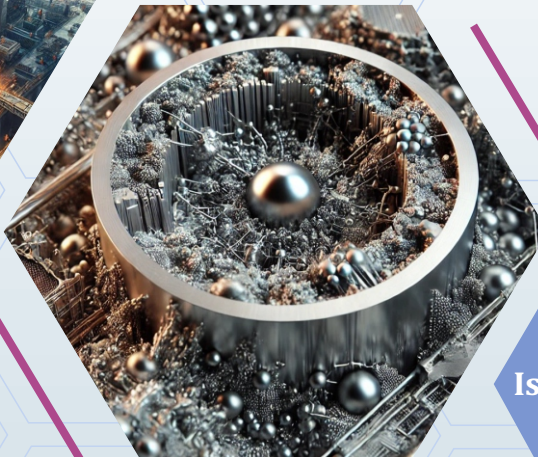




# Research on Engineering Structures and Materials



Volume 11  
Issue 1  
February 2025

The International Journal of **Research on Engineering Structures and Materials (RESM)** is a peer-reviewed open access journal (p-ISSN: 2148-9807; o-ISSN: 2149-4088) published by MIM Research Group. It is published in February, April, June, August, October, and December.

The main objective of RESM is to provide an International academic platform for researchers to share scientific results related to all aspects of mechanical, civil, and material engineering areas.

RESM aims the publication of original research articles, reviews, short communications technical reports, and letters to the editor on the latest developments in the related fields.

All expenditures for the publication of the manuscripts are most kindly reimbursed by *MIM Research Group*. Thus, authors do not need to pay for publishing their studies in the journal.

The scope of the journal covers (but not limited to) behavior of structures, machines and mechanical systems, vibration, impact loadings and structural dynamics, mechanics of materials (elasticity, plasticity, fracture mechanics), material science (structure and properties of concrete, metals, ceramics, composites, plastics, wood, etc.), nano-materials performances of new and existing buildings and other structural systems, design of buildings and other structural systems, seismic behavior of buildings and other structural systems, repair and strengthening of structural systems, case studies and failure of structural systems, safety and reliability in structural and material engineering, use of new and innovative materials and techniques in energy systems and mechanical aspects of biological systems (biomechanics and biomimetics).

#### **The topics covered in JRESM include:**

- Structural Engineering
- Mechanical Engineering
- Material Engineering
- Earthquake Engineering
- Nano-technology
- Energy Systems (Focus on Renewable)
- Biomechanics and Biomimetics
- Environment (Material and Engineering System Related Issues)
- Computer Engineering and Data Science (Material and Engineering System-Related Issues)

#### **Abstracting and Indexing**

Please visit <http://www.jresm.org> for more information.

#### **Graphics and Design**

Mehmet Yilmaz

[myilmaz@jresm.net](mailto:myilmaz@jresm.net)



**RESEARCH on  
ENGINEERING STRUCTURES &  
MATERIALS**



# RESEARCH on ENGINEERING STRUCTURES & MATERIALS

## Editorial Board

---

### Editor in Chief

Hayri Baytan Özmen

Usak University

Türkiye

---

### Editors

Canan Kandilli

Usak University

Türkiye

---

Antonio F. Miguel

University of Evora

Portugal

---

Michele Barbato

University of California Davis

USA

---

Mehmet Palancı

Arel University

Türkiye

---

Francesco D'Annibale

University of L'Aquila

Italy

---

Samson Olalekan  
Odeyemi

Kwara State University Maletе

Nigeria

---

Saifulnizan Jamian

Universiti Tun Hussein Onn  
Malaysia

Malaysia

---

Chitaranjan Pany

Vikram Sarabhai Space Centre

India

---

Badrinarayan Rath

Wollega University

Ethiopia

---

Taymaz Tabari

Jagiellonian University

Poland

---

Tamer  
Saracyakupoglu

İstanbul Gelisim University

Türkiye

---

Ivan Banović

University of Split

Croatia

---

Rayah Nasr Al-  
Dala'ien

Al-Balqa Applied University

Jordan

---

Abbasali Sadeghi

Islamic Azad University

Iran

---

Balasubramanian  
Ramesh

Dhanalakshmi Srinivasan  
University

India

---

## Editorial Office

---

### Publishing Manager

---

Mehmet Yılmaz

MIM Research Group

Türkiye

---

### Language Editors

---

Gaye Kuru

Uşak University

Türkiye

Mete Çal

MIM Research Group

Türkiye

---

---

**Editorial Board Members**

---

|                             |  |              |
|-----------------------------|--|--------------|
| Farid Abed-Meraim           | Arts et Metiers ParisTech                      | France       |
| P. Anbazhagan               | Indian Institute of Science                    | India        |
| Raffaele Barretta           | University of Naples Federico II               | Italy        |
| R.S. Beniwal                | Council of Scientific and Industrial Research  | India        |
| Antonio Caggiano            | University of Buenos Aires                     | Argentina    |
| Noel Challamel              | University of South Brittany                   | France       |
| Abdulkadir Çevik            | Gaziantep University                           | Türkiye      |
| J. Paulo Davim              | University of Aveiro                           | Portugal     |
| Hom Nath Dhakal             | University of Portsmouth                       | UK           |
| Ali Faghidian               | Islamic Azad University                        | Iran         |
| S. Amir M. Ghannadpour      | Shahid Beheshti University                     | Iran         |
| Ali Goodarzi                | Harvard University                             | USA          |
| Jian Jiang                  | National Institute of Standards and Technology | USA          |
| Ramazan Karakuzu            | Dokuz Eylül University                         | Türkiye      |
| Arkadiusz Kwiecien          | Cracow University of Technology                | Poland       |
| Stefano Lenci               | Universita Politecnica delle Marche            | Italy        |
| Silva Lozančić              | University of Osijek                           | Croatia      |
| Fabio Mazza                 | University of Calabria                         | Italia       |
| Yuan Meini                  | North University of China                      | China        |
| Stergios A. Mitoulis        | University of Surrey                           | UK           |
| Vinayagam Mohanavel         | Anna University                                | India        |
| Ehsan Noroozinejad Farsangi | Kerman Graduate University of Technology       | Iran         |
| Alaa M. Rashad              | Shaqra University                              | Saudi Arabia |
| Mohammad Mehdi Rashidi      | University of Tongji                           | China        |
| Pier Paolo Rossi            | University of Catania                          | Italy        |
| Neritan Shkodrani           | Polythecnic University of Tirana               | Albania      |
| Y.B. Yang                   | National Taiwan University                     | Taiwan       |

---

---

**Advisory Board Members**

---

|                           |  |          |
|---------------------------|--|----------|
| A. Abdelbary              | Alexandria University  | Egypt    |
| A.A.A. Sheha              | Petrogulfmistr Oil Company                                   | Egypt    |
| Aashish Roy               | S. S. Tegnoor Degree College                                 | India    |
| Abbasali Sadeghi          | Islamic Azad University,<br>Mashhad                          | India    |
| Abdelbaki Chikh           | Ibn Khaldoun University of<br>Tiaret                         | Algeria  |
| Abdelhalim Bensaada       | University of Yahia Fares of<br>Medea                        | Algeria  |
| Abdel-Hamid Ismail Mourad | United Arab Emirates<br>University                           | BAE      |
| Abdelkader Fidjah         | University of Djelfa   | Algeria  |
| Adil Mahdi Jabbar         | Wasit University   | Iraq     |
| Ahmet Demir               | Bolu University  | Türkiye  |
| Ahmet Devlet Ozcelik      | Istanbul Gelişim University                                  | Türkiye  |
| Alaa M. Rashad            | Building Materials Research<br>and Quality Control Institute | Egypt    |
| Aleksandar Savić          | University of Belgrade                                       | Serbia   |
| Ali Bagherkhani           | Shiraz University of<br>Technology                           | Iran     |
| Ali Raza                  | University of Engineering and<br>Technology                  | Pakistan |
| Ali Abbar Khleif          | University of Technology                                     | Iraq     |
| Ali Goodarzi              | Harvard University   | USA      |
| Alpay Tamer Erturk        | Kocaeli University   | Türkiye  |
| Alper Incesu              | Karabük University   | Türkiye  |
| Ameer Baiee               | University of Babylon  | Iraq     |
| Amiya Pandit              | University College Dublin<br>Ireland                         | Ireland  |
| Ammar Tawashi             | Al-Baath University  | Syria    |
| Anjishnu Biswas           | Indian Institute of Technology<br>Guwahati                   | India    |
| Ankang Kan                | Shanghai Maritime University                                 | China    |
| Arif Tuncal               | General Directorate of State<br>Airports                     | Türkiye  |
| Arife Kübra Yontar        | Ondokuz Mayıs University                                     | Türkiye  |
| Arunkumar K               | Kalsalingam Academy of<br>Research and Education             | India    |
| Ash-Shu'Ara Marafa Salman | Kwara State University                                       | Nigeria  |

---

---

|                             |   |            |
|-----------------------------|---|------------|
| Asimina Athanatopoulou      | Aristotle University                                  | Greece     |
| Atike İnce Yardımcı         | Uşak University                                       | Türkiye    |
| Ayoub Souileh               | University Mohammed V                                 | Morocco    |
| Berrin İkizler              | Ege University  | Türkiye    |
| Billel Rebai                | Abbes Laghrour University                             | Algeria    |
| Breetha Yesudhas Jayakumari | Chennai Institute of<br>Technology                    | India      |
| Brijesh Singh               | National Council for Cement<br>and Building Materials | India      |
| Bülent İmamoğlu             | Gedik University                                      | Türkiye    |
| Can Gonenli                 | Ege University  | Türkiye    |
| Catur Harsito               | Universitas Sebelas Maret                             | Indonesia  |
| Chella Gifta Christopher    | National Engineering College<br>Kovilpatti            | India      |
| Chitaranjan Pany            | Vikram Sarabhai Space Centre                          | India      |
| Chinenye Elizabeth Okere    | Federal University of<br>Technology                   | Nigeria    |
| Chuanjin Yu                 | Southwest Jiaotong University                         | China      |
| Daniel Cruze                | Mohamed Sathak A J College<br>of Engineering          | India      |
| Davide Forcellini           | University of San Marino                              | San Marino |
| Debasish Sen                | Ahsanullah University of<br>Science and Technology    | Bangladesh |
| Deniz Uner                  | Middle East Technical<br>University                   | Türkiye    |
| Dhirendra Patel             | Kalaniketan Polytechnic<br>College                    | India      |
| Dilay Uncu                  | Celal Bayar University                                | Türkiye    |
| Dipankar Das                | Tripura University                                    | India      |
| Diyar Qader                 | University of Kirkuk                                  | Iraq       |
| Abdul Razak Abdul Karim     | Universiti Malaysia Sarawak                           | Malaysia   |
| Anand Murthy Hc             | Adama Science & Tech.<br>University                   | Ethiopia   |
| Vera Ilyina                 | Institute of Geology Karelian<br>Research Centre      | Russia     |
| Dulce Franco Henriques      | Instituto Politécnico de Lisboa                       | Portugal   |
| Elavenil S                  | Vellore Institute of<br>Technology                    | India      |
| Elton Hala                  | Polytechnic University of<br>Tirana                   | Albania    |
| Emre Kemer                  | Usak University                                       | Türkiye    |

---



---

|                         |   |              |
|-------------------------|---|--------------|
| Enea Mustafaraj         | Epoka University, Tirana                                      | Albania      |
| Ercan Isık              | Bitlis Eren University  | Türkiye      |
| Esra Özer               | Tokat Gaziosmanpasa University                                | Türkiye      |
| Essam Mohamed           | South Valley University                                       | Egypt        |
| Fatoş Koç               | Ege University  | Türkiye      |
| Federico Scafati        | University of L'Aquila  | Italy        |
| Fokruddin Ahmad         | Washington State University                                   | USA          |
| Gaurav Dhadse           | G. H. Rasoni Institute of Engineering and Business Management | India        |
| Guobo Wang              | Wenzhou University  | China        |
| Gururaj Hatti           | KLS Vishwanathrao Deshpande Institute of Technology           | India        |
| Guy Louarn              | Université de Nantes  | France       |
| Habibe Demir            | İskenderun Teknik University                                  | Türkiye      |
| Hadj Bekki              | University Ibn Khaldoun of Tiaret                             | Algeria      |
| Hakan Sarıkaya          | Uşak University   | Türkiye      |
| Hakan Ulker             | Bursa Teknik University                                       | Türkiye      |
| Halil Murat Enginsoy    | Çanakkale Onsekiz Mart University                             | Türkiye      |
| Halil Yalcin Akdeniz    | Eskisehir Osmangazi University                                | Türkiye      |
| Hasan Ulus              | Selcuk University   | Türkiye      |
| Hemadri Prasad Raju     | Sree Vidyanikethan Engineering College                        | India        |
| Hints G. Gebremariam    | Addis Ababa University  | Ethiopia     |
| Hossein Kabir           | University of Illinois  | USA          |
| Hussein Hamada          | Al-Qalam University College                                   | Iraq         |
| I Gede Gegirang Wiryadi | Universitas Mahasaraswati Denpasar                            | Indonesia    |
| Ibrahim Sharaky         | Taif University   | Saudi Arabia |
| Ikram Kouidri           | University of Relizane  | Algeria      |
| Indra Mawardi           | Politeknik Negeri Lhokseumawe                                 | Indonesia    |
| Irakli Premti           | Polytechnic University of Tirana                              | Albania      |
| Isabel Milagre Martins  | Laboratório Nacional de Engenharia Civil                      | Portugal     |

---

---

|                          |   |           |
|--------------------------|---|-----------|
| Ivana Štimac Grandić     | University of Rijeka                                      | Croatia   |
| J. Jenix Rino            | Anna University   | India     |
| J. Paulo Davim           | University of Aveiro                                      | Portugal  |
| Jinxu Mo                 | Yangtze University  | China     |
| Jojok Widodo Soetjipto   | Universitas Jember  | Indonesia |
| Josephine Chang Hui Lai  | Universiti Malaysia Sarawak                               | Malaysia  |
| Juan Llorca-Schenk       | University of Alicante                                    | Spain     |
| K. Ashwini               | Jawaharlal Nehru<br>Technological University<br>Hyderabad | India     |
| Kabiru Mustapha          | Kwara State University                                    | Nigeria   |
| Kadir Gunaydın           | GE Aviation Marmara<br>Technology Center                  | Türkiye   |
| Kamel Chaoui             | Badji Mokhtar University                                  | Algeria   |
| Kanish Kapoor            | Dr B R Ambedkar National<br>Institute of Technology       | India     |
| Khairul Nizar Ismail     | Universiti Malaysia Perlis                                | Malaysia  |
| Konstantinos Kalfas      | University of Texas at Tyler                              | USA       |
| Lawrence Zahemen Tuleun  | University of Ilorin                                      | Nigeria   |
| Lomesh Mahajan           | Dr. Babasaheb Ambedkar<br>Technological University        | India     |
| Lyamine Briki            | University of Batna2                                      | Algeria   |
| M. Kalil Rahiman         | Saveetha School of<br>Engineering                         | India     |
| Magdalini Titirla        | Conservatoire National des<br>Arts et Métiers             | France    |
| Maher Chakhari           | Tunis El Manar University                                 | Tunisia   |
| Mahesh Gopal             | Wollega University, Nekemte                               | Ethiopia  |
| Maheswaran Chellapandian | Mepco Schlenk Engineering<br>College                      | India     |
| Mahmoud Mokhtar          | Housing & Building National<br>Research Center            | Egypt     |
| Majid Pouraminian        | Islamic Azad University                                   | Iran      |
| Maria Richert            | AGH University of Science and<br>Technology               | Poland    |
| Marina Sunara            | University of Split                                       | Croatia   |
| Marwa Enneffati          | Université Angers   | France    |
| Md. Saiful Islam         | Universiti Putra  | Putra     |
| Mehdi Panji              | Islamic Azad University                                   | Iran      |

---

---

|                          |  |            |
|--------------------------|--|------------|
| Mehmet Ada               | Uşak University  | Türkiye    |
| Mehmet Cemal Genes       | Eastern Mediterranean University                                   | Cyprus     |
| Mehrab Nodehi            | University of California Davis                                     | USA        |
| Mert Göksüzöğlü          | SAMPA Advanced Parts for Commercial Vehicles                       | Türkiye    |
| Mohammad .I Al Biajawi   | Universiti Malaysia Pahang Al-Sultan Abdullah                      | Malaysia   |
| Mohammad Afrazi          | Tarbiat Modares University   | Iran       |
| Mohammad Naeim Moradi    | Amirkabir University of Technology                                 | Iran       |
| Mohammad Saleh Baradaran | Islamic Azad University  | Iran       |
| Mohammed Bentahar        | Tahar Moulay University of Saida                                   | Algeria    |
| Mohammed Sarhan          | Mustansiriyah University   | Iraq       |
| Mohsen Hajizamani        | Graduate University of Advanced Technology                         | Iran       |
| Morchid Fatima Ezzahrae  | University of Hassan II Casablanca                                 | Morocco    |
| Muhammad Bilal Khan      | Ghulam Ishaq Khan Institute of Engineering Sciences and Technology | Pakistan   |
| Mustafa Akpolat          | Munzur University  | Türkiye    |
| Mustafa H. Omar          | Bilad Alrafidain University College                                | Iraq       |
| Mustafa Ozgunler         | Mimar Sinan Fine Arts University                                   | Türkiye    |
| Mustaqqim Abdul Rahim    | University Malaysia Perlis   | Malaysia   |
| Nadhim Hamah Sor         | University of Garmian  | Iraq       |
| Nagaraj Ekabote          | KLE Technological University                                       | India      |
| Nahida Nazim Musayeva    | Azerbaijan National Academy of Sciences                            | Azerbaijan |
| Navdeep Singh            | Dr. Babasaheb Ambedkar Technological University                    | India      |
| Nebab - Mokhtar          | University Hassiba Benbouali of Chlef                              | Algeria    |
| Nghia P. Tran            | The University of Melbourne  | Australia  |
| Nitin Kumar              | University of California Davis                                     | USA        |
| Olfa Maalej              | Monastir University  | Tunisia    |
| Olumoyewa D. Atoyebi     | Landmark University  | Nigeria    |
| Orhan Gülcan             | General Electric Aerospace   | Türkiye    |
| Osman M. Ramadan         | Cairo University, Giza   | Egypt      |

---

---

|                              |   |              |
|------------------------------|---|--------------|
| Ozgur Avsar                  | Eskisehir Technical University                                    | Türkiye      |
| Özgür Demircan               | Ondokuz Mayıs Üniversitesi  | Türkiye      |
| Partheeban Pachaivannan      | Chennai Institute of Technology                                   | India        |
| Peng Gao                     | University of Massachusetts Lowell                                | USA          |
| Peyman Beiranvand            | Razi University   | Iran         |
| Piya Chotickai               | Kasetsart University  | Tailand      |
| Pooja Sharma                 | Dr. Yashwant Singh Parmar University of Horticulture and Forestry | India        |
| Subash Thanappan             | KAAF University College   | Ghana        |
| Raif Sakin                   | Balıkesir University  | Türkiye      |
| Rajesh Kumar                 | KPR Institute of Engineering and Technology                       | India        |
| Rajesh M.                    | Hindustan Institute of Technology and Science                     | India        |
| Ramaswamy Palanivel          | Shaqra University   | Saudi Arabia |
| Rami Sldozian                | University of Technology-Iraq                                     | Iraq         |
| Rasheed Abdulwahab           | Kwara State University  | Nigeria      |
| Ravichandran M               | K.Ramakrishnan College of Engineering                             | India        |
| Revathi Srinivasan           | Mepco Schlenk Engineering College                                 | India        |
| Riadh Bennai                 | University Hassiba Benbouali of Chlef                             | Algeria      |
| Rianti Dewi Sulamet-Ariobimo | Universitas Trisakti  | Indonesia    |
| Roberto Nascimbene           | School of Advanced Studies IUSS Pavia                             | Italy        |
| Royal Madan                  | Chandigarh University   | India        |
| S. Ali Faghidian             | Islamic Azad University   | Iran         |
| Saeid Foroughi               | Konya Technical University  | Türkiye      |
| Sahar Ismail                 | Saint Joseph University of Beirut                                 | Lebanon      |
| Sajjad Hassanpour Kasanagh   | Middle East Technical University                                  | Türkiye      |
| Salmabanu Luhar              | National Taipei University of Technology                          | Taiwan       |
| Samer Adeeb                  | University of Alberta   | Canada       |
| Samia Bouzouaid              | Kasdi Merbah University   | Algeria      |
| Samuel Awe                   | Automotive Components Floby AB                                    | Sweden       |

---

---

|                          |   |            |
|--------------------------|---|------------|
| Sangeetha Palanivelu     | SSN College of Engineering  | India      |
| Sarmila Sahoo            | Heritage Institute of Technology Kolkata                                | India      |
| Sercan Serin             | Osmaniye Korkut Ata University  | Türkiye    |
| Shaish K. John           | College of Engineering Trivandrum                                       | India      |
| Shaohong Cheng           | University of Windsor   | Canada     |
| Sharmin Reza Chowdhury   | Ahsanullah University of Science and Technology                         | Bangladesh |
| Sivakumar N              | SSN College of Engineering  | India      |
| Solomon Olalere Ajamu    | Ladoke Akintola University  | Nigeria    |
| Somya Ranjan Patro       | Indian Institute of Technology Delhi                                    | India      |
| Sonal Thakkar            | Nirma University  | India      |
| Sophia Immanuel          | National Institute of Technology Tiruchirappalli                        | India      |
| Suliman Khan             | NFC Institute of Engineering and Fertilizer Research                    | Pakistan   |
| Sumanth Ratna Kandavalli | New York University   | USA        |
| Surajit Kumar Paul       | Indian Institute of Technology  | India      |
| Susmita Naskar           | University of Southampton   | Englang    |
| T.V. Reshma              | GITAM School of Technology  | India      |
| Taha Rashid              | Universiti Teknologi Malaysia   | Malaysia   |
| Tamer Saracyakupoglu     | TUSAŞ Academy   | Türkiye    |
| Taqiy Eddine Boukelia    | University of Jijel   | Algeria    |
| Tarun Kumar Rajak        | Shri Shankaracharya Institute of Professional Management and Technology | India      |
| Tasnia Ahmed             | Military Institute of Science and Technology                            | Bangladesh |
| Thaer Alrudaini          | University of Basrah  | Iraq       |
| Thi Loan Pham            | Civil Engineering, Hai Phong University                                 | Vietnamese |
| Thomás L. Resende        | Federal University of Jequitinhonha and Mucuri Valleys                  | Brazil     |
| Thomas Salonikios        | The Institute of Engineering Seismology and Earthquake Engineering      | Greece     |
| Toufik Sebbagh           | University of Skikda  | Algeria    |
| Tuan Anh Nguyen          | Thuyloi University  | Vietnamese |

---

---

|                            |  |           |
|----------------------------|--|-----------|
| Upendra K. Mallela         | Indian and Toubro<br>Technology                          | India     |
| Vedat Arda Küçük           | Çankırı Karatekin University                             | Türkiye   |
| Vineeth Kumar T. V.        | Siddaganga Institute of<br>Technology                    | India     |
| Víctor I. Fernandez-Davila | Pontifical Catholic University<br>of Peru                | Peru      |
| Victor Rizov               | University of Architecture                               | Bulgaria  |
| Vincent Sam Jebadurai      | Karunya Institute of<br>Technology and Sciences          | India     |
| Wahyu Dwi Lestari          | University of Pembangunan<br>Nasional Veteran Jawa Timur | Indonesia |
| Waleed A Abbas             | University of Technology,<br>Baghdad                     | Iraq      |
| Yamini Sreevalli I         | Vellore Institute of<br>Technology                       | India     |
| Yang Feng                  | Xi'an Jiaotong University                                | China     |
| Yang Yang                  | Southeast University                                     | China     |
| Yaser Acikbas              | Uşak Üniversitesi  | Türkiye   |
| Yonatan Ayele Abera        | Dilla University   | Ethiopia  |
| Yunika Kirana Abdul Khalik | University of Malaysia                                   | Malaysia  |
| Zafer Kaya                 | Dumlupınar University                                    | Türkiye   |
| Zahid Iqbal Khan           | Universiti Teknologi Malaysia                            | Malaysia  |
| Zikriye Ozbek              | Çanakkale Onsekiz Mart<br>University                     | Türkiye   |

---

## In This Issue

### Research Article

1 **Victor Rizov**

General analysis of the dissipation of strain energy in circular columns

### Review Article

21 **Nabaz Yassen Ezuldin, Saad Mahmood Raof, Alyaa Abbas Alattar, Hussein Hamada**

Factors affecting durability properties of GPC: A review

### Research Article

45 **Emre Kemer, Hasan Başak**

Performance analysis of fuzzy-LQR and fuzzy-LQG controllers for active vehicle suspension systems

### Research Article

59 **Mustapha Hadji, Mohamed Benamira, Rabia Khelif**

Reliability approach for lifetime prediction of the aluminum extrusion dies

### Research Article

73 **Sabrina Mammeri, Khaider Bouacha, Kamel Chaoui, Wafia Ghabeche, Khaoula Berkas**

Filament manufacturing via external grooving of an HDPE pipe wall: RSM optimization and mechanical tests validation

### Research Article

97 **Andi Yusra, Jasmi Jasmi, Hernanda Mirza Pratama Simatupang, Irwansyah Irwansyah, Lissa Opirina**

Optimizing concrete strength through pozzolan variation, heat treatment, and alkaline solution modulation: A comprehensive study

### Research Article

113 **Manel Djeddou, Mohamed Amieur, Rabah Chaid, Habib-Abdelhak Mesbah**

Development of eco-friendly self-compacting concrete using marble powder, blast furnace slag and glass fibre-reinforced plastic waste: Application of mixture design approach

### Research Article

139 **Utsav Koshtia, Sharadkumar Purohit**

Prototype silicone rubber based passive seismic damper: Development, characterization and implementation

Research Article

- 165 **A. Narender Reddy, G. Gautham Kishore Reddy, P. Narashima Reddy, K. Srinivas Reddy, B. Venkata Kavyateja**

Analyzing the impact of nano-sized silica on composite concrete: A static approach utilizing response surface method

Research Article

- 179 **Andi Yusra, Zakia, Surya Perdana, Fachruddin Fachruddin, Teuku Budi Aulia**

Effects of rattan fiber length variation on mechanical properties, characterization, and microstructure of concrete

Research Article

- 199 **Daniel Cruze, Balaji Ramalingam, Nedunchezian Krishnaraju**

Comparison of single and multi-coil self-powered MR damper subjected to cyclic and earthquake loading for structural vibration control

Research Article

- 213 **Abdelmalek Abdelhamid, Baizid Benahmed, Omar Laghrouche, Mehmet Palanci, Lakhdar Aidaoui**

Evaluation of damping reduction factors for displacement and acceleration spectra using code-compatible near-fault and far-fault ground motions depending on site conditions

Review Article

- 231 **Gudipati Chaitanya Avinash, N. Lingeshwaran**

Review on base and inter storey seismic isolation systems for high rise buildings

Research Article

- 273 **Rai Sujit Nath Sahai, Pravin Nana Jadhav, Achyut Sahebrao Raut, Sumit Shahaji Surve**

Study on performance of multiwall carbon nanotubes and functionalized multiwall carbon nanotubes/ poly aryl ether ketone polymer composite gears

Research Article

- 287 **Yi Zhanga, Tian Su**

Research on nonlinear corrosion law of epoxy coating on steel bridges based on image processing

Research Article

- 305 **Sara Hadidi, Denise-Penelope N. Kontoni, Imran Karimi**

Enhancing the seismic performance of a concentrically braced reinforced concrete frame using an I-shaped shear link made of low yield point steel



Research Article

333 **Mohammad Salim Kaiser, S Reaz Ahmed**

A study on the quantitative recrystallization of cold deformed copper affected by tin-lead solder

Research Article

351 **Hassan Shuaibu Abdulrahman, Ali Almusawi, Julide Oner, Nasiru Ibrahim Ahmed**

Statistical models for porous asphalt mixtures containing pulverized surface dressed pavement material/low-density polyethylene waste

Research Article

369 **Baran Ramadhan Omer, Ganjeena J. Khoshnaw**

Enriching asphalt binders' rheology by joining nano-copper oxide as a modifier

Review Article

383 **Nabam Tado, Salam Medhajit, Dibyendu Pal**

Forecasting California bearing ratio (CBR) of soil using machine learning algorithms: A review

Research Article

399 **Essam H. Mohamed**

Using digital modelling for the partial reconstruction of Sheikh Al-Arab Hammam citadel, situated in Farshout, Qena, Egypt

Free access to tables of content, abstracts and full text of papers for web visitors.

Copyright © 2023

Research on Engineering Structures & Materials

MIM Research Group Publications

P-ISSN: 2148-9807

E-ISSN: 2149-4088

<http://www.jresm.org>



## ABSTRACTING / INDEXING

The international journal of Research on Engineering Structures and Materials (RESM) is currently Abstracted/Indexed by Asos Indeks, CiteFactor, Cosmos, CrossRef, Directory of Research Journal Indexing, Engineering Journals (ProQuest), EZB Electronic Journal Library, Global Impact Factor, Google Scholar, International Institute of Organized Research (I2OR), International Scientific Indexing (ISI), Materials Science & Engineering Database (ProQuest), Open Academic Journals Index, Publication Forum, Research BibleScientific Indexing Service, Root Indexing, Scopus, Ulakbim TR Index (Tubitak), Universal Impact Factor and under evaluation by many other respected indexes.

Check web site for current indexing info, [www.jresm.org](http://www.jresm.org)



## General analysis of the dissipation of strain energy in circular columns

Victor Rizov<sup>a</sup>

Dept. of Technical Mechanics, University of Architecture, Civil Engineering and Geodesy, Sofia, Bulgaria

### Article Info

#### Article history:

Received 28 Dec 2023

Accepted 16 Apr 2024

#### Keywords:

*Circular Column;  
Dissipation of strain energy;  
General analysis*

### Abstract

This theoretical paper is concerned with general analysis of the strain energy dissipation in columns of circular cross-section. The columns are under longitudinal displacements that vary continuously with time. The columns exhibit non-linear viscoelastic behavior that is studied by mechanical models constructed by using non-linear springs and dashpots. Besides, the columns are functionally graded along the radius of the cross-sections. A simple expression for the dissipated strain energy in the columns under consideration is derived. The expression holds for columns having portions with different radius of the cross-section. Also, the expression derived is applicable for columns built-up by concentric layers. Results indicating how the dissipated strain energy is influenced by various factors (distribution of material properties, geometry of the columns and loading) are presented. These results are found by using a non-linear viscoelastic model with one spring and one dashpot. A check-up is performed by determining the dissipated strain energy through subtracting the strain energy in the spring of viscoelastic model from the whole strain energy in the column.

© 2025 MIM Research Group. All rights reserved.

## 1. Introduction

Since columns are widely used in various load-carrying engineering structures, it is important to study in detail the response of columns to different external loads and influences. Deepening of the knowledge for the column's response is an important condition for improving the safety and reliability of structures.

Dissipation of the strain energy is a momentous factor that has to be considered when studying columns of viscoelastic behavior. For instance, the dissipation of the strain energy has influence on such issues like fracture behavior, structural integrity and expected service-life of engineering constructions and facilities (it should be noted here that when the strain energy dissipation takes place in a structure, the fracture behavior has to be analyzed by using the strain energy cumulated in the structure reduced by the dissipated energy). Therefore, dissipation of the strain energy has to be taken into account in the design and use of structural members (including columns) having viscoelastic behavior. This, on its side, requires analyses of the strain energy dissipation.

The significance of the dissipation of strain energy for engineering structures with viscoelastic behavior is well-grounded in the scientific literature [1]. It should be underlined, however, that the majority of the strain energy analyses have been concerned with linear viscoelastic beam load-bearing structures [1 - 2]. Besides, the analyses usually are focused on particular problems [3 - 7]. The end-plate beam-to-column connection

<sup>a</sup>Corresponding author: [v\\_rizov\\_fhe@uacg.bg](mailto:v_rizov_fhe@uacg.bg)

<sup>a</sup>[orcid.org/0000-0002-0259-3984](https://orcid.org/0000-0002-0259-3984)

DOI: <http://dx.doi.org/10.17515/resm2024.134me1228rs>

Res. Eng. Struct. Mat. Vol. 11 Iss. 1 (2025) 1-19

under cyclic loading is evaluated [3]. It is shown that the neutral network model used is capable of characterizing pinching and stiffness degradation of the connection [3]. A

The significance of the dissipation of strain energy for engineering structures with viscoelastic behavior is well-grounded in the scientific literature [1]. It should be underlined, however, that the majority of the strain energy analyses have been concerned with linear viscoelastic beam load-bearing structures [1 - 2]. Besides, the analyses usually are focused on particular problems [3 - 7]. The end-plate beam-to-column connection under cyclic loading is evaluated [3]. It is shown that the neutral network model used is capable of characterizing pinching and stiffness degradation of the connection [3]. A framework that provides an optimal distribution of energy dissipation devices for framed buildings is presented in [4]. It is proved that the proposed framework is superior compared to the conventional machine learning algorithms for obtaining optimum retrofitting scheme for buildings considered [4]. Energy dissipation and damping capacity of reinforced concrete columns under uniaxial and biaxial conditions are investigated in [5]. The energy dissipation is studied in terms of cumulative dissipated energy. The study leads to obtaining of simplified expressions for equivalent viscous damping in columns under biaxial loading conditions [5]. The free vibration behavior of two-directional functionally graded multiple nanobeam systems are analyzed by considering Winkler elastic medium between them in [6]. It is assumed that the material properties vary along the length and thickness of the nanobeams. The effects of nonlocal parameter, slenderness ratio, functionally graded power index and boundary conditions are evaluated [6]. A nanobeam with a moving nanoparticle is studied in [7]. A mathematical model for the nanobeam-nanoparticle system is developed. The influence of various factors, including the nonlocal parameter, initial velocity and mass of nanoparticle are studied and discussed [7]. The fact that previous works deal with particular problems indicates that general analysis of the strain energy dissipation needs to be developed.

Therefore, the present paper is concerned with general analysis of the dissipated strain energy in columns exhibiting non-linear viscoelastic behavior. The columns under consideration have circular cross-section. The general analysis is developed assuming that columns are functionally graded along the cross-section radius. This assumption is made in view of the fact that functionally graded materials have become very attractive for a variety of applications in engineering structures and facilities in recent decades [8 - 13]. Due to their excellent properties, the functionally graded materials have begun to replace the widely used up to now homogeneous engineering materials like metals, alloys and fiber reinforced composites [14 - 19]. One of the basic advantages of the functionally graded materials is that their properties vary smoothly in a given structural member [20 - 25]. In this way, the stress concentrations are avoided which considerably reduces the probability of loss of stiffness, degradation of strength, shortening of expected service-life and even premature failure of the structure due to appearance and propagations of cracks [26 - 28]. Other widely used structural materials in modern engineering are multilayered systems having a high strength-to-weight and stiffness-to-weight ratio [29]. As known, the multilayered constructions represent systems of adhesively bonded layers made of different materials [30 - 34]. In view of the increased interest towards the multilayered materials and structures, general analysis of the dissipated strain energy is developed in the present paper also for multilayered columns built-up by concentric layers. The layers are functionally graded through thickness and have non-linear viscoelastic behavior.

The general analysis of the strain energy dissipation developed here uses non-linear viscoelastic models constructed by non-linear springs and dashpots. The analysis yielded a relatively simple expression for the dissipated strain energy. This expression holds for functionally graded (and multilayered) circular columns under longitudinal displacements which vary continuously with time. Besides in columns clamped at the bottom, the strain

energy dissipation is analyzed also in columns clamped at the bottom and the top. The results obtained are checked-up by determining the dissipated strain energy by subtracting the strain energy in the spring from the whole strain energy in the columns under consideration. The change of the dissipated strain energy caused by inhomogeneity of the material, the column geometry and the longitudinal displacements magnitude is studied.

## 2. General Analysis

The general analysis developed here is concerned with strain energy dissipation in the column which static schema is displayed in Fig. 1. The column under consideration has  $n$  longitudinal portions.

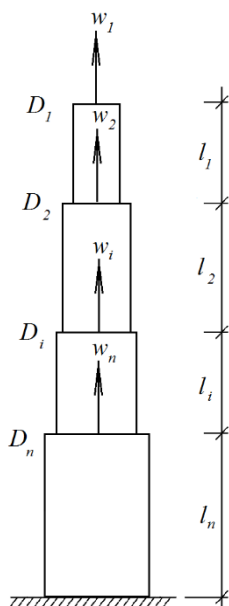


Fig. 1. Column under longitudinal displacements,  $w_i$

The cross-section of the column in each portion is a circle. The radius of the column cross-section in an arbitrary portion is marked by  $R_i$ . The length of the column arbitrary portion is marked by  $l_i$  (Fig. 1). The bottom of the column is clamped. The column has non-linear viscoelastic mechanical behavior. In an arbitrary column portion, the viscoelastic behavior is described by a stress-strain-time relationship written in the form

$$\sigma_i = f_i(\varepsilon_i, t) \tag{1}$$

$$i = 1, 2, \dots, n \tag{2}$$

where  $\sigma_i$  is the stress,  $\varepsilon_i$  is the strain and  $t$  is time. It should be underlined that  $f_i$  is a non-linear function of the strain. The present strain energy dissipation analysis uses viscoelastic models built-up by non-linear springs and dashpots for describing the column mechanical behavior. Therefore, stress-strain-time relationships (1) are derived by analyzing the stresses and strains in the viscoelastic model components. It should also be

underlined that the mechanical properties involved in the stress-strain-time relationships (1) are smooth functions of the running radius,  $R$ , where  $0 \leq R \leq R_i$  due to the fact that in each column portion the material is functionally graded in radial direction.

The column in Fig. 1 is under longitudinal displacements,  $w_i$ , which vary smoothly with time (the law controlling this variation is given). The displacements,  $w_i$ , are expressed through strains by formula (3), i.e.

$$w_i = \sum_{j=i}^{j=n} \varepsilon_j l_j \tag{3}$$

The strains in the column portions can be easily determined from (3). Then these strains can be applied on the viscoelastic model to determine the stresses. The strain energy dissipation in the column under consideration is modeled by the dashpots in the viscoelastic model. Therefore, the dissipated strain energy,  $U_{dse}$ , in the column can be expressed by using formula (4), i.e.

$$U_{dse} = \sum_{i=1}^{i=n} l_i \iint_{(A_i)} \sum_{k=1}^{k=p} u_{0ik} dA \tag{4}$$

where  $p$  is the number of dashpots in the viscoelastic model,  $u_{0ik}$  is the unit strain energy in the  $k$ -th dashpot in the  $i$ -th column portion,  $A_i$  is the cross-section area of the column in the  $i$ -th portion. Formula (5) is applied for determining the unit strain energy.

$$u_{0ik} = \int_0^{\varepsilon_{ik}} \sigma_{ik} d\varepsilon_{ik} \tag{5}$$

$$i = 1, 2, \dots, n \tag{6}$$

$$k = 1, 2, \dots, p \tag{7}$$

where  $\sigma_{ik}$  is the stress in the  $k$ -th dashpot of the viscoelastic model in the  $i$ -th portion of the column. The stress,  $\sigma_{ik}$ , is found by applying relationship (8), i.e.

$$\sigma_{ik} = g_{ik}(\dot{\varepsilon}_{ik}) \tag{8}$$

where  $\dot{\varepsilon}_{ik}$  is the first derivative of the strain in the dashpot under consideration with respect to time,  $g_{ik}$  is a non-linear function of  $\dot{\varepsilon}_{ik}$  (the type of this function depends on the viscoelastic model used).

If the column is built-up by concentric layers (the cross-section of such a column is displayed in Fig. 2) the dissipated energy can be derived by formula (9), i.e.

$$U_{dse} = \sum_{i=1}^{i=n} l_i \sum_{s=1}^{s=m} \iint_{(A_{is})} \sum_{k=1}^{k=p} u_{0isk} dA \tag{9}$$

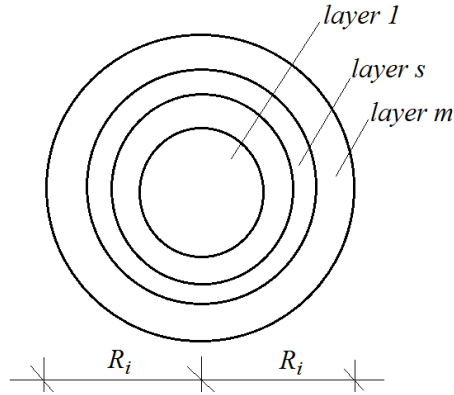


Fig. 2. Cross-section of a column built-up by concentric layers

where  $m$  is the number of layers,  $A_{is}$  is the cross-section area of the  $s$ -th layer in the  $i$ -th portion of the column,  $u_{0isk}$  is the unit strain energy in the  $k$ -th dashpot in the  $s$ -th layer in the  $i$ -th column portion. Here formula (10) can be used for deriving  $u_{0isk}$ .

$$u_{0isk} = \int_0^{\varepsilon_{isk}} \sigma_{isk} d\varepsilon_{isk} \tag{10}$$

where  $\sigma_{isk}$  and  $\varepsilon_{isk}$  are the stress and strain, respectively.

General analysis of the dissipated strain energy in columns in which the number of portions is higher than the number of given longitudinal displacements (refer to Fig. 3) can also be developed. For this purpose, additional equations have to be composed for determining the strains in the column portions (this is necessary because the number of equations composed by using (3) is less than the number of unknown strains). These additional equations consider the equilibrium of the axial forces on borders between column portions (for instance, for column in Fig. 3 such equations have to be composed for borders,  $D_i$  and  $D_n$ ). These equations can be written as

$$\iint_{(A_{i-1})} \sigma_{i-1} dA = \iint_{(A_i)} \sigma_i dA \tag{11}$$

where  $\sigma_{i-1}$  and  $\sigma_i$  are the stresses in the column cross-sections over and under border,  $D_i$ .

The stresses,  $\sigma_{i-1}$  and  $\sigma_i$ , are found by using the viscoelastic model. If the column is built-up by concentric layers, the additional equations for determining the strains in the column portions have the following form:

$$\sum_{s=1}^{s=m} \iint_{(A_{i-1s})} \sigma_{i-1s} dA = \sum_{s=1}^{s=m} \iint_{(A_{is})} \sigma_{is} dA \tag{12}$$

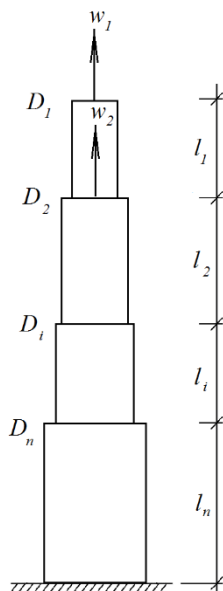


Fig. 3. Column in which the number of portions is higher than the number of longitudinal displacements,  $w_i$

analysis of the dissipated strain energy is developed also for the column that is clamped at the bottom and the top (the column static schema is displayed in Fig. 4). Here again the column is under longitudinal displacements,  $w_i$ .

The displacement of the column top is zero. Thus, we write

$$w_{D1} = \sum_{i=1}^{i=n} \varepsilon_i l_i = 0 \tag{13}$$

Also, we can write (Fig. 4)

$$w_i = \sum_{j=i}^{j=n-1} \varepsilon_{j+1} l_{j+1} \tag{14}$$

Where;

$$i = 1, 2, \dots, n - 1 \tag{15}$$

The strains in the column portions can be derived directly from equations (13) and (14). After that the dissipated strain energy can be obtained by using (4). If the column is made of concentric layers, the dissipated strain energy can be found by applying formula (9).

For columns in which the number of portions is higher than the number of the given longitudinal displacements like, for instance, column in Fig. 5, the strains can be derived by using additional equations of equilibrium (11) (or (12) when the column is made by concentric layers). After that formula (4) (or formula (9)) can be used for obtaining of dissipated strain energy.



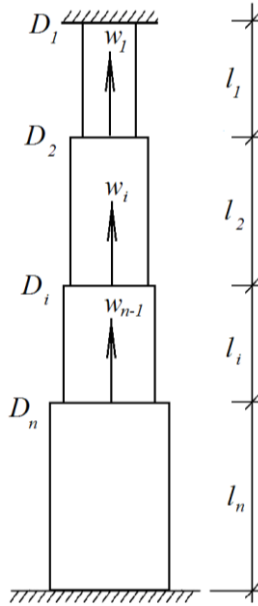


Fig. 4. Column clamped at the bottom and the top

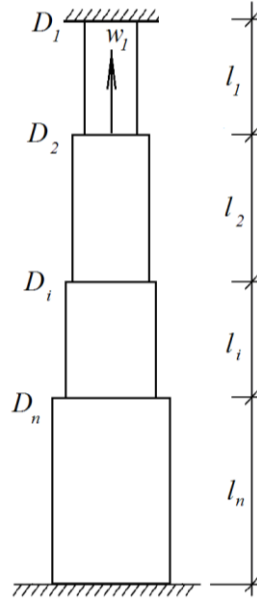


Fig. 5. Column clamped at the bottom and the top in which the number of portions is higher than the number of longitudinal displacements,  $w_i$

### 3. Practical Application of General Analysis

This section of the paper describes practical applications of the general analysis of the dissipated strain energy. The numerical results presented here are related to the functionally graded viscoelastic column with three portions displayed in Fig. 6.

The column is under longitudinal time-dependent displacements,  $w_i$ , where  $i = 1, 2, 3$ . Formula (16) describes the change of these displacements.

$$w_i = w_{ib} \cos(a_0 + \omega t) \tag{16}$$

where  $w_{ib}$ ,  $a_0$  and  $\omega$  are parameters.

The strains,  $\varepsilon_1$ ,  $\varepsilon_2$  and  $\varepsilon_3$ , in the column portions,  $D_1D_2$ ,  $D_2D_3$  and  $D_3D_4$ , are determined from equation (3) with taking into account (16). The result is;

$$\varepsilon_1 = \frac{1}{l_1} (w_{1b} - w_{2b}) \cos(a_0 + \omega t) \tag{17}$$

$$\varepsilon_2 = \frac{1}{l_2} (w_{2b} - w_{3b}) \cos(a_0 + \omega t) \tag{18}$$

$$\varepsilon_3 = \frac{1}{l_3} w_{3b} \cos(a_0 + \omega t) \tag{19}$$

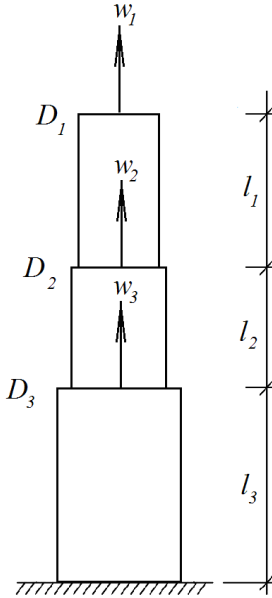


Fig. 6. Column with three portions under three longitudinal displacements,  $w_1$ ,  $w_2$  and  $w_3$

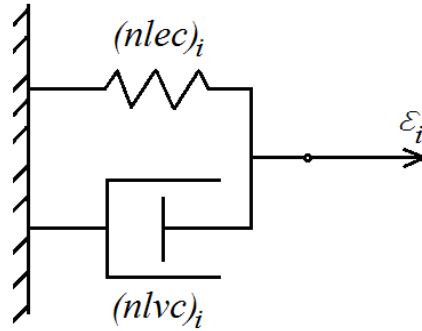


Fig. 7. Non-linear viscoelastic model

The stresses in the column portions are derived by using the non-linear viscoelastic mechanical model displayed in Fig. 7. This model has a non-linear elastic spring,  $(nlvc)_i$ , and a non-linear dashpot,  $(nlec)_i$ . The model is under strain,  $\varepsilon_i$ , whose change with time is presented by formulas (17), (18) and (19) for column portions,  $D_1D_2$ ,  $D_2D_3$  and  $D_3D_4$ , respectively. The choice of a relatively simple non-linear viscoelastic model (Fig. 7) with one spring and one dashpot is motivated by the fact that this model is mainly for illustration of the way for use of the general analysis. When a practical engineering problem is treated, a more complex non-linear viscoelastic model with more springs and dashpots may be applied.

Formula (20) defines the stress-strain relationship of the non-linear elastic spring in the viscoelastic model in Fig. 7 [35].

$$\sigma_{(nlec)_i} = Q_i \left[ 1 - \left( 1 - \frac{\varepsilon_i}{H_i} \right)^{\beta_i} \right] \quad (20)$$

where  $\sigma_{(nlec)_i}$  is the stress in the spring,  $Q_i$ ,  $H_i$  and  $\beta_i$  are material properties in the  $i$ -th portion of the column (here  $i = 1, 2, 3$ ). According to [35],  $Q_i$  is the ultimate strength,  $H_i$  is the strain that corresponds to the ultimate strength,  $\beta_i$  is the ratio of the

initial modulus of elasticity to the secant modulus at the ultimate strength (usually,  $\beta_i \geq 1$  [35]).

The constitutive relationship of the non-linear dashpot in the model shown in Fig. 7 is described by formula (21) [35], i.e.

$$\sigma_{(nlvc)i} = L_i \left[ 1 - \left( 1 - \frac{\dot{\varepsilon}_i}{B_i} \right)^{\delta_i} \right] \quad (21)$$

where  $\sigma_{(nlvc)i}$  is the stress in the dashpots,  $\dot{\varepsilon}_i$  is the first derivative of the strain with respect to time,  $L_i$ ,  $B_i$  and  $\delta_i$  are material properties in the  $i$ -th portion of the column (here again  $i = 1, 2, 3$ ). The stress,  $\sigma_i$ , in the viscoelastic model is determined as (Fig. 7)

$$\sigma_i = \sigma_{(nlec)i} + \sigma_{(nlvc)i} \quad (22)$$

In fact, formula (22) presents the stress-strain-time relationship of the non-linear viscoelastic model. Since the column is functionally graded in radial direction, the material properties,  $Q_i$ ,  $H_i$ ,  $\beta_i$ ,  $L_i$ ,  $B_i$  and  $\delta_i$ , which are involved in (20), (21) and (22) vary smoothly along the radius of the column cross-section. This variation is described by the following formulas:

$$Q_i = Q_{0i} e^{\alpha_i \frac{R}{R_i}} \quad (23)$$

$$H_i = H_{0i} e^{\varphi_i \frac{R}{R_i}} \quad (24)$$

$$\beta_i = \beta_{0i} e^{\lambda_i \frac{R}{R_i}} \quad (25)$$

$$L_i = L_{0i} e^{\mu_i \frac{R}{R_i}} \quad (26)$$

$$B_i = B_{0i} e^{\theta_i \frac{R}{R_i}} \quad (27)$$

$$\delta_i = \delta_{0i} e^{\rho_i \frac{R}{R_i}} \quad (28)$$

Where;

$$0 \leq R \leq R_i \quad (29)$$

$$i = 1, 2, 3 \quad (30)$$

In formulas (23) – (29),  $Q_{0i}$ ,  $H_{0i}$ ,  $\beta_{0i}$ ,  $L_{0i}$ ,  $B_{0i}$  and  $\delta_{0i}$  are the values of  $Q_i$ ,  $H_i$ ,  $\beta_i$ ,  $L_i$ ,  $B_i$  and  $\delta_i$  in the center of the column cross-section,  $\alpha_i$ ,  $\varphi_i$ ,  $\lambda_i$ ,  $\mu_i$ ,  $\theta_i$  and  $\rho_i$  are parameters which control the variation of the material properties.

Formula (22) can be used to calculate the stress in the column portions with taking into account the change of the material properties in the radial direction via formulas (23) – (28).

The dissipated strain energy in the column is determined by applying formula (4) (here  $n = 3$ ,  $p = 1$ ). The unit strain energy,  $u_{0ik}$ , in the dashpot of the viscoelastic model that is involved in (4) is determined by replacing of  $\sigma_{ik}$  with  $\sigma_{(nlvc)i}$  in formula (5). The MATLAB is used for integration in (4).

The dissipated strain energy solution for the column in Fig. 6 is checked-up in the following way. First, the axial forces,  $F_1$ ,  $F_2$  and  $F_3$ , in column cross-sections,  $D_1$ ,  $D_2$  and  $D_3$ , are derived by using the following dependences:

$$F_1 = \iint_{(A_1)} \sigma_1 dA \tag{31}$$

$$F_2 = \iint_{(A_2)} \sigma_2 dA - \iint_{(A_1)} \sigma_1 dA \tag{32}$$

$$F_3 = \iint_{(A_3)} \sigma_3 dA - \iint_{(A_2)} \sigma_2 dA \tag{33}$$

where  $A_1$ ,  $A_2$  and  $A_3$  are the areas of the column cross-section in portions,  $D_1D_2$ ,  $D_2D_3$  and  $D_3D_4$ , respectively (Fig. 6). Substitution of (22) in (31), (32) and (33) yields

$$F_1 = \iint_{(A_1)} [ \sigma_{(nlec)1} + \sigma_{(nlvc)1} ] dA \tag{34}$$

$$F_2 = \iint_{(A_2)} [ \sigma_{(nlec)2} + \sigma_{(nlvc)2} ] dA - \iint_{(A_1)} [ \sigma_{(nlec)1} + \sigma_{(nlvc)1} ] dA \tag{35}$$

$$F_3 = \iint_{(A_3)} [ \sigma_{(nlec)3} + \sigma_{(nlvc)3} ] dA - \iint_{(A_2)} [ \sigma_{(nlec)2} + \sigma_{(nlvc)2} ] dA \tag{36}$$

Formula (37) is applied to determine the strain energy,  $U$ , in the column.

$$U = \int_0^{w_1} F_1 dw_1 + \int_0^{w_2} F_2 dw_2 + \int_0^{w_3} F_3 dw_3 \tag{37}$$

The unit strain energy,  $u_{0i}$ , in the non-linear elastic spring of the viscoelastic model in Fig. 7 is found by formula (38), i.e.

$$u_{0i} = \int_0^{\varepsilon_i} \sigma_{(nlec)i} d\varepsilon_i \tag{38}$$

where the stress,  $\sigma_{(nlec)i}$ , in the spring is determined by using relationship (20). Then  $u_{0i}$  is integrated in the three portions of the column (Fig. 6), i.e.

$$U_{nlec} = \sum_{i=1}^{i=3} l_i \iint_{(A_i)} u_{0i} dA \tag{39}$$

Finally, the dissipated strain energy,  $U_{dse}$ , in the column is derived by subtracting of  $U_{nlec}$  from  $U$ .

$$U_{dse} = U - U_{nlec} \tag{40}$$

Actually, formula (40) is based on the fact that the spring in the viscoelastic model in Fig. 7 preserves the strain energy. Therefore, by subtracting of the strain energy in the spring,  $U_{nlec}$ , from the whole strain energy,  $U$ , we should derive the dissipated strain energy,  $U_{dse}$ .

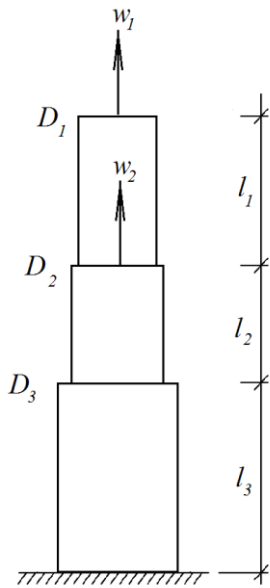


Fig. 8. Column with three portions under two longitudinal displacements,  $w_1$  and  $w_2$

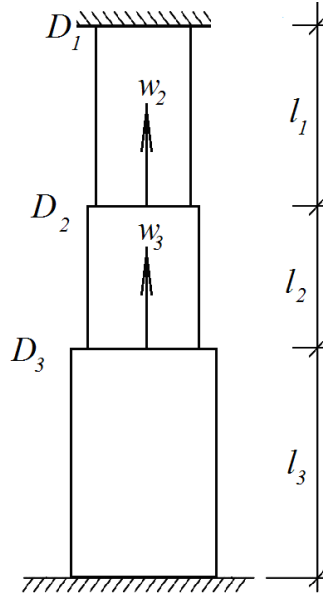


Fig. 9. Column clamped at the bottom and the top and having three portions under two longitudinal displacements,  $w_2$  and  $w_3$

The dissipated strain energy determined by using (40) matches that obtained by applying the general analysis through formula (4) (this is a check-up of the analysis).

The dissipated strain energy is determined also for the column displayed in Fig. 8 (this column is under two longitudinal displacements,  $w_1$  and  $w_2$ , which change according formula (16)). From equation (3) we obtain

$$\varepsilon_1 = \frac{1}{l_1}(w_1 - w_2) \tag{41}$$

$$w_2 = \varepsilon_2 l_2 + \varepsilon_3 l_3 \tag{42}$$

where  $\varepsilon_2$  and  $\varepsilon_3$  are unknown.

One additional equation is written by considering the equilibrium of the axial forces in section,  $D_3$ , of the column (Fig. 8), i.e.

$$\iint_{(A_3)} \sigma_3 dA = \iint_{(A_2)} \sigma_2 dA \tag{43}$$

where  $\sigma_2$  and  $\sigma_3$  are determined by using (22). Equations (42) and (43) are solved with respect to  $\varepsilon_2$  and  $\varepsilon_3$ . Then the dissipated energy in the column is found by using formula (4) (the result obtained is verified by (40)).

Analysis of the dissipated strain energy in the column clamped at the bottom and the top as displayed in Fig. 9 also is performed. The column is under longitudinal displacements,  $w_2$  and  $w_3$ , which change according to formula (16). Equations (13) and (14) are applied for determining the strains,  $\varepsilon_1$ ,  $\varepsilon_2$  and  $\varepsilon_3$ , in the column portions,  $D_1D_2$ ,  $D_2D_3$  and  $D_3D_4$ . The result is

$$\varepsilon_1 = \frac{1}{l_1}(-w_{2b}) \cos(a_0 + \omega t) \tag{44}$$

$$\varepsilon_2 = \frac{1}{l_2}(w_{2b} - w_{3b}) \cos(a_0 + \omega t) \tag{45}$$

$$\varepsilon_3 = \frac{1}{l_3} w_{3b} \cos(a_0 + \omega t) \tag{46}$$

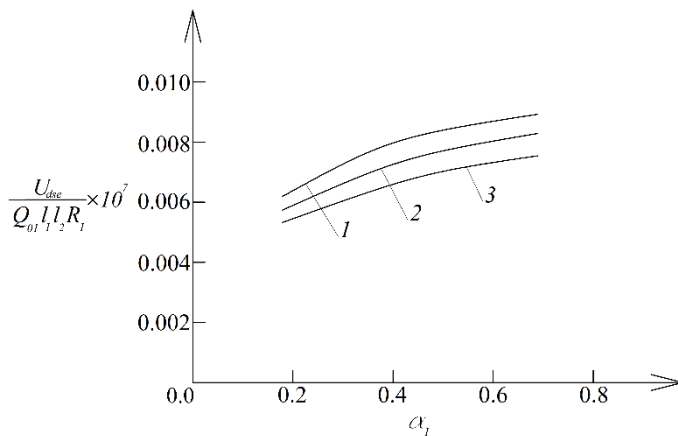


Fig. 10. Change of the normalized dissipated strain energy with increase of  $\alpha_1$  for the column with three portions under three longitudinal displacements,  $w_1$ ,  $w_2$  and  $w_3$  (curve 1 - at  $\varphi_1 = 0.2$ , curve 2 - at  $\varphi_1 = 0.5$  and curve 3 - at  $\varphi_1 = 0.8$  )

The viscoelastic model displayed in Fig. 7 is used for treating the column in Fig. 9. The change of material properties along the column cross-section radius is described by formulas (23) – (28). Formula (4) is applied to derive the dissipated strain energy in the column under consideration (Fig. 9). A check-up of the dissipated strain energy solution is carried-out via formula (40).

Further, we assume that the column in Fig. 9 is built-up by concentric layers. The column layers are inhomogeneous through their thickness. Formulas (47) – (52) are used for describing the smooth change of the material properties through thickness of the  $s$ -th layer in the  $i$ -th portion of the column.

$$Q_{is} = Q_{0is} e^{\alpha_{is} \frac{R-R_{is-1}}{R_{is}-R_{is-1}}} \quad (47)$$

$$H_{is} = H_{0is} e^{\varphi_{is} \frac{R-R_{is-1}}{(R_{is}-R_{is-1})}} \quad (48)$$

$$\beta_{is} = \beta_{0is} e^{\lambda_{is} \frac{R-R_{is-1}}{R_{is}-R_{is-1}}} \quad (49)$$

$$L_{is} = L_{0is} e^{\mu_{is} \frac{R-R_{is-1}}{R_{is}-R_{is-1}}} \quad (50)$$

$$B_{is} = B_{0is} e^{\theta_{is} \frac{R-R_{is-1}}{R_{is}-R_{is-1}}} \quad (51)$$

$$\delta_{is} = \delta_{0is} e^{\rho_{is} \frac{R-R_{is-1}}{R_{is}-R_{is-1}}} \quad (52)$$

Where;

$$R_{is-1} \leq R \leq R_{is} \quad (53)$$

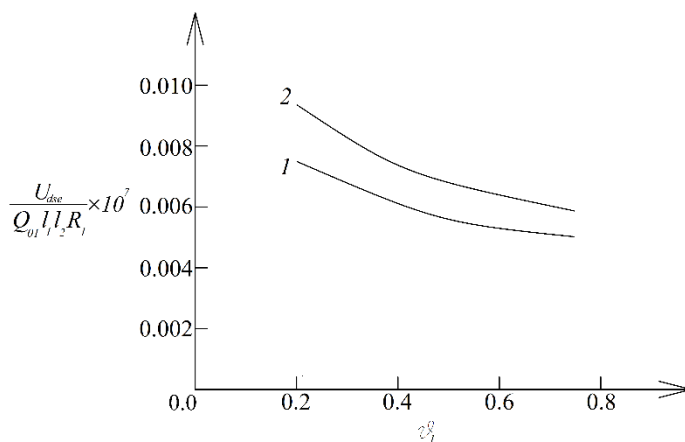


Fig. 11. Change of the normalized dissipated strain energy with increase of  $\theta_1$  (curve 1- for the column with three portions under two longitudinal displacements,  $w_1$  and  $w_2$ , curve 2 - for the column with three portions under three longitudinal displacements,  $w_1$ ,  $w_2$  and  $w_3$ )

In formulas (47) - (52),  $Q_{0is}$ ,  $H_{0is}$ ,  $\beta_{0is}$ ,  $L_{0is}$ ,  $B_{0is}$  and  $\delta_{0is}$  are the values of  $Q_{is}$ ,  $H_{is}$ ,  $\beta_{is}$ ,  $L_{is}$ ,  $B_{is}$  and  $\delta_{is}$  at  $R = R_{is-1}$  (here  $R_{is-1}$  and  $R_{is}$  are the radiuses of the internal and external surfaces of the layer, respectively). The dissipated strain energy in the column built-up by concentric layers is determined by applying formula (9). A check-up is performed by using expression (40).

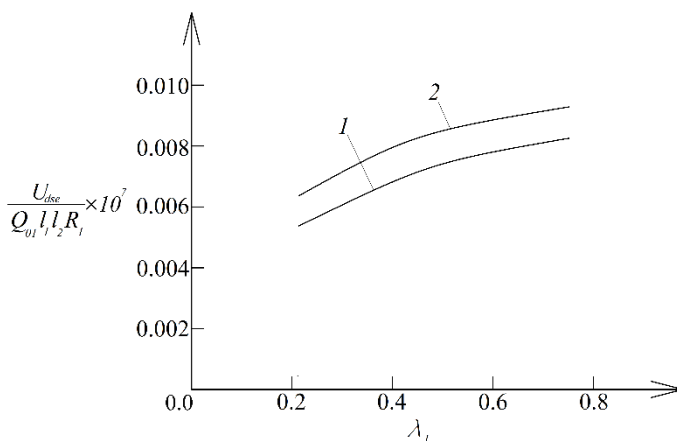


Fig. 12. Change of the normalized dissipated strain energy with increase of  $\lambda_1$  (curve 1- for the column clamped at the bottom and having three portions under three longitudinal displacements, curve 2 - for the column clamped at the bottom and the top and having three portions under two longitudinal displacements,  $w_2$  and  $w_3$ )



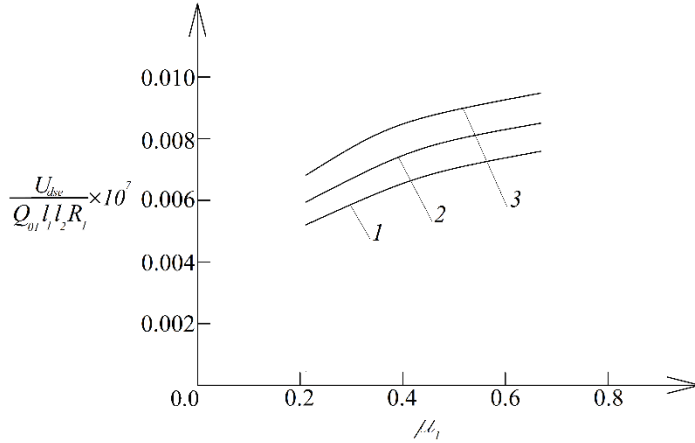


Fig. 13. Change of the normalized dissipated strain energy with increase of  $\mu_1$  for column clamped at the bottom and the top and having three portions under two longitudinal displacements,  $w_2$  and  $w_3$  (curve 1 - at  $w_{3b} = 0.003$  m, curve 2 - at  $w_{3b} = 0.004$  m and curve 3 - at  $w_{3b} = 0.005$  m)

The graphs displayed in Fig. 10, Fig. 11, Fig. 12, Fig. 13 and Fig. 14 illustrate how the dissipated strain energy in the non-linear viscoelastic inhomogeneous columns in Fig. 6, Fig. 8 and Fig. 9 changes under the influence of different factors (inhomogeneity of the material, the column geometry, parameters of the longitudinal displacements, etc.).

It is assumed that  $l_1 = 2$  m,  $l_2 = 3$  m,  $l_3 = 4$  m,  $R_1 = 0.15$  m,  $R_2 = 0.20$  m,  $R_3 = 0.25$  m,  $Q_{01} = 180000$  kPa,  $H_{01} = 0.001$ ,  $\beta_{01} = 1.3$ ,  $L_{01} = 1400$  kPa,  $B_{01} = 0.0015$  1/s,  $\delta_{01} = 1.2$   $\omega = 0.0003$  1/s and  $a_0 = 0.1$ .

The influence of  $\alpha_1$  and  $\varphi_1$  on the dissipated strain energy (the latter is presented in normalized (non-dimensional) form) for the column with three portions under three longitudinal displacements (refer to Fig. 6) is displayed in Fig. 10. The graphs in Fig. 10 indicate that the rise of  $\alpha_1$  causes growth of the dissipated strain energy. The rise of  $\varphi_1$  generates a reduction of the dissipated strain energy (Fig. 10).

Rise of  $\theta_1$  causes reduction of the dissipated strain energy as one can observe in Fig. 11. The graphs displayed in Fig. 11 reveal also that the dissipated strain energy in the column with three portions under three longitudinal displacements (refer to Fig. 6) is higher than that in the column with three portions under two longitudinal displacements (refer to Fig. 7).

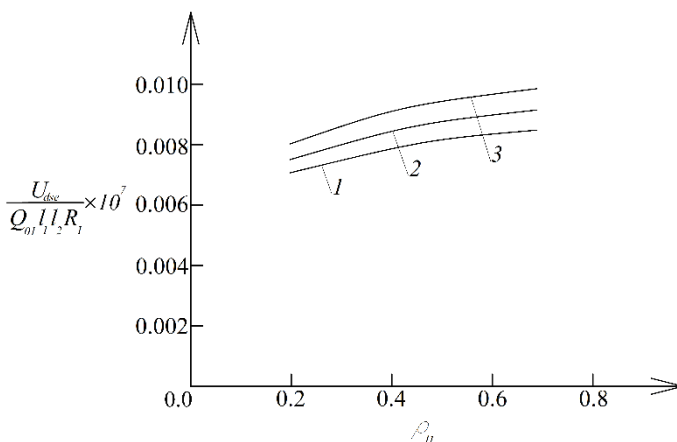


Fig. 14. Change of the normalized dissipated strain energy with increase of  $\rho_{11}$  for column clamped at the bottom and the top and having three portions under two longitudinal displacements,  $w_2$  and  $w_3$  (curve 1 - at  $l_3/l_1 = 1.5$ , curve 2 - at  $l_3/l_1 = 2.0$  and curve 3 - at  $l_3/l_1 = 2.5$ )

The effect of  $\lambda_1$  is studied for both columns displayed in Fig. 6 and Fig. 9. The corresponding graphs are displayed in Fig. 12. It can be seen that rise of  $\lambda_1$  causes smooth growth of the dissipated strain energy (Fig. 12). It can also be seen in Fig. 12 that the dissipated strain energy in the column clamped at the bottom and the top (refer to Fig. 9) is higher than that in the column clamped at the bottom end only (refer to Fig. 6).

One can observe in Fig. 13 how the dissipated strain energy changes with rise of  $\mu_1$  in the column clamped at the bottom and the top (refer to Fig. 9) at three values of  $w_{3b}$ . Graphs in Fig. 3 indicate growth of the dissipated strain energy with rise of  $\mu_1$  and  $w_{3b}$ .

How the dissipated strain energy varies with increase of  $\rho_{11}$  in the column clamped at the bottom and the top and built-up by concentric layers (the number of layers is 3, 5 and 7 in column portions,  $D_1D_2$ ,  $D_2D_3$  and  $D_3D_4$ , respectively) can be seen in Fig. 14. The graphs indicate rise of the dissipated strain energy with increase of  $\rho_{11}$  at each of the considered  $l_3/l_1$  ratios (Fig. 14).

#### 4. Conclusions

General analysis of the dissipation of the strain energy in columns under continuously varying with time longitudinal displacements is developed. The first step in the analysis is to determine the strains in the column. Then the strains are used to derive stresses. The analysis yields a simple expression for the dissipated strain energy in columns of circular cross-section. The columns are functionally graded in radial direction. Besides, the columns under consideration have non-linear viscoelastic behavior that is analyzed by viscoelastic mechanical models which are structured by using non-linear springs and dashpots. Actually, this is the basic assumption in the present study. This assumption

imposes an important limitation in sense that the approach developed here is applicable only when models with spring and dashpots are used (the dissipated energy is derived from the strain energy in the dashpots). The columns have an arbitrary number of portions with different radius of the cross-section. The general analysis is applicable also for determining of the dissipated strain energy in non-linear viscoelastic columns built-up by concentric layers. Each layer may have different material properties. Besides, the layers may be functionally graded through thickness. The expression obtained is used for determining the dissipated strain energy in a column clamped at the bottom. A column clamped at the bottom and the top also is studied. Since the columns are functionally graded along the radius of the cross-section, the material properties which are involved in the expression for the dissipated strain energy change continuously in radial direction. A check-up of the results obtained is performed by determining the dissipated strain energy by subtracting the strain energy in the spring from the whole strain energy cumulated in the column. It is found that increase of the value of  $\alpha_1$  generates growth of the dissipated strain energy. Growth of the dissipated strain energy is observed also when  $\lambda_1$ ,  $\mu_1$  and  $\rho_{11}$  rise. An opposite behavior, i.e. reduction of the dissipated strain energy is observed when  $\varphi_1$  and  $\theta_1$  rise. The increase of  $l_3/l_1$  ratio induces rise of the dissipated strain energy (this finding indicates that the dissipated strain energy in longer column is higher). The dissipated strain energy rises also when  $w_{3b}$  has higher values. It can be summarized that the main novelty of this paper is in the fact that general analysis of the dissipated energy in non-linear viscoelastic columns is presented. One of the practical implications of the derived expressions and the results is in fracture mechanics. For example, when fracture is analyzed in terms of the strain energy release rate, the latter has to be derived from the strain energy reduced by the dissipated energy that can be determined by applying the expressions obtained in the present paper.

## References

- [1] Dowling N. Mechanical Behavior of Materials, Pearson, 2007.
- [2] Rizov V. Analysis of temperature change effect on dissipation of energy in functionally graded beams. The Eurasia Proceedings of Science, Technology, Engineering & Mathematics (EPSTEM), 2023; 23: 406-412. <https://doi.org/10.55549/epstem.1371771>
- [3] Abdollahzadeh G, Hashemi SM, Tavakoli H et al. Determination of Hysteretic Behavior of Steel End-Plate Beam-to-Column Connection with Mechanical and Neural Network Modeling. Arab J Sci Eng, 2014; 39: 7661-7671. <https://doi.org/10.1007/s13369-014-1348-4>
- [4] Nouredin M, Ali A, Nasab MSE, Kim J. Optimum distribution of seismic energy dissipation devices using neural network and fuzzy inference system. Comput Aided Civ Inf, 2021; 36:1306-1321. <https://doi.org/10.1111/mice.12673>
- [5] Hugo Rodrigues, Humberto Varum, António Arêde, Aníbal Costa. A comparative analysis of energy dissipation and equivalent viscous damping of RC columns subjected to uniaxial and biaxial loading. Engineering Structures, 2012; 35: 149-164. <https://doi.org/10.1016/j.engstruct.2011.11.014>
- [6] Ahmadi I, Davarpanah M, Sladek J et al. A size-dependent meshless model for free vibration analysis of 2D-functionally graded multiple nanobeam system. J Braz. Soc. Mech. Sci. Eng., 2024; 46: 11. <https://doi.org/10.1007/s40430-023-04580-5>
- [7] Isa Ahmadi, Mohammad Naeim Moradi and Mahdi Davar Panah. Dynamic response analysis of nanoparticle-nanobeam impact using nonlocal theory and meshless method. Structural Engineering and Mechanics, 2024; 89: 135-153.

- [8] Kieback B, Neubrand A, Riedel H. Processing techniques for functionally graded materials. *Materials Science and Engineering: A*, 2003; 362: 81-106. [https://doi.org/10.1016/S0921-5093\(03\)00578-1](https://doi.org/10.1016/S0921-5093(03)00578-1)
- [9] Chen Y, Lin X. Elastic analysis for thick cylinders and spherical pressure vessels made of functionally graded materials. *Computational Materials Science*, 2008; 44: 581-581. <https://doi.org/10.1016/j.commatsci.2008.04.018>
- [10] Dias CMR, Savastano JrH, John V.M. Exploring the potential of functionally graded materials concept for the development of fiber cement. *Construction and Building Materials*, 2010; 24: 140-146. <https://doi.org/10.1016/j.conbuildmat.2008.01.017>
- [11] Tokovyy Y, Ma CC. Three-Dimensional Elastic Analysis of Transversely-Isotropic Composites. *Journal of Mechanics*, 2017; 33: 821-830. <https://doi.org/10.1017/jmech.2017.91>
- [12] Tokovyy Y, Ma CC. Elastic Analysis of Inhomogeneous Solids: History and Development in Brief. *Journal of Mechanics*, 2019; 18: 1-14. <https://doi.org/10.1017/jmech.2018.57>
- [13] Tokovyy Y. Solutions of Axisymmetric Problems of Elasticity and Thermoelasticity for an Inhomogeneous Space and a Half Space. *Journal of Mathematical Science*, 2019; 240: 86-97. <https://doi.org/10.1007/s10958-019-04337-3>
- [14] Gandra J, Miranda R, Vilaça P, Velhinho A, Teixeira J.P. Functionally graded materials produced by friction stir processing. *Journal of Materials Processing Technology*, 2011; 211: 1659-1668. <https://doi.org/10.1016/j.jmatprotec.2011.04.016>
- [15] Zhang Y, Ming-jie Sun, Zhang D. Designing functionally graded materials with superior load-bearing properties. *Acta Biomaterialia*, 2012; 8: 1101-1108. <https://doi.org/10.1016/j.actbio.2011.11.033>
- [16] Tejaswini N, Babu R, Ram S. Functionally graded material: an overview. *Int J Adv Eng Sci Technol*, 2013;4: 183-188.
- [17] Mino Naebe, Kamyar Shirvanimoghaddam. Functionally graded materials: A review of fabrication and properties. *Applied materials today*, 2016; 5: 223-245. <https://doi.org/10.1016/j.apmt.2016.10.001>
- [18] Toudeshdehghan J., Lim W., Foo1 K.E., Ma'arof M.I.N., Mathews J. A brief review of functionally graded materials. *MATEC Web of Conferences*, 2017; 131: 03010. <https://doi.org/10.1051/mateconf/201713103010>
- [19] Nikbakht S, Kamarian S, Shakeri M. A review on optimization of composite structures Part II: Functionally graded materials. *Composite Structures*, 2019; 214: 83-102. <https://doi.org/10.1016/j.compstruct.2019.01.105>
- [20] El-Galy IM, Saleh BI, Ahmed M.H. Functionally graded materials classifications and development trends from industrial point of view. *SN Appl. Sci.*, 2019; 1: 1378-1389. <https://doi.org/10.1007/s42452-019-1413-4>
- [21] Ekrem Tufekci, Ugurcan Eroglu, Serhan Aydin Aya (2016) Exact solution for in-plane static problems of circular beams made of functionally graded materials. *Mechanics Based Design of Structures and Machines*, 2016; 44: 476-494. <https://doi.org/10.1080/15397734.2015.1121398>
- [22] Hilal Koc & Ekrem Tufekci (2023) A novel approach of bending behavior of carbon nanotubes by combining the effects of higher-order boundary conditions and coupling through doublet mechanics. *Mechanics of Advanced Materials and Structures*. <https://doi.org/10.1080/15376494.2023.2263767>
- [23] Tufekci E, Aya SA, Oldac O. A unified formulation for static behavior of nonlocal curved beams. *Structural Engineering and Mechanics*, 2016; 59: 475-502. <https://doi.org/10.12989/sem.2016.59.3.475>
- [24] Mahamood RM, Akinlabi ET. *Functionally Graded Materials*, Springer, 2017. <https://doi.org/10.1007/978-3-319-53756-6>

- [25] Shrikantha Rao S, Gangadharan KV. Functionally graded composite materials: an overview, *Procedia Materials Science*, 2014; 5: 1291-1299. <https://doi.org/10.1016/j.mspro.2014.07.442>
- [26] Saiyathibrahim A, Subramaniyan R, Dhanapl P. Centrifugally cast functionally graded materials - review, In: *International Conference on Systems, Science, Control, Communications, Engineering and Technology*, 2016; 68-73.
- [27] Miyamoto Y, Kaysser WA, Rabin BH, Kawasaki A, Ford RG. *Functionally Graded Materials: Design, Processing and Applications*, Kluwer Academic Publishers, Dordrecht/London/Boston, 1999. <https://doi.org/10.1007/978-1-4615-5301-4>
- [28] Butcher RJ, Rousea, CE, Tippur HV. A functionally graded particulate composite: Measurements and Failure Analysis, *Acta. Mater.*, 1999; 47: 259-268. [https://doi.org/10.1016/S1359-6454\(98\)00305-X](https://doi.org/10.1016/S1359-6454(98)00305-X)
- [29] Rzhantsyn AR. *Built-up Bars and Plates*, Stroyizdat, 1986.
- [30] Dolgov NA. Effect of the elastic modulus of a coating on the serviceability of the substrate-coating system. *Strength of Materials*, 2002; 37: 422-431. <https://doi.org/10.1007/s11223-005-0053-7>
- [31] Dolgov NA. Determination of Stresses in a Two-Layer Coating, *Strength of Materials*, 2005; 37: 422-431. <https://doi.org/10.1007/s11223-005-0053-7>
- [32] Dolgov NA. Analytical Methods to Determine the Stress State in the Substrate-Coating System Under Mechanical Loads, *Strength of Materials*, 2016; 48: 658-667. <https://doi.org/10.1007/s11223-016-9809-5>
- [33] Finot M, Suresh S. Small and large deformation of thick and thin-film multilayers: effect of layer geometry and compositional gradients. *J Mech Phys Solids*, 1996: 44; 683-721. [https://doi.org/10.1016/0022-5096\(96\)84548-0](https://doi.org/10.1016/0022-5096(96)84548-0)
- [34] Kim JS, Paik KW, Oh SH. The Multilayer-Modified Stoney's Formula for Laminated Polymer Composites on a Silicon Substrate. *J. Appl. Phys.*, 1999; 86: 5474-5479. <https://doi.org/10.1063/1.371548>
- [35] Lukash P. *Fundamentals of non-linear structural mechanics*, Stroiizdat, 1978.

Blank Page

## Factors affecting durability properties of GPC: A review

Nabaz Yassen Ezuldin<sup>1,2,a</sup>, Saad Mahmood Raof<sup>2,b</sup>, Alyaa Abbas Alattar<sup>1,c</sup>, Hussein Hamada<sup>\*,3,d</sup>

<sup>1</sup>Technical Engineering College of Kirkuk, Northern Technical University, Kirkuk, Iraq

<sup>2</sup>College of Engineering, Tikrit University, Iraq

<sup>3</sup>Al-Qalam University College, Kirkuk 36001, Iraq

### Article Info

### Abstract

#### Article history:

Received 09 Jan 2024

Accepted 05 Apr 2024

#### Keywords:

Geopolymer concrete;  
Activator;  
Strength;  
Durability;  
Sustainable;  
Environment

The imperative to find sustainable alternatives to conventional cement, given its energy-intensive production and significant environmental impact, has driven research into alternative binder materials for civil infrastructure. This paper explores Geopolymer concrete (GPC), a polymer-based binder technology, as a promising solution to reduce the environmental footprint associated with traditional cement production. The study meticulously examines various aspects of GPC, focusing on its impact on crucial durability properties for infrastructure applications. This includes an in-depth analysis of GPC properties, elucidating characteristics influencing performance. In addition to fundamental properties, the paper critically evaluates the resistance of geopolymer pastes and concrete to a spectrum of extreme conditions. The discussion spans testing methodologies for both heat- and ambient-cured geopolymers, providing insights into their performance and durability across diverse environmental challenges. This comprehensive review aims to enhance the understanding of GPC technology, offering valuable insights for researchers, engineers, and industry professionals committed to sustainable and resilient infrastructure solutions.

© 2025 MIM Research Group. All rights reserved.

## 1. Introduction

Geopolymer concrete (GPC) stands as a groundbreaking advancement in concrete technology, emerging as a highly sophisticated alternative to conventional ordinary Portland cement (OPC) concrete [1]. This innovative approach in concrete production replaces traditional Portland cement with pozzolanic materials, specifically designed to address the environmental concerns associated with the widespread use of Portland cement [2]. As the second most utilized material globally after water, Portland cement production significantly contributes to carbon dioxide (CO<sub>2</sub>) emissions and entails substantial energy consumption, thereby presenting formidable environmental challenges [3].

In addition to its superior strength and durability, GPC offers a myriad of advantages, establishing itself as a compelling choice for contemporary construction practices [4]. Notably, GPC exhibits exceptional early-age strength and benefits from ambient curing conditions, contributing to accelerated construction timelines [5]. The intricacies of GPC's durability and strength hinge on various factors, including the selection of binders, the alkali-activating solution employed, and the nuances of the curing process [6]. This study aims to provide a comprehensive exploration of the inherent strength and durability

\*Corresponding author: [enghu76@gmail.com](mailto:enghu76@gmail.com)

<sup>a</sup>[orcid.org/0009-0005-0357-1444](https://orcid.org/0009-0005-0357-1444); <sup>b</sup>[orcid.org/0000-0002-6791-8268](https://orcid.org/0000-0002-6791-8268); <sup>c</sup>[orcid.org/0000-0003-1942-5458](https://orcid.org/0000-0003-1942-5458);

<sup>d</sup>[orcid.org/0000-0001-9911-8639](https://orcid.org/0000-0001-9911-8639)

DOI: <https://dx.doi.org/10.17515/resm2024.145ma0109rv>

Res. Eng. Struct. Mat. Vol. 11 Iss. 1 (2025) 21-43

characteristics of GPC, with a focal point on understanding the critical interplay of these variables.

Moreover, the incorporation of industrial by-products, such as fly ash (FA) and ground granulated blast-furnace slag (GGBS), into GPC reveals additional benefits, contributing to both environmental sustainability and resource efficiency. A notable environmental advantage lies in the reduced energy requirements for raw material extraction in GPC production [7]. This paper serves as a detailed examination of various facets of GPC, encompassing mix design techniques, the impact of fiber additions on durability and strength properties, and the overall performance of GPC structures.

Despite numerous studies investigating the effects of different factors on the strength and durability of GPC [8-10], geopolymer mortar [11-13], and both [14], recent literature lacks comprehensive reviews, especially within the last three years, focused on the factors affecting the durability of GPC. Hassan et al. [15] studied the mechanical and microstructure properties of GPC and did not address the fire resistance and water permeability of GPC. Johan et al. [13] focused in their study on the effect of source materials on the properties of geopolymer mortar and also did not study factors effecting the fire resistance and water permeability. Zhang et al. [11] investigated the mechanical properties of geopolymer mortar and did not address the GPC properties. Huseien et al. [16] investigated the geopolymer mortar as repair materials and did not focus on the factors effecting the durability of GPC. Ng et al. [14] investigated only compressive strength and microstructure of geopolymer paste, mortar, and concrete. Amran et al. [17] investigated the mechanical and physical properties of GPC only and did not address the durability properties of GPC. Zhang et al. [18] investigated the engineering and fabrication properties of concrete and GPC, but they did not address the fire resistance and water permeability of GPC, as well as did not address the repolymerization process in detail. Ahmed et al. [19] conducted a comprehensive literature review about the mechanical properties of GPC and its effect on the behavior of GPC beams. This paper aims to fill this gap, serving as a valuable resource for researchers, engineers, and practitioners. It offers a thorough understanding of the nuanced aspects of GPC and the factors influencing its strength and durability. The intent is to encourage further exploration and application of this innovative concrete technology in sustainable and resilient construction practices.

## **1.1 Background**

Geopolymers have emerged as a focal point in contemporary research and development, holding substantial promise as ecologically beneficial and sustainable alternatives to traditional cement-based materials [5]. The impetus behind geopolymer research lies in its potential to significantly alleviate the environmental impact associated with conventional Portland cement production [20]. Noteworthy is the fact that the synthesis of geopolymers typically occurs at lower temperatures, resulting in significant reductions in carbon dioxide emissions and overall environmental considerations [21]. Primarily derived from aluminosilicate source materials, geopolymers capitalize on industrial by-products such as fly ash from coal combustion or slag from metallurgical processes [22]. The versatility of these source materials is a central focus of ongoing research, underscoring the imperative to identify and optimize components suitable for geopolymer synthesis.

GPC, an innovative and environmentally friendly alternative to conventional Portland cement-based concrete, distinguishes itself through exceptional strength, durability, and sustainable characteristics [23]. At its core, GPC relies on geopolymers— inorganic materials with a polymer-like structure, often sourced from industrial by-products like fly ash, slag, or other aluminosilicates. The utilization of these industrial residues not only



enhances the sustainability of the concrete but also aligns with the principles of the circular economy by repurposing waste materials.

## **1.2 Importance of Study**

Geopolymer materials are gaining traction as substitutes for traditional construction components; however, many studies are confined to conditions involving heat curing. The widespread acceptance of geopolymer materials, encompassing both mortar and concrete, could be significantly broadened if they prove to be feasibly and economically viable under ambient curing conditions. This study aims to contribute to the ongoing advancements in geopolymer materials by exploring their potential enhancement through the incorporation of various mineral admixtures. The focus is on improving durability properties such as resistance to elevated temperatures, permeability, acid resistance, and sulfate resistance. Ambient curing, which refers to curing at room temperature without the need for specialized curing conditions like high temperatures or steam curing, is crucial for the practical application of geopolymers in real-world construction settings [24]. Generally, the addition of mineral admixtures such as fly ash, silica fume, or GGBFS can enhance the properties of GPC [25]. These admixtures can contribute to increased strength, reduced permeability, and improved durability of GPC [13]. However, the exact effects depend on the specific materials and mix proportions, highlighting the importance of understanding and optimizing these factors for the desired performance of geopolymers.

The continued development of geopolymer materials is crucial for addressing the practical challenges associated with their application, especially in the context of ambient curing conditions. This research seeks to advance the understanding of how different mineral admixtures can positively impact the durability characteristics of geopolymer materials, thereby expanding their practical utility. Of particular interest are properties such as resistance to elevated temperatures, acid resistance, sulfate resistance, and permeability, which play a pivotal role in determining the overall performance and lifespan of structures constructed with geopolymer materials.

## **2. Polymer and Polymerization Process**

The term "polymer process" encompasses a diverse range of activities related to the production, modification, or processing of polymers—large molecules composed of recurring structural units called monomers [26]. These versatile compounds play pivotal roles in numerous industries, including plastics, textiles, adhesives, and various biological applications [27, 28]. The polymer process spans diverse procedures, ranging from the synthesis of polymers to their transformation into practical and usable items [29]. In the context of geopolymer technology, the polymer process takes on a unique significance. An alkaline medium, typified by substances such as sodium hydroxide or potassium hydroxide, proves ideal for observing the polymerization process. Notably, the inclusion of silicates introduces an additional ionic composition, fostering excellent bonding effects within the resulting polymer structure. The concentration of alkali ions, particularly in higher molar concentrations, can expedite the chain reaction among reactants. However, a delicate balance must be struck, as elevated concentrations may lead to a rapid loss of consistency during mixing, given the accelerated pace of the polymerization reaction [30].

A noteworthy observation is the impact of sodium silicate addition on the sodium hydroxide solution's silicate content. This augmentation influences the gel formation, rendering it more prone to rapid polymerization [31]. Insights into the intricacies of the polymer process are pivotal for understanding and optimizing the synthesis of geopolymers, particularly as they pertain to achieving desired properties in GPC. This section illuminates the complex interplay of alkaline mediums, silicate content, and the

kinetics of polymerization, providing a foundational understanding of the polymer process crucial for advancing geopolymer research and application.

Geopolymers, classified as inorganic polymers, exhibit a chemical composition akin to zeolites, with a distinguishing microstructural feature of amorphousness rather than crystallinity [32]. The polymerization process involves a swift reaction facilitated by activator agents on Si-Al minerals, culminating in the formation of a 3D geopolymer chain and the establishment of Si-O-Al-O bonds [33], as shown in Figure 1. This key concept revolves around the amalgamation of Si/Al-rich materials with activator agents, fostering the development of Si-O-Al-O bonds through the polymerization process. GPC undergoes poly-condensation from Si and Al, along with a high alkali content, contributing to strength development [34].

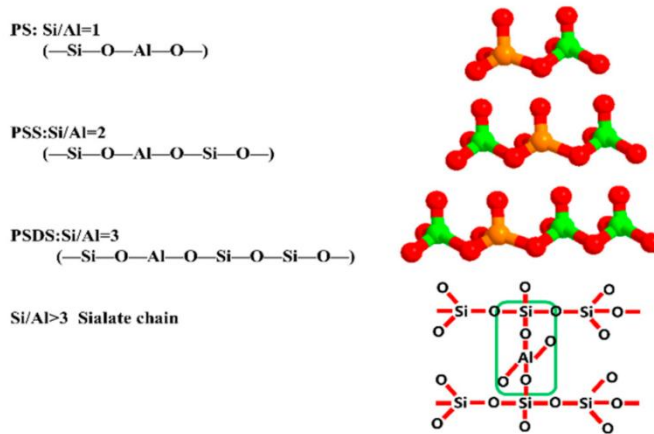


Fig. 1. Model of Geopolymer with various Si/Al molar [33]

Noteworthy is the amorphous nature of GPC, akin to synthetic zeolites, with a chemical composition resembling the zeolitic structure. The geopolymer framework comprises Si-O-Al units, distinct from zeolites, where alternate Si-Al tetrahedra are interconnected in three dimensions by oxygen atoms [35]. The coordination of Al with four oxygen atoms generates a negative disproportion, necessitating cations like Na<sup>+</sup> and K<sup>+</sup> to expedite the geopolymerization [36]. Upon the addition of water or additives to NaOH and KOH agents, a reaction ensues, liquefying silica and vigorously reacting with additives to form a geopolymer binder [37]. The incorporation of industrial waste rich in Si and Al enhances the strength of the resulting material [38]. A higher concentration of binder components such as fly ash, GGBS, rice husk ash (RHA), metakaolin (MK), etc., contributes to elevated Si, Al, and CaO content, thereby augmenting strength development. The wide reactivity range of fly ashes influences the evolution of the C-S-H matrix, enhancing tetra-coordination in interlayer spaces.

### 3. Properties of GPC Mixtures

Concrete, including GPC, which distinguishes itself from conventional Portland cement-based concrete. GPC relies on a unique binder system activated through industrial by-products such as fly ash or slag in combination with alkaline solutions [39]. Table 1 provides an overview of the chemical composition and types of binders employed by various authors in the context of GPC.

As shown in Table 1, silica and alumina oxides constitute the highest percentages among other components in the chemical composition of aluminosilicate materials. These

proportion significantly contributes to enhancing the durability of GPC by improving the hardness and density of GPC.

Table 1. Chemical compositions of each binder used in the previous studies

| Ref                           | Binder                | SiO <sub>2</sub> | Al <sub>2</sub> O <sub>3</sub> | Fe <sub>2</sub> O <sub>3</sub> | CaO   | MgO  | P <sub>2</sub> O <sub>5</sub> | K <sub>2</sub> O | Na <sub>2</sub> O | TiO <sub>2</sub> | L.O.I | SO <sub>3</sub> |
|-------------------------------|-----------------------|------------------|--------------------------------|--------------------------------|-------|------|-------------------------------|------------------|-------------------|------------------|-------|-----------------|
| Jindal et al. [40]            | RHA                   | 90               | 0.46                           | 0.43                           | 1.10  | 0.77 | NA                            | 4.6              | NA                | NA               | 3.9   | NA              |
|                               | Ultra-fine slag (UFS) | 33.9             | 22.6                           | 1.4                            | 32.8  | 7.8  | NA                            | NA               | NA                | NA               | NA    | 0.23            |
| Albegm prli et al., [41]      | Fly ash               | 38.4             | 22.2                           | 12.14                          | 0.88  | 1.81 | NA                            | NA               | 2.76              | NA               | 3.1   | 0.4             |
|                               | GGBS                  | 50.82            | 10.19                          | 0.76                           | 26.72 | 1.89 | NA                            | NA               | 0.24              | NA               | 1.9   | 1.02            |
| Mahdik hani and Sarvandi [42] | GGBS                  | 39.61            | 9.57                           | 1.45                           | 31.68 | 6.49 | 0.02                          | 1.97             | 0.51              | 0.95             | NA    | 2.5             |
| Petrus et al., [43]           | Fly ash               | 37.6             | 12.5                           | 20.8                           | 20.7  | NA   | 1.9                           | 2.0              | NA                | 1.3              | NA    | 2.1             |
| Kugler et al., [44]           | Fly ash               | 52.35            | 25.19                          | 6.22                           | 4.17  | 1.88 | NA                            | 2.09             | 1.09              | 1.15             | NA    | NA              |
|                               | Concrete rubble       | 59.5             | 3.12                           | 1.33                           | 17.85 | 1.42 | NA                            | 1.18             | 0.20              | 0.11             | NA    | NA              |
| Ahmed et al., [45]            | ferrosil icon slag    | 77.7             | 3.45                           | 11.50                          | 1.96  | 0.14 | NA                            | 0.35             | 0.26              | 0.11             | 3.85  | 0.39            |
|                               | alumin a waste        | 2.62             | 64.5                           | 0.46                           | 0.47  | 0.13 | NA                            | 3.61             | 4.29              | 0.13             | 2.74  | 0.42            |
| Pham et al., [46]             | Fly ash               | 58.7             | 22.87                          | 7.31                           | 0.98  | 0.85 | NA                            | 3.6              | 0.33              | 1.35             | 3.53  | NA              |
| Hamzah et al., [47]           | GGBFS                 | 35.02            | 13.56                          | 1.41                           | 38.6  | 8.18 | NA                            | 0.80             | 0.31              | 0.23             | 1.89  | NA              |
|                               | Fly ash               | 57.2             | 28.8                           | 3.7                            | 5.2   | 1.6  | NA                            | 0.9              | 0.1               | NA               | 0.22  | 0.1             |

#### 4. Effect of Curing on The Durability of Geopolymer Concrete

GPC undergoes a dynamic evolution of characteristics and behaviors, a transformation intricately linked to the specifics of its curing conditions [48]. Rigorous investigations, involving variations in both curing temperatures and durations, have been instrumental in unraveling the nuanced development of GPC [49]. Diverse studies have probed the behavior of GPC under different curing regimens, exemplified by the work of Chouksey et al. [50], who explored the impact of curing conditions on mechanical and physical properties. Their investigation, employing both oven-curing and ambient curing, revealed higher compressive, flexural, and tensile strengths in oven-cured samples compared to ambient-cured ones. Notably, dry shrinkage and density exhibited an inverse trend, with higher values for ambient-cured samples. Similarly, Poloju and Srinivasu [51], demonstrated the advantages of incorporating fly ash and GGBS with an alkaline activator (sodium silicate and sodium hydroxide) in GPC, comparing the outcomes of oven curing at

60°C for 24 hours and ambient curing. Their findings underscored the superior strength recorded in oven-cured samples relative to ambient-cured counterparts. Table 2 shows the effect of curing conditions on the GPC.

Table 2. Effect of different curing conditions on the durability and strength of HPC

| References                | Curing type  | Aluminosilicate  | Alkali activator                          | Effect of curing   |
|---------------------------|--|--|---|--|
| Gholampour et al. [52]    | Ambient and oven-curing                            | GGBS and fly ash   | NaOH and Na <sub>2</sub> SiO <sub>3</sub> | GPC samples cured by oven show a somewhat higher strength than that of GPC cured by ambient condition.   |
| Singh and Sandhu [53]     | 27 and 90 C  | Fly Ash and Alccofine                                      | NaOH and Na <sub>2</sub> SiO <sub>3</sub> | GPC samples have improved properties at 27 and 90 °C owing to the creation of polymer and hydration products.  |
| Suresh et al. [54]        | Ambient curing                                     | GGBS and bio-medical waste ash                             | NaOH and Na <sub>2</sub> SiO <sub>3</sub> | The addition of waste glass powder in GPC containing GGBS and biomedical waste ash at ambient curing led to an enhancement in the properties of GPC more than that of mixtures without waste glass powder to record a 28 days-compressive strength of 48.6 MPa |
| Dişçi and Polat [55]      | heat + water cured and heat + ambient 90 C for 72. | Perlite, Nano-CaO, and Nano-Al <sub>2</sub> O <sub>3</sub> | NaOH and Na <sub>2</sub> SiO <sub>3</sub> | The compressive strength and durability of GPC improved in the heat curing condition than the ambient curing condition.  |
| Poloju and Srinivasu [51] | Ambient curing and Oven curing with 60C            | GGBS and fly ash   | NaOH and Na <sub>2</sub> SiO <sub>3</sub> | The samples of GPC oven-cured recorded better performance compared to GPC samples that cured at ambient condition  |
| Arunkumar et al. [56]     | Ambient curing                                     | Fly ash and waste wood ash                                 | NaOH and Na <sub>2</sub> SiO <sub>3</sub> | Addition of waste wood ash as fly ash replacement and waste rubber tires as a fiber at ambient curing enhanced the GPC properties.   |
| Wang et al. [48]          | 20, 40, 60, 80 and 100 °C                          | GGBS and fly ash   | NaOH and Na <sub>2</sub> SiO <sub>3</sub> | The strength and durability of GPC increase as the curing temperature increases from 20 to 80 C. while, the performance of GPC starts to decrease as the curing temperature increases more than 80 °C.   |

|                          |  |                              |   |  |
|--------------------------|--|------------------------------|---|--|
| Saif et al. [57]         | ambient curing and 60 °C heat curing               | Fly ash, GGBS, and mtakaolin | NaOH and Na <sub>2</sub> SiO <sub>3</sub> | Heat curing enhance the durability properties of GPM containing MK more than ambient curing for all aggressive environments. |
| Noushini and Castel [58] | Ambient curing and thermal curing 60, 75, and 90 C | fly ash                      | NaOH and Na <sub>2</sub> SiO <sub>3</sub> | Thermal curing has a significant influence in improve durability properties of GPC made of low calcium fly ash.              |

The curing process for GPC unfolds in distinct stages, each contributing to the material's final properties. Initial heat curing involves subjecting specimens to varying temperatures in an oven, a critical step in determining the optimal curing temperature for complete polymerization over 24 hours [59]. Subsequently, a second phase employs steam curing in an accelerated curing tank at diverse temperatures for 18 hours, a method proven to enhance compressive strength significantly [60]. Following these accelerated curing steps, standard water curing is applied, culminating in the final stage of fixing the model at room temperature [61]. An alternative curing method involves microwave household curing at 2.45 GHz, where variations in wattage and duration impact the temperature profile in the center of the samples [62]. Furthermore, researchers have delved into the impact of both microwave and conventional curing methods on the compressive strength of geopolymer mortar. The investigation incorporated standard heat curing parameters at 65 °C, coupled with a 5-minute curing duration using a 90-W microwave. In parallel, diverse studies scrutinized alternative curing conditions, encompassing lime-water curing (LWC), sealed ambient curing, and heat curing, spanning both GPC and ordinary Portland cement concrete (OPCC) [63].

The alkaline activator in GPC mainly involves of a combination of sodium silicate (Na<sub>2</sub>SiO<sub>3</sub>) and sodium hydroxide (NaOH) [64]. The chemical composition can be represented as: Sodium Hydroxide (NaOH) and Sodium Silicate (Na<sub>2</sub>SiO<sub>3</sub>), and to calculate the Molar Ratios, should be applied the following calculations:

- Sodium Oxide (Na<sub>2</sub>O) molar mass = 62 g/mol
- Silicon Dioxide (SiO<sub>2</sub>) molar mass = 60.09 g/mol

As reported by Cheng et al. [65], the molar ratio of Na<sub>2</sub>O to SiO<sub>2</sub> in sodium silicate (Na<sub>2</sub>SiO<sub>3</sub>) is ranging between 1.38 and 1.93, and this proportion might be changed according to the mix design and specification required. This means that for every mole of Na<sub>2</sub>O in the sodium silicate, there are 1.38 moles of SiO<sub>2</sub>. The molar ratios of Na<sub>2</sub>O to SiO<sub>2</sub> in the alkaline activator can importantly affect the durability of GPC.

## 5. Durability of GPC

The durability of GPC consistently surpasses that of conventional Portland cement concrete, owing to its distinctive material composition and manufacturing method [66]. GPC exhibits exceptional resistance to acids and sulfates, attributed to the absence of gaps between binding materials, ensuring heightened durability [67]. This advantage extends to the preservation of the reinforcing steel's integrity within the concrete for extended periods, resulting in significantly less volume loss compared to normal concrete. Key durability properties of GPC encompass resistance to acid attacks, resistance to sulfate attacks, fire resistance, and permeability.

### 5.1. Resistance to Acid Attack

In a study comparing GPC (composed of fly ash and slag) with O.P.C. concrete in structural applications, slag demonstrated superior acid resistance when exposed to sulfuric acid [13]. A comprehensive durability examination involving exposure to seawater (5% NaCl), sulfate attack (5% sodium sulfate or 5% magnesium sulfate), and acid attack (5% sulfuric acid) confirmed the exceptional durability of GPC over normal concrete. Acid attack proved to be the most challenging for both geopolymer and standard concrete, with GPC consistently outperforming ordinary Portland cement specimens in all durability tests [68]. In a study by Valencia-Saavedra et al. [69], the exposure of normal concrete samples to H<sub>2</sub>SO<sub>4</sub> for 7, 28, 90, 180, and 360 days significantly affected the surface of the samples. Clear deterioration in the control concrete was observed after 28 days of exposure to H<sub>2</sub>SO<sub>4</sub>, intensifying over prolonged exposure periods. In contrast, the effect of the acid solution on GPC was notably lower compared to normal concrete, as illustrated in Figure 2. While, table 3 shows the resistance of geopolymer against acid attacks.

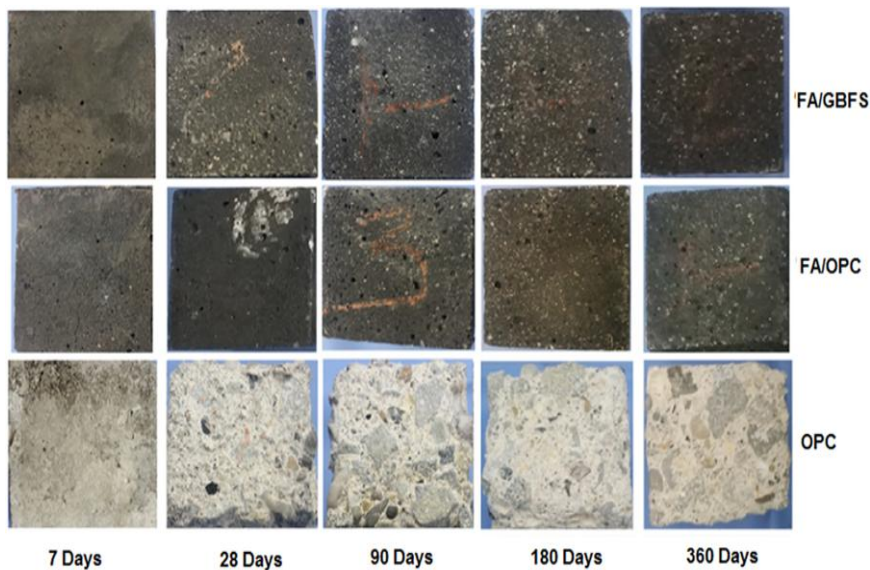


Fig. 2. Appearance of concrete samples exposed to H<sub>2</sub>SO<sub>4</sub> for different periods [69]

Table 3. Resistance of geopolymer against acid attacks

| References              | Type of acid                                      | Aluminosilicate           | Alkali activator                          | Effect on the GPC   |
|-------------------------|---|---------------------------|---|---|
| Albegmprli et al., [41] | H <sub>2</sub> SO <sub>4</sub> % in 0, 5, and 10% | GGBS, fly ash, and cement | NaOH and Na <sub>2</sub> SiO <sub>3</sub> | Even though the GPC has better resistance to acid attacks than cement concrete. However, degradation in the properties of GPC has been shown also due to exposure to the H <sub>2</sub> SO <sub>4</sub> , especially at a concentration of 10%. |

|                                |   |                                     |   |  |
|--------------------------------|---|-------------------------------------|---|--|
| Valencia-Saavedra et al., [69] | Acetic acid (CH <sub>3</sub> -COOH) and sulfuric acid (H <sub>2</sub> SO <sub>4</sub> ) | Fly ash, GGBS, and cement           | NaOH and Na <sub>2</sub> SiO <sub>3</sub> | The GPC samples exposed to the acid solutions had lower mass loss of up to 6%, while in the case of normal concrete reached up to 19%.                         |
| Yang et al. [70]               | H <sub>2</sub> SO <sub>4</sub>  | Metakaolin and fly ash              | NaOH and Na <sub>2</sub> SiO <sub>3</sub> | Minor deterioration was noted for samples of GPC exposed to H <sub>2</sub> SO <sub>4</sub> in terms of mass loss, neutralization depth, and visual appearance. |
| Pham et al. [71]               | H <sub>2</sub> SO <sub>4</sub>  | Ultrafine slag, cement, and fly ash | NaOH and Na <sub>2</sub> SiO <sub>3</sub> | GPC with crumb rubber showed poorer resistance to acid attacks (H <sub>2</sub> SO <sub>4</sub> and HCl).   |

## 5.2. Resistance to Sulfate Attacks

GPC is recognized for its potential durability advantages over traditional Portland cement concrete [72], particularly in terms of superior resistance to various chemical attacks, including sulfate attacks [73]. Sulfate attack is a concrete deterioration process initiated by the reaction of sulfates in the environment with concrete components, leading to the formation of expansive and disruptive compounds [74]. Unlike conventional Portland cement concrete, GPC employs industrial by-products like fly ash or slag as binders, contributing to an inherently improved resistance to sulfate attack [75].

The geopolymerization process involved in GPC results in the formation of a robust three-dimensional network structure, imparting greater resilience to chemical attacks when compared to the calcium silicate hydrate gel found in traditional concrete [76]. The resistance of GPC to sulfate attack is further influenced by factors such as specific mix design, curing conditions, and the type and concentration of sulfates in the environment [68, 75]. Numerous research studies have been conducted to evaluate the durability properties of GPC, with a specific focus on its resistance to sulfate attack. The insights gained from these studies contribute to an evolving understanding of the material's performance. Table 4 provides a summary of results obtained from previous studies related to the resistance of GPC to sulfate attacks.

Sulfate ions exist in water and soil in various forms [81]. These ions can penetrate concrete samples through the pores on the concrete surface, subsequently reacting with cement hydration to produce gypsum and ettringite. This reaction can lead to spalling and cracks in the concrete surfaces [82]. Lingyu et al. [83] observed that the permeability of GPC samples increases with an elevated Si/Al ratio in GPC made of metakaolin. Additionally, Nasir et al. [84] reported that exposure of GPC samples to sodium sulfate (Na<sub>2</sub>SO<sub>4</sub>) results

in a reduction in the Ca/Si ratio. The nature of GPC samples makes them more durable and has higher resistance against sulfate attacks as compared to normal concrete [75].

Table 4. Resistance of geopolymer against sulfate attacks

| References         | Aluminosilicate        | Alkali activator                          | Effect on the GPC  |
|--------------------|------------------------|---|--|
| Uğurlu et al. [77] | GGBS                   | Na <sub>2</sub> SiO <sub>3</sub> and NaOH | The resistance to sulfate attacks increases as the binder content amount in the GPC mix increases.   |
| Guo et al. [78]    | Metakaolin (MK)        | Na <sub>2</sub> SiO <sub>3</sub> and NaOH | The resistance against sulfate attacks improved due to the incorporation of hybrid fibers to reduce the stress, preventing the formation of pore cracks and prevent the development of micro-cracks. |
| Guo et al. [79]    | Fly ash and steel slag | Na <sub>2</sub> SiO <sub>3</sub> and NaOH | The addition of steel fiber into GPC mix enhanced the strength.<br>Also, the steel fiber has a significant role in the resistance of GPC mortar against sulfate attacks.                             |
| Kuri et al. [80]   | Slag and fly ash       | Na <sub>2</sub> SiO <sub>3</sub> and NaOH | The low content of calcium in slag assists in improving the resistance of the GPC samples against sulfate attacks.   |

### 5.3. Permeability of Geopolymer

Geopolymers, like other materials, demonstrate diverse permeability characteristics influenced by factors such as composition, curing conditions, and microstructure [85]. Inorganic geopolymers typically arise from the combination of aluminosilicate substances with an alkaline activator solution, known for their robust construction and chemical resistance [22]. Permeability, defined as the material's ability to allow the passage of gases, liquids, or ionic species, including water, is a critical attribute in assessing durability properties [86]. The presence of pores in concrete renders it vulnerable to the ingress of detrimental ions, leading to various adverse effects. Water, in particular, can induce ice formation in large paste pores, facilitate leaching of compounds from the paste, transport chlorides or acids into the paste, and result in the leaching of calcium hydroxide from the cement paste. Table 5 presents the factors affecting the permeability of GPC.

Table 5. Resistance of geopolymer against permeability

| References       | Aluminosilicate | Alkali activator                          | Effect on the GPC  |
|------------------|-----------------|---|--|
| Ross et al. [87] | Fly ash         | Na <sub>2</sub> SiO <sub>3</sub> and NaOH | The geopolymer paste has lower permeability compared to the cement |



|                   |                |                                    |   |
|-------------------|----------------|------------------------------------|---|
|                   |                |                                    | paste, its recorded only $0.26 \pm 0.09 \mu\text{D}$ at 28 curing days.   |
| Nasvi et al. [88] | Fly ash        | $\text{Na}_2\text{SiO}_3$ and NaOH | The permeability of GPC decreases due to increase of confining Pressure and decrease the connectivity of pores.   |
| Arafa et al. [89] | Fly ash        | $\text{Na}_2\text{SiO}_3$ and NaOH | The coefficient of water permeability for the GPC made of biomass aggregate was not considerably different from that of normal concrete prepared from normal aggregates. However, the use of agricultural waste improves waste management and encourages the adoption of eco-friendly concrete. |
| Zhang et al. [90] | MK and fly ash | $\text{Na}_2\text{SiO}_3$ and NaOH | The permeability significant affected by the pore connectivity, pore size, and porosity of the GP foam concrete.  |

#### 5.4. Fire Resistance

GPC, as a material, generally exhibits fire-resistant properties [91]. However, the dehydration and breakdown of crystalline hydrates, aggregate types, permeability, and other factors result in a residual strength of ordinary Portland cement (OPC) concrete typically not exceeding 20-30% after exposure to temperatures between 800°C and 1000°C [92]. The temperature range of 25-910°C induces structural changes in the cement gels of concrete PENLY and TEMELIN under heat load [93]. Alterations in micro- and mesoporous areas are studied through physical nitrogen adsorption and mercury porosimeter. Up to around 500°C, corresponding to the disintegration of  $\text{Ca}(\text{OH})_2$  into CaO, there is an observed increase in pore volume and surface area.

Table 6. Resistance of geopolymer against sulfate attacks

| References            | Aluminosilicate | Alkali activator                  | Effect on the GPC  |
|-----------------------|-----------------|-----------------------------------|--|
| Wang et al. [95]      | MK and fly ash  | NaOH and $\text{Na}_2\text{SO}_4$ | The addition of kaliophilite significantly enhanced the resistance against fire of GPC samples.  |
| Nuaklong et al. [96]  | Fly ash         | NaOH and $\text{Na}_2\text{SO}_4$ | The addition of granite waste into the oven-dried and air-dried aggregates of the GPC mixture has a minor effect on the fire resistance of GPC |
| Abd Razak et al. [97] | Fly ash         | NaOH and $\text{Na}_2\text{SO}_4$ | Increase the temperature from 500 C to 1200 C led to reduce the performance of GPC sample. However, the  |

|                      |   |   |
|----------------------|---|---|
|                      |   | GPC samples still better strength and durable than cement concrete. |
| Nuaklong et al. [98] | Fly ash, rice husk ash, and nano-silica | NaOH and Na <sub>2</sub> SO <sub>4</sub>                            |

Investigating geopolymers and geopolymer-aggregate composites derived from class F fly ash, samples heated to 800°C showed strength improvements of about 53% for geopolymers [94]. However, geopolymer/aggregate composites, using the same geopolymer binder compositions, experienced a strength decrease of up to 65%. Dilatometry measurements revealed linear growth in aggregate size with increasing temperature, expanding by approximately 1.5% to 2.5% at 800 °C. Conversely, the geopolymer matrix shrank by about 1% between 200 and 300 °C and an additional 0.6% between 700°C and 800°C [94]. Table 6 shows the resistance of GPC against the fire resistance. As indicated in Table 6, several factors influence the fire resistance of GPC. Nuaklong et al. [98], conducted a study on the impact of high calcium fly ash (HCFA), nano silica (nS), and rice husk ash (RHA) as binder materials in the production of GPC containing recycled aggregate concrete (RAC). They observed that the use of recycled aggregate (RCA) in GPC led to an enhancement in the loss of strength and durability during the initial 30 minutes of exposure to fire. However, GPC samples made of both RCA and natural aggregate no longer maintained their dimensional stability, as depicted in Figure 3.

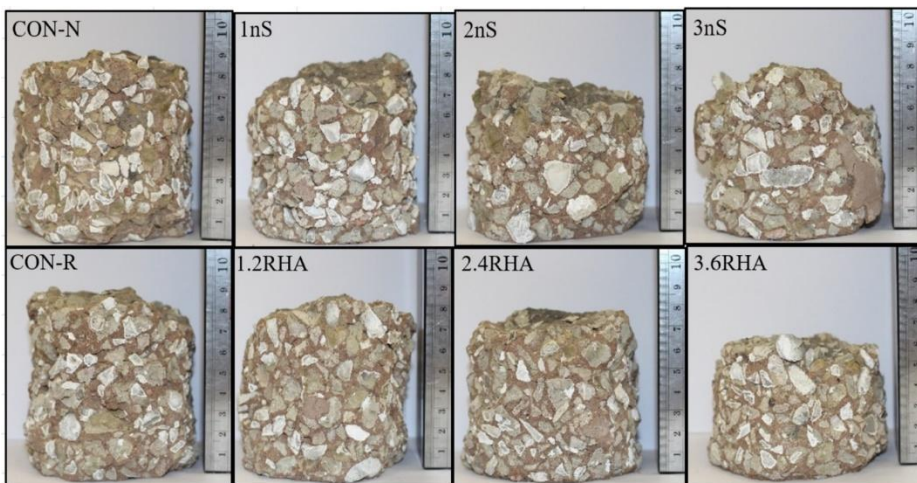


Fig. 3. Shape of fire-damaged samples exposed to fire for 90 minutes [98]

### 5.5 Chloride Ion Penetration

Chloride ion penetration is one of the important tests that determine the durability of GPC, and existence in marine and coastal areas. Chloride ions can penetrate the concrete matrix and reach the embedded steel reinforcement, leading to corrosion and ultimately compromising the structural integrity of the GPC. Factors influencing chloride ion penetration include the permeability and porosity of the concrete, the existence of cracks or other defects, the curing regime, and the type and content of SCMs. Saif et al. [57] examined the effect of curing conditions and MK content on the resistance against chloride penetration. They exposed the GPC samples to chemical solutions of (10% NaCl, H<sub>2</sub>SO<sub>4</sub> (pH=3, and 10% MgSO<sub>4</sub>) for 10 weeks then tested the compressive strength and change in

weight. They observed that the use of MK in GPM displays better performance than that of normal concrete when exposed to harsh environments. Another study by Okoye et al. [99] examined the effect of silica fume on the durability of GPC by immersing the samples in 5% sodium chloride (NaCl) and 2% sulfuric acid ( $H_2SO_4$ ) solutions. They measured the weight loss and compressive strength loss after exposure the samples for different periods. One of the samples was fixed as control mix made from OPC concrete for comparison, called M40. They observed that there was a minor losing in weight for the GPC samples due to exposure these samples to NaCl solution in different periods. However, the GPC samples have lower weight losses than that of M40 as shown in Figure 4, means that GPC samples have higher resistant against chloride attack.

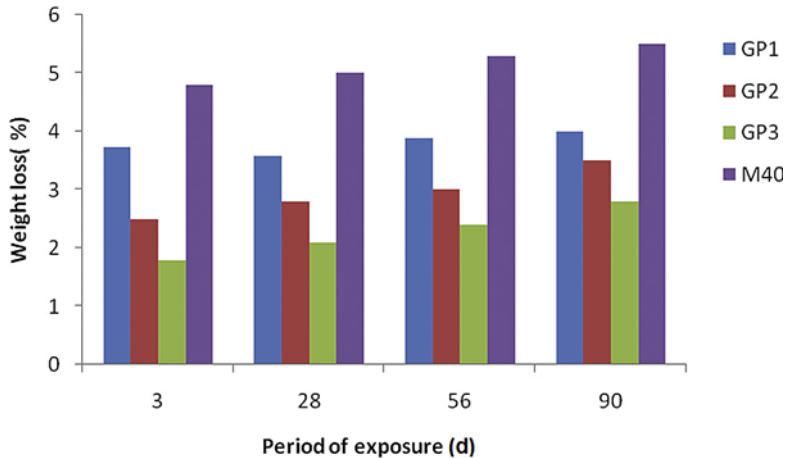


Fig. 4. Weight loss vs exposure periods for GPC and M40 samples in 5% NaCl [99]

Chindaprasirt and Chalee [100] investigated the influence of the concentration of sodium hydroxide on steel corrosion and chloride penetration of GPC containing fly ash at marine environment. They used different concentrations of sodium hydroxide from 8 to 18 molarity. The samples of GPC were tested for corrosion, chloride penetration, and compressive strength after three years exposure. They found that the increase concentration of sodium hydroxide led to reduce the corrosion and chloride penetration values. Therefore, it has a positive effect on the durability of GPC. Halim and Ekaputri [101] examined the effect of salt water on the performance of GPC made of sodium silicate and 8 molar sodium hydroxides as the alkali solution and fly ash as binder material. They immersed some samples in 3.5% concentration of salt water, while other samples were cured in normal water, as a control samples. They observed that the chloride penetration in GPC is higher than normal cement concretes, and GPC samples have higher compressive strength than that of normal cement concretes.

### 5.6 Dry Shrinkage

Dry shrinkage is one of the factors effecting the durability of GPC. It refers to the reduction in volume that occurs when moisture is lost from the concrete without the presence of any external factors such as loading or temperature changes. Dry shrinkage in GPC is primarily attributed to the evaporation of water from the pore structure, leading to a decrease in interparticle forces and subsequent shrinkage. Factors affecting dry shrinkage include the curing conditions, composition of the geopolymer binder, admixtures, and aggregate properties. Numerous researchers investigated the factors effecting dry shrinkage of GPC. For instance, Ahmed et al. [102] examined the effect of clay brick waste on the dry shrinkage of GPC made of metakaolin as a binder material. They used two groups of clay

brick waste, it was clay brick powder as partial metakaolin replacement in proportions of 10, 15 and 20% by weight, the other group involved of waste clay brick as a partial aggregate replacement in proportions of 10, 20 and 30% by volume. They observed that the drying shrinkage of GPC samples increased at early age, and then decreased after 28 days due to use of clay brick waste as powder in GPC, as shown in Figure 5.

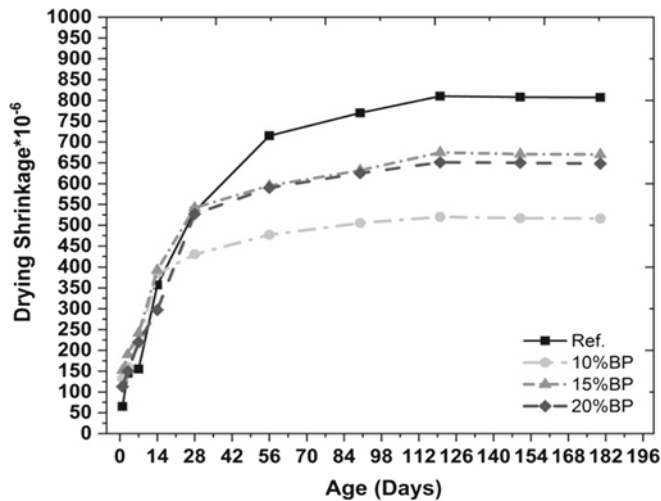


Fig. 5 Effect of clay brick waste powder (BP) on the drying shrinkage of GPC [102]

As mentioned before, drying shrinkage of GPC can be affected by different factors related to curing duration, materials sources and characteristics, mix design, and others. Riddirud et al. [103] conducted a study on the factors affecting the drying shrinkage of GPC made of fly ash. They investigate effect of NaOH concentration, curing temperature, liquid-to-ash ratio, and NaOH concentration on the drying shrinkage of GPC. The results obtained from their study indicated to that the drying shrinkage of GPC is mostly influenced by liquid-to-ash ratio and curing temperature. The increase in liquid-to-ash ratio from 0.4 to 0.7 led to significant increase the drying shrinkage of GPC. Neupane et al. [104] investigated the influence of two types of powders on the drying shrinkage of GPC, namely fly ash and cement at ambient curing condition. They observed that the drying shrinkage of cement concrete was similar to that of GPC. This value also depends on numerous factors such as additives types, workability, water content, and binder types.

### 5.7 Carbonation

Carbonation is an important durability concern for GPC structures, as it can lead to a reduction in alkalinity and subsequent corrosion of embedded steel reinforcement. Carbonation occurs when carbon dioxide from the atmosphere reacts with calcium hydroxide in the concrete to form calcium carbonate. This process reduces the pH of the concrete, which can accelerate the corrosion of steel reinforcement. Factors affecting carbonation include the content and type of alkaline activator, exposure to carbon dioxide, curing conditions, and the existence of SCMs. Grengg et al. [105] observed that the corrosion rates of GPC was ranging between (1.4 mm/a) and (13.3 mm/a), and reported that the well-designed GPC mixtures significantly contribute in enhancing resistance against carbonation. As reported by Law et al. [106], the carbonation is hypothesized as the reaction of the  $\text{CO}_2$  with sodium hydroxide (NaOH) making sodium carbonate  $\text{NaCO}_3 + \text{H}_2\text{O}$ . The lower content of 7.5% in geopolymer mortar having a somewhat lesser pH than those having content 15%. Zhuguo and Sha [107] investigated the effect of two waste

materials, namely GGBS and fly ash on the carbonation resistance of geopolymer mortars and GPC at various elapsed times. They found that the resistance against carbonation of GGBS and fly ash-based GPC treated at ambient curing is lower than those of normal cement concretes. Finally, they concluded that the increase of NaOH, GGBS ratios, and GGBS fineness, leads to increase of carbonation resistance of GPC and GP mortars. For long curing age, Pasupathy et al. [108] examined the carbonation resistance of GPC exposed to normal conditions for eight years. They detected that the carbonation degree of GPC is extremely affected by the activator materials of GPC. The first group of GPC samples including  $\text{Na}_2\text{SiO}_3$  activator, 25% GGBFS and 75% fly ash presented a weak resistance against carbonation compared to normal cement concretes. But, the second group of GPC samples involved 30% GGBS and 70% fly ash and without additional  $\text{Na}_2\text{SiO}_3$  activator, was alike to cement concrete samples.

## **6. Conclusion**

In conclusion, this paper underscores the remarkable potential of geopolymers as a cutting-edge and environmentally friendly class of materials, demonstrating numerous advantages over traditional Portland cement. The findings from this study shed light on the effect of various factors on the durability properties of GPC, emphasizing the following key points:

- Geopolymers significantly reduce the carbon footprint associated with construction materials by utilizing industrial by-products and scraps, thereby contributing to sustainable and eco-friendly practices in the construction industry.
- Geopolymers exhibit exceptional mechanical properties, including impressive compressive strength and durability. These attributes position geopolymers as promising alternatives to traditional building materials, enhancing overall structural integrity.
- The inherent resistance of geopolymers to a diverse range of chemical agents makes them invaluable in applications within the chemical industry and for waste encapsulation, broadening their utility across various sectors.
- Properly formulated and cured geopolymers can exhibit low permeability, proving advantageous in situations where resistance to water and gas penetration is crucial for the longevity of structures.
- Geopolymers showcase better resistance against acid and sulfate attacks as compared to normal concrete.
- Geopolymers showcase inherent fire-resistant characteristics, making them highly desirable for applications in fire-prone environments and the development of fireproof building materials.
- The GPC samples have better resistance against chloride and carbonation than that of normal cement concrete. Besides, numerous factors affect the carbonation and chloride penetration such as the permeability and porosity of the concrete, the existence of cracks, the curing regime, the SCM type, etc.

In light of their demonstrated durability, strength, and resilience to extreme climatic conditions, geopolymers emerge as a viable and sustainable alternative to conventional construction and building materials. As technology and knowledge progress, the increased integration of geopolymers holds the promise of fostering sustainable practices in building, infrastructure, and various industrial applications. The comprehensive exploration of durability properties, including resistance to acid and sulfate attacks, permeability, and fire resistance, contributes valuable insights for researchers, engineers, and practitioners engaged in the pursuit of resilient and environmentally friendly construction solutions.

## References

- [1] Danish A, Ozbakkaloglu T, Mosaberpanah MA, Salim MU, Bayram M, Yeon JH, et al. Sustainability benefits and commercialization challenges and strategies of geopolymer concrete: A review. *Journal of Building Engineering*. 2022;105005. <https://doi.org/10.1016/j.jobe.2022.105005>
- [2] Shehata N, Mohamed O, Sayed ET, Abdelkareem MA, Olabi A. Geopolymer concrete as green building materials: Recent applications, sustainable development and circular economy potentials. *Science of the Total Environment*. 2022;836:155577. <https://doi.org/10.1016/j.scitotenv.2022.155577>
- [3] Adesina A. Recent advances in the concrete industry to reduce its carbon dioxide emissions. *Environmental Challenges*. 2020;1:100004. <https://doi.org/10.1016/j.envc.2020.100004>
- [4] Pradhan P, Dwibedy S, Pradhan M, Panda S, Panigrahi SK. Durability characteristics of geopolymer concrete-Progress and perspectives. *Journal of Building Engineering*. 2022;105100. <https://doi.org/10.1016/j.jobe.2022.105100>
- [5] Sbahieh S, McKay G, Al-Ghamdi SG. Comprehensive Analysis of Geopolymer Materials: Properties, Environmental Impacts, and Applications. *Materials*. 2023;16(23):7363. <https://doi.org/10.3390/ma16237363>
- [6] Qaidi S, Najm HM, Abed SM, Ahmed HU, Al Dughaisi H, Al Lawati J, et al. Fly ash-based geopolymer composites: A review of the compressive strength and microstructure analysis. *Materials*. 2022;15(20):7098. <https://doi.org/10.3390/ma15207098>
- [7] Manzoor T, Bhat JA, Shah AH. Advancements in Geopolymer Concrete: A State-of-the-Art Analysis of Its Mechanical and Durability Features. *Iranian Journal of Science and Technology, Transactions of Civil Engineering*. 2023:1-40. <https://doi.org/10.1007/s40996-023-01261-0>
- [8] Amran YHM, Alyousef R, Alabduljabbar H, El-Zeadani M. Clean production and properties of geopolymer concrete; A review. *Journal of Cleaner Production*. 2020;251:119679. <https://doi.org/10.1016/j.jclepro.2019.119679>
- [9] Zhang P, Wang K, Li Q, Wang J, Ling Y. Fabrication and engineering properties of concretes based on geopolymers/alkali-activated binders - A review. *Journal of Cleaner Production*. 2020;258:120896. <https://doi.org/10.1016/j.jclepro.2020.120896>
- [10] Hassan A, Arif M, Shariq M. Use of geopolymer concrete for a cleaner and sustainable environment "A review of mechanical properties and microstructure. *Journal of Cleaner Production*. 2019;223:704-28. <https://doi.org/10.1016/j.jclepro.2019.03.051>
- [11] Zhang P, Zheng Y, Wang K, Zhang J. A review on properties of fresh and hardened geopolymer mortar. *Composites Part B: Engineering*. 2018;152:79-95. <https://doi.org/10.1016/j.compositesb.2018.06.031>
- [12] Fahim Huseien G, Mirza J, Ismail M, Ghoshal SK, Abdulameer Hussein A. Geopolymer mortars as sustainable repair material: A comprehensive review. *Renewable and Sustainable Energy Reviews*. 2017;80:54-74. <https://doi.org/10.1016/j.rser.2017.05.076>
- [13] John SK, Nadir Y, Girija K. Effect of source materials, additives on the mechanical properties and durability of fly ash and fly ash-slag geopolymer mortar: A review. *Construction and Building Materials*. 2021;280:122443. <https://doi.org/10.1016/j.conbuildmat.2021.122443>
- [14] Ng C, Alengaram UJ, Wong LS, Mo KH, Jumaat MZ, Ramesh S. A review on microstructural study and compressive strength of geopolymer mortar, paste and concrete. *Construction and Building Materials*. 2018;186:550-76. <https://doi.org/10.1016/j.conbuildmat.2018.07.075>
- [15] Hassan A, Arif M, Shariq M. Use of geopolymer concrete for a cleaner and sustainable environment "A review of mechanical properties and microstructure. *Journal of cleaner production*. 2019;223:704-28. <https://doi.org/10.1016/j.jclepro.2019.03.051>

- [16] Huseien GF, Mirza J, Ismail M, Ghoshal S, Hussein AA. Geopolymer mortars as sustainable repair material: A comprehensive review. *Renewable and Sustainable Energy Reviews*. 2017;80:54-74. <https://doi.org/10.1016/j.rser.2017.05.076>
- [17] Amran YM, Alyousef R, Alabduljabbar H, El-Zeadani M. Clean production and properties of geopolymer concrete; A review. *Journal of Cleaner Production*. 2020;251:119679. <https://doi.org/10.1016/j.jclepro.2019.119679>
- [18] Zhang P, Wang K, Li Q, Wang J, Ling Y. Fabrication and engineering properties of concretes based on geopolymers/alkali-activated binders-A review. *Journal of Cleaner Production*. 2020;258:120896. <https://doi.org/10.1016/j.jclepro.2020.120896>
- [19] Ahmed HU, Mahmood LJ, Muhammad MA, Faraj RH, Qaidi SM, Sor NH, et al. Geopolymer concrete as a cleaner construction material: An overview on materials and structural performances. *Cleaner Materials*. 2022;5:100111. <https://doi.org/10.1016/j.clema.2022.100111>
- [20] Mortada Y, Masad E, Kogbara RB, Mansoor B, Seers T, Hammoud A, et al. Development of Ca (OH) 2-based Geopolymer for Additive Manufacturing Using Construction Wastes and Nanomaterials. *Case Studies in Construction Materials*. 2023:e02258. <https://doi.org/10.1016/j.cscm.2023.e02258>
- [21] Freire AL, Jos   HJ, Moreira RdFPM. Potential applications for geopolymers in carbon capture and storage. *International Journal of Greenhouse Gas Control*. 2022;118:103687. <https://doi.org/10.1016/j.ijggc.2022.103687>
- [22] Luhar I, Luhar S. A comprehensive review on fly ash-based geopolymer. *Journal of Composites Science*. 2022;6(8):219. <https://doi.org/10.3390/jcs6080219>
- [23] Abdellatif M, Abd Elrahman M, Abadel AA, Wasim M, Tahwia A. Ultra-high performance concrete versus ultra-high performance geopolymer concrete: Mechanical performance, microstructure, and ecological assessment. *Journal of Building Engineering*. 2023;79:107835. <https://doi.org/10.1016/j.jobe.2023.107835>
- [24] Zhang H, Li L, Yuan C, Wang Q, Sarker PK, Shi X. Deterioration of ambient-cured and heat-cured fly ash geopolymer concrete by high temperature exposure and prediction of its residual compressive strength. *Construction and Building Materials*. 2020;262:120924. <https://doi.org/10.1016/j.conbuildmat.2020.120924>
- [25] Singh RP, Vanapalli KR, Cheela VRS, Peddireddy SR, Sharma HB, Mohanty B. Fly ash, GGBS, and silica fume based geopolymer concrete with recycled aggregates: Properties and environmental impacts. *Construction and Building Materials*. 2023;378:131168. <https://doi.org/10.1016/j.conbuildmat.2023.131168>
- [26] Hossain KR, Jiang P, Yao X, Wu J, Hu D, Yang X, et al. Additive Manufacturing of Polymer-Based Lubrication. *Macromolecular Materials and Engineering*. 2023;308(11):2300147. <https://doi.org/10.1002/mame.202300147>
- [27] Mukherjee C, Varghese D, Krishna J, Boominathan T, Rakeshkumar R, Dineshkumar S, et al. Recent Advances in Biodegradable Polymers  Properties, Applications and Future Prospects. *European Polymer Journal*. 2023;112068. <https://doi.org/10.1016/j.eurpolymj.2023.112068>
- [28] El-Ghoul Y, Alminderej FM, Alsubaie FM, Alrasheed R, Almousa NH. Recent Advances in Functional Polymer Materials for Energy, Water, and Biomedical Applications: A Review. *Polymers*. 2021;13(24):4327. <https://doi.org/10.3390/polym13244327>
- [29] El Itawi H, Fadlallah S, Allais F, Perre P. Green assessment of polymer microparticles production processes: a critical review. *Green Chemistry*. 2022;24(11):4237-69. <https://doi.org/10.1039/D2GC00578F>
- [30] Mao J, Li C, Jiang H, Zhang H, Yang X, Lin C, et al. Preparation of a novel polymer suspensions with high stabilization, and their superior performances in high salinity. *Journal of Molecular Structure*. 2024;1297:136922. <https://doi.org/10.1016/j.molstruc.2023.136922>
- [31] Dai X, Aydin S, Yardimci MY, De Schutter G. Rheology and structural build-up of sodium silicate-and sodium hydroxide-activated GGBFS mixtures. *Cement and*

- Concrete Composites. 2022;131:104570.  
<https://doi.org/10.1016/j.cemconcomp.2022.104570>
- [32] Ozen S, Uzal B. Effect of characteristics of natural zeolites on their geopolymerization. Case Studies in Construction Materials. 2021;15:e00715.  
<https://doi.org/10.1016/j.cscm.2021.e00715>
- [33] Wang H, Wu H, Xing Z, Wang R, Dai S. The effect of various Si/Al, Na/Al molar ratios and free water on micromorphology and macro-strength of metakaolin-based geopolymer. Materials. 2021;14(14):3845. <https://doi.org/10.3390/ma14143845>
- [34] Ahmed HU, Mohammed AA, Rafiq S, Mohammed AS, Mosavi A, Sor NH, et al. Compressive strength of sustainable geopolymer concrete composites: a state-of-the-art review. Sustainability. 2021;13(24):13502.  
<https://doi.org/10.3390/su132413502>
- [35] Elgarahy AM, Maged A, Eloffy M, Zahran M, Kharbish S, Elwakeel KZ, et al. Geopolymers as sustainable eco-friendly materials: Classification, synthesis routes, and applications in wastewater treatment. Separation and Purification Technology. 2023;124631. <https://doi.org/10.1016/j.seppur.2023.124631>
- [36] Shilar FA, Ganachari SV, Patil VB, Khan TY, Khadar SDA. Molarity activity effect on mechanical and microstructure properties of geopolymer concrete: A review. Case Studies in Construction Materials. 2022;16:e01014.  
<https://doi.org/10.1016/j.cscm.2022.e01014>
- [37] Farooq F, Jin X, Javed MF, Akbar A, Shah MI, Aslam F, et al. Geopolymer concrete as sustainable material: A state of the art review. Construction and Building Materials. 2021;306:124762. <https://doi.org/10.1016/j.conbuildmat.2021.124762>
- [38] Liu J, Doh J-H, Dinh HL, Ong DE, Zi G, You I. Effect of Si/Al molar ratio on the strength behavior of geopolymer derived from various industrial waste: A current state of the art review. Construction and Building Materials. 2022;329:127134.  
<https://doi.org/10.1016/j.conbuildmat.2022.127134>
- [39] de Oliveira LB, de Azevedo AR, Marvila MT, Pereira EC, Fediuk R, Vieira CMF. Durability of geopolymers with industrial waste. Case Studies in Construction Materials. 2022;16:e00839. <https://doi.org/10.1016/j.cscm.2021.e00839>
- [40] Jindal BB, Jangra P, Garg A. Effects of ultra fine slag as mineral admixture on the compressive strength, water absorption and permeability of rice husk ash based geopolymer concrete. Materials Today: Proceedings. 2020;32:871-7.  
<https://doi.org/10.1016/j.matpr.2020.04.219>
- [41] Albegmprli HM, Al-Qazzaz ZK, Rejeb SK. Strength performance of alkali activated structural lightweight geopolymer concrete exposed to acid. Ceramics International. 2022;48(5):6867-73. <https://doi.org/10.1016/j.ceramint.2021.11.240>
- [42] Mahdikhani M, Hatamiyan Sarvandani M. Assessment of the bending bearing capacity of the GGBFS-based geopolymer concrete beams exposed to acidic environment. Archives of Civil and Mechanical Engineering. 2021;21:1-20.  
<https://doi.org/10.1007/s43452-021-00223-5>
- [43] Petrus HTBM, Fairuz FI, Sa N, Olvianas M, Astuti W, Jenie SA, et al. Green geopolymer cement with dry activator from geothermal sludge and sodium hydroxide. Journal of Cleaner Production. 2021;293:126143.  
<https://doi.org/10.1016/j.jclepro.2021.126143>
- [44] Kugler F, Karrer J, Krcmar W, Teipel U. Setting behavior and mechanical properties of concrete rubble fly ash geopolymers. Open Ceramics. 2022;11:100286.  
<https://doi.org/10.1016/j.oceram.2022.100286>
- [45] Ahmed MM, El-Naggar K, Tarek D, Ragab A, Sameh H, Zeyad AM, et al. Fabrication of thermal insulation geopolymer bricks using ferrosilicon slag and alumina waste. Case Studies in Construction Materials. 2021;15:e00737.  
<https://doi.org/10.1016/j.cscm.2021.e00737>



- [46] Pham DQ, Nguyen TN, Le ST, Pham TT, Ngo TD, editors. The structural behaviours of steel reinforced geopolymer concrete beams: An experimental and numerical investigation. Structures; 2021: Elsevier. <https://doi.org/10.1016/j.istruc.2021.04.077>
- [47] Hamzah HK, Huseien GF, Asaad MA, Georgescu DP, Ghoshal S, Alrshoudi F. Effect of waste glass bottles-derived nanopowder as slag replacement on mortars with alkali activation: Durability characteristics. Case Studies in Construction Materials. 2021;15:e00775. <https://doi.org/10.1016/j.cscm.2021.e00775>
- [48] Wang J, Xie J, Wang C, Zhao J, Liu F, Fang C. Study on the optimum initial curing condition for fly ash and GGBS based geopolymer recycled aggregate concrete. Construction and Building Materials. 2020;247:118540. <https://doi.org/10.1016/j.conbuildmat.2020.118540>
- [49] Zia ul Haq M, Sood H, Kumar R, editors. AI-Assisted Geopolymer Concrete Mix Design: A Step Towards Sustainable Construction. International Conference on Artificial Intelligence of Things; 2023: Springer. [https://doi.org/10.1007/978-3-031-48781-1\\_26](https://doi.org/10.1007/978-3-031-48781-1_26)
- [50] Chouksey A, Verma M, Dev N, Rahman I, Upreti K. An investigation on the effect of curing conditions on the mechanical and microstructural properties of the geopolymer concrete. Materials Research Express. 2022;9(5):055003. <https://doi.org/10.1088/2053-1591/ac6be0>
- [51] Poloju KK, Srinivasu K. Impact of GGBS and strength ratio on mechanical properties of geopolymer concrete under ambient curing and oven curing. Materials Today: Proceedings. 2021;42:962-8. <https://doi.org/10.1016/j.matpr.2020.11.934>
- [52] Gholampour A, Ozbakkaloglu T, Ng C-T. Ambient-and oven-cured geopolymer concretes under active confinement. Construction and Building Materials. 2019;228:116722. <https://doi.org/10.1016/j.conbuildmat.2019.116722>
- [53] Singh A, Sandhu V. Effects of alccofine and curing conditions on properties of low calcium fly ash-based geopolymer concrete. Materials Today: Proceedings. 2020;32:620-5. <https://doi.org/10.1016/j.matpr.2020.02.763>
- [54] Suresh K, Muthukannan M, Arun K, Chithambar G, Kanniga D. Influence of incinerated biomedical waste ash and waste glass powder on the mechanical and flexural properties of reinforced geopolymer concrete. Australian Journal of Structural Engineering. 2022;23(3).
- [55] DiÅŸi E, Polat R. The influence of nano-CaO and nano-Al<sub>2</sub>O<sub>3</sub> and curing conditions on perlite based geopolymer concrete produced by the one-part mixing method. Construction and Building Materials. 2022;346:128484. <https://doi.org/10.1016/j.conbuildmat.2022.128484>
- [56] Arunkumar K, Muthukannan M, Sureshkumar A, Chithambarganesh A, Devi RK. Mechanical and durability characterization of hybrid fibre reinforced green geopolymer concrete. Research on Engineering Structures and Materials. 2022;8(1):19-43.
- [57] Saif MS, El-Hariri MOR, Sarie-Eldin AI, Tayeh BA, Farag MF. Impact of Ca<sup>+</sup> content and curing condition on durability performance of metakaolin-based geopolymer mortars. Case Studies in Construction Materials. 2022;16:e00922. <https://doi.org/10.1016/j.cscm.2022.e00922>
- [58] Noushini A, Castel A. The effect of heat-curing on transport properties of low-calcium fly ash-based geopolymer concrete. Construction and Building Materials. 2016;112:464-77. <https://doi.org/10.1016/j.conbuildmat.2016.02.210>
- [59] Gunasekara C, Dirgantara R, Law DW, Setunge S. Effect of curing conditions on microstructure and pore-structure of brown coal fly ash geopolymers. Applied Sciences. 2019;9(15):3138. <https://doi.org/10.3390/app9153138>

- [60] Azarsa P, Gupta R. Comparative study involving effect of curing regime on elastic modulus of geopolymer concrete. *Buildings*. 2020;10(6):101. <https://doi.org/10.3390/buildings10060101>
- [61] Hasnaoui A, Ghorbel E, Wardeh G. Effect of curing conditions on the performance of geopolymer concrete based on granulated blast furnace slag and metakaolin. *Journal of Materials in Civil Engineering*. 2021;33(3):04020501. [https://doi.org/10.1061/\(ASCE\)MT.1943-5533.0003606](https://doi.org/10.1061/(ASCE)MT.1943-5533.0003606)
- [62] Muthukrishnan S, Ramakrishnan S, Sanjayan J, editors. Buildability of geopolymer concrete for 3D printing with microwave heating. Second RILEM International Conference on Concrete and Digital Fabrication: Digital Concrete 2020. [https://doi.org/10.1007/978-3-030-49916-7\\_90](https://doi.org/10.1007/978-3-030-49916-7_90)
- [63] Gholampour A, Ozbakkaloglu T. Oven-cured alkali-activated concrete. *Handbook of advances in Alkali-activated Concrete*: Elsevier; 2022; 157-86. <https://doi.org/10.1016/B978-0-323-85469-6.00019-2>
- [64] Ghafoor MT, Khan QS, Qazi AU, Sheikh MN, Hadi M. Influence of alkaline activators on the mechanical properties of fly ash based geopolymer concrete cured at ambient temperature. *Construction and Building Materials*. 2021;273:121752. <https://doi.org/10.1016/j.conbuildmat.2020.121752>
- [65] Cheng H, Lin K-L, Cui R, Hwang C-L, Chang Y-M, Cheng T-W. The effects of SiO<sub>2</sub>/Na<sub>2</sub>O molar ratio on the characteristics of alkali-activated waste catalyst metakaolin based geopolymers. *Construction and Building Materials*. 2015;95:710-20. <https://doi.org/10.1016/j.conbuildmat.2015.07.028>
- [66] Amran M, Debbarma S, Ozbakkaloglu T. Fly ash-based eco-friendly geopolymer concrete: A critical review of the long-term durability properties. *Construction and Building Materials*. 2021;270:121857. <https://doi.org/10.1016/j.conbuildmat.2020.121857>
- [67] Alyousef R, Ebid AAK, Huseien GF, Mohammadhosseini H, Alabduljabbar H, Poi Ngian S, et al. Effects of Sulfate and Sulfuric Acid on Efficiency of Geopolymers as Concrete Repair Materials. *Gels*. 2022;8(1):53. <https://doi.org/10.3390/gels8010053>
- [68] Kumar R, Verma M, Dev N. Investigation on the effect of seawater condition, sulphate attack, acid attack, freeze-thaw condition, and wetting-drying on the geopolymer concrete. *Iranian Journal of Science and Technology, Transactions of Civil Engineering*. 2022:1-31.
- [69] Valencia-Saavedra WG, de Gutierrez RM, Puertas F. Performance of FA-based geopolymer concretes exposed to acetic and sulfuric acids. *Construction and Building Materials*. 2020;257:119503. <https://doi.org/10.1016/j.conbuildmat.2020.119503>
- [70] Yang W, Zhu P, Liu H, Wang X, Ge W, Hua M. Resistance to sulfuric acid corrosion of geopolymer concrete based on different binding materials and alkali concentrations. *Materials*. 2021;14(23):7109. <https://doi.org/10.3390/ma14237109>
- [71] Pham TM, Lim YY, Malekzadeh M. Effect of pre-treatment methods of crumb rubber on strength, permeability and acid attack resistance of rubberised geopolymer concrete. *Journal of Building Engineering*. 2021;41:102448. <https://doi.org/10.1016/j.jobe.2021.102448>
- [72] Parathi S, Nagarajan P, Pallikkara SA. Ecofriendly geopolymer concrete: A comprehensive review. *Clean Technologies and Environmental Policy*. 2021;23:1701-13. <https://doi.org/10.1007/s10098-021-02085-0>
- [73] Srinivas T, Rao NR. Studies on the behaviour of sulphate attack resistance of low calcium fly ash and slag based geopolymer concrete. *IJCIET*. 2019;10(02):510-8.
- [74] Kanaan D, Soliman AM, Safhi AeM. External Sulfate Attack of Ambient-Cured One-Part Alkali-Activated Self-Consolidating Concrete. *Sustainability*. 2023;15(5):4127. <https://doi.org/10.3390/su15054127>
- [75] Singh RP, Vanapalli KR, Jadda K, Mohanty B. Durability assessment of fly ash, GGBS, and silica fume based geopolymer concrete with recycled aggregates against acid and

- sulfate attack. Journal of Building Engineering. 2023:108354. <https://doi.org/10.1016/j.jobe.2023.108354>
- [76] Ralli ZG, Pantazopoulou SJ. State of the art on geopolymers. International Journal of Structural Integrity. 2021;12(4):511-33. <https://doi.org/10.1108/IJSI-05-2020-0050>
- [77] Ugurlu Al<sup>o</sup>, Karakoç MB, Özcan A. Effect of binder content and recycled concrete aggregate on freeze-thaw and sulfate resistance of GGBFS based geopolymer concretes. Construction and Building Materials. 2021;301:124246. <https://doi.org/10.1016/j.conbuildmat.2021.124246>
- [78] Guo L, Wu Y, Xu F, Song X, Ye J, Duan P, et al. Sulfate resistance of hybrid fiber reinforced metakaolin geopolymer composites. Composites Part B: Engineering. 2020;183:107689. <https://doi.org/10.1016/j.compositesb.2019.107689>
- [79] Guo X, Xiong G. Resistance of fiber-reinforced fly ash-steel slag based geopolymer mortar to sulfate attack and drying-wetting cycles. Construction and Building Materials. 2021;269:121326. <https://doi.org/10.1016/j.conbuildmat.2020.121326>
- [80] Kuri JC, Nuruzzaman M, Sarker PK. Sodium sulphate resistance of geopolymer mortar produced using ground ferronickel slag with fly ash. Ceramics International. 2023;49(2):2765-73. <https://doi.org/10.1016/j.ceramint.2022.09.258>
- [81] Duan X, Yang S, Waclawek S, Fang G, Xiao R, Dionysiou DD. Limitations and prospects of sulfate-radical based advanced oxidation processes. Journal of Environmental Chemical Engineering. 2020;8(4):103849. <https://doi.org/10.1016/j.jece.2020.103849>
- [82] Zhuang Z, Mu S, Guo Z, Liu G, Zhang J, Miao C. Diffusion-reaction models for concrete exposed to chloride-sulfate attack based on porosity and water saturation. Cement and Concrete Composites. 2023:105378. <https://doi.org/10.1016/j.cemconcomp.2023.105378>
- [83] Lingyu T, Dongpo H, Jianing Z, Hongguang W. Durability of geopolymers and geopolymer concretes: A review. Reviews on Advanced Materials Science. 2021;60(1):1-14. <https://doi.org/10.1515/rams-2021-0002>
- [84] Nasir M, Johari MAM, Maslehuddin M, Yusuf MO. Sodium sulfate resistance of alkali/slag activated silico-manganese fume-based composites. Structural Concrete. 2021;22:E415-E29. <https://doi.org/10.1002/suco.202000079>
- [85] Hassan A, Arif M, Shariq M. Influence of microstructure of geopolymer concrete on its mechanical properties—A review. Advances in Sustainable Construction Materials and Geotechnical Engineering: Select Proceedings of TRACE 2018. 2020:119-29. [https://doi.org/10.1007/978-981-13-7480-7\\_10](https://doi.org/10.1007/978-981-13-7480-7_10)
- [86] Milla J, Cavalline TL, Rupnow TD, Melugiri-Shankaramurthy B, Wang K, Lomboy G. Methods of test for concrete permeability: a critical review. Advances in Civil Engineering Materials. 2021;10(1):172-209. <https://doi.org/10.1520/ACEM20200067>
- [87] Ross JH, Genedy M, Juenger MC, van Oort E. Permeability recovery by self-healing of class F fly ash-based geopolymers. Cement. 2022;10:100048. <https://doi.org/10.1016/j.cement.2022.100048>
- [88] Nasvi M, Ranjith P, Sanjayan J. The permeability of geopolymer at down-hole stress conditions: Application for carbon dioxide sequestration wells. Applied energy. 2013;102:1391-8. <https://doi.org/10.1016/j.apenergy.2012.09.004>
- [89] Arafa S, Milad A, Yusoff NIM, Al-Ansari N, Yaseen ZM. Investigation into the permeability and strength of pervious geopolymer concrete containing coated biomass aggregate material. Journal of materials research and technology. 2021;15:2075-87. <https://doi.org/10.1016/j.jmrt.2021.09.045>
- [90] Zhang X, Zhang X, Li X, Tian D, Ma M, Wang T. Optimized pore structure and high permeability of metakaolin/fly-ash-based geopolymer foams from Al- and H<sub>2</sub>O<sub>2</sub>-

- sodium oleate foaming systems. *Ceramics International*. 2022;48(13):18348-60. <https://doi.org/10.1016/j.ceramint.2022.03.094>
- [91] Hassan A, Arif M, Shariq M, Alomayri T, Pereira S. Fire resistance characteristics of geopolymers for environmental sustainability: a review of thermal, mechanical and microstructure properties. *Environment, Development and Sustainability*. 2023;25(9):8975-9010. <https://doi.org/10.1007/s10668-022-02495-0>
- [92] Alhamad A, Yehia S, Lubal<sup>3</sup>y Å%, Elchalakani M. Performance of different concrete types exposed to elevated temperatures: a review. *Materials*. 2022;15(14):5032. <https://doi.org/10.3390/ma15145032>
- [93] Ma G, Jia K, Xie P, Ruhan A, Wang L, Ding X, et al. Physical, mineralogical, thermal, and mechanical properties of aerogel-incorporated concrete exposed to elevated temperatures. *Cement and Concrete Composites*. 2023;140:105089. <https://doi.org/10.1016/j.cemconcomp.2023.105089>
- [94] Kong DL, Sanjayam JG. Damage behavior of geopolymers exposed to elevated temperatures. *Cement and Concrete Composites*. 2008;30(10):986-91. <https://doi.org/10.1016/j.cemconcomp.2008.08.001>
- [95] Wang J, Chen X, Li C, Zhou Z, Du P, Zhang X. Evaluating the effect of kaliophilite on the fire resistance of geopolymers. *Journal of Building Engineering*. 2023:106975. <https://doi.org/10.1016/j.jobe.2023.106975>
- [96] Nuaklong P, Worawatnalunart P, Jongvivalsakul P, Tangaramvong S, Pothisiri T, Likitlersuang S. Pre-and post-fire mechanical performances of high calcium fly ash geopolymers containing granite waste. *Journal of Building Engineering*. 2021;44:103265. <https://doi.org/10.1016/j.jobe.2021.103265>
- [97] Abd Razak SN, Shafiq N, Nikbakht EH, Mohammed BS, Guillaumat L, Farhan SA. Fire performance of fly-ash-based geopolymers: Effect of burning temperature on mechanical and microstructural properties. *Materials Today: Proceedings*. 2022;66:2665-9. <https://doi.org/10.1016/j.matpr.2022.06.491>
- [98] Nuaklong P, Jongvivalsakul P, Pothisiri T, Sata V, Chindaprasirt P. Influence of rice husk ash on mechanical properties and fire resistance of recycled aggregate high-calcium fly ash geopolymers. *Journal of Cleaner Production*. 2020;252:119797. <https://doi.org/10.1016/j.jclepro.2019.119797>
- [99] Okoye FN, Prakash S, Singh NB. Durability of fly ash based geopolymers in the presence of silica fume. *Journal of Cleaner Production*. 2017;149:1062-7. <https://doi.org/10.1016/j.jclepro.2017.02.176>
- [100] Chindaprasirt P, Chalee W. Effect of sodium hydroxide concentration on chloride penetration and steel corrosion of fly ash-based geopolymers under marine site. *Construction and Building Materials*. 2014;63:303-10. <https://doi.org/10.1016/j.conbuildmat.2014.04.010>
- [101] Halim LN, Ekaputri JJ, editors. The influence of salt water on chloride penetration in geopolymers. *MATEC Web of Conferences*; 2017: EDP Sciences. <https://doi.org/10.1051/mateconf/20179701002>
- [102] Ahmed MF, Khalil WI, Frayeh QJ. Effect of waste clay brick on the modulus of elasticity, drying shrinkage and microstructure of metakaolin-based geopolymers. *Arabian Journal for Science and Engineering*. 2022;47(10):12671-83. <https://doi.org/10.1007/s13369-022-06611-0>
- [103] Ridditirum C, Chindaprasirt P, Pimraksa K. Factors affecting the shrinkage of fly ash geopolymers. *International Journal of Minerals, Metallurgy, and Materials*. 2011;18(1):100-4. <https://doi.org/10.1007/s12613-011-0407-z>
- [104] Neupane K, Kidd P, Chalmers D, Baweja D, Shrestha R. Investigation on compressive strength development and drying shrinkage of ambient cured powder-activated geopolymers. *Australian Journal of Civil Engineering*. 2016;14(1):72-83. <https://doi.org/10.1080/14488353.2016.1163765>

- [105] Grengg C, Ukrainczyk N, Koraimann G, Mueller B, Dietzel M, Mittermayr F. Long-term in situ performance of geopolymer, calcium aluminate and Portland cement-based materials exposed to microbially induced acid corrosion. *Cement and Concrete Research*. 2020;131:106034. <https://doi.org/10.1016/j.cemconres.2020.106034>
- [106] Law DW, Adam AA, Molyneaux TK, Patnaikuni I, Wardhono A. Long term durability properties of class F fly ash geopolymer concrete. *Materials and Structures*. 2015;48:721-31. <https://doi.org/10.1617/s11527-014-0268-9>
- [107] Zhuguo L, Sha L. Carbonation resistance of fly ash and blast furnace slag based geopolymer concrete. *Construction and Building Materials*. 2018;163:668-80. <https://doi.org/10.1016/j.conbuildmat.2017.12.127>
- [108] Pasupathy K, Berndt M, Castel A, Sanjayan J, Pathmanathan R. Carbonation of a blended slag-fly ash geopolymer concrete in field conditions after 8 years. *Construction and Building Materials*. 2016;125:661-9. <https://doi.org/10.1016/j.conbuildmat.2016.08.078>

Blank Page



## Performance analysis of fuzzy-LQR and fuzzy-LQG controllers for active vehicle suspension systems

Emre Kemer<sup>\*1,a</sup>, Hasan Başak<sup>2,b</sup>

<sup>1</sup>Faculty of Eng. and Natural Sciences, Electrical-Electronics Eng., Uşak University, Uşak, Türkiye

<sup>2</sup>Faculty of Eng., Electrical-Electronics Eng., Artvin Çoruh University, Artvin, Türkiye

### Article Info

### Abstract

#### Article history:

Received 07 Feb 2024

Accepted 14 Apr 2024

#### Keywords:

FLQR control;

FLQG control;

Road disturbance;

Ride comfort;

Quarter-car suspension system

Suspension systems in vehicles are crucial to both ride quality and driving security. The challenge of creating an effective control mechanism for automotive active suspension systems is addressed in this work. In the event of unforeseen road disturbances, the active suspension systems are intended to deliver a more pleasant ride and good handling. Fuzzy-Linear Quadratic Gaussian (FLQG) and Fuzzy-Linear Quadratic Regulator (FLQR) controllers adapting to road disturbances are proposed to enhance vehicle comfort through the reduction of the driver's overall body acceleration. The simulation findings demonstrate that the FLQR and FLQG controllers are efficient in adjusting the automotive suspension configuration under varying road profiles compared to those of the conventional LQR and LQG controllers.

© 2024 MIM Research Group. All rights reserved.

## 1. Introduction

The suspension systems of vehicles maintain the wheels in a near position with the chassis while travelling. The currently available vehicle suspension technology can be categorized as active, semi-active and passive suspension systems. Energy absorption in passive suspensions reduces road impacts without active control, while semi-active suspensions offer dynamic adjustments to stiffness or damping, optimizing flexibility across different road surfaces [1]. An actuator in the active suspension system introduces additional forces between the tires and the vehicle, implementing an active control strategy. This system creates adjustable suspension control forces to guarantee that the vehicle's handling is smooth and stable [2]. Active suspension systems in vehicles aim to ensure ride comfort, road holding, and passenger safety for different road irregularities. To utilize the potential of active suspension systems, the control algorithms should deal with changing road profiles. The control objectives of active suspension systems are passenger comfort, minimum vehicle body acceleration, and road handling. In the literature, various control algorithms have been designed for active suspension systems. Adaptive control [3] enables the suspension system to adapt its parameters in real-time based on feedback signals, thus ensuring adaptability to changing road conditions and vehicle dynamics. However, adaptive control suffers from computational complexity and tuning challenges. Sliding mode control [4,5], employs discontinuous control laws to provide robust performance in the presence of uncertainties and disturbances. Nevertheless, it can exhibit chattering phenomena and require careful design to mitigate undesirable effects. Despite efforts to address chattering, the phenomenon may still affect the stability of the system. Therefore,

\*Corresponding author: [emre.kemer@usak.edu.tr](mailto:emre.kemer@usak.edu.tr)

<sup>a</sup>orcid.org/0000-0001-8716-1971; <sup>b</sup>orcid.org/0000-0002-3724-6819

DOI: <http://dx.doi.org/10.17515/resm2024.177ce0207rs>

Res. Eng. Struct. Mat. Vol. 11 Iss. 1 (2025) 45-57

combining sliding mode control with PI/PID and fuzzy control can be addressed to obtain a control algorithm that can manage chattering while ensuring stable and robust performance [6, 7]. Model predictive control [8], utilizes predictive models of vehicle dynamics to generate optimal control actions over a finite time horizon, offering precise control while considering future system states and constraints. However, model predictive control may entail high computational demands and require accurate models for effective implementation. Fuzzy control [9] utilizes linguistic variables and fuzzy rules to achieve adaptive and intuitive control of suspension systems. Fuzzy control may lack robustness in handling uncertainties and external disturbances. Therefore,  $H_\infty$  control theory combines fuzzy logic to achieve robust performance and disturbance rejection [10]. Yet, it may introduce complexity in controller design and tuning due to the integration of multiple control strategies. PID controller based on the genetic algorithm [8] offers a straightforward yet effective approach to suspension control. Nonetheless, PID controllers exhibit limited adaptability to varying operating conditions. Adaptive fuzzy PID control [9] integrates fuzzy logic with PID control to enhance adaptability and robustness. However, it suffers from complexity in design and tuning due to the combination of multiple control techniques. A state feedback optimal control law namely Linear Quadratic Regulator (LQR) is designed to obtain optimal performance without deteriorating conflict design requirements [11,12]. LQR offers guaranteed stability, robustness, and a structured design method for multiple-input multiple-output systems. The LQR approach computes an optimal state-feedback gain by minimizing a quadratic performance index, which consists of the state and input variables penalized by the weighting matrices. Linear Quadratic Gaussian (LQG) control [13] combines optimal control theory with state estimation techniques to design controllers that minimize a quadratic cost function while accounting for uncertainties and noise.

Fuzzy logic can capture the complex and nonlinear relationships inherent in suspension dynamics. By encoding expert knowledge and linguistic variables into fuzzy rule sets, fuzzy logic enables the controller to make intuitive and adaptive decisions in response to varying road conditions. On the other hand, LQR and LQG controllers provide robust mathematical frameworks for optimal control design. These controllers leverage system models and performance criteria to synthesize control laws that minimize the system's performance such as ride comfort and handling stability. In this study, Fuzzy-LQR (FLQR) and Fuzzy-LQG (FLQG) controllers are proposed for enhancing the performance of the active suspension system. FLQR and FLQG approaches integrate the adaptive and intuitive decision-making capabilities of fuzzy logic with the rigorous optimization principles of LQR and LQG control. This combination enables the controller to effectively adapt to changing operating conditions while optimizing the system's performance. The developed fuzzy controllers are evaluated by comparing their performances with those of the standard LQR and LQG controllers in terms of vehicle body acceleration, suspension deflection, and tire deflection. Simulation results have shown that the designed fuzzy controllers can achieve better closed-loop responses.

The structure of the remaining article is as follows: Section 2 introduces the model of an active suspension system, followed by the development of FLQR and FLQG controllers in Section 3. Section 4 gives simulation results and provides a discussion of the outcomes, and Section 5 gives the conclusions of the paper.

## **2. Material and Method**

### **2.1. Quarter Active Suspension System**

This section outlines the dynamic equations that govern the behavior of a quarter-active suspension system. The quarter active suspension system is depicted in Fig. 1. The system



has two inputs (control input  $F$  and the road surface position,  $z_r$ ). The vehicle body displacement and the tire displacement are denoted by  $z_s$  and  $z_{us}$  from the ground respectively.

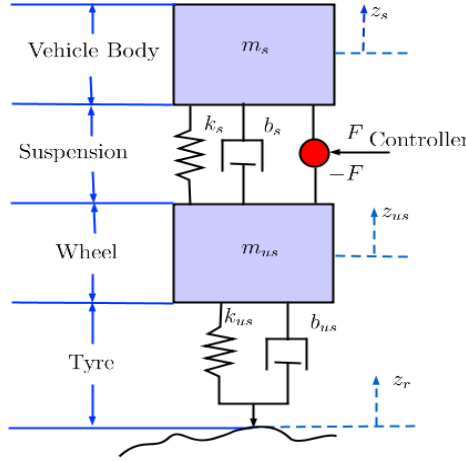


Fig. 1. Diagram of the quarter active vehicle suspension system

The quarter active suspension system equations of motion are derived in [14] using the Newton law as follows:

$$m_{us}\ddot{z}_{us} = -b_{us}\dot{z}_{us} - b_s\dot{z}_{us} - F + b_s\dot{z}_s + b_{us}\dot{z}_r - (z_{us} - z_s)k_s - (z_{us} - z_r)k_{us} \quad (1)$$

$$m_s\ddot{z}_s = b_s\dot{z}_{us} + F - b_s\dot{z}_s - (z_s - z_{us})k_s \quad (2)$$

Eqs. (1)-(2) can be given in the state-space realization as:

$$\begin{aligned} \dot{x}(t) &= \mathcal{A}x(t) + \mathcal{B}u(t) \\ y(t) &= \mathcal{C}x(t) + \mathcal{D}u(t) \end{aligned} \quad (3)$$

where the state variable vector is  $x = [x_1 \ x_2 \ x_3 \ x_4] = [(z_s - z_{us}) \ \dot{z}_s \ (z_{us} - z_r) \ \dot{z}_{us}]^T$  and the input vector is  $u = [\dot{z}_r \ F]^T$  and the output vector is  $y = [(z_s - z_{us}) \ \ddot{z}_s]^T$ .  $(z_s - z_{us})$  and  $(z_{us} - z_r)$  are the suspension and tyre deflections,  $\dot{z}_s$  and  $\dot{z}_{us}$  are the body and the tyre vertical velocities respectively. The following matrices are obtained:

$$\begin{aligned} \mathcal{A} &= \begin{bmatrix} 0 & 1 & 0 & -1 \\ \frac{-k_s}{m_s} & \frac{-b_s}{m_s} & 0 & \frac{b_s}{m_s} \\ 0 & 0 & 0 & 1 \\ \frac{k_s}{m_{us}} & \frac{b_s}{m_{us}} & \frac{-k_{us}}{m_{us}} & \frac{-(b_s+b_{us})}{m_{us}} \end{bmatrix}, & \mathcal{B} &= \begin{bmatrix} 0 & 0 \\ 0 & \frac{1}{m_s} \\ -1 & 0 \\ \frac{b_{us}}{m_{us}} & \frac{-1}{m_{us}} \end{bmatrix} \\ \mathcal{C} &= \begin{bmatrix} 1 & 0 & 0 & 0 \\ \frac{-k_s}{m_s} & \frac{-b_s}{m_s} & 0 & \frac{b_s}{m_s} \end{bmatrix}, & \mathcal{D} &= \begin{bmatrix} 0 & 0 \\ 0 & \frac{1}{m_s} \end{bmatrix}. \end{aligned} \quad (1)$$

Table 1 provides the specifications of the quarter active suspension system.

Table 1. Model parameters [14]

| Symbol   | Value   | Definition    |
|----------|---------|---------------|
| $m_s$    | 2.45 kg | Sprung Mass   |
| $m_{us}$ | 1 kg    | Unsprung Mass |

|          |          |   |
|----------|----------|---|
| $k_s$    | 900 N/m  | Suspension Stiffness                    |
| $k_{us}$ | 1250 N/m | Tire Stiffness                          |
| $b_s$    | 7.5 Ns/m | Suspension Inherent Damping coefficient |
| $b_{us}$ | 5 Ns/m   | Tire Inherent Damping coefficient       |

### 2.1.1 Performance Requirements

The active suspension system's performance criteria are given in [15] as:

- 1) **Ride comfort:** The vehicle body acceleration  $\ddot{z}_s$  must be reduced by the active suspension system.
- 2) **Suspension deflection:** The active suspension system has to maintain the suspension deflection within the allowable interval to avoid vehicle damage.  $|z_s - z_{us}| \leq \bar{z}$ ,  $\bar{z}$  is the greatest acceptable suspension deflection ( $\bar{z} = 0.038$ ).
- 3) **Road handling:** The wheel assembly has to stay in firm contact with the road to ensure passenger safety. Therefore, the tire's dynamic load has to be smaller than its static load ( $|k_s(z_{us} - z_r)| \leq (m_s + m_{us})g$ ).

## 3. Fuzzy-LQR and Fuzzy-LQG Controller Development

### 3.1. LQR Control

Consider the following linear time-invariant system:

$$\begin{aligned} \dot{x}(t) &= \mathcal{A}x(t) + \mathcal{B}u(t), & x(0) &= x_0 \\ y(t) &= \mathcal{C}x(t) + \mathcal{D}u(t) \end{aligned} \tag{5}$$

in which  $x(0)$  is the initial condition. The purpose is to find the optimal control law,  $u(t)$  which can drive the state variables of the dynamics to demand ones by optimizing the following equation:

$$J = \int_0^{\infty} x^T(t)Qx(t) + u^T(t)\mathcal{R}u(t)dt, \tag{6}$$

Here  $Q$  is the positive semi-definite and  $\mathcal{R}$  is the positive-definite weighting matrices. Diagonal weighting matrices are generally selected. The order of  $Q$  and  $\mathcal{R}$  matrices are equal to the number of states and inputs. Bryson's rule is used to obtain acceptable  $Q$  and  $\mathcal{R}$  matrices in the literature. Initially  $Q = I$  and  $\mathcal{R} = \gamma I$  can be used. Assume that  $(\mathcal{A}, \mathcal{B})$  is stabilisable and  $(\mathcal{A}, \mathcal{C})$  is observable, then the LQR controller computes as follows:

$$u(t) = -Kx(t) \tag{7}$$

in which  $K$  is the optimal state-feedback gain computed by  $K = \mathcal{R}^{-1}\mathcal{B}^T\mathcal{P}$  that is called the Lagrange multiplier based on optimization. The positive definite-matrix,  $\mathcal{P}$  is obtained from the solution of the following Algebraic Riccati Equation [16]:

$$\mathcal{A}^T\mathcal{P} + \mathcal{P}\mathcal{A} + Q - \mathcal{P}\mathcal{B}\mathcal{R}^{-1}\mathcal{B}^T\mathcal{P} = 0 \tag{8}$$

### 3.2. Fuzzy-LQR Control

Fuzzy-LQR controller consists of an LQR control and a fuzzy control. The FLQR control structure is given in Fig. 2. A linear fusion function is used including error (E) and error change (EC) which reduces the number of rules for the fuzzy logic control [17]. The linear fusion function,  $F_1(X)$  is given as follows.

$$F_1(X) = \begin{vmatrix} K_{x_1} & 0 & K_{x_3} & 0 \\ 0 & K_{x_2} & 0 & K_{x_4} \end{vmatrix} \tag{2}$$

and E and EC are computed as:

$$\begin{vmatrix} E \\ EC \end{vmatrix} = F_1(X) \begin{vmatrix} x_1 \\ x_2 \\ x_3 \\ x_4 \end{vmatrix} \tag{3}$$

$$E = K_{x_1} x_1 + K_{x_3} x_3 \tag{4}$$

$$EC = K_{x_2} x_2 + K_{x_4} x_4$$

Here, the purpose of developing the Mamdani-type fuzzy model is to set the closed-loop state-feedback gains. The transformation of the input variables (E and EC) and the output variable (Fc) into linguistic variables is performed as: (ZE-zero error, PS-positive small, PM-positive medium, PB-positive big, NB-negative big, NM-negative medium, NM-negative small) [18]. The fuzzy rules of the controller are given in Table 2. As can be seen from the table, there exist 49 rules which are implemented to control the active suspension system.

Table 2. Fuzzy Logic Rules

| E  | EC |    |    |    |    |    |    |
|----|----|----|----|----|----|----|----|
|    | NB | NM | NS | ZE | PS | PM | PB |
| NB | NB | NB | NB | NM | NM | NS | ZE |
| NM | NB | NB | NB | NM | NS | ZE | PS |
| NS | NS | NM | NM | NS | ZE | PS | PM |
| ZE | NM | NM | NS | ZE | PS | PM | PB |
| PS | NM | NS | ZE | PS | PM | PM | PB |
| PM | NS | ZE | PS | PM | PM | PB | PB |
| PB | ZE | PS | PM | PM | PB | PB | PB |

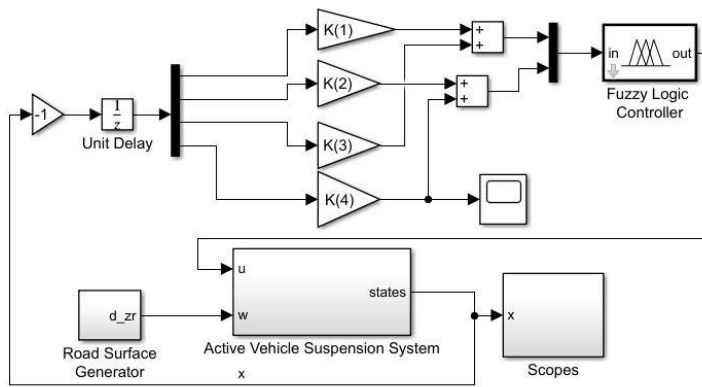


Fig. 2. FLQR control structure

The input variables, E and EC vary in intervals [-10 10 cm]. The output variable changes in the interval [-38.5 38.5 N]. The input and output variables are inferred graphically using triangular membership functions. Figs. 3, 4 and 5 illustrate the membership of the input and output variables. The relationship between the FLC's inputs and outputs is depicted in Fig. 6

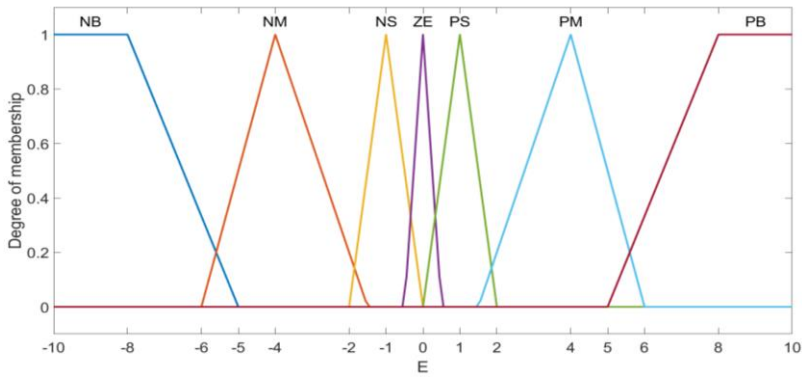


Fig. 3. The membership functions of the input variable, E

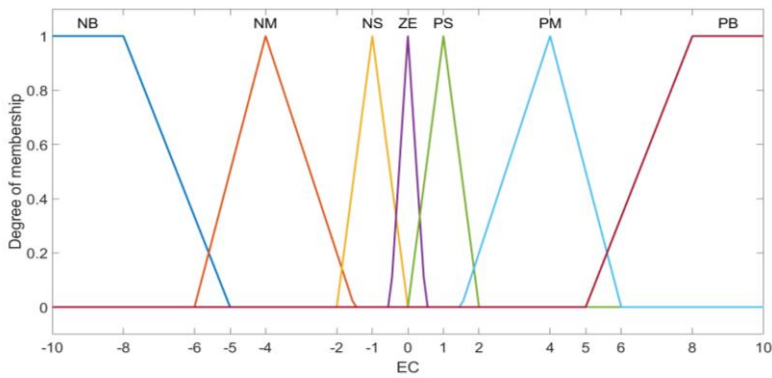


Fig. 4. The membership functions of the input variable, EC

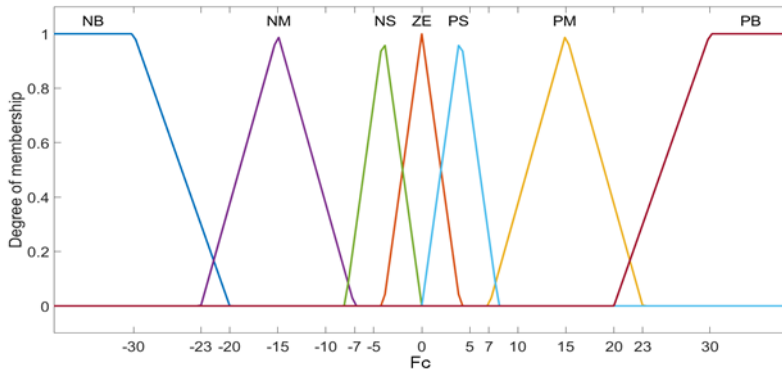


Fig. 5. The membership functions of the input variable, Fc

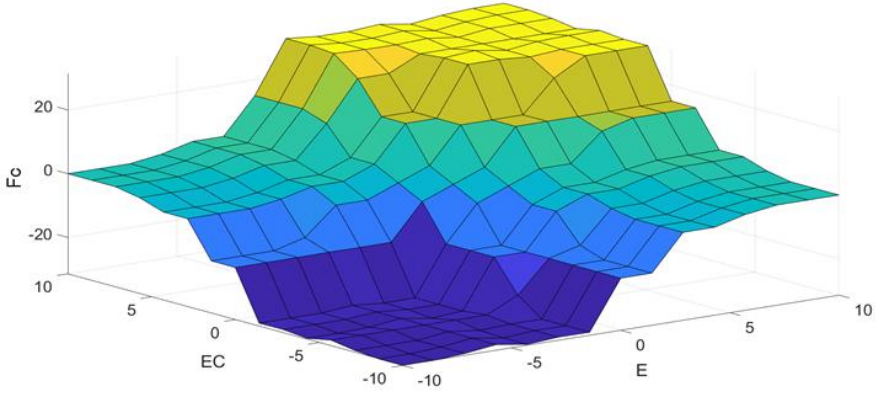


Fig. 6. Fuzzy logic surface

### 3.3. Fuzzy-LQG Control

In the LQR control design, all states are assumed to be available. This assumption is not valid in practice. Kalman filter (Fig. 7) estimates the system states from the information of input and output in Fig. 8. The state space model of the active suspension system with the zero mean Gaussian white noise is given as follows:

$$\begin{aligned} \dot{x}(t) &= \mathcal{A}x(t) + \mathcal{B}u(t) + n_d \\ y(t) &= \mathcal{C}x(t) + n_y \end{aligned} \quad (5)$$

where the pair  $(\mathcal{A}, \mathcal{C})$  is detectable, and the pair of  $(n_d, n_y)$  represents white noise satisfies that

$$E[n_d n_d^T] = \tilde{Q}, E[n_y n_y^T] = \tilde{R} \text{ and } E[n_d n_y^T] = 0 \quad (6)$$

with  $\tilde{Q} \geq 0$  and  $\tilde{R} > 0$ . Let  $\tilde{P}$  satisfy the following Riccati equation.

$$\mathcal{A}^T \tilde{P} + \tilde{P} \mathcal{A} + \tilde{Q} - \tilde{P} \mathcal{C}^T \tilde{R}^{-1} \mathcal{C} \tilde{P} = 0 \quad (7)$$

Kalman filter is given as following dynamic equations:

$$\begin{aligned} \hat{x}(t) &= \mathcal{A}\hat{x}(t) + \mathcal{B}u(t) + K_F(y - \hat{y}) \\ y(t) &= \mathcal{C}\hat{x}(t) \end{aligned} \quad (8)$$

Where;

$$K_F = \tilde{P} \mathcal{C}^T \tilde{R}^{-1} \quad (9)$$

Kalman filter minimizes the prediction of the error covariance when presumed conditions are met [19].

FLQG controller is obtained by combining the LQG controller and fuzzy logic controller as shown in Fig. 9. Kalman filter estimates the state variables using the input and measured output variables of the active suspension system. The estimated variables can be used for the FLQR which completes the design of the FLQG given in Fig. 9. The simulation results will be given in the next section.

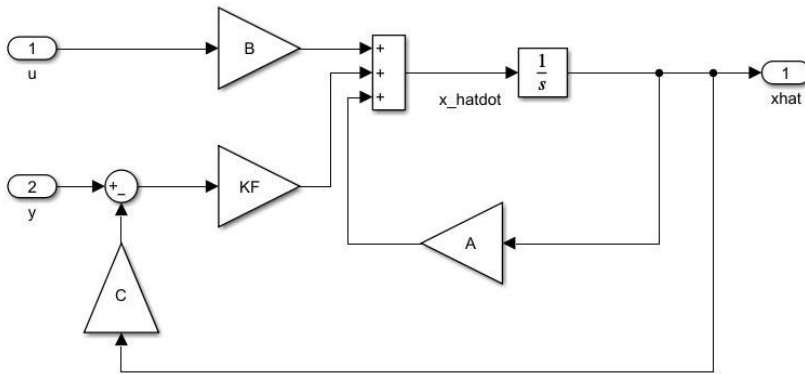


Fig. 7. The structure of the Kalman filter

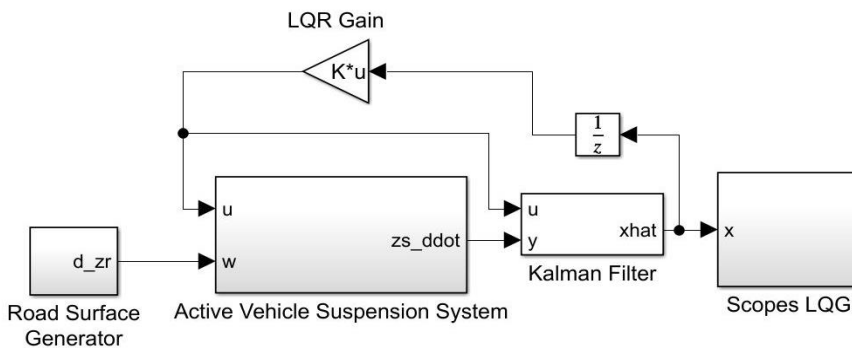


Fig. 8. LQG control structure of the active vehicle suspension system

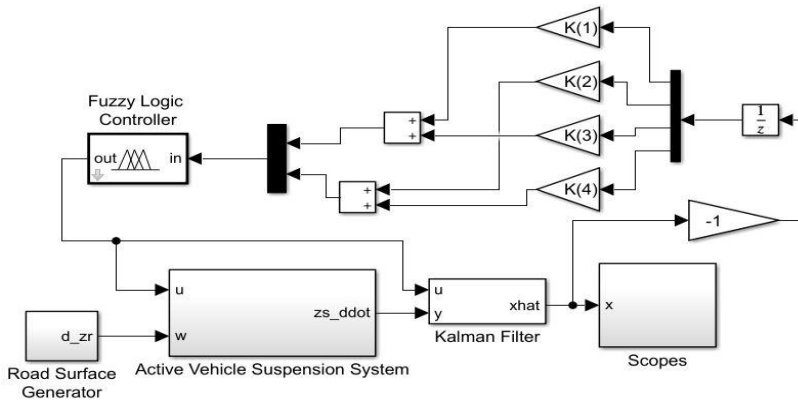


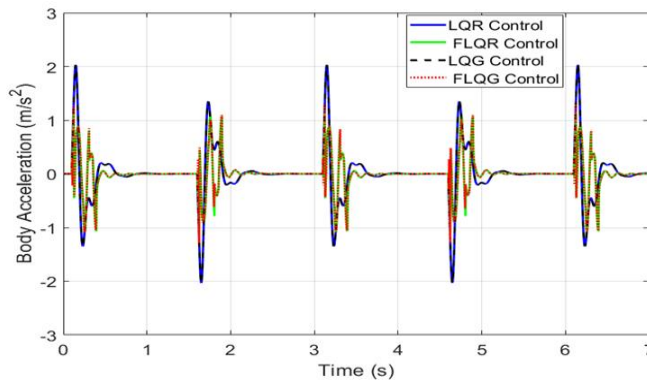
Fig. 9. FLQG control structure of the active vehicle suspension system

#### 4. Simulation Results and Discussion

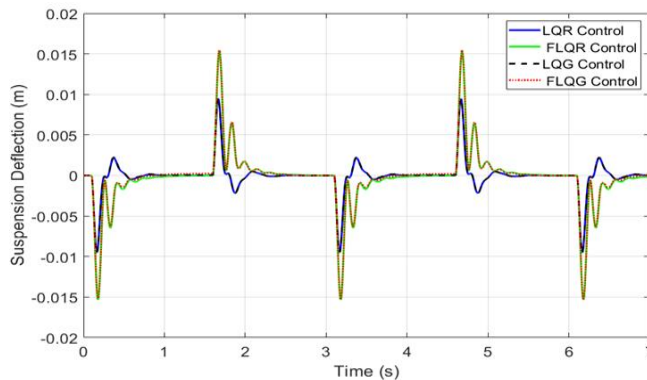
This section presents simulation results to show the effectiveness of the active suspension system with the FLQR and the FLQG controllers against random road disturbances. Two cases of road disturbances are taken into consideration as follows: Case 1 is a square signal with an amplitude of 0.01 m and frequency of 0.3 Hz. Case 2 is a chirp signal, which begins at a frequency of 1Hz and an amplitude of 0.0015 m, which reaches a frequency of 8 Hz at

25s. The FLQR and the FLQG controllers are compared with the conventional LQR and LQG controllers under the mentioned road disturbances.

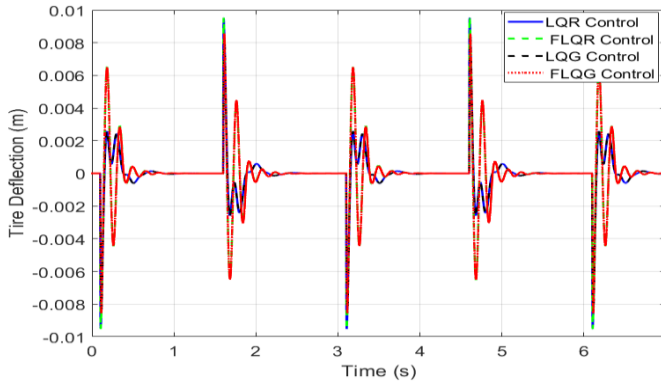
Fig. 10(a) compares the vehicle body acceleration closed-loop responses for the square road profile. It can be seen that the FLQR controller (green line) provides lower body acceleration than the conventional LQR does. To void structural damage, the absolute value of the suspension deflection should be less than 0.038 m ( $|z_s - z_{us}| \leq 0.038$  m). Figs. 10(b) and 10(c) display the vehicle suspension and tire deflections respectively. Fig. 10(a) also compares the vehicle body acceleration closed-loop responses with the LQG and FLQG controllers. It can be seen that the FLQG controller (red dashed line) obtains a body acceleration,  $0.055 \text{ m/s}^2$  which is lower than the result of the conventional LQG controller. The vehicle suspension and tire deflection results of the LQG and FLQG controller are seen in Figs. 10(b) and 10(c) respectively. The results of suspension deflections with controllers provide that  $|z_s - z_{us}| \leq 0.015$  m which is within the acceptable range. For road handling requirements, the tire's dynamic load has to be smaller than its static load ( $(m_s + m_{us})g = 33.84 \text{ N}$ ). All controllers satisfy this performance requirement. More precisely, the active suspension system with the classical LQR and LQG controllers has tire's dynamic load,  $|k_s(z_{us} - z_r)| = 8.6 \text{ N}$  and  $7.7 \text{ N}$  respectively. The maximum tire's dynamic loads of the active suspension system with the FLQR and FLQG controllers are  $8.57 \text{ N}$  and  $7.6 \text{ N}$  respectively. As a result, the FLQR and FLQG controllers have a dynamic load within the permissible range.



(a)



(b)



(c)

Fig. 10. Comparison of closed-loop responses (Case 1)

Next, test results of controllers in the presence of chirp road disturbance are given as follows. Closed-loop responses are given in Fig.11. Vehicle body vertical acceleration plots are given in Fig.10(a) to evaluate the passenger ride comfort. The FLQR provides an improvement of 70% over the conventional LQR controller and the FLQG controller has an improvement of 75.5% over the conventional LQG controller. Fig. 11(b) indicates the suspension deflection. The LQR controller increases the suspension deflection to improve ride comfort. The FLQR and FLQR controllers having the maximum value of the suspension deflection are 0.002 m and 0.0019 m respectively, which are less than the permissible travel range of 0.038 m. Lastly, the tire deflection is depicted in Fig. 11(c). The dynamic loads with LQR, FLQR, LQG and FLQG controllers are 1.04 N, 0.37 N, 0.96 N and 0.33 N respectively, which are lower than the tire’s static load. Furthermore, the FLQG controller achieves the best tire deflection amongst all designed controllers. The FLQR and FLQG controllers reduce the suspension in the presence of chirp road disturbance. Root-mean-square (RMS), minimum (Min), maximum (Max) and peak-to-peak values are reported in Table 3 under the square road condition. Closed-loop responses with the FLQR and FLQG controllers achieve the lowest RMS indices.

Table 3. Statistical analysis of the body acceleration with different controllers (Case 1)

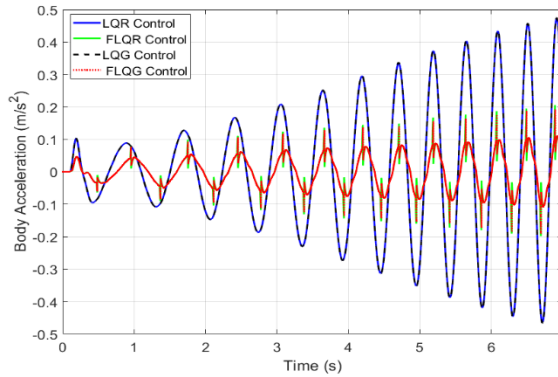
| Controller   | LQR    | Fuzzy-LQR     | LQG    | Fuzzy-LQG     |
|--------------|--------|---------------|--------|---------------|
| Max          | 2.029  | <b>1.141</b>  | 2.029  | <b>1.291</b>  |
| Min          | -2.029 | <b>-1.138</b> | -2.029 | <b>-1.286</b> |
| Peak to Peak | 4.058  | <b>2.279</b>  | 4.058  | <b>2.576</b>  |
| RMS          | 0.4648 | <b>0.2839</b> | 0.4658 | <b>0.2844</b> |

Furthermore, statistical analysis of the body acceleration with the FLQR and the FLQG controllers under the chirp road disturbance is given in Table 4. According to Table 4, the FLQR and the FLQG controllers improve the performance of the active suspension system. Simulation and statistical results show that the fuzzification of the LQR and LQG controllers improves ride comfort and reduces suspension and tire deflections under different road disturbances.

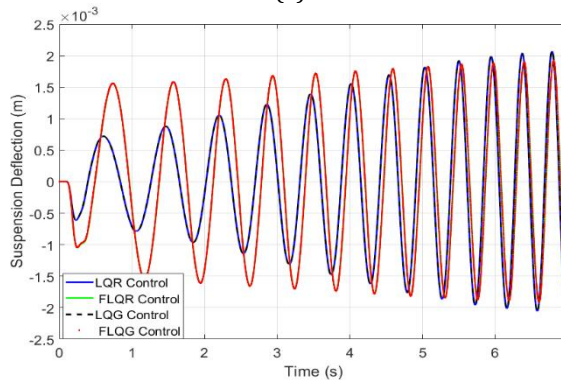


**Table 4. Statistical analysis of the body acceleration with different controllers (Case 2)**

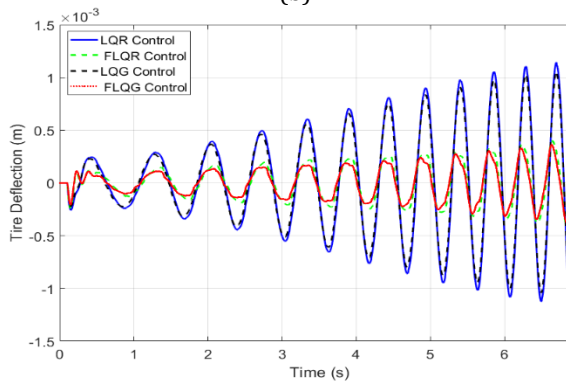
| Controller   | LQR     | Fuzzy-LQR      | LQG     | Fuzzy-LQG      |
|--------------|---------|----------------|---------|----------------|
| Max          | 0.4729  | <b>0.2055</b>  | 0.475   | <b>0.1905</b>  |
| Min          | -0.4646 | <b>-0.1984</b> | -0.4667 | <b>-0.1892</b> |
| Peak to Peak | 0.9374  | <b>0.404</b>   | 0.9416  | <b>0.3797</b>  |
| RMS          | 0.2027  | <b>0.05218</b> | 0.2037  | <b>0.05263</b> |



(a)



(b)



(c)

**Fig. 11. Comparison of closed-loop responses (Case 2)**

## 5. Conclusions

The active suspension system of a vehicle plays a crucial role in evaluating dynamic performance metrics such as ride comfort, road handling, and suspension deflection. Enhancing ride comfort and handling stability in active suspension systems relies heavily on the effectiveness of the active suspension controller. Thus, this study focuses on the development of Fuzzy-LQR and Fuzzy-LQG control approaches for active suspension systems, specifically targeting the active quarter suspension system without considering road input signals.

Using the active quarter suspension system as the study subject, Fuzzy-LQR and Fuzzy-LQG controllers were designed independently of road input signals. Simulation studies were conducted using the MATLAB/Simulink environment to evaluate the performance of these controllers. Comparative analysis was performed against both passive suspension and active suspension systems employing standard LQR/LQG control approaches.

Simulation results demonstrate the efficacy of Fuzzy-LQR and Fuzzy-LQG controllers in improving ride quality compared to standard LQR and LQG controllers. The fuzzy controllers effectively reduce vehicle body acceleration while maintaining permissible suspension deflection in the presence of road disturbances. Specifically, the Fuzzy-LQR and Fuzzy-LQG controllers reduce the root mean square (RMS) values of vertical body acceleration in the presence of square road disturbances by 38.7% and 38.9%, respectively. Moreover, in the presence of chirp road disturbances, the Fuzzy-LQR and Fuzzy-LQG controllers achieve even greater reductions, lowering RMS values of vertical body acceleration by 73.9% and 74.25%, respectively.

Future research directions will focus on experimental validation of the proposed controllers, addressing several key points. Firstly, the application of the suggested control mechanisms will be extended to nonlinear active suspension systems to provide a more accurate representation of genuine suspension dynamics. Secondly, efforts will be directed towards developing fuzzy controllers for dynamic models encompassing entire car active suspensions, with the ultimate goal of implementing these controllers in real-world suspension systems. This emphasis on experimental validation will contribute to bridging the gap between theoretical advancements and practical implementation, enhancing the overall effectiveness and applicability of active suspension control strategies.

## References

- [1] Tang L, Ren NL and Funkhouser S. Semi-active Suspension Control with PSO Tuned LQR Controller Based on MR Damper. *International Journal of Automotive and Mechanical Engineering*, 2023; 20(2): 10512-10522. <https://doi.org/10.15282/ijame.20.2.2023.13.0811>
- [2] Hua C, Chen J, Li Y, and Li L. Adaptive prescribed performance control of half-car active suspension system with unknown dead-zone input. *Mechanical Systems and Signal Processing*, 2018; 111: 135-148. <https://doi.org/10.1016/j.ymsp.2018.03.048>
- [3] Fialho I, Balas GJ. Road adaptive active suspension design using linear parameter-varying gain-scheduling. *IEEE Trans. Control Syst. Technol.*, 2002; 10(1): 43-54. <https://doi.org/10.1109/87.974337>
- [4] Deshpande VS, Mohan B, Shendge PD and Phadke SB. Disturbance observer based sliding mode control of active suspension systems. *J. Sound Vib.*, 2014; 333 (11): 2281-2296. <https://doi.org/10.1016/j.jsv.2014.01.023>
- [5] Nguyen DN, Nguyen TA. Evaluate the stability of the vehicle when using the active suspension system with a hydraulic actuator controlled by the OSMC algorithm. *Scientific reports*, 2022; 12(1): 19364. <https://doi.org/10.1038/s41598-022-24069-w>

- [6] Nguyen DN, Nguyen TA. Proposing an original control algorithm for the active suspension system to improve vehicle vibration: Adaptive fuzzy sliding mode proportional-integral-derivative tuned by the fuzzy (AFSPIDF). *Heliyon*, 2023; 9(3). <https://doi.org/10.1016/j.heliyon.2023.e14210>
- [7] Nguyen TA. A novel approach with a fuzzy sliding mode proportional integral control algorithm tuned by fuzzy method (FSMPIDF). *Scientific Reports*, 2023; 13(1): 7327. <https://doi.org/10.1038/s41598-023-34455-7>
- [8] Papadimitrakis M, Alexandridis A. Active vehicle suspension control using road preview model predictive control and radial basis function networks. *Applied soft computing*, 2022; 120: 108646. <https://doi.org/10.1016/j.asoc.2022.108646>
- [9] Cao J, Li P, and Liu H. An interval fuzzy controller for vehicle active suspension systems. *IEEE Trans. Intell. Transp. Syst.*, 2010; 11(4): 885-895. <https://doi.org/10.1109/TITS.2010.2053358>
- [10] Shao X, Naghdy F, and Du H. Reliable fuzzy  $H_{\infty}$  control for active suspension of in-wheel motor driven electric vehicles with dynamic damping. *Mech. Syst. Signal Process.*, 2017; 87: 365-383. <https://doi.org/10.1016/j.ymsp.2016.10.032>
- [11] Nagarkar MP, Bhalerao YJ, Vikhe Patil GJ, and Zaware Patil RN. GA-based multi-objective optimization of active nonlinear quarter car suspension system-PID and fuzzy logic control. *Int. J. Mech. Mater. Eng.*, 2018; 13(10). <https://doi.org/10.1186/s40712-018-0096-8>
- [12] Han SY, Dong JF, Zhou J and Chen YH. Adaptive fuzzy PID control strategy for vehicle active suspension based on road evaluation. *Electronics*, 2022; 11(6) : 921. <https://doi.org/10.3390/electronics11060921>
- [13] Gomonwattanapanich O, Pannucharoenwong N, Rattanadecho P, Echaroj S and Hemathulin S. Vibration control of vehicle by active suspension with LQG algorithm. *International Journal of Automotive and Mechanical Engineering*, 2020; 17(2): 8011-8018. <https://doi.org/10.15282/ijame.17.2.2020.19.0600>
- [14] Quanser, Active Suspension System: User Manual, Quanser Corporation, Ontario, Canada, 2009.
- [15] Manna S, Mani G, Ghildiyal S, Stonier AA, Peter G, Ganji V and Murugesan S. Ant colony optimization tuned closed-loop optimal control intended for vehicle active suspension system. *IEEE Access*, 2022; 10: 53735-53745. <https://doi.org/10.1109/ACCESS.2022.3164522>
- [16] Fu Q, Wu J, Yu C, Feng T, Zhang N and Zhang J. Linear Quadratic Optimal Control with the Finite State for Suspension System. *Machines*, 2023; 11(2): 127. <https://doi.org/10.3390/machines11020127>
- [17] Luhao W, Zhanshi S. LQR-Fuzzy control for double inverted pendulum. In 2010 International Conference on Digital Manufacturing & Automation, 1, 900-903, 2010. <https://doi.org/10.1109/ICDMA.2010.170>
- [18] Hazem ZB, Fotuhi MJ and Bingül Z. A study of anti-swing fuzzy LQR control of a double serial link rotary pendulum. *IETE Journal of Research*, 2023; 69(6): 3443-3454. <https://doi.org/10.1080/03772063.2021.1911690>
- [19] Welch G, Bishop G. An introduction to the Kalman filter, University of North Carolina, North Carolina, 1995.

Blank Page

## Reliability approach for lifetime prediction of the aluminum extrusion dies

Mustapha Hadji<sup>1,\*</sup>, Mohamed Benamira<sup>2,b</sup>, Rabia Khelif<sup>2,c</sup>

<sup>1</sup>Mechanics of Materials and Plant Maintenance Research Laboratory (LR3MI), Mechanical Eng. Dept, Faculty of Technology, Badji Mokhtar-Annaba University, Algeria

<sup>2</sup>Industrial Mechanics (LMJ), Mechanical Eng. Dept, Faculty of Technology, Badji Mokhtar-Annaba University, Algeria

### Article Info

#### Article history:

Received 02 Dec 2023  
Accepted 15 May 2024

#### Keywords:

Reliability;  
Critical damage;  
Die life;  
Extrusion

### Abstract

This paper introduces a probabilistic approach for predicting the lifetime of extrusion dies using a structural reliability method known as stress-strength interference. In our investigation, we have integrated the assessment of the die's cycle life by following behavioral and rheological law. The approach relies on estimating the reliability index through a combination of a behavioral model and a reliability analysis of the hot extrusion process. Subsequently, the reliability analysis is conducted using a mechanical model to depict the most likely failure conditions. In this regard, the rheological law of Hansel & Spittel emerges as the most suitable choice, as it incorporates the mechanical properties of the materials employed in the fabrication of hot tools. The proposed mechano-reliability approach enables us to estimate reliability and its sensitivity by adjusting the parameters controlling the input process in die formation. Numerous scenarios involving extrusion dies were considered. The results demonstrate that temperature's impact on the die during the extrusion process is manifested through fatigue and damage parameters, as well as the first equivalent strain, which affect the evolution of the reliability index  $\beta$  and subsequently enhance the number of billets extruded.

© 2024 MIM Research Group. All rights reserved.

## 1. Introduction

In a world characterized by rapid changes and significant technical advancements, the global aluminum extrusion market has seen considerable growth. In the realm of extruded aluminum manufacturing, particularly related to our research paper, extrusion tools and molds have garnered significant attention due to their role in enhancing efficiency and reducing costs, encompassing material expenses, research expenditures, and manufacturing costs with thermal processing. Our research is dedicated to enhancing the quality of metals and controlling their properties to extend die life.

Die life is primarily determined by the number of billets extruded in relation to profile size requirements, making it a critical concern. Controlling die failure mechanisms, such as thermal fatigue and surface wear, is essential for achieving economically viable tool longevity. Additional load effects may also be caused by fatigue damage [1]. 70% of die-casting die failures are caused by thermal fatigue, one of the several failure modes. [2], stands out.

The user may choose material parameters, especially crack growth statistics, from a menu, which is a handy feature of the program. The kinetics of crack formation can be

\*Corresponding author: [mustapha.hadji@univ-annaba.dz](mailto:mustapha.hadji@univ-annaba.dz)

<sup>a</sup> orcid.org/0009-0003-0130-7012; <sup>b</sup> orcid.org/0009-0009-3257-2138; <sup>c</sup> orcid.org/0009-0000-2113-5754  
DOI: <http://dx.doi.org/10.17515/resm2024.104ma1202rs>

represented by a variety of models. [1]. Compared to other steels in its class, AISI H13 is a hot work tool steel containing 5% chromium and a higher-than-average amount of vanadium by virtue of its high hardenability, material chemical composition presented in Table 1 [3,4]. It exhibits a combination of desirable properties including toughness, strength, ductility, and thermal conductivity [5,6]. Consequently, H13 tool steel finds extensive applications in casting, extrusion, and forging processes. Its resistance to thermal fatigue cracking, a result of repeated heating and cooling cycles in hot working setups, is attributed to its hot hardness, which is synonymous with hot strength [7].

Table 1. H13 chemical composition

| Element | C    | Si   | Mn  | Cr   | Mo   | V    |
|---------|------|------|-----|------|------|------|
| Wt %    | 0.39 | 0.99 | 0.4 | 5.23 | 1.34 | 0.95 |

The value of the first effective strain, which is a critical parameter that requires careful evaluation, is closely related to the effect of temperature on die life [8]. The most pronounced die wear occurs near the die bearing, posing a higher risk of die failure due to significant plastic deformation, elevated die temperature, and interface pressure [9]. During the hot extrusion cycle, especially under high-temperature and high-speed conditions, localized heating due to friction at the billet-tool interface results in a temperature increase close to the melting point, accompanied by high tension stress [10]. Improving and controlling scrap production and assessing its impact on product quality is dependent on variables related to extrusion temperature, time, ram speed, pressure, and die geometry [11].

Aluminum alloy 6063 with main chemical composition of 0.47% Si and 0.55% Mg is known to be one of the properties that influences the die's life during the extrusion process. This is due to the metal's quality, particularly when utilizing the secondary melting alloy especially from mixed scrap, which enhances the quality of the coefficient of friction's reduction. This raises the temperature, which in turn shortens the die's lifetime.

Several vital parameters, including equipment conditions, operating conditions, temperatures, pressures, and die quality, significantly influence the extrusion process. Despite diligent efforts by manufacturers, various challenges in the process still lead to product defects [12]. Many defects and wastage are linked to the choice of billet size for extrusion and involve factors such as surface quality, temperature, speed, die geometry, and weld joints. To mitigate these issues, it is imperative to maintain control over all relevant parameters, including extrusion billet size, cutter position, puller speed, die entry angle, conveyor roller surfaces, temperature, and speed [13].

In light of the aforementioned considerations and recent research on extrusion die behavior and defects, the primary objective of our research paper is to determine the reliability index by considering die material elements and their influencing factors. To achieve this goal, we have developed a model to analyze the behavior of the extrusion process by integrating mechanical reliability and key influencing factors. This has led to the development of a mechanical model that combines the rheological model with the damage model.

In the present work, a model is developed to analyze the behavior of the most essential tool (die) in the aluminum extrusion process by coupling mechanical reliability to obtain different key factors. This leads to the development of a mechanical model coupling the rheological model to the damage model to evaluate the reliability index  $\beta$  and determine the sensitivity of variations in the random values of the input parameters from the aluminum extrusion process. The probabilities of die failure can be predicted using the

combined model, which is defined in terms of the reliability index  $\beta$  determined by the reliability simulations in PHIMECASoft® as a limit state function.

## 2.Failure Mode and Analysis of Extrusion Die

Die failure encompasses various wear factors, predominantly influenced by the material quality and temperatures experienced during extrusion processes. The die is responsible for forming the shape of the extrusion, and it is kept in place by the die holder/ring so that it does not collapse or fracture. The die backer is responsible for providing support for the die. The extrusion load is transferred from the die to the pressure ring, transferring the force to the press platen. This process prevents the bolster from deflecting and ensures the weight is correctly transferred. The complete die set, which includes the die ring and the bolster, is being held in the press by the die slide, it also withstands a high degree of stress based on AISI H13 material used, and its high properties to withstand stress and fatigue. [14,15], as illustrated in Fig 1.

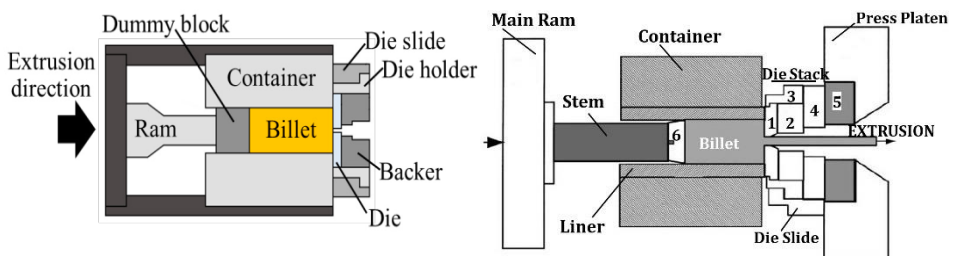


Fig. 1. Extrusion tooling used in hot extrusion. [10, 15], 1, solid die; 2, backer; 3, die holder ; 4, bolster; 5, pressure pad; and 6, dummy block



Fig. 2. The most important failures of aluminum extrusion dies

Factors contributing to die wear involve abrupt temperature fluctuations and prolonged exposure to high temperatures, resulting in friction between the aluminum flow and the

die's surface. Among the factors mentioned, temperature and extrusion speed are of paramount importance. The speed of extrusion and the temperature increase at the die bearing are directly interrelated [15]. The extrusion die is susceptible to various categories of defects, with the most influential ones being those that are irreparable, including cracking, deflection, friction, and wear. Fig 2 illustrates some of these defects: (C, D) depict cracking in its advanced stages, while (B, F) illustrate deflection, and (A, E) showcase wear. Each of these defects contributes to a damage model in hot extrusion. A statistical examination of the primary types of die failure and their subcategories, as well as a greater understanding of die failure modes and processes, was conducted by AFM ARIF [16]. Indeed, the presence of various irreversible effects like wear, deflection, and cracks in a damaged die underscores the need to establish a reliability index and conduct a statistical analysis. This analytical approach is essential for pinpointing the pivotal factors that impact the cycle life of the die.

### **3. Model Identification**

#### **3.1 Basic Equations**

As a general rule, it is important to note that cracks are often found in dies and extruders as a result of metal alloy die manufacturing processes. These cracks are usually about 0.01 mm deep during processes such as surface hardening of the bearing zone [17].

The increase in crack intensity, influenced by various material properties, results in heightened stress levels. This, in turn, accelerates crack growth at a certain rate. When the material is subjected to a specific stress intensity factor  $K$  for a given number of extrusions  $\Delta N$ , the fracture length is accelerated and experiences a notable increase represented by the parameter 'a.' The rate of crack growth acceleration is determined by the changing property of interest within a strain resistance range, [18] expressed as the ratio  $\Delta a/\Delta N$ . Consequently, we present the rate of acceleration of crack length, denoted as  $da/dN$ .

$$\frac{da}{dN} = C(\Delta K)^m \tag{1}$$

Constants unique to the material and environment under consideration are the factors  $C$  and  $m$ . In the case of the extrusion die steel.

#### **3.2 Lifetime determination**

By substituting the definitions of maximum and minimum stress into the stress range formula, we can derive a valuable alternative definition of the stress range:

$$\Delta K = \alpha \Delta \sigma \sqrt{\pi a} \tag{2}$$

Here,  $\alpha$  represents the crack geometry factor. In general cases, the rate of propagation of a given crack under constant amplitude loading depends on several factors, including the duration of the extrusion cycle, the end stresses of the fatigue cycle ( $\sigma_{max}$ ,  $\sigma_{min}$ ), and the length of the crack. In simpler scenarios where the similarity condition is met, the concept of stress intensity factor allows us to consider the two principal components by utilizing the range of stress intensity factor. This is because the extrusion cycle commences with the minimum load ( $\Delta \sigma = \sigma_{max} - \sigma_{min}$ ) =  $\sigma_{max}$ .

By substituting Equation 2 into Equation 1 and integrating it, we can determine the total number of extrusions allowed before reaching the end of the fatigue life. The fatigue life ( $N_f$ ) was determined by the number of cycles until fracture failure [19].



$$Nf = \frac{(a_0)^{1-\frac{m}{2}} - (a_c)^{1-m/2}}{C\left(\frac{m}{2} - 1\right)\alpha^m \pi^{m/2} \sigma_{max}^m} \tag{3}$$

Considering that H13 tool steel belongs to the category of ultrahigh strength steel, it is possible to determine the values of C and m for this type of steel by referring to standard sources. As previously mentioned, heat-treated and surface-hardened H13 steel has preexisting cracks (a0) that fall within a range of 0.05 to 0.1 mm. It is possible to set the geometry factor (alpha) value at 1.12 if the kind of fracture is an edge crack [17].

The equation  $\alpha = f(a/w)$  is a function of the normalized crack length (a/w) and serves to eliminate surface tensile stresses. Using mode-I stress intensity factor according to its typical definition, while disregarding the finite-size factor  $f(a/W)$ , and recognizing that the crack becomes unstable ( $a=a_c$ ) when  $KI = KIC$ , we can derive the following relationship [7].

$$a_c = \frac{1}{\pi} \left( \frac{K_{IC}}{\alpha \sigma_{max}} \right)^2 \tag{4}$$

The behavior of the production system is governed by a mathematical law that describes the required deformations needed to shape a billet into a profile with the desired dimensions and shape. In the context of extrusion, the most suitable choice is the rheological law developed by Hansel & Spittel. The Hansel-Spittel model was selected due to its strong support for establishing a simple connection between variables such as strain, strain rate, and temperature. This enables the modelling of flow stress by considering the strain's dependence in accordance with the rheological law parameters [20,21]. It has been integrated into many alloys [22,23,]. The modeling of behavior characterized by Hansel & Spittel's law has been seamlessly integrated into FORG shaping calculation codes.

$$\sigma_{max} = A e^{m_1 T} T^{m_9} \varepsilon^{m_2} e^{m_4/\varepsilon} (1 + \varepsilon)^{m_5 T} e^{m_7 \varepsilon} \dot{\varepsilon}^{m_3} \varepsilon^{m_8 T} \tag{5}$$

Most referenced material has null values for parameters  $m_5$  to  $m_9$ . Thus, it is possible therefore simplify the equation like this (equation 6).

$$\sigma_{max} = A e^{m_1 T} \varepsilon^{m_2} e^{m_4/\varepsilon} \dot{\varepsilon}^{m_3} \tag{6}$$

In the given context, A represents the material's cohesion, T denotes the die temperature, and  $m_1$  signifies the material's sensitivity to temperature. Additionally,  $m_2$  and  $m_4$  dictate the material's sensitivity to tension, while  $m_3$  is contingent upon the material's sensitivity to the strain rate. Equation (3) is employed to substitute the term  $a_c$ .

$$Nf = \frac{(a_0)^{1-\frac{m}{2}} - \left( \frac{1}{\pi} \left( \frac{K_{IC}}{\alpha (A e^{m_1 T} \varepsilon^{m_2} e^{m_4/\varepsilon} \dot{\varepsilon}^{m_3})} \right)^2 \right)^{1-m/2}}{C\left(\frac{m}{2} - 1\right)\alpha^m \pi^{m/2} \sigma_{max}^m} \tag{7}$$

The reliable geometric mechanical model is derived from the following equation (Equation 8). By combining the material model based on Hansel-Spittel with the mechanical model for lifespan analysis, we have developed a comprehensive mechanistic model for conducting reliability analyses.

$$Nf = \frac{(a_0)^{1-\frac{m}{2}} - \left( \frac{1}{\pi} \left( \frac{K_{IC}}{\alpha(Ae^{m_1 T} \varepsilon^{m_2} e^{m_4/\varepsilon \dot{\varepsilon}^{m_3}})} \right)^2 \right)^{1-m/2}}{C \left( \frac{m}{2} - 1 \right) \alpha^m \pi^{m/2} (Ae^{m_1 T} \varepsilon^{m_2} e^{m_4/\varepsilon \dot{\varepsilon}^{m_3}})^m} \tag{8}$$

Lemaître and Chaboche are modelled the damage expressed as a function of n/Nf is: (Equation 9) [21, 24].

$$D = 1 - \left[ 1 - \left( \frac{n}{Nf} \right)^{\frac{1}{1-\alpha}} \right]^{\frac{1}{\beta+1}} \tag{9}$$

Where  $\alpha$  is given by:

$$\alpha(\sigma_{max}, \bar{\sigma}) = 1 - a \left( \frac{\sigma_{max} - \sigma_I(\bar{\sigma})}{\sigma_u - \sigma_{max}} \right) \tag{10}$$

Equation 11, which describes a model correlating the Hansel–Spittel model, is thus the method by which the reliability engineering mechanical model is obtained [23]. (Equation 6) presents the mechanical model for reliability evaluations by combining it with the Lemaître–Chaboche model (equation 9) [21, 24].

$$D = 1 - \left[ 1 - \left( \frac{(a_0)^{1-\frac{m}{2}} - \left( \frac{1}{\pi} \left( \frac{K_{IC}}{\alpha(Ae^{m_1 T} \varepsilon^{m_2} e^{m_4/\varepsilon \dot{\varepsilon}^{m_3}})} \right)^2 \right)^{1-m/2}}{C \left( \frac{m}{2} - 1 \right) \alpha^m \pi^{m/2} (Ae^{m_1 T} \varepsilon^{m_2} e^{m_4/\varepsilon \dot{\varepsilon}^{m_3}})^m} \right)^{1/_{1-1-a \left( \frac{\sigma_{max}-\sigma_I(\bar{\sigma})}{\sigma_u-\sigma_{max}} \right)}} \right]^{\frac{1}{\beta+1}} \tag{11}$$

And then we construct failure steps from (equation 11) using the reliability statement with limit state functions to achieve the reliability index of the extrusion dies.

#### 4. Die Reliability Assessment

When delving into the realm of reliability within mechanics, it is essential to first establish the context in which the proposed approach operates. Reliability encompasses both well-established methods, such as the implementation of statistical techniques for manufacturing control, and emerging methods that focus on failure and risk assessment. The latter approach stems from a relatively new philosophy that must be contextualized.

Our interest lies in methods primarily developed in the context of material and structural modeling. These methods allow mechanics to draw upon the wealth of knowledge derived from fields like probability theory and the experiences gained in the domain of aluminum extrusion die manufacturing.

Embracing a probabilistic approach, reliability methods in mechanics enable us to calculate the reliability index and sensitivity to failure. The success of the dimensioning process is validated by confirming an equality function, which relates the number of extruded billets (determining die lifetime, Nf) to critical damage (Dc) and the acting damage (D) as time-independent output variables. This approach allows us to describe the structural state through a single global random variable known as the margin, representing the elementary resistance-solicitation case.

The limit state function, denoted as  $G(X_i)$ , quantifies the lifetime limit, presented as the variation between the number of billets extruded into the die and the required number for satisfactory performance (Equation 12).

$$G(X_i) = D_c - D(X_i) \tag{12}$$

according to the literature [26,27,28,29],  $D_c$  is defined by:  $0.2 \leq D_c \leq 0.5$

The reliability index  $\beta$  is employed to describe the probability of failure, which is defined as the shortest distance in the middle of the origin and the domain of failure in the equivalent Gaussian space  $u_i$ .

$$\beta = \text{minimise} \sqrt{\sum_i u_i^2} \text{ subjected to } G(X_i) \leq 0 \tag{13}$$

Ensuring the reliability of structures is a fundamental criterion when it comes to making choices in terms of design and maintenance. For each dimensioning rule, a failure scenario is described by means of a performance function  $G(X_i) = R(X_i) - S(X_i)$

( $X_i$ ) being the basic random variables,  $R(X_i)$  the resistance and  $S(X_i)$  the stress.  $G(x_i) > 0$  indicates the state of safety  $G(x_i) \leq 0$  while reflects the state of failure.

The objective is to evaluate a probability of failure,  $P_f$  that of being in a situation of failure. Within the framework of the first-order approximation, the calculation of  $P_f$  is equivalent to the evaluation of an indicator called the reliability index  $\beta$ , the probability of failure of the system can be expressed as:

$$P_f = p_r[G(X) \leq 0] = \Phi(-\beta) \tag{14}$$

The reliability software PHIMECASoft® can be applied to calculate the reliability index  $\beta$  and failure probability, where  $\Phi(.)$  is the cumulative Gaussian probability function in the die environment and  $\text{Pr}[.]$  is the probability function, there are four primary factors that contribute to determining the reliability index. These factors include material rheological parameters, die temperature, fatigue damage parameters, and strain, all of which are expressed as random variables.

Table 2. Random elements and their associated variables for fatigue and damage

| Type of var.   | Symbol   | Description                     | Probability distribution model | Mean value            | Coefficient of variation (%) | Source  |
|----------------|----------|---------------------------------|--------------------------------|-----------------------|------------------------------|---------|
| Fatigue param. | $a_0$    | Constant material               | Normal                         | 0.01018               | 11.78                        | [17]    |
|                | $\beta$  | Coefficient of the damage model | Determinist                    |                       | 2.94                         | [30]    |
|                | $K_{IC}$ | fracture toughness              | Normal                         | 83.6                  | 5.98                         | [17]    |
|                | $C$      | Paris constants                 | Normal                         | $3.13 \times 10^{-7}$ | 12.65                        | [31]    |
| Damage param.  | $D_c$    | Critical damage                 | Normal                         | 0.4                   | 16.03                        | [26,27] |

The uncertainties associated with the die are linked to various states, including geometry, loading, manufacturing, and service conditions. The results obtained are presented in Tables 2 and 3, which separately list the random variables and their corresponding variables. Table.2 contains the fatigue and damage parameters, while Table.3 presents the rheological law parameters for the selected random variables during the initial extrusion phase (as per Equation 11).

Table 3. Random elements and their associated variables of the rheological law

| Type of var.           | Symbol         | Description  | Probability distribution model | Mean value | Coefficient of variation (%) | Source           |
|------------------------|----------------|--|--------------------------------|------------|------------------------------|------------------|
| Rheological law Param. | A              | Material coherence   | Determinist                    | 2821.246   | 1                            | baseFPD1.3FORGE® |
|                        | m <sub>1</sub> | Sensitivity of material to temperature                     | Determinist                    | 0.0029     | 1                            | baseFPD1.3FORGE® |
|                        | m <sub>2</sub> | Sensitivity of material to stress                          | Determinist                    | -0.10727   | 1                            | baseFPD1.3FORGE® |
|                        | m <sub>3</sub> | Sensitivity of material according to strain rate           | Determinist                    | 0.13444    | 1                            | baseFPD1.3FORGE® |
|                        | m <sub>4</sub> | Sensitivity of material to strain                          | Determinist                    | -0.0462    | 1                            | baseFPD1.3FORGE® |
|                        | ε              | Equivalent strain resulting from the first extrusion cycle | Normal                         | 0.04       | 10                           | baseFPD1.3FORGE® |
|                        | T              | Die temperature  | Normal                         | 485        | 9.27                         | [32]             |

### 5. Variable Sensitivities

Variable sensitivities are crucial in understanding the impact of random variables on die cycle life. In Fig 3, we can observe the variable sensitivity  $\alpha^2$  for an accepted reliability index value of 3.7273, with the number of extruded billets increased to 1157. There are five primary elements considered in regulating die cycle life: die temperature (T), die material rheological characteristics, equivalent plastic strain after one extrusion cycle, critical damage (Dc), and fatigue damage associated variables.

Among these factors, critical damage (Dc) stands out as the most significant, contributing to 79% of all global factors influencing die life. Paris constants, accounting for less than 7%, follows in importance. Equivalent plastic strain represents 4% of the impact, with the remaining percentage attributed to all other factors. This analysis underscores the critical role of Dc in die life determination, with other factors playing a comparatively lesser role.

The reliability assessment proceeds in two main steps:

- 1. Comparison of Time-Based Life Prediction Models: Initially, the assessment centers on comparing time-based life prediction models and evaluating the parameters within the applied model. This step aims to determine how sensitive the model is to uncertainties associated with the die.
- 2. Analysis of Parameter Sensitivity in the Mechanical Model: In the second step, the assessment delves into the sensitivity of the parameters within the mechanical model, taking into account both the data of the random variables and deterministic factors.

These steps collectively provide insights into the reliability of the die and its susceptibility to various uncertainties and factors.

Importance of the random variables in aluminum extrusion die.

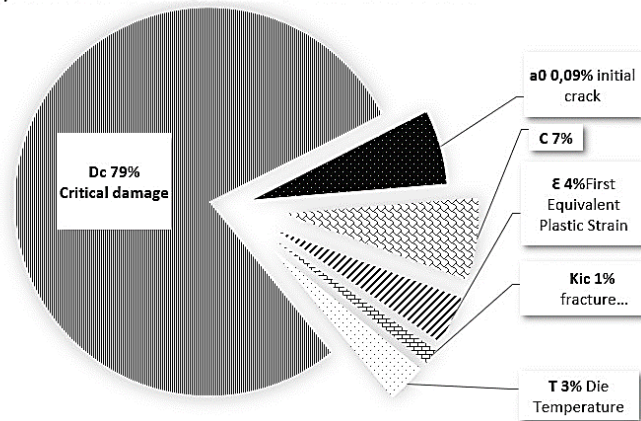
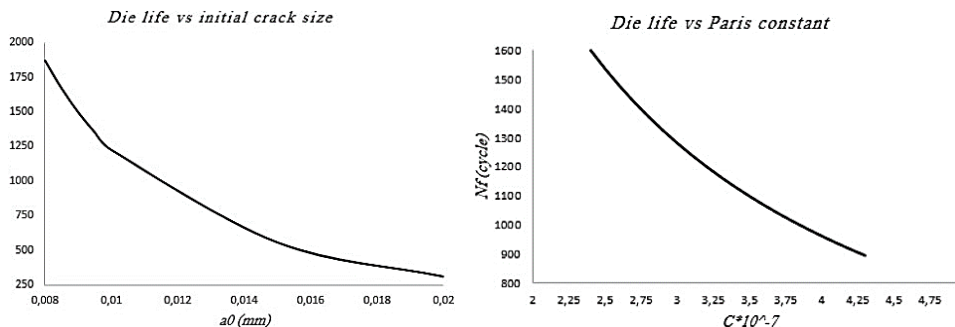


Fig. 3. The significance of the variables in a hot aluminum extrusion die (random variables and parameters founded on Table 2).

Fig.4 illustrates the sensitivity values for die life are evaluated with respect to a range of geometrical parameters, including fracture toughness, initial crack size, maximum stress, and material-specific constants, following the previously described method. Die temperature remains a critical variable in extrusion, as it can be significantly affected during the extrusion process. To minimize uncertainties in the work described, meticulous care should be exercised when selecting material parameters and the mechanical model that governs die life. It is noteworthy that, for a reliability index ( $\beta$ ) value of 3.72, there is a noteworthy observation regarding the cycle life number. This observation underscores the significance of managing die temperature and the careful selection of material parameters and mechanical models to ensure desired reliability levels in the extrusion process.

The impact of temperature on the die during the extrusion process is depicted in Fig 5. These figures are correlated with the value of the reliability index and the cycle life achieved under specific conditions. In this analysis, a 15% variation in fatigue parameters and a 10% variation in damage parameters were considered.



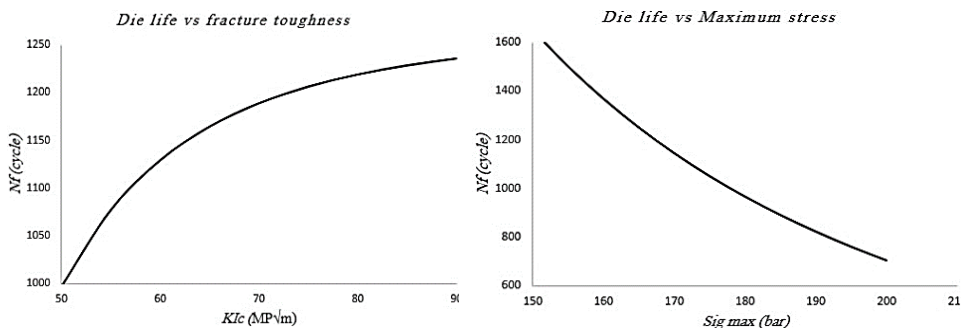


Fig. 4. Variation of die life against geometrical parameters

Additionally, the first equivalent strain was increased from 0.06 by a coefficient variation of 10% in the die temperature, which was maintained at 511°C. These findings provide valuable insights into how changes in temperature, fatigue parameters, and damage parameters can affect the reliability index and cycle life of the die during extrusion.

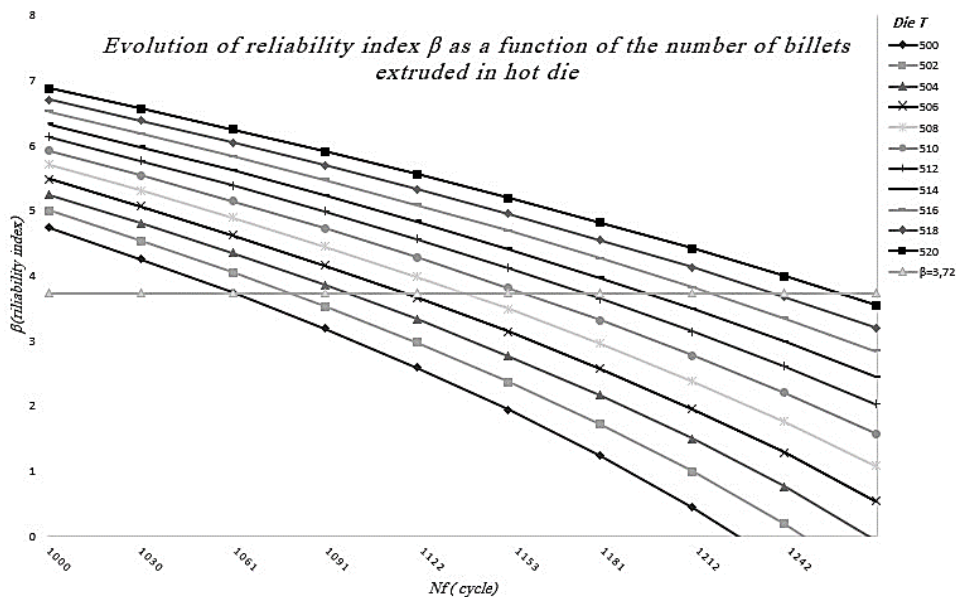


Fig. 5. Evolution of reliability index  $\beta$  as a function of the number of billets extruded in hot die

The analysis presented in Fig 6 demonstrates the evolution of the reliability index ( $\beta$ ) at a level of 3.72. It's noteworthy that under these conditions, the cycle number of extruded billets increases to 1157 pushes when the die temperature is maintained at 511.11°C. This result represents a favorable average of the key parameters, indicating improved die performance and a longer operational lifespan for extrusion processes at this temperature.

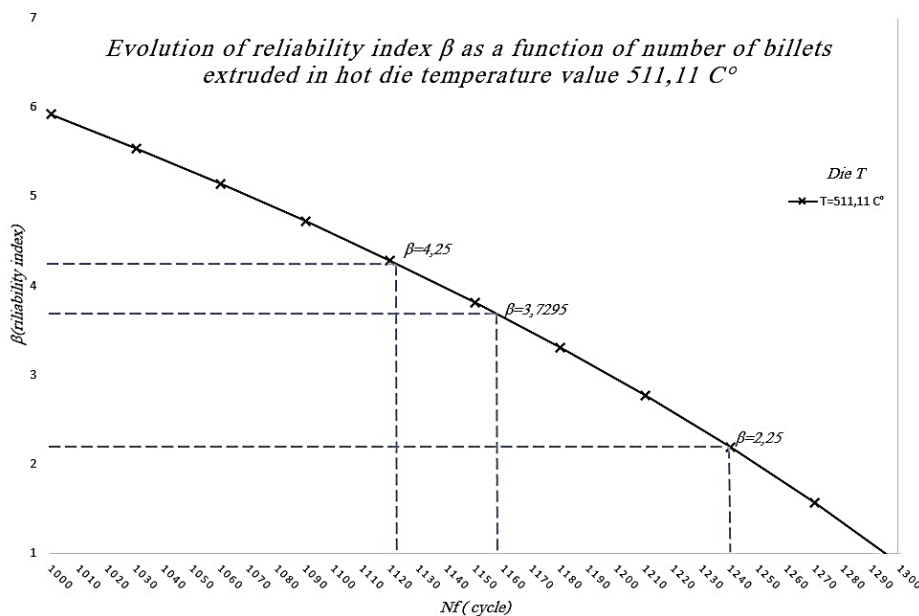


Fig. 6. Evolution of reliability index  $\beta$  as a function of the number of billets extruded in hot die temperature value  $T=511.11^{\circ}\text{C}$

### 6. Conclusions

A mechanical engineering model that aims to prolong the life of extrusion dies has been successfully constructed using the probabilistic methodology provided, based on the Paris and rheological laws. By considering various geometrical and material characteristics, this model has allowed us to improve the die reliability significantly. However, several factors affect an extrusion die's reliability index, with temperature and equivalent strain notably significant in producing damage areas, particularly fatigue crack propagation. Considering the model's parameter uncertainties is crucial for an in-depth reliability evaluation. The complete analysis shown in Figs. 5 and 6 shows that temperature, first equivalent strain, and model parameters have a more significant impact on die safety than differences in other components and geometric precision. The developed mechanical model offers quantitative instructions that relate important extrusion factors to cycles before the necessity for die replacement or maintenance, as indicated by the limited stat. Die material fatigue parameters, rheological law parameters, and other damage parameters are mapped to estimate longevity. By combining simulations with the reliability index, we believe it will be possible to predict operating limits, giving die designers an essential direction for extending the life of extrusion dies.

The study examined the probabilistic behavior of solid and hollow die failures in commercial aluminum extrusion based on its material, The aluminum extrusion industry has benefited from the data-driven insights that have been gained to boost productivity and competitiveness. These results imply that careful parameter management and adjustment in accordance with service and operational conditions can lead to optimal die life. This strategy will reduce possible sources of failure and damage while improving the extrusion processes' reliability and productivity. The extrusion process and die mechanics including thermal alignment, process control, extrusion metallurgy, quenching, and more have been covered from an operational and best practices perspective.

To sum up, a mechanical engineering model that aims to prolong the life of extrusion dies has been effectively constructed using the probabilistic methodology that has been described. The key focus is demonstrating tangible ways the predictive model facilitates actively modifying and improving the parameters in the mechanical model and probabilistic study using PHIMECASoft®. The model accounts for several geometrical and material characteristics, allowing us to improve significantly die reliability. In practical terms, these findings suggest that achieving optimal die performance and longevity can be achieved by carefully managing and adjusting parameters in accordance with service and operational conditions. This approach will help enhance the reliability and efficiency of extrusion processes to minimize potential sources of damage and failure.

## References

- [1] Abdulla W, Menzemer C. Fatigue life prediction of steel bridge connections using Fracture Mechanics Models. *Research on Engineering Structures and Materials*. 2021. <https://doi.org/10.17515/resm2021.264st0310>
- [2] Jiang QC, Zhao XM, Qiu F, Ma TN, Zhao QL. The relationship between oxidation and thermal fatigue of martensitic hot-work die steels. *Acta Metallurgica Sinica (English Letters)*. 2017;31(7):692–698. <https://doi.org/10.1007/s40195-017-0699-8>
- [3] Parishram P, Malshe AP, Fulton A. Laser melt processing of H13 Tool Steel. *Manufacturing Engineering and Textile Engineering*. 2006. <https://doi.org/10.1115/imece2006-15243>
- [4] Li G, Li X, Wu J. Study of the thermal fatigue crack initial life of H13 and H21 steels. *Journal of Materials Processing Technology*. 1998;74(1-3):23–26. [https://doi.org/10.1016/s0924-0136\(97\)00244-6](https://doi.org/10.1016/s0924-0136(97)00244-6)
- [5] Birol Y. Response to thermal cycling of duplex-coated hot work tool steels at elevated temperatures. *Materials Science and Engineering: A*. 2011;528(29–30):8402–8409. <https://doi.org/10.1016/j.msea.2011.08.038>
- [6] Duan Z, Pei W, Gong X, Chen H. Superplasticity of Annealed H13 Steel. *Materials*. 2017;10(8):870. <https://doi.org/10.3390/ma10080870>
- [7] Qamar SZ, Sheikh AK, Arif AFM. A CVN-K(K<sub align="right">IC) correlation for H13 Tool Steels</sub>. *International Journal of Materials and Product Technology*. 2008;33(4):421. <https://doi.org/10.1504/ijmpt.2008.022519>
- [8] Bendjoudi Y, Becker E, Bigot R, Amirat A. Contribution in the evaluation of a performance index of hot forging dies. *The International Journal of Advanced Manufacturing Technology*. 2016;88(5–8):1187–1201. <https://doi.org/10.1007/s00170-016-8829-4>
- [9] Zhang C, Zhao G, Li T, Guan Y, Chen H, Li P. An investigation of die wear behavior during aluminum alloy 7075 tube extrusion. *Journal of Tribology*. 2012;135(1). <https://doi.org/10.1115/1.4023081>
- [10] Ngernbamrung S, Suzuki Y, Takatsuji N, Dohda K. Investigation of surface cracking of hot-extruded AA7075 Billet. *Procedia Manufacturing*. 2018;15:217–224. <https://doi.org/10.1016/j.promfg.2018.07.212>
- [11] Ferrás AF, Almeida FD, e Silva EC, Correia A, Silva FJG. Scrap production of extruded aluminum alloys by direct extrusion. *Procedia Manufacturing*. 2019;38:1731–1740. <https://doi.org/10.1016/j.promfg.2020.01.100>
- [12] Gadekar SS. Defects in Extrusion Process And their Impact on product Quality. *International Journal of Mechanical engineering And robotics research*. July-2014.
- [13] Ferrás AF, Almeida FD, e Silva EC, Correia A, Silva FJG. Scrap production of extruded aluminum alloys by direct extrusion. *Procedia Manufacturing*. 2019;38:1731–1740. <https://doi.org/10.1016/j.promfg.2020.01.100>



- [14] Assaad W, Geijselaers HJ, Chinesta F, Chastel Y, El Mansori M. Coupled analysis of material flow and die deflection in direct aluminum extrusion. AIP Conference Proceedings. 2011. <https://doi.org/10.1063/1.3552494>
- [15] Saha PK. Aluminum Extrusion Technology. 2000. <https://doi.org/10.31399/asm.tb.aet.9781627083362>
- [16] Arif AFM, Sheikh AK, Qamar SZ. A study of die failure mechanisms in aluminum extrusion. Journal of Materials Processing Technology. 2003;134(3):318–328. [https://doi.org/10.1016/s0924-0136\(02\)01116-0](https://doi.org/10.1016/s0924-0136(02)01116-0)
- [17] Qamar SZ, Pervez T, Siddiqui RA, Sheikh AK, Arif AFM. Sensitivity analysis in life prediction of extrusion dies. Journal of Achievements in Materials and Manufacturing Engineering. 2007;25(1).
- [18] Pöhlandt K. Materials Testing for the Metal Forming Industry. 1989. <https://doi.org/10.1007/978-3-642-50241-5>
- [19] Balcioglu HE, Sakin R, Gün H. The design of multi-sample flexural fatigue device and fatigue behavior of glass/epoxy laminated composites. Research on Engineering Structures and Materials. 2018. <https://doi.org/10.17515/resm2018.67me0917>
- [20] Hansel A, Pittel T-S. Kraft- und Arbeitsbedarf Bildsamer Formgebungs Verfahren. VEB Deutscher Verlag für Grundstoffindustrie, Lipsk; 1979.
- [21] Lemaitre J, Chaboche J-L. Mechanics of Solid Materials. 1990. <https://doi.org/10.1017/cbo9781139167970>
- [22] Meyer LW, Weise A, Hahn F. Comparison of constitutive flow curve relations in cold and hot forming. Le Journal de Physique IV. 1997;07(C3). <https://doi.org/10.1051/jp4:1997305>
- [23] Chadha K, Shahriari D, Jahazi M. An approach to develop Hansel–Spittel constitutive equation during ingot breakdown operation of low alloy steels. Frontiers in Materials Processing, Applications, Research and Technology. 2017:239–246. [https://doi.org/10.1007/978-981-10-4819-7\\_20](https://doi.org/10.1007/978-981-10-4819-7_20)
- [24] Herblant T, Cailletaud G, Quilici S, Jaffal H. A new technique for the fatigue life prediction in notched components. Senlis: Cetim; 2009. cetim.fr
- [25] Hensel A, Spittel T. Kraft- und Arbeitsbedarf bildsamer Formgebungs verfahren. Leipzig: VEB Deutscher Verlag für Grundstoffindustrie; 1978.
- [26] Lemaitre J, Desmorat R. Engineering damage mechanics: Ductile, creep, fatigue and brittle failures. Springer-eBooks; 2005. DOI: 10.1007/b138882. ISBN: 978-3-540-27293-9.
- [27] Lemaitre J. A Course on Damage Mechanics. Berlin, Heidelberg: Springer; 1996. DOI: 10.1007/978-3-642-18255-6. ISBN: 978-3-642-18255-6.
- [28] Nordmann J, Naumenko K, Altenbach H. Cohesive Zone models—theory, numerics and usage in high-temperature applications to describe cracking and delamination. In: Advances in Mechanics of High-Temperature Materials. 2019. p. 131–168. DOI: 10.1007/978-3-030-23869-8\_7.
- [29] Abed FH, Al-Tamimi AK, Al-Himairee RM. Characterization and modeling of ductile damage in structural steel at low and intermediate strain rates. Journal of Engineering Mechanics. 2012;138(9):1186–1194. [https://doi.org/10.1061/\(asce\)em.1943-7889.0000415](https://doi.org/10.1061/(asce)em.1943-7889.0000415)
- [30] Herblant T. Une méthode de correction élastoplastique pour le calcul en fatigue des zones de concentration de contraintes sous chargement cyclique multiaxial non proportionnel [dissertation]. Paris: École Nationale Supérieure des Mines de Paris; 2009.
- [31] Granta CES EduPack. Tool steel, chromium alloy, AISI H13 (hot work). 2009.
- [32] ALGALPLUS, Algerian Aluminum Extrusion Factory. M'sila industrial zone. Bpn°702, M'sila, Algeria, 28000. [algalplus.com](http://algalplus.com)

Blank Page

## Filament manufacturing via external grooving of an HDPE pipe wall: RSM optimization and mechanical tests validation

Sabrina Mammeri<sup>1,2,a</sup>, Khaider Bouacha<sup>2,b</sup>, Kamel Chaoui<sup>\*,1,c</sup>, Wafia Ghabeche<sup>3,d</sup>, Khaoula Berkas<sup>1,e</sup>

<sup>1</sup>*Mechanics of Materials and Plant Maintenance Research Laboratory (LR3MI), Mechanical Eng. Dept., Faculty of Technology, Badji Mokhtar University, Annaba, Algeria*

<sup>2</sup>*Faculty of Sciences and Technology, Mohamed-Chérif Messaadia University, Souk-Ahras, Algeria*

<sup>3</sup>*Mechanics of Materials and Plant Maintenance Research Laboratory (LR3MI), Mechanical Eng. Dept., LR3MI, Elect. Eng. Dept., Faculty of Technology, A. Mira University of Bejaia, Algeria*

| Article Info   | Abstract   |
|--|--|
| <p><i>Article history:</i></p> <p>Received 14 Jan 2024<br/>Accepted 12 May 2024</p> <p><i>Keywords:</i></p> <p>Polyethylene pipe;<br/>Machining;<br/>RSM optimization;<br/>Filament;<br/>Stress-strain behavior;<br/>Mechanical properties</p> | <p>In order to explore the possibilities of manufacturing and testing specimens from extruded HDPE pipes to retrace material inherent properties, continuous filaments are circumferentially machined by grooving. The proposed protocol imposes to keep to a strict minimum damage effects since semi-crystalline polyethylene is sensitive to deformation and heat. A Taguchi plan is adopted with inputs (cutting speed; feed rate; depth of cut). The modeled performance characteristics are roughness criteria (Rt; Ra) and temperature (T°). Using ANOVA and response surface methodology, the optimized values are 137.0 m/min, 0.4 mm/rev and 4.0 mm respectively for Vc, f and ap. At the highest desirability, the values of Rt (1.100 μm), Ra (0.223 μm) and T (36.44 °C) are satisfactory compared to turning data. Tensile tests on specimens from outer, middle and inner pipe show that (σ-ε) curves are reproducible with a pronounced drawing zone, especially for the inner pipe layers. Practically, the elasticity modulus is increased by 43% from outer to inner layers while the utmost difference in the elastic limit is ~ 5%. Concerning failure strain, the increase is 47% meaning that the material shows a great predisposition to ductility. This behavior is related to the higher crystallinity in internal pipe layers.</p> |

© 2024 MIM Research Group. All rights reserved.

### 1. Introduction

Copolymerized high-density polyethylene (HDPE) pipes continue to find yet greater relevance fields as technical, durable and economical solutions compared to standard metals. New applications involving plastic pipes need an increased deal of safety, more diligence and reliable protective methods especially in pressurized installations such as oil and gas industries [1,2] and nuclear installations [3,4]. To achieve these goals, durability studies are imperative together with rigorous follow-ups of polyethylene pipes properties in order to guarantee optimal performance levels as required by procedural standards. Accessing the local properties of an extruded and rigid polymer bulk, such as thick pipes or reservoirs, is not an easy task, and in many cases, may require the use of slitting and material removal techniques. For instance, given the sensitivity of HDPE to various external parameters, conventional machining operations by material removal must take place under well-studied and appropriately defined conditions. Several studies have

\*Corresponding author: [kamel.chaoui@univ-annaba.dz](mailto:kamel.chaoui@univ-annaba.dz)

<sup>a</sup> [orcid.org/0009-0002-1961-8305](https://orcid.org/0009-0002-1961-8305); <sup>b</sup> [orcid.org/0000-0002-9349-5967](https://orcid.org/0000-0002-9349-5967); <sup>c</sup> [orcid.org/0000-0001-6532-9462](https://orcid.org/0000-0001-6532-9462);

<sup>d</sup> [orcid.org/0000-0003-1423-3203](https://orcid.org/0000-0003-1423-3203); <sup>e</sup> [orcid.org/0009-0004-4393-2817](https://orcid.org/0009-0004-4393-2817)

DOI: <http://dx.doi.org/10.17515/resm2024.150me0714rs>

Res. Eng. Struct. Mat. Vol. 11 Iss. 1 (2025) 73-96

investigated the machinability of semi-crystalline polymers such as HDPE, PP (polypropylene) and PA (polyamide). Published studies involving semicrystalline polymers are much more limited to turning, milling, sawing and drilling processes, but the case of grooving remains, until now, deprived of explicit optimized experimental data [5-11].

In the review authored by Alauddin et al. [5], key manufacturing processes such as orthogonal turning, milling, grinding and drilling for both thermoplastics and thermosets were briefly presented together with comments on optimal machining conditions. Also, important properties of plastic materials in relation to machining such as hardness, strength, heat and chemical effects were reviewed. On the other hand, Kaiser et al. [6] considered a comparative study of machined surfaces in three commercial polymers (Acrylic, uPVC and HDPE) while taking into account hardness, temperature, roughness and chip deformation. As expected, it was observed that better surface finish is obtained at higher cutting speed ( $V_c$ ) combined with low depth of cut ( $a_p$ ). Also, it noted that the surface hardness decreased as the temperature raised up due to the nature of amorphous thermoplastic. At the same time, the average temperature at chip-tool interface and the chip deformation were augmented with  $V_c$  and  $a_p$ . The study established that the surface finish was better for acrylics than uPVC and HDPE. At higher  $V_c$  and  $a_p$ , chip microstructure revealed that numerous crack-like flaws were created, while only fewer cracks were noticed at higher  $V_c$  and lower  $a_p$  [6]. Carr and Feger [7] employed single-point diamond to machine several polymers and they found that material type and its viscoelastic properties play a critical role in determining final surface roughness. As properties dependence on time and temperature is high, changing of parameters such as cutting velocity can alter the cutting mechanism from brittle fracture with rough irregular surfaces to ductile material removal with smooth surfaces. Usually, materials with the ability to deform in a ductile manner, tend to react to external cutting tools by rolling around the edge and for lower molecular weight polymers, cracking occurs well before the ductile regime is attained. On the other side, brittle fracture usually occurs in polymers having high glass transition temperature. They concluded that compressibility and tensile strength have significant effects on the relationship between tool rake angle and resultant workpiece surface roughness [7]. Kiass et al. [8] were the first to investigate the variability of mechanical properties across an HDPE-80 pipe using an original idea based on regular filaments machined by grooving. At that time, no optimization study of the machining conditions was performed. It was found that stress properties are increasing when going from outer diameter towards the inner one while strain properties did not show a clear tendency. The root causes of such behavior were attributed to the inherent stress state and crystallinity distribution across wall thickness as a result of differential cooling during melt extrusion and the subsequent temperature gradients. A linear relationship between filament yielding stress and Young's modulus was presented with supporting data from literature. Kaddeche et al. [9] proposed to search for the minimum required surface roughness which corresponds to the lowest cutting forces using Taguchi and grey relational analysis (GRA) methods when machining HDPE-100 pipes. It was found that the prevalent grey relational grade is best described by a recommended turning regime with  $V_c = 188$  m/min,  $f = 0.14$  mm/rev and  $a_p = 3$  mm. Based on the order of importance, the study established that roughness criteria was mostly controlled by  $a_p$  and  $V_c$  while specific cutting force is dominated by  $f$  and  $a_p$ . Hamlaoui et al. [10] employed RSM and ANOVA to study correlations between machining parameters on one side, and on the other side, HDPE surface roughness and cutting temperature. They concluded that the most influencing regime parameter on surface roughness criteria minimization is also  $f$  (feed rate) as all contributions fell within the interval (96-86%). Conversely, both cutting speed and depth of cut remained the main influencing parameters for the cutting temperature. For high industrial productivity, they proposed to use an optimized regime (119 m/min,

0.12 mm/rev and 0.5 mm) which ensures a limited cutting temperature of  $T^{\circ} \leq 32^{\circ}\text{C}$ , well below the maximum allowed as suggested by standardized practices of PE pipes and reservoirs.

Salles and Gonçalves [11] investigated the influence of both cutting speed and feed rate on surface roughness of UHMWPE under turning operation using hard metallic tools. They concluded that UHMWPE reaction is similar that of aluminum and wood turning. Although, cutting temperature was supposed to show noticeable influence on the surface finish, the cutting speed effect remained low. While many investigations related to plastic materials have concluded that  $V_c$  is the main significant parameter, the situation is somewhat different for UHMWPE as  $f$  was found to be the most sensitive factor in roughness creation. The generated chip was continuous and, according to literature, it indicates the utmost attainable industrial quality. Alternatively, Xiao and Zhang [12] found that the viscous deformation of machined thermoplastics (e.g., HDPE) shows a significant impact cutting forces, surface quality and chip geometry. They concluded that the optimal machining regime should not go beyond a limit which provokes visco-plastic tearing or brittle cracking and ought to take into account molecular mobility, polymer tenacity and glass transition temperature [7].

Recently, Mammeri et al. [13] devoted a study to filament manufacturing from HDPE-100 pipe by an orthogonal turning process. Two chief difficulties were encountered: (i) in-plane filament curvature, and (ii) slightly bowed rectangular filament section. Such technical hitches cannot be completely sidestepped because of the nature of material removal by turning operations. However, it was possible to reduce both of them to technically acceptable minimum levels. Besides optimizing cutting temperature and roughness, it was compulsory to introduce a diligent geometric parameter to account for and monitor filament curvature cutback throughout the evolution of the study. Both filament curvature and unbalanced cross-sectional area reduce the possibilities to prepare satisfactory straight-lined tensile specimens which are anticipated for property assessment across pipe wall. RMS and ANOVA results led to an interesting cutting regime combined with an adequate tool geometry ensuring acceptable filament shape and a cutting temperature below  $33^{\circ}\text{C}$ . The right cutting edge ( $\kappa_r$ ) and rake ( $\gamma$ ) angles were experimentally established and discussed in the case of tough PE turning [13]. Although several studies related to the machining of different polymers and composites have been published, the fact remains that this literature does not include any specific study to the specific grooving operation and its optimization for such viscoelastic materials. Usually, general recommendations with extended intervals are proposed in some guides but do not fulfill the sought solutions for a rigorous work. Besides cutting parameters ( $V_c$ ,  $a_p$  and  $f$ ), important limitations on temperature and roughness are not provided following an optimization approach.

The main objective of this research is to optimize cutting conditions of uniform and regular filaments by grooving operations from an HDPE gas pipe. The filament should cover the entire pipe thickness, i.e., it includes all (technically possible) layers ranging from the outer surface towards the inner one. Subsequently, a series of specimens, with predetermined dimensions, is subjected to tensile tests to reveal effects of the thermomechanical history induced by extrusion on the various embedded mechanical properties.

## 2. Experimental Methods

### 2.1. Material

As mentioned earlier, the experimental strategy was to prepare polyethylene filaments under specific machining conditions in order to study inherent properties as distributed within the pipe wall. The material was an extruded polyethylene pipe from an HDPE-100

resin according to European (EN 1555-2) and Algerian (NA 7591-2) standards. It was purchased from a local supplier of the CHIALI Co. (Sidi Bel-Abbès, Algeria) in the form of a 12 m section pigmented with carbon black [14]. The pipe standard dimension ratio (SDR) is 17.6 and its outer diameter is 200 mm [13-15]. Tables 1 and 2 summarize some key plastic pipe characteristics, based on approved standards, and regularly provided for product quality assurance.

Table 1. Major physical properties

| Property  | Method      | Value                      |
|---|-------------|----------------------------|
| Density   | ISO 1183    | 0.959 (g/cm <sup>3</sup> ) |
| Fluid Flow Index (190 °C/5.0 kg)                  | ISO 1133    | 0.23 (g/10 min.)           |
| Softening Temperature Vicat (VST/B/50 K/h (50 N)) | ISO 306     | 74 (°C)                    |
| Crystallinity                                     | ISO 11357-3 | 65.63 (%)                  |
| OIT (210 °C)                                      | EN 728      | 30 (min.)                  |
| Carbon Black Content                              | ISO 6964    | 2.25 (%)                   |

Table 2. Key mechanical properties for quality assessment

| Property  | Method      | Value                   |
|---|-------------|-------------------------|
| E (23 °C, V = 1 mm/min.)                        | ISO 527-1   | 900 (MPa)               |
| $\sigma_Y$ (23 °C, V = 50 mm/min.)              | ISO 527-1   | 23 (MPa)                |
| Tensile Creep Modulus (1000 h)                  | ISO 899-1   | 360 (MPa)               |
| Flexural Creep Modulus (4-Point Method, 2000 h) | DIN 19537-2 | 330 (MPa)               |
| Notched Charpy Impact (23 °C)                   | ISO 179     | 26 (kJ/m <sup>2</sup> ) |
| Shore Hardness (Shore D; 3 sec)                 | ISO 868     | 63                      |

## 2.2. Grooving Procedure

Fig. 1 shows the machining system specially developed for grooving operations of PE pipe. For this purpose, it is necessary to find a suitable clamping device so as not to damage the pipe surface by spindle jaws. Therefore, a self-tightening sleeve was manufactured to grasp the HDPE pipe segment with sufficient pressure and allow the grooving operation to take place according to the chosen parameters (Fig. 1).

After equilibrating the mounted pipe segment during rotation, machining must be done progressively given that small cylindricity defects in manufactured plastic pipes are common and are tolerated to a certain standard limit. It is essential to note any continuous chip portion damaged or lost due to cylindricity problems is recorded to be considered when identifying the actual length of the obtained strand at the end of one grooving operation. Each cutting step provides one continuous long chip (i.e., filament) in addition of one pipe ring having a pre-fixed width (between 2 mm and 24 mm) according to the nature of the next mechanical tests. Each cutting condition was carried out several times and only the filaments which meet the requirements set by the experimental protocol were

kept. Any filament obtained and presenting defects during machining will be rejected because it ought to represent the entire thickness of the pipe.

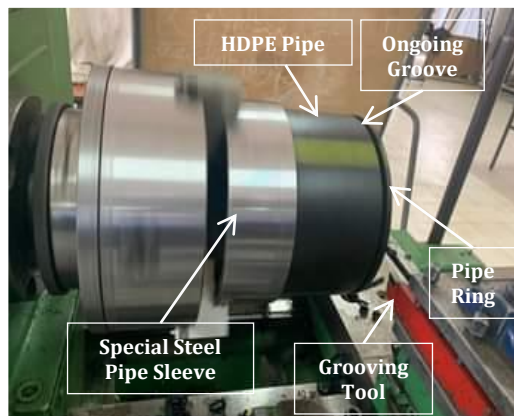


Fig. 1. View of external grooving of an HDPE pipe

Taguchi's planning method was applied for grooving operations in order to organize and carry out the experimental program [10,13,16]. In addition, such optimization is needed to get mathematical models describing the cutting process. Starting with input ( $V_c$ ,  $f$  and  $a_p$ ) and output ( $T$ ,  $R_a$ ,  $R_t$  and filament regularity) factors, the method helped determining the necessary number of tests. Grooving experiments were completed under dry conditions using a SN-40 parallel lathe having 6.6 kW spindle power as explained in literature [9,10,13,15,16]. So as to consider tool geometry, three commercial carbide tools (Type K20) with varying cutting-edge widths were employed. Automatic feeding, in each operation, is given only to the transverse carriage trolley keeping the longitudinal one stationary. The grooving machining conditions allowed to reduce Taguchi L27 plan to L9 while keeping orthogonality and as much as possible output information.

Taking advantage from the method given by Mammeri et al. [13], some choices were straightforward for tool geometry when switching from turning to grooving operations. Ultimately, a  $15^\circ$  positive rake angle ( $\gamma$ ) is defined and both clearance angle ( $\alpha$ ) and cutting-edge inclination angle ( $\lambda$ ) are respectively set equal to  $6^\circ$  and  $0^\circ$ . The cutting-edge angle ( $\kappa_r$ ), which is also called the steering angle, is formed by the cutting edge and the feed direction. It directly affects the cutting length ( $L_c$ ) and resulting chip (or filament) thickness ( $h$ ). The geometrical relationships expressing  $h$  and  $L_c$  as a function of machining conditions ( $f$  and  $a_p$ ) for any angle  $\kappa_r$  are given by equations (1) and (2) [17]:

$$h = f \cdot \sin(\kappa_r) \quad (1)$$

$$L_c = \frac{a_p}{\sin(\kappa_r)} \quad (2)$$

Since grooving operations on HDPE pipe are characterized by a  $90^\circ$  cutting-edge angle ( $\kappa_r$ ); therefore,  $L_c$  and  $h$  are respectively identified as depth of cut ( $a_p$ ; mm) and feed rate ( $f$ ; mm/rev). Consequently, filament regularity was easily checked as no out-of-plane bending or deviation ought to occur; i.e., curvature is obviously nil. This situation is sought by such experimental program for subsequent uniaxial filament testing. It should be noted that commercial HDPE pipes are not perfectly circular at outer and inner surfaces. Thus, complete grooving of a continuous filament took place after some initial pipe revolutions to correct cylindricity along its z-axis.

### 2.3. Roughness and Temperature Measurements

Roughness measurements were carried out in the longitudinal direction of the filament's outer side using a MITUTOYO SurfTest 301M roughness meter as explained elsewhere for turning and grooving [13,15]. Two roughness criteria (i.e., Ra and Rt) were chosen in order to have a comprehensive understanding of the readily accessible filament surface. This choice is kept alike for all experiments with 3 different measurements.

Filament surface temperature was measured as close as possible to the cutting zone. Its determination was achieved during the machining operations with a CAT-S60 smartphone equipped with a Lepton 2.5 sensor for the FLIR (Forward Looking InfraRed) thermal camera (Fig. 2). With an accuracy of  $\pm 2.0$  °C, it allows temperature measurements in the range of -20 to 120 °C with a good thermal sensitivity well-adapted to moving parts and black objects [13,18].



Fig. 2. Temperature measurement set-up using CAT S60 smartphone [13]

A special support was engineered to fix the camera with the possibility of orienting it according to the demand. The support consists of two mechanisms: the first one allows to hold firmly the smartphone to the upper tool holder trolley via a switching magnet and the second one is an articulated support commanding camera movement in three directions. Preliminary tests were carried out to delimit the measurement zone and the principal thermal scene parameters (i.e., emissivity, remoteness, atmospheric temperature, reflection, measurement angle and color palette). For each test, at least three measurements were taken during machining stabilization period towards the end of the operation.

### 2.4. Stress-Strain Tests

Mechanical In the second part of this work, variances of mechanical properties across pipe wall were investigated using monotonic tensile tests of filament specimens based on the general recommendations of ISO 527 standard. The stress-strain curves ( $\sigma$ - $\epsilon$ ) are obtained on a universal Zwick/Roell testing machine Type BT 1-FR2.5TN.D14. Its load cell type is a KAP-TC with a force limit of 2 kN. The operating system and data acquisition are controlled by the TestXpert® 2.0 Software, as indicated in Fig. 3.

Finite specimens were cut from the original long filament extending from outer pipe surface all-the-way through the wall. Each specimen is associated with a unique numeral, checked for any damage, then calibrated and the necessary observations are documented.



As a whole, the obtained filament is accepted as a wide-ranging representation of juxtaposed material layers forming the pipe wall thickness.

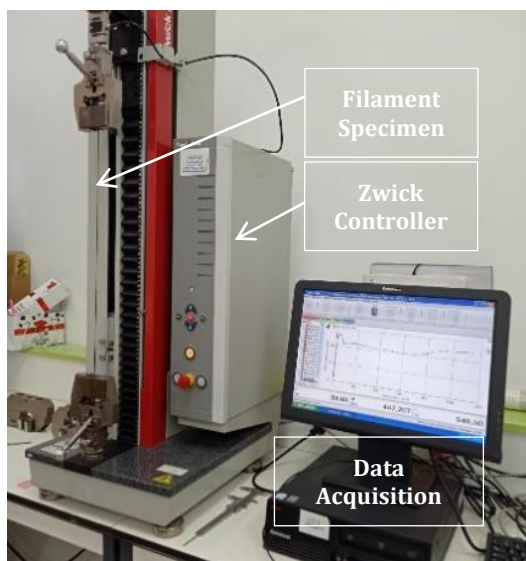


Fig. 3. Zwick universal tensile testing machine and TestXpert data acquisition system

The numbered layers can be assumed as a series of circumscribed rings with decreasing diameters from the outer side towards the inner side of the pipe. From each layer, an ordered succession of specimens of finite size ( $120 \times 4 \times 0.4 \text{ mm}^3$ ) was prepared and the remaining piece whose length is below 120 mm were saved for other purposes. The stress-strain curves ( $\sigma$ - $\epsilon$ ) are obtained at 50 mm/min.

### 3. Results and Discussion

#### 3.1. Filament Assessment

Fig. 4 shows the resulting machined filament by grooving as it starts at the outer pipe surface (Yellow mark) and it ends at the inner side (Deformed end). Throughout the machining operation, the cutting process is closely monitored to guarantee steadiness and continuousness of the removed material (i.e., the filament). The latter is considered as a manufactured product known conditions (cutting regime, cutting temperature, tool geometry, and at a given position along the pipe length) and hence, can be used for characterization (mechanical, structural, etc.). Each obtained filament is carefully spool-lose and stored in a plastic bag with an appropriate identification to avoid any alteration or damage.

In this study, the conditions for machining and tool selection have been improved compared to previous studies [8-10,16], making it possible to get even smaller filament thicknesses. However, these improvements unveiled the limits of quality parameters of marketed HDPE pipes especially for out-of-roundness and thickness tolerances. In fact, if the pipe is not accurately cylindrical, dimensional approximations must be made to reach thresholds which helps identifying the positional coordinates (radial and circumferential) of the specimen for each 0.4 mm thick layer. In other words, it is sometimes tolerated to lose a few layers, at the machining start-up, until the cutting process becomes unfluctuating and the produced filament is continuous and regular. Therefore, it is

necessary to consider these inevitable difficulties, since rectifications altering the pipe stress state or the polymer structure are not tolerated herein.

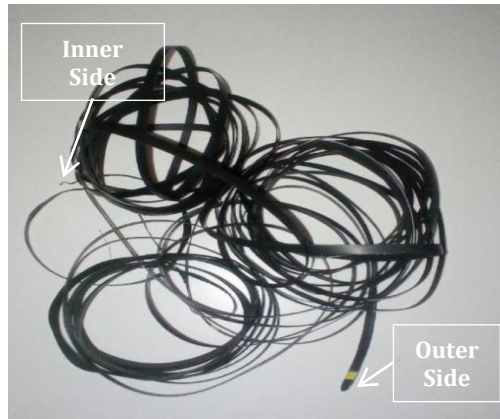


Fig. 4. A overall filament manufactured by grooving

The same approach is also effective for some layers at the innermost side which might be lost due to excessive deformations and material distortions. In all cases, it is necessary to take these adverse events into account during each cut. In addition, it is advised to make the appropriate choices to reduce the width and the mass of the resulting ring associated with each prepared filament.

### 3.2 Machining Optimization

#### 3.2.1 Taguchi Orthogonal Plan

The three cutting parameters levels are chosen based on published data, guidelines for plastics machining and on specific previous studies for similar polycrystalline polymers [8-11,19-21]. Following a previous study on turning of HDPE pipe material [13,15], lower and upper limits for  $V_c$ ,  $f$  and  $a_p$  are respectively (100 – 560 m/min), (0.34 – 0.63 mm/rev) and (2 – 3 mm) whereas, the intermediate levels are 140 m/min, 0.49 mm/rev and 4 mm as indicated in Table 3.

Table 3. Selected levels for cutting parameters

| Level | $V_c$   | $f$      | $a_p$ |
|-------|---------|----------|-------|
|       | (m/min) | (mm/rev) | (mm)  |
| 1     | 100     | 0.34     | 2     |
| 2     | 140     | 0.49     | 3     |
| 3     | 560     | 0.63     | 4     |

Conventional cutting factors ( $V_c$ ,  $f$  and  $a_p$ ) are considered as input parameters while performance characteristics comprise ( $T$ ,  $R_a$ ,  $R_t$  and  $L$ ). The geometrical parameter  $L$ (mm), defined in [13] as a gap representing a specified deviation between bent and straight filaments observed in the case of turning. Output parameters are recorded during or after the grooving operation depending on the case using a simplified Taguchi L9 mixed level (Table 4). In grooving operations, the parameter  $L$  representing the height of filament bent is visually and physically checked against a metallic straight ruler. As expected for grooving and the for the selected tool geometry, it is nil all the times (i.e., no curvature) and this is a reliable corroboration for the filament uniformness and levelness. It is observed that high  $V_c$  (560m/min) for all  $f$  levels (0.49; 0.63 and 0.34 mm/rev) produced unacceptable cutting

temperatures which exceeded or nearly equated the 40°C limit; thus, level 3 cannot lead to desirable machining regime regardless of ap values.

Table 4. L9 Taguchi experimental plan for HDPE grooving operations

| Run N° | Cutting Parameters |            |         | Performance Characteristics |         |         |        |
|--------|--------------------|------------|---------|-----------------------------|---------|---------|--------|
|        | Vc (m/min)         | f (mm/rev) | ap (mm) | T (°C)                      | Ra (µm) | Rt (µm) | L (mm) |
| 1      | 100                | 0.34       | 2       | 32.9                        | 0.44    | 0.97    | 0      |
| 2      | 100                | 0.49       | 3       | 35.3                        | 0.45    | 1.05    | 0      |
| 3      | 100                | 0.63       | 4       | 36.2                        | 0.49    | 1.13    | 0      |
| 4      | 140                | 0.34       | 4       | 35.9                        | 0.20    | 0.82    | 0      |
| 5      | 140                | 0.49       | 2       | 34.1                        | 0.29    | 0.88    | 0      |
| 6      | 140                | 0.63       | 3       | 34.8                        | 0.31    | 0.97    | 0      |
| 7      | 560                | 0.34       | 3       | 39.4                        | 0.29    | 0.75    | 0      |
| 8      | 560                | 0.49       | 4       | 44.3                        | 0.23    | 0.86    | 0      |
| 9      | 560                | 0.63       | 2       | 43.5                        | 0.30    | 0.93    | 0      |

It is understood that heat generation is intensely triggered when polymers are subjected to rapid frictional material removal operations. The lowest roughness value (Ra: 0.20 µm) is recorded at 140 m/min and 0.34 mm/rev which corresponds to an acceptable measured T (35.9 °C). From literature of polymer machining, it is known that lowering Vc, f and ap can lower the generated heat but, usually it follows that roughness criteria are catastrophically degraded [13,19,20].

3.2.2 ANOVA Approach

ANOVA conclusions on how initial regime factors affected the selected output parameters (Ra, Rt and T) are depicted in the following Tables 5–7. In all cases, Vc can be considered as the most significant factor among the regime parameters while ap is the less affecting factor.

Table 5. ANOVA of Ra

| Source            | DF | Seq SS   | Contribution | Adj SS   | Adj MS   | F-Value | P-Value |
|-------------------|----|----------|--------------|----------|----------|---------|---------|
| Model             | 5  | 0.082779 | 99.26%       | 0.082779 | 0.016556 | 79.97   | 0.002   |
| Linear            | 3  | 0.027935 | 33.49%       | 0.059173 | 0.019724 | 95.27   | 0.002   |
| Vc                | 1  | 0.021162 | 25.37%       | 0.051872 | 0.051872 | 250.55  | 0.001   |
| f                 | 1  | 0.004756 | 5.70%        | 0.002144 | 0.002144 | 10.35   | 0.049   |
| ap                | 1  | 0.002017 | 2.42%        | 0.004245 | 0.004245 | 20.50   | 0.020   |
| Square            | 1  | 0.051105 | 61.28%       | 0.051105 | 0.051105 | 246.84  | 0.001   |
| Vc*Vc             | 1  | 0.051105 | 61.28%       | 0.051105 | 0.051105 | 246.84  | 0.001   |
| 2-Way Interaction | 1  | 0.003739 | 4.48%        | 0.003739 | 0.003739 | 18.06   | 0.024   |
| Vc*f              | 1  | 0.003739 | 4.48%        | 0.003739 | 0.003739 | 18.06   | 0.024   |
| Error             | 3  | 0.000621 | 0.74%        | 0.000621 | 0.000207 |         |         |
| Total             | 8  | 0.083400 | 100.00%      |          |          |         |         |

Table 6. ANOVA of Rt

| Source            | DF | Seq SS   | Contribution | Adj SS   | Adj MS   | F-Value | P-Value |
|-------------------|----|----------|--------------|----------|----------|---------|---------|
| Model             | 5  | 0.100591 | 99.77%       | 0.100591 | 0.020118 | 260.62  | 0.000   |
| Linear            | 3  | 0.073017 | 72.42%       | 0.096247 | 0.032082 | 415.60  | 0.000   |
| Vc                | 1  | 0.039764 | 39.44%       | 0.062300 | 0.062300 | 807.06  | 0.000   |
| f                 | 1  | 0.032187 | 31.92%       | 0.033796 | 0.033796 | 437.80  | 0.000   |
| ap                | 1  | 0.001067 | 1.06%        | 0.002191 | 0.002191 | 28.38   | 0.013   |
| Square            | 1  | 0.025725 | 25.52%       | 0.025725 | 0.025725 | 333.25  | 0.000   |
| Vc*Vc             | 1  | 0.025725 | 25.52%       | 0.025725 | 0.025725 | 333.25  | 0.000   |
| 2-Way Interaction | 1  | 0.001849 | 1.83%        | 0.001849 | 0.001849 | 23.95   | 0.016   |
| Vc*f              | 1  | 0.001849 | 1.83%        | 0.001849 | 0.001849 | 23.95   | 0.016   |
| Error             | 3  | 0.000232 | 0.23%        | 0.000232 | 0.000077 |         |         |
| Total             | 8  | 0.100822 | 100.00%      |          |          |         |         |

For Ra, cutting speed contribution is in the lead with Vc and Vc<sup>2</sup> (respectively 25.37% and 61.28%). Similarly, for Rt, both forms of speed (Vc and Vc<sup>2</sup>) dominate with respective contributions of 39.44% and 25.52%. When it comes to cutting temperature which is supposed as the main limiting parameter in this process, the effect of Vc is much more pronounced since it explains 83.87% of total differences. It is noted that the contributions of ap in both cases did not exceed 3%. 7).

Table 7. ANOVA of T

| Source            | DF | Seq SS  | Contribution | Adj SS  | Adj MS  | F-Value | P-Value |
|-------------------|----|---------|--------------|---------|---------|---------|---------|
| Model             | 4  | 133.142 | 98.76%       | 133.142 | 33.285  | 79.54   | 0.000   |
| Linear            | 3  | 125.603 | 93.17%       | 132.310 | 44.103  | 105.40  | 0.000   |
| Vc                | 1  | 113.075 | 83.87%       | 112.159 | 112.159 | 268.04  | 0.000   |
| f                 | 1  | 6.726   | 4.99%        | 11.049  | 11.049  | 26.40   | 0.007   |
| ap                | 1  | 5.802   | 4.30%        | 10.803  | 10.803  | 25.82   | 0.007   |
| 2-Way Interaction | 1  | 7.538   | 5.59%        | 7.538   | 7.538   | 18.02   | 0.013   |
| Vc*f              | 1  | 7.538   | 5.59%        | 7.538   | 7.538   | 18.02   | 0.013   |
| Error             | 4  | 1.674   | 1.24%        | 1.674   | 0.418   |         |         |
| Total             | 8  | 134.816 | 100.00%      |         |         |         |         |

The feed rate contribution is important for Rt as the latter represents the height change between the topmost and the deepest points within a given measuring section while Ra is just an average variation of the roughness profile from a reference line. The averaging operation leads to lower Ra than actual roughness variations and keeps them always well below corresponding Rt measurements. For cutting temperature, it is concluded that Vc is dominant with more than 83% contribution (Table

Alternatively, Fig. 5 represents the variation of the responses in terms of Ra, Rt and T as a function of the most influencing input parameters (f and Vc) as deduced from the ANOVA section. As anticipated, both Ra and Rt describe a comparable shape represented by a steep decrease up to ~300 m/min followed by a sharp rise at higher speeds (Figs. 5a-5b). It appears that 300 m/min is a critical point which indicates the lowest values of Ra and Rt especially when feed rate f is at its minimum.

The effect of f on roughness criteria remains small within the range shown (0.30-0.66 mm/rev) and at low cutting speeds, the corresponding variations ( $\Delta Ra$ ) and ( $\Delta Rt$ ) are respectively  $\sim 0.2 \mu\text{m}$  and  $\sim 0.5 \mu\text{m}$ . In both cases, the global roughness values are lowermost for speeds in the range 250-350 m/min. However, when invoking temperature as a limiting criterion for material integrity, it is observed that at higher speeds ( $V_c > 300$  m/min), generated heat becomes a detrimental factor and lead to material degradation (Fig. 5c) especially at higher feed rates.

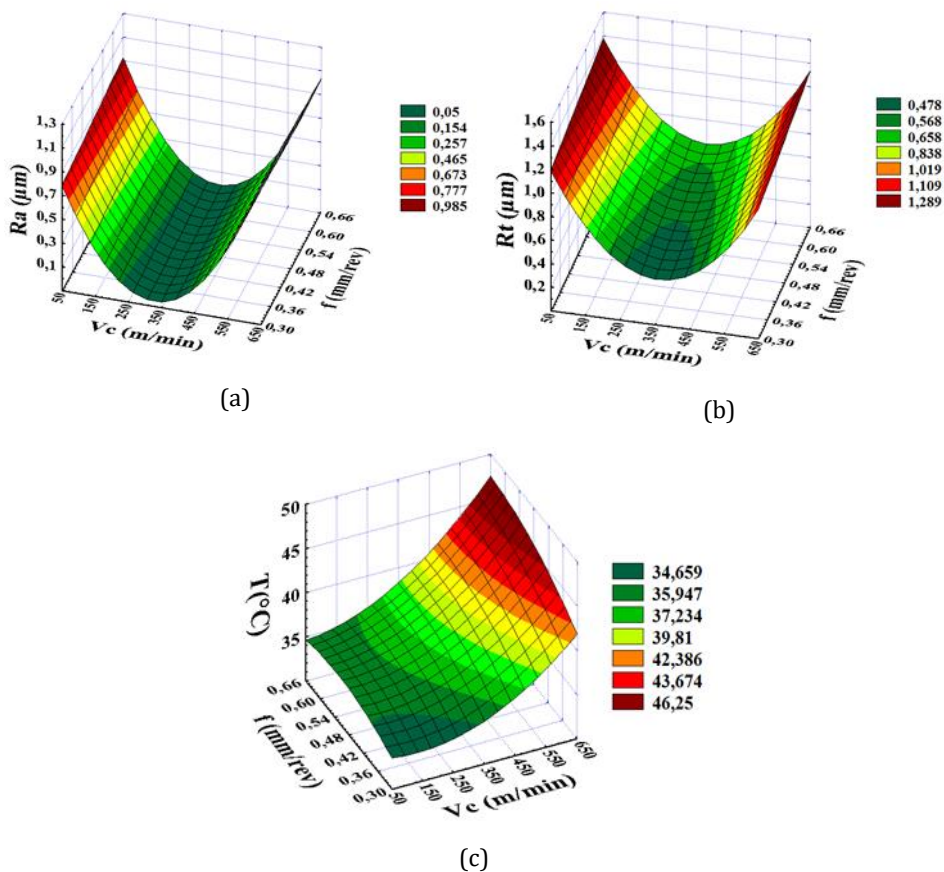


Fig. 5. Estimated response surface of performance characteristics versus Vc and f

### 3.2.3 Grooving Conditions Optimization

The optimization results are presented Table 8. The case evoking no constraints on both roughness criteria and cutting temperature is chosen. The reason is that only one most significant input factor (i.e., Vc) is found and there is a high probability that the associated

limiting temperature is well below the maximum set by the standards as shown from the experimental results.

Table 8. Parameters (8a) and optimization (8b) solution

|      | Response Parameters | Goal   | Lower | Target | Upper | Weight | Importance |
|------|---------------------|--------|-------|--------|-------|--------|------------|
| (8a) | Rt                  | Target | 0.95  | 1.10   | 1.33  | 1      | 1          |
|      | T                   | Target | 32.90 | 36.50  | 44.30 | 1      | 1          |
|      | Ra                  | Target | 0.20  | 0.22   | 0.49  | 1      | 1          |

| (8b) | Vc (m/min) | f (mm/tr) | ap (mm) | T (°)  | Ra (µm) | Rt (µm) | Composite Desirability |
|------|------------|-----------|---------|--------|---------|---------|------------------------|
|      | 137.194    | 0.4       | 4       | 36.448 | 0.223   | 1.100   | 0.991034               |

The targeted performance values with identical weights and importance levels together with the optimized parameters are shown in Tables 8a and 8b. When using the optimal desirability, the anticipated practical solution for grooving consists principally of a moderate cutting speed (137 m/min) and an acceptable cutting temperature (36.5 °C). HDPE literature does not report temperature data for grooving but for turning there is some similarities [9,10,13,16]. It is concluded that this optimization gives satisfactory parameters for the sought application under grooving process and the filaments can be employed to investigate property variances across the pipe wall. Fig. 6 indicates the response optimization for T, Ra and Rt.

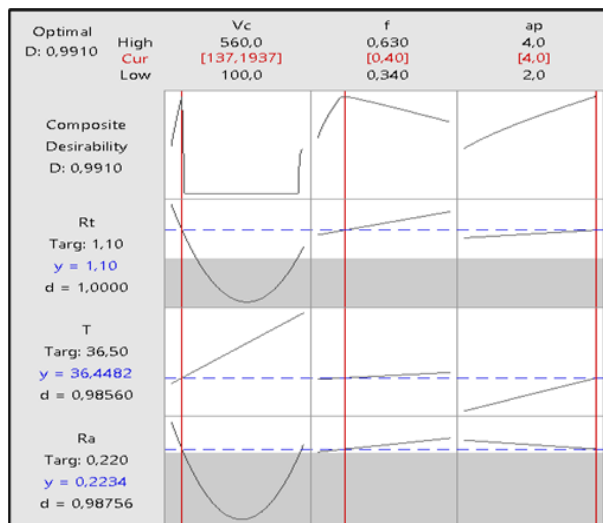


Fig. 6. Response optimization for T, Ra and Rt

Again, it is revealed that Vc is the most influencing factor for grooving process and its important effects on T are evident. On the other hand, both f and ap show limited effects on output parameters. As discussed in literature, PE is subject to heat induced phenomenon which may ultimately cause irreversible damage [11,12].

At this stage, it is interesting to discuss the corresponding regression equations which include all parameters and their interactions. It is understood that the models are reduced by eliminating terms with no significant effects on the responses. The final models of response equations in terms of input factors are as follows:

$$R_a = 0.9665 - 6.926 \cdot 10^{-3} V_c + 0.4336 f - 0.02887 a_p + 1.1 \cdot 10^{-5} V_c^2 - 8.98 \cdot 10^{-4} V_c \cdot f \tag{3}$$

$$R_t = 1.4870 - 5.686 \cdot 10^{-3} V_c + 0.3366 f + 0.02074 a_p + 7.0 \cdot 10^{-6} V_c^2 + 6.31 \cdot 10^{-4} V_c \cdot f \tag{4}$$

$$T = 30.15 - 2.59 \cdot 10^{-3} V_c - 3.45 f + 1.456 a_p + 0.04032 V_c \cdot f \tag{5}$$

In order to appreciate the goodness-of-fit, calculated R<sup>2</sup>, adjusted R<sup>2</sup> and standard error of the estimate are summarized in Table 9. It is observed that the coefficients R<sup>2</sup> (i.e., the percentage of the variation in the response that is explained by the model) and R<sup>2</sup> adjusted (i.e., which represents R<sup>2</sup> when adjusted for the number of predictors in the model relative to the number of experimental observations; filament roughness criteria and temperature) are very satisfactory for all output model parameters. The standard errors of the regression (or standard errors of the estimate) indicated by (S) are also very satisfactory compared to the experimentally measured data.

Table 9. R<sup>2</sup>, R<sup>2</sup> adj. and s for output parameters

| Output model parameter | R <sup>2</sup> (%) | R <sup>2</sup> Adjusted (%) | S          |
|------------------------|--------------------|-----------------------------|------------|
| T                      | 98.76%             | 97.52%                      | 0.6468 °C  |
| Ra                     | 99.26%             | 98.01                       | 0.01438 μm |
| Rt                     | 99.77%             | 99.39                       | 0.00878 μm |

It is accepted that common deviation sources between actually measured and statistically estimated data are diverse and they can be imputed to many circumstances proper to this study: (i) each experimental value used in the modeling is the result of an average value issued from 3 distinctive and consecutive measurements for the same test; (ii) in fact, the obtained statistical models are just approximation models and not interpolation functions; (iii) both uncertainties and engendered errors accumulated during testing may be in relation with the machine-tool condition, the chosen measuring instruments (roughness and temperature), the operator etc.; and finally, (iv) residual errors created when carrying out ANOVA analysis following the hypothesis of 95% confidence interval.

The following Table 10 illustrates cutting regime parameters adopted in different studies devoted to polyethylene machining and typical limits for various outputs. It is observed that both feed rates and depths of cut are well positioned in specific intervals dictated by polymer thermal and structural properties which are a basis for the corresponding industrial standards. However, cutting speed is variable over a wide range as it greatly influences production objectives (material removal rate) and product quality. It is found that the majority of optimization studies indicate Vc < 200 m/min. limit. In comparison to turning, reducing Vc for the grooving process contributes to obtain acceptable properties for the machined filaments.

Table 10. Comparison of literature data for PE martials machining

| machining process  | Cutting parameters |                 |            | Output parameters  |           | Refs         |
|--------------------|--------------------|-----------------|------------|--|-----------|--------------|
|                    | f (tr/min.)        | ap (mm)         | Vc (m/min) | T (°C)   | Ra (μm)   |              |
| Turning            | Constant (0.254)   | 0.5-4           | 3-27.5     | 33-45  | 3.5-6.8   | [6]          |
| Grooving, HDPE-80  | 0.5                | 2               | 17.66      | Variability of ( $\sigma$ - $\epsilon$ ) behavior across pipe wall |           | [8]          |
| Turning, HDPE-100  | 0.14               | 3               | 188        | <40  | 2.25      | [9]          |
| Turning, HDPE-100  | 0.12               | 0.5             | 119        | 32   | 0.86      | [10]         |
| Turning, UHMWPE    | 0.025-0.3          | Constant (~0.4) | 160 - 400  | Max. advisable service T°: 93°C                                    |           | [11] *       |
| Turning, HDPE      | 0.01               | 1.47            | 50         | Lowest surface roughness   |           | [21]         |
|                    |                    | 1               | 150        | Highest material removal   |           |              |
|                    |                    | 1.5             | 100        | Largest chip thickness   |           |              |
| Turning, HDPE-100  | 0.37-0.67          | 2-4             | 100-560    | 28.5-39.5  | 0.41-1.55 | [13]         |
|                    | 0.5                | 4               | 160        | 32   | 0.46      |              |
| Grooving, HDPE-100 | 0.34-0.63          | 2-4             | 100-560    | 32.5-44.3  | 0.20-0.49 | **This study |
|                    | 0.4                | 4               | 137        | 36   | 0.223     |              |

\*: Min. Mw = 3.1x10<sup>6</sup> g/mol.; Chip formation study; \*\*: based on optimized regime parameters of [13].

### 3.3 Mechanical Properties Crosswise Pipe Wall

In this second part, the outlines of a practical validation are considered in order to complete the procedure of manufacturing and testing filament specimens. At this stage, the primary objective was to obtain stress-strain behaviors and analyze few specific mechanical properties to get a first sense of the tendencies across the wall pipe.

#### 3.3.1 Assorting Test Specimens

The matching process for specimens made out of the overall filament is summarized in Fig. 7. Indeed, just after machining and recording the production parameters, the global filaments (chip) can be viewed in “rolled-up” (Fig. 7a) or “scrambled” (Fig. 7b) forms which are influenced by relieved internal stresses [21-23]. The latter is not particularly preferred as it increases the probability of filament entanglements and unwanted deformations during handling and storage. After identification of the yellow marks (external surface), dimensional measurements and examination of the 2 filament tips, the positions of the layers are identified and finally separated from each other (Fig. 7c). As the cumulative set of layers represents the pipe wall thickness; then, the length of one given layer is equivalent to the pipe diameter at that radial specified position.

It is necessary to record the sequential order of each 120 mm long segment as it appears and in a clockwise direction to obtain the number of specimens per layer of material. For instance, in Figs. 7c-d, the operation provided 4 effective specimens and one residue (i.e.; specimen length < 120 mm). This operation is repeated for the next layer until all layers are completed.



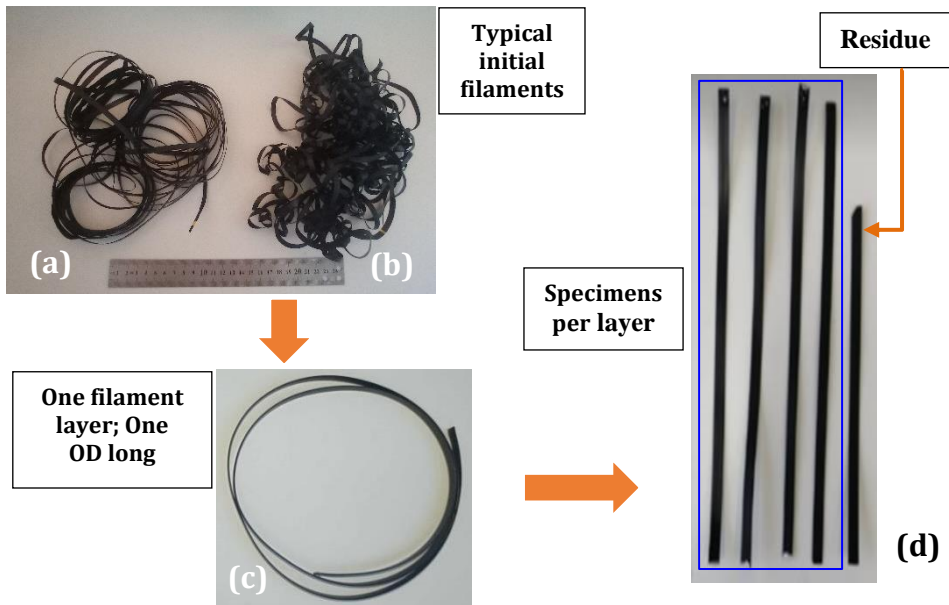


Fig. 7. Steps for testing specimen cutting

### 3.3.2 Tensile Characterization

Specimens subjected to monotonic traction show similar stretching behavior characterized by single or multiple necking zones as illustrated in Fig. 8. Initiation locations of drawn-out zones propagation direction remain aleatory. In some cases, one drawn zone begins around the specimen's mid-span and at the same time, starts propagating towards both grips (Fig. 8a). In other cases, the opposite occurs and the necking begins on the side of the jaws and evolves towards the middle of the specimen, forming one or multiple "spindles" of unstretched material (Fig. 8b).

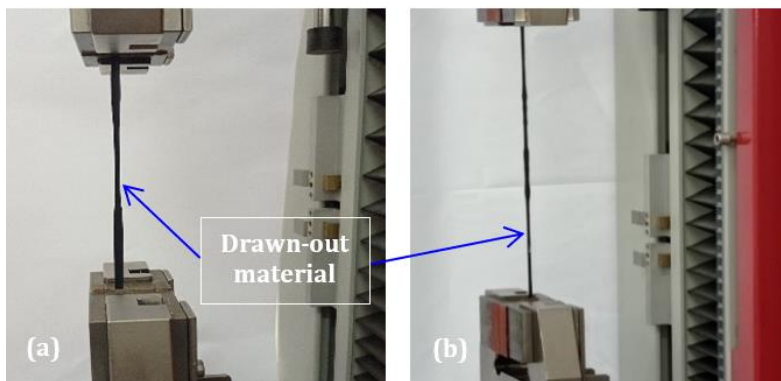
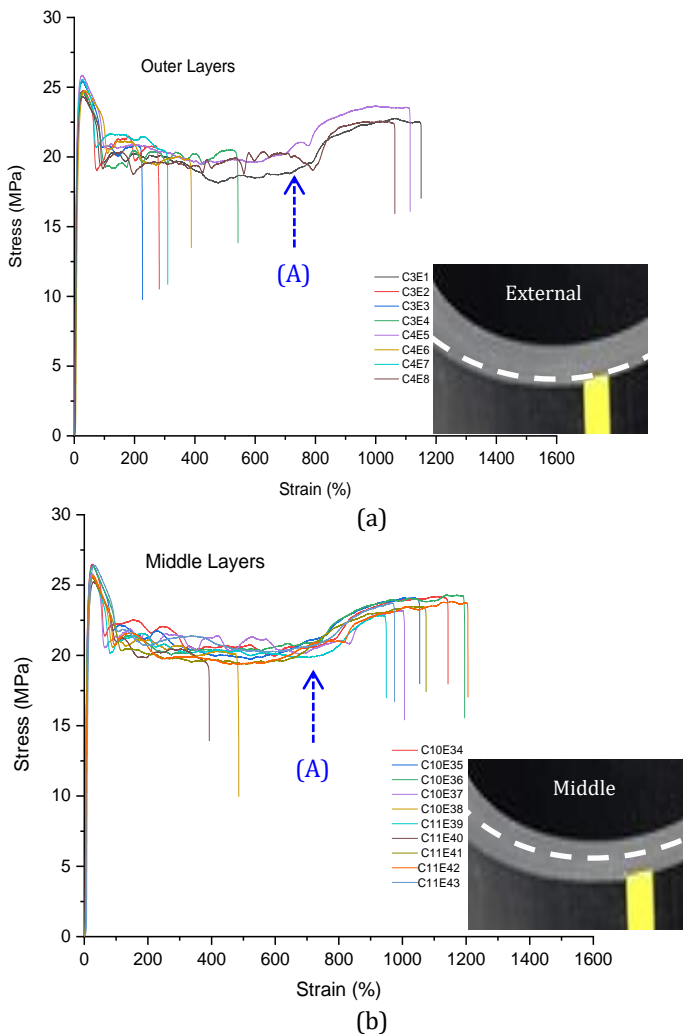


Fig. 8. Photographs of filament behavior under monotonic traction

In Fig. 9, a series of 25 tensile tests, carried out in the same laboratory conditions, is shown. They portray 3 different batches of successive layers located at average diameters of 196 mm, 188.6 mm and 179.2 mm respectively for outermost (Fig. 9a), intermediate (Fig. 9b) and innermost (Fig. 9c) layers. Each batch can be regarded as a cylindrical envelope with a total thickness  $\leq 4$  mm. In all cases, stress-strain ( $\sigma$ - $\epsilon$ ) curves replicate global similarities including a relatively narrow elastic zone and a widened plastically drawn zone as it is typically observed for semi-crystalline polymers. Physically, the last zone associates a cold drawing part which occurs at relatively constant stress and a final phase including plastic hardening and a tremendous rise in polymer chain orientation.

This behavior has already been observed in the literature for HDPE filaments and standard specimens in virgin and chemically aged conditions from engineering stress-strain curves [8,23-28]. Comparing behaviors of outer and inner layers (Figs. 9a, 9c), it is observed that the measured deformations at break increased significantly (from  $\sim 1100\%$  up to  $\sim 1500\%$ ) and the elastic resistance is also gradually increasing (from  $\sim 25$  MPa up to  $\sim 28$  MPa). On the other hand, the cold drawing part (middle zone) has rather shrunk in favor of increased plastic hardening and chain orientation [12,29-32].



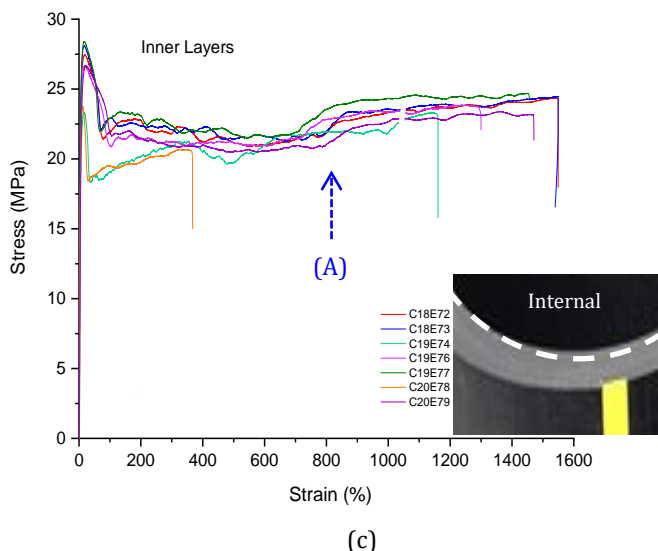


Fig. 9. Stress-Strain curves: (a) outer, (b) middle and (c) inner pipe layers

This suggests that the inner layers are much stronger than the outer layers. Undoubtedly, the pipe extrusion process is at the origin of these variations which were possible to reveal via such experimental methodology. Indeed, the abrupt cooling by intense water showers allows stored heat to be evacuated from the bulky mass of polyethylene while it is in the solidification phase. Also, this action does not allow material stress relaxation in a uniform manner, i.e., the internal layers remain sufficiently hot and experience slow cooling by natural convection as opposed to the external layers. These conditions favor embedding residual (internal) stresses and morphology variances in the pipe structure in terms of crystalline and amorphous parts [21-24,29-32].

### 3.3.3 Mechanical Properties Variability

The quantitative analysis of  $\sigma$ - $\epsilon$  curves makes it possible to extract several mechanical properties relating to resistance, elasticity and ductility. Table 11 shows the values of Young's modulus, elastic limit, yield strain and strain at break as a function of position in the pipe wall. In this case, 3 distinctive locations in the pipe wall are chosen with corresponding layer samples to elucidate differences. The values shown in Table 11 are averages of several tests for each layer as deduced from Fig. 9. Analyzing these results across the pipe wall (i.e., from outermost to innermost envelope), it appears that tendencies are manifested by an increase in  $E$ ,  $\sigma_y$  and  $\epsilon_f$  while  $\epsilon_y$  is showing a manifest decline. When switching from one layer to the next one, it is possible to perceive the variation (or the progression) of illustrated properties from one layer to another within one given envelope. At this level, it is noted that this progression does not follow only one trend, as the averages of most measured values for the innermost envelope are effectively fluctuating. Also, the greatest dispersion of results is found for the strain at failure, which is predictable because of the large stretching values especially for the layers located on the pipe internal side. Usually, the structure is supposed to be much more crystalline and what remains from the positive residual stresses is added to the applied load.

Fig. 10 depicts averaged properties for each of the 3 envelopes (outermost, midway and innermost). It is found that pronounced trends characterize these properties along the pipe radial direction. For both  $E$  and  $\sigma_y$ , the innermost layers are found to be more rigid and more resistant (Figs. 10a-b). These findings corroborate with the structural properties such as the degree of crystallinity and the morphology (e.g., lamellae thickness, tie-

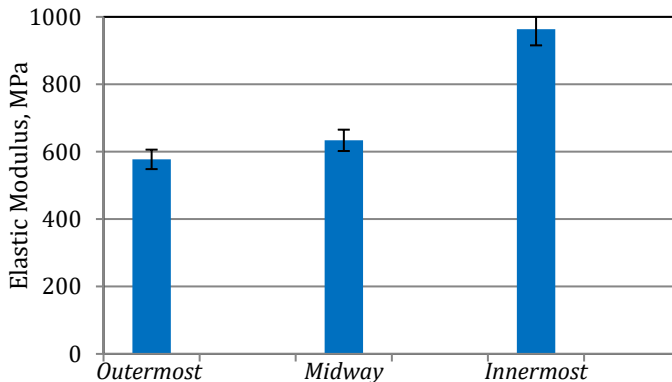
molecules density, etc.). On the other hand, as shown in Figs. 10c-d, the properties related to yield and failure strains are in opposite evolutions. The highest property variation between outermost and innermost envelopes is recorded for  $\epsilon_f$  with +51.3% followed respectively by E (+40.1%),  $\epsilon_y$  (-39,5%) and  $\sigma_y$  (+10.3%).

Table. 11. Mechanical properties of HDPE tube through the wall

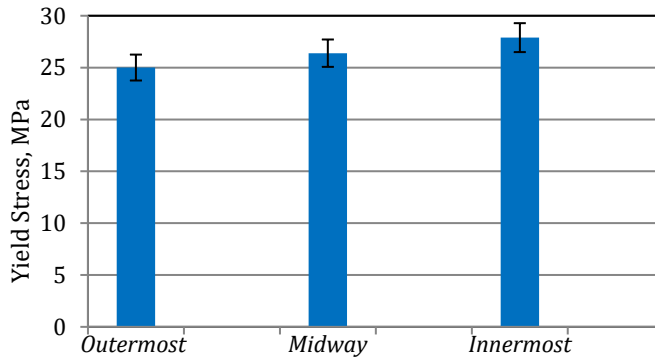
| Position in Pipe Wall | Layer Nb | Nb of specimens* | E (MPa)            | $\sigma_y$ (MPa)  | $\epsilon_y$ (%) | $\epsilon_f$ (%)     |
|-----------------------|----------|------------------|--------------------|-------------------|------------------|----------------------|
| Outermost             | 3        | (4)              | 573.75<br>(±38.75) | 24.86<br>(±28)    | 27.03<br>(±1.26) | 560.69<br>(±30.75)   |
|                       | 4        | (4)              | 580.60<br>(±31.75) | 25.15<br>(±0.49)  | 27.35<br>(±1.14) | 801.40<br>(±24.46)   |
| Midway                | 10       | (5)              | 651.20<br>(±38.64) | 26.42<br>(±0.18)  | 25.87<br>(±1.04) | 1113.65<br>(±83.35)  |
|                       | 11       | (5)              | 616.17<br>(±8.75)  | 26.36<br>(±0.29)  | 26.36<br>(±0.29) | 1050.38<br>(±88.87)  |
| Innermost             | 18       | (2)              | 1005.99<br>(±1.11) | 28.45<br>(±0.015) | 16.37<br>(±0.37) | 1500**<br>(-)        |
|                       | 19       | (3)              | 923.25<br>(±86.22) | 28.19<br>(±0.30)  | 16.24<br>(±0.38) | 1327.61<br>(±101.14) |
|                       | 20       | (2)              | 961.89<br>(±38.00) | 27.05<br>(±0.95)  | 16.75<br>(±0.25) | 1467.95<br>(±543.97) |

\* Valid; \*\*Maximum machine crosshead displacement reached.

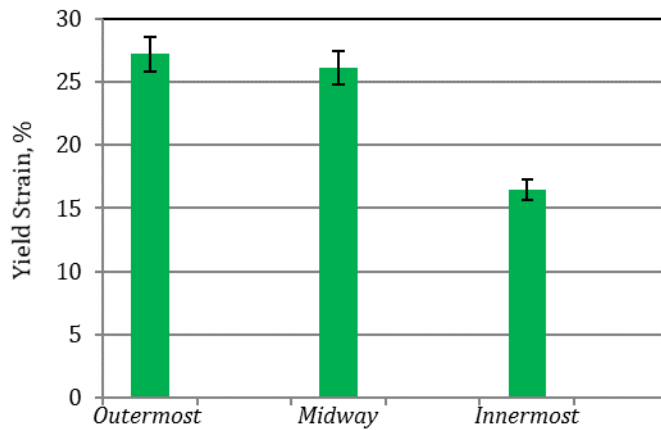
Furthermore, when the pipe wall thickness is conceived as 2 concentric envelopes: (i) an external one extending from outer-to-middle and, (ii) an internal envelope laying from middle-to-inner, the observed variations are quite different. Fig. 10 shows that the inner envelope (midway–innermost) presents the dominating variations for both E (+34.2%) and  $\epsilon_y$  (-37.0%). Inversely, the highest variation for  $\epsilon_f$  is associated with the outer envelope (outermost–midway) with 37.1%. In the case of yield stress, there is an equivalent contribution for both sides with roughly 5%. Although it is not easy to explain what happens during a traction test from the macromolecular point of view but polymer characterization techniques helped to disclose some understandings in the course of the last thirty years [31,32]. Some foremost conclusions on tensile behavior of polyethylene are reviewed in the following paragraphs.



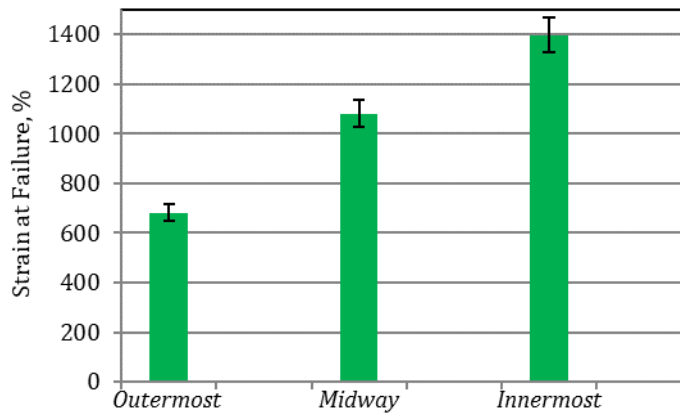
(a)



(b)



(c)



(d)

Fig. 10. Evolution of (a)  $E$ , (b)  $\sigma_y$ , (c)  $\epsilon_y$  and (d)  $\epsilon_f$  as a function in pipe wall

Using X-ray diffraction, Addiego et al. [31] concluded that monotonic traction of HDPE is associated with a significant volume change caused by local polymer chain

transformations affecting the semi-crystalline structure. The strained structure shows a progressive crazing mechanism at the spherulitic level followed by a cavitation phenomenon and subsequently, intense fibrillation restricting conventional chain movements. They also explained that a rivalry opposes volume increase and chain compaction respectively generated by crystallinity diminution (narrowing of the ordered domain) and chain orientation especially occurring throughout drawing and strain hardening phases. It is understood that both homogenous and inhomogeneous processes characterize the HDPE structure. In the first mechanism, the spherulites' dilatation is global (multidirectional) while for the following one, subsequent yielding occurs unevenly favoring the formation of crazes [30-32].

At another level, the interlamellar connections known as tie-molecules usually work as draw back momentum towards the original material state upon unloading. They contribute in conveying present loads from extended amorphous regions towards crystalline ones which undergo plastic deformation [32,33]. Séguéla [33] concludes that stress concentration on infinitesimal structural weaknesses lead to unexpected crazing mechanism which develops slow crack growth (SCG). Also, fragmented lamellae and unfolded polymer chains contribute to the fibrillar structure which constitutes drawn material which prolongs from the strain at yield location up to the onset of plastic strain hardening designated by arrow (A) in Fig. 9. This is one good reason to prefer the copolymerization process for HDPE as it favors the increase of intercrystallite tie-molecules and hence, ameliorates the long-term pipe resistance. According to an in-situ investigation carried out on the strain hardening occurrence in PE, it was confirmed that it is the result of the highly stretched tie-molecules fraction bonding the well-ordered chains [34].

## 5. Conclusion

Although a lot of research studies on plastics and composites machining are available, very few of them investigated the grooving process of semicrystalline polymers. The practicality of this work lies in the manufacture of filament specimens to retrace the thermomechanical history of an extruded pipe from copolymerized HDPE resins. The following conclusions may be drawn:

- Based of RSM, this study investigated the optimization of grooving regime to manufacture continuous polyethylene filaments from HDPE-100 gas pipe. The grooving operation is initiated from outer to inner pipe surface.
- In order to preserve the filament integrity, more attention is paid to cutting temperature as a key limiting parameter in this process. The effect of  $V_c$  is more pronounced as it explained 83.87% of total differences while the contribution of  $a_p$  did not exceed the 5% threshold. As expected,  $R_a$  and  $R_t$  described a comparable behavior illustrated by one "decrease-increase" sequence with a minimum around 300 m/min. It appears the 300 m/min cutting speed is an interesting point when searching for the lowest  $R_a$  and  $R_t$  values for a minimum feed rate. However, when considering cutting temperature, it is found that as  $V_c$  goes beyond this limit ( $V_c > 300$  m/min), more heat is generated and becomes a detrimental factor for material integrity especially at greater feed rates.
- The optimized solution (for a desirability  $\sim 1$ ) is characterized by very satisfactory roughness criteria and cutting temperature. The latter is well below the 40 °C imposed by HDPE pipes standards. A cutting speed of 137 m/min is also acceptable as the process of filament grooving should be carried out meticulously in order to increase reliability of afterward measured mechanical and/or structural properties.

- In all tested cases, the stress-strain curves as a function of 3 radial pipe wall locations duplicated overall similarities comprising a narrow elastic zone and a widened plastic one (drawing and hardening phases) typically observed for semi-crystalline polymers. However, they revealed interesting variances in terms of mechanical properties which are in phase with structural explanations given in literature.
- Young's modulus, yield stress and strain at break increased from outermost to innermost layers which suggests that pipe inner layers are much more stiff, resistant and show significant ductility. Across the pipe wall, the increases of  $E$ ,  $\sigma_y$  and  $\epsilon_f$  are respectively +40.1%, +10.3% and +51.3%. Inversely,  $\epsilon_y$  decreased by more than 39% when moving towards the innermost layer. Such differences may imply a way to equilibrate the high failure strain and the larger drawing zone observed at innermost layers when compared to outermost ones.
- Such variances need to be explained from the characterization of strained polymer layers (outermost, middle and innermost) as they undergo significant volume changes caused by localized polymer chain transformations that disturb the polyethylene semi-crystalline structure. In literature, it is proposed that spherulitic crazing, tie-molecules and cavitation mechanisms are behind the heterogeneous behavior of layers across the pipe wall during extrusion and cooling stages.
- The proposed grooving procedure and the established filament testing protocol are found to be suitable to investigate mechanical heterogeneities and quantify the associated variances. Also, structural analyses can be carried out at very localized points or layers within the pipe wall.

### Acknowledgements

Part of this research is achieved within the 2019 PRFU project: "Mechanical behavior and remaining life of HDPE pipes subjected to operating and environmental conditions" (Code A11N01UN230120190008). The authors are grateful to the Algerian Ministry of Higher Education and Scientific Research (DGRSDT-MESRS), the National Higher School of Mining and Metallurgy (Annaba) and the CRTI (Annaba). Commitment, investment and persistence in laboratory work of one author (Mrs. S. Mammeri) for the accomplishment of this research are highly praised. Fruitful discussions with lab researchers, master students (M2) and lab staff are very appreciated (Dr L. Alimi, Dr N. Hamlaoui, C. Djendi, F. Zoghba, A. Guenouche, I. Lalaymia, and A. Aoussat).

### Nomenclature:

|                          |   |
|--------------------------|---|
| ap:                      | Depth of cut (mm)   |
| DL:                      | Degrees of freedom  |
| $f$ :                    | Feed rate (mm/rev)  |
| F:                       | Fisher test   |
| HDPE:                    | High Density Polyethylene                                   |
| L:                       | Filament height bend (or curvature) (mm).                   |
| P:                       | Error value compared at 5%                                  |
| PE:                      | Polyethylene  |
| P-value:                 | Probability value   |
| R <sup>2</sup> :         | Determination coefficient                                   |
| R <sup>2</sup> Adjusted: | Response % variation explained by the model                 |
| Ra:                      | Arithmetic mean roughness ( $\mu\text{m}$ )                 |
| RSM:                     | Response Surface Methodology                                |
| Rt:                      | Total roughness ( $\mu\text{m}$ )                           |
| SDR:                     | Pipe diameter to thickness ratio (Standard Dimension Ratio) |
| T:                       | Temperature ( $^{\circ}\text{C}$ )                          |
| Vc:                      | Cutting speed (mm/min)                                      |

Greek Letters:

|                |                                      |
|----------------|--------------------------------------|
| $\alpha$ :     | Clearance angle (°)                  |
| $\sigma_y$ :   | Yield stress (MPa)                   |
| $\epsilon_f$ : | Failure strain (%)                   |
| $\epsilon_y$ : | Yield strain (%)                     |
| $\gamma$ :     | Rake angle (°)                       |
| $\kappa r$ :   | Cutting-edge (or steering) angle (°) |
| $\lambda$ :    | Cutting edge inclination angle (°).  |

References

- [1] PPI, Historical review of pressure rating methods for PE and PEX pipe in gas applications. Technical Report TR-55, 2023, 22.  
<https://www.plasticpipe.org/EnergyPipingSystems/EnergyPipingSystems/Publications/Energy-Technical-PPI-Literature.aspx>
- [2] PPI, Polyethylene Piping Distribution Systems for Components of Liquid Petroleum Gases. Technical Report TR-22, 2013, 7.  
<https://www.plasticpipe.org/common/Uploaded%20files/Technical/TR-22.pdf>
- [3] US Nuclear Regulatory Commission, Review of literature on the use of polyethylene (PE) piping in nuclear power plant safety-related class 3 service water systems. Report to The US NRC under NRC Contract No. DR-04-07-072 EMC2, 2007, 30.  
<https://www.nrc.gov/docs/ML1426/ML14266A208.pdf>
- [4] NESCC, Polymer Piping Codes and Standards for Nuclear Power Plants Current Status and Recommendations for Future Codes and Standards Development, Polymer Piping Task Group, 2013, 70.  
[https://share.ansi.org/shared%20documents/Meetings%20and%20Events/NESCC/NESCC\\_Final\\_Report\\_HDPE\\_Task\\_Group.pdf](https://share.ansi.org/shared%20documents/Meetings%20and%20Events/NESCC/NESCC_Final_Report_HDPE_Task_Group.pdf)
- [5] Alludin M, Choudhury IA, El Badarie MA, Hashmi MSJ. Plastics and their machining: A review. J. Mater. Proc. Technol., 1995; 54(1-4): 40-46.  
[https://doi.org/10.1016/0924-0136\(95\)01917-0](https://doi.org/10.1016/0924-0136(95)01917-0)
- [6] Kaiser MS, Fazlullah F, Ahmed SR. A comparative study of characterization of machined surfaces of some commercial polymeric materials under varying machining parameters. J. Mech. Eng., Automation & Control Syst. 2020;1(2):75-88.  
<https://doi.org/10.21595/jmeacs.2020.21643>
- [7] Carr WJ, Feger C. Ultraprecision machining of polymers. Precision Engineering, 1993; 15(4): 221-237. [https://doi.org/10.1016/0141-6359\(93\)90105-J](https://doi.org/10.1016/0141-6359(93)90105-J)
- [8] Kiass N, Khelif R, Boulanouar L, Chaoui K. Experimental Approach to Mechanical Property Variability through a High-Density Polyethylene Gas Pipe Wall. Journal of Applied Polymer Science. 2005; 97:272-281. <https://doi.org/10.1002/app.21713>
- [9] Kaddeche M, Chaoui K, Yaltese MA. Cutting parameters effects on the machining of two high density polyethylene pipes resins. Mechanics & Industry, 2012;13(5):307-316.  
<https://doi.org/10.1051/meca/2012029>
- [10] Hamlaoui N, Azzouz S, Chaoui K, Azari Z, Yaltese MA. Machining of tough polyethylene pipe material: surface roughness and cutting temperature optimization. Int. J. Adv. Manuf. Technol. 2017;92, 5(8):2231-2245.  
<https://doi.org/10.1007/s00170-017-0275-4>
- [11] Salles JLC, Gonçalves MTT. Effects of machining parameters on surface quality of the ultra-high molecular weight polyethylene (UHMWPE). Materia. 2002;8(1):1-10.
- [12] Xiao KQ, Zhang LC. The role of viscous deformation in the machining of polymers. Int. J. Mech. Sci. 2002;44(11):2317-2336.  
[https://doi.org/10.1016/S0020-7403\(02\)00178-9](https://doi.org/10.1016/S0020-7403(02)00178-9)



- [13] Mammeri S, Chaoui K, Bouacha K. Manufacturing of testing specimens from tough HDPE-100 pipe: Turning parameters optimization, Int. J. Res. Eng. Struct. Mat. (In press, Accepted: Nov., 1st, 2023, Online First).  
<https://doi.org/10.17515/resm2023.38ma0714rs>
- [14] Technical documents on HDPE gas pipes. CHIALI Co., 2023. <https://www.groupe-chiali.com>
- [15] Mammeri S, Bouacha K, Chaoui K. Optimization of HDPE material orthogonal machining. 1st Nat. Conf. on Sci. & Technol., Mascara University, 27-28 June 2023.
- [16] Belhadi S, Kaddeche M, Chaoui K, Yaltese M-A. Machining Optimization of HDPE Pipe Using the Taguchi Method and Grey Relational Analysis. Int. Polym. Process. XXXI 2016;4:491-502. <https://doi.org/10.3139/217.3271>
- [17] Vasques B. Étude du comportement du rayon d'arête et de son influence sur l'intégrité de surface en tournage à sec, Ph.D. Dissertation, Tours Univ., France, 2005.
- [18] Cat. S60 Smartphone, User Manual. Caterpillar, 2016.  
<https://www.catphones.com/download/User-Manuals/S60-Smartphone/S60-User-Manual-English.pdf>
- [19] Mitsubishi Chemical Group. Guide To Machining Plastic Parts, Metric System. Machinist's Toolkit (2023).  
<https://www.mcam.com/mam/41701/MCG-Machinist-Toolkit-A4-EU-metric.pdf>
- [20] Curbell Plastics, Inc. Plastic Turning Machining Guidelines (2003).  
<https://www.curbellplastics.com/services-capabilities/fabrication-machined-parts/plastic-machining-guidelines/plastic-turning-machining-guidelines/>
- [21] Alateyah AI, El-Taybany Y, El-Sanabary S, El-Garaihy WH, Kouta H. Experimental investigation and optimization of turning polymers using RSM, GA, Hybrid FFD-GA, and MOGA Methods. Polymers. 2022;14,3585. <https://doi.org/10.3390/polym14173585>
- [22] Chaoui K, Chudnovsky A, Moet A. Effect of residual stress on crack propagation in MDPE pipes. J. Mater. Sci. 1987;22:3873-3879. <https://doi.org/10.1007/BF01133334>
- [23] Patel Y. The Machining of Polymers. Ph.D. Dissertation, Imperial College London, UK, 2008. <https://spiral.imperial.ac.uk/bitstream/10044/1/4435/1/Patel-Y-2009-PhD-Thesis.pdf>
- [24] Rehab-Bekkouche S, Ghabeche W, Kaddeche M, Kiass N, Chaoui K. Mechanical behaviour of machined polyethylene filaments subjected to aggressive chemical environments. MECHANIKA. 2009;77(3):40-46.
- [25] Ghabeche W, Chaoui K, Zeghib N. Mechanical properties and surface roughness assessment of outer and inner HDPE pipe layers after exposure to toluene methanol mixture. Int. J. Adv. Manuf. Technol. 2019;103:2207-2225.  
<https://doi.org/10.1007/s00170-019-03651-z>
- [26] Djendi C. Étude expérimentale du vieillissement du HDPE dans un environnement de dichlorométhane liquide (DCM) : Analyses de la sorption et des propriétés mécaniques. Master's Thesis, Mech. Eng. Dept., Badji Mokhtar University, Annaba, Algeria, 2023. (in French).
- [27] Almomani A, Mourad AI, Deveci S, Wee JW, Choi B-H. Recent advances in slow crack growth modeling of polyethylene materials. Materials & Design. 2023;227:111720.  
<https://doi.org/10.1016/j.matdes.2023.111720>
- [28] Wang Y, Lin D, Xiang M, Cui M, Liu N. Experimental study on aging performance of polyethylene gas pipelines. 3rd Int. Conf. on Air Pollution & Environmental Eng., IOP Conf. Series: Earth and Environmental Science. 2021;631:012066.  
<https://doi.org/10.1088/1755-1315/631/1/012066>
- [29] Humbert S, Lame O, Vigier G. Polyethylene yielding behaviour: What is behind the correlation between yield stress and crystallinity? Polymer. 2009; 50:3755-3761.  
<https://doi.org/10.1016/j.polymer.2009.05.017>

- [30] G'Sell C, Dahoun A, Royer FX, Philippe MJ. The influence of the amorphous matrix on the plastic hardening at large strain of semicrystalline polymers. *Modelling & Simulation in Mater. Sci. & Eng.* 1999;7(5):817-828.  
<https://doi.org/10.1088/0965-0393/7/5/313>
- [31] Addiego F, Dahoun A, G'Sell C, Hiver JM. Characterization of volume strain at large deformation under uniaxial tension in high-density polyethylene. *Polymer.* 2006;47:4387-4399 <https://doi.org/10.1016/j.polymer.2006.03.093>
- [32] Addiego F, Dahoun A, G'Sell C., Hiver JM, Godard O. Effect of microstructure on crazing onset in polyethylene under tension. *Polymer Eng. & Sci.* 2009;49(6):1198-1205.  
<https://doi.org/10.1002/pen.21194>
- [33] Séguéla R. critical review of the molecular topology of semicrystalline polymers: The origin and assessment of intercrystalline tie molecules and chain entanglements. *J. Polym. Sci. Part B: Polym. Phys.* 2005;43(14):1729-1748.  
<https://doi.org/10.1002/polb.20414>
- [34] Kida T, Hiejima Y, Nitta K-H, Yamaguchi M. Evaluation of microscopic structural changes during strain hardening of polyethylene solids using In situ Raman, SAXS, and WAXD measurements under step-cycle test. *Polymer.* 2022;250:124869.  
<https://doi.org/10.1016/j.polymer.2022.124869>

# Optimizing concrete strength through pozzolan variation, heat treatment, and alkaline solution modulation: A comprehensive study

Andi Yusra<sup>\*1, a</sup>, Jasmi Jasmi<sup>1, b</sup>, Hernanda Mirza Pratama Simatupang<sup>1, c</sup>, Irwansyah Irwansyah<sup>2, d</sup>, Lissa Opirina<sup>1, e</sup>

<sup>1</sup>Department of Civil Engineering, Teuku Umar University, Aceh, Indonesia

<sup>2</sup>Department of Mechanical Engineering, Syiah Kuala University, Aceh, Indonesia

## Article Info

## Abstract

### Article history:

Received 05 Feb 2024

Accepted 05 May 2024

### Keywords:

Pozzolan;

Rice husk ash;

Palm shell ash;

Concrete strength;

Functional groups of compounds

The study aimed to assess concrete characteristics and mechanical properties by incorporating pozzolan variations, heat treatments, and alkaline solution molarities. It focused on identifying the optimal pozzolan addition percentage for achieving maximum concrete strength. Specimens underwent heat treatments at 60°C, 90°C, and exposure to alkaline solutions with molarity levels of 6M for rice husk ash and 8M for palm shell ash (PSA). Compressive strength testing at 28 days revealed the most optimal strength of 25.80 MPa in concrete without heat treatment, with 10% Palm Shell Ash pozzolan addition. Non-pozzolan concrete subjected to 1 day of 90°C heat treatment exhibited a strength of 21.99 MPa. The lowest strength observed in concrete without heat treatment, with 15% rice husk ash, resulting in 12.50 MPa. FTIR analysis focused on the chemical aspects of concrete, particularly changes in molecular structure due to different parameters. Composite concrete samples incorporating rice husk ash pozzolan and varying alkaline solution concentrations showed negligible differences. Further analysis found that mixing concrete with 15% Palm shell ash without heat treatment resulted in optimal compressive strength of 22.60 MPa, highlighting PSA's potential in increasing concrete strength. The research also emphasized the effect of temperature on concrete strength, with non-pozzolan concrete heated at 90°C for 1 day showing decreased strength. Comparison of pozzolan influence revealed that Rice Husk Ash tended to reduce concrete strength, especially at higher percentages, indicating a different response to pozzolan types. FTIR analysis identified chemical components in Rice Husk Ash (RHA) pozzolan concrete, laying the foundation for understanding pozzolan-concrete matrix interaction. However, further analysis needed for accurate interpretation of FTIR results and understanding the mechanism behind pozzolan's influence on concrete strength.

© 2024 MIM Research Group. All rights reserved.

## 1. Introduction

The significance of mineral admixture concrete as a prominent new material globally for both new construction and rehabilitation purposes is evident. The studies indicate that mineral admixtures, including blast furnace slag, fly ash, and silica fume, contribute to the improvement of concrete strength and durability. Ongoing research over years has dedicated to exploring the use of mineral admixtures to enhance concrete properties. Additionally, economic advantages, such as lower cement requirements, and

\*Corresponding author: [andiyusra@utu.ac.id](mailto:andiyusra@utu.ac.id)

<sup>a</sup>[orcid.org/0000-0003-4779-0815](https://orcid.org/0000-0003-4779-0815); <sup>b</sup>[orcid.org/0009-0005-7727-5410](https://orcid.org/0009-0005-7727-5410); <sup>c</sup>[orcid.org/0009-0009-5859-3578](https://orcid.org/0009-0009-5859-3578);

<sup>d</sup>[orcid.org/0000-0001-8987-2507](https://orcid.org/0000-0001-8987-2507); <sup>e</sup>[orcid.org/0009-0003-4495-9723](https://orcid.org/0009-0003-4495-9723)

DOI: <http://dx.doi.org/10.17515/resm2024.175ma0205rs>

Res. Eng. Struct. Mat. Vol. 11 Iss. 1 (2025) 97-111

environmental considerations, play a crucial role in the increasing utilization of mineral admixtures, [1-5].

The utilization of supplementary cementitious materials (SCMs) in concrete has gained significance due to reasons. Concrete, recognized as the second most utilized material globally, constitutes over 20% of ordinary Portland cement (OPC), raising environmental concerns owing to its association with approximately 8% of worldwide carbon dioxide emissions during manufacturing, [1-3]. In response to the escalating demand in the global construction industry, scholars and academics are actively exploring sustainable alternatives, [4-6].

Over the last few decades, there has been a notable shift towards incorporating supplementary cementitious materials (SCMs), which derived from industrial by-products or natural pozzolan materials, as partial substitutes for cement. These SCMs include fly ash (FA), ground granulated blast furnace slag (GGBS), silica fume (SF), metakaolin (MK), limestone, fine glass powder, among others, [7-9]. This strategic use of SCMs not only contributes to cost reduction in concrete production but also imparts technical advantages, [10-12]. The incorporation of SCMs in concrete shown to decrease the heat of hydration and enhance the overall durability of the concrete structure.

The efficacy of curing practices for pozzolanic cement concrete is a focal point of concern, given the strong dependency of the pozzolanic reaction on proper curing, [13-14]. Over the last few decades, there has been a notable shift towards incorporating supplementary cementitious materials (SCMs), which derived from industrial by-products or natural pozzolan materials, as partial substitutes for cement. These SCMs include fly ash (FA), ground granulated blast furnace slag (GGBS), silica fume (SF), metakaolin (MK), limestone, fine glass powder, among others, [15-19].

Concrete is a highly popular construction material, frequently employed as a key component in building planning and design. This popularity stems from advantages it offers, such as high compressive strength, ease of manufacture and maintenance, the abundance of raw materials in nature, and economic feasibility. Sometimes, to achieve optimal quality in execution, admixtures, fibers, or non-chemical construction materials can be added with proper proportions and employing appropriate mixing and execution techniques, enhancing the overall result, [20-23].

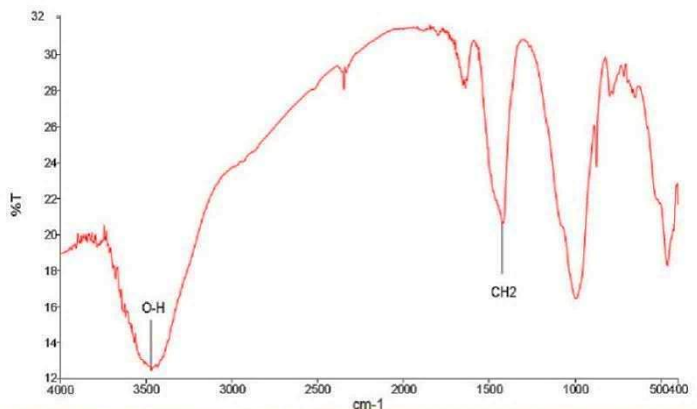


Fig. 1. Compound functional group test results on non-pozzolan concrete by FTIR [27]

The Fourier Transform Infrared (FTIR) analysis method utilized to elucidate the chemical aspects of concrete. This involves examining alterations in the molecular structure of concrete induced by various parameters, such as variations in pozzolan, heat treatment, and exposure to alkaline solutions, [24-26]. Figure 1 displays the results of FTIR testing on concrete without using pozzolan, which only reveals two chemical bonds: O-H and CH<sub>2</sub>. This limitation arises because non-pozzolan concrete involves solely a chemical reaction between the cement material and water, with no other chemical reactions occurring. In FTIR analysis, visible absorption bands provide insights into the chemical bonds within the sample. However, interpreting FTIR results for non-pozzolan concrete may be more constrained, often only serving to identify the presence of organic compounds or polymers in the concrete mixture. The research aims to comprehend the characteristics of concrete and its mechanical attributes. This entails examining the influence of varied factors, such as pozzolan variations, various heat treatments, and different molarity levels of alkaline solutions, on concrete properties. The primary objective is to determine the optimal percentage of pozzolan addition for achieving the highest concrete strength.

The materials utilized in this investigation consist of Portland Cement, palm kernel shell ash pozzolan, and rice husk ash, with pozzolan addition percentages varying at 5%, 10%, and 15%. The study involves subjecting concrete specimens to different heat treatments at temperatures of 60°C and 90°C, which is expected to offer insights into the effects of heat on concrete mechanical properties. Compressive Strength Testing: The research includes conducting compressive strength testing at 28 days to evaluate the performance of different concrete mixtures. The goal is to determine the most optimal compressive strength under various conditions. Additionally, the study employs Fourier Transform Infrared (FTIR) analysis to focus on the chemical aspects of concrete. This involves examining changes in the molecular structure of concrete due to different parameters such as pozzolan variations, heat treatments, and alkaline solutions.

Composite concrete, also known as fibre concrete, is a type of concrete reinforced by adding fibres to the concrete mixture. This reinforcement enhances strength, resistance to cracking, and overall mechanical performance. Commonly used fibres include polypropylene, glass, steel, or other types that provide additional support to concrete, [27-29]. Overall, the aim of the study was to investigate factors that can affect concrete strength and then optimize them. By analysing variations in pozzolan use, heat treatment, and modulation of alkaline solutions, the study aims to provide a better understanding of how to improve concrete performance in construction applications. The differences between this study and previous studies. Research Variations: This study includes a wider range of additional variations in terms of the types of pozzolan used (such as rice husk ash and palm shell ash), different heat treatments, and different concentrations of alkaline solutions. This suggests a more comprehensive approach in analysing the influence of factors on the mechanical properties of concrete.

- **Research Focus:** This study focuses more on finding out the optimal pozzolan variation in achieving optimal concrete strength. This suggests that the study has a clearer and more specific focus on identifying the most important parameters in improving concrete strength.
- **Use of FTIR Analysis:** This study also uses FTIR analysis to examine the chemical aspects of concrete, especially changes in molecular structure due to different parameters. This suggests that the study broadens its scope for understanding the chemical interactions between pozzolan and concrete matrices.
- **Additional Findings:** The study found that the addition of oil palm shell ash without heat treatment resulted in optimal compressive strength in concrete, while the addition of rice husk ash tended to reduce the strength of concrete, especially at a

higher percentage. This is an additional discovery that provides new insights in the selection of the right pozzolan to improve the quality of concrete.

- Research Expansion: Nonetheless, the study also highlights the need for further analysis to interpret FTIR results more accurately and understand the mechanisms behind pozzolan's influence on concrete strength. This suggests that this study provides a foundation for advanced research in this topic.

## 2. Methods and Mix Design

### 2.1. Material Preparation

The materials used to make normal-quality concrete include Portland Cement Composite (PCC), coarse aggregate (natural stone), fine aggregate (sand), shell powder, wicker fibre, and water. The cement chosen for this study is PCC cement. Laboratory examination of this cement not conducted because it adheres to standards. Visual inspection will only conduct on the cement bag to ensure there are no damages such as tears and no hard lumps present.

Coarse aggregates derived from natural stone and fine aggregates derived from sand sourced from the KRUENG MEUREUBO River, Aceh Barat Regency. Inspection of coarse aggregates (natural stone) and fine aggregates (sand) as raw materials for concrete requires an examination of physical properties to meet planned standards. This examination includes aggregate properties such as specific gravity, absorption, bulk density, and sieve analysis. Figure 2 shows the process of making an alkaline solution with a molarity of M6, and 10M.



Fig. 2. Preparation of alkaline solutions

Pozzolan Variations is Palm shell ash and rice husk ash. Pozzolan addition percentages is 5%, 10%, and 15%. The objective is to identify the optimum pozzolan content for optimal concrete strength. Heat Treatments, temperatures: 60°C and 90°C. Heat-treated specimens at 1 and 2 days. The goal is to assess the impact of different heat treatments on concrete properties. Alkaline Solutions, molarity levels 6M for rice husk ash and 8M for palm shell ash. The objective is to investigate the influence of alkaline solutions on concrete characteristics. FTIR Analysis, focus on chemical aspects and molecular structure changes. Parameters affecting the molecular structure include pozzolan content, heat treatments, and alkaline solutions. The objective is to understand the chemical variations in concrete due to different parameters. Composite Concrete Samples, incorporate rice husk ash and palm shell ash pozzolan with varying alkaline solution concentrations (0% to 15%). Negligible differences observed in bonding and compound types across concentrations. Image analysis demonstrates uniformity in bonding and compound types.

Figure 3 shows the palm shell ash slag material to use as a binder, and Figure 4 displays Rice Husk Ash. Firstly, 'palm shell ash' refers to the ash from palm kernel burning, while 'Rice Husk Ash' derived from burned rice husks. These materials used as binders in composite concrete. Here are their potential benefits and uses, palm shell ash Slag. This material can provide additional strength to concrete, making it more resistant to pressure and loads. Utilizing palm shell ash and slag as binders can aid in waste utilization and support recycling practices. Rice Husk Ash can help reduce pores in concrete, increasing material density and strength. The use of rice husk ash in composite concrete can reduce the need for conventional materials, thereby improving the energy efficiency of concrete production. The use of these two types of ash as binders in composite concrete can offer economic and ecological advantages. However, it is crucial to note that the formulation and proportions of these ingredients must be carefully considered to ensure the desired mechanical and functional properties of concrete. Laboratory tests and analysis also required to validate the performance of composite concrete using these materials.



Fig. 3. Slag from burning palm shell ash



Fig. 4. Rice Husk Ash

Figure 4 shows the location of the rice processing plant, where Rice Husk Ash (RHA) waste observed utilized as a natural pozzolan in the production of composite concrete. This process involves incorporating an RHA binder and an alkaline solution, with sodium silicate serving as an activator.

## 2.2 Mix Design

The research will employ a concrete mixture with a targeted strength of 20 MPa. The concrete mix design methodology follows the guidelines outlined in the American Concrete Institute (ACI) 211.1-22 standard. The standard specimen for testing will be cylindrical, with a diameter of 15 cm and a height of 30 cm, and it will contain aggregate with a maximum diameter of 19 mm.

The design of the test specimens in this study includes evaluating the characteristics and mechanical properties of concrete with variations in the addition of pozzolan, different heat treatments, and variations in the molarity of alkaline solutions. The following outlines the design of the test specimens, including the materials used: Portland Cement, Palm Shell Ash, Pozzolan Rice Husk Ash, and aggregate. Pozzolan addition variations are set at 5%, 10%, and 15%, while heat treatments are conducted at 60°C and 90°C. The alkaline solution has a molarity of 6M for rice husk ash and 8M for palm shell ash. Test specimen creation involves mixing concrete with varying percentages of pozzolan addition. Concrete specimens then created and grouped based on heat treatment conditions and alkaline solution concentrations. Detailed information about the test specimens provided in Table 1.

Table 1. Test specimen design

| Specimens            | Age of test<br>Day | Molarity Alkaline |     |     | Thermal Curing |          |          |
|----------------------|--------------------|-------------------|-----|-----|----------------|----------|----------|
|                      |                    | 0 M               | 6 M | 8 M | Thermal        |          |          |
|                      |                    | I                 | II  | III | 0°C            | 60°C     | 90°C     |
| Concrete<br>Cylinder | 14 Days            | 3                 | 0   | 0   | 0              | 1 D 60°C | 2 D 90°C |
|                      | 28 Days            | 3                 | 0   | 0   | 0              | 1 D 60°C | 2 D 90°C |
| CRHA 0%              | 14 Days            | 0                 | 3   | 0   | 0              | 1 D 60°C | 2 D 90°C |
|                      | 28 Days            | 0                 | 3   | 0   | 0              | 1 D 60°C | 2 D 90°C |
| CRHA 5%              | 14 Days            | 0                 | 3   | 0   | 0              | 1 D 60°C | 2 D 90°C |
|                      | 28 Days            | 0                 | 3   | 0   | 0              | 1 D 60°C | 2 D 90°C |
| CRHA 10%             | 14 Days            | 0                 | 3   | 0   | 0              | 1 D 60°C | 2 D 90°C |
|                      | 28 Days            | 0                 | 3   | 0   | 0              | 1 D 60°C | 2 D 90°C |
| CRHA 15%             | 14 Days            | 0                 | 3   | 0   | 0              | 1 D 60°C | 2 D 90°C |
|                      | 28 Days            | 0                 | 3   | 0   | 0              | 1 D 60°C | 2 D 90°C |
| Total<br>specimens   |                    | 6                 | 18  |     |                |          |          |
| CPSA 5%              | 14 Days            | 0                 | 0   | 3   | 0              | 1 D 60°C | 2 D 90°C |
|                      | 28 Days            | 0                 | 0   | 3   | 0              | 1 D 60°C | 2 D 90°C |
| CPSA10%              | 14 Days            | 0                 | 0   | 3   | 0              | 1 D 60°C | 2 D 90°C |
|                      | 28 Days            | 0                 | 0   | 3   | 0              | 1 D 60°C | 2 D 90°C |
| CPSA 15%             | 14 Days            | 0                 | 0   | 3   | 0              | 1 D 60°C | 2 D 90°C |
|                      | 28 Days            | 0                 | 0   | 3   | 0              | 1 D 60°C | 2 D 90°C |
| Total<br>specimens   |                    |                   |     | 18  |                |          |          |

For test specimens without the addition of pozzolan and alkali solution, there are 6 pieces. Evaluate specimens with the addition of rice husk ash (RHA) and using alkaline solution with a 6M molarity consist of 18 test specimens. Assess specimens with Palm Shell Ash (PSA) pozzolan and alkaline solution with an 8M molarity also consist of 18 test specimens. For more details, refer to Table 1, which shows variations in the addition of pozzolan, variations in heat treatment, variations in the heating period, as well as variations in heating temperature.

In this study, Super Plasticizer used at a rate of 1% of the weight of cement, which amounts to 0.127 kg, for each variation with the addition of pozzolan, except for concrete with 0% pozzolan, where super plasticizer not added. The cement used in this study is Portland Composite Cement class 2.



**Table 2. Mix design**

| No | Specimen | Materials   |               |            |                     |                       |                        |
|----|----------|-------------|---------------|------------|---------------------|-----------------------|------------------------|
|    |          | Cement (kg) | Pozzolan (kg) | Water (kg) | Fine aggregate (kg) | Coarse Aggregate (kg) | Alkaline solution (kg) |
| 1  | CRHA 0%  | 12.717      | 0             | 6.613      | 16.760              | 25.179                | 0.24                   |
| 2  | CRHA 5%  | 12.717      | 0.64          | 6.613      | 16.478              | 24.717                | 0.24                   |
| 3  | CRHA 10% | 12.717      | 1.27          | 6.613      | 16.170              | 24.255                | 0.24                   |
| 4  | CRHA 15% | 12.717      | 1.91          | 6.613      | 15.682              | 23.793                | 0.24                   |
| 5  | CPSA 5%  | 12.717      | 0.64          | 6.613      | 16.478              | 24.717                | 0.24                   |
| 6  | CPSA 10% | 12.717      | 1.27          | 6.613      | 16.170              | 24.255                | 0.24                   |
| 7  | CPSA 15% | 12.717      | 1.91          | 6.613      | 15.682              | 23.793                | 0.24                   |
|    | Totals   | 89.190      | 7.63          | 46.29      | 113.426             | 170.709               | 1.68                   |

**2.3 Compressive Strength Testing**

The Indonesian National Standard (SNI) is a set of technical guidelines published by the National Standardization Agency (BSN) in Indonesia. SNI 03-2834-2000 is the standard for testing the compressive strength of concrete in Indonesia, [30-33]. The following provides an explanation of concrete compressive strength testing based on SNI. The primary purpose of compressive strength testing of concrete is to determine its resistance to applied pressure, ensuring that the concrete used in construction meets established strength standards. Before the test begins, concrete specimens must be prepared in accordance with the provisions outlined in the SNI (National Indonesian Standard). This includes selecting the size and shape of the specimen to be representative of the structure or concrete work to be evaluated.

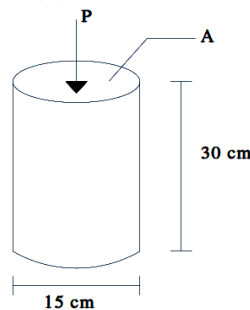


**Fig. 5. Specimen setting for compression test [35]**

Concrete compressive strength testing conducted using a concrete compressive testing machine. The concrete specimen placed inside the testing machine and subjected to a gradually increasing load until failure occurs. The load measured and recorded during the test. Two types of specimens commonly used: concrete cylinders (with certain diameters and heights) and concrete cubes (with specific sides). SNI provides guidance on selecting specimen types based on specific project needs or conditions. Compressive Strength Measurement: Test results expressed in units of pressure (MPa) or N/mm<sup>2</sup>, representing the maximum compressive strength a concrete specimen can withstand before failure. This value offers a reliable indication of concrete strength under certain conditions. SNI sets the minimum limit of compressive strength that concrete must meet to accept in construction

projects. If the compressive strength value of concrete meets or exceeds the limit, the concrete considered to meet the standard requirements.

Test results reported in full, including information about the concrete specimen, test conditions, loads applied, and compressive strength values obtained. This report is useful for documenting and evaluating the quality of the concrete used. It is important to always refer to the latest version of the applicable SNI standard, as test requirements and procedures may change over time. Figure 5 shows the setting of the specimen in the compressive strength testing process [35].

Room conditions for the tested sample. This is important because room conditions can affect test results and data consistency. The examples of specifications that included in room conditions are. Temperature: For example, the room is set at a certain constant temperature, such as 25°C, to ensure consistency in the test. The relative humidity of a room can also be set to remain constant, for example, at 50% RH, to minimize the influence of humidity on the sample. If the test requires visual observation, the light intensity in the room should be set consistently to ensure uniform test conditions. In cases, such as testing materials under certain conditions, atmospheric pressure in the room can be set to meet the test requirements. Other factors such as ventilation, noise, and environmental contamination also need to consider and regulated if possible.

### **2.4 FTIR Testing**

FTIR (Fourier Transform Infrared Spectroscopy) testing on geopolymer concrete is an infrared spectroscopic analysis method used to understand the chemical composition and molecular structure of geopolymer concrete, [36]. Geopolymer concrete, a type of concrete that utilizes geopolymer binders instead of conventional Portland cement, is examined through FTIR to provide insights into the chemical bonds between atoms in geopolymer concrete samples, [37].

FTIR spectrum analysis provides valuable insights into the chemical structure and composition of geopolymer concrete. Peaks in the spectrum offer clues about the chemical bonds and molecules present in the sample. FTIR results are instrumental in verifying the presence of the desired geopolymer in concrete, with specific peaks ensuring the proper formation of geopolymer bonds. By delving into the molecular structure and composition of materials, FTIR testing on geopolymer concrete contributes to a deeper understanding and aids in the development and refinement of geopolymer concrete performance, [38].



**Fig. 6. Sample preparation for FTIR testing**

Here are the general steps involved in FTIR testing on geopolymer concrete. Sample preparation, geopolymer concrete samples crushed into a fine powder, as shown in Figure

6. The concrete powder then placed on a transparent substrate suitable for FTIR analysis, such as glass or calcium fluoride. Spectrum measurement, the sample positioned inside the FTIR spectrometer. Infrared light directed to the sample, and the resulting infrared spectrum recorded. This process measures a series of intensified waves produced by chemical bonds in the sample. The resulting spectrum shows peaks associated with specific chemical bonds in the sample. These peaks identified and associated with specific components in geopolymer concrete, such as Si-O-Si (silica) bonds, Al-O-Si (aluminosilicate) bonds, and geopolymer bonds.

### 3. Results and Discussion

The research aimed to examine the attributes and mechanical behaviours of concrete in various scenarios, including changes in pozzolan levels, heat treatments, and alkaline solution concentrations. The primary focus was on determining the most effective amount of pozzolan addition for enhancing concrete strength. Portland Cement, palm kernel shell ash pozzolan, and rice husk ash utilized as materials, with pozzolan ratios set at 5%, 10%, and 15%. Figure 7 shows the condition of the composite concrete specimen after compressive testing, experiencing columnar cracking which means its strength is not too high because it undergoes heating for two days with a temperature of 90°C. Where the age of testing at the age of 14 days.



Fig. 7. Sample concrete after compression test

After subjecting the specimens to different treatments, the compressive strength testing at 28 days revealed notable findings. The most optimal compressive strength of 22.60MPa observed in concrete without heat treatment, with the addition of 15% palm shell ash (PSA) pozzolan. The compressive strength of non-pozzolan concrete subjected to 1 day of heat treatment at 90°C was slightly lower at 21.99MPa. On the contrary, the lowest compressive strength observed in concrete without heat treatment, with the addition of 15% rice husk ash, resulting in a compressive strength of 12.50MPa. More details of compressive strength test results with pozzolan variations, differences in alkaline solution molarity, and heat treatment shows in Table 3 and Figure 8.

Table 3 shows that the data include research results related to the strength of concrete containing various percentages of Concrete Rice Husk Ash (CRHA) and Concrete Palm Shell Ash (CPSA) under different concrete aging conditions (test life) and various thermal treatment conditions. The compressive strength of concrete measured in Megapascals (MPa). In the data matrix, the numbers represent the compressive strength of concrete under specific conditions. For example, on the 0% CRHA line with Thermal Curing II (60°C) and a test life of 14 days, the compressive strength of concrete is 19.84 MPa. In the matrix, general findings drawn. In general, the addition of CRHA (Residue High Alumina) shows a

decrease in concrete strength, especially at higher percentages. This observed in rows with CRHA percentages (5%, 10%, 15%) under various thermal treatment conditions. In general, the addition of CPSA shows variations in concrete strength, depending on the percentage and thermal treatment conditions.

Table. 3 Compressive strength test results

| Specimens         | Age of test<br>Day | Molarity Alkaline |           |            | Thermal Curing |            |             | Strength (MPa) |       |       |
|-------------------|--------------------|-------------------|-----------|------------|----------------|------------|-------------|----------------|-------|-------|
|                   |                    | I<br>0 M          | II<br>6 M | III<br>8 M | I<br>0°C       | II<br>60°C | III<br>90°C | I              | II    | III   |
| Concrete Cylinder | 14 Days            | 3                 | 0         | 0          | 0 D            | 1 D        | 2 D         | 19.84          | 14.70 | 12.55 |
|                   | 28 Days            | 3                 | 0         | 0          | 0 D            | 1 D        | 2 D         | 20.10          | 21.99 | 17.70 |
| CRHA 0%           | 14 Days            | 0                 | 3         | 0          | 0 D            | 1 D        | 2 D         | 15.55          | 18.10 | 19.80 |
|                   | 28 Days            | 0                 | 3         | 0          | 0 D            | 1 D        | 2 D         | 17.27          | 20.11 | 21.20 |
| CRHA 5%           | 14 Days            | 0                 | 3         | 0          | 0 D            | 1 D        | 2 D         | 12.20          | 8.90  | 15.60 |
|                   | 28 Days            | 0                 | 3         | 0          | 0 D            | 1 D        | 2 D         | 16.70          | 15.50 | 17.80 |
| CRHA 10%          | 14 Days            | 0                 | 3         | 0          | 0 D            | 1 D        | 2 D         | 12.60          | 17.40 | 20.02 |
|                   | 28 Days            | 0                 | 3         | 0          | 0 D            | 1 D        | 2 D         | 12.50          | 15.60 | 18.70 |
| CRHA 15%          | 14 Days            | 0                 | 0         | 3          | 0 D            | 1 D        | 2 D         | 17.70          | 14.90 | 13.80 |
|                   | 28 Days            | 0                 | 0         | 3          | 0 D            | 1 D        | 2 D         | 21.70          | 15.90 | 12.60 |
| CPSA 5%           | 14 Days            | 0                 | 0         | 3          | 0 D            | 1 D        | 2 D         | 25.30          | 9.80  | 15.40 |
|                   | 28 Days            | 0                 | 0         | 3          | 0 D            | 1 D        | 2 D         | 25.80          | 21.30 | 20.00 |
| CPSA10%           | 14 Days            | 0                 | 0         | 3          | 0 D            | 1 D        | 2 D         | 17.80          | 16.80 | 11.30 |
|                   | 28 Days            | 0                 | 0         | 3          | 0 D            | 1 D        | 2 D         | 22.60          | 17.50 | 19.10 |
| CPSA 15%          | 14 Days            | 0                 | 0         | 3          | 0 D            | 1 D        | 2 D         | 17.80          | 16.80 | 11.30 |
|                   | 28 Days            | 0                 | 0         | 3          | 0 D            | 1 D        | 2 D         | 22.60          | 17.50 | 19.10 |

The optimal strength achieved in PSA pozzolan concrete with a 10% addition at the age of 28 days, exhibiting a heat treatment rate of 25.8 MPa. Conversely, the lowest compressive strength was observed in non-pozzolan concrete at the age of 14 days, subjected to a heat treatment of 60°C for 1 day. In the case of RHA pozzolan concrete, the most favourable strength was attained at the age of 28 days with a two-day heat treatment, while the weakest strength occurred at the age of 14 days with a heat treatment of 60°C for one day, registering at 8.9 MPa. For PSA pozzolan concrete, the lowest compressive strength was recorded at a heat treatment of 60°C for one day, with a testing duration of 14 days.

From Figures 1, 9 and 10 it can be seen that there are differences in compound functional groups Where in Figure 1, namely concrete without additional pozzolan there are only O-H and CH<sub>2</sub> compound bonds, while in figures 9 and 10 show the addition of compound functional groups, namely there are two O-H bonds, then the presence of C=O and CH<sub>3</sub> bonds, this shows that concrete with additions has additional compound functional groups that contribute strength to concrete with the addition of material Pozzolan. Pozzolan PSA is more suitable for addition to composite concrete because it has more calcium oxide content than RHA, so PSA is more concrete which proven from variations in heating tests resulting in PSA concrete decreasing in strength when heated. Conversely, in RHA there

are more silica elements so that it is more influential on the polymer process, this can be proven by heating variations, where RHA concrete experiences an increase in compressive strength when applied, although overall the compressive strength produced by RHA concrete does not increase too much compressive strength compared to PSA concrete.

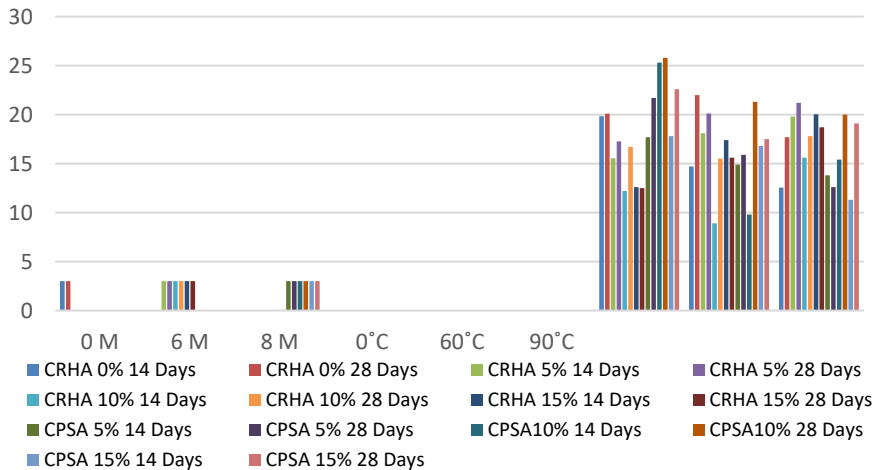


Fig. 8. Compressive strength relationship with age of testing, heat treatment and molarity of alkaline solutions

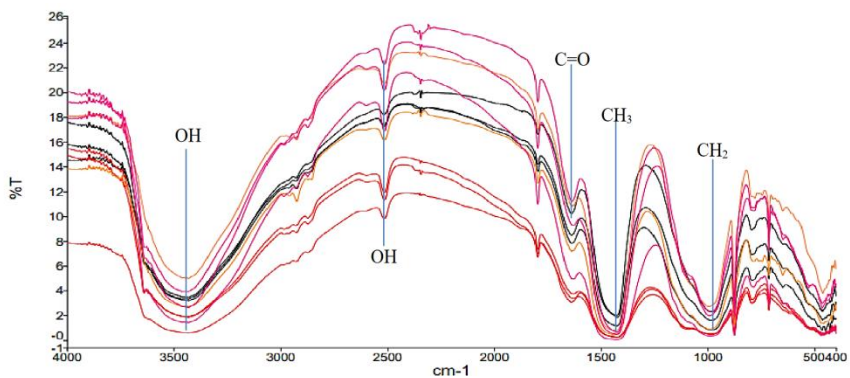


Fig. 9. FTIR test results on RHA and PSA pozzolan concrete

Fig. 9 show the wavenumbers of the test results from FTIR. In Figure 10 of RHA and PSA pozzolan concrete shows the occurrence of 5 groups of chemical compounds, namely O-H, O = H, C = O, CH<sub>3</sub>, and CH<sub>2</sub>. FTIR (Fourier Transform Infrared) testing is an infrared spectroscopy method used to analyse molecular structures based on the absorption of infrared light by molecules. The wavenumber recorded in FTIR test results can provide information about functional groups in a compound.

Here are common interpretations of compound groups that shows in the FTIR results of pozzolan concrete RHA (Rice Husk Ash): O-H (Hydroxyl): The wavenumber range is about 3200-3600 cm<sup>-1</sup>. Hydroxyl can come from water or from hydroxyl groups in organic compounds. O=H (Hydroxy Group): The wavenumber range is about 3000-3500 cm<sup>-1</sup>. This group can also refer to hydroxyl, especially hydroxyl bonded to oxygen atoms in

compounds. C=O (Carbonyl Group): The wavenumber range is about 1700-1750  $\text{cm}^{-1}$ . The carbonyl group derived from compounds such as ketones or aldehydes. CH<sub>3</sub> (Methyl): The wavenumber range is about 2800-3000  $\text{cm}^{-1}$ . This indicates the presence of methyl groups in the compound. CH<sub>2</sub> (Methylene): The wavenumber range is about 2800-3000  $\text{cm}^{-1}$ . This group indicates the presence of a carbon chain consisting of two carbon atoms. FTIR results reflecting the presence of these groups can provide information on the chemical composition and molecular structure of RHA pozzolan concrete. However, a more detailed and accurate interpretation requires a further understanding of the test conditions and the specific characteristics of the sample assessed.

#### 4. Conclusions

The objective of the research was to evaluate the properties and compressive strength of concrete incorporating different proportions of pozzolan additives, namely palm kernel shell ash (PSA) and rice husk ash (RHA), under various thermal treatment conditions and concentrations of alkaline solution. From the results and distribution data, the following conclusions drawn:

- Concrete without pozzolan, subjected to 1 day of heat treatment at 90°C, exhibited a slightly lower compressive strength of 21.99 MPa.
- The lowest compressive strength observed in concrete without heat treatment, with the addition of 15% rice husk ash, recording at 12.50 MPa.
- Pozzolan Effects: The addition of Concrete Rice Husk Ash (CRHA) led to a decrease in concrete strength, especially at higher percentages, under various thermal treatment conditions.
- Concrete Palm Shell Ash (CPSA) addition showed variations in strength, depending on the percentage and thermal treatment conditions.
- Optimal Conditions: The highest compressive strength 25.8MPa achieved in PSA pozzolan concrete with a 10% addition at the age of 28 days.
- The weakest strength occurred in non-pozzolan concrete at the age of 14 days, subjected to a heat treatment of 60°C for 1 day.
- FTIR Analysis: FTIR analysis revealed chemical compounds in RHA pozzolan concrete, including O-H, O=H, C=O, CH<sub>3</sub>, and CH<sub>2</sub> groups.
- Interpretations of wavenumbers suggested the presence of hydroxyl, hydroxy groups, carbonyl groups, methyl groups, and methylene groups in the RHA pozzolan concrete.
- Detailed analyses, considering specific test conditions and sample characteristics, required for a more accurate interpretation of FTIR results.

In summary, this study provides valuable insights into the impact of pozzolan addition, thermal treatment, and alkaline solution molarity on the characteristics and compressive strength of concrete, offering a foundation for future research in optimizing concrete mixtures for enhanced performance. Recommendations for Further Research: Further investigations needed to understand the specific mechanisms behind the observed effects of pozzolan on concrete strength.

The novelty of this research lies in its comprehensive investigation into the properties and compressive strength of concrete incorporating various proportions of pozzolan additives, specifically palm kernel shell ash (PSA) and rice husk ash (RHA), under diverse thermal treatment conditions and alkaline solution concentrations. The key findings contribute to advancing the understanding of pozzolan effects on concrete performance in significant ways:

- **Effect of Thermal Treatment:** The study elucidates how different thermal treatment conditions impact concrete strength, highlighting variations in compressive strength under distinct temperatures and durations.
- **Pozzolan Influence:** By analysing the effects of CRHA and CPSA additions on concrete strength, the research identifies trends in strength variations, particularly emphasizing the decrease in strength associated with higher percentages of CRHA addition.
- **Optimal Conditions:** The identification of optimal conditions for achieving the highest compressive strength, notably 25.8 MPa in PSA pozzolan concrete with a 10% addition at 28 days, offers valuable insights for concrete mixture optimization.
- **FTIR Analysis:** The use of FTIR analysis to characterize chemical compounds in RHA pozzolan concrete unveils molecular changes, providing a deeper understanding of the interaction between pozzolan additives and the concrete matrix.
- **Recommendations for Further Research:** The call for further investigations into the specific mechanisms behind observed pozzolan effects on concrete strength sets the stage for future studies aimed at unravelling the underlying mechanisms and optimizing concrete mixtures for enhanced performance.

This research fills gaps in current knowledge by systematically examining the impact of pozzolan additives, thermal treatment, and alkaline solution molarity on concrete properties and compressive strength, laying a foundation for future endeavours in the field of concrete material science and engineering.

## References

- [1] Dey S, Kumar VP, Goud KR, Basha SKJ. State of art review on self-compacting concrete using mineral admixtures. *J Build Pathol Rehabil.* 2021;6(1):18. <https://doi.org/10.1007/s41024-021-00110-9>
- [2] Imbabi MS, Carrigan C, McKenna S. Trends and developments in green cement and concrete technology. *Int J Sustain Built Environ.* 2012;1(2):194-216. <https://doi.org/10.1016/j.ijsbe.2013.05.001>
- [3] Nair NA, Sairam V. Research initiatives on the influence of wollastonite in cement-based construction material-A review. *J Clean Prod.* 2021;283:124665. <https://doi.org/10.1016/j.jclepro.2020.124665>
- [4] Pacheco-Torgal F, Melchers RE, Shi X, De Belie N, Van Tittelboom K, Perez AS. *Eco-efficient repair and rehabilitation of concrete infrastructures.* Woodhead Publishing; 2017.
- [5] Bastos G, Patiño-Barbeito F, Patiño-Cambeiro F, Armesto J. Admixtures in cement-matrix composites for mechanical reinforcement, sustainability, and smart features. *Materials.* 2016;9(12):972. <https://doi.org/10.3390/ma9120972>
- [6] Tayeh BA, Hasaniyah MW, Zeyad AM, Yusuf MO. Properties of concrete containing recycled seashells as cement partial replacement: A review. *J Clean Prod.* 2019;237:117723. <https://doi.org/10.1016/j.jclepro.2019.117723>
- [7] Sharma R, Khan RA. Effect of different supplementary cementitious materials on mechanical and durability properties of concrete. *J Mater Eng Struct.* 2016;3(3):129-147.
- [8] Ndashirwa D, Zmamou H, Lenormand H, Leblanc N. The role of supplementary cementitious materials in hydration, durability and shrinkage of cement-based materials, their environmental and economic benefits: A review. *Clean Mater.* 2022;5:100123. <https://doi.org/10.1016/j.clema.2022.100123>
- [9] Sakir S, Raman SN, Safiuddin M, Kaish AA, Mutalib AA. Utilization of by-products and wastes as supplementary cementitious materials in structural mortar for sustainable construction. *Sustainability.* 2020;12(9):3888. <https://doi.org/10.3390/su12093888>

- [10] Yaphary YL, Lam RH, Lau D. Chemical technologies for modern concrete production. *Procedia Eng.* 2017;172:1270-1277. <https://doi.org/10.1016/j.proeng.2017.02.150>
- [11] Snellings R, Suraneni P, Skibsted J. Future and emerging supplementary cementitious materials. *Cem Concrete Res.* 2023;171:107199. <https://doi.org/10.1016/j.cemconres.2023.107199>
- [12] Sobolev K, Kozhukhova M, Sideris K, Menéndez E, Santhanam M. Alternative supplementary cementitious materials. In: *Prop. Fresh Hardened Concrete Contain. Suppl. Cem. Mater. State---Art Rep. RILEM Tech. Comm. 238-SCM Work. Group 4.* 2018:233-282. [https://doi.org/10.1007/978-3-319-70606-1\\_7](https://doi.org/10.1007/978-3-319-70606-1_7)
- [13] Zhang J, Chen T, Gao X. Incorporation of self-ignited coal gangue in steam cured precast concrete. *J Clean Prod.* 2021;292:126004. <https://doi.org/10.1016/j.jclepro.2021.126004>
- [14] McCarthy MJ, Dyer TD. Pozzolanas and pozzolanic materials. In: *Lea's Chem. Cem. Concrete.* 2019:363-467. <https://doi.org/10.1016/B978-0-08-100773-0.00009-5>
- [15] Mermerdaş K, Arbili MM. Explicit formulation of drying and autogenous shrinkage of concretes with binary and ternary blends of silica fume and fly ash. *Constr Build Mater.* 2015;94:371-379. <https://doi.org/10.1016/j.conbuildmat.2015.07.074>
- [16] Nochaiya T, Wongkeo W, Chaipanich A. Utilization of fly ash with silica fume and properties of Portland cement-fly ash-silica fume concrete. *Fuel.* 2010;89(3):768-774. <https://doi.org/10.1016/j.fuel.2009.10.003>
- [17] Radlinski M, Olek J. Effects of Curing Conditions on Properties of Ternary (Ordinary Portland Cement/Fly Ash/Silica Fume) Concrete. *ACI Mater J.* 2015;112(1). <https://doi.org/10.14359/51687307>
- [18] Singh NB, Kalra M, Kumar M, Rai S. Hydration of ternary cementitious system: Portland cement, fly ash and silica fume. *J Therm Anal Calorimetry.* 2015;119:381-389. <https://doi.org/10.1007/s10973-014-4182-8>
- [19] Vance K, Aguayo M, Oey T, Sant G, Neithalath N. Hydration and strength development in ternary Portland cement blends containing limestone and fly ash or metakaolin. *Cem Concrete Compos.* 2013;39:93-103. <https://doi.org/10.1016/j.cemconcomp.2013.03.028>
- [20] Conner JR, Hoeffner SL. A critical review of stabilization/solidification technology. *Crit Rev Environ Sci Technol.* 1998;28(4):397-462. <https://doi.org/10.1080/10643389891254250>
- [21] Ramalingam M, Narayanan K, Sivamani J, Kathirvel P, Murali G, Vatin NI. Experimental Investigation on the Potential Use of Magnetic Water as a Water Reducing Agent in High Strength Concrete. *Materials.* 2022;15(15):5219. <https://doi.org/10.3390/ma15155219>
- [22] Thakur RK, Singh KK. Abrasive waterjet machining of fibre-reinforced composites: A state-of-the-art review. *J Braz Soc Mech Sci Eng.* 2020;42(7):381. <https://doi.org/10.1007/s40430-020-02463-7>
- [23] Amritha PS, Vinod V, Harathi PB. A critical review on extraction and analytical methods of phthalates in water and beverages. *J Chromatography A.* 2022;1675:463175. <https://doi.org/10.1016/j.chroma.2022.463175>
- [24] Firdous R, Stephan D, Djobo JNY. Natural pozzolan based geopolymers: A review on mechanical, microstructural and durability characteristics. *Constr Build Mater.* 2018;190:1251-1263. <https://doi.org/10.1016/j.conbuildmat.2018.09.191>
- [25] Bondar D, Lynsdale CJ, Milestone NB, Hassani N, Ramezaniapour AA. Effect of heat treatment on reactivity-strength of alkali-activated natural pozzolans. *Constr Build Mater.* 2011;25(10):4065-4071. <https://doi.org/10.1016/j.conbuildmat.2011.04.044>
- [26] Hidalgo A, Petit S, Domingo C, Alonso C, Andrade C. Microstructural characterization of leaching effects in cement pastes due to neutralisation of their alkaline nature: Part I: Portland cement pastes. *Cem Concrete Res.* 2007;37(1):63-70. <https://doi.org/10.1016/j.cemconres.2006.10.002>



- [27] Yusra A, Meliana H, Opirina L, Satria A. Investigation of normal concrete properties with the addition of micro reinforcement. *Res. Eng. Struct. Mater.*, 2023; 9(3): 875-884. <https://doi.org/10.17515/resm2023.693ma0218tn>
- [28] Hussain I, Ali B, Akhtar T, Jameel MS, Raza SS. Comparison of mechanical properties of concrete and design thickness of pavement with different types of fiber-reinforcements (steel, glass, and polypropylene). *Case Stud Constr Mater.* 2020;13:e00429. <https://doi.org/10.1016/j.cscm.2020.e00429>
- [29] Ali B, Qureshi LA, Kurda R. Environmental and economic benefits of steel, glass, and polypropylene fibre reinforced cement composite application in jointed plain concrete pavement. *Compos Communications.* 2020;22:100437. <https://doi.org/10.1016/j.coco.2020.100437>
- [30] Orouji M, Zahrai SM, Najaf E. Effect of glass powder & polypropylene fibres on compressive and flexural strengths, toughness and ductility of concrete: an environmental approach. In: *Structures.* Elsevier; 2021:4616-4628. <https://doi.org/10.1016/j.istruc.2021.07.048>
- [31] Yuwana HP, Purnomo S. The effect of variations in the composition of cement and fine aggregate on the compressive strength of mortar used in the cementation process of radioactive waste. In: *AIP Conference Proceedings.* AIP Publishing; 2023. <https://doi.org/10.1063/5.0173135>
- [32] Ginting A, Pradikta DH, Santosa B, Adi P. Comparison of Compressive Strength of Concrete Using White Portland Cement with Gray Cement. *J Tek SIPIL Dan PERENCANAAN.* 2022;24(1):1-7. <https://doi.org/10.15294/jtsp.v24i1.32390>
- [33] Mansyur M, Tumpu M. Compressive strength of normal concrete using local fine aggregate from Binang River in Bombana district, Indonesia. In: *AIP Conference Proceedings.* AIP Publishing; 2022. <https://doi.org/10.1063/5.0072888>
- [34] Siregar AC, Liana UWM, Yatnikasari S, Agustina F, Rahma A. The Effect of Rainwater in Concrete Mixture on Concrete Compressive Strength. *FONDASI J Tek SIPIL.* 2023;12(1):121-130. <https://doi.org/10.36055/fondasi.v12i1.19561>
- [35] SNI 03-1974-1990. Concrete compressive strength test methods. Penerbit Badan STANDARISASI Nas.; 1990.
- [36] Kani EN, Mehdizadeh H. Investigating gel molecular structure and its relationship with mechanical strength in geopolymers based on natural pozzolan using in situ ATR-FTIR spectroscopy. *J Mater Civ Eng.* 2017;29(8):04017078. [https://doi.org/10.1061/\(ASCE\)MT.1943-5533.0001917](https://doi.org/10.1061/(ASCE)MT.1943-5533.0001917)
- [37] Yusuf MO. Bond characterization in cementitious material binders using Fourier-transform infrared spectroscopy. *Appl Sci.* 2023;13(5):3353. <https://doi.org/10.3390/app13053353>
- [38] Shilar FA, Ganachari SV, Patil VB, Khan TY, Almakayeel NM, Alghamdi S. Review on the relationship between nano modifications of geopolymers concrete and their structural characteristics. *Polymers.* 2022;14(7):1421. <https://doi.org/10.3390/polym14071421>

Blank Page



Research Article

## Development of eco-friendly self-compacting concrete using marble powder, blast furnace slag and glass fibre-reinforced plastic waste: Application of mixture design approach

Manel Djeddou<sup>\*1,a</sup>, Mohamed Amieur<sup>1,b</sup>, Rabah Chaid<sup>2,c</sup>, Habib-Abdelhak Mesbah<sup>3,d</sup>

<sup>1</sup>LTPiTE Laboratory, Ecole Nationale Supérieure des Travaux Publics-Francis Jeanson, Kouba, Algeria

<sup>2</sup>Research Unit: Materials, Processes and Environment, M'hamed Bougarra University of Boumerdes, Algeria

<sup>3</sup>INSA de Rennes, Université de Rennes 1, L.G.C.G.M. Laboratory, Rennes, France

### Article Info

### Abstract

#### Article history:

Received 08 Feb 2024

Accepted 05 May 2024

#### Keywords:

Marble;

Slag;

Plastic;

Glass;

Fibre;

Concrete;

Mixture design

The present paper investigates the valorisation of three local Algerian waste materials, namely Marble Powder (MP), Ground Granulated Blast Furnace Slag (GGBS), and Glass Fibre-Reinforced Plastic Waste (GFRPW), as mineral additions in Self-Compacting Concrete (SCC). A mixture design modelling approach was used to evaluate the impact of these waste materials and their interactions on the fresh and hardened properties of SCC. Experimental tests were performed, including slump flow, V-funnel, L-box, air content, and compressive strength tests. Regression models were developed to understand the behaviour of SCC based on the proportions of MP, GGBS, and GFRPW in both binary and ternary systems. The statistical analysis software Minitab was employed for the modelling. The results revealed that the combination of MP, GGBS and GFRPW in ternary systems has a synergistic effect on slump flow and L-box ratio. The highest slump flow value and L-box ratio were achieved at proportions of approximately 38% MP, 37% GGBS, and 25% GFRPW. The V-funnel time was affected by the proportions of the waste materials, decreasing with higher MP and GFRPW proportions and increasing with a higher GGBS proportion. In GFRPW-based systems, a higher GFRPW proportion increased the air content, but combining GFRPW with GGBS significantly reduced it. Furthermore, the interaction between GGBS and GFRPW enhanced the development of the 28-day compressive strength, where the highest value of 54 MPa was reached at the combination of 32% GFRPW and 68% GGBS. After 90 days of curing, the SCC mixtures containing 100% GGBS exhibited the highest compressive strength value of 66 MPa. This study provides valuable insights for optimising the use of MP, GGBS, and GFRPW in SCC, potentially leading to more sustainable and cost-effective concrete production.

© 2024 MIM Research Group. All rights reserved.

## 1. Introduction

Self-compacting concrete (SCC) is a modern form of concrete developed in Japan in 1988 to improve the durability of concrete structures. It was a response to the durability problems that had arisen two decades after post-war reconstruction, where the focus on rapid project delivery had compromised the quality of construction (1). Prof. Hajime Okamura identified insufficient concrete compaction as a major cause of structural deterioration and proposed SCC as a solution (1). This new technology allows concrete to be placed into the formwork under its own weight without the need for vibration. As well as improving the durability of concrete structures, SCC has helped to address the shortage

\*Corresponding author: [m.djeddou@enstp.edu.dz](mailto:m.djeddou@enstp.edu.dz)

<sup>a</sup> [orcid.org/0009-0002-5007-9944](https://orcid.org/0009-0002-5007-9944); <sup>b</sup> [orcid.org/0000-0002-6650-942X](https://orcid.org/0000-0002-6650-942X); <sup>c</sup> [orcid.org/0000-0002-7008-4161](https://orcid.org/0000-0002-7008-4161);

<sup>d</sup> [orcid.org/0000-0003-1705-4681](https://orcid.org/0000-0003-1705-4681)

DOI: <http://dx.doi.org/10.17515/resm2024.178ma0208rs>

Res. Eng. Struct. Mat. Vol. 11 Iss. 1 (2025) 113-138

of skilled labour in the construction industry. The SCC mix design necessitates a high cement content with a compatible rate of superplasticizer. This composition is essential for the concrete to achieve fresh properties, including segregation resistance, filling ability, and passing ability, that characterise SCC and contribute to its self-place ability. However, the adoption of this technology in the construction industry can increase the cost of concrete production and its carbon footprint (2). Many researchers have proposed the use of industrial by-products such as marble dust, granulated blast furnace slag, and glass fibre-reinforced plastic waste, as mineral additions in SCC. This approach offers several benefits, such as material cost reduction, decreased environmental impact, and enhanced concrete performance.

Marble is a metamorphic rock composed mainly of carbonate minerals such as dolomite and calcite. Valued for its durability, resistance, and wide range of colours, it has long been used as a building material and decorative element. The extensive global production of this stone has resulted in negative impacts on the environment and public health. Dust generated during the processing, cutting, and polishing of marble is collected and discharged near the manufacturing plants. The high alkalinity of these deposits reduces soil fertility and increases the risk of water contamination (3,4). In addition, the fine marble particles suspended in the air can cause respiratory, visual, and skin disorders (5), (6). To mitigate the environmental impact of MP, numerous researchers have attempted to use this waste material in the production of SCC. Meera et al. (7) analyzed the rheological and mechanical behavior of SCC containing up to 360 kg/m<sup>3</sup> of MP. Most of the mixes were classified within the VS2/VF1 and VS2/VF2 categories of the EFNARC specifications. The authors concluded that MP can be used in low-strength SCC up to 360 kg/m<sup>3</sup> and in high-strength SCC up to 230 kg/m<sup>3</sup>. Gupta et al. (2) conducted a study to investigate the use of marble waste (MP), silica fume (SF), and fly ash (FA) in different combinations for the design of high-performance self-compacting concrete (HPSCC). The addition of both MP and FA was found to enhance the fresh properties of HPSCC. The use of 10% MP combined with 15% FA and 5% SF exhibited the best mechanical performance and microstructure of HPSCC. Sadeek et al. (8) highlighted that the incorporation of MP without cement substitution enhances the mechanical performance of SCC. Mechanical strength showed an increase with higher incorporation rates of MP. Mahmood et al. (9) concluded that substituting 5% of fine aggregate with marble powder and 15% with rice husk ash resulted in optimum mechanical performance for both short and long-term applications in SCC.

Blast furnace granulated slag is a by-product of iron production that is typically landfilled, causing environmental damage such as soil degradation and water pollution. Ground granulated blast furnace slag (GGBS) is a well-known material that, due to its latent hydraulic reactivity, is widely used as a partial substitute for cement in cement-based materials. Several studies have focused on its use in SCC and reported various results. Bayat et al. (10) found that substituting cement with up to 40% GGBS generates SCC mixes with reduced flowability, viscosity and passing ability. However, the incorporation of GGBS at 30% cement replacement optimized mechanical strength. Sara et al. (11) showed that the addition of GGBS as a cement substitute in self-compacting mortar based on recycled concrete sand reduced the demand for superplasticizers. The highest compressive strength was achieved at a cement substitution rate of 20%. By investigating the behaviour of SCC after replacing up to 60% of cement with GGBS, Mohammed et al. (12) reported that the mechanical strength increased, reaching an optimum value of 84 MPa at a substitution rate of 40% and a water/cement ratio of 0.26. According to Ofuyatan et al. (13), the use of GGBS results in a decrease in flowability and an increase in viscosity and passing ability. The SCC mixes exhibited optimum mechanical strength at 20% cement substitution.

Glass Fibre-Reinforced Plastic (GFRP) is a composite material consisting of glass fibres immersed in a thermosetting resin. GFRP is known for its exceptional properties that

combine lightness with high mechanical and durability performance. These properties have facilitated its widespread adoption in various industries, including aerospace, construction, and automotive. The growing global market demand for composite materials has resulted in the accumulation of waste generated during their production, including machining, cutting, and polishing. The GFRP products are also expected to reach the end of their service life, leading to the accumulation of even larger quantities of this material. The accumulation of GFRPW is a significant challenge that requires sustainable waste management and recycling practices. Mechanical recycling is a promising approach for the management of GFRPW, as it is cost-effective and environmentally friendly [14]. This method involves shredding or grinding the waste into small pieces that can then be used as raw materials for new products. Other methods of recycling GFRW, such as chemical and thermal recycling, are also being explored, but are generally more expensive and energy-intensive (16). The incorporation of mechanically recycled GFRP powder in cement-based materials offers a promising solution for waste management in the construction sector, helping to mitigate the negative impact of this waste on the environment. Most studies on the incorporation of recycled GFRP powder as a replacement for fine aggregates in concrete and mortar have reported a loss of workability and a degradation of mechanical strength (17–21). However, recent research has shown that the use of a small amount of recycled GFRPW in cement-based materials can improve their mechanical performance. Asokan et al. discovered that oven curing allows the mechanical strength of GFRP powder-based concrete to develop (20). The same authors, in another study, found a significant improvement in mechanical strength when GFRPW is incorporated with a high dosage of superplasticizer (22). Farinha et al. also reported a continuous increase in the mechanical strength of mortar by substituting natural silica sand with GFRP powder obtained from the cutting process of floor elements (23). Tittareli and Moriconi (24) have used GFRP powder in SCC by replacing the calcareous filler at rates of 25% and 50%. The authors reported a considerable loss in mechanical resistance despite the improvement of some durability-related properties.

The extensive investigation of the potential for recycling MP, GGBS and GFRPW as alternatives to cement or fine aggregates has been the focus of numerous research efforts. These studies have mainly concentrated on the use of these waste materials alone or in combination with other mineral additions such as pozzolan (PZ) (25), fly ash (FA), and silica fume (SF)(2). However, to date, no studies have examined the simultaneous use of these wastes in SCC or other cement-based materials.

The objective of this work is to investigate the effect of combining the three types of waste (MP, GGBS, and GFRPW) in binary and ternary systems on the fresh and hardened properties of SCC. The waste additions were ground to a consistent Blaine fineness of 4500 cm<sup>2</sup>/g to eliminate the influence of this physical property on the concrete's performance. The fresh properties of SCC were evaluated through a series of tests, including slump flow, V-funnel time, L-box ratio, and air content. Additionally, the mechanical properties were assessed through compression tests after 28 and 90 days of curing. In this study, the mixture design method, a statistical approach, was employed to analyse the individual and combined effects of MP, GGBS, and GFRPW on the properties of the SCC under investigation. This approach provides a comprehensive understanding of the impact of these waste materials on the performance of SCC.

## **2. Experimental Program**

### **2.1. Mixture Design Approach**

The mixture design method is a statistical modelling tool specifically tailored to analyse the behaviour of mixtures (blends). This approach is particularly valuable in construction materials such as concrete, where it enables the design of experiments, prediction of

concrete behaviour, and optimisation of the proportion of its components to achieve the best performance. The mixture plan is an experimental design characterised by a fundamental constraint indicating that the proportion of all the mixture components must add up to 100%. This constraint is expressed in equation (1), where  $X_i$  denotes the proportion of the constituent  $i$  (26).

$$\sum_{i=1}^{i=n} X_i = 1 \quad (1)$$

The mixture design of experiments is beneficial in understanding the relationship between the behaviour of a mixture, referred to as "response  $Y$ ," and the proportion of its constituents  $X_i$ , termed factors. It is evident that the factors are non-independent, where the proportion of a specific component depends on the combined proportions of the other ingredients. The experimental programme can be defined based on the type of mixture design adopted. The simplex lattice, simplex centroid, and extreme vertex are traditional mixture designs that help determine the number of mixtures to be prepared with the proportions of their analysed constituents. Once the experiments have been conducted on these mixtures, the regression equation can be developed to describe the association between the response  $Y$  and the factors  $X_i$ . The regression equation provides insights into the impact of each constituent and their interactions on the behaviour of the mixtures. Furthermore, it enables the effective prediction of the mixtures' performance based on the proportions of their constituents. The validity of the regression equation is subsequently assessed using specific parameters, including the coefficients  $R^2$ ,  $R^2_{adj}$ , and  $R^2_{pred}$ , analysis of variance (ANOVA), and the distribution of errors between the experimental and predicted results (residuals) (27). This evaluation process is essential for determining the accuracy and reliability of the regression model in describing the data and making predictions.

$$Y = B_1 \times MP + B_2 \times GGBS + B_3 \times GFRPW + B_4 \times (MP \cdot GGBS) + B_5 \times (MP \cdot GFRPW) + B_6 \times (GGBS \cdot GFRPW) + B_7 \times (MP \cdot GGBS \cdot GFRPW) \quad (2)$$

In this study, a ternary system composed of MP, GGBS, and GFRPW was evaluated for its suitability as a mineral addition in self-compacting concrete. The traditional augmented simplex-centroid mixture plan, based on three factors, was employed, resulting in 10 combinations to be processed, as illustrated in Fig. 1. The special cubic model of Scheffé was selected for the regression equation, which includes the individual factors MP, GGBS, and GFRPW, along with their binary and ternary interactions, as detailed in equation (2). The coefficients of the regression model ( $B_i$ ) were calculated using the least squares method, which minimises the sum of the squares of the errors. These coefficients represent the contribution of the associated terms to the response variable "Y". A high coefficient indicates a strong influence on the response, while a negative coefficient suggests an adverse influence on the variable "Y". The mixture design approach was applied in this investigation using the Minitab statistical software.

## 2.2. Materials

The used cement is a blended Portland cement of type CEM II/A-L 52.5 N, manufactured by the CILAS cement plant (Ciment Lafarge Souakri) in accordance with the European Standard EN 197-1 (Fig. 3(a)).

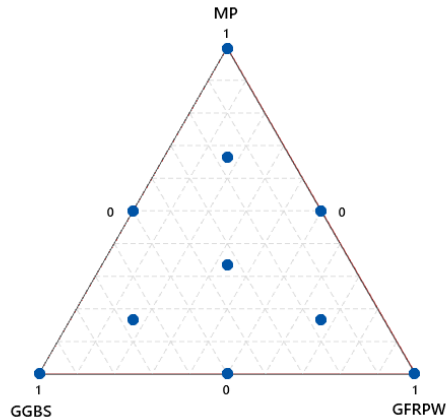


Fig. 1. Illustration of centroid-simplex augmented design with three factors: MP, GGBS and GFRPW

Three Algerian industrial by-products, MP, GGBS, and GFRPW, were utilised as mineral additions in SCC. The MP was obtained from the El-Khroub quarry near the city of Constantine, whilst the GGBS was from the El-Hadjar steel factory in Annaba (Algeria). The GFRPW was recovered from the “Maghreb Pipe Industries” factory located in M’sila (Algeria), which specialises in the production of GFRP piping systems. This waste material is generated as a by-product of the GFRP pipe-cutting process. The cutting equipment includes a vacuum system that collects and stores the GFRP waste in bags (Fig. 2). The GFRP itself was produced using polyester thermosetting resin and E-glass fibres. The chemical composition of cement, MP, GGBS and GFRPW obtained with X-ray fluorescence (XRF) analysis is presented in Table 1.



(a)



(b)

Fig. 2. (a) Cutting process of GFRP pipes with the vacuum system, (b) GFRPW Storage bags

All the waste materials (MP, GGBS, and GFRPW) were ground separately using a ball mill until their Blaine-specific surface area reached  $4500 \text{ cm}^2/\text{g}$  (Fig. 3(b), (c), (d)). Scanning electron microscopy (SEM) analysis was conducted to examine the morphology and surface texture of the waste particles after the grinding process. The marble particles were found to possess a relatively rounded shape with a smooth surface (Fig. 4 (a)), whereas the

GGBS consisted of angular particles with a rough surface (Fig. 4 (b)). The GFRPW was characterised by the irregular shape and size of its particles (Fig. 4 (c)). The physical properties and particle size distribution of MP, GGBS, GFRPW, and cement are presented in Table 2 and Fig. 5, respectively.



Fig. 3. (a) General aspect of Cement, (b) MP, (c) GGBS and (d) GFRPW

Table 1. Chemical composition of Cement, MP, GGBS and GFRPW

| Materials | SiO <sub>2</sub> | Al <sub>2</sub> O <sub>3</sub> | Fe <sub>2</sub> O <sub>3</sub> | CaO   | MgO  | SO <sub>3</sub> | K <sub>2</sub> O | Na <sub>2</sub> O | TiO <sub>2</sub> | LOI   |
|-----------|------------------|--------------------------------|--------------------------------|-------|------|-----------------|------------------|-------------------|------------------|-------|
| Cement    | 19.47            | 4.89                           | 2.97                           | 64.58 | 1.63 | 2.28            | 0.74             | 0.12              | -                | 2.97  |
| MP        | 0.06             | -                              | 0.01                           | 55.73 | 0.12 | 0.07            | -                | -                 | 0.01             | 43.65 |
| GGBS      | 35.65            | 7.86                           | 4.83                           | 40.87 | 3.50 | 1.62            | 0.63             | 0.12              | 0.28             | 0.02  |
| GFRPW     | 33.44            | 8.29                           | 0.24                           | 11.85 | 1.56 | 0.08            | 0.06             | 0.42              | 0.25             | 44.32 |

Table 2. Physical properties of MP, GGBS, GFRPW and Cement

| Materials                            | MP   | GGBS | GFRPW | Cement | Specifications |
|--------------------------------------|------|------|-------|--------|----------------|
| Specific Gravity                     | 2.72 | 2.92 | 1.77  | 3.09   | EN 1097-7      |
| Blaine fineness (m <sup>2</sup> /Kg) | 450  | 450  | 450   | 390    | EN 196-6       |

Three fractions of crushed natural aggregates were utilised in this work: gravel (3/8), gravel (8/15), and sand (0/4) obtained from the Kef-Azrou quarry located in Medea (Algeria), and dune sand of class (0/1) collected from Bou-Saada in southern Algeria. The physical characteristics and gradation curves of the fine and coarse aggregates are presented in Table 3 and Fig. 6, respectively.



A polycarboxylate-based superplasticizer, Sika ViscoCrete Tempo 12, with a specific density of 1.06 and a solid content of 30%, was used.

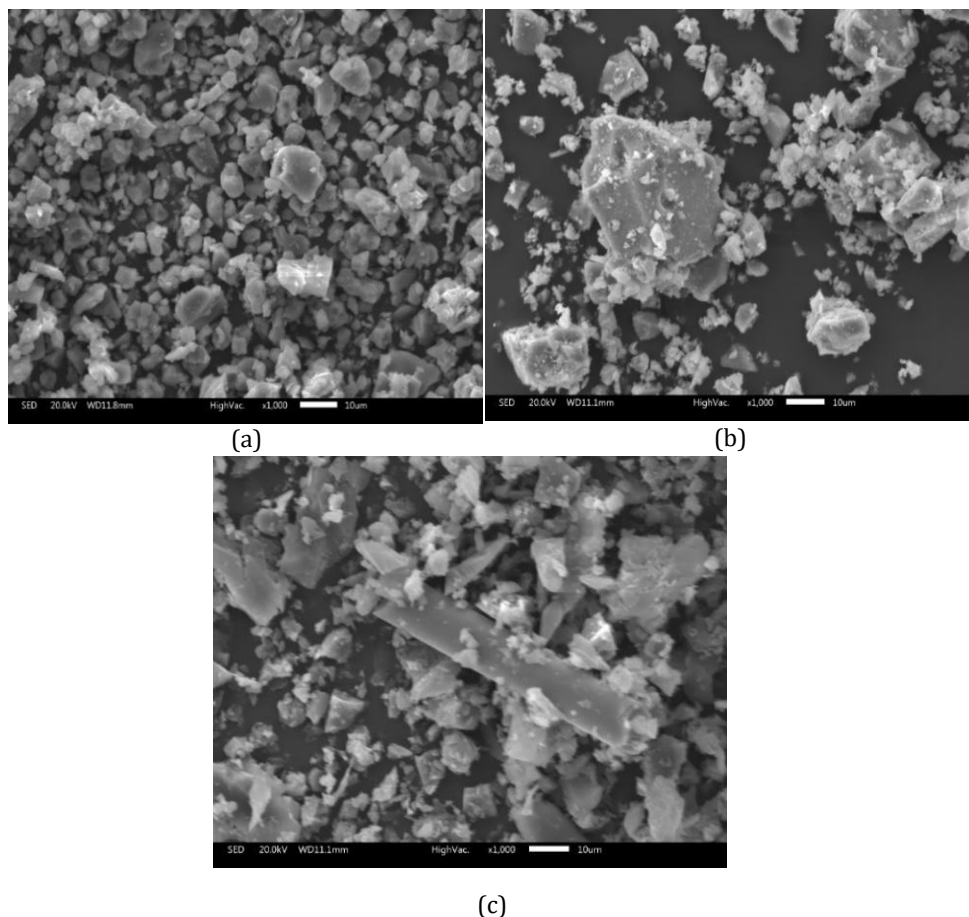


Fig. 4. SEM observation of MP (a), GGBS (b), and GFRPW (c)

Table 3. Physical characteristics of aggregates

| Materials                 | Gravel 1<br>(8/15) | Gravel 2<br>(3/8) | Crushed Sand<br>(0/4) | Dune Sand<br>(0/1) | Specifications |
|---------------------------|--------------------|-------------------|-----------------------|--------------------|----------------|
| Specific Gravity          | 2.62               | 2.64              | 2.74                  | 2.62               | EN 1097-6      |
| Coefficient of absorption | 1.01               | 1.19              | 0.73                  | 0.55               |                |
| Flakiness index           | 11.46              | 14.37             | -                     | -                  | EN 933-3       |
| Sand equivalent (%)       | -                  | -                 | 60.78                 | 75.75              | EN 933-8       |
| Methylene Blue Value      | -                  | -                 | 0.17                  | 1.83               | EN 933-9       |
| Fineness Modulus          | 5.93               | 5.24              | 3.06                  | 1.03               | NF P 18-540    |

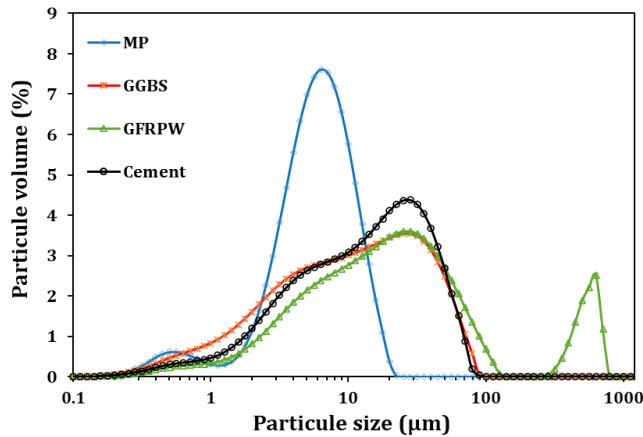


Fig. 5. The gradation curves of MP, GGBS, GFRPW and Cement

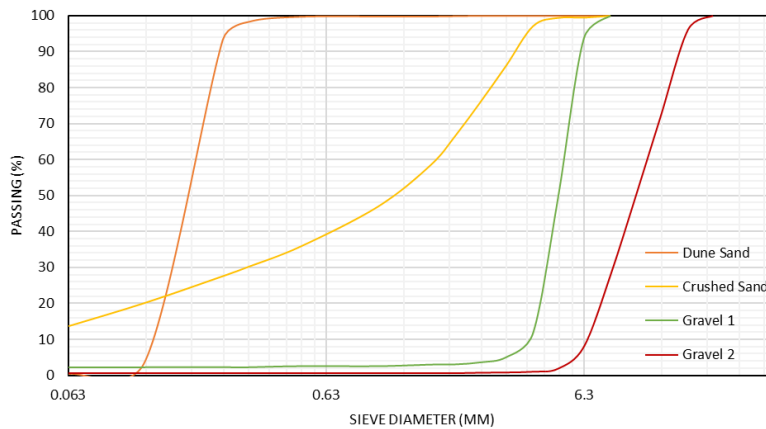


Fig. 6. The gradation curves of Dune sand, crushed sand, gravel 1 and gravel 2

### 2.3. Mixture Proportions

This study involves the preparation of 10 mixtures of SCC. The mineral addition, consisting of MP, GGBS, and GFRPW, was incorporated into the SCC mixtures at a proportion of 15% of the cement mass. The proportions of MP, GGBS, and GFRPW were determined according to the mixture design plan, as shown in Table 4. The quantities of the additional components, such as cement, gravel, sand, water and superplasticizer (SP), in the SCC mixture were kept constant, and their specific values are detailed in Table 5.

### 2.4. Testing Procedure

The experimental evaluation of the SCC mixtures included tests to assess their fresh and hardened properties. The tests conducted to evaluate the fresh properties included the slump flow (EN 12350-8), V-funnel time (EN 12350-9), and L-box (EN 12350-10) tests. The slump flow test was conducted by using a slump cone mould to contain the SCC mixture. The process involved filling the slump cone with the SCC sample without any compaction and lifting it vertically to allow the concrete to flow freely. After lifting the

slump cone, the final diameter of the resulting concrete spread was measured in two directions (Fig. 7(a)). For the V-funnel test, the SCC sample was poured into a V-funnel apparatus until it reached the top. The trap door was then opened, and the time it took for the concrete to flow out was recorded. The L-box test involved the use of an L-shaped box apparatus consisting of a vertical section connected to a horizontal section through a control gate. To perform the L-box test, the SCC sample was initially poured into the vertical section. The control gate was then removed to allow the SCC to flow through the horizontal part. The heights of the concrete at the end (H2) and the beginning (H1) of the L-box horizontal section were measured after the fresh concrete flow ceased (Fig. 7(b)). The blocking ratio was calculated as H2/H1. The air void content of the fresh SCC mixtures was measured using an air meter (ASTM C 231), as shown in Fig. 7(c). SCC specimens were cast in cylindrical moulds measuring  $\phi$  100 x 200 mm and placed in a controlled chamber at  $20\pm 5^\circ\text{C}$  for 24 hours. Following demoulding, the concrete specimens were immersed in water at  $20\pm 2^\circ\text{C}$ . The compressive strength test (EN 12390-3) was carried out on the hardened concrete specimens after 28 and 90 days of water curing, as shown in Fig. 7(d). The results of these tests are detailed in Table 4.

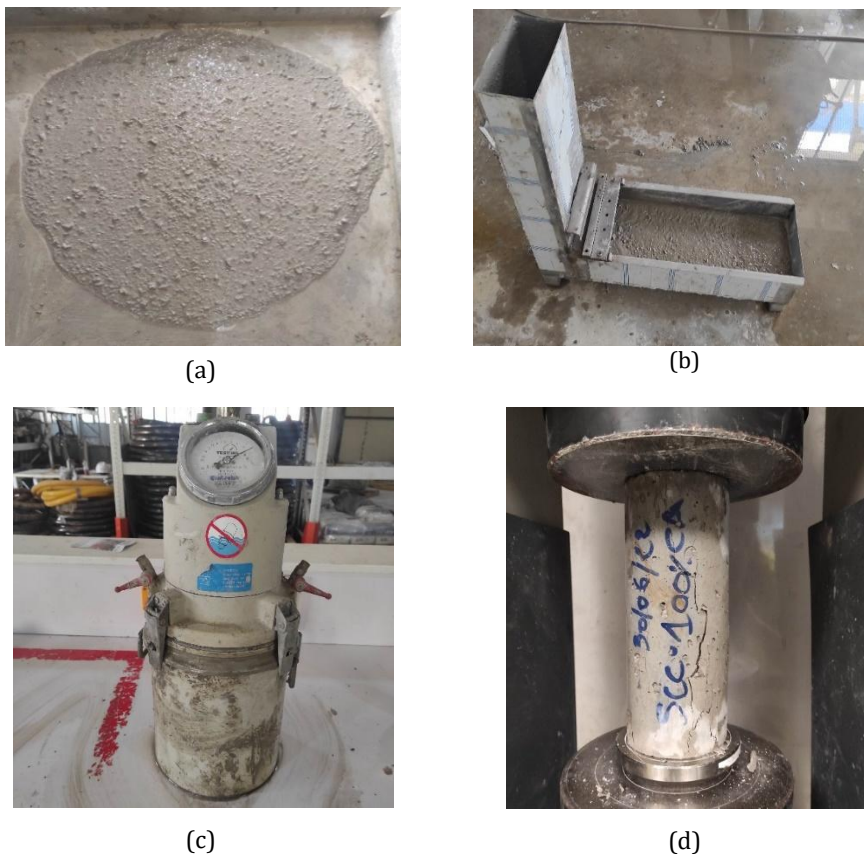


Fig. 7. (a) Tests for SCC: Slump flow, (b) L-box, (c) Air content, (d) Compressive strength

Table 4. Waste materials combinations and experimental results of prepared SCC mixtures

| Mix. N° | Waste materials combinations |      |      | Fresh Properties |                   |                     |                 | Compressive strength (MPa) |       |
|---------|------------------------------|------|------|------------------|-------------------|---------------------|-----------------|----------------------------|-------|
|         | MP                           | GGBS | GRPW | Slump Flow (mm)  | V-funnel time (s) | L-box ratio (H2/H1) | Air Content (%) | Rc28                       | Rc90  |
| 1       | 1                            | 0    | 0    | 695              | 10                | 0.87                | 2.30            | 49.38                      | 51.99 |
| 2       | 0                            | 1    | 0    | 700              | 23                | 0.86                | 3.00            | 51.02                      | 66.12 |
| 3       | 0                            | 0    | 1    | 590              | 10                | 0.84                | 3.90            | 41.65                      | 48.57 |
| 4       | 1/2                          | 1/2  | 0    | 690              | 14                | 0.86                | 2.10            | 48.72                      | 49.82 |
| 5       | 1/2                          | 0    | 1/2  | 615              | 9                 | 0.80                | 3.10            | 44.04                      | 51.69 |
| 6       | 0                            | 1/2  | 1/2  | 625              | 18                | 0.78                | 2.30            | 53.29                      | 61.73 |
| 7       | 1/3                          | 1/3  | 1/3  | 720              | 15                | 0.92                | 2.35            | 49.63                      | 55.54 |
| 8       | 2/3                          | 1/6  | 1/6  | 730              | 12                | 0.91                | 2.00            | 50.67                      | 51.77 |
| 9       | 1/6                          | 2/3  | 1/6  | 740              | 16                | 0.89                | 2.10            | 53.90                      | 59.03 |
| 10      | 1/6                          | 1/6  | 2/3  | 650              | 10                | 0.85                | 3.20            | 45.58                      | 53.72 |

Table 5. Quantities of SCC mixture constituents kept constant

| Materials                     | Gravel 1 | Gravel 2 | Crushed Sand | Dune Sand | Cement | Mineral addition* | Water | SP   |
|-------------------------------|----------|----------|--------------|-----------|--------|-------------------|-------|------|
| Quantity (Kg/m <sup>3</sup> ) | 297      | 445      | 868          | 96        | 400    | 60                | 206   | 2.76 |

\*(MP+GGBS+GFRPW)

### 3. Statistical Analysis of Regression Models

The regression models are established to evaluate the effect of MP, GGBS, and GFRPW proportions, and their interactions, on each of the SCC properties investigated. The analysis of variance (ANOVA) is a statistical method that helps to estimate and verify regression models through the P-value that determines the statistical significance of the model terms. A P-value less than 0.05 indicates that the model terms are significant, whilst a P-value greater than 0.05 identifies non-significant terms at a 95% confidence level. The presence of non-significant terms in the regression model can affect its descriptive and predictive quality. This work applies the stepwise elimination method to eliminate non-significant terms from the developed models. In the stepwise regression process, terms are systematically added to or removed from the model based on their statistical significance. Table 6 shows the final form of all established regression models, along with their respective  $R^2$ ,  $R^2_{adj}$ , and  $R^2_{pred}$  coefficients. In regression analysis, the  $R^2$  and  $R^2_{adj}$  coefficients are used to evaluate the goodness of fit of the derived model with the experimental results, while the  $R^2_{pred}$  coefficient is used to assess the predictive capacity of the model for new observations that deviate from the initial dataset. The validation of the statistical models also involves residual diagnostics, which include analysing the residuals against the predicted responses, as presented in Fig. 8. A random distribution of residuals in these plots indicates that the data does not exhibit any systematic patterns, such as reliability, periodicity, or interference (28). This randomness provides evidence that the model is validated and can be considered appropriate for the given application.

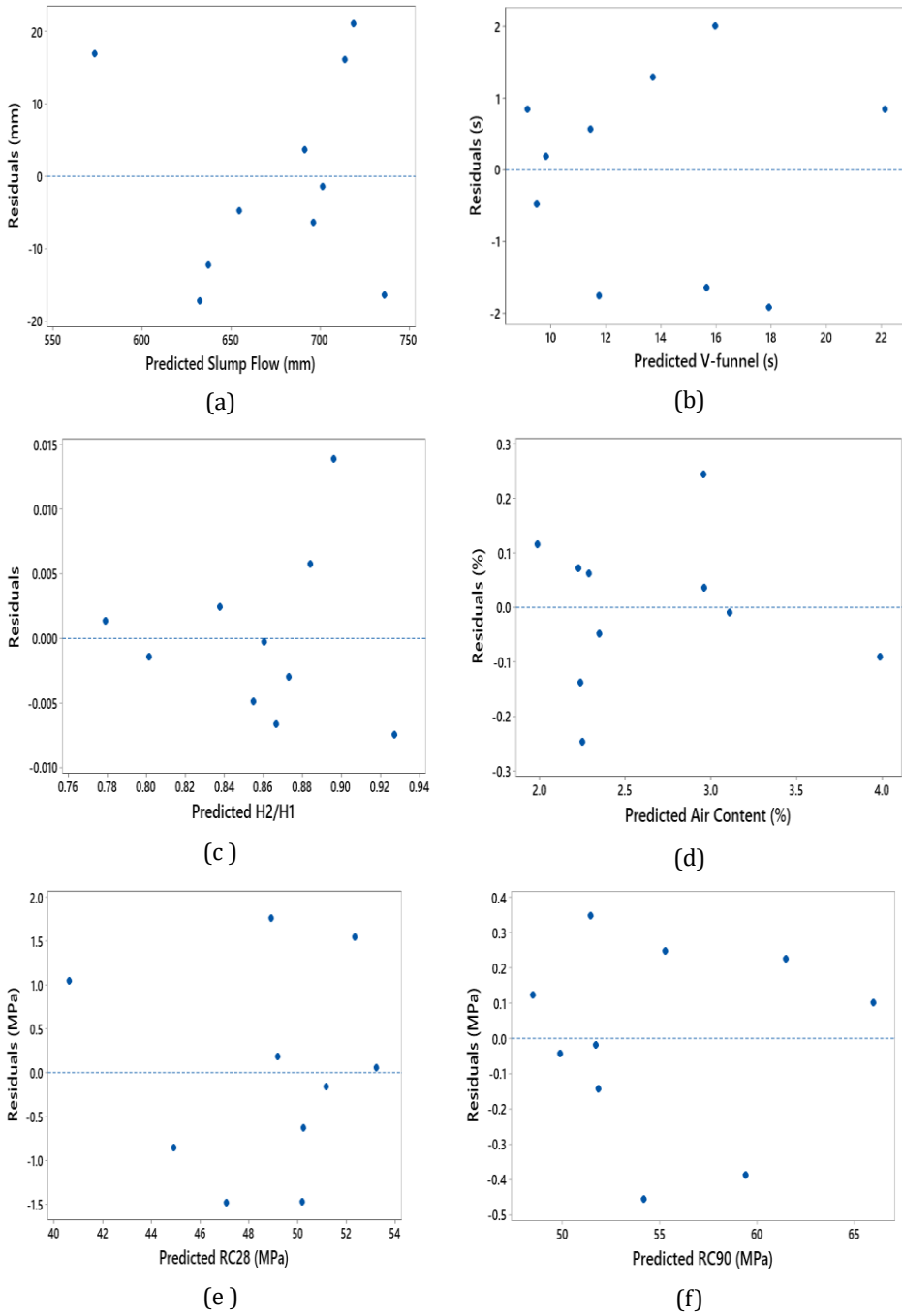


Fig. 8. Residual plots for: (a) Slump flow, (b) V-funnel, (c) H2/H1, (d) Air Content, (e) RC28, (f) RC90

Table 6. Regression equations developed by the mixture design approach and respective square

| Response        | Equation  | R <sup>2</sup> | R <sup>2</sup> <sub>adj</sub> | R <sup>2</sup> <sub>pred</sub> |
|-----------------|---|----------------|-------------------------------|--------------------------------|
| Slump Flow (mm) | $691.3*MP + 701.3*GGBS + 573.0*GFRPW + 2190*MP*GGBS*GFRPW$  | 92.71          | 89.06                         | 76.19                          |
| V-funnel (s)    | $9.14*MP + 22.14*GGBS + 9.81*GFRPW$   | 90.27          | 87.49                         | 82.02                          |
| H2/H1           | $0.873*MP + 0.860*GGBS + 0.837*GFRPW + 3.393*MP*GGBS*GFRPW - 0.281*GGBS*GFRPW - 0.216*MP*GGBS*GFRPW$          | 97.89          | 95.26                         | 82.76                          |
| Air content (%) | $2.227*MP + 2.963*GGBS + 3.991*GFRPW - 4.517*GGBS*GFRPW - 2.444*MP*GGBS$                                      | 95.09          | 91.16                         | 75.15                          |
| Rc28 (MPa)      | $49.19*MP + 51.18*GGBS + 40.60*GFRPW + 29.38*GGBS*GFRPW$  | 91.32          | 86.97                         | 75.28                          |
| Rc90 (MPa)      | $51.83*MP + 66.01*GGBS + 48.45*GFRPW - 36.26*MP*GGBS + 17.09*GGBS*GFRPW + 6.28*MP*GFRPW + 34.9*MP*GGBS*GFRPW$ | 99.78          | 99.34                         | 92.94                          |

## 4. Results and Discussion

### 4.1. Slump Flow

The trace plot established by Minitab helps in understanding the individual effect of each component on the response value (28). According to the response trace plot of slump flow, illustrated in Fig. 9, it can be seen that the three components, MP, GGBS, and GFRPW, have a positive effect in a particular range where the slump flow value increases, followed by a negative effect where the slump flow value decreases. It can also be seen that the MP and GGBS have a similar effect on the slump flow value, which is demonstrated by the superposition of their corresponding curves. This behaviour can be explained by these two components having the same specific surface area. The amount of water required to lubricate the surface of GGBS and MP particles can be the same, making the MP- and GFRPW-based SCC mixes exhibit similar slump flow diameters (23). However, the curve corresponding to GFRPW shows a significant drop in slump flow value, even though its specific surface area is the same as that of MP and GGBS. Correia et al. (19) reported a similar observation, which was attributed to the irregularity and non-uniformity in size and shape of GFRPW particles as compared to the spherical and uniform particles of recycled stone slurry. Oliveira et al. (17) explained the increased water consumption resulting from the incorporation of GFRPW due to the irregular dimensions of its particles, as shown in Fig. 4(c). Zhou et al. (29) also highlighted the effect of GFRPW-particle size distribution on workability. The authors observed that GFRW, consisting of two dominant particle sizes, namely short glass fibres and angular resin particles, negatively affects the workability of mortar. As shown in Fig. 5, the GFRPW used in our study is dominated by two main particle sizes, which may explain the slump flow drop. Furthermore, the presence of cylindrical-shaped particles in GFRPW (Fig. 4(c)) results in a loss of workability and a reduction in slump flow diameter as the proportion of GFRPW increases (30). Hadigheh et al. (14) attributed the decrease in slump flow diameter observed with a higher GFRPW dosage to the conglomeration of fibrous and granular recycles, thus increasing the water demand.

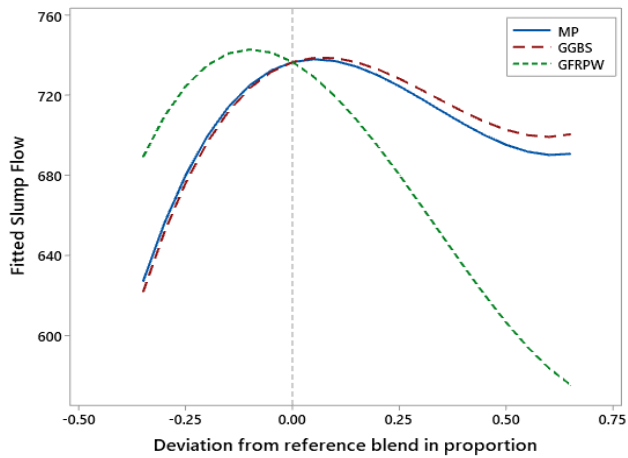


Fig. 9. Trace plot for Slump flow

The statistical model derived for the slump flow (Table 6) indicates that the latter is mainly influenced by the combination factor  $MP*GGBS*GFRPW$  in a ternary system (2190). It can be seen that the interaction between the three additions generates a synergistic effect on the slump flow. This effect better elucidates the observed increase in slump flow values shown in Fig. 9. Dada et al. reported similar behaviour in a ternary system combining marble powder, pozzolana, and cement. They explained the decrease in workability that followed the synergistic effect by an increase in the compactness of the mixes (31). The ternary contour plot in Fig. 10 illustrates the effect of MP, GGBS and GFRPW proportions on slump flow in ternary and binary systems. This figure shows that SCC mixes containing more than 0.5 GFRPW proportion in the GFRPW-GGBS and GFRPW-MP binary systems exhibited slump flow diameters of less than 650mm, which falls outside the range recommended by EFNARC (32).

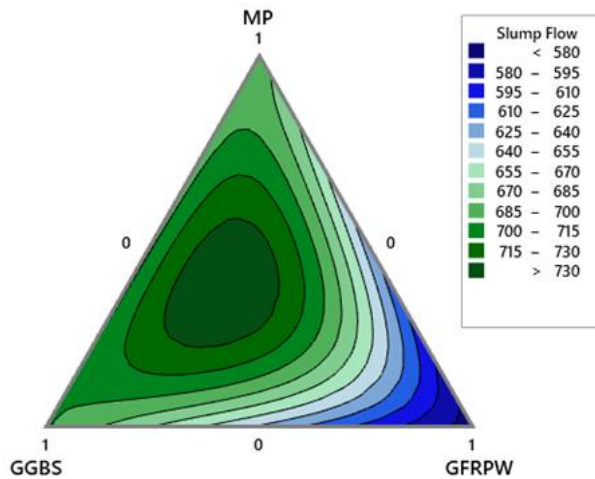


Fig. 10. Contour plot for Slump flow

For the MP-GGBS binary system, all SCC mixes produced slump flow values that met this recommendation. For the MP-GGBS binary system, increasing the MP content slightly increases the slump flow diameter. The optimum slump flow value is 742.69mm, corresponding to the mix proportions of 37% PM, 39% LA and 23% PV.

#### 4.2. V-funnel

The V-funnel time allows the evaluation of the viscosity of SCC mixtures, where a high flow time reflects high viscosity and a low flow time indicates low viscosity. The results illustrated in Fig. 11 show that the addition of MP and GGBS in SCC mixtures leads to a decrease in the V-funnel time values. Several researchers have attributed the reduction in viscosity of MP-based cementitious systems to the thixotropic property of this mineral addition (2,33,34). Biricik et al. (34) stated that the incorporation of MP can diminish the thixotropy of cement-based materials due to its inert nature. The authors also reported that the smooth surface texture and rounded shape of the MP particles, as shown in Fig. 4(a), can improve the flow behaviour. Spherically shaped particles with a smooth surface create a ball-bearing effect, allowing the particles to slide easily over each other, thus reducing interparticle friction.

The GFRPW particles, characterised by their low specific gravity (Table 2), exhibit SCC mixtures with a high paste volume. The increase in cement paste volume helps to minimise the interaction and friction between the aggregate particles. Moreover, the addition of GFRPW causes an increase in the air content percentage, as shown in Fig. 12. According to Meko et al., the increase in air bubbles tends to decrease the friction between mortar and coarse aggregate (35). It is evident that the ability of MP and GFRPW particles to mitigate internal friction allows SCC mixtures to flow through the V-funnel more easily and quickly. Tittarelli et al. (18) also reported that the presence of surfactants at the surface of the polymer particles of GFRPW may allow for better dispersion, thus reducing the viscosity of cement paste.

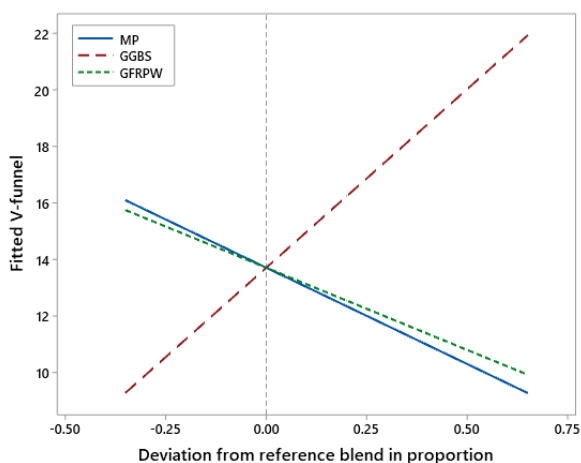


Fig. 11. Trace plot for V-funnel time

However, incorporating GGBS in the SCC mixes significantly increases the V-funnel time, as illustrated in Fig. 11. This behaviour can be explained by GGBS particles having a more angular shape and rough texture than MP particles, as shown in Fig. 4. Furthermore, the high specific gravity of GGBS particles (Table 2) contributes to decreasing the paste volume and, hence, increasing the internal friction of the SCC mixtures. Previous studies have also reported an increase in viscosity with the addition of GGBS (13,36,37).



The statistical model derived for V-funnel time is presented in Table 6. The model indicates that the V-funnel time is only influenced by the individual factors MP, GGBS, and GFRPW. Bouziani et al. (26) obtained comparable results when assessing the impact of three types of sand on the V-funnel flow time of SCC mixtures. The statistical model derived for V-funnel time was found to be independent of both ternary and binary interactions between the different sand types.

The effect of MP, GGBS, and GFRPW proportions on V-funnel time in binary and ternary systems is illustrated in Fig. 12. This figure indicates that the V-funnel time increases with increasing GGBS proportion in the GGBS-GFRPW, GGBS-MP, and MP-GFRPW-GGBS systems. Several studies have observed similar trends when incorporating GGBS in combination with different mineral admixtures (37). The figure also revealed that a GGBS proportion higher than 0.2 resulted in SCC mixtures with V-funnel times greater than 12 s, which is the upper limit recommended by EFNARC (32). On the other hand, the SCC mixtures in the GFRPW-MP binary system exhibited V-funnel time values ranging from 9 s to 10 s, meeting the EFNARC recommendations. The V-funnel time values ranged from a maximum of 22 s for 100% GGBS to a minimum of 9 s for 100% MP.

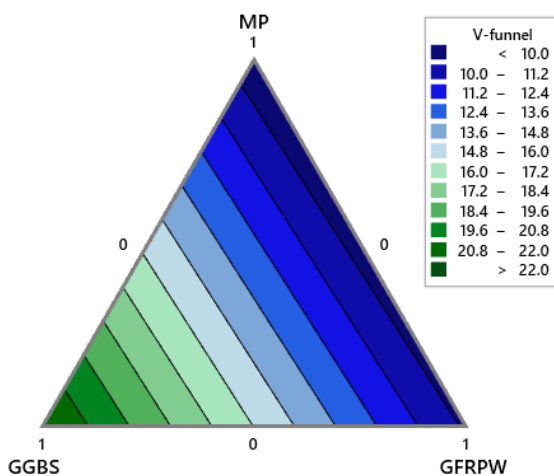


Fig. 12. Contour plot for V-funnel time

### 4.3. L-Box

The L-box ratio ( $H_2/H_1$ ) assesses the filling and passing ability of the SCC mixtures. The trace plot of the L-box ratio ( $H_2/H_1$ ), illustrated in Fig. 13, indicates that each of the additions MP, GGBS and GFRPW increases the L-box ratio at low proportions and then decreases it at high proportions. It is important to note that there is a proportional relationship between the L-box ratios and the slump flow values; the L-box ratio increases as the slump flow value increases, and vice versa. Nutan et al. (38) identified a good correlation between the L-box ratio and the yield stress of SCC mixtures, indicating that the L-box decreases as the yield stress increases. However, the GFRPW curve does not exhibit a significant drop in the L-box ratio, as observed in the slump flow. The reason can be attributed to the decrease in viscosity, illustrated in the V-funnel trace plot, which prevents a significant drop in the L-box ratio (39).

The statistical model of the L-box ratio indicates that the ternary combination MP\*GGBS\*GFRPW has the most significant influence, followed by the single factors MP, GGBS and GFRPW, respectively. The binary combinations GFRPW\*GGBS and MP\*GFRPW have a negative impact on the blocking ratio.

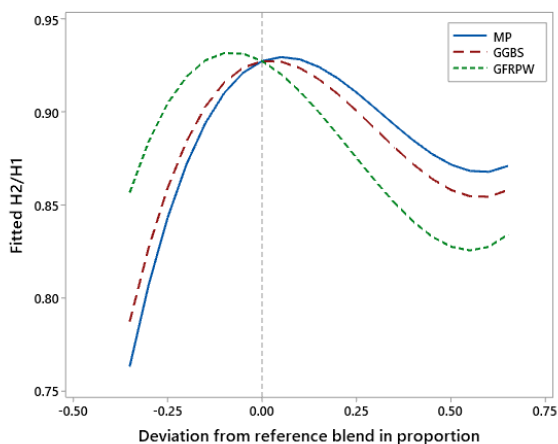


Fig. 13. Trace plot for L-Box ratio

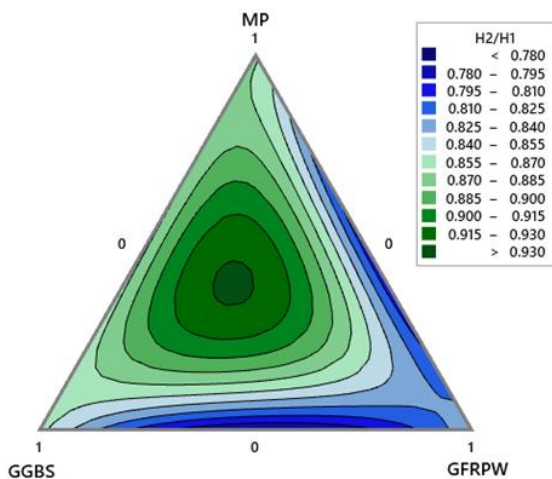


Fig. 14. Contour plot for L-Box ratio

From the contour plot of the L-Box ratio, illustrated in Fig. 14, it can be seen that all the blocking ratios in the MP-GGBS and MP-GFRPW binary systems fall within the range of 0.8 to 1 recommended by EFNARC. It can also be seen that the interaction between GGBS\*GFRPW and MP\*GFRPW exhibits an antagonistic effect on the blocking ratio. Mohammed et al. reported a similar effect between GGBS and FA, attributing it to the interlocking mechanism between the two types of particles (12). In the GFRPW-GGBS binary system, the L-box ratio falls below 0.8 when the GFRPW and GGBS proportions are between 0.3 and 0.7. According to EFNARC, a blocking ratio below 0.8 indicates a risk of mixture blockage (32). The SCC mix proportions of 39% PM, 36% LA and 25% PV yielded the optimum L-box ratio of 0.93.

#### 4.4. Air Content

The air content measured using the pressure method provides insight into the air voids or bubble content in the fresh concrete. The majority of air bubbles are formed during the concrete mixing process and get entrapped between colliding fine aggregates (40). It can

be seen from the trace plot in Fig. 15 that the air content has a low sensitivity to the MP content. The slight negative slope in the corresponding curve reflects the adverse impact of MP on air content. Different parameters can contribute to the negative effect of MP addition on the air content. Zeng et al. reported that the low viscosity of fresh concrete facilitates the escape of air bubbles during mixing and placing (40). Puthipad et al. also found that particles of spherical shape may promote the coalescence of fine air bubbles into larger ones, making their collapse easier (41,42). In addition, the slight decrease in air content can reflect the minor effect of MP particles on improving the compactness of the mixes (43–45).

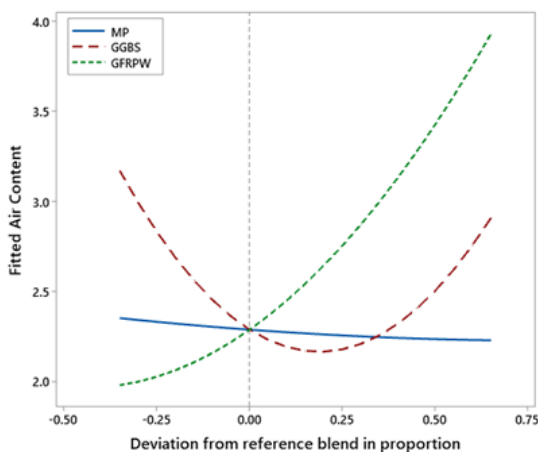


Fig. 15. Trace plot for Air content

Fig. 15 also shows that the addition of GGBS decreases the air content within a specific range and then increases it at high proportions. This observation can be related to the effect of GGBS particles on the mix's compactness. Initially, the GGBS particles probably fill the voids between the larger particles, making the mixes more compact and reducing the air content. Once the larger voids have been filled, the GGBS particles may start to create voids between each other, impairing the compactness of the mixes and increasing the air content (23,36). Moreover, the curve corresponding to GGBS demonstrates a good relationship between slump flow and air content of the SCC mixtures. Özcan et al. obtained a strong correlation between flow diameter and air content of non-air entrained concrete (46). It is well-known that low workability can generate a high amount of entrapped air due to improper placement of concrete mixes in the mould (46–48).

The air content trace plot (Fig. 15) illustrates the significant positive effect of GFRPW proportion on the air content. Most of the studies conducted on GFRPW incorporation in cementitious systems reported similar observations [24] (18,21,23,49). Coppola et al. found an anomalous air entrapment in fresh concrete, which was mitigated by a defoamer (21). Dehghan et al. attributed the increase in air content to the morphology of the GFRPW fibres, which promotes air entrapment (50). It is worth noting that the addition of GFRPW contributes to the loss of workability, as shown in Fig. 9, which may explain the increase in air entrapment in the SCC mixtures. Oliveira et al. also demonstrated that the poor hydrophilicity of the GFRPW particles prevents water absorption and facilitates the formation of air bubbles inside the mixtures (17). In a recent study, Zhou et al. (29) found that the addition of GFPW triggers apparent expansion in fresh mortar. The researchers identified that the amine curing agent of the resin and metallic oxides in the GFRPW react in an alkaline solution, resulting in gas production and fresh expansion. The expansion

generated during mixing could potentially explain the increase in the air content of the SCC mixtures (29,51).

The statistical model for air content (Table 6) indicates that the factors influencing air content are, in order of importance, GGBS\*GFRPW, GFRPW, GGBS, MP\*GGBS, and MP. The binary combination GGBS\*GFRPW has the most significant impact on air content (-4.517). According to Ma et al., the pozzolanic reaction consumes the OH<sup>-</sup> ions in cement paste, potentially mitigating the fresh-state expansion reaction and reducing gas generation (51). The combined effect of GGBS in improving the mixture compactness and reducing the expansion reaction with its pozzolanic reactivity might explain the notable negative impact of the GGBS\*GFRPW combination on air content.

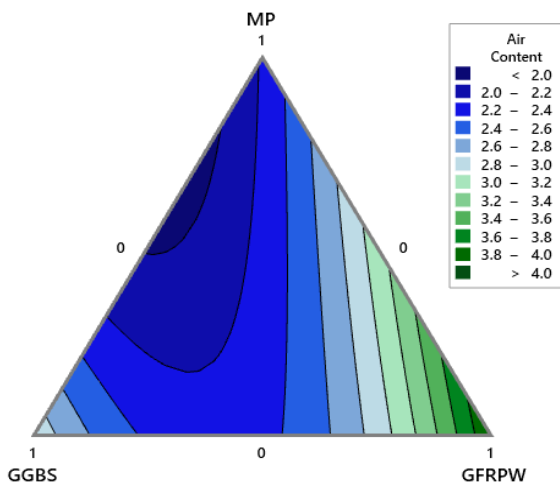


Fig. 16. Contour plot for Air content

The contour plot, illustrated in Fig. 16, shows that increasing the GFRPW content in the binary system MP-GFRPW elevates the air content in the SCC mixes. The binary combination of GGBS with MP and GFRPW produces an antagonistic effect on the air content. As depicted in Fig. 15, the addition of GGBS enhances the compactness of the SCC mixes within a specific range before decreasing it.

The highest air content percentage is 3.99%, recorded with 100% GFRPW. The highest air content percentage does not exceed the 5% allowed for SCC mixtures (51). It can be inferred that the addition of GFRPW contributes to the frost resistance of SCC (47). However, the lowest air content percentage is 1.93%, which was recorded with the combination of 65% MP and 35% GGBS.

#### 4.5. Compressive Strength

Figs. 17 and 18 illustrate the trace plot of the compressive strength at 28 days (Rc28) and 90 days (Rc90), respectively. It can be seen from Fig.17 that the addition of GFRPW leads to a decrease in the 28-day compressive strength, as indicated by the downward trend of the corresponding curve. This decrease in 28-day strength can be attributed to the increase in the air content resulting from the addition of GFRPW, as illustrated in Fig. 15. Similar observations have been reported by several authors (21,49). Corinaldesi et al. successfully mitigated a 10% loss in compressive strength in SCC mixes containing GFRPW by adding a defoamer that decreased air entrapment (49). The reduction in compressive strength can also be related to the lower strength of the plastic particles compared to that of MP and GGBS particles. Tittarelli et al. reported that replacing calcareous filler with GFRPW

impairs the mechanical performance of SCC (24). Furthermore, the interaction zone between the GFRPW particles and the cement matrix may affect the concrete strength. The low hydrophilicity of GFRPW particles can lead to an accumulation of free water around their surface, which reduces the microstructure of their interaction zone with the cement matrix (52). Oliveira et al. attributed the loss of compressive strength to the weak bond between the polymer fraction of the GFRPW and the cement paste (17). Correia et al. also reported that the cylindrical shape of the GFRPW particles negatively impacts the interaction zone between the concrete's components (19). Upon examining the SEM images of GFRPW-based concrete, Zhao et al. observed that the GFRPW fibres were pulled out rather than broken, indicating a weak bond between the fibres and the matrix (53).

The negative effect of GFRPW on the 28-day compressive strength tends to decrease as the GFRPW proportion decreases. This tendency can be observed as the slope of the GFRPW curve decreases with the GFRPW content. A similar trend was observed by Correia et al., who reported a slight decrease in the 28-day compressive strength at low GFRPW incorporation rates(19).

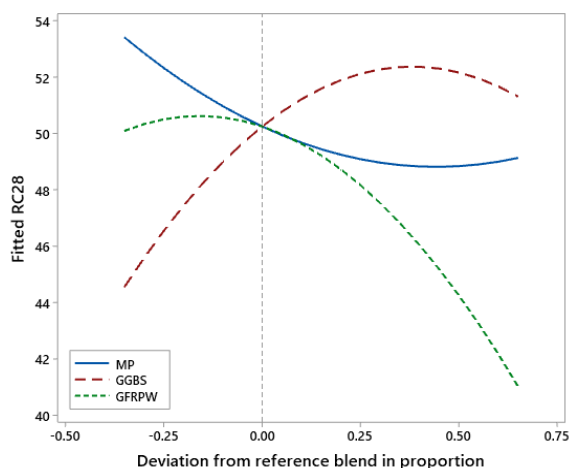


Fig. 17. Trace plot for RC28

It is worth noting that the influence of GFRPW on compressive strength changes at a later age. According to the GFRPW curve shown in Fig. 18, this waste material has a positive effect on the 90-day compressive strength in a specific range. The reason for the increase in the 90-day strength can be attributed to the presence of the chemical components SiO<sub>2</sub>, CaO and Al<sub>2</sub>O<sub>3</sub>, which contribute to the hydration reaction and, thus, to the mechanical strength development (22). As the increase in mechanical strength was observed after 90 days of curing, it can be inferred that this behaviour is a result of the pozzolanic reactivity of GFRPW. Baturki et al. reported that GFRPW exhibits a high pozzolanic activity, which is mainly controlled by its silicate content and fineness (54).

However, beyond a certain threshold, the 90-day compressive strength decreases with increasing GFRPW content, as illustrated in Fig. 18. It is evident that a high proportion of GFRPW leads to the accumulation of more voids and poor interaction zones, which in turn weakens the concrete microstructure and reduces its strength. These results are in agreement with previous research (53,55).

The trace plot curve corresponding to MP, illustrated in Fig. 17 and 18, shows that MP has a negative impact on both 28-day and 90-day compressive strengths. It can be noticed that the slope of the MP curves steepens with age. These observations corroborate the earlier

suggestions that MP is an inert mineral addition with no pozzolanic activity (2,39,43). The inert nature of the MP prevents its involvement in the hydration process, limiting its ability to contribute to the development of the concrete's mechanical performance (56). In addition, excessive fines can weaken the bond between the aggregates and the cement matrix in the interfacial transition zone (ITZ), decreasing the strength of concrete. Meera and Gupta attributed the decrease in the concrete compressive and splitting strength after the incorporation of MP to the presence of a large amount of fines (57).

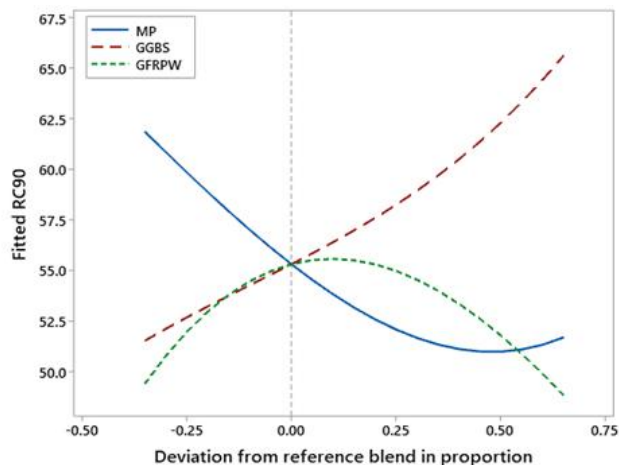


Fig. 18. Trace plot for Rc90

Fig. 17 and 18 also demonstrate that GGBS has a positive effect on compressive strengths at both ages. This influence becomes more pronounced at 90 days as the GGBS-related curve slope increases. According to Moula et al., GGBS particles act as nucleation sites for the formation and growth of hydrates, which enhances short-term strength and promotes the production of Portlandite for the long-term pozzolanic reaction (58). The trace plot curve related to GGBS, illustrated in Fig. 17, also shows a slight decrease in 28-day strength at high GGBS proportions. This result is consistent with that of air content. It is therefore possible to explain this loss of compressive strength by the increased porosity of the SCC mixtures. The loss in compressive strength was recovered after 90 days due to the long-term pozzolanic reactivity of GGBS. The long-term pozzolanic reaction of GGBS produces more hydrated calcium silicates (C-S-H) at a later age, which reduces the size of capillary pores, densifies the microstructure, and develops strength (11).

The statistical models for compressive strength at 28 days (Rc28) and 90 days (Rc90) are presented in Table 6. The factors influencing the compressive strength at 28 days are GGBS, MP, GFRPW and GGBS\*GFRPW, respectively. The binary combination GGBS\*GFRPW contributes to an increase in the 28-day compressive strength. It is evident that the significant influence of this parameter on reducing the air content (Table 6) enabled the development of compressive strength. Özcan et al. also reported an inverse relationship between 28-day compressive strength and air content (46), where the compressive strength increases as the air content of the fresh concrete decreases.

For the 90-day compressive strength, the influencing factors in order of importance are, GGBS, MP, GFRPW, MP\*GGBS, MP\*GFRPW\*GGBS, GGBA\*GFRPW, and MP\*GFRPW. It is clear that the interaction terms MP\*GGBS\*GFRPW and MP\*GFRPW promote the development of the 90-day compressive strength. Several researchers have reported that the use of pozzolanic additions in combination with MP improves the mechanical performance of concrete [9]. Choudhary et al. found that despite the negative effect of MP on mechanical

strength, the addition of FA improved the mechanical strength of SCC after 90 days of curing (2). However, the interaction term GGBS\*MP has a negative influence on the 90-day compressive strength. Belaidi et al. obtained a reduction in compressive strength with the addition of PZ and MP (25). The authors stated that PZ incorporation causes a slow evolution of the compressive strength of MP-based concrete mixtures.

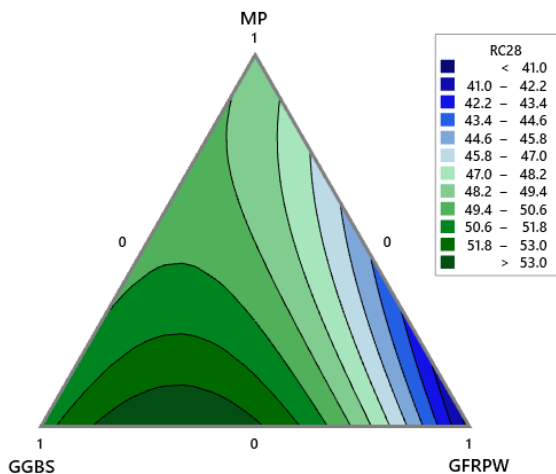


Fig. 19. Contour plot for RC28

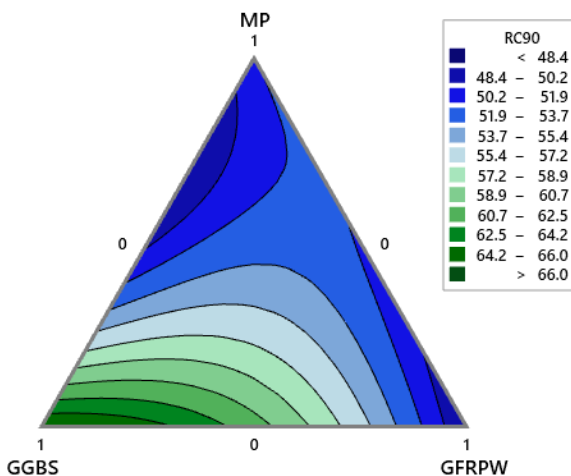


Fig. 20. Contour plot for RC90

The contour plot for compressive strength at 28 days is shown in Fig. 19. The figure shows that as the GFRPW content increases in the binary system MP-GFRPW, the compressive strength decreases. This behaviour can be attributed to the increase in air content in the SCC mixtures with increasing GFRPW proportion in the MP-GFRPW combination (Fig. 16). In the case of the GGBS-MP binary combination, the 28-day compressive strength improves with an increase in GGBS content due to the pozzolanic reactivity of this mineral addition, unlike the inert nature of MP. However, in the GGBS-GFRPW system, the increase in GGBS content increases the compressive strength to a maximum value of 54.19MPa, corresponding to the combination of 32% GFRPW with 68% GGBS, and then decreases it. These results are consistent with those for air content in the GGBS-GFRPW binary system,

where GGBS reduces the air content of SCC mixes before subsequently increasing it. The minimum 28-day compressive strength value is 40.60 MPa, corresponding to the 100% GFRPW proportion.

Regarding the 90-day compressive strength, it can be seen from Fig. 20 that the effect of the mineral additions in both the binary and ternary systems change with time. Increasing the GGBS proportion in the GGBS-GFRPW binary system develops the compressive strength to a maximum value of 66.02 MPa, corresponding to the mix proportion of 100% GGBS, and shows no decreasing effect. This suggests that the long-term pozzolanic reactivity of GGBS contributes to the refinement of the capillary pores that negatively affect the 28-day strength. The interaction in the MP-GGBS binary system causes an antagonistic effect on the 90-day compressive strength. This behaviour is not consistent with the air content results, where the binary combination MP-GGBS shows the minimum air content percentage. This implies that the air content of the fresh concrete is not the only parameter that can explain the development of concrete strength. As for the 28-day compressive strength, the minimum 90-day compressive strength corresponds to the proportion of 100% GFRPW and is equal to 48.44 MPa.

## 5. Conclusions

The mixture design modeling approach was adopted in this study to evaluate the impact of combining three local waste materials, namely MP, GGBS, and GFRPW, as mineral additions on the performance of SCC. Based on the results obtained, the following conclusions can be drawn:

- MP, GGBS, and GFRPW exhibited a similar effect on slump flow, with the slump flow value increasing within a specific range and then decreasing. When the proportion of GFRPW in the GFRPW-based binary systems exceeded 0.5, the SCC mixes produced slump flow values below the lower limit of 650 mm recommended by EFNARC. The interaction between the three components MP\*GGBS\*GFRPW promoted an increase in slump flow, reaching a maximum value of 742.69 mm at proportions of 37% MP, 39% GGBS, and 23% GFRPW.
- GFRPW and MP had a similar decreasing effect on the V-funnel time, while GGBS demonstrated an increasing effect. When the proportion of GGBS exceeded 0.2 in the GGBS-based systems, the SCC mixtures resulted in V-funnel time values above 12s, which does not meet the EFNARC recommendations.
- MP, GFRPW, and GGBS had a similar effect on the blocking ratio, with the L-box ratio increasing within a specific range before decreasing. The ternary interaction MP\*GFRPW\*GGBS contributed to an increase in the L-box ratio, reaching a maximum value of 0.93 at proportions of 39% MP, 36% GGBS, and 25% GFRPW. However, the binary interactions GFRPW\*GGBS and GFRPW\*MP caused a decrease in the blocking ratio. In the GGBS-GFRPW binary system, when the proportion of GFRPW was between 0.3 and 0.7, the SCC mixtures had L-box ratios below the EFNARC recommended lower limit of 0.8.
- GFRPW had a significant effect on increasing the air content of fresh SCC mixtures, with the maximum value of 3.99% recorded at a mixture proportion of 100% GFRPW. The interaction in the binary systems GFRPW-MP and GFRPW-GGBS resulted in a decrease in the air content. MP had a minimal impact on the air content, while GGBS initially decreased the air content within a specific range before increasing it.
- Increasing the amount of GRPW resulted in a decrease in compressive strength at 28 and 90 days, reaching a minimum value of 40.60 MPa and 48.44 MPa, respectively, for 100% GRPW. The interaction between GGBS and GFRPW gave a maximum 28-day compressive strength of 54.19 MPa for a mix containing 68%



GGBS and 32% GFRPW. The maximum 90-day compressive strength was 66.02 MPa for 100% GGBS.

## References

- [1] De Schutter G, editor. Self-compacting concrete. Dunbeath: Whittles Publ. [u.a.]; 2008. 296 p.
- [2] Choudhary R, Gupta R, Nagar R. Impact on fresh, mechanical, and microstructural properties of high strength self-compacting concrete by marble cutting slurry waste, fly ash, and silica fume. *Constr Build Mater.* 2020;239:117888. <https://doi.org/10.1016/j.conbuildmat.2019.117888>
- [3] Iqbal Q, Musarat MA, Ullah N, Alaloul WS, Rabbani MBA, Al Madhoun W, et al. Marble dust effect on the air quality: An environmental assessment approach. *Sustainability.* 2022;14(7):3831. <https://doi.org/10.3390/su14073831>
- [4] Sufian M, Ullah S, Ostrowski KA, Ahmad A, Zia A, Śliwa-Wieczorek K, et al. An experimental and empirical study on the use of waste marble powder in construction material. *Materials.* 2021;14(14):3829. <https://doi.org/10.3390/ma14143829>
- [5] Singh M, Choudhary K, Srivastava A, Sangwan KS, Bhunia D. A study on environmental and economic impacts of using waste marble powder in concrete. *J Build Eng.* 2017;13:87-95. <https://doi.org/10.1016/j.jobe.2017.07.009>
- [6] Butt IM, Mustafa T, Rauf S, Razzaq A, Anwer J. Pulmonary function parameters among marble industry workers in Lahore, Pakistan. *F1000Research* [Internet]. 2021 [cited 2024 Mar 23];10. <https://doi.org/10.12688/f1000research.52749.1>
- [7] Meera M, Dash AK, Gupta S. Rheological and strength properties of self-compacting concrete incorporating marble and granite powders. *Mater Today Proc.* 2020;32:1005-13. <https://doi.org/10.1016/j.matpr.2020.08.531>
- [8] Sadek DM, El-Attar MM, Ali HA. Reusing of marble and granite powders in self-compacting concrete for sustainable development. *J Clean Prod.* 2016;121:19-32. <https://doi.org/10.1016/j.jclepro.2016.02.044>
- [9] Mahmood MS, Elahi A, Zaid O, Alashker Y, Şerbănoiu AA, Grădinaru CM, et al. Enhancing compressive strength prediction in self-compacting concrete using machine learning and deep learning techniques with incorporation of rice husk ash and marble powder. *Case Stud Constr Mater.* 2023;19:e02557. <https://doi.org/10.1016/j.cscm.2023.e02557>
- [10] Bayat H, Banar R, Nikravan M, Farnood P, Ramezaniyanpour AM, Kashani A. Durability, mechanical, workability, and environmental assessment of self-consolidating concrete containing blast furnace slag and natural zeolite. *J Build Eng.* 2024;108737. <https://doi.org/10.1016/j.jobe.2024.108737>
- [11] Sara B, Mhamed A, Otmame B, Karim E. Elaboration of a Self-Compacting mortar based on concrete demolition waste incorporating blast furnace slag. *Constr Build Mater.* 2023;366:130165. <https://doi.org/10.1016/j.conbuildmat.2022.130165>
- [12] Mohammed AM, Asaad DS, Al-Hadithi AI. Experimental and statistical evaluation of rheological properties of self-compacting concrete containing fly ash and ground granulated blast furnace slag. *J King Saud Univ-Eng Sci.* 2022;34(6):388-97. <https://doi.org/10.1016/j.jksues.2020.12.005>
- [13] Ofuyatan OM, Adeniyi AG, Ijie D, Ighalo JO, Oluwafemi J. Development of high-performance self compacting concrete using eggshell powder and blast furnace slag as partial cement replacement. *Constr Build Mater.* 2020;256:119403 <https://doi.org/10.1016/j.conbuildmat.2020.119403>
- [14] Hadigheh SA, Wei Y. Recycling of glass fibre reinforced polymer (GFRP) composite wastes in concrete: A critical review and cost benefit analysis. In: *Structures* [Internet]. Elsevier; 2023 [cited 2024 Jan 27]. p. 1540-56. <https://doi.org/10.1016/j.istruc.2023.05.018>

- [15] Gonçalves RM, Martinho A, Oliveira JP. Recycling of reinforced glass fibers waste: Current status. *Materials*. 2022;15(4):1596. <https://doi.org/10.3390/ma15041596>
- [16] Oliveira PS, Antunes MLP, da Cruz NC, Rangel EC, de Azevedo ARG, Durrant SF. Use of waste collected from wind turbine blade production as an eco-friendly ingredient in mortars for civil construction. *J Clean Prod*. 2020;274:122948. <https://doi.org/10.1016/j.jclepro.2020.122948>
- [17] Tittarelli F, Shah SP. Effect of low dosages of waste GRP dust on fresh and hardened properties of mortars: Part 1. *Constr Build Mater*. 2013;47:1532-8. <https://doi.org/10.1016/j.conbuildmat.2013.06.043>
- [18] Correia JR, Almeida NM, Figueira JR. Recycling of FRP composites: reusing fine GFRP waste in concrete mixtures. *J Clean Prod*. 2011;19(15):1745-53. <https://doi.org/10.1016/j.jclepro.2011.05.018>
- [19] Asokan P, Osmani M, Price AD. Assessing the recycling potential of glass fibre reinforced plastic waste in concrete and cement composites. *J Clean Prod*. 2009;17(9):821-9. <https://doi.org/10.1016/j.jclepro.2008.12.004>
- [20] Coppola L, Cadoni E, Forni D, Buoso A. Mechanical characterization of cement composites reinforced with fiberglass, carbon nanotubes or glass reinforced plastic (GRP) at high strain rates. *Appl Mech Mater*. 2011;82:190-5. <https://doi.org/10.4028/www.scientific.net/AMM.82.190>
- [21] Asokan P, Osmani M, Price AD. Improvement of the mechanical properties of glass fibre reinforced plastic waste powder filled concrete. *Constr Build Mater*. 2010;24(4):448-60. <https://doi.org/10.1016/j.conbuildmat.2009.10.017>
- [22] Farinha CB, de Brito J, Veiga R. Assessment of glass fibre reinforced polymer waste reuse as filler in mortars. *J Clean Prod*. 2019;210:1579-94. <https://doi.org/10.1016/j.jclepro.2018.11.080>
- [23] Tittarelli F, Moriconi G. Use of GRP industrial by-products in cement based composites. *Cem Concr Compos*. 2010;32(3):219-25. <https://doi.org/10.1016/j.cemconcomp.2009.11.005>
- [24] Belaidi ASE, Azzouz L, Kadri E, Kenai S. Effect of natural pozzolana and marble powder on the properties of self-compacting concrete. *Constr Build Mater*. 2012;31:251-7. <https://doi.org/10.1016/j.conbuildmat.2011.12.109>
- [25] Bouziani T. Assessment of fresh properties and compressive strength of self-compacting concrete made with different sand types by mixture design modelling approach. *Constr Build Mater*. 2013;49:308-14. <https://doi.org/10.1016/j.conbuildmat.2013.08.039>
- [26] Mendes BC, Pedroti LG, Vieira CMF, de Carvalho JMF, Ribeiro JCL, de Souza CMM. Application of mixture design of experiments to the development of alkali-activated composites based on chamotte and waste glass. *Constr Build Mater*. 2023;379:131139. <https://doi.org/10.1016/j.conbuildmat.2023.131139>
- [27] Chen C, Li X, Chen X, Chai J, Tian H. Development of cemented paste backfill based on the addition of three mineral additions using the mixture design modeling approach. *Constr Build Mater*. 2019;229:116919. <https://doi.org/10.1016/j.conbuildmat.2019.116919>
- [28] Zhou B, Zhang M, Ma G. Multi-scale experimental study on the effect of crushed GFRP powder and dust on physical-mechanical properties of cement mortar. *J Build Eng*. 2022;57:104853. <https://doi.org/10.1016/j.jobbe.2022.104853>
- [29] Chen CH, Huang R, Wu JK, Yang CC. Waste E-glass particles used in cementitious mixtures. *Cem Concr Res*. 2006;36(3):449-56. <https://doi.org/10.1016/j.cemconres.2005.12.010>
- [30] Dada H, Belaidi ASE, Soualhi H, Kadri EH, Benabed B. Influence of temperature on the rheological behaviour of eco-mortar with binary and ternary cementitious blends of natural pozzolana and marble powder. *Powder Technol*. 2021;384:223-35. <https://doi.org/10.1016/j.powtec.2021.02.019>

- [31] EFNARC F. Specification and guidelines for self-compacting concrete. Eur Fed Spec Constr Chem Concr Syst. 2002;
- [32] Prakash B, Saravanan TJ, Kabeer KSA, Bisht K. Exploring the potential of waste marble powder as a sustainable substitute to cement in cement-based composites: A review. Constr Build Mater. 2023;401:132887.
- [33] Biricik Ö, Aytekin B, Mardani A. Effect of waste binder material usage rate on thixotropic behaviour of cementitious systems. Constr Build Mater. 2023;403:133197. <https://doi.org/10.1016/j.conbuildmat.2023.133197>
- [34] Meko B, Ighalo JO, Ofuyatan OM. Enhancement of self-compactability of fresh self-compacting concrete: A review. Clean Mater. 2021;1:100019. <https://doi.org/10.1016/j.clema.2021.100019>
- [35] Revilla-Cuesta V, Skaf M, Santamaría A, Hernández-Bagaces JJ, Ortega-López V. Temporal flowability evolution of slag-based self-compacting concrete with recycled concrete aggregate. J Clean Prod. 2021;299:126890. <https://doi.org/10.1016/j.jclepro.2021.126890>
- [36] Khodair Y, Bommareddy B. Self-consolidating concrete using recycled concrete aggregate and high volume of fly ash, and slag. Constr Build Mater. 2017;153:307-16. <https://doi.org/10.1016/j.conbuildmat.2017.07.063>
- [37] Nguyen TLH, Roussel N, Coussot P. Correlation between L-box test and rheological parameters of a homogeneous yield stress fluid. Cem Concr Res. 2006;36(10):1789-96. <https://doi.org/10.1016/j.cemconres.2006.05.001>
- [38] Uysal M, Yilmaz K. Effect of mineral admixtures on properties of self-compacting concrete. Cem Concr Compos. 2011;33(7):771-6. <https://doi.org/10.1016/j.cemconcomp.2011.04.005>
- [39] Zeng X, Lan X, Zhu H, Liu H, Umar HA, Xie Y, et al. A review on bubble stability in fresh concrete: Mechanisms and main factors. Materials. 2020;13(8):1820. <https://doi.org/10.3390/ma13081820>
- [40] Wang Y, Lu H, Xiao R, Hu W, Huang B. Experimental Study on the Stability and Distribution of Air Voids in Fresh Fly Ash Concrete. Materials. 2022;15(23):8332. <https://doi.org/10.3390/ma15238332>
- [41] Puthipad N, Ouchi M, Attachaiyawuth A. Effects of fly ash, mixing procedure and type of air-entraining agent on coalescence of entrained air bubbles in mortar of self-compacting concrete at fresh state. Constr Build Mater. 2018;180:437-44. <https://doi.org/10.1016/j.conbuildmat.2018.04.138>
- [42] Alyousef R, Benjeddou O, Soussi C, Khadimallah MA, Mustafa Mohamed A. Effects of incorporation of marble powder obtained by recycling waste sludge and limestone powder on rheology, compressive strength, and durability of self-compacting concrete. Adv Mater Sci Eng [Internet]. 2019 [cited 2024 Jan 31];2019. <https://doi.org/10.1155/2019/4609353>
- [43] Ahmad J, Zhou Z, Deifalla AF. Self-Compacting Concrete with Partially Substitution of Waste Marble: A Review. Int J Concr Struct Mater. 2023 Apr 17;17(1):25. <https://doi.org/10.1186/s40069-023-00585-5>
- [44] Danish A, Mosaberpanah MA, Salim MU, Fediuk R, Rashid MF, Waqas RM. Reusing marble and granite dust as cement replacement in cementitious composites: A review on sustainability benefits and critical challenges. J Build Eng. 2021;44:102600. <https://doi.org/10.1016/j.jobe.2021.102600>
- [45] Özcan F, Koç ME. Influence of ground pumice on compressive strength and air content of both non-air and air entrained concrete in fresh and hardened state. Constr Build Mater. 2018;187:382-93. <https://doi.org/10.1016/j.conbuildmat.2018.07.183>

- [46] Topcu IB, Bilir T, Uygunoğlu T. Effect of waste marble dust content as filler on properties of self-compacting concrete. *Constr Build Mater.* 2009;23(5):1947-53. <https://doi.org/10.1016/j.conbuildmat.2008.09.007>
- [47] Ahmad J, Zhou Z. Mechanical performance of waste marble based self compacting concrete reinforced with steel fiber (Part I). *J Build Eng.* 2023;78:107574. <https://doi.org/10.1016/j.jobbe.2023.107574>
- [48] Corinaldesi V. Influence of lightweight aggregates and GRP by-product powders on the properties of self-compacting concretes. *Adv Mater Res.* 2012;548:215-20. <https://doi.org/10.4028/www.scientific.net/AMR.548.215>
- [49] Dehghan A, Peterson K, Shvarzman A. Recycled glass fiber reinforced polymer additions to Portland cement concrete. *Constr Build Mater.* 2017;146:238-50. <https://doi.org/10.1016/j.conbuildmat.2017.04.011>
- [50] Ma G, Zhou B, Zhang M, Sanjayan J. Understanding and eliminating of expansion caused by recycled glass fiber reinforced plastic powder in concrete. *Constr Build Mater.* 2022;347:128542. <https://doi.org/10.1016/j.conbuildmat.2022.128542>
- [51] Aravecchia N, Bañuls-Ciscar J, Caverzan A, Ceccone G, Cuenca E, Ferrara L, et al. On the feasibility of using Polyester (PE) waste particles from metal coating industry as a secondary raw materials in concrete. *Clean Mater.* 2023;100193. <https://doi.org/10.1016/j.clema.2023.100193>
- [52] Zhao T, Lv Y, Chen J, Song P, Sun M, Zhang X, et al. Effect of Glass Fiber-Reinforced Plastic Waste on the Mechanical Properties of Concrete and Evaluation of Its Feasibility for Reuse in Concrete Applications. *Materials.* 2023;16(20):6772. <https://doi.org/10.3390/ma16206772>
- [53] Baturkin D, Hisseine OA, Masmoudi R, Tagnit-Hamou A, Massicotte L. Valorization of recycled FRP materials from wind turbine blades in concrete. *Resour Conserv Recycl.* 2021;174:105807. <https://doi.org/10.1016/j.resconrec.2021.105807>
- [54] Aziz F, Tan AR, Bakar NB, Nasir NAM. Properties of concrete with glass fibre reinforced polymer waste as partial replacement of fine aggregate. In: *Journal of Physics: Conference Series* [Internet]. IOP Publishing; 2023.; 012015. <https://doi.org/10.1088/1742-6596/2521/1/012015>
- [55] Meera M, Gupta S. Performance evaluation of marble powder and fly ash concrete for non-structural applications. *J Build Eng.* 2024;84:108499. <https://doi.org/10.1016/j.jobbe.2024.108499>
- [56] Essam A, Mostafa SA, Khan M, Tahwia AM. Modified particle packing approach for optimizing waste marble powder as a cement substitute in high-performance concrete. *Constr Build Mater.* 2023;409:133845. <https://doi.org/10.1016/j.conbuildmat.2023.133845>
- [57] Moula S, Fraj AB, Wattez T, Bouasker M, Ali NBH. Mechanical properties, carbon footprint and cost of ultra-high performance concrete containing ground granulated blast furnace slag. *J Build Eng.* 2023;79:107796. <https://doi.org/10.1016/j.jobbe.2023.107796>

## Prototype silicone rubber based passive seismic damper: Development, characterization and implementation

Utsav Koshti<sup>a</sup>, Sharadkumar Purohit<sup>\*b</sup>

Dept. of Civil Eng., School of Engineering, Institute of Technology, Nirma University, Ahmedabad, India

### Article Info

#### Article history:

Received 29 Feb 2024

Accepted 14 May 2024

#### Keywords:

Silicone rubber;  
Kelvin-Voigt model;  
Benchmark building;  
Passive damper

### Abstract

Passive damping devices are mostly preferred owing to their relatively lower cost, low maintenance, and stability over a wide range of frequencies during seismic events. Currently, these devices with temperature in-sensitive viscoelastic material are being explored. The paper aims to develop a prototype piston-cylinder based passive damper with silicone rubber particles and characterize it with varied amplitude and frequency of sinusoidal input. The device Silicone Rubber Particle Packed Damper, so developed, was then implemented in the benchmark building for seismic response control. Silicone rubber particles with lower hardness were produced through compressed molding technology to improve the damping efficiency of the device. The device was later converted to an Air Damping Device by removing silicone rubber particles for a natural comparison of efficacy. Hysteresis curves of devices, elliptical in shape, obtained through characterization were mathematically modelled using the Kelvin-Voigt model, and parameters were identified using multivariable linear regression to implement them with the benchmark building. Uncontrolled and controlled responses of benchmark building fitted with, both, damping devices were determined under strong motion (El Centro, Hachinohe) and pulse-type (Kobe, Northridge) seismic excitations. Seismic response parameters; peak displacement, peak interstorey drift, peak acceleration, and peak damper force was estimated. Each seismic response parameter yields substantial reduction for controlled benchmark building with Silicone Rubber Particle Packed Damper. The efficacy of damping devices was established by Performance Indices in terms of peak interstorey ratio, level acceleration, base shear, and control force. Though both passive damping devices were found effective in seismic response control of benchmark building, Silicone Rubber Particle Packed Damper outperforms Air Damping Device. The developed prototype damping devices are a low cost and easy to maintain.

© 2024 MIM Research Group. All rights reserved.

## 1. Introduction

Earthquakes, one of the natural disasters, are the most destructive force in nature as they disrupt infrastructure and human lives. In the last couple of decades, earthquakes contributed nearly about 8,10,000 fatalities, worldwide [1]. The recent past has seen a surge in the frequency of earthquakes, especially in seismically active areas, e.g., Japan (2024), Afghanistan (2023), Turkey (2023), and Italy (2016/17). Such earthquakes cause varied degrees of damage to buildings, public infrastructures, industrial and lifeline structures made from concrete, steel and precast materials that can be identified through field observations [2] and quantified by advanced imagery based techniques [3]. It becomes imperative to enhance the seismic resistance of buildings and structures by employing evolving structural control technologies and reducing seismic vulnerability.

\*Corresponding author: [sharad.purohit@nirmauni.ac.in](mailto:sharad.purohit@nirmauni.ac.in)

<sup>a</sup>orcid.org/0000-0001-8652-5868; <sup>b</sup>orcid.org/0000-0002-2678-4320

DOI: <http://dx.doi.org/10.17515/resm2024.201ma0229rs>

Res. Eng. Struct. Mat. Vol. 11 Iss. 1 (2025) 139-163

Retrofitting strategies to improve the reduced stiffness of structural elements through jacketing, fibre wrapping, the addition of lateral load resisting elements and providing passive/active damper are other ways to safeguard buildings and structures from future Earthquakes [4]. Developed countries like the USA, Japan, Italy and New Zealand have proactive retrofitting strategies leading to improved seismic resistance for buildings, as evident in recent earthquakes [5]. In developing countries like India, many buildings are seismically vulnerable and at risk of strong earthquakes with the rapid increase in new construction projects [6].

The earthquake induced structural vibrations can be controlled by modifying mass, stiffness, damping or shape and by externally supplying passive or active counter forces. Various methods of structural control have been implemented successfully, and efforts are going on to improve the efficiency of such methods utilizing the mechanical properties of diversified materials. These advanced structural control methodologies are broadly classified as Active, Passive, Hybrid and Semi-active control. Realizing improved structural seismic response of buildings with the implementation of these control devices, it is recommended that such devices are further improved on energy efficient approaches and reduced cost [7]. Owing to mechanical simplicity, reduced power requirement, and relatively higher controllable force capacity, a semi-active system forms an attractive alternative to an active control system [8]. Numerous studies conducted have proved that such systems, when implemented appropriately, perform better than passive devices and yield at par with the performance of fully active systems. However, acceptance of such a system depends on important parameters like construction cost, long-term effect and maintenance along with improved performance. Additionally, structural systems are a combination of various structural elements and thus, integration of such innovative devices with structural systems becomes complex and challenging. In light of these, research efforts are still continued in developing new and modifying existing passive devices for improved seismic response of structures as they are relatively low-cost, offer less maintenance and ensure safety under seismic events owing to their robustness [9].

Passive energy dissipation devices have been under development for many years, beginning with the 1990's. The fundamental principle of these devices is to decrease the inelastic energy dissipation demand of the framing system of structures [10]. The most common passive devices used for seismic response control are viscous fluid dampers, friction dampers and metallic yield dampers, which are classified as rate-dependent and rate-independent devices. Since viscous damping offered by viscous damper is temperature sensitive and material proportion of friction damper tends to decrease and suffered to fatigue effect, there is a need to develop an innovative passive damper for seismic response control of the buildings. Out of these, rate-dependend passive energy dissipation devices are in continuous mode of redevelopment with a major focus on the viscoelastic damper (VED). VED has mechanical properties sensitive to various parameters, such as temperature, strain amplitude, excitation frequency, amplitude, hardness, etc., and thus offers diversified damper configuration compared to other passive energy dissipating devices. The performance of VED is largely dependent on vulcanized viscoelastic materials (VEM) made from a composite material, including matrix, vulcanized system, filler system and anti-ageing system. VEM is required to satisfy specific requirements: (i) damping and loss factor, (ii) reduced heat generation with good heat dissipation, (iii) good working performance, (iv) large temperature range, and (v) good durability properties which are difficult to mate with. Current research work focuses on utilizing innovative VEMs which are less sensitive to temperature variation. Therefore, silicone rubber and Nitrile Butadiene Rubber (NBR) were developed and are being studied as potential alternatives to standard VEMs of VEDs [11]. It has been proposed through experiments that the Kelvin-Voigt model of viscoelasticity within certain conditions can

fairly depict the hysteresis behaviour of VEDs [10]. The model comprises of displacement and velocity components represented by a linear spring placed in parallel to a linear viscous dashpot, respectively, as shown in Figure 1(b) [10].

Recently, Particle Impact Damper (PID) that use silicone rubber, Nitrile Butadiene Rubber etc., are gaining momentum that demonstrate enhanced stiffness and natural damping properties [12]. Owing to particle-particle, particle-wall friction and inelastic collision, the kinetic energy of the particle is dissipated, and thus, the vibration of vibration systems gets attenuated by particle damping devices [13], [14]. Out of various types of configurations of particle damper, piston-based particle damper converts mechanical energy of vibration to elastic energy as piston collide and press particles together. Piston-based particle dampers with and without glass and steel particles were tested under transient vibration by Bai et al. [15] revealed that energy dissipation was due to friction contact of particles while young's modulus has little effect on damping. However, density has a greater effect on overall damping performance.

A novel means of vibration attenuation using Vacuum Packed Particles (VPP) as energy dissipating material was proposed by Bartkowski et al. [14]. Three types of granular ball shaped grains of 3 mm diameters made up of polyethylene were tested under triangular constant loading function. A modified Bouc-Wen hysteresis model was fitted through parameter identification with experimental data that showed good agreement [14]. Toyouchi et al. [16] developed dual-chamber single rod type damper with elastomer particles to improve damping characteristics and damper force. A set of experiments were conducted on the damper with elastomer particles varying in diameters 3, 4 and 5 mm. Parametric studies were carried out in terms of Particle Packing Ratio (PPR), vibration frequency and material of particles of the damper, revealing that damping energy increases in the damper [16].

It has been realized that particle dampers utilizing silicone rubber particles need to be studied beyond their experimental characterization as a potential seismic response control damping device, which has not yet been explored. The reported research studies used a few specific PPRs of the silicone rubber particle and hardness value. An independent experimental investigation on particle damper by fitting the PPR value to the existing study set will expand the data set of similar studies. Further, the use of a lower hardness value for silicone rubber particles than in previous studies may further improve the damping characteristics of particle dampers. The present paper aims to develop a prototype passive energy-damping device filled with silicone rubber particles of hardness value 23 and PPR 0.67. The proposed damper was characterized to understand its hysteresis behaviour under cyclic excitations of varied frequencies and amplitudes. For an immediate comparison of the efficiency of the prototype Silicone Rubber Particle Packed Damper (SPPD), silicone rubber particles were removed from the cylinder converting the device to Air Damping Device (ADD). Later on, the efficacy of developed dampers in seismic response attenuation was studied by fitting the damper devices with three storey Benchmark building [17] at the ground storey only. The hysteresis behaviour of the dampers was studied. It was fitted well with the Kelvin-Voigt model, where two modal parameters, stiffness and damping co-efficient, were identified using the multivariable linear regression method. Seismic response parameters, peak displacement, acceleration, interstorey drift and damper force were evaluated. Performance Indices (PIs) related to interstorey drift ratio, level acceleration, base shear and control force were determined for strong and pulse-type seismic excitations.

## 2. Development of Prototype Silicone Rubber Particle Packed Damper

This section provides details of a prototype passive damping device developed for seismic response control application during the present study. It covers various parameters and aspects of design considered for the development of the device in the following two Subsections: Piston-based cylinder and elastomer damping material.

### 2.1. Piston-based Cylinder

A piston-based cylinder, typically employed in a variety of mechanical systems, was repurposed in the present study, firstly filled with ball shaped silicone rubber particles and secondly, without particles but filled with air to be used as seismic response control devices. It comprises a cylinder of 50 mm diameter and 2.7 mm thickness supported by a square accumulator of 63 mm × 63 mm dimensions with an air valve of diameter 8 mm at both ends of the cylinder. The cylinder with the accumulator is a single casting aluminum body with a screwing mechanism so the accumulator can be detached from the cylinder part. A piston has a 305 mm rod connected with a circular plate of 35 mm thickness and 20 mm diameter at one end and is made of stainless steel. Overall assembly of the cylinder with an end framing system are made airtight.

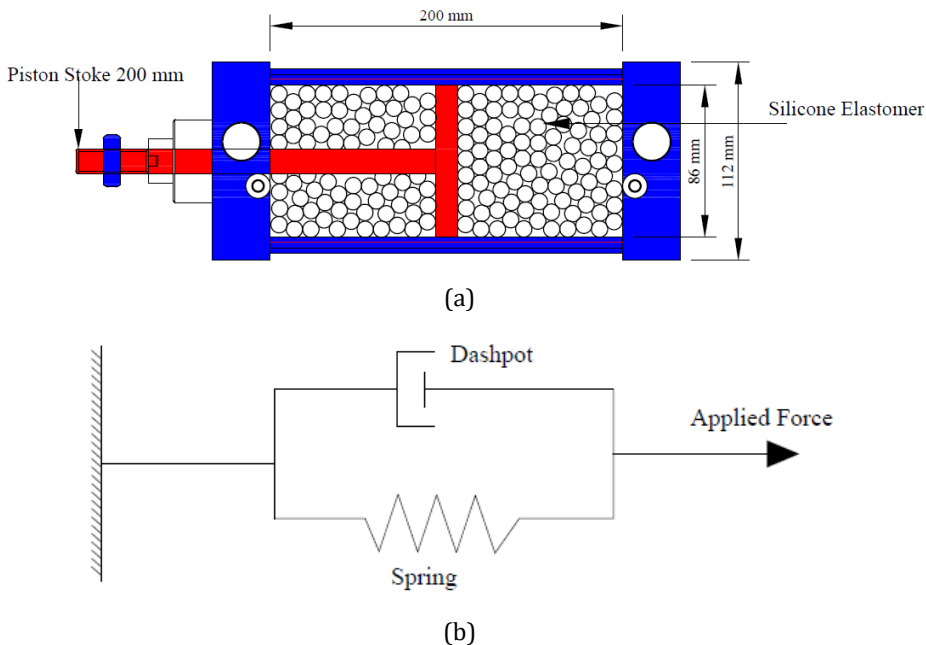


Fig. 1. Pistone based cylinder damper (a) schematic diagram (b) Kelvin-Voigt mathematical Model [10]

Thus, air can only travel in and out of the cylinder through the air valve provided at each end, which acts upon the pressure-suction principle. The piston-based cylinder packed with silicone rubber particles with the central position of the piston is shown schematically in Figure 1(a). The mathematical model of the damper described in section 5 is shown in Figure 1(b). The device has a maximum peak-to-peak displacement amplitude of  $\pm 20$  mm and is lightweight, having 2 kg weight with air and 2.2 kg weight with silicone rubber filled inside the cylinder. The device was developed with the aim of implementing it with the benchmark building problem [17] with negligible mass vis-à-vis storey mass. The device provides flexibility to carry out damping characteristic studies using a variety of



elastomers, nitrile butadiene rubber (NBR) and other materials under cyclic excitation in the laboratory, repetitively establishing the robustness of the piston-based cylinder device. The fabrication cost of a piston-based device is approximately INR 4725, and the same can be procured commercially at a reasonable price with respect to its fabrication cost. The device doesn't require any additional accessories and preparation before using as a passive damping device for cyclic testing.

### 2.2 Elastomer Damping Material

Rubber, a class of viscoelastic materials, is a composite material comprising of matrix, vulcanization system and anti-ageing system. There are two types of matrices, currently widely used, natural rubber and synthetic rubber. As compared to natural rubber, synthetic rubber can be more effectively produced with controllable chemical and physical properties. The Vulcanization process includes melting of rubber in the mold with high pressure to convert elastomer into elastic and dimensionally stable form and to yield temperature independent physical properties. Figure 2 shows silicone rubber produced through a compressed molding process in a ball shape with 5 mm diameter by heating followed by cooling to form the shape. At a time, 56 nos. of silicone rubber particles can be produced with the mold fabricated from stainless steel material. It also shows silicone rubber particles are consistent in dimension, weight and homogeneity. The weight of single silicone rubber particles was evaluated and reported in Table 1. The particle packing ratio, also referred as packing fraction [15] is defined as,

$$PPR = \frac{\text{Total mass of the Particles}}{\text{Volume of the space in the container} \times \text{Density of the Particle}} \quad (1)$$

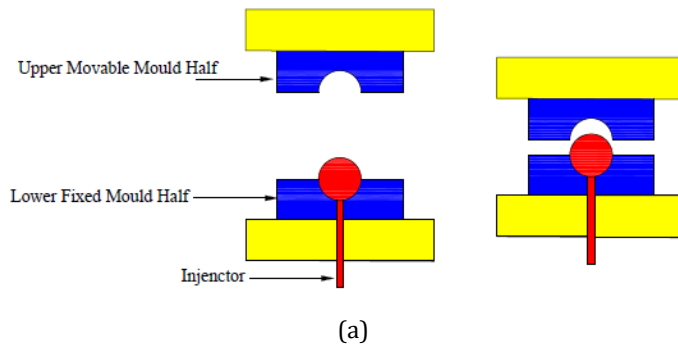


Fig. 2. Compression molding process of silicone rubber particle production and silicone rubber particles

The PPR evaluated using Equation (1) was 0.65, which is different than the PPR considered in other research [14], [15] and, thus, adds value to the existing set of research outcomes. Additionally, these research studies have used elastomer particle damping material with durometer hardness values  $\sim 60$ , classified as harder than the hardness value of 23, indicating soft material for shore A scale of durometer, measured for the produced silicone rubber particle for the study. This will improve the damping characteristic of silicone rubber particles as soft particles will undergo relatively larger deformation under sinusoidal input to the damping device. The silicone rubber particle with lower density, when used to fill space in a piston-based cylinder shall not greatly increase the mass of the SPPD.

Table 1. Physical and mechanical properties of silicone rubber particle

| Material Type      | Identification No. | Diameter (mm) | Density (g/cm <sup>3</sup> ) | Particle Packing Ratio | Durometer Hardness (Shore A) | Tensile Strength (MPa) |
|--------------------|--------------------|---------------|------------------------------|------------------------|------------------------------|------------------------|
| Silicone Elastomer | KE-520 -U          | 5             | 1.06                         | 0.67                   | 23                           | 11                     |

### 3. Characterization of Silicone Rubber Particle Packed Damper:

A detailed experimental program was developed to characterize SPPD in terms of hysteresis behaviour under varying frequencies and amplitude of the sinusoidal dynamic input. Characterization studies were conducted in two phases: firstly, SPPD, with a Particle Packing Ratio of 0.65, was tested and secondly, silicone particles were removed from the piston-based cylinder and the volume of the space in the cylinder was left with the atmospheric air transforming SPPD to ADD. A specialized experimental test set-up comprising a dynamic loading frame with a hydraulic piston controlled by an electric stepper motor capable of varying frequency was prepared at the workshop laboratory by the mechanical engineering department. The loading frame is capable of imposing cyclic loading to the attached specimen in the forcing frequency ranges between 0.5 Hz to 3.5 Hz through adjustable variable drive depending upon amplitude ranges from 5 mm to 40 mm. A specialized attachment was fabricated to connect the piston of SPPD with the hydraulic piston of the dynamic loading frame. An instrumental layout for the measurement of force and displacement was prepared. A dynamic force transducer of capacity 500 kg was installed between the reaction beam of the frame and the bottom of the piston-based cylinder having piston attachment assemblies. A piezoelectric based accelerometer of 10 g capacity was attached with a reciprocating plate connected to the hydraulic piston of the frame. Both force and acceleration sensors were attached to the data acquisition system-National Instruments (NI) for logging real-time force and acceleration data. The data acquisition system was connected to the computer system for compilation and post-processing of the data. Acceleration measurement in real-time was integrated twice to measure displacement input to the SPPD. A bandpass filter was used to remove noises from the measurement. A schematic diagram of the experimental set-up comprising of dynamic loading frame SPPD device, damper, force and acceleration sensors, data acquisition system and computer system is shown in Figure 3.

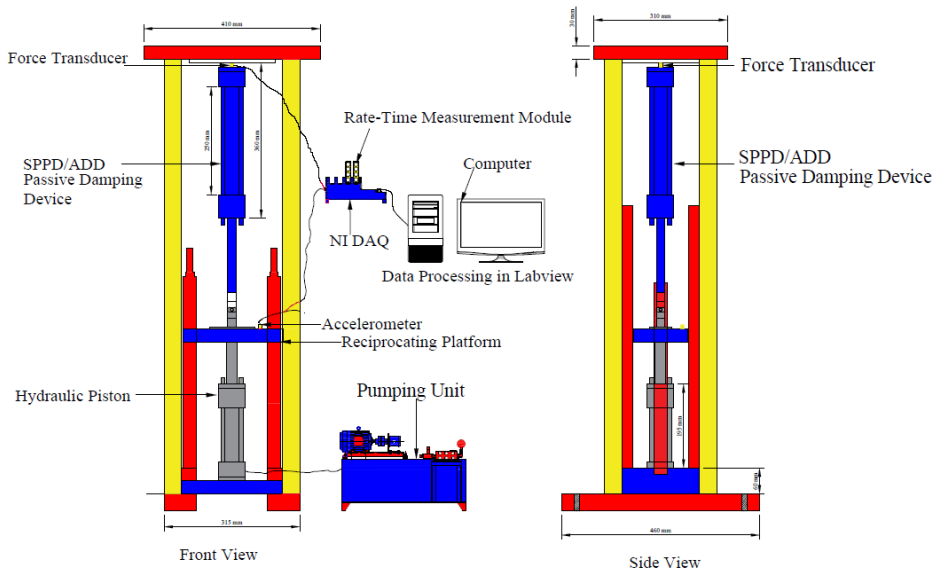


Fig. 3. Schematic diagram of experimental test set-up and instrumentation diagram for characterization of SPPD and ADD

Three sets of displacement inputs were applied to the SPPD and ADD through the hydraulic piston of the dynamic loading frame, as shown in Table 2.

Table 2. Details of sinusoidal displacement input used for characterization of passive damping devices

| Displacement Input | Amplitude (mm) | Forcing Frequency (Hz) |
|--------------------|----------------|------------------------|
| Sinusoidal         | ~ 5            | 0.5, 1, 2, 3, 3.5      |
|                    | ~ 10           | 0.5, 1, 1.5, 2         |
|                    | ~ 15           | 0.5, 1                 |

It is evident from Table 2 that as the amplitude of displacement input increases, the forcing frequency applied decreases, and thus experiments related to few frequencies for 10 mm and 20 mm amplitude could not be performed. It should be observed that the amplitude of displacement is controlled by a proxy sensor attached to the main columns of the loading frame. There are two proxy sensors for controlling peak-to-peak displacement amplitude with an adjustable knob to set the required displacement amplitude input. It was realized that achieving consistent displacement amplitude with different frequencies offers challenges as the proxy sensor controls peak amplitude when reciprocating the platform sensed by it while passing across it over its circular surface on covering some part of it to reverse the velocity of the platform. It was observed that with increasing frequency of the input displacement, the peak displacement amplitude set to a particular number was overshooted. Thus, despite center-to-center displacement between two proxy sensors, fixed displacement amplitude shows variation either higher or lower for different frequency inputs.

The prototype SPPD device was developed with the objective to implement it for seismic response control of building structures. Therefore, it was decided to study the prototype SPPD under earthquake predominant ground motions comprising of strong motion and pulse-type seismic excitation to assess the efficacy of damping characteristics of the SPPD.

Two strong ground motions, El Centro and Hachinohe excitation and two pulse-type ground motions, Kobe and Northridge ground motions, were selected from the seismic excitations data set and the frequency content of each seismic excitation was evaluated through Fast Fourier Transform (FFT) analysis. Table 3 reports peak amplitude, acceleration, velocity and displacement along with predominant frequencies of the seismic excitations. It is evident that predominant frequencies across all seismic excitation ranges between 0.5 Hz to 7 Hz. Therefore, forcing frequencies of sinusoidal displacement inputs were applied between 0.5 Hz to 3.5 Hz, where the upper value of forcing frequency was driven by the maximum amplitude of displacement that aimed to be applied by the dynamic loading frame. Since the characterization of SPPD and ADD should be carried out under varying frequencies and amplitudes of the input sinusoidal displacement loading, various levels of frequencies and amplitude were considered for the present study, as defined by Table 3. In the very recent past piston-type cylinder dampers with viscoelastic material were developed, tested and implemented for vibration response control [14], [16]. However, most of these dampers were found to exhibit no/weak damper force while piston is pulled from its mean position. Additionally, most of these damping devices were used for mechanical and aerospace systems and implementation of such devices for seismic response control of building structures is yet to be explored. The present study, thus, focuses on developing low cost, low maintenance, easily replaceable and effective passive damping devices, SPPD and ADD, to be implemented with benchmark building to establish their effectiveness in seismic response control.

Table 3. Details of seismic excitations with predominant frequencies

| Seismic Excitation | Peak Acceleration (g) | Peak Velocity (cm/sec) | Peak Displacement (cm) | Predominant Frequency (Hz) |
|--------------------|-----------------------|------------------------|------------------------|----------------------------|
| El Centro          | 0.32                  | 31.50                  | 14.13                  | 1.95, 2.68, 6.71           |
| Hachinohe          | 0.23                  | 25.63                  | 7.42                   | 1.04, 1.68, 2.15           |
| Kobe               | 0.34                  | 27.67                  | 9.69                   | 2.93, 4.76                 |
| Northridge         | 0.57                  | 51.820                 | 9.03                   | 6.10                       |

#### 4. Hysteresis behavior of SPPD and ADD

Passive damping devices, SPPD and ADD, when tested under varying forcing frequencies and amplitude sinusoidal excitation, demonstrated a tilted elliptical hysteresis loop from its mean position, indicating energy dissipation capabilities due to particle-particle and particle-wall interaction. The hysteresis behavior of SPPD and ADD were studied in terms of parameters, frequency, amplitude, displacement, velocity and damper force under sinusoidal input. Peak displacement of the SPPD and ADD were plotted for steady-state conditions. A peak velocity plot was also plotted to understand the effect of the damping characteristic. Overall hysteresis behavior of SPPD and ADD was studied under four categories: (i) effects of frequency dependency, (ii) effect of amplitude dependency, (iii) effect of velocity dependency, and (iv) frequency-dependent damper force.

##### 4.1 Effects of Frequency Dependency

Damper force produced by SPPD and ADD damping devices under three peak displacement amplitudes as indicated by Table 4 were derived for varying frequencies. Figure 4(a) to Figure 4(c) show the damper force vs displacement relationship of SPPD and ADD, respectively. It has been observed that, each damper device has energy dissipation capability as the damper force to displacement relationship yields a hysteresis loop. It is evident that damper force is a function of the forcing frequency of displacement input since damper force increases with an increase in forcing frequency. This is due to the elastic deformation of silicone rubber particles as the piston transfers the force through particle-

particle interaction. An increase in damper force for each device for a given amplitude of displacement function can be verified from Table 4 as well. Further, it can be observed that the hysteresis loop grows with an increase in forcing frequency under a given amplitude of displacement input, indicating an increase in energy dissipation and, thus, improvement in damping.

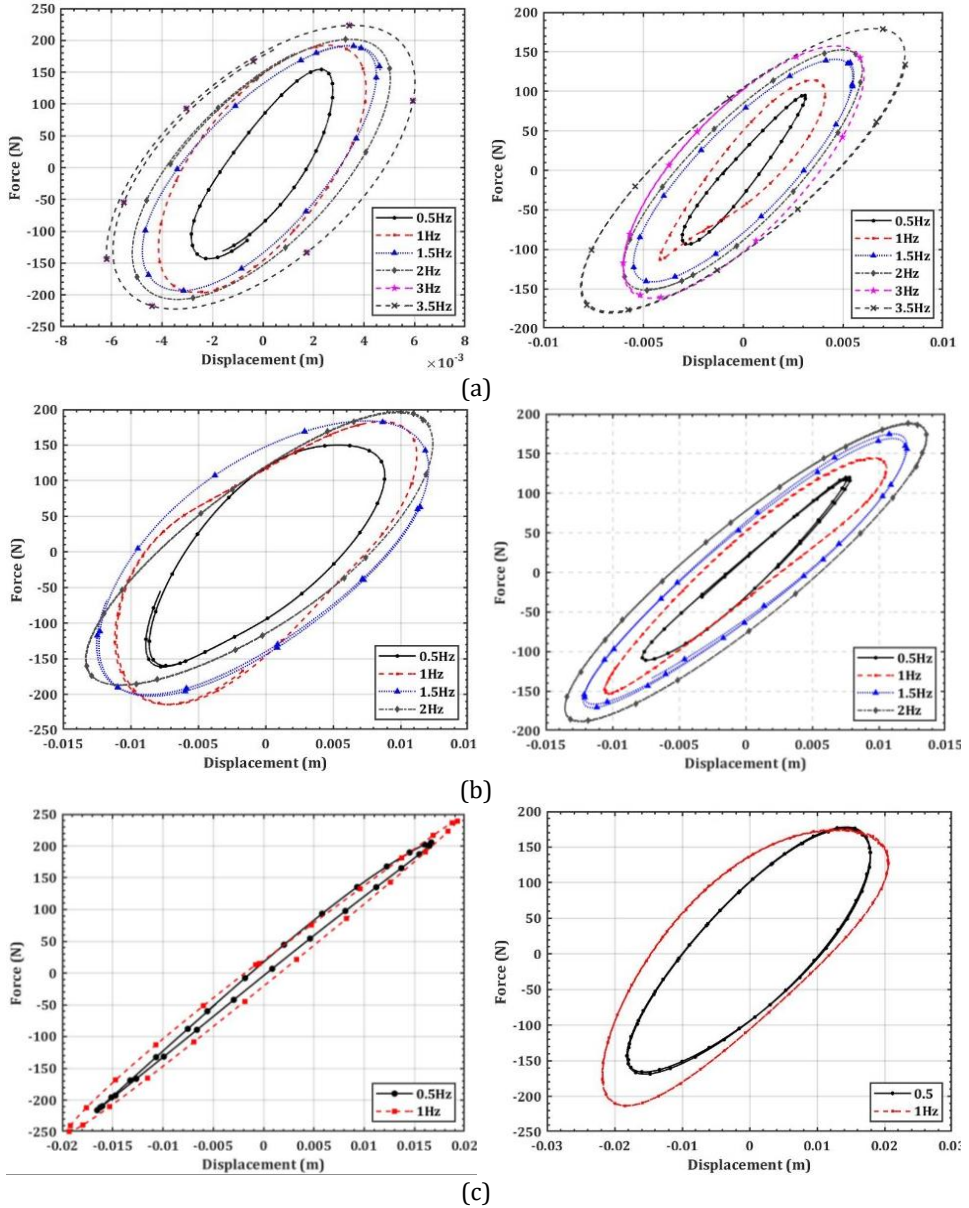


Fig. 4. Hysteresis behavior of SPPD and ADD under variable frequencies of sinusoidal input (a) with displacement amplitude of 5mm (b) with displacement amplitude of 10 mm and (c) with displacement amplitude of 20 mm

Comparing hysteresis loops of SPPD with ADD, it can be concluded that SPPD yields higher damper force and damping coefficient vis-à-vis ADD under each amplitude of displacement input. Hysteresis loops obtained for both SPPD and ADD show a force-displacement relation elliptical, very similar to those of viscous damping devices but with an inclination indicating that passive damping devices are dependent on displacement and velocity of the input motion. This attribute makes them more suitable for seismic response control of building structures as compared to the viscous dampers, which are only velocity dependent. On comparing hysteresis loops with those of reported results [16], it can be realized that level of force and energy dissipation capacities improve a lot.

#### 4.2 Effect of Amplitude Dependency

In order to understand the effect of displacement amplitude on the damping force of SPPD and ADD, damper forces are plotted for various amplitudes under forcing frequencies, 0.5 Hz to 1 Hz. Figure 5(a) and Figure 5(b) show the damper force-displacement relationship for two forcing frequencies, 0.5 Hz and 1 Hz only since high amplitude limits the forcing frequency of the dynamic frame. It is evident that damper force is a function of the amplitude of displacement amplitude input since damper force increases. It can also be realized that SPPD yields a damper higher force as compared to ADD. While increment in the damper force for ADD was quite evident with an increase in displacement amplitude of the sinusoidal input, SPPD yield a similar slight, lower damper force for displacement amplitude of ~10 mm of the input.

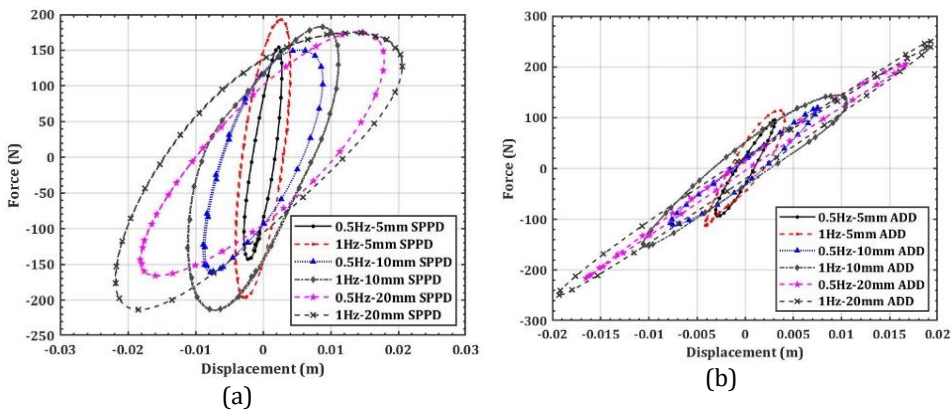


Fig. 5. Hysteresis behavior of passive damper devices under variable amplitudes of sinusoidal displacement input (a) SPPD with 0.5 Hz and 1 Hz frequencies (b) ADD with 0.5 Hz and 1 Hz frequencies

#### 4.3 Effect of Velocity Dependency Study

The velocity of the SPPD and ADD passive damping devices were plotted against the damping force, as shown in Figure 6(a) to Figure 6(c). It can be realized that stable hysteresis loops observed by the devices indicate that passive damper force is a function of the velocity since it increases with an increase in the velocity. Similar to the displacement damper force relationship, it can be seen that the width of the hysteresis loop increases with higher frequencies, which confirms the energy dissipation capabilities of dampers. It can be observed that with an increase in the forcing frequency of sinusoidal displacement input, the hysteresis loop starts deviating from its vertical portion at low velocity.

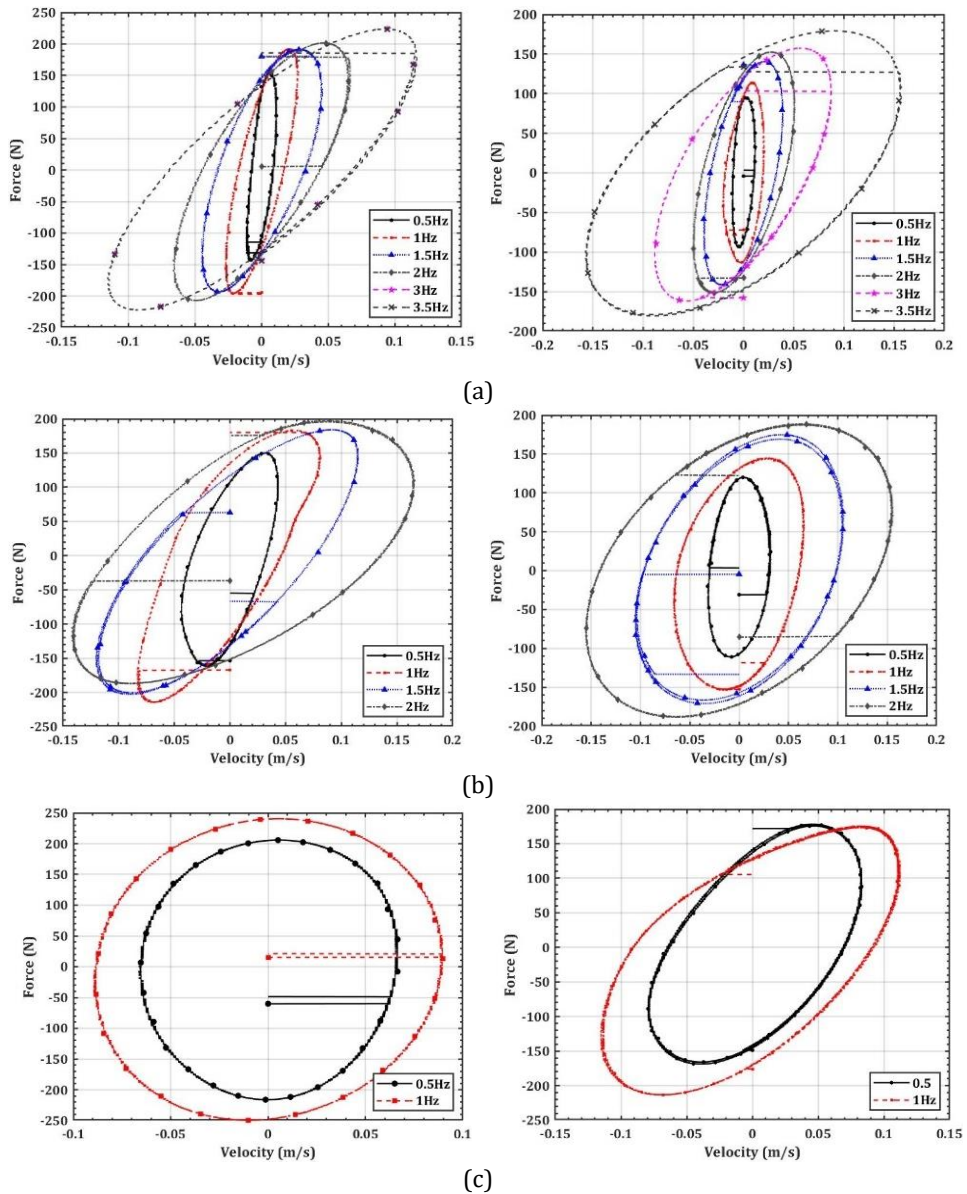


Fig. 6. Hysteresis behavior of SPPD and ADD to input velocity under variable frequencies of sinusoidal input (a) with displacement amplitude of 5mm (b) with displacement amplitude of 10 mm and (c) with displacement amplitude of 20 mm

#### 4.4 Combined Force to Frequency Relationship

In order to study the efficacy of both passive damping devices, SPPD and ADD in terms of their damper force generation capabilities, damper force is plotted against various forcing frequencies of the displacement input. Figure 7 presents a holistic view of damper force to forcing frequencies across all frequencies applied to SPPD and ADD. It is evident that SPPD yields higher damper force as compared to ADD across each forcing frequency and displacement amplitude except for ADD with  $\sim 20$  mm displacement amplitude. It is clearly evident that both damper devices were found effective in generating a reasonable amount

of damper force. However, SPPD outperforms ADD and thus, expected to effectively control seismic parameters of building filled with SPPD.

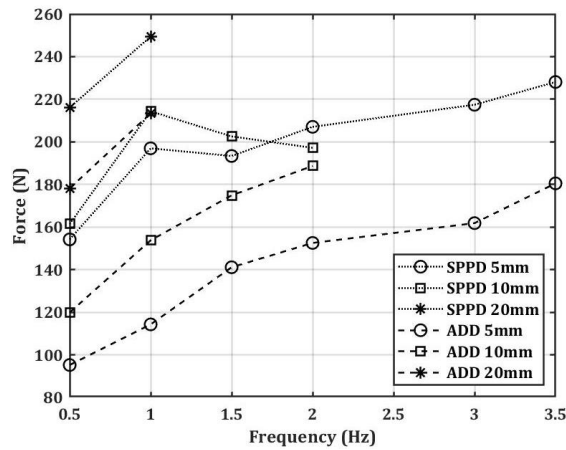


Fig. 7. Damper force produced by SPPD and ADD to various frequencies of sinusoidal displacement input

## 5. The Kelvin-Voigt Hysteresis Model

It was evident from Figure 4 to Figure 6 that the hysteresis behavior of both SPPD and ADD shows dependency on displacement and displacement rate (velocity) of the sinusoidal input. Therefore, the hysteresis loop obtained from a force-displacement and force-velocity relationship can be represented by an idealized physical model comprising of spring and dashpot elements, as shown in Figure 1(b) subjected to displacement input, producing hysteresis damper force. The said model is popularly known as the Kelvin-Voigt hysteresis model, which gets activated at low displacement and can be fitted well with a linear system and, thus, produces a simplified damper model. The physical model depicted by the physical model as shown in Figure 1(b) has a component of the damper force, the restoring force, proportional to the displacement and another component of the damper force, the damping force, proportional to the velocity and therefore, the damper has the ability to store energy in addition to dissipation energy [10].

Since the Kelvin-Voigt model is a linear combination of two independent variables, 'K' and 'C', the multivariable linear regression method [18] was used to evaluate the variable. A computer program on the MATLAB platform was written to fit experimental data of force with respect to 'K' and 'C'. Coefficient of determination,  $R^2$ , was determined for each set of experimental data of force-displacement, and velocity was measured for both SPPD and ADD devices. In order to prove the efficacy of predictive variables 'K' and 'C', the experimental force-displacement relationship was fitted with the force-displacement relationship. A comparison of experimental data of force and predicted plot of force shows very good agreement, which is evident from Figure 8 as well as from the value of  $R^2$ , which is tabulated in Table 4. Consistent high values of  $R^2$ , i.e. very close to 1 obtained for varying amplitude and forcing frequencies, confirm that the Kelvin-Voigt model with predicted values of variables K and C are well optimized. There is barely any difference visible to force-displacement hysteresis loops for experimentally measured data to that predicted through multivariable linear regression analysis as shown in representative Figure 8(a) for SPPD with 5 mm amplitude and few forcing frequencies and in Figure 8(b) for ADD. It is evident from Table 4 the stiffness values predicted for SPPD vis-a-vis ADD are higher for



a lower amplitude of sinusoidal function and are observed to be decreasing with increasing frequency and amplitude of displacement input.

However, the damping co-efficient, 'C', is found to increase with the amplitude and frequency of sinusoidal displacement inputs for SPPD air to ADD. It can be seen that, the hysteresis loop expands with an increase in amplitudes and forcing frequencies, indicating improvement in energy damping characteristics of the SPPD and ADD devices and thus, both energy dissipation damping devices are expected to be effective in controlling seismic response control of the building in which they are implemented.

Table 4. Damper force under various frequencies and amplitudes of sinusoidal input with stiffness and damping parameters of the Kelvin-Voigt Model

| Types of Damper | Forcing Frequency (Hz) | Maximum Force P <sub>max</sub> (N) | Minimum Force P <sub>min</sub> (N) | Stiffness K (N/m) | Damping Coefficient C (N.S/m) | Coefficient of Determination R <sup>2</sup> |
|-----------------|------------------------|------------------------------------|------------------------------------|-------------------|-------------------------------|---|
| 5 mm Amplitude  |                        |                                    |                                    |                   |                               |   |
| SPPD            | 0.5                    | 154.19                             | -143.04                            | 40309.41          | 8000.38                       | 0.9933                                      |
| ADD             |                        | 95.21                              | -93.51                             | 28833.80          | 2477.95                       | 0.9962                                      |
| SPPD            | 1                      | 192.16                             | -196.96                            | 29955.46          | 3046.04                       | 0.9966                                      |
| ADD             |                        | 114.28                             | -113.03                            | 21488.60          | 1977.56                       | 0.9998                                      |
| SPPD            | 1.5                    | 191.28                             | -193.36                            | 30126.35          | 5443.16                       | 0.9985                                      |
| ADD             |                        | 140.47                             | -141.10                            | 26186.95          | 2031.12                       | 0.9908                                      |
| SPPD            | 2                      | 201.59                             | -207.05                            | 27013.15          | 2297.59                       | 0.9985                                      |
| ADD             |                        | 152.53                             | -151.49                            | 20968.58          | 1724.36                       | 0.9993                                      |
| SPPD            | 3                      | 223.56                             | -221.99                            | 20638.51          | 1421.67                       | 0.9987                                      |
| ADD             |                        | 157.31                             | -161.83                            | 18031.05          | 666.13                        | 0.9995                                      |
| SPPD            | 3.5                    | 228.10                             | -225.41                            | 23210.95          | 1705.25                       | 0.9991                                      |
| ADD             |                        | 179.21                             | -180.50                            | 20144.90          | 1170.42                       | 0.9990                                      |
| 10 mm Amplitude |                        |                                    |                                    |                   |                               |   |
| SPPD            | 0.5                    | 150.07                             | -161.45                            | 13766.50          | 2446.54                       | 0.9938                                      |
| ADD             |                        | 119.92                             | -110.91                            | 14705.25          | 787.13                        | 0.9964                                      |
| SPPD            | 1                      | 183.06                             | -214.33                            | 10068.90          | 1240.59                       | 0.9984                                      |
| ADD             |                        | 144.76                             | -153.77                            | 13051.67          | 590.67                        | 0.9992                                      |
| SPPD            | 1.5                    | 183.96                             | -202.56                            | 11285.20          | 1740.72                       | 0.9900                                      |
| ADD             |                        | 174.87                             | -170.85                            | 13219.88          | 654.64                        | 0.9951                                      |
| SPPD            | 2                      | 197.18                             | -187.12                            | 11867.58          | 770.02                        | 0.9965                                      |
| ADD             |                        | 188.67                             | -188.51                            | 12651.02          | 498.91                        | 0.9998                                      |
| 20 mm Amplitude |                        |                                    |                                    |                   |                               |   |
| SPPD            | 0.5                    | 205.67                             | -216.08                            | 7848.79           | 1220.05                       | 0.9981                                      |
| ADD             |                        | 175.64                             | -165.92                            | 12821.50          | 148.61                        | 0.9985                                      |
| SPPD            | 1                      | 240.43                             | -249.44                            | 7076.47           | 1068.89                       | 0.9896                                      |
| ADD             |                        | 175.23                             | -213.38                            | 12795.54          | 245.67                        | 0.9993                                      |

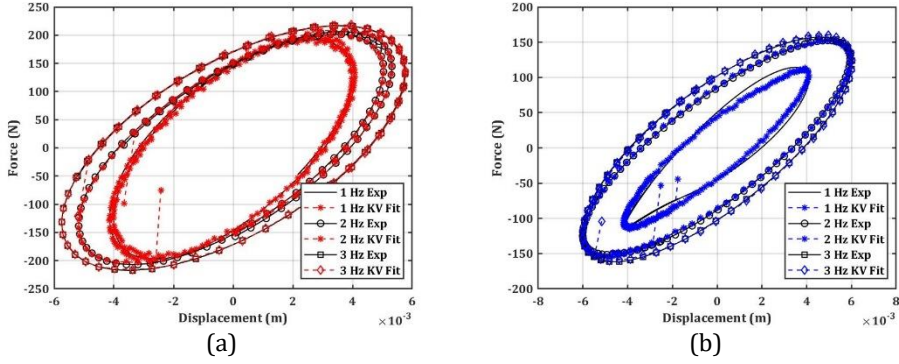


Figure 8: Validation of the Kelvin-Voigt model with experimental data of the force-displacement for sinusoidal displacement amplitude of 5 mm (a) SPPD (b) ADD

### 6. The Benchmark Building: Problem Formulation

The ASCE committee in 1997 developed a benchmark building problem to innovate various types of dampers for seismic response control and test them against set performance specifications. The present study considers the first generation three-storey benchmark building developed by Spencer et al. [19] as shown in Figure 9. The geometrical properties of the buildings were defined in terms of mass matrix,  $M$  and stiffness matrix,  $K$ . A Rayleigh damping, which is proportional to the mass and stiffness of the building, is defined as a damping matrix,  $C$ . The building is a laboratory based scaled model subjected to seismic excitation at the base. The dynamic equilibrium equation for the said building model can be defined as,

$$M \ddot{x}(t) + C \dot{x}(t) + K x(t) = -M L \ddot{x}_g(t) \tag{2}$$

where  $M$  is a mass matrix,  $C$  is a damping matrix,  $K$  is the stiffness matrix,  $L$  is the influence vector indicating force applied at each floor,  $x(t)$ ,  $\dot{x}(t)$  and  $\ddot{x}(t)$  are displacement, velocity and acceleration of the mass. The Mass, stiffness and damping matrices are defined by Dyke et al. as,

$$M = \begin{bmatrix} 98.3 & 0 & 0 \\ 0 & 98.3 & 0 \\ 0 & 0 & 98.3 \end{bmatrix} kg; \quad k = \begin{bmatrix} 12 & -6.84 & 0 \\ -6.84 & 13.7 & -6.84 \\ 0 & -6.84 & 6.84 \end{bmatrix} N/m; \tag{3}$$

$$C = \begin{bmatrix} 175 & -50 & 0 \\ -50 & 100 & -50 \\ 0 & -50 & 50 \end{bmatrix} Ns/m; \quad L = \begin{bmatrix} 1 \\ 1 \\ 1 \end{bmatrix} N/m; \tag{4}$$

$$K_d = \begin{bmatrix} 19430 & 0 & 0 \\ 0 & 0 & 0 \\ 0 & 0 & 0 \end{bmatrix} N/m; \quad C_d = \begin{bmatrix} 2533 & 0 & 0 \\ 0 & 0 & 0 \\ 0 & 0 & 0 \end{bmatrix} N.s/m; \tag{5}$$

The prototype passive, SPPD and ADD were placed at the ground storey of the benchmark building to control the seismic response of the building. The passive damping devices offered damper force as described by the Kelvin-Voigt model, and thus, the dynamic equilibrium equation stated by Equation (2) will be modified as,

$$M \ddot{x}(t) + C \dot{x}(t) + K x(t) + F_d(t) = -M L \ddot{x}_g(t) \tag{6}$$

Substituting Equation (2) into Equation (6), the dynamic equilibrium equation becomes,

$$M \ddot{x}(t) + (C + C_d) \dot{x}(t) + (K + K_d) x(t) + F_d(t) = -M L \ddot{x}_g(t) \tag{7}$$

It is evident from Equation (7) that passive SPPD and ADD improve the damping and stiffness characteristics of the modified benchmark building with the damper. The natural frequencies of the benchmark building model under free vibration were calculated as,  $\omega_{ni} = \{5.46, 15.81, 23.64\}$ , rad/sec. where  $i = 1, 2, 3$ . The modified natural frequencies of the modal building with damper at ground storey were found to be  $\omega_{ni} = \{5.52, 15.90, 23.67\}$ , rad/sec. Differential equations, representing modal benchmark buildings with and without passive damping devices; SPPD and ADD, represented through Equation (2) to Equation (7) were subjected to two types of seismic excitation; strong motion and pulse-type. Seismic excitation defined as strong motion are; El Centro excitation (1940, NS component, 3.42 m/s<sup>2</sup> PGA) and Hachinohe excitation (1968, 2.25 m/s<sup>2</sup> PGA), while pulse-type ground motion includes; Kobe excitation (1995, 8.18 m/s<sup>2</sup> PGA) and Northridge excitation (1994, 8.27 m/s<sup>2</sup> PGA).

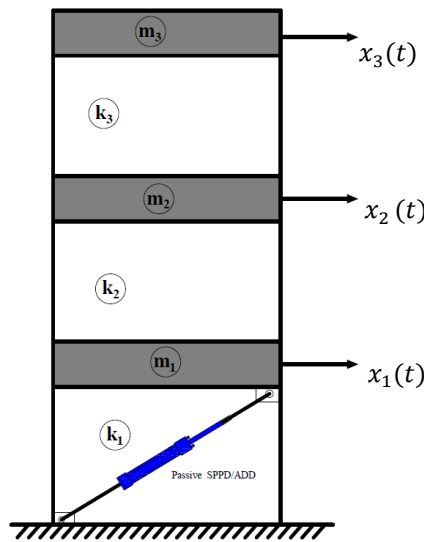


Fig. 9. schematic diagram of first-generation benchmark building filled with passive damping devices; SPPD/ADD

In order to evaluate the efficacy of the prototype passive damping devices, SPPD and ADD, seismic response parameters determined for controlled model building, i.e., model building fitted with SPPD or ADD at the ground storey, were compared with uncontrolled model buildings, i.e., model building without SPPD and ADD fitted to it. The evaluation was carried out through normalized Performance Indices as defined by Ohtori et al. [20], specifically, Peak Interstorey Ratio,  $J_1$ , Level Acceleration,  $J_2$ , Base Shear,  $J_3$  and Control Force  $J_{11}$ . Out of four performance indices considered three indices;  $J_1$ ,  $J_2$  and  $J_3$  is related to the building response while  $J_{11}$  is related to control device. Each of these performance indices are defined as,

$$J_1 = \max \left\{ \frac{\max_{t,i} |d_i(t)|}{\delta^{max}} \right\} \quad J_2 = \max \left\{ \frac{\max_{t,i} |\ddot{x}_{ai}(t)|}{\ddot{x}_{ai}^{max}} \right\} \tag{8}$$

$$J_3 = \max_t \left\{ \frac{\max |\sum_i m_i \ddot{x}_{ai}(t)|}{F_b^{\max}} \right\} \quad J_{11} = \max_{t,l} \left\{ \frac{\max |f_1(t)|}{W} \right\} \quad (9)$$

where  $d_i(t)$  is the interstorey drift of the above ground level,  $h_i$  is the height of the stories, and  $\delta_{\max}$  is the maximum uncontrolled interstorey drift given by  $\frac{|d_i(t)|}{h_i}$ ,  $\ddot{x}_{ai}(t)$  and  $\ddot{x}_a^{\max}$  are the absolute accelerations of  $i^{\text{th}}$  level for controlled and uncontrolled buildings, respectively.  $m_i$  is the seismic mass of the  $i^{\text{th}}$  level.  $F_b^{\max}$  is maximum uncontrolled base shear,  $f_1(t)$  is the force produced by dampers, and  $W$  is the seismic weight of the modal building.

### 7. Results and Discussion

A modal building fitted with passive damping devices, SPPD and ADD, represented by Figure 9, was mathematically modelled as a lumped-mass system and dynamic equilibrium equations defined by Equation (2) to Equation (7) were derived. A Rayleigh damping was assumed for modal building and nonlinear hysteresis behaviour, as characterized under cyclic loading, described in section 3, and was linearized through the linear Kelvin-Voigt model. A detailed computer program on the MATLAB platform was developed to evaluate the seismic response of the benchmark building subjected to strong motion and pulse-type seismic excitation.

Table 5: Validation of uncontrolled structural response with Dyke et al. and controlled structural response of benchmark building under El Centro seismic excitation

| Seismic Response Parameters           | Storey | Uncontrolled Response |                  | Controlled Response |                     |                   |
|---------------------------------------|--------|-----------------------|------------------|---------------------|---------------------|-------------------|
|                                       |        | Dyke et al.           | Present Study    | MR Damper Off Case  | Passive Dyke et al. | SPPD              |
| Peak Displacement (cm)                | 1      | 0.54                  | 0.55<br>(-0.02)  | 0.21<br>(-60.78)    | 0.31<br>(-43.64)    | 0.41<br>(-25.46)  |
|                                       | 2      | 0.82                  | 0.87<br>(6.00)   | 0.36<br>(-56.46)    | 0.52<br>(-40.23)    | 0.68<br>(-21.84)  |
|                                       | 3      | 0.96                  | 1.00<br>(4.00)   | 0.46<br>(-52.70)    | 0.65<br>(-38.10)    | 0.84<br>(-20.00)  |
| Peak Interstorey Drift (cm)           | 1      | 0.54                  | 0.55<br>(1.85)   | 0.21<br>(-60.78)    | 0.31<br>(-43.64)    | 0.41<br>(-25.46)  |
|                                       | 2      | 0.32                  | 0.34<br>(6.25)   | 0.15<br>(-52.04)    | 0.22<br>(-35.29)    | 0.28<br>(-17.65)  |
|                                       | 3      | 0.20                  | 0.19<br>(-5.26)  | 0.10<br>(-48.76)    | 0.13<br>(-31.58)    | 0.16<br>(-15.79)  |
| Peak Acceleration (m/s <sup>2</sup> ) | 1      | 8.56                  | 8.33<br>(-2.69)  | 4.20<br>(-50.93)    | 4.32<br>(-48.13)    | 5.43<br>(-34.78)  |
|                                       | 2      | 10.30                 | 10.21<br>(-0.87) | 4.80<br>(-53.40)    | 6.31<br>(-38.19)    | 8.47<br>(-17.03)  |
|                                       | 3      | 14.00                 | 13.44<br>(-4.00) | 7.17<br>(-48.79)    | 9.03<br>(-32.78)    | 11.21<br>(-16.54) |
| Damper Force (N)                      |        |                       |                  | 258.00              | 277.11              | 164.73            |

The numerical solution of Equation (6) was obtained through Newmark-beta numerical integration with the linear acceleration method. The solution was obtained for a time step of 12 seconds, ensuring stability and the accuracy of the numerical solution. Seismic response parameters, peak displacement, peak interstorey drift, peak acceleration and

peak damper force was evaluated for controlled building. The efficacy of passive damping devices, SPPD and ADD considers as passive control devices were evaluated through seismic response performance indices  $J_1$ ,  $J_2$ ,  $J_3$  an  $J_{11}$ . Uncontrolled model building under strong motion (El Centro, Hachinohe) and pulse type (Kobe, Northridge) seismic excitation was solved first, and seismic response parameter peak displacement, peak interstorey drift, and peak acceleration were determined. The results were validated by comparing them with results represented by Dyke et al. [17] for El Centro seismic excitation. Table 5 summarize seismic response parameters of uncontrolled model building by Dyke et al. and simulation results from the present study with percentage difference provided in the parenthesis. It is evident that results from the present study show close agreement with results for El Centro excitation of Dyke et al. and thus validate numerical simulation carried out through a computer program.

Seismic response parameters of controlled benchmark buildings fitted with SPPD and ADD obtained under seismic excitation are represented in Table 6 with percentage difference in the parenthesis w.r.to uncontrolled response. It is evident that passive damping device, SPPD and ADD, both effectively reduces seismic response parameters. It can be seen that a controlled building with SPPD yields a substantial reduction in each seismic parameter, while it is moderate for ADD-fitted model building. Peak displacement of the roof floor is found to be reduced by 38.10% and 20% controlled building with SPPD and ADD, respectively. Similarly, peak acceleration of the roof storey yields a reduction of 32.88% and 16.54%, respectively. Peak interstorey drift at the first storey shows a reduction of 43.64% and 25.75%, respectively. It can be proved that a double side silicone rubber filled piston-based cylinder, SPPD, device yields better seismic response performance vis-à-vis air filled piston-based cylinder, ADD. This is attributed to elastic deformability and low-hardness silicone rubber. SPPD device can produce damper force of the order 277.11 N which is 68.22% higher as compared to ADD.

Figure 10(a) to Figure 10(d) show the peak displacement response of uncontrolled and controlled buildings for each storey under all seismic excitations considered in the study. It can be observed that the SPPD device yields a substantial reduction in peak displacement at every storey for each seismic excitation. While displacement response shows substantial (~36%~59%) reduction for El Centro, Hachinohe and Kobe seismic excitations, it is moderate (~13% to 20%) for Northridge seismic excitations since it is of relatively high PGA and consists of a shallow band of earthquake frequencies. It can further be realized that the SPPD device outperformed ADD in terms of peak displacement seismic response performance. Maximum reduction in peak displacement response (~58%) was obtained by a controlled building filled with SPPD and ADD under strong motion type Hachinohe seismic excitation.

Peak interstorey drift for the uncontrolled and controlled model building was determined under each seismic excitation and is plotted through Figure 11(a) to Figure 11(d). It is evident that peak interstorey drift at the first floor shows a substantial reduction under each seismic excitation since SPPD and ADD were provided on the ground floor only. It is apparent that the reduction in peak interstorey drift in upper stories lowered as compared to the first storey. Peak interstorey drift of controlled building with SPPD, at first storey, reduced by 43.64% and 59.68% under El Centro and Hachinohe seismic excitations, respectively and by 40.82% and 20.37% under Kobe and Northridge seismic excitation, respectively. Controlled building with ADD yields a reduction in peak interstorey drift by 25.46%, and 40.32% under El Centro and Hachinohe seismic excitation, respectively and by 21.77% and 11.11% under Kobe and Northridge seismic excitations. It can be realized that the trend of reduction in this seismic response parameter for different seismic excitations storey-wise is very similar to these peak displacements for different seismic excitations.

Table 6. Uncontrolled and controlled structural responses of the benchmark building under Hachinohe, Kobe, and Northridge seismic excitations

| Seismic Response Parameter            | Storey | Controlled Response  |               |               |       |                 |                |       |                |                       |                |                |      |
|---------------------------------------|--------|----------------------|---------------|---------------|-------|-----------------|----------------|-------|----------------|-----------------------|----------------|----------------|------|
|                                       |        | Hachinohe Excitation |               |               |       | Kobe Excitation |                |       |                | Northridge Excitation |                |                |      |
|                                       |        | Uncontrolled         | SPPD          | ADD           | SPPD  | Uncontrolled    | SPPD           | ADD   | SPPD           | Uncontrolled          | SPPD           | ADD            | SPPD |
| Peak Displacement (cm)                | 1      | 0.62                 | 0.25 (-59.68) | 0.37 (-40.32) | 1.47  | 0.87 (-40.82)   | 1.15 (-21.77)  | 0.54  | 0.87 (-40.82)  | 1.15 (-21.77)         | 0.43 (-20.37)  | 0.48 (-11.11)  |      |
|                                       | 2      | 0.99                 | 0.40 (-59.60) | 0.59 (-40.40) | 2.25  | 1.42 (-36.89)   | 1.76 (-21.78)  | 0.74  | 1.42 (-36.89)  | 1.76 (-21.78)         | 0.59 (-20.27)  | 0.65 (-12.16)  |      |
|                                       | 3      | 1.19                 | 0.49 (-58.82) | 0.71 (-40.34) | 2.72  | 1.74 (-36.03)   | 2.09 (-23.16)  | 0.79  | 1.74 (-36.03)  | 2.09 (-23.16)         | 0.68 (-13.92)  | 0.72 (-8.86)   |      |
| Peak Interstorey Drift (cm)           | 1      | 0.62                 | 0.25 (-59.68) | 0.37 (-40.32) | 1.47  | 0.87 (-40.87)   | 1.15 (-21.77)  | 0.54  | 0.87 (-40.87)  | 1.15 (-21.77)         | 0.43 (-20.37)  | 0.48 (-11.11)  |      |
|                                       | 2      | 0.36                 | 0.15 (-58.33) | 0.22 (-38.89) | 0.83  | 0.55 (-33.73)   | 0.65 (-21.69)  | 0.28  | 0.55 (-33.73)  | 0.65 (-21.69)         | 0.24 (-14.29)  | 0.26 (-7.14)   |      |
|                                       | 3      | 0.20                 | 0.08 (-60.00) | 0.12 (-40.00) | 0.520 | 0.31 (-40.39)   | 0.41 (-21.15)  | 0.22  | 0.31 (-40.39)  | 0.41 (-21.15)         | 0.18 (-18.18)  | 0.19 (-13.64)  |      |
| Peak Acceleration (m/s <sup>2</sup> ) | 1      | 7.83                 | 3.18 (-59.32) | 4.70 (-39.96) | 27.20 | 15.14 (-44.32)  | 21.35 (-21.51) | 15.48 | 15.14 (-44.32) | 21.35 (-21.51)        | 12.04 (-22.23) | 13.79 (-10.94) |      |
|                                       | 2      | 11.58                | 4.82 (-58.30) | 7.11 (-38.51) | 30.72 | 17.02 (-44.57)  | 22.52 (-26.69) | 12.01 | 17.02 (-44.57) | 22.52 (-26.69)        | 10.06 (-16.20) | 11.21 (-6.67)  |      |
|                                       | 3      | 13.91                | 5.81 (-58.20) | 8.40 (-39.61) | 35.91 | 21.79 (-39.34)  | 28.63 (-20.29) | 14.97 | 21.79 (-39.34) | 28.63 (-20.29)        | 12.65 (-15.49) | 13.14 (-12.22) |      |
| Peak Damper Force (N)                 |        |                      |               |               |       |                 |                |       | 739.87         | 497.00                | 328.13         | 182.35         |      |

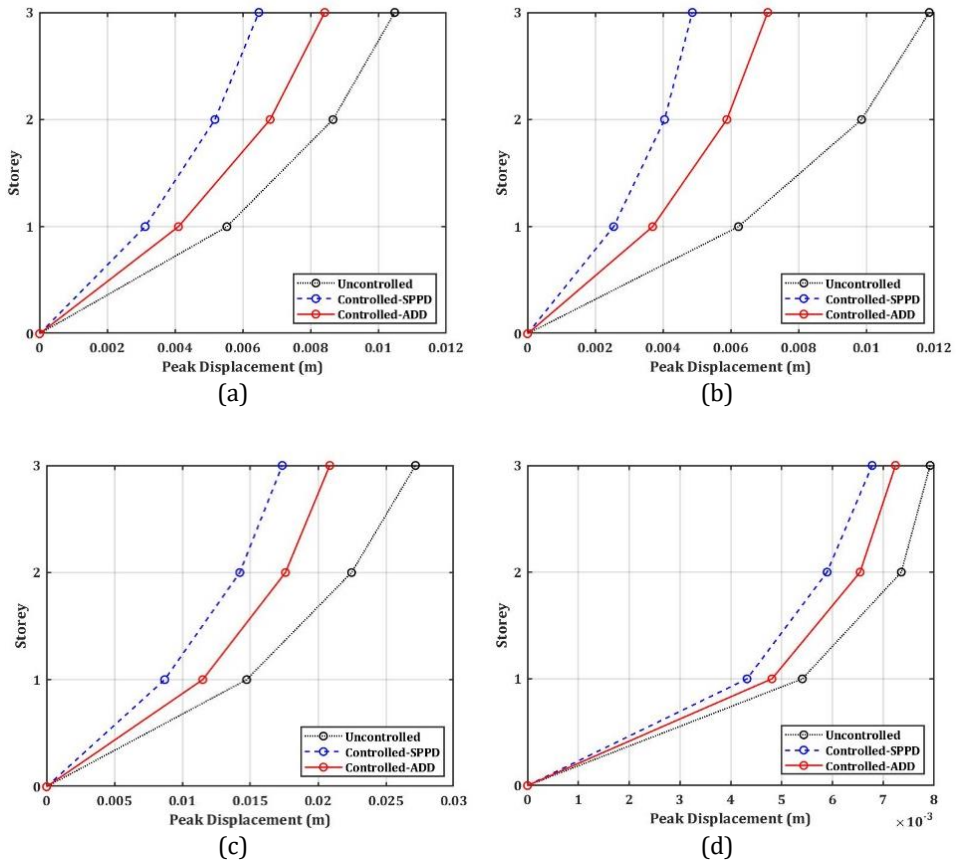


Fig. 10. Peak displacement structural response of uncontrolled and controlled benchmark buildings with SPPD and ADD under seismic excitation (a) El Centro (b) Hachinohe (c) Kobe (d) Northridge

The peak acceleration response of controlled buildings with SPPD and ADD follows similar results in terms of storey-wise reduction as that of peak displacement and peak interstorey drift response parameter. Figure 12(a) to Figure 12(d) demonstrate the storey-wise peak acceleration response of uncontrolled and controlled modelled buildings with passive damping devices. The controlled building attached with SPPD yields a reduction in peak acceleration at each storey under both strong motion and pulse-type seismic excitations. Peak acceleration at the roof storey of the controlled building yields a reduction of 48.13% and 59.32% for El Centro and Hachinohe seismic excitation, respectively. The same reduces by 44.32% and 22.23% for Kobe and Northridge seismic excitation, respectively. On the other hand, ADD fitted with controlled buildings shows a reduction in peak roof acceleration of 34.78%, 39.78%, 21.51% and 10.94% for El Centro, Hachinohe, Kobe and Northridge seismic excitation, respectively. Seismic response parameters, peak displacement, peak interstorey drift, peak acceleration along with peak damper force of SPPD device and ADD of uncontrolled and controlled buildings are reported in Table 6 for all seismic excitations, except El Centro seismic excitation, which is available in Table 5.

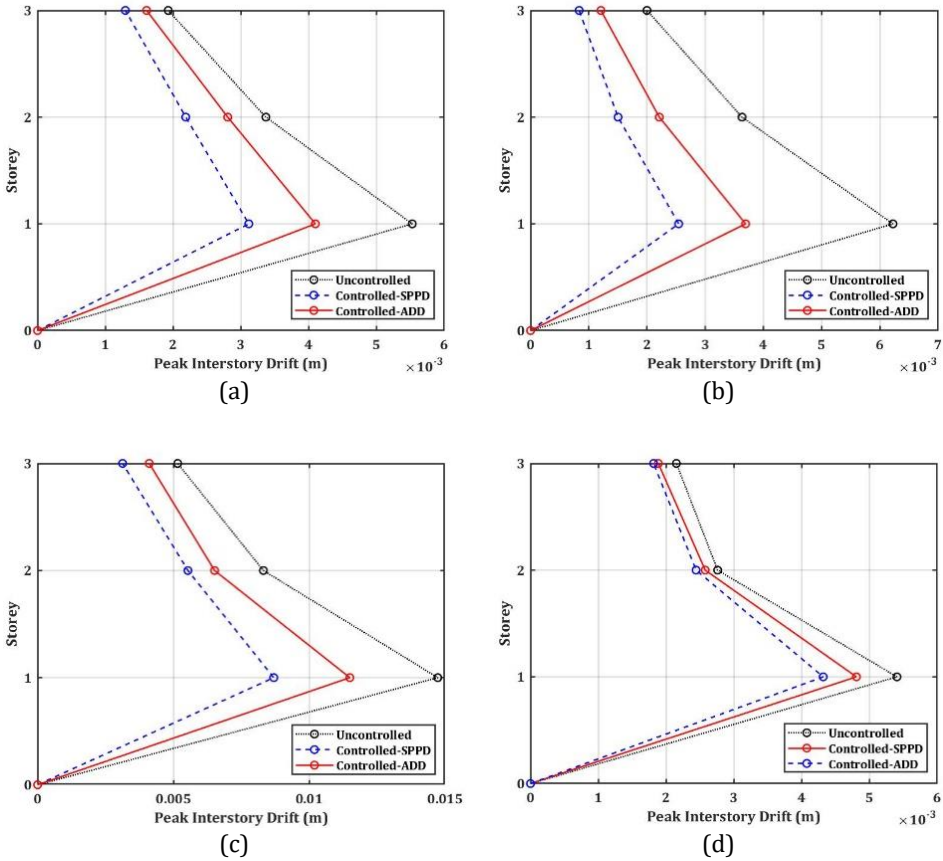


Fig. 11. Peak interstorey structural response of uncontrolled and controlled benchmark buildings with SPPD and ADD under seismic excitation (a) El Centro (b) Hachinohe (c) Kobe (d) Northridge

It is evident from Table 6 that SPPD offers a higher amount of damper force as compared to ADD and, thus, performs better in reducing seismic response parameters. The SPPD warrants a reasonably small amount of damper force under all seismic excitation, except Kobe excitation, where the required damper force is relatively higher. ADD could generate lower damper force vis-à-vis SPPD and, thus, becomes relatively less effective in controlling seismic response parameters. It should be noted that the force generated by SPPD of the present study yields a damper force of the same order or higher when compared with another dual-chamber single-rod-type damper with identical PPR but with higher hardness of silicone rubber [16] which produces force only on the compression side. The efficacy of passive damping devices, SPPD, and ADD, in improving seismic response control of benchmark building has been proved through performance indices defined by Equation (8) and Equation (9) as defined by Ohtori et al. Out of the total performance indices defined [20], only four important PIs most relevant to passive damping devices considered are Peak Interstorey Ratio  $J_1$ , Level Acceleration,  $J_2$ , Base Shear,  $J_3$  and Control Force,  $J_{11}$ . Table 7 summarizes numerical values for PIs  $J_1$ ,  $J_2$ ,  $J_3$  and  $J_{11}$  under all seismic excitations of the study. It can be observed from the table that both damping devices show good seismic control in terms of parameters represented by PIs as each PIS value < 1.



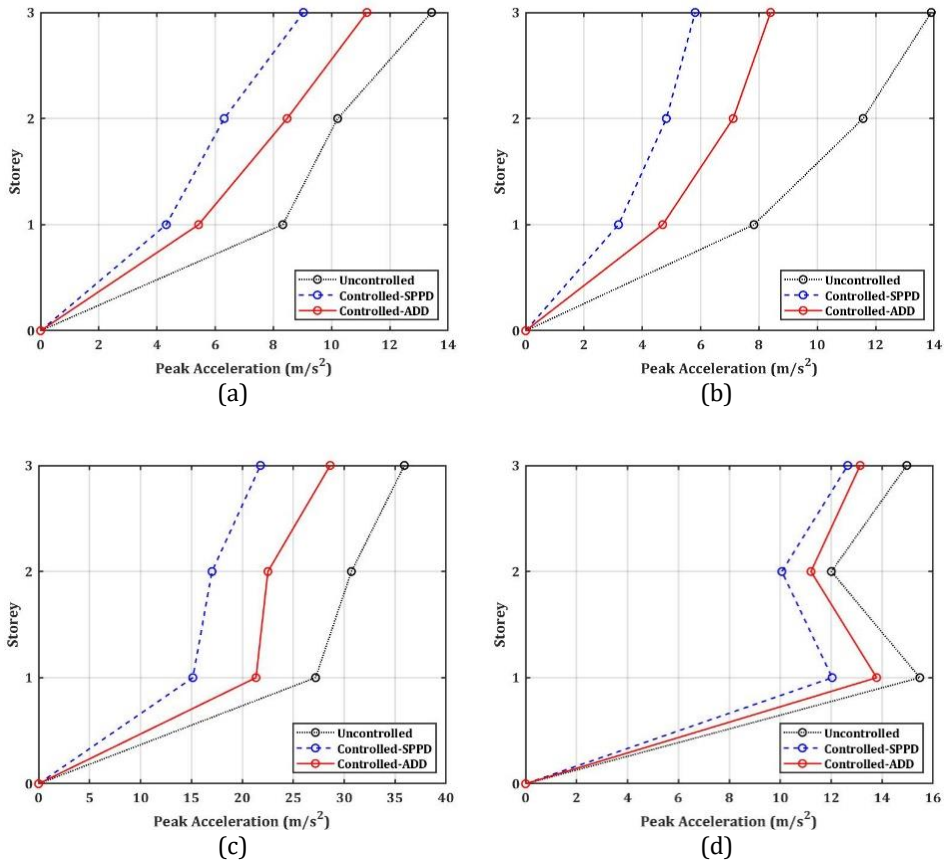


Fig. 12. Peak acceleration structural response of uncontrolled and controlled benchmark buildings with SPPD and ADD under seismic excitation (a) El Centro (b) Hachinohe (c) Kobe (d) Northridge

The lower value of  $PI-J_1$  reveals that the peak interstorey drift of the benchmark building gets better controlled by both SPPD and ADD passive devices. However, the relatively higher value of  $PI-J_2$  indicate that controlling peak acceleration of benchmark buildings under Northridge seismic excitation is a challenge due to the high PGA and low duration of the earthquake. Base shear  $PI-J_3$  depicts a similar understanding as lateral load acting on the benchmark building is higher with respect to weight, thus leading to a higher  $J_3$  value. The lower value of  $PIs J_1, J_2$  and  $J_3$  for SPPD as compared to ADD establishes better efficiency of the former over the latter. The same can be reflected in  $PI-J_{11}$ , where values are higher for SPPD vis-à-vis ADD. The relatively lower value of  $PI-J_{11}$  for each passive damping device; SPPD and ADD indicate that effective seismic control of benchmark building is achieved with a very low value of the damper fore, which means a handy, low-weight prototype damping device is enough for the seismic control. Peak seismic response parameters, peak displacement, peak interstorey drift, peak acceleration and peak damper force reported in Table 6 and performance indices as shown in Table 7 established well that controlled buildings filled with both passive damping devices, SPPD and ADD perform well vis-à-vis uncontrolled building. A time history response of controlled benchmark building under all seismic excitation considered in the study are plotted in Figure 13 and Figure 14.

Table 7. Seismic response Performance Indices for controlled benchmark building under seismic excitations

| Seismic Excitation | Damper Type | Performance Indices |                |                |                 | Peak Damper Force (N) |
|--------------------|-------------|---------------------|----------------|----------------|-----------------|-----------------------|
|                    |             | J <sub>1</sub>      | J <sub>2</sub> | J <sub>3</sub> | J <sub>11</sub> |                       |
| El Centro          | ADD         | 0.4692              | 0.8346         | 0.7686         | 0.0569          | 164.733               |
|                    | SPPD        | 0.3568              | 0.6722         | 0.5956         | 0.0958          | 277.107               |
| Hachinohe          | ADD         | 0.3755              | 0.6149         | 0.6071         | 0.0507          | 146.793               |
|                    | SPPD        | 0.2585              | 0.4179         | 0.415          | 0.0738          | 213.423               |
| Kobe               | ADD         | 0.4939              | 0.7971         | 0.8207         | 0.1718          | 497.003               |
|                    | SPPD        | 0.3735              | 0.6066         | 0.5998         | 0.2557          | 739.874               |
| Northridge         | ADD         | 0.5628              | 0.9333         | 0.9117         | 0.0630          | 182.351               |
|                    | SPPD        | 0.5055              | 0.8451         | 0.8109         | 0.1134          | 328.132               |

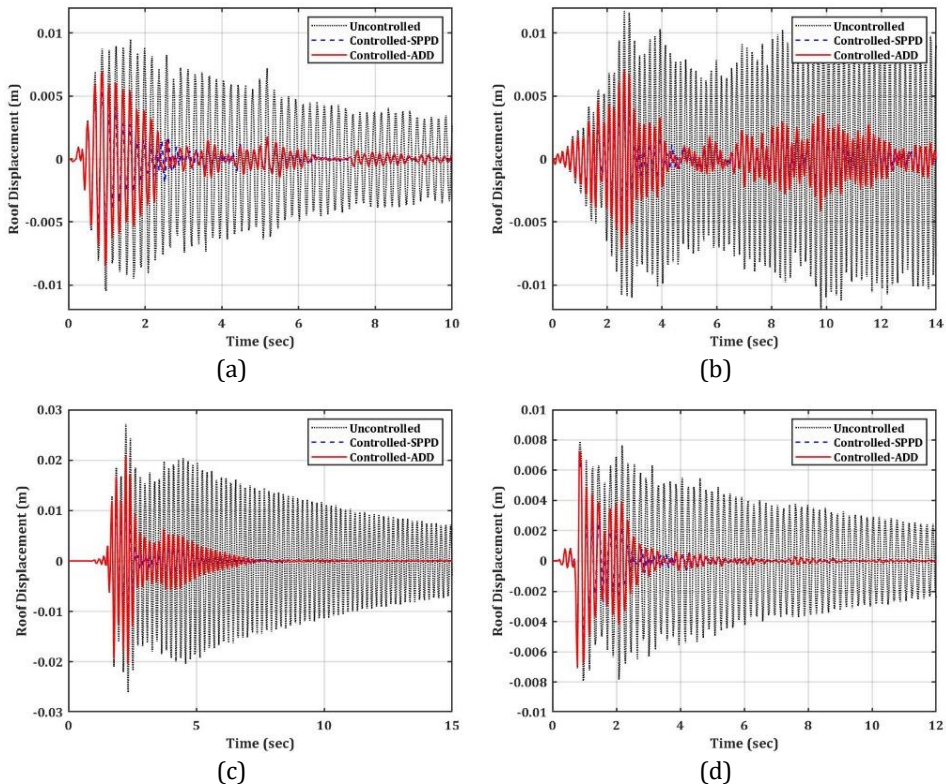


Fig. 13. Roof displacement time history response of uncontrolled and controlled benchmark building under seismic excitation (a) El Centro (b) Hachinohe (c) Kobe (d) Northridge

However, this quantity of controlled benchmark buildings should be plotted with respect to real-time to ensure that passive damping produces the damper force but also remains stable through the presence of seismic excitation. It can be seen that controlled benchmark

buildings with SPPD and ADD yield good displacement control under strong motion and pulse-type seismic excitation throughout the time span as compared to uncontrolled displacement response. The Peak roof displacement of uncontrolled response occurs at 0.96, 9.8, 2.24 and 0.96 sec for El Centro, Hachinohe, Kobe and Northridge seismic excitation, respectively, while the same occurs at 0.96, 2.52, 1.78 and 0.84 sec for controlled response for SPPD. It is evident from Figure 13(a) to Figure 13(d) that the controlled building shows much reduced displacement (almost stopped vibrating) after 7 sec under pulse-type seismic excitation. However, through nicely controlled, displacement of controlled benchmark building sustained under strong motion type seismic excitation, especially, Hachinohe seismic excitation. A similar trend of roof acceleration time history response was achieved for controlled benchmark building under all seismic excitations, as reported in Figure 14(a) to Figure 14(d). Peak roof acceleration of uncontrolled response occurs at 0.98, 9.8, 2.4 and 1.06 sec for El Centro, Hachinohe, Kobe and Northridge seismic excitation, respectively, while the same occurs at 0.96, 2.50, 2.24 and 0.84 sec for controlled response for SPPD. It is evident that both SPPD and ADD passive damping devices are effective in controlling roof acceleration of controlled buildings as compared to uncontrolled buildings under each seismic excitation considered for the study.

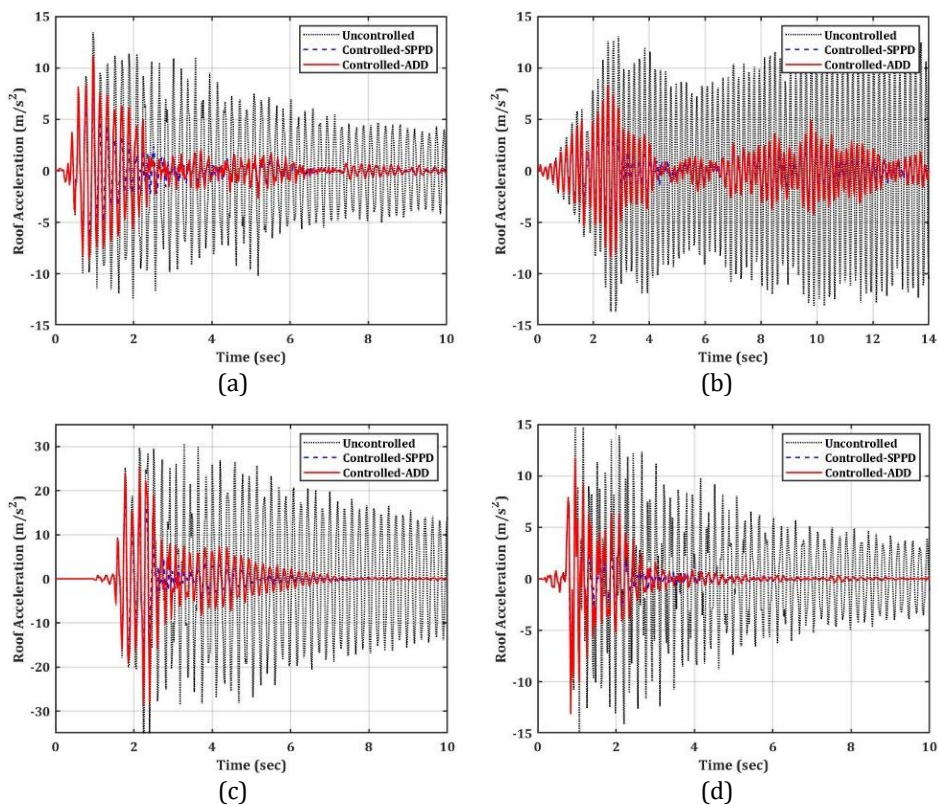


Fig. 14. Roof Acceleration Time History Response of Controlled Model Building to Seismic Excitation (a) El Centro (b) Hachinohe (c) Kobe (d) Northridge

## 8. Conclusions

Prototype passive damping devices; SPPD, ADD were developed and characterized under varied amplitude and frequency of sinusoidal displacement inputs. Both devices

demonstrate a stable hysteresis loop of elliptical shape, ensuring the presence of viscoelastic properties. Hysteresis behaviour was modelled using the Kelvin-Voigt model. SPPD and ADD were fitted at the ground storey of the benchmark building and were subjected to strong ground motion and pulse-type seismic excitations. Seismic response parameters, peak displacement, peak interstorey drift, peak acceleration and peak damper force of controlled benchmark building was evaluated. The efficacy of passive damping devices was established through PIs;  $J_1$ ,  $J_2$ ,  $J_3$  and  $J_{11}$ . Time history response of roof displacement and roof acceleration were plotted over entire seismic events considered for the study.

Major outcomes derived from the present study are summarized as follows.

- Characterization of SPPD and ADD under sinusoidal input with varied amplitude and frequency exhibits stable hysteresis behaviour, ensuring good damping dissipation characteristics over wide frequencies.
- Parameter identification of the Kelvin-Voigt model by a multivariable linear regression approach yields very good agreement with experimental data of hysteresis curves for SPPD and ADD.
- The SPPD outperforms ADD by yielding a substantial reduction (> 31%) in peak seismic response parameters of the benchmark building when fitted at the ground storey under strong motion and pulse-type seismic excitations. However, under Northridge (pulse-type) seismic excitation the reduction is moderate (>13%).
- The PIs;  $J_1$ ,  $J_2$ ,  $J_3$  and  $J_{11}$  evaluated for controlled benchmark building establish the efficacy of the SPPD. Though relatively higher than the SPPD, ADD also yields good controlled PIs except  $J_{11}$ , which yields a lower value due to the relatively lower damper force produced.
- The Time history response of a controlled benchmark building fitted with SPPD and ADD shows a consistent reduction of roof displacement and roof acceleration over entire seismic events, demonstrating the effectiveness and stability of the damping devices.
- The damper force produced by SPPD and ADD ranges from ~150 N to ~739 N under various seismic excitations, establishing its potential for full-scale implementation.

Seismic response parameters were evaluated for the benchmark building fitted with the SPPD with a particular value of the PPR. Effective seismic response control of the benchmark building with different PPR values for the SPPD using the same or different hardness values of silicone rubber particles may be explored. The proposed passive damping devices, SPPD and ADD may be scaled-up for full-scale implementation.

## **Acknowledgement**

The authors deeply acknowledge the financial assistance received from Nirma University under the minor Research Project for the academic year 2022-2023 and 2023-2024 to conduct the present research work.

## **References**

- [1] World Health Organization. Resilient reconstruction: 20 years after Gujarat earthquake [Internet]. 2021 [Accessed January 26, 2021].
- [2] Belleri A, Brunesi E, Nascimbene R, Pagani M, Riva P. Seismic performance of precast industrial facilities following major earthquakes in the Italian territory. *J Perform Constr Facil.* 2015;29(5):1-10. [https://doi.org/10.1061/\(ASCE\)CF.1943-5509.0000617](https://doi.org/10.1061/(ASCE)CF.1943-5509.0000617)

- [3] Nascimbene R. Investigation of seismic damage to existing buildings by using remotely observed images. *Eng Fail Anal.* 2024;161(April):108282. <https://doi.org/10.1016/j.engfailanal.2024.108282>
- [4] Kaushik HB, Dasgupta K. Assessment of seismic vulnerability of structures in Sikkim, India, based on damage observation during two recent earthquakes. *J Perform Constr Facil.* 2013;27(6):697-720. [https://doi.org/10.1061/\(ASCE\)CF.1943-5509.0000380](https://doi.org/10.1061/(ASCE)CF.1943-5509.0000380)
- [5] Zhang Y, Fung JF, Johnson KJ, Sattar S. Review of seismic risk mitigation policies in earthquake-prone countries: lessons for earthquake resilience in the United States. *J Earthq Eng.* 2022;26(12):6208-6235. <https://doi.org/10.1080/13632469.2021.1911889>
- [6] Jain SK. Earthquake safety in India: achievements, challenges and opportunities. *Bull Earthq Eng.* 2016;14(5):1337-1436. <https://doi.org/10.1007/s10518-016-9870-2>
- [7] Housner GW, Bergman LA, Caughey TK, Chassiakos AG, Claus RO, Masri SF, Skelton RE, Soong TT, Spencer BF, Yao JTP. Structural control: past, present, and future. *J Eng Mech.* 1997;123:897-971. [https://doi.org/10.1061/\(ASCE\)0733-9399\(1997\)123:9\(897\)](https://doi.org/10.1061/(ASCE)0733-9399(1997)123:9(897))
- [8] Spencer Jr. BF, Nagarajaiah S. State of the art of structural control. *J Struct Eng.* 2003;129(7):845-856. [https://doi.org/10.1061/\(ASCE\)0733-9445\(2003\)129:7\(845\)](https://doi.org/10.1061/(ASCE)0733-9445(2003)129:7(845))
- [9] Soong TT, Spencer BF. Supplemental energy dissipation: state-of-the-art and state-of-the-practice. *Eng Struct.* 2002;24(3):243-259. [https://doi.org/10.1016/S0141-0296\(01\)00092-X](https://doi.org/10.1016/S0141-0296(01)00092-X)
- [10] Symans MD, Charney FA, Whittaker AS, Constantinou MC, Kircher CA, Johnson MW, McNamara RJ. Energy dissipation systems for seismic applications: current practice and recent developments. *J Struct Eng.* 2008;134(1):3-21. [https://doi.org/10.1061/\(ASCE\)0733-9445\(2008\)134:1\(3\)](https://doi.org/10.1061/(ASCE)0733-9445(2008)134:1(3))
- [11] Sadek F, Mohraz B, Taylor AW, Chung RM, Kantar M, Prabhakar AA. Passive energy dissipation devices for seismic applications. National Institute of Standards and Technology; 1996. <https://doi.org/10.6028/NIST.IR.5923>
- [12] Lu Z, Wang Z, Zhou Y, Lu X. Nonlinear dissipative devices in structural vibration control: A review. *J Sound Vib.* 2018;423:18-49. <https://doi.org/10.1016/j.jsv.2018.02.052>
- [13] Lu Z, Wang Z, Masri SF, Lu X. Particle impact dampers: past, present, and future. *Struct Control Heal Monit.* 2018;25(1):1-25. <https://doi.org/10.1002/stc.2058>
- [14] Bartkowski P, Zalewski R, Chodkiewicz P. Parameter identification of Bouc-Wen model for vacuum packed particles based on genetic algorithm. *Arch Civ Mech Eng.* 2019;19(2):322-333. <https://doi.org/10.1016/j.acme.2018.11.002>
- [15] Bai XM, Shah B, Keer LM, Wang QJ, Snurr RQ. Particle dynamics simulations of a piston-based particle damper. *Powder Technol.* 2009;189(1):115-125. <https://doi.org/10.1016/j.powtec.2008.06.016>
- [16] Toyouchi A, Hanai M, Ido Y, Iwamoto Y. Damper force characteristics of a separated dual-chamber single-rod-type damper using an elastomer-particle assemblage. *J Sound Vib.* 2020;488:1-15. <https://doi.org/10.1016/j.jsv.2020.115625>
- [17] Dyke SJ, Spencer BF, Saint MK, Carison JD. Seismic response reduction using magnetorheological Dampers. *Smart Mater Struct.* 1996;5(5):565-575. <https://doi.org/10.1088/0964-1726/5/5/006>
- [18] Chapra SC, Canale RP. Numerical Methods for Engineers. McGraw-Hill Education; 2015.
- [19] Spencer BF, Dyke SJ, Deoskar HS. Benchmark problems in structural control: Part I - Active Mass Driver system. *Earthq Eng Struct Dyn.* 1998;27(11):1127-1139. [https://doi.org/10.1002/\(SICI\)1096-9845\(199811\)27:11<1127::AID-EQE774>3.0.CO;2-F](https://doi.org/10.1002/(SICI)1096-9845(199811)27:11<1127::AID-EQE774>3.0.CO;2-F)
- [20] Ohtori Y, Christenson RE, Spencer BF, Dyke SJ. Benchmark control problems for seismically excited nonlinear buildings. *J Eng Mech.* 2004;130(4):366-385. [https://doi.org/10.1061/\(ASCE\)0733-9399\(2004\)130:4\(366\)](https://doi.org/10.1061/(ASCE)0733-9399(2004)130:4(366))

Blank Page



Research Article

## Analyzing the impact of nano-sized silica on composite concrete: A static approach utilizing response surface method

A. Narender Reddy<sup>\*1,a</sup>, G. Gautham Kishore Reddy<sup>2,b</sup>, P. Narashima Reddy<sup>3,c</sup>, K. Srinivas Reddy<sup>1,d</sup>, B. Venkata Kavyateja<sup>4,e</sup>

<sup>1</sup>Department of Civil Engineering, Guru Nanak Institutions Technical Campus, Hyderabad, India

<sup>2</sup>Department of Civil Engineering, Vignan Institute of Technology and Science, Hyderabad, India

<sup>3</sup>Department of Civil Engineering, Sri Venkateshwara College of Engineering and Technology, Chittoor, India

<sup>4</sup>Department of Civil Engineering, JNTUA College of Engineering, Kalikiri, India

### Article Info

### Abstract

#### Article history:

Received 02 Feb 2024

Accepted 28 May 2024

#### Keywords:

Fly Ash;

Alcofine;

Nano silica;

Tetranary blended

nano concrete;

Statistical analysis;

Response surface

method

The utilization of composite materials as alternatives to Ordinary Portland Cement (OPC) is essential in mitigating the environmental impact of cement production. This study investigates the potential of industrial by-products rich in silica and alumina, such as fly ash (FA), alcofine (ALC), and nano silica (CNS), to partially replace OPC in concrete. Tetranary blended nano concrete (TBNC) compositions, incorporating 25% FA, 10% ALC, and varying proportions of CNS (0%, 0.5%, 1%, 2%, and 3%), were examined for their compressive strength in M30 and M60 grade concrete following a 90-day curing period. Results demonstrate the significant influence of CNS on compressive strength of TBNC. To validate these findings, Response Surface Methodology (RSM) was employed for mathematical modeling and statistical analysis, predicting compressive strength values and comparing them with experimental data. This research underscores the viability of utilizing industrial by-products in concrete production, thereby promoting sustainable construction practices.

© 2024 MIM Research Group. All rights reserved.

## 1. Introduction

Utilization of concrete is increasing every year with increase in the infrastructure. Concrete manufactured by using Ordinary Portland Cement (OPC) is widely used throughout the world because of availability and flexibility in easy operation [1]. The production of OPC requires a substantial amount of thermal energy and emits a large quantity of greenhouse gases, such as carbon dioxide (CO<sub>2</sub>), which have severe environmental consequences and contribute to global warming [2,3]. OPC production has been reported to be liable for about 3% and 9% of worldwide energy consumption and anthropogenic emission of CO<sub>2</sub>, respectively [4,5]. So, there is a need to search for the alternate materials, which can help to reduce the usage of OPC and produce sustainable construction materials in construction industry. The solution to this problem is to utilizing the industrial by-product which process pozzolanic nature as supplementary cementations materials (SCMs) in concrete [6]. The solid waste generated from industries creates disturbance in environment due to air pollution, land filings and pollutes the ground water by leachate. The by-products such as Fly Ash (FA), Rice Husk Ash (RHA), Ground Granulated Blast Furnace Slag (GGBS), Red mud (RM), Alcofine (ALC), Silica Fume (SF), Metakaolin (MK) etc., which are pozzolanic in nature can be used as SCMs [7,8]. Blending different types of pozzolans with cement improves the properties (durability and mechanical) of concrete [9,10]. The most

\*Corresponding author: [avnarenderreddy9@gmail.com](mailto:avnarenderreddy9@gmail.com)

<sup>a</sup> [orcid.org/0000-0003-3887-5147](https://orcid.org/0000-0003-3887-5147); <sup>b</sup> [orcid.org/0000-0002-0556-2548](https://orcid.org/0000-0002-0556-2548); <sup>c</sup> [orcid.org/0000-0001-8856-9741](https://orcid.org/0000-0001-8856-9741);

<sup>d</sup> [orcid.org/0000-0002-2010-7169](https://orcid.org/0000-0002-2010-7169); <sup>e</sup> [orcid.org/0000-0003-3447-4741](https://orcid.org/0000-0003-3447-4741)

DOI: <http://dx.doi.org/10.17515/resm2024.172ma0202rs>

important effects of Pozzolan admixture enhances the microstructure of concrete or cement paste by altering the interfacial transition zone (ITZ) and reducing pore structure via pozzolanic reaction [11,12]. In the present study, industrial by-products of pozzolanic nature, such as FA and ALC, are substituted for cement in concrete. By substituting these materials for cement in concrete, pollution-causing gas emissions from the cement production process will be reduced.

Moreover, the introduction of nanoparticles like colloidal nano silica (CNS) presents an opportunity to enhance concrete properties further [3]. CNS, with its high pozzolanic nature, can accelerate pozzolanic reactions within concrete, resulting in improved mechanical and physical properties. By incorporating CNS into concrete mixes, we can achieve greater strength and durability while reducing environmental impact [5]. Several studies have investigated the impact of nano-sized silica on the compressive strength, tensile strength, and flexural strength of concrete [9-12]. Research indicates that the addition of nano-sized silica particles improves the packing density of concrete mixtures, resulting in higher compressive strength [10]. Furthermore, nano-sized silica enhances the ITZ between cement paste and aggregates, leading to increased bond strength and improved mechanical properties [11]. Moreover, nano-sized silica has been found to enhance the durability of concrete by reducing permeability and increasing resistance to chloride ion penetration, sulfate attack, and alkali-silica reaction [13,14]. The fine particles of nano-sized silica fill in the pores and capillary voids within the concrete matrix, effectively reducing water ingress and preventing the ingress of deleterious substances [15]. Pervious research studies suggest that nano-sized silica can act as a viscosity-modifying admixture, improving the workability and flowability of concrete mixtures. This property is particularly advantageous in high-performance concrete and self-compacting concrete applications. Furthermore, investigations into the hydration kinetics of nano-sized silica in cementitious systems have revealed its role in accelerating cement hydration and promoting the formation of additional calcium silicate hydrate (C-S-H) gel. This accelerated pozzolanic reaction contributes to early strength development and improved long-term mechanical properties of concrete [9-15].

In this study, we focus on investigating the combined effects of 25% FA, 10% ALC, and varying amounts of CNS on the compressive strength of Ternary Blended Nano Concrete (TBNC) for M30 and M60 grade concrete over a 90-day curing period. By examining the influence of these materials on concrete strength, we aim to contribute to the development of sustainable construction practices and the utilization of industrial waste. Additionally, we have employed Response Surface Methodology (RSM) to develop regression equations for the compressive strength of M30 and M60 grade concretes separately. RSM helps to model and optimize complex processes, such as concrete strength development, by analyzing the interactions between multiple variables [16]. In RSM utilizing the design of experiments (DOE) method, several mathematical models have been developed and employed. One common model is the quadratic model, which assumes a second-order relationship between the independent variables and the response [17]. By utilizing RSM, we can gain insights into the optimal combination of materials to achieve desired concrete properties, thereby enhancing the efficiency and effectiveness of this research. The relevance of the static approach lies in its ability to provide precise and reliable data on the performance of concrete mixtures over time [16,17]. By subjecting the TBNC specimens to a consistent curing environment, we can accurately evaluate the long-term effects of incorporating FA, ALC, and CNS on concrete strength. This method allows us to capture the gradual development of concrete strength and assess the durability of the composite material. Moreover, the static approach enables us to systematically investigate the individual and combined contributions of FA, ALC, and CNS to the mechanical properties of TBNC. By maintaining a stable testing environment throughout the curing period, we can isolate the effects of each material and analyze their synergistic interactions on



concrete strength. The static approach facilitates the comparison of different concrete mix designs and helps identify optimal combinations of supplementary materials for achieving desired performance characteristics [16]. This structured methodology enhances the reliability and reproducibility of findings, ensuring robust conclusions regarding the efficacy of TBNC in sustainable construction practices. The static approach serves as a fundamental tool in this research, allowing for a detailed and structured analysis of the influence of supplementary materials on the compressive strength of TBNC. Through this approach, we aim to provide valuable insights into the development of sustainable concrete mixtures and contribute to the utilization of industrial waste in construction applications [16,17].

## 2. Research Significance

The primary challenge in modern construction lies in attaining the requisite strength of standard concrete, predominantly reliant on OPC. However, the surge in industrialization has led to the accumulation of non-engineered industrial waste, posing detrimental effects on the environment and ecosystems. The main aim of the present research is to explore the alternative building materials with industrial solid waste, potentially beneficial for the construction sector. This study investigates the potential of utilizing pozzolanic industrial solid waste as a cementitious supplement, offering a sustainable alternative to OPC. By advocating for the incorporation of industrial waste as admixtures or partial cement replacements, efforts are directed towards reducing cement consumption and addressing environmental contamination attributed to industrial byproducts. In particular, our research explores the effects of a composite mixture comprising FA, ALC, and CNS on the compressive strength of M30 and M60 grade concrete. By examining the influence of these materials on concrete strength, we aim to contribute to sustainable construction practices and mitigate the environmental impact of industrial waste. The adoption of RSM in our study serves to enhance the efficiency and effectiveness of our research. RSM allows for the modeling and optimization of complex processes, such as concrete strength development, by analyzing the interactions between multiple variables. In the context of our research, the RSM model enables us to systematically investigate the combined effects of fly ash, alccofine, and colloidal nano silica on the compressive strength of M30 and M60 grade concrete. By utilizing RSM, we can develop regression equations that provide insights into the optimal combination of materials to achieve desired concrete properties. Overall, the use of RSM facilitates a comprehensive understanding of the relationship between input variables and concrete strength, enabling us to optimize concrete mixtures for enhanced mechanical performance while minimizing environmental impact.

## 3. Materials

This research utilizes OPC of 53-grade as the binder in the experimental setup. Coarse and fine aggregates serve as filler materials, supplemented with super-plasticizers, specifically poly-carboxylic ether. The OPC utilized adheres to the standards set by the Bureau of Indian Standards (IS) with reference to IS: 12269-2013 [18]. The OPC exhibits a specific gravity of 3.12, fines of 6.50%, and initial and final setting times of 50 minutes and 420 minutes, respectively. The fine and coarse aggregates undergo testing according to IS: 383-1970 [19]. The angular shaped locally available crushed stone was used coarse aggregates, 20 mm downgraded, feature a specific gravity of 2.78, fineness modulus of 7.2%, and water absorption of 0.86%. Meanwhile, the fine aggregates, 4.75 mm downgraded and falling within the II grading zone as per IS 383-1970 [19], exhibit a specific gravity of 2.68, fineness modulus of 2.7%, and water absorption of 1.02%. Low calcium FA (Class F type) is sourced from the Vijayawada Thermal Plant in Andhra Pradesh, aligning with the specifications outlined in IS 3812-2013 [20]. This FA boasts a specific gravity of 2.3 and a fines modulus of 1.19%. ALC-1203, obtained from Ambuja Cement Ltd in Goa, conforms to

American Society for Testing and Materials (ASTM) C989-1999 [21] and possesses a specific gravity of 2.9. ALC is characterized as an ultrafine slag material and glass-based SCM sourced from steel or iron industries. Notably, ALC comprises fine solid glass spheres of non-crystalline polymorph or amorphous silicon dioxide. The high specific surface area of ALC particles exerts a significant influence on both the fresh and hardened state properties of concrete, as documented in various studies. In the study, scanning electron microscope (SEM) analysis was conducted to examine the morphology and microstructure of fly ash and alccofine particles used in our composite concrete. The SEM images revealed essential insights into the characteristics of these materials. The chemical properties of FA obtained from SEM and Energy Dispersive X-ray Analysis (EDAX) are given below and in figure1, the figure 1 revealed that the elemental characteristics in terms of weight percentage and atomic percentage. The analysis discerns four major elements, with distinctive compositions as follows:

1. C K (Carbon):
  - Weight Percentage: 59.2%
  - Atomic Percentage: 68.02%
2. O K (Oxygen):
  - Weight Percentage: 31.9%
  - Atomic Percentage: 27.6%
3. Al K (Aluminium):
  - Weight Percentage: 2.7%
  - Atomic Percentage: 1.4%
4. Si K (Silicon):
  - Weight Percentage: 6.07%
  - Atomic Percentage: 2.9%

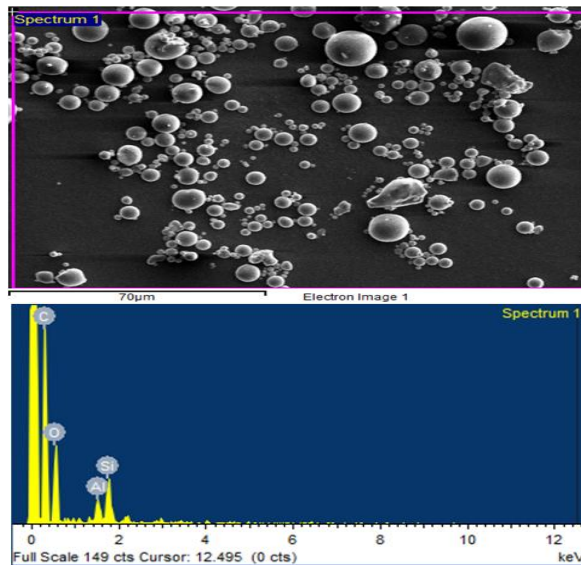


Fig. 1. SEM and EDAX image of FA

From figure 1, the SEM images revealed essential insights into the characteristics of these materials. For fly ash, the SEM observations indicated an amorphous structure, with spherical particles ranging in size from 0.5  $\mu\text{m}$  to 70  $\mu\text{m}$ . This spherical morphology is consistent with previous research findings [30,31] and is known to contribute to improved packing density and reduced water demand in concrete mixtures. The predominant presence of Carbon and Oxygen, comprising 59.2% and 68.02% in weight and 31.9% and 27.6% in atomic percentages, respectively, highlights their significant role in the elemental composition of the FA. Aluminum and Silicon are found in lower concentrations, with 2.7% and 1.4% in weight and 6.07% and 2.9% in atomic percentages, respectively as shown in figure 1. These chemical properties elucidate the elemental composition of FA, offering valuable insights into its potential impact on concrete properties and its suitability for use as a supplementary cementitious material. The data provided by EDAX contributes to a comprehensive understanding of the composition of FA, essential for informed decisions in concrete mix design and sustainable construction practices [22,23].

The chemical properties of ALC derived from EDAX are given figure 2, delineating the elemental characteristics in terms of weight percentage and atomic percentage. From the figure 2, the SEM analysis revealed an amorphous structure with angular particles, with sizes ranging from 0.5  $\mu\text{m}$  to 30  $\mu\text{m}$ . This angular morphology is advantageous for

enhancing the pozzolanic activity of ALC, promoting better interfacial bonding with cementitious materials and resulting in enhanced mechanical properties of concrete [22,23] and the EDAX analysis reveals the composition of five major elements as follows. The predominant presence of Carbon and Oxygen, comprising 45.6% and 57.6% in weight and 35.2% and 33.3% in atomic percentages, respectively, underscores their substantial role in the elemental composition of ALC. Aluminium, Silicon, and Calcium are found in comparatively lower concentrations, emphasizing the multifaceted composition of ALC. These chemical properties offer insights into the elemental composition of ALC, crucial for understanding its potential impact on concrete properties. The presence of Calcium suggests its pozzolanic nature, contributing to enhanced durability and strength characteristics in concrete. The data provided by EDAX facilitates informed decision-making in concrete mix design, particularly when incorporating ALC as a supplementary cementitious material in construction practices. These SEM observations provide valuable insights into the microstructural characteristics of FA and ALC, which are essential for understanding their influence on the properties of composite concrete [22,23].

1. C K (Carbon):
  - Weight Percentage: 45.6%
  - Atomic Percentage: 57.6%
2. O K (Oxygen):
  - Weight Percentage: 35.2%
  - Atomic Percentage: 33.3%
3. Al K (Aluminium):
  - Weight Percentage: 4.01%
  - Atomic Percentage: 2.2%
4. Si K (Silicon):
  - Weight Percentage: 6.3%
  - Atomic Percentage: 3.4%
5. Ca K (Calcium):
  - Weight Percentage: 8.6%
  - Atomic Percentage: 3.2%

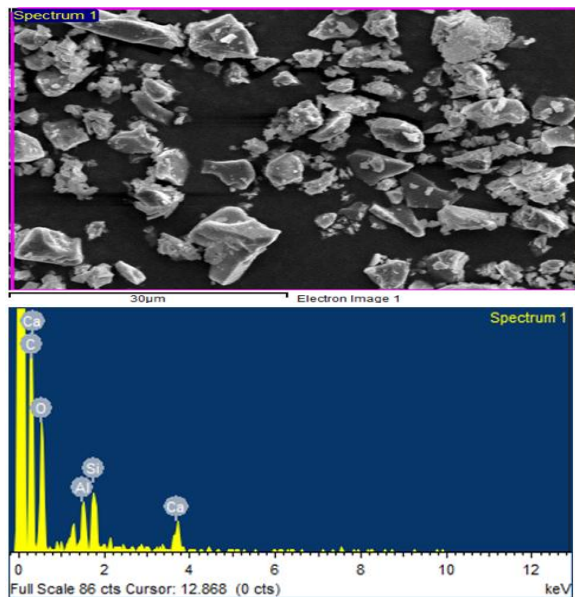


Fig. 2. SEM and EDAX image of ALC

CNS, procured from Bee-Chems Chemicals in Kanpur, boasts a specific gravity of 1.21, particle size ranging from 10-20 nm, and a surface area of 150-180 m<sup>2</sup>/g. A high-range water-reducing admixture primarily composed of poly-carboxylic ether, in accordance with ASTM-C494 [24] standards, is employed throughout the study. In the study, nano-sized silica, particularly in colloidal form, plays a critical role in enhancing the performance of composite concrete. The fine particles of CNS help densify the concrete microstructure, filling voids and pores, thereby improving packing density, reducing permeability, and enhancing mechanical properties [11]. Additionally, CNS promotes better adhesion between the cement paste and aggregates, leading to improved bond strength and overall mechanical performance of the concrete [12]. Through our research, we aim to elucidate the significant role of colloidal nano silica in composite concrete and its incorporation method, contributing to the advancement of sustainable and durable construction materials. The concrete preparation utilizes portable tap water available on the university premises, featuring a pH value of 7-8, adhering to the recommendations outlined in IS 456-2000 [25].

#### 4. Mix Design

M30 and M60 grade of mix designs were prepared as per the guidelines given in IS: 10262-2009 [26] and American Concrete Institute (ACI) 211.4R-2008 [27] respectively. The design mix of 1:2.06:3.63 with w/c ratio 0.43 was adopted for casting of M30 grade of concrete and for M60 grade the design mix of 1:1.6:2.19 with w/c ratio 0.30 was adopted. The details of mix design and proportions are given in Table 1. The OPC was partial replaced by combination of 25% FA, 10% ALC and with varying amounts of CNS (i.e. 0%, 0.5%, 1%, 2% and 3%). The quantity of all ingredients of concrete was determined according to the design ratio of the mixes. The CNS is incorporated by first mixing it with water to form a stable suspension, ensuring uniform dispersion throughout the concrete mix. Once dispersed, nano silica contributes to improving various aspects of concrete properties. Its high surface area facilitates enhanced pozzolanic activity, reacting with calcium hydroxide in the cement paste to form additional C-S-H gel, thus enhancing strength and durability. The ingredients were mixed thoroughly until the mix obtained uniform colour. The cubes of 100x100x100 mm were filled with concrete and vibrated with the help of table vibrator. The specimens were allowed for air curing for 24 hrs and de-moulded. They are allowed for 7-, 28-, 56- and 90-days curing periods and tested for compressive strength.

Table 1. Details of mix design and proportions

| GC  | MN   | OPC<br>(kg/m <sup>3</sup> ) | FA<br>(kg/m <sup>3</sup> ) | ALC<br>(kg/m <sup>3</sup> ) | CNS<br>(kg/m <sup>3</sup> ) | CNS<br>content | Fine<br>Aggregate<br>(kg/m <sup>3</sup> ) | Coarse<br>Aggregate<br>(kg/m <sup>3</sup> ) | Water<br>(kg/m <sup>3</sup> ) |
|-----|------|-----------------------------|----------------------------|-----------------------------|-----------------------------|----------------|---|---|-------------------------------|
| M30 | C1   | 350.2                       | -                          | -                           | -                           | -              | 721.5                                     | 1273.8                                      | 150.59                        |
|     | T0   | 236.4                       | 87.5                       | 26.3                        | -                           | 0%             | 721.5                                     | 1273.8                                      | 150.59                        |
|     | T0.5 | 235.2                       | 87.5                       | 26.3                        | 1.18                        | 0.5%           | 721.5                                     | 1273.8                                      | 150.59                        |
|     | T1   | 234.06                      | 87.5                       | 26.3                        | 2.37                        | 1%             | 721.5                                     | 1273.8                                      | 150.59                        |
|     | T2   | 231.7                       | 87.5                       | 26.3                        | 4.73                        | 2%             | 721.5                                     | 1273.8                                      | 150.59                        |
|     | T3   | 229.33                      | 87.5                       | 26.3                        | 7.10                        | 3%             | 721.5                                     | 1273.8                                      | 150.59                        |
| M60 | C2   | 540.1                       | -                          | -                           | -                           | -              | 625.5                                     | 1180.8                                      | 162.03                        |
|     | S0   | 364.5                       | 135.02                     | 40.5                        | -                           | 0%             | 625.5                                     | 1180.8                                      | 162.03                        |
|     | S0.5 | 362.7                       | 135.02                     | 40.5                        | 1.8                         | 0.5%           | 625.5                                     | 1180.8                                      | 162.03                        |
|     | S1   | 360.9                       | 135.02                     | 40.5                        | 3.6                         | 1%             | 625.5                                     | 1180.8                                      | 162.03                        |
|     | S2   | 357.3                       | 135.02                     | 40.5                        | 7.3                         | 2%             | 625.5                                     | 1180.8                                      | 162.03                        |
|     | S3   | 353.7                       | 135.02                     | 40.5                        | 10.9                        | 3%             | 625.5                                     | 1180.8                                      | 162.03                        |

GC- Grade of Concrete, MN- Mix Notation, C1- M30 Grade Conventional Concrete

T0 - M30 grade blended concrete mix containing 25% FA, 10% ALC and 0% CNS

T0.5 - M30 grade blended concrete mix containing 25% FA, 10% ALC and 0.5% CNS

T1 - M30 grade blended concrete mix containing 25% FA, 10% ALC and 1% CNS

T2 - M30 grade blended concrete mix containing 25% FA, 10% ALC and 2% CNS

T3 - M30 grade blended concrete mix containing 25% FA, 10% ALC and 3% CNS,

C2 - M60 grade Conventional Concrete mix,

S0 - M30 grade blended concrete mix containing 25% FA, 10% ALC and 0% CNS

S0.5 - M30 grade blended concrete mix containing 25% FA, 10% ALC and 0.5% CNS

S1 - M30 grade blended concrete mix containing 25% FA, 10% ALC and 1% CNS

S2 - M30 grade blended concrete mix containing 25% FA, 10% ALC and 2% CNS

S3 - M30 grade blended concrete mix containing 25% FA, 10% ALC and 3% CNS

CNS content - Percentage by weight of cement

## 5. Experimental Setup

The prepared specimen is mounted on the lower platen of a compression testing machine, ensuring proper alignment to prevent eccentric loading as per the guidelines provided in IS 516:2018 [28]. A compressive load is at  $1.4\text{N/mm}^2/\text{minute}$  applied gradually to the specimen at a specified rate until failure occurs, which is typically characterized by visible cracking or crushing. Throughout the test, data on applied load and deformation are continuously recorded. After testing, the data are analyzed to determine the compressive strength of the concrete specimen, providing valuable insights into its structural performance and integrity.

## 6. Results

### 6.1 Compressive Strength (CS)

The compressive strength results of M30 grade and M60 grade blended concrete with combination of 25% FA, 10% ALC and varying percentages of CNS (0%, 0.5%, 1%, 2% and 3%) at a curing period of 7, 28, 56 and 90 days are shown in Figure 3 and Figure 4.

From the Figure 3 and Figure 4 it is noticed that a minor improvement in compressive strength is achieved with combination of 25% FA, 10% ALC and 0% CNS (T0 and S0 mixes), the strength increased by 9.8%, 7.08%, 7.07%, 7.04% and 12.8%, 9.03%, 8.9%, 8.5% for the ages of 7, 28, 56 and 90 days respectively, in comparison to the M30 grade and M60 grade conventional concrete mixes C1 and C2, which is attributed to the reason that the concrete matrix gets densified due to the plugging of pores by ALC particles [12]. The compressive strength is further enhanced significantly with CNS, The compressive strength of T0 - T3 mixes containing 0.5%, 1%, 2% and 3% CNS is increased by 20.6%, 26.8%, 23.9%, 14.1% and 9.8%, 14.09%, 12.17%, 8.78%, for the ages of 7 and 28 days respectively, in comparison to the M30 Grade conventional concrete mix C1.

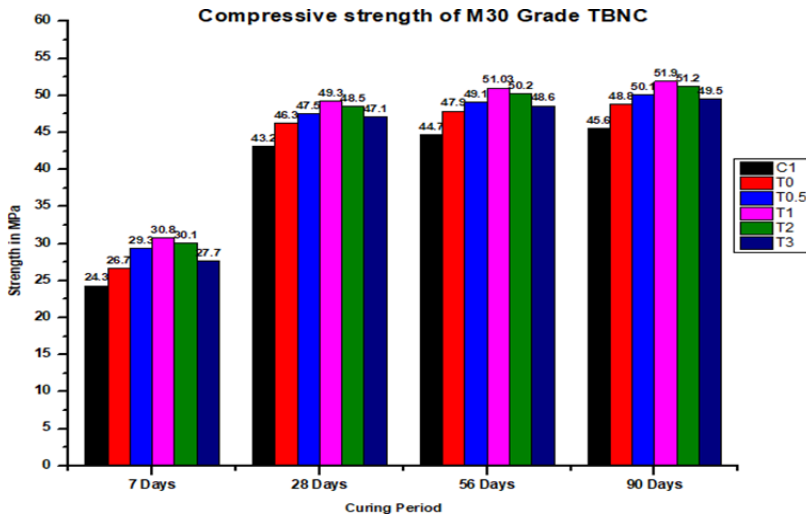


Fig. 3. Compressive Strength of M30 Grade of concrete

Whereas for M60 grade of concrete, the compressive strength of S0 - S3 mixes containing 0.5%, 1%, 2% and 3% CNS is increased by 21.5%, 25.1%, 23.5%, 20.9% and 13.7%, 17.5%, 16.3%, 12.8%, for the ages of 7 and 28 days respectively, in comparison to the conventional concrete mix C2. The enhancement in the initial age (7 day) compressive strength of blended concrete is due to accelerated hydration reaction in concrete on the addition of CNS [29,30]. In hydration process CNS helps in accelerating the pozzolanic reaction by

formation of more Calcium Hydroxide (CH) resulting in quick hydration of tricalcium silicate (C<sub>3</sub>S) and Dicalcium silicate (C<sub>2</sub>S) resulting in formation of more C-S-H which helps in formation of denser matrix in concrete structure resulting in high improvement in early age strength [31]. In the hydration reaction, the nucleation effect by nano silica accelerates the consumption of C<sub>3</sub>S, which results in release of more CH [32]. The better dispersion of CNS particles with cement showed enhancement in compressive strength for all the blended mixes. The enhancement of compressive strength continued till the CNS concentration increased up to 1% and reduces slightly for 2% and 3%. The reason for the decrease in compressive strength may be due to the separation of particles because of excess number of nano particles or due to the higher potential of agglomeration, due to poor dispersion of nano particle in mixture leads to effect of pore structure of concrete resulting in strength decrement [33]. The later age (i.e. 56 and 90 days) compressive strength showed a negligible change for 28 days compressive strength which is because of accelerated heat of hydration process, moreover, the addition of micro and nano sized SCM's are responsible for the development of denser microstructure. It is also noticed that most of the hydration process gets completed at 28 days curing period which becomes very slow and will continue over time, thus showing minimum variations in compressive strength at a curing period of 56 and 90 days [34].

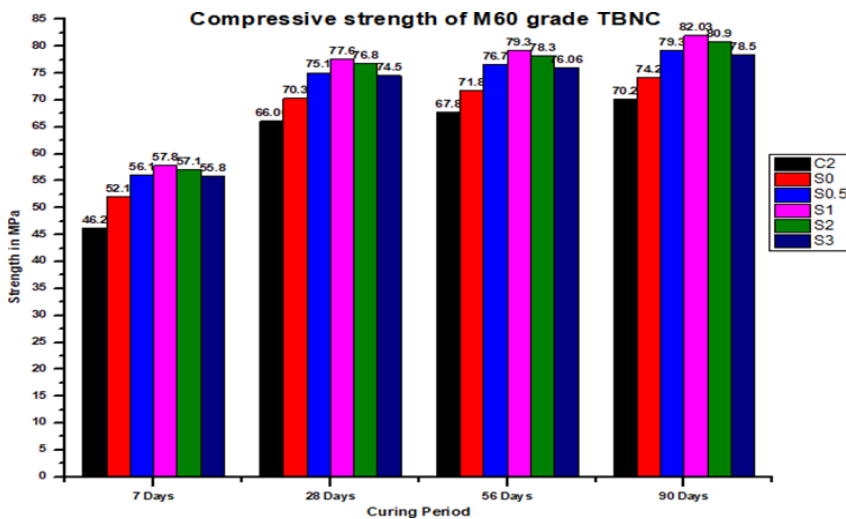


Fig. 4. Compressive Strength of M60 Grade of concrete

**6.2 Design of experiments (DOE) by Response Surface Method (RSM):**

In our study, RSM was utilized to assess the compressive strength (CS) of TBNC through a structured DOE. RSM, a statistical tool widely employed in industry and research, facilitated mathematical modeling and statistical analysis to predict the validity of experimental CS values. We adopted a second-order polynomial equation, as opposed to a linear model, to comprehensively evaluate the input variables responses. The response can be represented by the equation mentioned below equation 1.

$$y = F(\epsilon_1, \epsilon_2, \epsilon_3 \dots \epsilon_k) + \epsilon \tag{1}$$

Where the input variables are represented by  $\epsilon_1, \epsilon_2, \epsilon_3 \dots \epsilon_k$ , approximate response function is denoted by F and static residual error is denoted by  $\epsilon$ , in the present analytical study for evaluating the input variables response, the second order polynomial equation was used instead of the linear polynomial. In this study experimental design, was mainly

focused on one response variable, CS, and two independent variables: Curing Period (CP) and Colloidal Nano Silica Percentage (%CNS). Through regression analysis conducted using MINITAB software, we obtained coefficient values to construct a quadratic prediction model equation, as per equation 2. This equation allowed us to predict CS based on varying CP and %CNS combinations. Subsequently, DOE was employed to evaluate the goodness of fit of our model, assessing its effectiveness in representing the observed data accurately. Additionally, RSM facilitated the development of response surface graphs and residual plot graphs, aiding in visualizing the relationships between CP, %CNS, and CS. This systematic approach enabled us to optimize TBNC formulations and enhance our understanding of the factors influencing its compressive strength.

$$Z = A + BX1 + CY1 + DX12 + EY12 + F X1 Y1 \tag{2}$$

In the equation X1 represents the %CNS, Y1 represents the CP and Z represents the CS. By RSM analysis the following polynomial regression equation 3 is obtained for M30 grade of concrete

$$CS = 23.39 + 3.99 \%CNS + 0.851 CP - 1.266 \%CNS \times \%CNS - 0.006436 CP \times CP + 0.0001 \%CNS \times CP \tag{3}$$

By RSM analysis the following polynomial regression equation 4 is obtained for M60 grade of concrete:

$$CS = 48.36 + 7.94 \%CNS + 0.830 CP - 2.325 \%CNS \times \%CNS - 0.00603 CP \times CP + 0.0011 \%CNS \times CP \tag{4}$$

Table 2. Experimental and predicted values by using RSM regression expression for m30 grade of TBNC

| %CNS | CP | CS (Actual) | CS (Predicted) | Residual Error | R <sup>2</sup> (Actual) | R <sup>2</sup> (Predicted) |
|------|----|-------------|----------------|----------------|-------------------------|----------------------------|
| 0    | 7  | 26.7        | 29.03326       | -2.33326       |                         |                            |
| 0.5  | 7  | 29.3        | 30.71313       | -1.41313       |                         |                            |
| 1    | 7  | 30.8        | 31.76004       | -0.96004       |                         |                            |
| 2    | 7  | 30.1        | 31.95497       | -1.85497       |                         |                            |
| 3    | 7  | 27.7        | 29.61806       | -1.91806       |                         |                            |
| 0    | 28 | 46.3        | 42.18122       | 4.11878        |                         |                            |
| 0.5  | 28 | 47.5        | 43.86229       | 3.637712       |                         |                            |
| 1    | 28 | 49.3        | 44.91039       | 4.389606       |                         |                            |
| 2    | 28 | 48.5        | 45.10772       | 3.392276       | 90.62%                  | 82.28%                     |
| 3    | 28 | 47.1        | 42.77321       | 4.326791       |                         |                            |
| 0    | 56 | 47.9        | 50.88107       | -2.98107       |                         |                            |
| 0.5  | 56 | 49.1        | 52.56374       | -3.46374       |                         |                            |
| 1    | 56 | 51.03       | 53.61344       | -2.58344       |                         |                            |
| 2    | 56 | 50.2        | 53.81397       | -3.61397       |                         |                            |
| 3    | 56 | 48.6        | 51.48265       | -2.88265       |                         |                            |
| 0    | 90 | 48.8        | 47.87722       | 0.922781       |                         |                            |
| 0.5  | 90 | 50.1        | 49.56183       | 0.538174       |                         |                            |
| 1    | 90 | 51.9        | 50.61347       | 1.286529       |                         |                            |
| 2    | 90 | 51.2        | 50.81788       | 0.382121       |                         |                            |
| 3    | 90 | 49.5        | 48.49044       | 1.009558       |                         |                            |

The actual CS and predicted CS by RSM for M30, M60 grades and their residual errors are represented in Table 2 and Table 3 respectively. From the RSM analysis the regression coefficient ( $R^2$ ) of CS (Actual) is 90.62%, CS (Predicted) is 82.28% and for M30 grade of TBNC concrete and the  $R^2$  of CS (Actual) is 90.19% and  $R^2$  of CS (Predicted) is 82.45% for M60 grade of TBNC concrete.

Table 3. Experimental and Predicted values by using RSM regression expression for M60 Grade of TBNC

| %CNS | CP | CS (Actual) | CS (Predicted) | Residual Error | $R^2$ (Actual) | $R^2$ (Predicted) |
|------|----|-------------|----------------|----------------|----------------|-------------------|
| 0    | 7  | 52.1        | 53.88003       | -1.78003       |                |                   |
| 0.5  | 7  | 56.1        | 57.27344       | -1.17344       |                |                   |
| 1    | 7  | 57.8        | 59.50422       | -1.70422       |                |                   |
| 2    | 7  | 57.1        | 60.47791       | -3.37791       |                |                   |
| 3    | 7  | 55.8        | 56.8011        | -1.0011        |                |                   |
| 0    | 28 | 70.3        | 66.88768       | 3.412317       |                |                   |
| 0.5  | 28 | 75.1        | 70.29297       | 4.807034       |                |                   |
| 1    | 28 | 77.6        | 72.53562       | 5.064377       |                |                   |
| 2    | 28 | 76.8        | 73.53306       | 3.266938       |                |                   |
| 3    | 28 | 74.5        | 69.88          | 4.620001       |                |                   |
| 0    | 56 | 71.8        | 75.96168       | -4.16168       |                |                   |
| 0.5  | 56 | 76.7        | 79.38279       | -2.68279       |                |                   |
| 1    | 56 | 79.3        | 81.64128       | -2.34128       |                |                   |
| 2    | 56 | 78.3        | 82.67039       | -4.37039       | 90.19%         | 82.45%            |
| 3    | 56 | 76.06       | 79.049         | -2.989         |                |                   |
| 0    | 90 | 74.2        | 74.27442       | -0.07442       |                |                   |
| 0.5  | 90 | 79.3        | 77.71477       | 1.585234       |                |                   |
| 1    | 90 | 82.03       | 79.99248       | 2.037516       |                |                   |
| 2    | 90 | 80.9        | 81.06004       | -0.16004       |                |                   |
| 3    | 90 | 78.5        | 77.4771        | 1.022897       |                |                   |

6.2.1 Residual Plots form RSM Analysis

From the RSM analysis, Normal probability plot and 3D response surface plots were obtained. The figure 5 represents the normal probability plot and figure 6 represents the 3D response surface plots for M30 and M60 grade of TBNC.

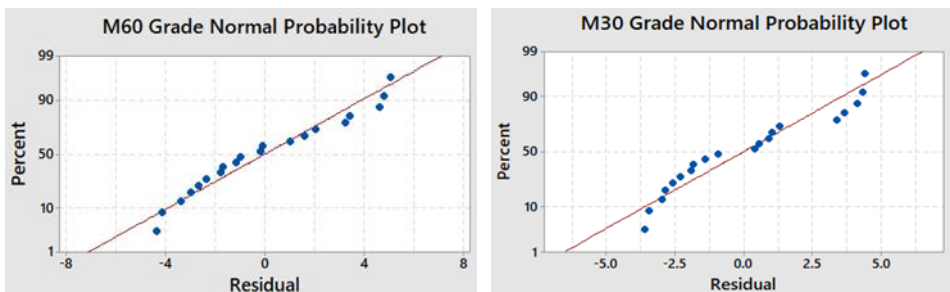


Fig. 5. Normal probability plot for M30 grade and M60 grade of TBNC from RSM analysis



The points which are present nearer to the reference line indicates low error and the points far from the reference line indicate more error. From the figure 5 it is clearly seen that the CS plot was approximated well in a line and the points are closer to the reference line. It can be concluded that the percentage of residual error is less and the probability between percentage and residual values is satisfied. From this analysis it can be concluded that the obtained CS results are in acceptable range for both M30 and M60 grade of TBNC.

Figure 6 depicts a 3D response surface plot with CS vs %CNS and CP from the developed model. The surface plot's curvature suggests that the CS of TBNC mix is highly dependent on its CNS concentration. Development in CS with the progression of curing age is usual, however in TBNC, high early age strength is achieved, and the graphical depiction does not indicate a sharp rise in terms of curing age.

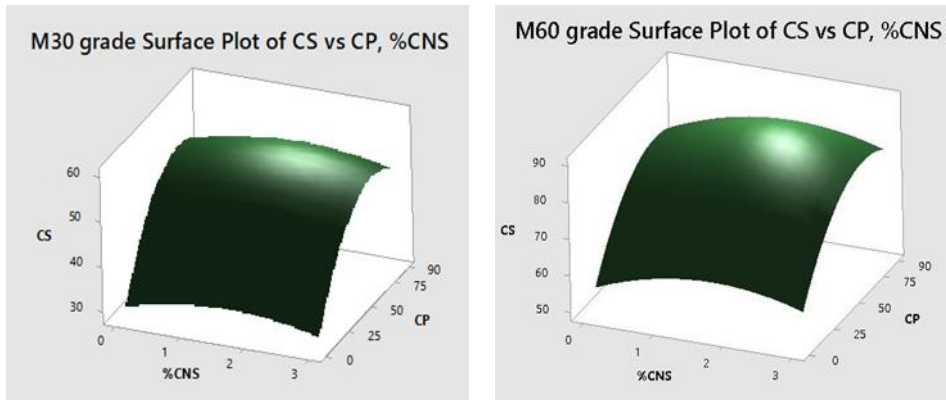


Fig. 6. Normal probability plot for M30 grade and M60 grade of TBNC from RSM analysis

From the RSM analysis it is clearly seen that the percentage of residual error is less than 5%, So that it can be concluded that the obtained results confidence level is about 95% for both M30 and M60 grade of TBNC [16]. In the study, it was aimed to investigate the synergistic effects of incorporating nano-sized silica alongside industrial pozzolanic materials, namely FA and ALC, in concrete mixes to enhance mechanical properties while reducing environmental impact. Through rigorous experimentation and analysis, we evaluated the compressive strength of composite concrete mixes containing varying concentrations of nano-sized silica over a 90-day curing period. The findings demonstrated that the addition of CNS in combination with FA and ALC led to significant improvements in compressive strength compared to traditional concrete mixes [17]. This result aligns with previous literature suggesting that nano-sized silica enhances the mechanical properties of concrete by improving packing density, enhancing bond strength, and reducing permeability [16,17]. Furthermore, the study contributes to the advancement of sustainable construction practices by highlighting the efficacy of utilizing industrial by-products as supplementary cementitious materials. By linking the results to the research objectives and relevant literature, we emphasize the potential of incorporating nano-sized silica in concrete formulations to achieve high-performance and environmentally friendly construction materials [16,17].

## 7. Conclusions

The combination of constant percentages of FA and ALC quantity showed moderate enhancement in compressive strength of concrete at all ages. With 25% FA, 10% ALC and 1% CNS showed better enhancement in compressive strength at all ages form both M30 and M60 grade of TBNC concrete. CNS helped to accelerate the hydration reaction which

helped the TBNC to improve early strength gaining capacity. At early age the strength had improved about 26.8% for M30 grade and 25.1% for M60 grade when compared with conventional concrete mixes for 7 days curing period, not only the early age enhancement the CNS helped to improve the long-term strength property also the strength enhancement was about 14.09%, 14.08%, 13.72% for M30 grade and 17.5%, 16.94%, 16.8% for M60 grade when compared with conventional concrete mixes for 28-, 56- and 90-days curing period. Incorporation of CNS in blended concrete can be considered as an effective way for enhancing the overall performance of the concrete. The better dispersion of CNS particles with cement showed enhancement in compressive strength for all the blended mixes. The enhancement of compressive strength continued till the CNS concentration increased up to 1% and reduces slightly for 2% and 3%. The decrease in CS may be attributable to the separation of particles as a result of an excess of nanoparticles or to a higher potential for agglomeration as a result of poor dispersion of nanoparticles in the mixture, which has an effect on the pore structure of concrete, resulting in a decrease in strength. The experimental CS was predicted using the RSM approach in order to forecast the CS values, and the residual error was found to be within an acceptable range, indicating a valid prediction. The replacement of cement in TBNC with a combination of FA, ALC, and CNS led to the development of high-strength TBNC concrete. This subsequently leads to the development of TBNC by combining several SCMs that may contribute to cost savings and sustainability

## References

- [1] Aly M, M S J Hashmi, A G Olabi, M Messeiry E F Abadir and A I Hussain. Effect of colloidal nano-silica on the mechanical and physical behaviour of waste-glass cement mortar. *Materials and Design*. 2012; 33: 127-135. <https://doi.org/10.1016/j.matdes.2011.07.008>
- [2] Singh L P, Karade S R, Bhattacharyya S K, Yousuf M M and Ahalawat S. Beneficial role of nanosilica in cement-based materials -A review. *Construction and Building Materials*. 2013; 47:1069-1077. <https://doi.org/10.1016/j.conbuildmat.2013.05.052>
- [3] Reddy A N and Meena T. An experimental study to find the optimum dosage of admixtures in blended concrete, *International Journal of Recent Technology and Engineering*. 2019; 7: 1062-1065
- [4] Berra Mario, Fabio Carassiti, Teresa Mangialardi, A E Paolini and Marco Sebastiani. Effects of nanosilica addition on workability and compressive strength of Portland cement pastes. *Construction and Building Materials*. 2012; 35: 666-675. <https://doi.org/10.1016/j.conbuildmat.2012.04.132>
- [5] Ravi teja G, A Narendra Reddy and Meena T. Experimental study on the strength and durability of high performance nano silica concrete. *International Journal of Innovative Technology and Exploring Engineering*. 2019; 8: 1141-1144.
- [6] P Kathirvel, V Saraswathy, S P Karthik and A S S Sekar. Strength and durability properties of quaternary cement concrete made with fly ash rice husk ash and limestone powder. *Arabian journal of science and technology*. 2012; 38: 589-598. <https://doi.org/10.1007/s13369-012-0331-1>
- [7] Jalal Mostafa, Esmaeel Mansouri, Mohammad Sharifipour and Ali Reza Pouladkhan. Mechanical, rheological, durability and microstructural properties of high performance self-compacting concrete containing SiO<sub>2</sub> micro and nanoparticles. *Materials & Design*, 2012; 34: 389-400. <https://doi.org/10.1016/j.matdes.2011.08.037>
- [8] Reddy A N and Meena T. The effect of alccofine on blended concrete under compression. *Lecture Notes on Multidisciplinary Industrial Engineering*. 2020; Part F248: 27-37. <https://doi.org/10.1007/978-981-13-7968-03>

- [9] Lincy V, Rao V V L K and Lakshmy P. A study on nanosilica and microsilica concretes under different transport mechanisms. Magazine of Concrete Research. 2018; 70: 1205-1216. <https://doi.org/10.1680/jmacr.16.00504>
- [10] Reddy A Narendar, P Mounika and R Moulika. Study on effect of alccofine and nano silica on properties of concrete-A review. International Journal of Civil Engineering and Technology. 2018; 9: 559-565.
- [11] Reddy A N and Meena T. Acid resistance of ternary blended nanosilica concrete incorporating fly ash and alccofine. Civil Engineering and Architecture. 2021; 9: 500-506. <https://doi.org/10.13189/cea.2021.090222>
- [12] Chithra S, Senthil Kumar S R R and Chinnaraju K. The effect of colloidal nano-silica on workability, mechanical and durability properties of high-performance concrete with copper slag as partial fine aggregate. Construction and Building Materials. 2016; 113,794- 804. <https://doi.org/10.1016/j.conbuildmat.2016.03.119>
- [13] Riahi Sh and Nazari A. Physical, mechanical and thermal properties of concrete in different curing media containing ZnO<sub>2</sub> nanoparticles. Energy Buildings. 2011; 43, 1977-1984. <https://doi.org/10.1016/j.enbuild.2011.04.009>
- [14] Reddy A N and Meena T. A study on the effect of colloidal nano-silica on blended concrete containing fly ash and alccofine. Revista Romana de Materiale.2019; 49, 217-224.
- [15] Reddy A N and Meena T. A study on influence of nano silica on mechanical properties of blended concrete. Journal of Computational and Theoretical Nanoscience. 2019; 16: 2006-2011. <https://doi.org/10.1166/jctn.2019.7840>
- [16] Udayasree B, Reddy AN, Suvidha Y, Kulkarni P, Kumar CA, Kavyatheja B. Strength prediction of modified self-compacting concrete using response surface method. Pollack Periodica. 2024; 1, 27-32. <https://doi.org/10.1556/606.2023.00948>
- [17] Reddy A N, Reddy P N and Kavyateja B V. Influence of nanomaterial on high-volume fly ash concrete: a statistical approach. Innovative Infrastructure Solutions. 2020; 5, 88. <https://doi.org/10.1007/s41062-020-00340-9>
- [18] IS 12269. Ordinary portland cement 53 grade-specification, New Delhi, India.2013
- [19] IS 383. Specification for coarse and fine aggregates from natural sources for concrete, New Delhi, India. 2016.
- [20] IS 3812. Pulverized fuel ash - specification, part 1 for use as pozzolana in cement, cement mortar and concrete, New Delhi, India. 2013.
- [21] ASTM C989. Standard specification for ground granulated blast-furnace slag for use in concrete and mortars, West Conshohocken, USA.1991.
- [22] Srinath B S, Patnaikuni C K and Raviteja N. Comparative studies of cement and alccofine and their suitability for concrete. Civil Engineering and Architecture. 2022; 10(4), 1327-1339. <https://doi.org/10.13189/cea.2022.100408>
- [23] Kavyateja B V, Jawahar J G and Sashidhar C. Effectiveness of alccofine and fly ash on mechanical properties of ternary blended self-compacting concrete. Materials Today: Proceedings. 2020; 33, 73-79. <https://doi.org/10.1016/j.matpr.2020.03.152>
- [24] ASTM C494. Standard specification for chemical admixture for concrete, West Conshohocken, USA. 2017.
- [25] IS 456. Plain and reinforced concrete - code of practice is an indian standard code of practice for general structural use of plain and reinforced concrete, New Delhi, India. 2017.
- [26] IS 10262. Concrete Mix Proportioning - Guidelines, New Delhi, India. 2019.
- [27] ACI211.4R. Standard specification for mix design for concrete, West Conshohocken, USA.2018.
- [28] IS 516. Methods of Tests for Strength of Concrete, New Delhi, India.1959.
- [29] Raj D S, Ganesan N Abraham R and Raju A. Behavior of geopolymer and conventional concrete beam column joints under reverse cyclic loading. Advances in concrete construction. 2016; 4: 161-172. <http://dx.doi.org/10.12989/acc.2016.4.3.161>

- [30] Zhang M H and Li H. Pore structure and chloride permeability of concrete containing nano-particles for pavement. *Construction Building Materials*. 2011; 25: 608-616. <https://doi.org/10.1016/j.conbuildmat.2010.07.032>
- [31] Anjali R and G Venkatesan. Optimization of mechanical properties and composition of M-sand and pet particle added concrete using hybrid deep neural network-horse herd optimization algorithm. *Construction and Building Materials*. 2022; 347, 128334. <https://doi.org/10.1016/j.conbuildmat.2022.128334>
- [32] Abhilash P P, Dheeresh Kumar Nayak, Bhaskar Sangoju, Rajesh Kumar and Veerendra Kumar. Effect of nano-silica in concrete- a review. *Construction and Building Materials*, 2021; 278, 122347. <https://doi.org/10.1016/j.conbuildmat.2021.122347>
- [33] Kumar Akash and Gurpreet Singh. Effect of nano silica on the fresh and hardened properties of cement mortar. *International Journal of Applied Engineering Research*. 2018; 13, 11183-11188.
- [34] Gupta Sakshi. Application of silica fume and nanosilica in cement and concrete-A review. *Journal on Today's Ideas-Tomorrow's Technologies*. 2013; 2, 85-98. <https://doi.org/10.15415/jotitt.2013.12006>

## Effects of rattan fiber length variation on mechanical properties, characterization, and microstructure of concrete

Andi Yusra<sup>\*1, a</sup>, Zakia<sup>1, b</sup>, Surya Perdana<sup>1, c</sup>, Fachruddin Fachruddin<sup>1, d</sup>, Teuku Budi Aulia<sup>2, e</sup>

<sup>1</sup>Department of Civil Engineering, Teuku Umar University, Meulaboh, Indonesia

<sup>2</sup>Department of Civil Engineering, Syiah Kuala University, Banda Aceh, Indonesia

### Article Info

### Abstract

#### Article history:

Received 05 Mar 2024

Accepted 31 May 2024

#### Keywords:

Microstructure;  
Characterization;  
Fiber concrete;  
Concrete strength

The study aimed to test how variations in fiber length affect the behavior of microstructures in concrete, as well as to characterize and analyze their mechanical properties. This research covers several specific objectives, including understanding the influence of different fiber lengths on micro and macrostructural aspects of concrete, assessing the mechanical properties of reinforced concrete with fibers of various lengths, and examining the relationship between fiber length and the mechanical performance of concrete. The results showed that the addition of rattan fibers in concrete can increase or even reduce tensile strength depending on the length of the fibers and their material characteristics. The addition of rattan fibers with a length of 30 mm results in a significant increase in tensile strength, while longer or shorter fiber lengths do not yield equally favorable results. Analysis of the chemical composition of concrete shows that the elements oxygen (O), calcium (Ca), and silicon (Si) predominate, with the addition of carbon (C), iron (Fe), aluminum (Al), magnesium (Mg), and Sulphur (S) elements in concrete with rattan fibers. Morphological observations using SEM on concrete, both with fibers and without fibers, provide an in-depth understanding of the structure of concrete surfaces microscopically.

© 2024 MIM Research Group. All rights reserved.

## 1. Introduction

Concrete is a widely utilized construction material due to its exceptional compressive strength, ease of production and maintenance, raw material availability, and cost-effectiveness [1,2]. When supplemented with admixtures, fibers, or alternative materials, concrete can achieve enhanced properties, contributing to superior final outcomes [3-7]. Composite concrete, often referred to as fiber concrete, involves reinforcing concrete through the addition of fibers to the mixture. This reinforcement bolsters strength, crack resistance, and overall mechanical performance [8]. Commonly employed fibers such as polypropylene, glass, steel, among others, augment both tensile and compressive strength, acting as supplementary reinforcement to mitigate cracking and fortify concrete [9,10].

Fiber-reinforced composites have garnered significant attention in various industries due to their exceptional mechanical properties and versatility in applications. Among the myriad of fibers utilized in composite manufacturing, rattan fibers stand out for their unique characteristics and potential contributions to composite material properties [11]. However, understanding the effects of different fiber lengths, particularly rattan fibers, on

\*Corresponding author: [andiyusra@utu.ac.id](mailto:andiyusra@utu.ac.id)

<sup>a</sup> [orcid.org/0000-0003-4779-0815](https://orcid.org/0000-0003-4779-0815); <sup>b</sup> [orcid.org/0009-0004-5007-9906](https://orcid.org/0009-0004-5007-9906); <sup>c</sup> [orcid.org/0009-0001-9153-3712](https://orcid.org/0009-0001-9153-3712);

<sup>d</sup> [orcid.org/0009-0001-1959-8677](https://orcid.org/0009-0001-1959-8677); <sup>e</sup> [orcid.org/0000-0003-1807-1088](https://orcid.org/0000-0003-1807-1088)

DOI: <http://dx.doi.org/10.17515/resm2024.208me0305rs>

Res. Eng. Struct. Mat. Vol. 11 Iss. 1 (2025) 179-197

the structural and chemical properties of composites requires comprehensive investigation.

**Effect of Fiber Length on FTIR Analysis.** Fourier Transform Infrared Spectroscopy (FTIR) serves as a powerful tool for analyzing the chemical composition and molecular structure of materials [12]. Literature studies suggest that varying fiber lengths can influence the FTIR spectra of composite materials [13]. Rattan fibers, with their distinct chemical composition and arrangement, may exhibit nuanced spectral signatures that elucidate their role in composite structures [14].

**Impact on Macro and Microstructure.** Macro and microstructural characteristics play pivotal roles in determining the mechanical behavior and performance of composite materials [15]. The arrangement and alignment of fibers, influenced by their length, significantly impacts structural integrity and overall properties. Investigations into the macro and microstructure provide insights into the interfacial interactions between fibers and matrix, thereby facilitating the optimization of composite design and fabrication processes [16].

Despite the evident significance of studying the effects of fiber length, particularly rattan fibers, on FTIR analysis, macro, and microstructure, a comprehensive examination remains scarce in the existing literature. This knowledge gap underscores the need for further research to elucidate the intricate relationships between fiber characteristics and composite properties, thereby unlocking the full potential of rattan fibers in composite applications [17]. Fiber concrete exhibits notable resistance to cracking, attributed to the control of small cracks induced by factors like drying, temperature fluctuations, or structural loads [18]. Its application is prevalent in earthquake-resistant construction, as fibers mitigate vibrations, averting severe structural damage during seismic events [19]. Certain fiber types, like polypropylene, offer increased strength without a significant weight increase, facilitating material transportation and manipulation [20]. Moreover, fibers such as glass or polymer variants provide corrosion resistance, enhancing durability in aggressive environments [21].

The utilization of composite concrete offers extensive design flexibility, permitting intricate architectural designs [22]. Indonesia, endowed with extensive forest resources covering over half of its territory, notably produces rattan, prized for its lightweight nature and exceptional tensile strength, [23]. Incorporating rattan into concrete holds promise for enhancing flexibility and durability in both compressive and tensile strength. Rattan fiber, commonly integrated into concrete mixtures, is recognized as 'micro reinforced concrete' or 'fiber concrete' (FC) [24]. The inclusion of rattan fiber reinforces concrete, reducing cracks induced by shrinkage or temperature changes and enhancing resistance to environmental and chemical pollutants [25]. Furthermore, rattan fibers improve concrete's tensile strength, elasticity, and resistance to vibrations and earthquakes, thereby preventing structural damage. They also increase bending strength, rendering concrete more resilient to loads and deformations while reducing overall structure weight, consequently conserving energy during construction and transportation processes [26,27].

The length of fibers significantly influences concrete's performance, impacting aspects like tensile strength, crack resistance, and durability. Short fibers are adept at controlling micro-cracking, while long fibers span larger cracks, collectively enhancing concrete's durability against dynamic loads [28]. Scanning Electron Microscope (SEM) and Energy Dispersive X-ray Spectroscopy (EDS) analyses offer insights into fiber distribution, chemical composition, and interaction with concrete matrices, aiding in evaluating mechanical performance and guiding concrete formulation improvements [29-33]. Additionally, Fourier Transform Infrared Spectroscopy (FTIR) facilitates the identification

of concrete components, quality assessment, and pollution monitoring, crucial for optimizing composite concrete performance [34]. By varying fiber lengths, the study aims to enhance mechanical properties, targeting increased strength, ductility, and crack resistance, aligning with engineering specifications for superior structural performance [35].

In the study, we will explore the influence of fiber length variations, particularly rattan fibers, on various structural aspects of concrete, including FTIR (Fourier Transform Infrared Spectroscopy) analysis, macrostructure, and microstructure. Rattan fibers have become an attractive additive in concrete, but the influence of fiber length on the mechanical properties and structure of concrete is still not fully understood. By combining FTIR techniques with macro- and microstructural analysis, this study aims to provide in-depth insights into how rattan fiber length affects the chemical and physical characteristics of concrete, as well as how it relates to its mechanical performance. One of the novelties offered by this article compared to previous ones is the focus on the influence of variations in rattan fiber length on the behavior of concrete microstructure. The article not only covers the characterization of the mechanical properties of concrete with fiber additions but also examines how the distribution of fibers within the concrete matrix and the overall structure change with varying fiber lengths. This provides a deeper understanding of how the micro composition of concrete reacts to changes in fiber length.

The novelty discovered in this study lies in the observation of maximum compressive strength in concrete mixes utilizing a fiber length of 30 mm. Typically, prior research has shown that the highest compressive strength was achieved when fibers with lengths ranging from 2 to 2.5 mm were used, as documented by [36]. Additionally, this study presents a novel finding regarding the emergence of compound functional groups, with distinctions between non-fiber concrete and rattan fiber concrete. The incorporation of clam shell ash at a 4% dosage resulted in a significant enhancement of compressive strength. Despite the relatively low cement content in the samples, a substantial increase in compressive strength was achieved through the combination of 30 mm rattan fibers and a 4% addition of clam shell ash.

## **2. Materials and Testing Method**

### **2.1. Materials**

Materials used to make normal-quality concrete include Portland Cement Composite (PCC), coarse aggregate (natural stone), fine aggregate (sand), shell powder, rattan fiber, and water. The cement chosen for this study is PCC cement. Laboratory examination of this cement will not be carried out because it adheres to standards. Visual inspection will only be done on the cement bag to ensure there is no damage such as tears and no hard lumps present. Portland cement composite is a mixture of materials consisting of Portland cement and other additives such as fillers, additives, or fibers to improve the performance of concrete.

The Chemical and Physical Properties of Portland Cement Composite are as follows. One of the main properties of Portland cement is its ability to react with water, forming strong hydration. This hydration process produces products such as calcium silicate hydrate (CSH) and calcium hydroxide (CH), which give strength and hardness to concrete. The chemical composition of Portland cement is mainly composed of cement clinker, which contains tricalcium silicate ( $C_3S$ ), dicalcium silicate ( $C_2S$ ), tricalcium aluminate ( $C_3A$ ), and tetra calcium alumina ferrite ( $C_4AF$ ). The relative proportions of each of these minerals can affect the performance and properties of the resulting concrete. Portland cement composites generally contain silica, which plays an important role in forming CSH during the hydration process. Silica can also increase concrete's resistance to corrosion and

chemical attack. Portland cement composite also contains an additive, pozzolan. In the past, PCC was known as Portland Pozzolan Cement (PPC); this type of cement is also referred to as Type II cement [37].

Portland cement has a relatively high density, ranging from 3.10 to 3.25 g/cm<sup>3</sup>, depending on the composition and manufacturing process. Portland cement composite exhibits a hardness that is not excessively high when compared to Type I cement or Portland Cement (PC) after the hydration process is complete, yet it provides the mechanical strength necessary for construction applications. The optimum hardness period of PCC cement (Type II cement) is slower compared to PC cement (Type I cement). Concrete made from Portland cement composite tends to have varying porosity, depending on the composition of the mixture and the casting method [38]. This porosity can affect the physical and chemical properties of concrete, such as resistance to chemical attack and water permeability.

Clam shell ash, a common additive in concrete production, has varied physical and chemical traits. It typically presents as fine powder with diverse particle sizes based on production methods. Its low density facilitates even distribution within concrete mixtures. The ash's porous nature enhances concrete permeability and moisture absorption. Rich in calcium carbonate, derived from shellfish, it may contain other minerals. Its reactive properties influence cement hydration, fostering additional hydration products for concrete enhancement. The ash's calcium carbonate content can elevate concrete pH, impacting its chemical behavior. Table 1 details clam shell ash's chemical composition.

Table 1. Chemical composition of CSA [39]

| Oxides  | SiO <sub>2</sub> | Al <sub>2</sub> O <sub>3</sub> | Fe <sub>2</sub> O <sub>3</sub> | CaO   | MgO  | SO <sub>3</sub> | K <sub>2</sub> O | Na <sub>2</sub> O | P <sub>2</sub> O <sub>5</sub> | Cl   | Sr   | LOI  |
|---------|------------------|--------------------------------|--------------------------------|-------|------|-----------------|------------------|-------------------|-------------------------------|------|------|------|
| CSA (%) | 6.95             | 2.59                           | 2.40                           | 81.60 | 3.07 | 1.20            | 0.30             | 0.00              | 0.55                          | 0.20 | 0.50 | 0.77 |

Coarse aggregates derived from natural stone and fine aggregates derived from sand will be sourced from the KRUENG Nagan River, Nagan Raya Regency. Inspection of coarse aggregate (natural stone) and fine aggregate (sand) as raw materials for concrete requires an examination of physical properties to meet planned standards. This examination includes aggregate properties such as specific gravity, absorption, bulk density, and sieve analysis.

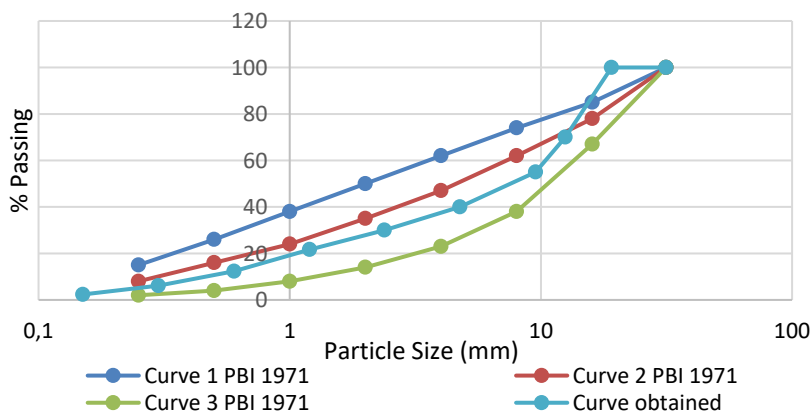


Fig. 1. Particle size distribution of aggregates



The shells used will be obtained from UJONG BAROH Village, Johan PAHLAWAN District, West Aceh Regency. The next step involves cleaning and drying the shells, after which they will be crushed until they reach a powder form with a size that can pass through sieve number 200. Figure 1 shows the granular gradient used in this study. The rattan fiber to be used will be sourced from the SIEMEULUE Regency area. After obtaining the rattan, the material will undergo a drying process to reduce water content. Next, the rattan will be cut into short segments and then split to obtain fiber strands with a thickness of about  $\pm 1$  mm. Afterward, the fibers will be cut to the planned lengths of 20 mm, 30 mm, and 40 mm. Figure 1 shows the rattan fiber material used in this study. The length of rattan fiber mixed into fresh concrete has different lengths, namely 20 mm, 30mm and 40 mm with an average diameter of 1 - 2 mm.



Fig. 2. (a) Rattan fiber, (b) clam shell ash

Shell ash is a solid remnant resulting from the burning of clam shells. The chemical properties of clam shell ash may vary depending on the type of shellfish used and the combustion process applied. Here are some common chemical properties of clam shell ash: Mineral Content: Shell ash generally contains minerals such as calcium carbonate ( $\text{CaCO}_3$ ) which is the main component of clam shells. In addition, shell ash can also contain small amounts of other minerals such as silica ( $\text{SiO}_2$ ), alumina ( $\text{Al}_2\text{O}_3$ ), and iron oxide ( $\text{Fe}_2\text{O}_3$ ). Calcium oxide ( $\text{CaO}$ ) is the main component produced from the burning of calcium carbonate in the shell of the shell. The  $\text{CaO}$  content in the shell ash of the shells can contribute to the hydraulic binding properties in the concrete mixture. Silica Content, some types of shell ash also contain silica ( $\text{SiO}_2$ ), which is a common component in pozzolanic materials. Silica in the ash of clam shells can provide pozzolanic reactivity, which can increase the strength of concrete. The chemical properties of shell ash are also affected by the carbonate content that remains in the shell of the shell that has not yet fully burned. This residual carbonate can affect the chemical properties and reactivity of shell ash shells in the concrete mixture. Heavy Metal Content although in small amounts, clamshell ash can also contain heavy metals such as lead ( $\text{Pb}$ ), cadmium ( $\text{Cd}$ ), and mercury ( $\text{Hg}$ ) that can affect the environment and human health if not managed properly. An understanding of the chemical properties of shellfish ash is important in its use as an additive in concrete mixtures. By understanding the chemical composition of clam shell ash, engineers can design optimal concrete mixtures by improving the performance and durability of concrete and minimizing negative impacts on the environment and human health.

In the study, to obtain the gradation value of the aggregate, it was obtained from sieve analysis data which was carried out by filtering the aggregate using a set sieve / sieve. Data obtained from sieve analysis is used to see the granular arrangement of aggregates used in concrete mixtures. The results of the calculation of sieve analysis and Fineness Modulus can be seen in Table 2.

Table 2. The value of the modulus fineness (FM) of the aggregate.

| No. | Type of Aggregates         | Modulus Fineness | Reference |
|-----|----------------------------|------------------|-----------|
|     |                            | FM (%)           | ASTM      |
| 1   | Coarse Aggregate (8-12 mm) | 5.983            | 5.5 – 8.5 |
| 2   | Fine Sand (0-2 mm)         | 3.1              | 2.2 – 3.1 |

From Table 2, the calculation of the value of Fineness Modulus against coarse aggregate is 5.983%. The Fineness Modulus value of coarse aggregate (coarse aggregate) meets ASTM requirements, which ranges from 5.5 - 8.5%. While the calculation of the Fineness Modulus value for fine sand, which is 3.1%, has met ASTM [26] requirements, which ranges from 2.2 - 3.1%.

### 2.2. Mix Design

This research will use a concrete mixture with a plan quality of 20 MPa. The concrete mix planning method refers to the method issued by the American Concrete Institute, [40]. The standard specimen to be used is cylindrical with a diameter of 15 cm and a height of 30 cm, with a maximum aggregate diameter of 19 mm. The planning process for a 20 MPa concrete mix starts with determining the slump test value, followed by calculating water quantity based on slump test and maximum aggregate. Then, the Cement Water Factor (w/c) is determined for concrete quality. Cement weight is found by subtracting pre-calculated water amount from w/c. Coarse aggregate amount is calculated based on maximum aggregate diameter and fine aggregate's fineness modulus. Fine aggregate quantity is determined from total concrete weight minus water, cement, and coarse aggregate. The study focuses on comparing concrete non fiber (CNF) with concrete containing rattan fiber (RF) of 20 mm, 30 mm, and 40 mm lengths, each at 0.5% fiber ratio, and 4% clam shell ash added to cement weight.

Table 3. Material composition for each test specimen variation

| No | Material            | 24 Specimens |          |          |          | Total  | Unit |
|----|---------------------|--------------|----------|----------|----------|--------|------|
|    |                     | CNF          | RF 20 mm | RF 30 mm | RF 40 mm |        |      |
| 1  | Cement              | 14.9         | 14.9     | 14.9     | 14.9     | 59.7   | Kg   |
| 2  | Water               | 7.7          | 7.7      | 7.7      | 7.7      | 30.966 | Kg   |
| 3  | Coarse Aggregate    | 41.4         | 41.4     | 41.4     | 41.4     | 165.8  | Kg   |
| 4  | Fine Aggregate      | 26.2         | 26.2     | 26.2     | 26.2     | 105.1  | Kg   |
| 5  | Clam Shell Ash (4%) | 0.0          | 0.6      | 0.6      | 0.6      | 1.8    | Kg   |
| 6  | Rattan Fibre (0,5%) | 0.0          | 75.0     | 75.0     | 75.0     | 225.0  | gr   |

The implementation of this research will be made a total of 24 test objects with a cylindrical shape (Ø 15 cm, T = 30 cm), the test specimens will be carried out by

distinguishing the length of rattan fiber as an added material, namely concrete without fiber, fiber concrete 20 mm, fiber concrete 30 mm, and fiber concrete 40 mm. The mix design is for 24 test specimens, there are 4 specimen's variations, namely CNF, CRF 20mm, CRF 30mm and CRF 40 mm, each variant is made with 3 tests for compressive tests and 3 pieces for concrete split tensile strength, the total number of test objects is all 24 pieces.

### **2.3. Compressive Strength**

The concrete compressive strength testing scheme (concrete cylinder), and to carry out concrete compressive strength testing will follow several stages as follows. The specimen will be placed on the press centrally in a vertical position. The press will be run with constant load additions ranging from 2 to 4 kg/cm<sup>2</sup> per second; Loading will be carried out until the specimen is destroyed, and the maximum load that occurs during the specimen inspection is recorded, [44,45].

### **2.4. Scanning Electron Microscope-EDS (SEM-EDS)**

SEM testing, among other techniques, can be utilized to ascertain information about surface properties, particle shape and size, as well as particle distribution and arrangement. Our scanning electron microscope (SEM) equipped with energy-dispersive X-ray spectroscopy (EDS) (ZEISS EVOMA10) facilitates such testing [41]. SEM-EDS (Scanning Electron Microscope-Energy Dispersive X-ray Spectroscopy) is a test equipment used to test material samples, including composite concrete samples.

Here are some of the uses of the SEM-EDS test equipment in testing composite concrete samples. Surface Morphology Analysis: SEM offers high-resolution views of composite concrete surface structures, aiding in crack, porosity, and phase distribution identification. Integrated with SEM, EDS enables chemical element identification and mapping on sample surfaces, facilitating the understanding of chemical element distribution and phase distribution. EDS permits the chemical composition analysis of composite concrete samples, ensuring material quality and performance. SEM-EDS aids in identifying material phases in composite concrete samples, enhancing understanding of material microstructure and properties. Thus, SEM-EDS significantly contributes to the characterization of composite concrete, enhancing understanding of its structure, composition, and properties, [1,8,9, 10,18,29,30,42]

### **2.5. FTIR**

FT-IR is used to determine functional groups in materials through the study of molecular interactions, which are demonstrated by the transmission of infrared light in various forms. This study focuses on the effect of treatment on the functional groups of composite concrete and fibers, as well as differences in the expression of functional groups in conventional concrete, [31-33]. The specimens used in the Fourier Transform Infrared Spectroscopy (FTIR) test will be taken from cylindrical specimens with additional variations of rattan fiber and shell powder that have been used in compressive strength and tensile strength tests, in the form of small flakes. The application of FTIR Analysis for fiber concrete testing involves sample preparation with KBr pellet making. The sample is refined with mortar to homogenize it. A small amount of sample is then placed into the barn, and KBr powder is added in a ratio of 1:10. The sample and KBr powder are ground until homogeneous, after which the mixture is inserted into the KBr pellet dies. The KBr pellet dies are then closed and pressed using a mini-Press KBr pellet. The formed KBr pellet is inserted into the sample holder in the FTIR. The FTIR test scheme can be seen in Figure 3., and to carry out the FTIR test, several stages must be followed as follows: Concrete samples are cleaned from contaminants or dust that may affect test results. The FTIR Spectrometer is turned on, and the system is allowed to reach stable operating conditions, ensuring that all optical components and instrument detectors are in good condition. The

concrete sample is placed on the IR (infrared) glass, ensuring that it is flat on the IR glass to produce accurate test results. FTIR spectrum measurements are then performed by directing infrared light onto the concrete sample. After the measurement is complete, the FTIR analysis software will identify the chemicals and main components in the concrete sample.

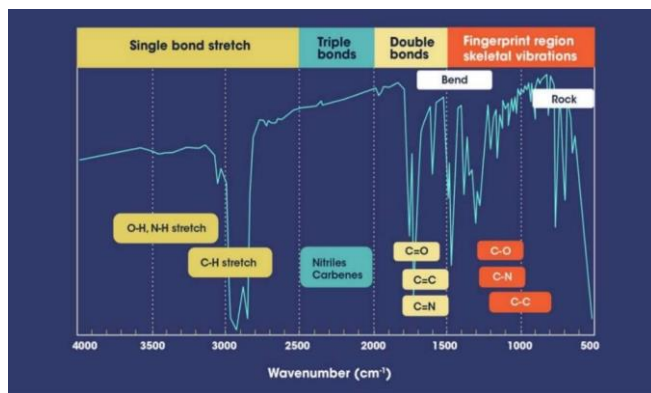


Fig. 3. Infrared absorption area, [34]

### 3. Results and Discussion

#### 3.1 Sump test

In normal concrete, slump testing is carried out which aims to determine the viscosity of the concrete mixture. This factor is due to the addition of fiber to the concrete mixture.

The data obtained from the results of the slump test in each casting of each fiber variation are shown in Figure 2. From these data, the value of the concrete mortar slump ranges from 7.5 cm – 10 cm, which means that it is in accordance with the height of the planned slump.

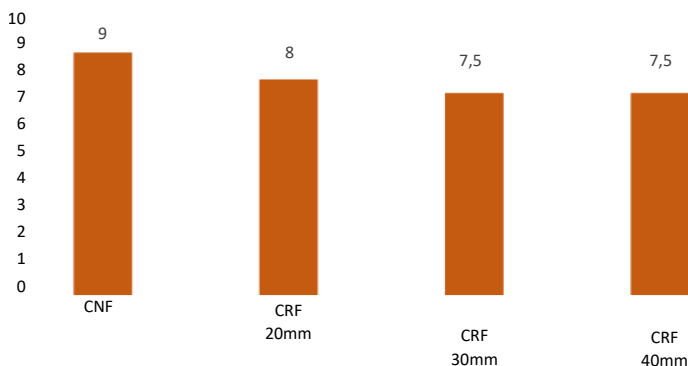


Fig. 4. Slump test results graph

Fig. 4 shows that the shape of the slump has a difference. In this study, the resulting high slump test showed that the value of the slump value was influenced by the percentage of fiber mixed into the concrete mortar. The graph below shows that the lowest slump values are in 30 mm and 40 mm 2 rattan fibers, while in normal concrete without the addition of rattan fibers and shell ash produces the highest slump values of 9 cm. This shows that the higher the length of rattan fiber used, the higher the water absorption of concrete.

### 3.2 Strength of Concrete

After the specimen is removed from the soaking bath following the treatment process, tests can be performed as shown in Fig. 5. Then, the specimen is left for 24 hours until it reaches a surface dry state. After that, the specimens are weighed to determine the weight per specimen. Next, compressive strength testing is performed on the test specimen using a pressure testing machine. Normal concrete compressive strength testing is carried out according to the planned life, which is 28 days concrete life. Data on concrete compressive strength test results at 28 days of age, compressive strength graphs can be seen in Figure 4.

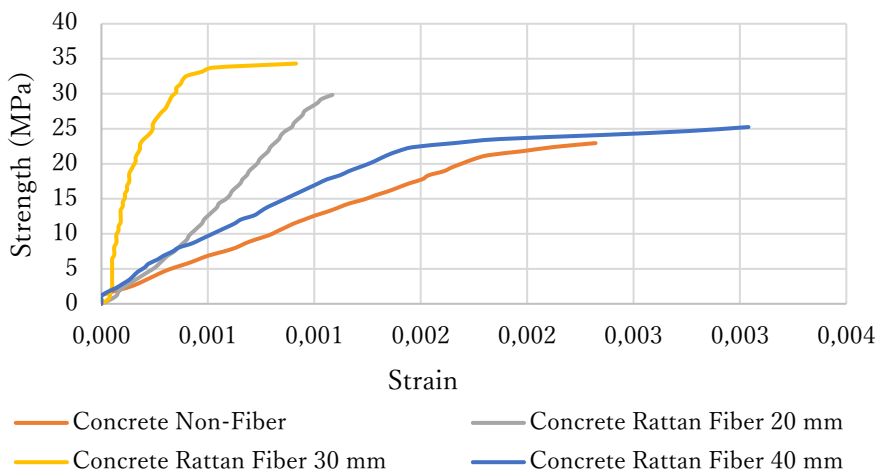


Fig. 6. Stress-strain relationship of rattan fiber concrete with variations in fiber length

Based on Figure 6, it can be observed that composite concrete using a 40 mm fiber length exhibits greater deformation compared to both non-fiber concrete and fiber concrete variations with 20mm and 30mm fiber lengths. This indicates that fiber concrete with a length of 40mm displays more ductility compared to fiber concrete with shorter fiber lengths, despite the compressive strength of the former being 40mm lower than that of the latter. According to Figure 6, the obtained compressive strengths are as follows: CNF 22.120MPa, CRF 20mm 23.488MPa, CRF 30mm 31.011MPa, and CRF 40mm 19.085MPa. This suggests that the optimum strength of fiber concrete is achieved with a 30mm CRF fiber length.

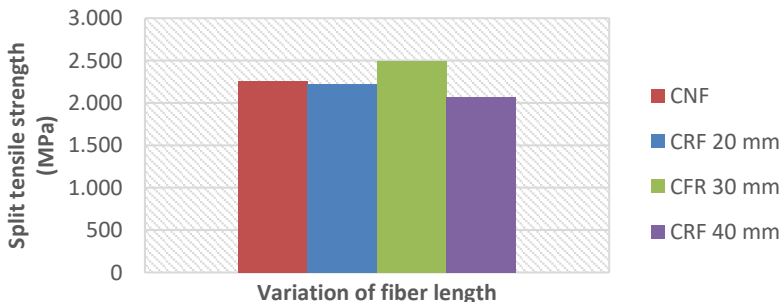


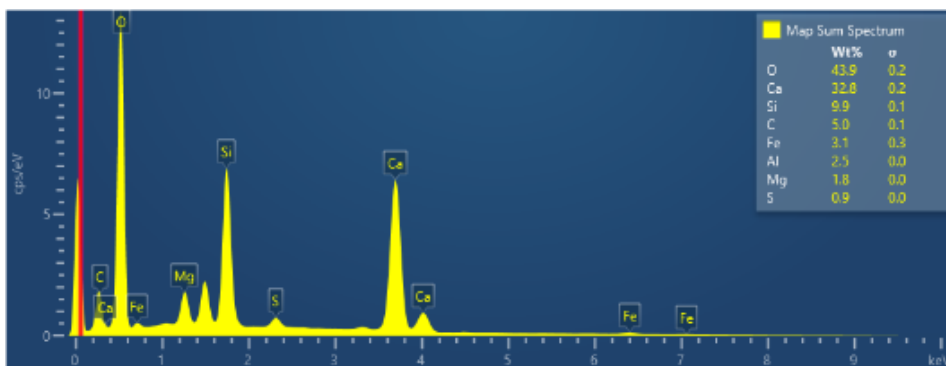
Fig. 7. Split tensile strength of CRF with variations in fiber length

In Fig. 7 above, the results of tensile strength tests conducted on fiber concrete at the age of 28 days are presented. Tensile strength is a measure obtained by breaking a concrete cylinder into two parts with a force applied perpendicular to its long axis. The tensile strength of each specimen is measured in units of  $N/mm^2$ . Additionally, there is a column showing the increase in tensile strength from one specimen type to another, calculated in units of  $N/mm^2$  and as a percentage. Here is a discussion of the tensile strength data provided. CNF (Concrete Non-Fiber), Tensile strength  $2.265N/mm^2$ . No change in strength compared to CNF (0%). CRF 20 mm (Concrete with 20 mm rattan Fiber), Tensile strength  $2.218 N/mm^2$ . Decrease of -2.1% compared to CNF. CRF 30 mm (Concrete with 30 mm Steel Fiber), Tensile strength  $2.501N/mm^2$ . Increase of 9.4% compared to CNF. CRF 40 mm (Concrete with 40 mm Steel Fiber): Tensile strength  $2.076N/mm^2$ . Decrease of -9.1% compared to CNF. Conclusion: Adding steel fibers to concrete can increase or decrease tensile strength depending on fiber length and material characteristics. 30 mm steel fibers significantly increase tensile strength, while longer or shorter fibers do not yield similar results. From the discussion above, it can be concluded that the addition of steel fibers in concrete can increase or even reduce tensile strength depending on the length of the fibers and their material characteristics. In these cases, the addition of 30 mm steel fibers results in a significant increase in tensile strength, while longer or shorter fiber lengths do not yield equally good results.

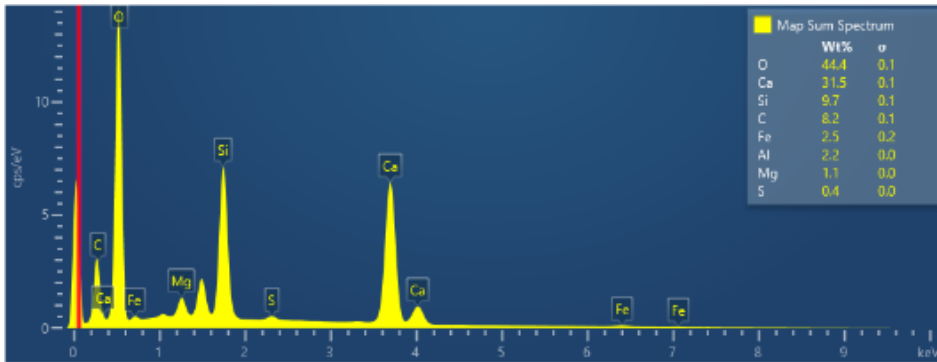
### 3.3 SEM-EDS Analysis

The findings of the study suggest that incorporating rattan fibers into concrete can result in either an increase or decrease in tensile strength, depending on the fiber length and material characteristics. Specifically, the inclusion of 30 mm rattan fibers notably enhances tensile strength, while longer or shorter fiber lengths do not produce similarly favorable outcomes. Furthermore, chemical composition analysis of the concrete reveal’s variations upon the addition of rattan fibers, indicating changes in elemental composition. Morphological observations conducted using Scanning Electron Microscopy (SEM) offer detailed insights into the microscopic structure of concrete surfaces, both with and without fibers.

Fig. 8.a shows the results of the chemical composition of sample (a) non-fiber concrete. The data provided has the weight percentage (Wt.%) of the various elements in the sample. Where describe the result as follows. Chemical analysis shows that Oxygen (O) has a weight percentage of 43.9%, Calcium (Ca) is 32.8%, Silicon (Si) has two entries, namely 9.9% and 0.9%, Carbon (C) is 5.0%, Iron (Fe) is 3.1%, Aluminum (Al) is 2.5%, and Magnesium (Mg) is 1.8%. This chemical composition indicates that Oxygen, Calcium, and Silicon are the most dominant elements in non-fiber concrete samples.



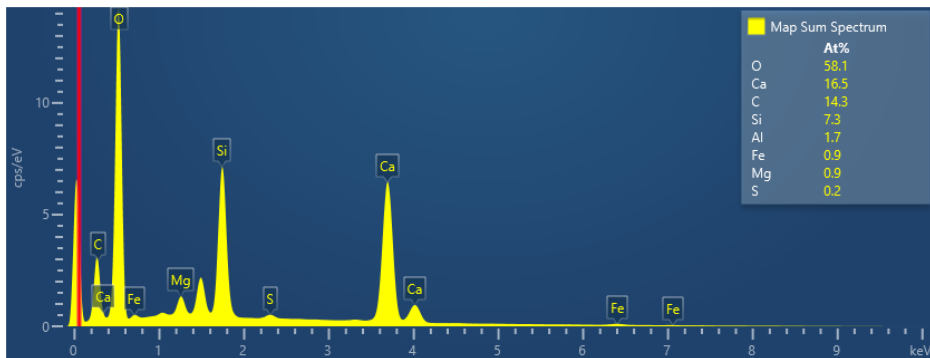
(a) Non-Fiber concrete



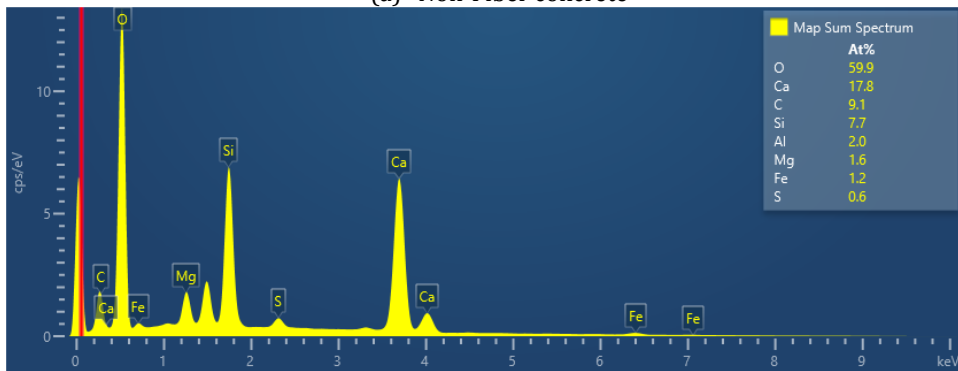
(b) Fiber concrete

Fig. 8. SEM-EDS test results of concrete base the weight percentage (Wt.%)

Figure 8.b illustrates the distribution of chemical elements in a concrete specimen with rattan fibers, shown in weight percentages. Oxygen dominates at 43.9%, followed by Calcium at 32.8%, Silicon at 9.9%, Carbon at 5.0%, Iron at 3.1%, Aluminum at 2.5%, Magnesium at 1.8%, and Sulphur at 0.9%. These proportions suggest the presence of oxide, calcium-rich, silicate, organic, iron-containing, aluminum-rich, magnesium-containing, and Sulphur-containing compounds, respectively. This data provides insight into the sample's chemical composition, aiding further analysis to identify specific minerals or compounds.



(a) Non-Fiber concrete

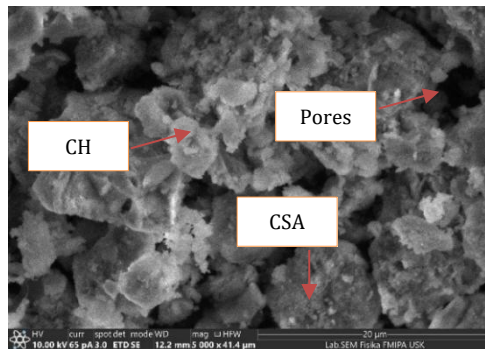


(b) Fiber concrete

Fig. 9. SEM-EDS test results of non-fiber concrete (At%).

Fig. 9.b visualizes the percentage composition of elements in a sample. Oxygen (O) dominates with 59.9%, followed by Calcium (Ca) at 17.8%, Carbon (C) at 9.1%, Silicon (Si)

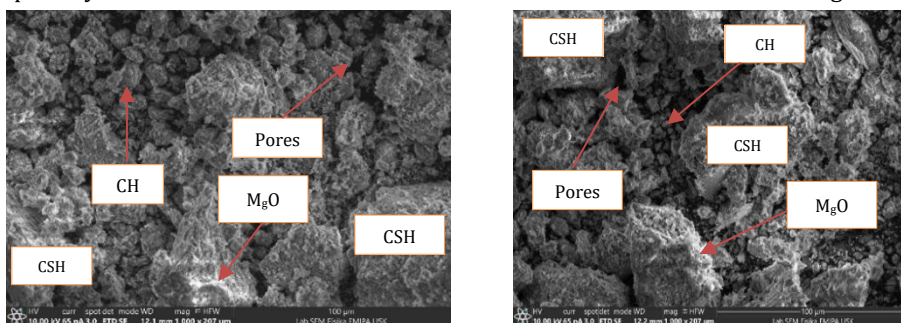
at 7.7%, Aluminum (Al) at 2.0%, Magnesium (Mg) at 1.6%, Iron (Fe) at 1.2%, and Sulphur (S) at 0.6%. The diagram shows the relative proportions of each element with sectors proportional to their percentage composition. Figure 9.b depicts composition Map spectra, showing the relative proportions of chemical elements in a sample. Data highlights the percentages of elements: Oxygen (O): 43.9%, Calcium (Ca): 32.8%, Silicon (Si): 9.9%, Carbon (C): 5.0%, Iron (Fe): 3.1%, Aluminum (Al): 2.5%, Magnesium (Mg): 1.8%, Sulphur (S): 0.9%. These visuals provide insight into element distribution, with Oxygen (O) being the highest, followed by Calcium (Ca), and so on. Figure 10 shows the difference between CNF concrete and fiber concrete with the addition of clam shell ash (CSA), the amount of element C (Carbon) is higher in concrete with the addition of CSA. In Figure 9, fiber concrete has a higher oxygen and carbon value compared to non-fiber concrete.



Fiber concrete

Fig. 10. Micromorphological form of concrete by SEM

Fig. 10 shows the hydration results of cement. There are  $MgO$ , CSA, CH, and micropores measuring 5 microns. The fiber concrete microstructure with quite a lot of pores marked in black in the figure. There is a matrix shape of cement and CSA and sand, but the number of white fibers is not too visible. Calcium Silicate Hydrate (CSH), This compound is formed during the hydration process of Portland cement, which is the main component of concrete. CSH provides strength and durability to concrete. Also formed during hydration of Portland cement, CH is a byproduct of chemical reactions and contributes to the performance of concrete. Magnesium Oxide ( $MgO$ ), Also present in some composite concrete mixtures,  $MgO$  can affect the chemical and physical properties of concrete, especially in the context of resistance to chemical attack and mechanical strength.



(a) Non-Fiber concrete

(b) Fiber concrete

Fig. 11. Micromorphological form of CNF structure (a), CRF (b)

Fig. 11.a shows CH compounds that occur due to imperfect cement hydration process. Fig. 10 and 11 shows SEM analysis revealing the surface structure of concrete materials on a microscopic scale. With high resolution, SEM scanning enables detailed observation of



surface structures such as pores, cracks, and aggregates, providing important insights into the quality and strength of concrete. The microstructure of non-fiber concrete, including pore size, can be observed. Pore size and particle size in non-fiber concrete are visible through SEM analysis within the range of 20 microns. Morphological differences between non-fiber concrete and fiber concrete, especially with the addition of shell ash, are evident. In Figure 11, rattan fibers are shown attached to the concrete matrix, contributing to strong tensile strength in concrete. Concrete with rattan fiber exhibits greater tensile strength compared to other concrete variations. In Figures 11.a and 11.b, shows the difference in crystal shape between non-fiber concrete and fiber concrete. In fiber concrete with added shell ash, the distance between particles is smaller compared to non-fiber concrete. The denser condition of fiber concrete to which shell ash is added is visibly apparent on the surface than in the SEM Image. Figure 11 depict Morphological Analysis at magnifications of 1000, and Fig. 10 5000 times, respectively. SEM analysis unveils the surface structure conditions of concrete materials on a microscopic scale. With high resolution, SEM scanning facilitates detailed observations of surface structures such as pores, cracks, and aggregates, offering crucial insights into the quality and strength of concrete. Microscopic conditions of non-fiber concrete structures, including the cement paste matrix and cement-sand matrix, can be observed. Pore sizes and elements in non-fiber concrete become visible through SEM analysis in the 100-micron range. In Figure 9.a, many small grains seem to separate from each other, possibly due to the addition of shell ash in concrete, as indicated in Figure 9.b. The SEM analysis in Figure 8.b reveals the surface characteristics of the fiber concrete material at the microscopic level, including pore size. SEM analysis can detect pore and particle sizes in non-fiber concrete up to 20 microns. In the figure, smaller pores are visible compared to non-fiber concrete, suggesting that fiber material may be filling these pores in concrete.

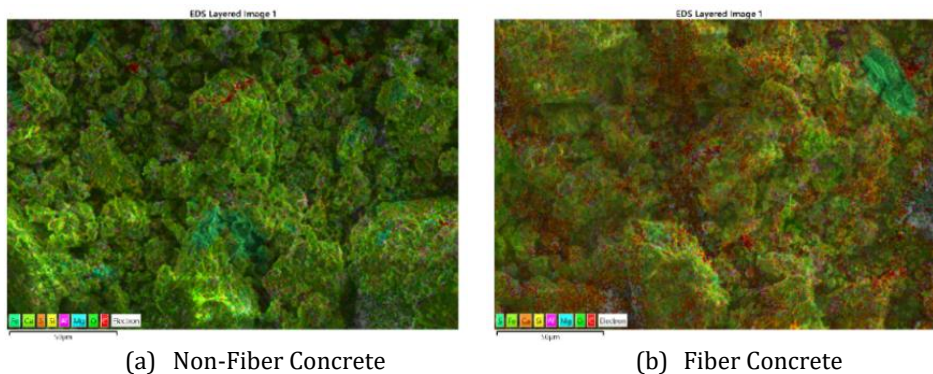


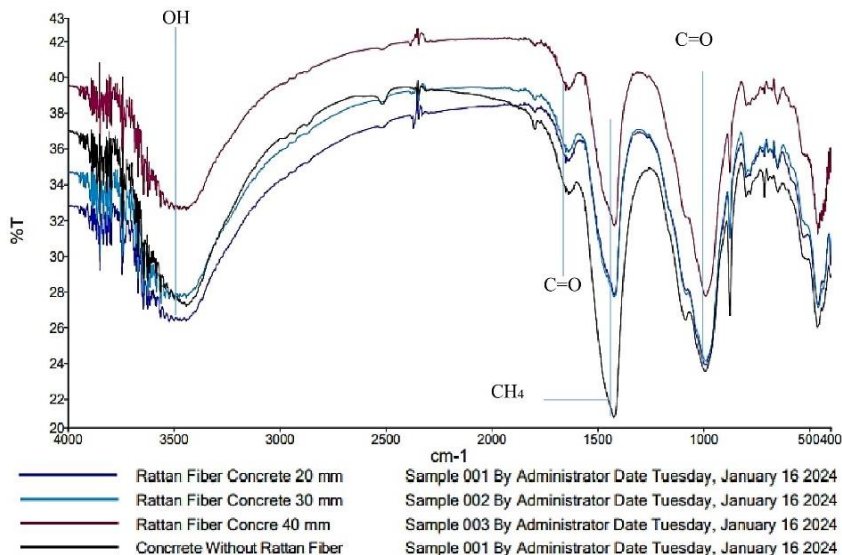
Fig. 12. The form of distribution of chemical elements in concrete

Based on Fig.9, and Figure 12.a, the chemical elements in non-fiber concrete are dispersed as follows: Oxygen (O): 59.9%, mainly found in oxide compounds like Calcium Oxide and SiO<sub>2</sub>. Calcium (Ca): 17.8%, associated with compounds like calcium silicate and calcium hydroxide. Carbon (C): 9.1%, typically in carbonate or organic form. Silicon (Si): 7.7%, mainly in silicate compounds like SiO<sub>2</sub>. Aluminum (Al): 2.0%, found in compounds like aluminum oxide. Magnesium (Mg): 1.6%, present in various minerals in aggregates. Iron (Fe): 1.2%, derived from compounds like iron oxide. Sulphur (S): 0.6%, likely in sulphate form. Figure 12 shows the distribution of chemical elements in non-fiber concrete visually, while Figures 12.a and 12.b provide further details. Additionally, in Figure 6.b, representing fiber concrete with clam shell ash, Carbon (C) distribution surpasses that of non-fiber concrete. Figure 4.b illustrates the spectra of composition maps, indicating the proportions of chemical elements within a given sample. The data showcases the percentages of elements as follows: Oxygen (O) constitutes 43.9%, Calcium (Ca) comprises

32.8%, Silicon (Si) accounts for 9.9%, Carbon (C) represents 5.0%, Iron (Fe) constitutes 3.1%, Aluminum (Al) contributes 2.5%, Magnesium (Mg) makes up 1.8%, and Sulphur (S) is at 0.9%. These visuals offer insights into the distribution of elements, with Oxygen (O) being the most abundant, followed by Calcium (Ca), and so forth.

### 3.4 FTIR Result

Based on Fig. 13 and Table 3, FTIR data from various types of concrete with and without rattan fiber, differences in absorption patterns indicate variations in the type and concentration of compounds present in the concrete. For instance, in concrete containing 20 mm rattan fiber, an absorption peak at 3.525.54 cm<sup>-1</sup> suggests the stretching of O-H bonds, typically associated with the presence of carboxylic acids. Conversely, in concrete without rattan fibers, an absorption peak at 3.590.86 cm<sup>-1</sup> indicates the presence of O-H stretch bonds, potentially suggesting the existence of phenols or alcohols.



| Sample Name   | Description                                    | Quality Checks  |
|---|--|---|
| Rattan Fiber Concrete 20 mm – 40 mm & Concrete Without Rattan Fiber | By Administrator Date Tuesday, January 16 2024 | The Quality Checks give rise to multiple warnings for the sample. |

Fig. 13. Compound groups in concrete

Table 4. Test results of functional groups of rattan fiber concrete compounds

| Concentrate (%) | Absorption Area (cm <sup>-1</sup> ) | Compound Type           | Bounds And Types of Functional Group | Intensity  |
|-----------------|-------------------------------------|-------------------------|--------------------------------------|------------|
| CRF 20 mm       | 3,525.54                            | carboxylic acid monomer | O-H Stretching                       | Medium     |
|                 | 1,651.00                            | Alkene                  | C=O Stretching                       | Capricious |
|                 | 1,420.00                            | Alkane                  | CH <sub>4</sub> Bending              | Strong     |
|                 | 894.38                              | Alkene                  | C=O Stretching                       | Strong     |
| CRF 30 mm       | 3,590.91                            | phenol, alcohol monomer | O-H Stretching                       | Capricious |
|                 | 3,500.08                            | carboxylic acid monomer | O-H Stretching                       | Medium     |

|           |          |                               |                         |            |
|-----------|----------|-------------------------------|-------------------------|------------|
|           | 1,638.24 | Alkene                        | C=O Stretching          | Capricious |
|           | 1,420.12 | Alkane                        | CH <sub>4</sub> Bending | Strong     |
|           | 988.35   | Alkene                        | C=O Stretching          | Strong     |
| CRF 40 mm | 3,564.10 | hydrogen bond alcohol, phenol | O-H Stretching          | Capricious |
|           | 1,650.97 | Alkene                        | C=O Stretching          | Capricious |
|           | 1,420.12 | Alkane                        | CH <sub>4</sub> Bending | Strong     |
|           | 989.03   | Alkene                        | C=O Stretching          | Strong     |
| CNF       | 3,590.86 | hydrogen bond alcohol, phenol | O-H Stretching          | Capricious |
|           | 1,637.55 | Alkene                        | C=O Stretching          | Capricious |
|           | 1,424.42 | Alkane                        | CH <sub>4</sub> Bending | Strong     |
|           | 992.07   | Alkene                        | C=O Stretching          | Strong     |

Based on Table 4, it can be inferred that 30mm CRF fiber concrete exhibits stronger compressive strength compared to normal concrete, as it possesses 5 bond compounds as opposed to CNF fiber concrete, which only has 4 bonding compounds. Similarly, other variations of fiber concrete exhibit only 4 compound bonds. Regarding the condition of 40 mm CRF concrete, it is anticipated to have lower compressive strength than other concrete variations due to the excessive length of the fiber, resulting in many areas of concrete being filled with fiber beyond the standard 20mm fiber length, leading to reduced compressive strength. However, it boasts advantages in tensile strength with greater deformation than other concrete variations. For a more comprehensive study, the author plans to continue the research by conducting tests on the pure bending strength of fiber concrete. The data are interpreted in Figure 13 and Table 4, all based on the guidelines in Figure 3 Infrared absorption area [34].

#### 4. Conclusions

This study presents significant findings regarding the effect of rattan fiber length variations on the mechanical properties, characterization, and microstructure of concrete. Based on the test results and discussions that have been presented, several conclusions can be drawn to provide a deeper understanding of this topic.

- First, from the results of the slump test, the addition of rattan fiber to concrete affects the slump value, where the highest slump value occurs in normal concrete without the addition of rattan fiber, while the lowest slump value occurs in concrete with the addition of 30 mm and 40 mm rattan fibers. This shows that the longer the rattan fiber used, the higher the water absorption by concrete.
- Furthermore, from the results of the compressive strength test, it was found that concrete with a fiber length of 30 mm has optimal compressive strength compared to other concrete. Despite having lower compressive strength than fibreless concrete, concrete with a fiber length of 30 mm shows a significant increase in compressive strength compared to concrete with a longer or shorter fiber length.
- Later, in terms of tensile strength, it was found that the addition of steel fibers to concrete can increase or decrease tensile strength depending on the length of the fibers and material characteristics. Steel fibers with a length of 30 mm significantly increase the tensile strength of concrete, while fibers with longer or shorter lengths do not give the same results.
- In terms of chemical characterization, composition analysis shows that the chemical composition of concrete changes with the addition of rattan fibers. Rattan fibers enrich concrete with elements such as oxygen, calcium, silicon, carbon, iron,

aluminum, magnesium, and sulfur, all of which affect the chemical properties and reactivity of concrete.

- In microstructural analysis using SEM, significant differences were found between concrete microstructures with and without rattan fibers. Rattan fibers fill the pores of concrete and improve aggregate distribution, which can affect the overall physical and mechanical properties of concrete.
- In addition, the results of FTIR analysis show that variations in the absorption patterns of the spectrum show differences in the types and concentrations of compounds present in concrete. This suggests that the addition of rattan fibers can also affect the overall chemical properties of concrete.

Based on the FTIR testing data presented, this scientific work highlights several novelties that can be a significant contribution to materials research. Here are some identifiable points of novelty:

- **Analysis of Differences in Absorption Patterns:** In the FTIR test, there are differences in absorption patterns between CRF (Concrete Rattan Fiber) fibers with lengths of 20 mm, 30 mm, and 40 mm, and CNF (Concrete non-fiber) fibers. This indicates that fiber length has a significant influence on the chemical properties of the resulting material. This diversity of absorption patterns indicates that each type of fiber has unique chemical characteristics.
- **Functional Group Identification:** FTIR data shows the presence of various functional groups detected in each type of fiber. For example, carboxylic acid monomer groups were detected in 20 mm and 30 mm CRF fibers, as well as hydrogen bond alcohol and phenol in 40 mm CRF and CNF. The determination of these functional groups provides further understanding of the chemical composition of the fibers used in this study.
- **Absorption Intensity:** The level of absorption intensity in each functional group can also provide additional insight into the quantity or concentration of each compound involved. For example, the intensity of the medium in the carboxylic acid monomer group on 20 mm CRF fibers indicates a significant concentration of these compounds in the material.
- **Comparison Between Fiber Types:** Through the analysis of FTIR data, this scientific work makes it possible to compare chemical responses between different types of fibers, such as CRF of different lengths and CNF. Differences in absorption patterns and functional groups detected between fiber types can provide valuable information about the potential uses of each fiber in specific material applications.

This research provides a deeper understanding of the effect of rattan fiber length on the mechanical properties, characterization, and microstructure of concrete. The results of this research have important implications for the development of more efficient and sustainable construction materials in the future. Therefore, for follow-up studies, it is recommended to continue the research considering aspects such as environmental durability, dimensional stability, and long-term performance of concrete with rattan fiber. Thus, greater progress can be achieved in the field of construction materials engineering.

### **Acknowledgement**

First and foremost, we extend our deepest appreciation to our supervisor, Prof. Ishak Hasan, for their invaluable guidance, continuous support, and insightful feedback throughout the duration of this study. Their expertise and encouragement have been instrumental in shaping this research and pushing it towards excellence. We are also grateful to the members of our research team, Putri ZURIATI, whose dedication, and hard work significantly contributed to the execution of experiments, data analysis, and discussions, enriching the quality of this work. Furthermore, we acknowledge the support

provided by the Teuku Umar University, including the resources, facilities, and funding that facilitated the smooth progress of this research project. We extend our appreciation to all individuals and organizations who generously helped, resources, and expertise essential for the completion of this study. I wish to express gratitude for the financial assistance provided by Internal Research Grant was funded in June 2022 by LPPM – Teuku Umar University under contract number 013/UN59.7/SPK-PPK/06, which significantly facilitated the experimental work and acquisition of necessary materials. Additionally, heartfelt thanks go to my family and friends for their constant support and understanding throughout the demanding phases of this research project. Lastly, we would like to express our heartfelt thanks to our families and friends for their unwavering support, understanding, and encouragement throughout this academic journey. Without the collective efforts and support of all mentioned above, this research would not have been possible. Thank you all for your invaluable contributions.

## References

- [1] Li Z, Zhou X, Ma H, Hou D. Advanced concrete technology. John Wiley & Sons; 2022. <https://doi.org/10.1002/9781119806219>
- [2] Setareh M, Darvas R. Concrete structures. Springer; 2007.
- [3] Zhong K, Zhou J, Zhao C, Yun K, Qi L. Effect of interfacial transition layer with CNTs on fracture toughness and failure mode of carbon fiber reinforced aluminum matrix composites. *Compos. Part Appl. Sci. Manuf.* 2022;163:107201. <https://doi.org/10.1016/j.compositesa.2022.107201>
- [4] Abou-Zeid M, et al. Control of cracking in concrete structures. *Rep ACI Comm.* 2001;224:12-16.
- [5] Paul SC, van Zijl GP, Šavija B. Effect of fibers on durability of concrete: A practical review. *Materials.* 2020;13(20):4562. <https://doi.org/10.3390/ma13204562>
- [6] Wang L, et al. The influence of fiber type and length on the cracking resistance, durability and pore structure of face slab concrete. *Constr. Build. Mater.* 2021;282:122706. <https://doi.org/10.1016/j.conbuildmat.2021.122706>
- [7] Perry JI, Walley SM. Measuring the effect of strain rate on deformation and damage in fibre-reinforced composites: A review. *J. Dyn. Behav. Mater.* 2022;8(2):178-213. <https://doi.org/10.1007/s40870-022-00331-0>
- [8] Nurazzi NM, et al. A review on natural fiber reinforced polymer composite for bullet proof and ballistic applications. *Polymers.* 2021;13(4):646. <https://doi.org/10.3390/polym13040646>
- [9] Hu YT, Ting Y, Hu JY, Hsieh SC. Techniques and methods to study functional characteristics of emulsion systems. *J. Food Drug Anal.* 2017;25(1):16-26. <https://doi.org/10.1016/j.jfda.2016.10.021>
- [10] Qu F, Li W, Dong W, Tam VW, Yu T. Durability deterioration of concrete under marine environment from material to structure: A critical review. *J. Build. Eng.* 2021;35:102074. <https://doi.org/10.1016/j.jobe.2020.102074>
- [11] Sinha S, Devnani GL. Natural fiber composites: processing, characterization, applications, and advancements. CRC Press; 2022. <https://doi.org/10.1201/9781003201724>
- [12] Fan M, Dai D, Huang B. Fourier transform infrared spectroscopy for natural fibres. *Fourier Transform-Mater. Anal.* 2012;3:45-68. <https://doi.org/10.5772/35482>
- [13] Alvarez VA, Vázquez A. Influence of fiber chemical modification procedure on the mechanical properties and water absorption of MaterBi-Y/sisal fiber composites. *Compos. Part Appl. Sci. Manuf.* 2006;37(10):1672-1680. <https://doi.org/10.1016/j.compositesa.2005.10.005>
- [14] Rogers CW. Structures of Building Design Standards: Leveraging Network Analysis to Understand Perceived Complexity [dissertation]. University of Pittsburgh; 2023.

- [15] Shaw A, Sriramula S, Gosling PD, Chryssanthopoulos MK. A critical reliability evaluation of fibre reinforced composite materials based on probabilistic micro and macro-mechanical analysis. *Compos. Part B Eng.* 2010;41(6):446-453. <https://doi.org/10.1016/j.compositesb.2010.05.005>
- [16] Feng Y, Hao H, Lu H, Chow CL, Lau D. Exploring the development and applications of sustainable natural fiber composites: A review from a nanoscale perspective. *Compos. Part B Eng.* 2024;111369. <https://doi.org/10.1016/j.compositesb.2024.111369>
- [17] Fidan I, Naikwadi V, Alkunte S, Mishra R, Tantawi K. Energy Efficiency in Additive Manufacturing: Condensed Review. *Technologies.* 2024;12(2):21. <https://doi.org/10.3390/technologies12020021>
- [18] Gebremariam HG, Taye S, Tarekegn AG. Disparity in research findings on parent concrete strength effects on recycled aggregate quality as a challenge in aggregate recycling. *Case Stud. Constr. Mater.* 2023;19. <https://doi.org/10.1016/j.cscm.2023.e02342>
- [19] Terzić A, et al. The effect of alternations in mineral additives (zeolite, bentonite, fly ash) on physico-chemical behavior of Portland cement based binders. *Constr. Build. Mater.* 2018;180:199-210. <https://doi.org/10.1016/j.conbuildmat.2018.06.007>
- [20] Nurshamila SB, Ismail H, Othman N. The effects of rattan filler loadings on properties of rattan powder-filled polypropylene composites. *BioResources.* 2012;7(4):5677-5690. <https://doi.org/10.15376/biores.7.4.5677-5690>
- [21] Fang H, Bai Y, Liu W, Qi Y, Wang J. Connections and structural applications of fibre reinforced polymer composites for civil infrastructure in aggressive environments. *Compos. Part B Eng.* 2019;164:129-143. <https://doi.org/10.1016/j.compositesb.2018.11.047>
- [22] Yusra A, et al. Effect of the Addition of Natural Fibers on the Mechanical Properties of Concrete. *E3S Web of Conferences.* EDP Sciences; 2024;01027. <https://doi.org/10.1051/e3sconf/202447601027>
- [23] Topić Popović N, Lorencin V, Strunjak-Perović I, Čož-Rakovac R. Shell waste management and utilization: Mitigating organic pollution and enhancing sustainability. *Appl. Sci.* 2023;13(1):623. <https://doi.org/10.3390/app13010623>
- [24] Kim MO, Lee MK. Strength and Microstructural Changes in Cementitious Composites Containing Waste Oyster Shell Powder. *Buildings.* 2023;13(12):3078. <https://doi.org/10.3390/buildings13123078>
- [25] Ahmad R, Hamid R, Osman SA. Physical and chemical modifications of plant fibres for reinforcement in cementitious composites. *Adv. Civ. Eng.* 2019;2019. <https://doi.org/10.1155/2019/5185806>
- [26] C on C Aggregates. Standard test method for compressive strength of cylindrical concrete specimens. *ASTM international*; 2014.
- [27] Nasional BS. SNI 03-1974-1990 Metode Pengujian Kuat Tekan Beton. *Badan Stand. Nas. Indones.*; 1990.
- [28] Waani JE, Elisabeth L. Substitusi material pozolan terhadap semen pada kinerja campuran semen. *J. Tek. Sipil.* 2017;24(3):237-245.
- [29] Durdziński PT, Dunant CF, Haha MB, Scrivener KL. A new quantification method based on SEM-EDS to assess fly ash composition and study the reaction of its individual components in hydrating cement paste. *Cem. Concr. Res.* 2015;73:111-122. <https://doi.org/10.1016/j.cemconres.2015.02.008>
- [30] Georget F, Schmatz J, Wellmann E, Matschei T. A critical catalogue of SEM-EDS multispectral maps analysis methods and their application to hydrated cementitious materials. *J. Microsc.* 2023. <https://doi.org/10.1111/jmi.13245>
- [31] Rollakanti CR, Prasad CVS, Poloju KK, Al Muharbi NMJ, Arun YV. An experimental investigation on mechanical properties of concrete by partial replacement of cement with wood ash and fine sea shell powder. *Mater. Today Proc.* 2021;43:1325-1330. <https://doi.org/10.1016/j.matpr.2020.09.164>

- [32] Hospodarova V, Singovszka E, Stevulova N. Characterization of Cellulosic Fibers by FTIR Spectroscopy for Their Further Implementation to Building Materials. *Am. J. Anal. Chem.* 2018;09(06):303-310. <https://doi.org/10.4236/ajac.2018.96023>
- [33] Rahmawati C, Aprilia S, Saidi T, Aulia TB. Mineralogical, Microstructural and Compressive Strength Characterization of Fly Ash as Materials in Geopolymer Cement. *Elkawnie.* 2021;7(1):1-17. <https://doi.org/10.22373/ekw.v7i1.7787>
- [34] Prasad DD, Ravande K. Fourier transformed-infrared spectroscopy (FTIR) studies on the concrete/cement mortar mass made of cent percentage recycled coarse and fine aggregates. *Int J Adv Res Eng Technol.* 2021;12(1):387-400.
- [35] Zhang D, Yu J, Wu H, Jaworska B, Ellis BR, Li VC. Discontinuous micro-fibers as intrinsic reinforcement for ductile Engineered Cementitious Composites (ECC). *Compos. Part B Eng.* 2020;184:107741. <https://doi.org/10.1016/j.compositesb.2020.107741>
- [36] Harle S, Dhawale V. Comparison of Different Natural Fiber Reinforced Concrete. *Int J Eng Sci Res Technol.* 2014;3:605-607.
- [37] Güneyisi E, Gesoğlu M. Properties of self-compacting portland pozzolana and limestone blended cement concretes containing different replacement levels of slag. *Mater. Struct.* 2011;44:1399-1410. <https://doi.org/10.1617/s11527-011-9706-0>
- [38] Zhao J, Gao X, Chen S, Lin H, Li Z, Lin X. Hydrophobic or superhydrophobic modification of cement-based materials: A systematic review. *Compos. Part B Eng.* 2022;243:110104. <https://doi.org/10.1016/j.compositesb.2022.110104>
- [39] Nduka DO, Akanbi ET, Ojo DO, Babayemi TE, Jolayemi KJ. Investigation of the Mechanical and Microstructural Properties of Masonry Mortar Made with Seashell Particles. *Materials.* 2023;16(6):2471. <https://doi.org/10.3390/ma16062471>
- [40] Committee ACI. State of the Art Report in Fiber Reinforced Concrete. ACI Am. Concr. Inst. Farmington Hills MI USA; 1982.
- [41] Alvee AR, et al. Experimental study of the mechanical properties and microstructure of geopolymer paste containing nano-silica from agricultural waste and crystalline admixtures. *Case Stud. Constr. Mater.* 2022;16 <https://doi.org/10.1016/j.cscm.2021.e00792>
- [42] Mobasher B. Mechanics of fiber and textile reinforced cement composites. CRC press; 2011. <https://doi.org/10.1201/b11181>

Blank Page



## Comparison of single and multi-coil self-powered MR damper subjected to cyclic and earthquake loading for structural vibration control

Daniel Cruze<sup>\*a</sup>, Balaji Ramalingam<sup>b</sup>, Nedunchezhian Krishnaraju<sup>c</sup>

Department of Civil Engineering Hindustan Institute of Technology and Science, Chennai, Tamil Nadu, India

### Article Info

### Abstract

#### Article history:

Received 06 Mar 2024

Accepted 26 May 2024

#### Keywords:

Self-powered MR damper;  
Energy harvesting system;  
Seismic mitigation;  
Electromagnetic Induction

A promising solution for semi-active vibration control of different dynamic systems is to use magnetorheological (MR) dampers. In the present study, the investigation focuses on developing a novel single and multi-coil self-powered magnetorheological (MR) damper system using electromagnetic induction (EMI) for seismic mitigation. The conventional MR dampers, which rely on external power sources, can be unreliable and impractical in earthquake-prone locations. Thus, the EMI device connected to the MR damper can be used as an effective and alternative power source for the MR damper, results in a self-powered system. The proposed energy-harvesting system is an MR damper placed above the top of the piston. The coil is wound around the piston, and the outer casing with a ferrite magnet is fixed. As the mechanical energy of the piston is converted into electrical energy, its self-tuning capacity is a perfect fit for structural vibration control applications. The MR damper is subjected to cyclic and time-history loading. At a maximum amplitude of 15 mm, the damper generated 1767.8 N for cyclic loading and -1780 N for earthquake loading, the El Centro earthquake 1940 is considered for the study. By placing EMI, the mechanical energy is converted into electrical energy and powers the damper to avoid external power. The experimental results showcase enhanced damping forces and adaptability, thereby establishing it as an innovative and effective it can be alternative to conventional MR dampers for vibration control in future.

© 2024 MIM Research Group. All rights reserved.

## 1. Introduction

Indeed, the progress in earthquake engineering has led to the development of control systems for structures and infrastructure, focusing on monitoring and minimizing the impact of seismic vibrations. A key technological innovation is the use of self-powered Magnetorheological (MR) dampers, which can convert vibrating energy into electrical energy, making them highly favored semi-active damping devices. Li et al. [1] explored the development of self-powered MR dampers aimed at enhancing reliability and reducing costs in remote locations by converting vibration energy into electricity. Bui et al. [2] designed a washing machine damper utilizing magnets to convert machine vibrations into electricity, effectively minimizing vibration, while investigating electromagnetic parameters and energy conversion efficiency in vehicle suspension systems. Gao et al. [3] developed self-powered MR dampers, showcasing their potential in reducing installation space and costs. Hu et al. [4] introduced MR dampers with self-powered capabilities, eliminating size, cost, and energy consumption concerns. Taking it a step further, Hu et al. [5] combined energy harvesting with automatic vibration detection, providing an innovative solution. Wang et al. [6] introduced methods for tackling cable vibration.

\*Corresponding author: [danielckarunya@gmail.com](mailto:danielckarunya@gmail.com)

<sup>a</sup> orcid.org/0000-0002-4024-4742<sup>b</sup> orcid.org/0009-0004-4341-0197; <sup>c</sup> orcid.org/0009-0007-3274-3852

DOI: <http://dx.doi.org/10.17515/resm2024.209st0306rs>

Res. Eng. Struct. Mat. Vol. 11 Iss. 1 (2025) 199-211

Jamshidi et al. [7] presented a self-powered MR damper that generates electricity from movement, significantly reducing vibration. Dyke et al. [8] explored an adaptive damper harvesting vibration energy for more autonomous and efficient structures, integrating vibration sensors and a small power source to automatically adjust building dampers. Chen et al. [9] proposed an MR damper combining energy harvesting, sensing, and damping, making it smaller, cheaper, and self-powered for various applications. Zhu et al. [10] replaced conventional dampers with energy-harvesting linear electromagnetic dampers for vibration mitigation, emphasizing their effectiveness in energy storage and performance. Wang et al. [11] advocate for the substitution of conventional dampers with energy-harvesting linear electromagnetic dampers, highlighting their dual advantages of dissipation and power generation. Wang et al. [12] developed a self-sensing MR damper with improved control and sensing capabilities for cost-effective and intelligent vibration control applications. Choi et al. [13] discussed the self-powered MR damper utilizing vibration energy to enhance vibration isolation in structures. Lam et al. [14] investigated the MR damper with built-in sensors for real-time control of building vibrations. Lai et al. [15] integrated an IRDS sensor into commercial dampers, optimizing their performance for self-sensing purposes in advanced vibration control applications. Chen et al. [16] developed a self-powered MR damper integrating energy harvesting, sensing, and damping for benefits such as lower cost, smaller size, and higher reliability. Choi et al. [17] developed an energy-harvesting vibration control system based on an electromagnetic device, demonstrating its efficiency in reducing structural responses. Sapinski et al. [18] introduced a self-energized MR damper with an internal vibration power generator, eliminating the need for external power sources for vibration control. Chen et al. [19] demonstrated a self-energized MR damper with multifaceted design potential, offering significant benefits in areas such as robotics, prosthetics, and vehicle suspension. Cruze et al. [20] evaluated six MR fluids, incorporating different carrier liquids and carbonyl-iron (CI) particle ratios, for their rheological performance. Notably, MRF 80 outperformed the retail MRF 132 DG in damping, showcasing a peak force of 0.536 kN in cyclic load tests with a 1-mm annular gap. This suggests its potential for applications requiring precise and adaptable damping forces across diverse fields. Utami et al. [21] evaluated the performance variation of MR fluid under extended cyclic stress. The investigation revealed a substantial increase in the damping force of the MR damper, both in on and off modes, growing by 44% for the on-state condition and 90% for the off-state condition after 170,000 operational cycles. Changes in magnetic particle sizes and shapes within the MR fluid were attributed to an inadequate grasp of technology (IUT) and a viscosity decrease due to oxidation during extended operation. Wang et al. [22] explored the impact mitigation potential of magnetorheological fluids (MRFs) under magnetic fields using rheological analysis with a speed-controlled capillary magneto rheometer. The study demonstrated consistent shear-thinning behavior and correlated viscosity uniformity across various excitation levels with the strength of the magnetic field, enhancing the technical application of MRFs in impact mitigation. Daniel et al. [23] conducted a study on the sedimentation rates of grease, lubricant oil, and silicone oil as three base fluids for MR fluids. Results indicated that MR fluid with silicone oil exhibited the lowest sedimentation rate, emphasizing the crucial role of base fluid selection in maximizing MR fluid performance for real-world applications. Xu et al. [24] conducted a study comparing three control strategies for MR damper-equipped building structures: bi-state, modified bi-state, and intelligent control. The results indicated that while bi-state control might lead to parameter overruns, the modified strategy mitigated this issue. Intelligent control, which integrated neural network prediction, effectively reduced earthquake responses, emphasizing the efficacy of intelligent strategies for optimal MR damper performance in reducing dynamic responses. Xu et al. [25] developed a novel real-time control approach using MR dampers for earthquake mitigation in structures. They established the Bingham model for MR dampers and demonstrated their efficacy in reducing seismic responses

through numerical analysis. Results showed that the proposed real-time control method outperformed traditional approaches. It was aided by the highly efficient Levenberg-Marquardt algorithm for training the control neural network, highlighting the effectiveness of MR dampers and innovative real-time control strategies in earthquake hazard mitigation. Yang et al. [26] investigated the dynamic characteristics of three-coil MR dampers, revealing full hysteresis curves and significant energy dissipation capacity, with damping force saturation beyond 1.2 A excitation current. Energizing all coils enhanced damping force amplitude and saturation, while the proposed modified micromodels accurately simulated force-velocity hysteresis curves and magnetic saturation. These findings offer insights for optimizing control strategies and enhancing the seismic performance of structures with multicoil MR dampers. Yang et al. [27] explored a micro-macro mathematical model incorporating MR fluid microstructure parameters into classic models. This model accurately described the MR damper's dynamic properties. Validation confirmed efficacy, while numerical analysis highlighted nonlinear hysteretic behavior, providing insights for optimizing MR fluid formulations and enhancing damper efficiency. Daniel et al. [28] studied the importance of building safer structures in response to earthquake-related losses and explored MR dampers as a potential solution. Experimental investigations on a scaled-down RC frame with a single piston shear mode MR damper demonstrated a 40–50% reduction in displacement and a 45–60% increase in energy dissipation capacity. The study highlighted the effectiveness of MR dampers in enhancing vibration reduction, with analytical and experimental results confirming their efficiency and potential for seismic resilience in civil engineering applications. Cruze et al. [29] developed a novel approach to MR damper design, emphasizing its semi-active vibration control capabilities. They conducted experimental and numerical investigations on a new MR damper design featuring multi-coils for enhanced shear force production. Results demonstrated significant displacement reduction and increased damping force under seismic events, highlighting its effectiveness in improving seismic resilience. The proposed device showcased superior performance over conventional control devices, offering a promising solution for seismic mitigation in earthquake-prone areas. Hu et al. [30] investigates the performance of a self-powered, multi-coil MR damper under simulated seismic excitation. It employs simulations to analyze the damper's response to various earthquake loading scenarios. The findings highlight the effectiveness of the multi-coil design, demonstrating how the coil configuration and control strategies can be optimized to achieve superior damping performance, potentially offering a significant advantage in mitigating the impact of earthquakes on structures. Kariganaur et al. [31] presents a comparative study on the effects of single-coil and multi-coil magnetorheological (MR) dampers using finite element analysis. The study finds that multi-coil MR dampers offer superior performance in controlling vibrations compared to single-coil dampers. The results suggest significant potential for multi-coil designs in enhancing the stability and safety of structures subjected to dynamic loads.

In the proposed research, the comparison of a single and multi-coil self-powered MR damper subjected to cyclic and earthquake loading is investigated. The main focus of this study is to conduct a comprehensive analysis of single and multi-coil MR dampers. It begins with the 3D modelling of self-powered MR dampers using AutoCAD. Then, the models are fabricated using mild steel. After the fabrication process, the MR dampers are assembled, the piston coils are wound with copper coils, and the EMI systems are placed at the top of the piston. Then, MR fluid is filled inside the cylinder. The MR dampers are tested by cyclic loading at three different displacement levels of 5, 10, and 15 mm. For time history loading, El Centro has been considered for the study.

## 2. Self-Powered MR Dampers

In general, supplying of current is required to activate the electromagnetic coils in an MR damper. There are several ways for a self-powered MR damper to convert mechanical energy into electrical energy in the event of high-magnitude earthquake. However, the amount of electrical energy produced is enough to create the damping force needed to keep the buildings from vibrating during a seismic event. Thus, self-power mechanisms are essential for civil engineering applications, particularly for seismic resistant buildings.

## 3. MR Fluid

A blend of magnetic particles and oil makes up MR Fluid, a smart liquid. The particles in the liquid align themselves when exposed to a magnetic field, changing the liquid's viscosity, yield stress, and magnetic susceptibility. The fluid's high receptivity makes precise control possible. Through testing, the most efficient mixture was found to be carbonyl iron and synthetic oil without the inclusion of surfactants. The carbonyl iron's spherical form facilitates good suspension in the fluid, and its high saturation magnetization adds to its potency. To synthesize the fluid, carbonyl iron of grade R is mixed with the carrier fluid and stirred for 8 hours at room temperature. The final mixture contains 50% carbonyl iron and 50% carrier fluid. This proposed MRF 50 shows a maximum yield stress of about 93.34 kPa and a viscosity of 0.28 Pa s. [20]. Fig. 1

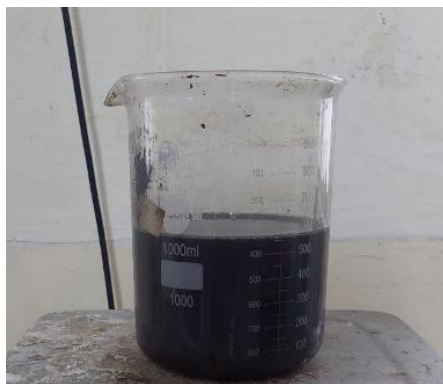


Fig. 1. Magnetorheological fluid

## 4. Electromagnetic Induction System

Electromagnetic induction (EMI) is the production of an electromotive force (EMF) across an electrical conductor in a changing magnetic field. It can also be described as the creation of current by moving an electric conductor through a static magnetic field. MR dampers incorporate EMI systems for self-power. MR dampers have EMI components that include a permanent magnet and a copper coil. As movement occurs, kinetic energy converts into electrical energy, resulting in changes in the damping capabilities of the device. Fig. 2.



Fig. 2. Electromagnetic induction system

### 5. Self-Powered Single Coil MR Damper

The configuration of the MR damper was designed and fabricated using mild steel material. The external structure includes a hollow cylinder, MR fluid, magnet, and magnet casing components, as depicted in Fig. 3. The proposed self-powered single-coil MR damper consists of a single-coil piston rod wound with a standard wire gauge (SWG) 22 copper coil 0.8  $\mu$ . The damper consists of a cylindrical casing with an external diameter of 60 mm and an internal diameter of 50 mm, with a depth of 280 mm. The piston has a diameter of 25 mm and a length of 130 mm, wound with a copper coil, which has a 0.8 mm diameter with 1462 coil turns [28], as shown in Fig. 4.

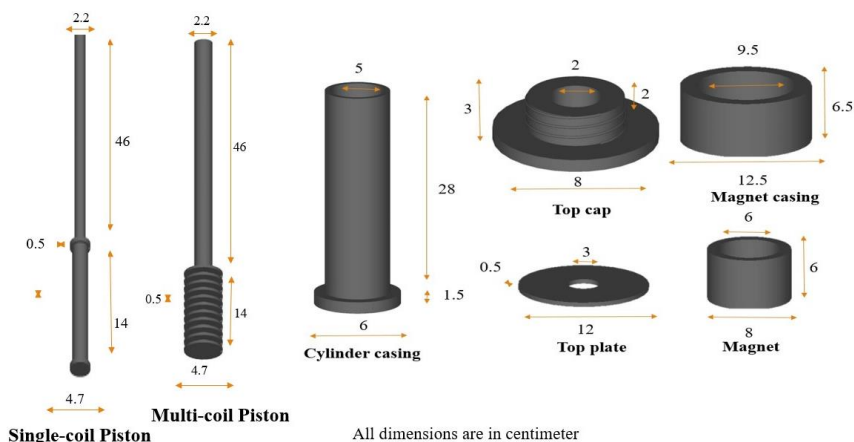


Fig. 3. Dimensions detailing of self-power single and multi-coil MR Damper

A self-powered magnet casing is placed at the top, measuring 60 mm in height and 80 mm in diameter at the center. Ferrite magnet grade N 42 is used for the study to create a self-powered MR damper. A ferrite magnet is placed to produce self-powered energy to activate the MR damper. In the self-powered single-coil piston head, 326 turns of coil were wound with a copper coil of 0.8  $\mu$  parallel to the magnet to generate EMI. The annular gap of 1 mm is maintained for the flow of MR fluid. The EMI system is placed above the cylinder cap. During operation, the piston rod moves in response to external movement, allowing the

MR fluid to flow throughout the annular gap of the cylinder. When the copper coil is magnetized using a self-powered system, the rheology of the MR fluid within the flow channel generates shear stress, impeding the relative motion of the piston head.

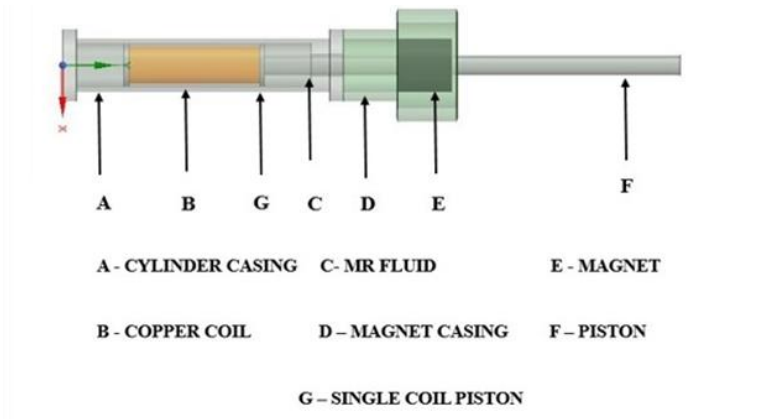


Fig. 4. 3D model self-power single-coil MR Damper

### 6. Self-powered Multi Coil MR Damper

The fluid flow through two adjacent cores in the piston is strengthened by the alternating polarities in the magnetic field, which benefits from utilizing the tothing system in the piston configuration. In contrast, 11 piston poles and 10 coils with a uniform distance of 5 mm and a depth of 10 mm were constructed in the proposed MR damper to increase the amount of shear force [29]. Shear forces on the piston's sides increase as the number of flow gaps increases with the number of piston poles, as shown in Fig. 5. The suggested self-powered MR damper has the capacity to produce a maximum damping force of 1.7 kN. The design indicates that an electromagnetic circuit can generate more flux lines in the flow gaps in milliseconds to produce 1.7 kN of damping force. The fluid is strengthened through two adjacent cores when the tothing system is used in the piston configuration because of the magnetic field's alternating polarities within the piston.

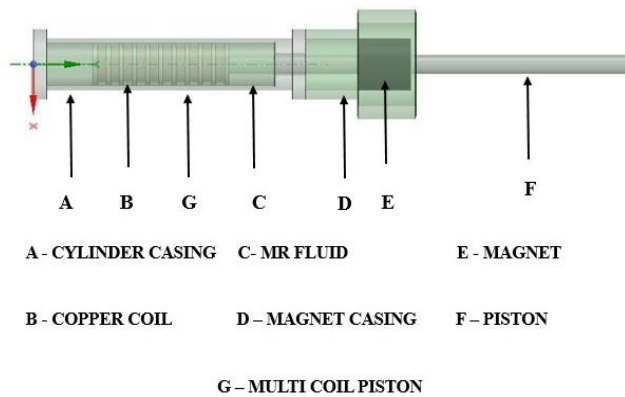


Fig. 5. 3D model self-power Multi-coil MR Damper

### 7. Working Principle

A new self-powered MR damper operates based on a mechanical mechanism. Figs. 4 and 5 depict a 3D model of the self-powered MR damper. The device comprises a piston, top cap, MR fluid, SWG 22 copper coil, magnet, and magnet casing. Vibration energy is converted into electrical energy to power the self-powered MR damper, thus eliminating the need for external electrical energy. During operation, the piston rod moves vertically, and a coil wound around the top of the piston cap, parallel to the magnet, generates electromagnetic induction (EMI) by producing electromagnetic force due to changes in the magnetic field. Therefore, the self-powered MR damper can perform adaptive damping adjustment without any external power supply equipment, reducing the impact of various exterior disturbances on the device's performance and improving its practicality and reliability. The main dimensional parameters of the proposed self-powered MR damper are tabulated in Table 1.

Table 1. Dimensional detailing of the proposed self-powered MR damper

| Parameters                 | Single coil MR damper        | Multi coil MR damper         |
|----------------------------|------------------------------|------------------------------|
| Cylinder casing            | 295 mm                       | 295 mm                       |
| Diameter of copper coil    | 0.8 mm                       | 0.8 mm                       |
| No. of turns (copper coil) | 1462 turns                   | 122 turns for each pole      |
| MR fluid (ratio)           | 50:50                        | 50:50                        |
| Piston length              | 600 mm                       | 600 mm                       |
| No. of piston pole         | -                            | 10 nos                       |
| Magnet                     | Ferrite magnet grade N<br>42 | Ferrite magnet grade N<br>42 |
| Magnet size                | 80 mmx60 mm                  | 80 mmx60 mm                  |
| Magnet casing              | 125 mmx65 mm                 | 125 mmx65 mm                 |
| Coil turns at top          | 326 turns                    | 326 turns                    |

### 8. Experimental Investigation on Self-Powered MR Damper

The performance of the MR damper can be determined by subjecting it to cyclic loading in the MTS Universal Testing Machine (UTM) at the Structural Engineering Laboratory of Karunya Institute of Technology and Science, Coimbatore.

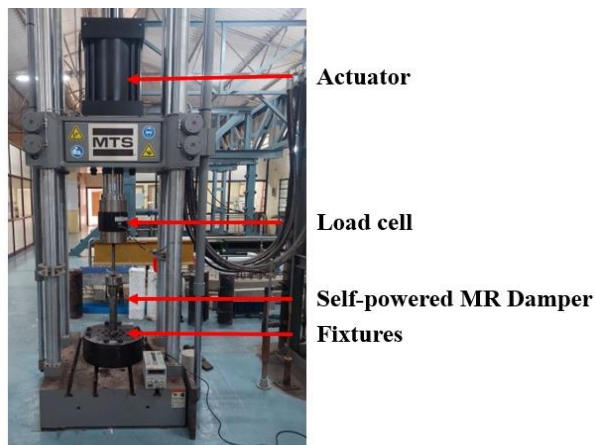


Fig. 6. Testing of self-Powered MR damper

The single and multi-coil self-powered MR dampers were tested at various displacements ranging from 5 mm to 15 mm. The experimental setup for the cyclic loading test on a single- and multi-coil self-powered MR damper is presented in Fig. 6. The setup includes a load cell, a base plate or fixtures, and a hydraulic actuator. The piston base is fixed to the UTM base plate using a fixture, while the piston rod is attached to the load cell. The input to the UTM is controlled by a computer-regulated hydraulic actuator.

### 9. Cyclic Loading

Cyclic loading on a self-powered MR damper involves subjecting it to repeated force or displacement cycles to assess its durability and performance under real-world conditions. At a frequency of 0.2 Hz for 10 repetition cycles, the displacement values of 5, 10, and 15 are used to determine the maximum force exerted by the self-powered MR damper. The experimental results of damping force are plotted in Figs. 7, 8, and 9. The results are tabulated in Table 2.

Table 2. Difference between single and multi-coil self-sensing MR damper on cyclic loading

| Single Coil Self-Sensing Mr Damper |          | Multi Coil Self-Sensing Mr Damper |          |
|------------------------------------|----------|-----------------------------------|----------|
| Displacement                       | Load     | Displacement                      | Load     |
| 5mm                                | 1256.4 N | 5mm                               | 1350.8 N |
| 10mm                               | 1392.6 N | 10mm                              | 1570.8 N |
| 15mm                               | 1566.8 N | 15mm                              | 1767.8 N |

The observed results for the single-coil self-powered MR damper indicate a maximum damping force of 1256.4 N at a 5mm displacement, 1392.6 N at a 10 mm displacement, and 1566.89 N at a 15 mm displacement. Multi-coil MR dampers typically exhibit higher damping forces compared to single-coil dampers due to the presence of multiple coils generating magnetic fields. Additionally, multi-coil dampers are capable of generating higher shear forces in the MR fluid compared to single-coil MR dampers.

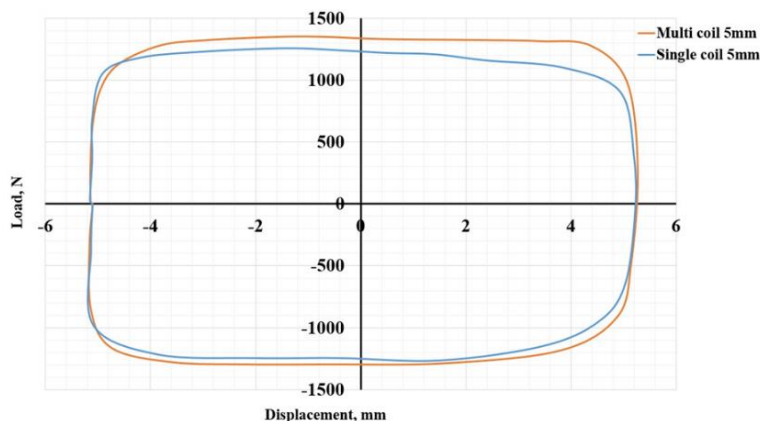


Fig. 7. Force and Displacement graph for single and multi-coil Self-power MR Damper for 5 mm displacement



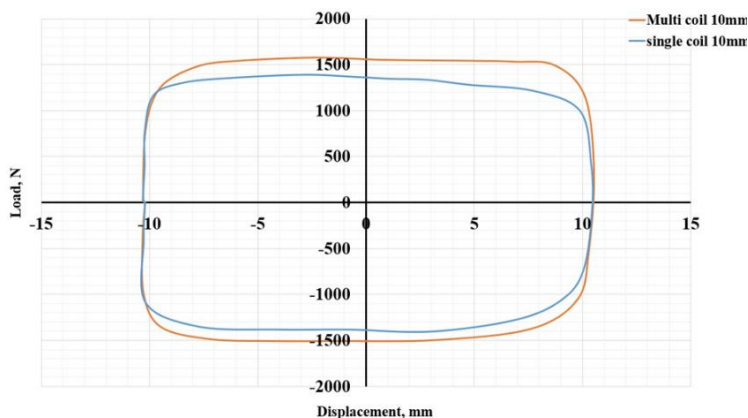


Fig. 8. Force and Displacement graph for single and multi-coil Self-power MR Damper for 10 mm displacement

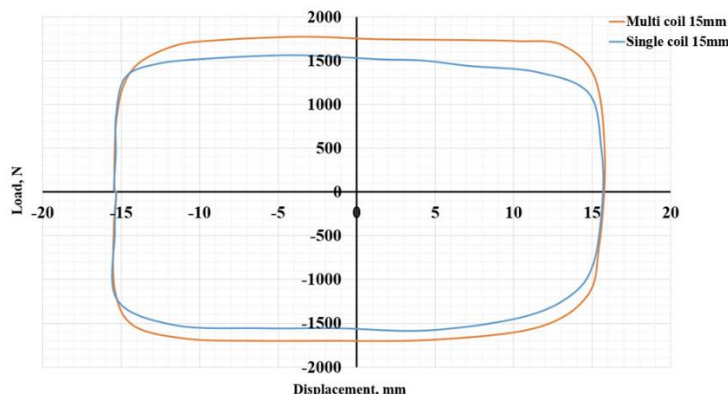


Fig. 9. Force and Displacement graph for single and multi-coil Self-power MR Damper for 15 mm displacement

### 10. Earthquake Loading

Earthquake loading on self-powered MR dampers involves adaptation to dynamic forces. These dampers utilize MR fluids, offering real-time adjustments in viscosity and mitigating structural vibrations during seismic events. In this study, the El Centro earthquake of 1940 was a significant seismic event in California, USA.

Table 3. Difference between single and multi-coil self-sensing MR damper on earthquake loading

| El-Centro 1940 Earthquake Loading  |           |
|------------------------------------|-----------|
| Self-Powered Single-Coil MR Damper | -1259.7 N |
| Self-Powered Multi-Coil MR Damper  | -1780.0 N |

Fig. 10 shows the time history loading ground acceleration converted to displacement and employed to simulate the response of self-powered MR dampers. The objective is to determine the earthquake loading capacity of both single and multi-coil MR dampers. The experimental results of earthquake loading are plotted in Fig. 11, and the results are tabulated in Table 3.

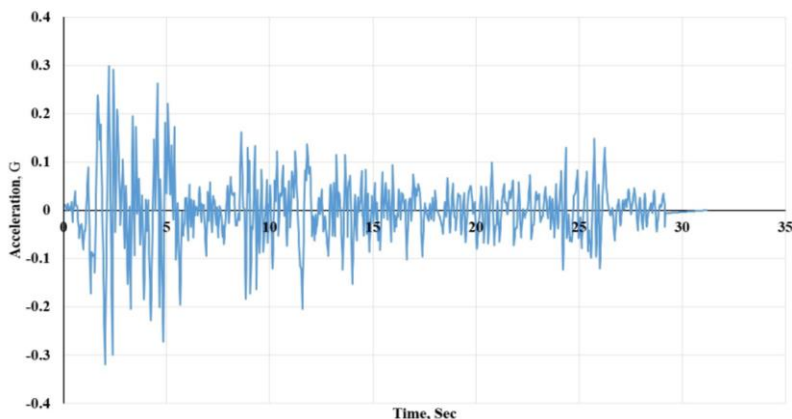


Fig. 10. Time history of El Centro earthquake, 1940

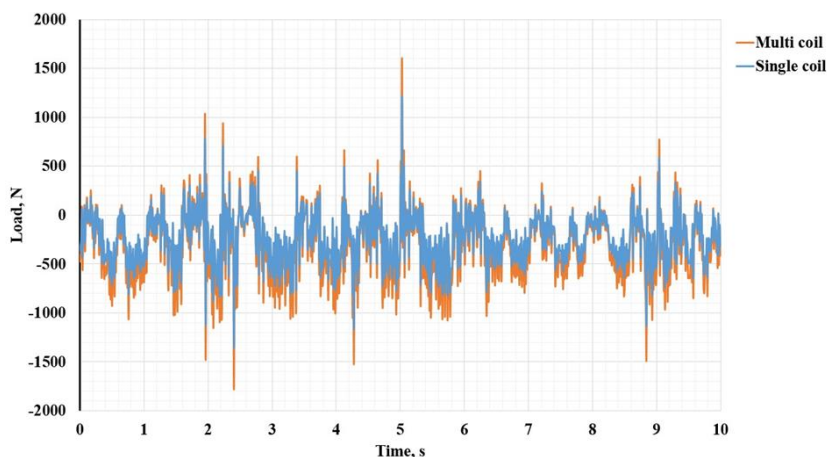


Fig. 11. Earthquake loading of single and multi-coil Self-power MR Damper

### 11. Conclusion

In this study, a novel functional-integration MR damper was designed, fabricated, and tested. The results indicate that the proposed self-powered single-coil MR damper exhibits a damping force of 1566.8 N at a 15 mm displacement, while the self-powered multi-coil MR damper demonstrates a damping force of 1767.8 N under cyclic loading; this represents a 12.8% increase in damping force compared to the single-coil self-powered MR damper. For earthquake loads, the single-coil self-powered MR damper shows a damping force of -1289.7 N, whereas the multi-coil self-powered MR damper has a compression value of -1780 N in seismic conditions; the multi-coil self-powered MR damper displays a 34.2% increase in damping force compared to the single-coil self-powered MR damper. The stiffness of a single-coil MR damper is 104.45, while the stiffness of a multi-coil MR damper is 117.8. Compared to the single-coil MR damper, the multi-coil MR damper has greater stiffness, representing a 12.7% increase in stiffness. Additionally, the multi-coil MR damper has a 16% reduction in the volume of MR fluid compared to the single-coil MR damper, which has a volume of 409.76 ml. In conclusion, the experimental investigation demonstrates that the proposed self-powered multi-coil MR damper device has better performance compared to a single-coil MR damper because a multi-coil piston

produces more magnetic field compared to a single-coil piston. This is due to the presence of piston poles in the multi-coil design. Additionally, the volume of MR fluid is lower in the multi-coil piston compared to the single-coil piston. Therefore, it can be considered an innovative and effective alternative for enhancing a building's seismic durability in seismically active areas in the future, effectively protecting structures from seismic resistance issues. In the future, the damper will be placed diagonally in the RC frame, and the performance of the damper will be studied when the frame is subjected to cyclic loading and real-time earthquake loading.

### **Acknowledgements**

The authors thank the Centre for Research & Consultancy, Hindustan Institute of Technology and Science, Padur, Chennai for the seed grant (SEED/CRC/HITS/2022-23/005).

### **References**

- [1] Li L, Hu G, Yu L, Qi H. Development and performance analysis of a new self-powered magnetorheological damper with energy-harvesting capability. *Energies*. 2021 Sep 27;14(19):6166. <https://doi.org/10.3390/en14196166>
- [2] Bui QD, Nguyen QH, Nguyen TT, Mai DD. Development of a magnetorheological damper with self-powered ability for washing machines. *Applied Sciences*. 2020 Jun 14;10(12):4099 <https://doi.org/10.3390/app10124099>
- [3] Gao X, Niu J, Jia R, Liu Z. Influential characteristics of electromagnetic parameters on self-powered MR damper and its application in vehicle suspension system. *Proceedings of the Institution of Mechanical Engineers, Part K: Journal of Multi-body Dynamics*. 2020 Mar;234(1):38-49. <https://doi.org/10.1177/1464419319870338>
- [4] Hu G, Ru Y, Li W. Design and development of a novel displacement differential self-induced magnetorheological damper. *Journal of Intelligent Material Systems and Structures*. 2015 Mar;26(5):527-40. <https://doi.org/10.1177/1045389X14533429>
- [5] Hu G, Yi F, Liu H, Zeng L. Performance analysis of a novel magnetorheological damper with displacement self-sensing and energy harvesting capability. *Journal of Vibration Engineering & Technologies*. 2021 Jan;9:85-103. <https://doi.org/10.1007/s42417-020-00212-7>
- [6] Wang Z, Chen Z, Gao H, Wang H. Development of a self-powered magnetorheological damper system for cable vibration control. *Applied Sciences*. 2018 Jan 15;8(1):118. <https://doi.org/10.3390/app8010118>
- [7] Jamshidi M, Chang CC. A new self-powered electromagnetic damper for structural vibration control. In *Sensors and Smart Structures Technologies for Civil, Mechanical, and Aerospace Systems 2017* 2017 Apr 12 (Vol. 10168, pp. 680-689). SPIE. <https://doi.org/10.1117/12.2256657>
- [8] Dyke SJ, Spencer Jr BF, Sain MK, Carlson JD. Modeling and control of magnetorheological dampers for seismic response reduction. *Smart materials and structures*. 1996 Oct 1;5(5):565. <https://doi.org/10.1088/0964-1726/5/5/006>
- [9] Chen C, Liao WH. A self-sensing magnetorheological damper with power generation. *Smart Materials and Structures*. 2012 Jan 25;21(2):025014. <https://doi.org/10.1088/0964-1726/21/2/025014>
- [10] Zhu S, Shen WA, Xu YL. Linear electromagnetic devices for vibration damping and energy harvesting: Modeling and testing. *Engineering Structures*. 2012 Jan 1;34:198-212. <https://doi.org/10.1016/j.engstruct.2011.09.024>
- [11] Wang DH, Bai XX, Liao WH. An integrated relative displacement self-sensing magnetorheological damper: prototyping and testing. *Smart Materials and Structures*. 2010 Aug 6;19(10):105008. <https://doi.org/10.1088/0964-1726/19/10/105008>

- [12] Wang DH, Wang T. Principle, design and modeling of an integrated relative displacement self-sensing magnetorheological damper based on electromagnetic induction. *Smart Materials and Structures*. 2009 Jul 17;18(9):095025. <https://doi.org/10.1088/0964-1726/18/9/095025>
- [13] Choi YT, Wereley NM. Self-powered magnetorheological dampers.
- [14] Lam KH, Chen ZH, Ni YQ, Chan HL. A magnetorheological damper capable of force and displacement sensing. *Sensors and Actuators A: Physical*. 2010 Mar 1;158(1):51-9. <https://doi.org/10.1016/j.sna.2009.12.022>
- [15] Lai DK, Wang DH. Principle, modeling, and validation of a relative displacement self-sensing magnetorheological damper. In *Smart Structures and Materials 2005: Smart Structures and Integrated Systems 2005* May 17 (Vol. 5764, pp. 130-141). SPIE. <https://doi.org/10.1117/12.602672>
- [16] Chen C, Liao WH. A self-sensing magnetorheological damper with power generation. *Smart Materials and Structures*. 2012 Jan 25;21(2):025014. <https://doi.org/10.1088/0964-1726/21/2/025014>
- [17] Choi KM, Jung HJ, Lee HJ, Cho SW. Feasibility study of an MR damper-based smart passive control system employing an electromagnetic induction device. *Smart Materials and Structures*. 2007 Oct 10;16(6):2323. <https://doi.org/10.1088/0964-1726/16/6/036>
- [18] Sapiński B. Vibration power generator for a linear MR damper. *Smart Materials and Structures*. 2010 Aug 6;19(10):105012. <https://doi.org/10.1088/0964-1726/19/10/105012>
- [19] Chen C, Liao WH. A self-powered, self-sensing magnetorheological damper. In *2010 IEEE International Conference on Mechatronics and Automation 2010* Aug 4 (pp. 1364-1369). IEEE. <https://doi.org/10.1109/ICMA.2010.5589157>
- [20] Cruze D, Gladston H, Loganathan S, Dharmaraj T, Solomon SM. Study on Magnatec oil-based MR fluid and its damping efficiency using MR damper with various annular gap configurations. *Energy, Ecology and Environment*. 2021 Feb;6:44-54. <https://doi.org/10.1007/s40974-020-00170-6>
- [21] Utami D, Ubaidillah, Mazlan SA, Imaduddin F, Nordin NA, Bahiuddin I, Abdul Aziz SA, Mohamad N, Choi SB. Material characterization of a magnetorheological fluid subjected to long-term operation in damper. *Materials*. 2018 Nov 6;11(11):2195. <https://doi.org/10.3390/ma11112195>
- [22] Daniel C, Sarala L, Tensing D, Sundar Manoharan S. Magnetorheological fluid with nano Fe<sub>3</sub>O<sub>4</sub> for performance enhancement of MR damper for seismic resistance of steel structures. *Key Engineering Materials*. 2018 Mar 14;763:975-82. <https://doi.org/10.4028/www.scientific.net/KEM.763.975>
- [23] Wang M, Chen Z, Wereley NM. Magnetorheological damper design to improve vibration mitigation under a volume constraint. *Smart Materials and Structures*. 2019 Oct 9;28(11):114003 <https://doi.org/10.1088/1361-665X/ab4704>
- [24] Xu ZD, Shen YP. Intelligent bi-state control for the structure with magnetorheological dampers. *Journal of intelligent material systems and structures*. 2003 Jan;14(1):35-42. <https://doi.org/10.1177/1045389X03014001004>
- [25] Xu ZD, Shen YP, Guo YQ. Semi-active control of structures incorporated with magnetorheological dampers using neural networks. *Smart materials and structures*. 2003 Jan 10;12(1):80. <https://doi.org/10.1088/0964-1726/12/1/309>
- [26] Yang Y, Xu ZD, Guo YQ, Sun CL, Zhang J. Performance tests and microstructure-based sigmoid model for a three-coil magnetorheological damper. *Structural Control and Health Monitoring*. 2021 Nov;28(11):e2819. <https://doi.org/10.1002/stc.2819>
- [27] Yang Y, Xu ZD, Xu YW, Guo YQ. Analysis on influence of the magnetorheological fluid microstructure on the mechanical properties of magnetorheological dampers. *Smart Materials and Structures*. 2020 Sep 30;29(11):115025. <https://doi.org/10.1088/1361-665X/abadd2>

- [28] Daniel C, Hemalatha G, Magdalene A, Tensing D, Sundar Manoharan S. Magnetorheological damper for performance enhancement against seismic forces. In *Facing the Challenges in Structural Engineering: Proceedings of the 1st GeoMEast International Congress and Exhibition, Egypt 2017 on Sustainable Civil Infrastructures 1* 2018 (pp. 104-117). Springer International Publishing. [https://doi.org/10.1007/978-3-319-61914-9\\_9](https://doi.org/10.1007/978-3-319-61914-9_9)
- [29] Cruze D, Gladston H, Farsangi EN, Loganathan S, Dharmaraj T, Solomon SM. Development of a multiple coil magneto-rheological smart damper to improve the seismic resilience of building structures. *The Open Civil Engineering Journal*. 2020 Jun 5;14(1). <https://doi.org/10.2174/1874149502014010078>
- [30] Hu G, Lu Y, Sun S, Li W. Performance analysis of a magnetorheological damper with energy harvesting ability. *Shock and Vibration*. 2016;2016:1-0. <https://doi.org/10.1155/2016/6928686>
- [31] Kariganaur AK, Kumar H, Mahalingam A. Comparative study on the effect of single coil and multi coil magnetorheological damper through finite element analysis. In *Journal of Physics: Conference Series* 2020 Dec 1 (Vol. 1706, No. 1, p. 012193). IOP Publishing. <https://doi.org/10.1088/1742-6596/1706/1/012193>

Blank Page



Research Article

## Evaluation of damping reduction factors for displacement and acceleration spectra using code-compatible near-fault and far-fault ground motions depending on site conditions

Abdelmalek Abdelhamid<sup>1,2,a</sup>, Baizid Benahmed<sup>\*1,b</sup>, Omar Laghrouche<sup>3,c</sup>, Mehmet Palanci<sup>4,d</sup>, Lakhdar Aidaoui<sup>1,e</sup>

<sup>1</sup>Development Laboratory in Mechanics and Materials, University of Djelfa, Djelfa, Algeria

<sup>2</sup>Department of Science & Technology, University of Tissemsilt, Tissemsilt, Algeria

<sup>3</sup>Institute for Infrastructure and Environment, Heriot-Watt University, Edinburgh, UK

<sup>4</sup>Civil Engineering Department, Istanbul Arel University, Istanbul, Türkiye

### Article Info

### Abstract

#### Article history:

Received 09 Feb 2024

Accepted 15 June 2024

#### Keywords:

Damping reduction factors;

Ground motion selection;

Response spectra;

Site conditions;

EC8

Damping Reduction Factors (DRFs) are widely employed in design standards to adjust the structural response due to varied levels of the structural damping, higher or lower than the common value of 5% for response spectra or time history analyses. Research findings highlighted that DRFs are sensitive not only to damping and period, but also to the seismological parameters and site conditions. Nevertheless, effect of ground motions on the DRFs compiled to code-based target spectrum are not investigated. For this purpose, Eurocode-8 (EC8) compatible real ground motions were carefully selected for three soil classes, namely, A, B, and C, considering near- and far-fault ground motions and DRFs were derived from the displacement and acceleration response spectra through, Single Degree of Freedom (SDOF) systems, dynamic analyses. Near- and far-fault ground motions were considered to investigate the effect of the distance on DRFs. The distributions of DRFs were then subjected to a comparison with code-based and existing literature DRF models and bias between the models were calculated. The findings demonstrated that near- and far-fault ground motions produced different outcomes and DRFs obtained from acceleration spectra were, on average, approximately 25% higher than those obtained from displacement spectra. It was also observed that DRFs were sensitive to soil classes, especially to soil class B. The maximum near/far fault ratios determined for site class B were 1.20, 1.45 and 1.71 for damping ratios of 10, 20, and 40%, respectively. In addition, results indicated that the DRF values provided by EC8 were generally non-conservative. Therefore, it is important that the code-based definitions should be refined to consider important parameters that affect DRFs such as distance and soil classes.

© 2024 MIM Research Group. All rights reserved.

## 1. Introduction

Response spectrum analysis is one of the most widespread seismic design approaches in earthquake engineering, using a viscous damping ratio of 5%. To perform such analysis to other damping ratios, DRFs are used, and seismic codes define DRFs as function of damping ratio and structural period. On the other hand, recent studies have shown that the DRFs are also sensitive to seismological characteristics such as magnitude, distance, near- and far-fault ground motion, fault type, near-source forward directivity, and site conditions etc. [1]–[3]. Therefore, empirical expressions are proposed. However, most of these parameters have not been taken into consideration in seismic codes yet.

\*Corresponding author: [benahmed.tp@univ-djelfa.dz](mailto:benahmed.tp@univ-djelfa.dz)

<sup>a</sup> [orcid.org/0009-0004-2414-070X](https://orcid.org/0009-0004-2414-070X); <sup>b</sup> [orcid.org/0000-0003-4924-0059](https://orcid.org/0000-0003-4924-0059); <sup>c</sup> [orcid.org/0000-0002-2439-2753](https://orcid.org/0000-0002-2439-2753);

<sup>d</sup> [orcid.org/0000-0002-9223-5629](https://orcid.org/0000-0002-9223-5629); <sup>e</sup> [orcid.org/0000-0003-0488-3800](https://orcid.org/0000-0003-0488-3800)

DOI: <http://dx.doi.org/10.17515/resm2024.153ea0209rs>

Res. Eng. Struct. Mat. Vol. 11 Iss. 1 (2025) 213-230

Firstly, Newmark and Hall [4], [5] proposed the first formulation for the DRFs that has been adopted in many standards and codes, for example, ATC-40 [6], FEMA-273 [7], UBC (1997) [8], ASCE7-05 (2006) [9], and FEMA-356 [10]. Kawashima and Aizawa [11] findings were introduced in the Caltrans Seismic Design Criteria [12]. Ashour's [13] relationship has been introduced in UBC (1994) [14] and NEHRP [15]. Bommer *et al.* [16] formulation was adopted in EC8 [17]. The equation of Ramirez *et al.* [18] was implemented in NEHRP [19] and that of Otani and Kanai [20] has been adopted in the Japanese Seismic Design Code [21]. Priestley [22] suggested an empirical formula that takes into consideration the structural period and near-fault (NF) ground motion for a modified version of EC8. The Zhou *et al.* [23] model was acknowledged in Chinese seismic code [24]. Benahmed [25] proposed an expression of the DRF based on a nonlinear regression, which was introduced in the Algerian Seismic Regulation (RPA 99 version 2003) [26] considering the structural period and damping ratio.

Besides the studies on improving DRF values, Hubbard and Mavroeidis [27] concluded that the DRF models proposed in most standards and codes are based on far-fault (FF) seismic excitation, and these DRF values are non-conservative for NF records. They formulated a conservative model by utilizing NF motions characterized by diverse velocity pulses. Pu *et al.* [28] stated that DRFs derived from FF motions are not appropriate to be used in a design for NF effects and this situation can lead to erroneous results. Li and Chen [29] stated that DRF values derived from FF motion in NF cases may lead to accuracy problems. In addition, Atkinson and Pierre [1] have found that DRFs are sensitive to the moment of magnitude and distance. Based on Hatzigeorgiou [2], on the other hand, DRFs were independent of the distance, but sensitive to soil types ranging from hard rock to soft soil.

Lin and Chang [30] investigated the soil conditions, according to the NEHRP soil classification, and their impact on DRFs obtained from displacement (DRFd) and acceleration (DRFa) response spectra. They concluded that the DRFs derived from displacement spectra were very similar for A, B, and D soil classes, whereas for C soil class, they were slightly different. In addition, it was indicated that DRFa values are more vulnerable to soil conditions than DRFd values. They suggested that DRFa should be used when the structural damping ratio determined from the hysteretic behavior. Otherwise, DRFd must be used if high levels of damping are implemented into the structure when using energy dissipation devices. Hatzigeorgiou [2] stated that the existing methods proposed for DRFs from displacement (Sd) and pseudo-acceleration (PSa) spectra provide a good correlation with the displacement response. This is crucial for high-damping systems because smaller DRFs are obtained from PSa spectra and may cause a significant underestimation of the seismic design forces. Accordingly, the different DRFs should be adopted.

Hao *et al.* [3] concluded that moment magnitude has a notable impact on the DRFs compared to the closest distance and site conditions, especially for classes B-D according to NEHRP [19]. Moreover, these parameters had more influence on DRFa compared to DRFd and DRFv. Zhao *et al.* [31] noticed that the impact of earthquake characteristics and soil types on DRFa are similar to those DRFd for a spectral periods up to 0.3s. At spectral periods longer than 0.3s, earthquake characteristics and soil conditions have a larger impact on DRFa compared to DRFd. Davila and Mendo [32] determined that significant differences exist in the DRFs computed from displacements compared to those computed from acceleration and velocity for periods greater than 0.2s. They found that the values of DRFd for site classes S1, S2, and S3 as per the ASCE 7-16 [33] exhibit similarity and can be adequately approximated by their average for all damping ratios and periods higher than 2.0s. They highlighted that this was not valid for DRFa and DRFv specifically for damping ratios higher than 20%. It was suggested that deriving DRF equations from acceleration and velocity response spectra specific to each soil type would be more appropriate.



Benahmed [34] investigated the damping uncertainty effects on the DRFs for both displacement and acceleration response spectra. It was highlighted that the DRF<sub>d</sub> values are more susceptible to the uncertainties inherent in damping than the DRF<sub>a</sub> values. Also, Abdelhamid *et al.* [35] have studied the uncertainties in DRFs using artificial neural networks for acceleration, velocity, and displacement spectra. Their conclusion highlighted that DRFs derived from acceleration spectra exhibit greater sensitivity to the inherent damping uncertainties compared to DRFs derived from displacement and velocity spectra.

Benahmed [25] found that there is a weak dependency between the DRFs from different soil types and concluded that the influence of the soil type can be omitted. Pavlou and Constantinou [36] examined the accuracy of DRFs implemented in NEHRP when applied to NF motions; however, they did not propose any equations. Daneshvar and Bouaanani [37] considered eastern Canada ground motions for the proposition of a DRFs empirical expression for a wide range of damping ratios, from 1% to 40%, taking into account magnitude, distance, and soil types. The obtained DRFs were dependent on the spectral period and magnitude at high periods, while the effect of distance was observed to have a limited impact. Different studies can be also found in the literature that investigate and propose DRF equations considering different structures, soil types, seismological effects etc. [38]–[43].

UBC97 [8] is the first seismic code to specify consideration of NF effects. It defines near-source factors based on source type and closest distance to the known seismic source. In the Chinese seismic code [24], construction sites are categorized into three groups based on the proximity to the ruptured fault and it recommends to use a larger response spectrum for closer ruptured faults. It is clear that increasing the response spectrum amplification leads to a more conservative design.

### 1.1 Contribution of the Paper

Discussions of the above studies indicate that the dependency of the DRFs on the different considered parameters does lead to different conclusions. Therefore, based on the ground motion database and building topologies, the influence of different seismological and geotechnical factors on DRFs needs further investigation. In addition, the relationship between NF and FF motions and their impact on dynamic response factors remain as open questions. For example, are DRF values observed for NF and FF motions comparable, or is there a significant difference? Do DRFs vary between the values derived from acceleration spectra and those derived from displacement spectra? Can we overlook the impact of soil type on DRFs? In addition to these open questions, the effect of NF and FF ground motions on DRFs are not evaluated in terms of code-compatible ground motions. Accordingly, this is the first study that investigates the effects of NF and FF motions on DRFs considering the spectral shape defined in the seismic code.

For this purpose, the present study investigates the influence of the NF and FF motions on DRFs considering different soil classes of EC8 design spectra. Real earthquake ground motions were taken from European Strong Motion Database [44] and Pacific Earthquake Engineering Research (PEER) Database [45]. These were grouped into six categories considering NF and FF motions as well as site classes of A, B, and C defined in EC8. Selected records were then subjected to a spectral matching algorithm developed by Kayhan *et al.* [46] and code-compatible ground motions records were obtained. Linear dynamic analyses were conducted for damping ratios of 5%, 10%, 20%, and 40% to determine DRFs using displacement and acceleration response spectra. The obtained results were then analysed and compared with DRF equations recommended in EC8 and two other known prediction equation models found in the literature [2], [30].

## 2. Selection of Ground Motions

Ground motion selection is an integral method for the success of time history analysis [47]–[51]. Appropriately selected records, for a given soil class considering seismological parameters, increase the accuracy and lead to realistic results [46]. According to Graizer and Kalkan [52], several earthquake characteristics that have an effect on the accelerogram spectral shape should be considered. Since there is no specific building or building group used in this study, the period interval for spectral matching was assumed between 0.1s and 4.0s which covers different heights of buildings. Three soil classes, namely, A, B, and C defined in EC8 were considered and earthquake records were classified according to shear wave velocity  $V_{s,30}$  as given in Table 1. By this way, the influence of site conditions on DRFs will be examined. NF records were acquired when ground motions were within 20 km of the epicenter, while FF records were gathered for ground motions at epicentral distance exceeding 20 km. Pulse-like motion effects were not taken into account in this study. Using the different ground motion source databases [44], [45], ground motion records were collected (see Fig. 1). Based on the sources, moment magnitude of the records in the database varied between 5.2 and 7.7. Ground motion records were then post processed by the software developed by Kayhan *et al.* [46] to obtain code-compatible records for the analyses.

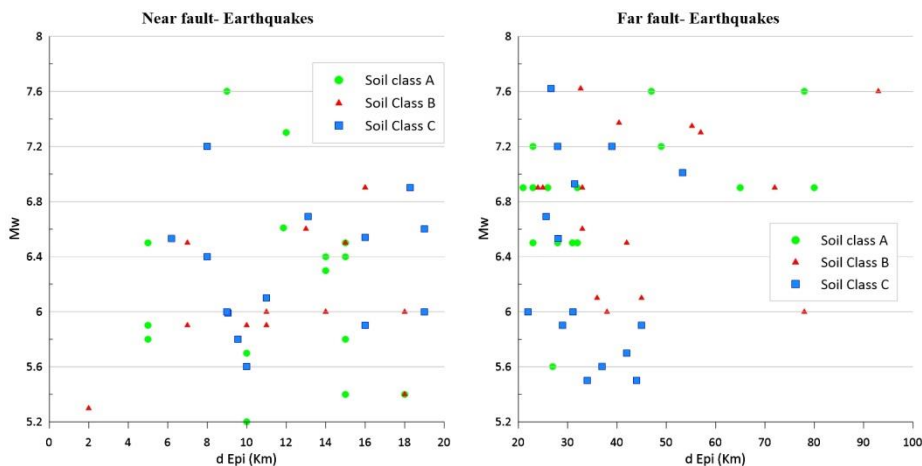


Fig. 1. The distribution of moment magnitude against epicentral distance for selected earthquakes, (left) near-fault and (right) far-fault

DRFs were computed from the acceleration and displacement response spectra of SDOF systems for each of the horizontal components of the records separately (i.e., unidirectional analysis was performed) for both NF and FF records (see Tables 2 to 4). It was difficult to choose original ground motions owing to strict constraints such as moment magnitude, soil categorization, and target spectrum. As a result, original ground motion records were, when necessary, scaled. Records selection constraints and procedures defined in the code [17] were used as input in the software and a total of 15 scaled records for each soil group were determined that match the target design spectrum. The target spectrum was constructed using 5% damping ratio and a peak ground acceleration of 0.35g. Although the effect of scaling factors were found statistically independent of the building responses, if the spectral shape matching is satisfied [53], [54], [55], it is worth stating that the scaling factors (used when necessary) were less than 2.0 [47], [48], [56]. It should be noted that an in-house computer program coded by the authors were used for the linear analysis of earthquakes using the Newmark's step by step time integration method [57]. Spectral acceleration and displacement history of selected earthquakes (i.e.,

$S_a$  and  $S_a$ ) for the period interval between 0.02s and 4.00s with increments of 0.02s considering the damping ratios of 5%, 10%, 20% and 40%, were computed by this program.

Table 1. Soil classes defined in EC8 [17]

| Soil Class | Description of ground type  | $V_{s,30}$ (m/s) | NSPT (bl/30cm) | $C_u$ (kPa) |
|------------|---|------------------|----------------|-------------|
| A          | Rock or other rock-like geological formation, including at most 5 m of weaker material at the surface.  | > 800            | -              | -           |
| B          | Deposits of very dense sand, gravel, or very stiff clay, at least several tens of meters in thickness, characterized by a gradual increase of mechanical properties with depth. | 360 - 800        | > 50           | > 250       |
| C          | Deep deposits of dense or medium dense sand, gravel or stiff clay with thickness from several tens to many hundreds of meters.  | 180 - 360        | 15 - 50        | 70 - 250    |

The list of selected records, for each soil type for both cases of NF and FF earthquake records, are listed in Tables 2 to 4. The acceleration spectrum of EC8, the spectral acceleration of obtained ground motions and their mean corresponding to site classes are plotted in the Figures 2 to 4.

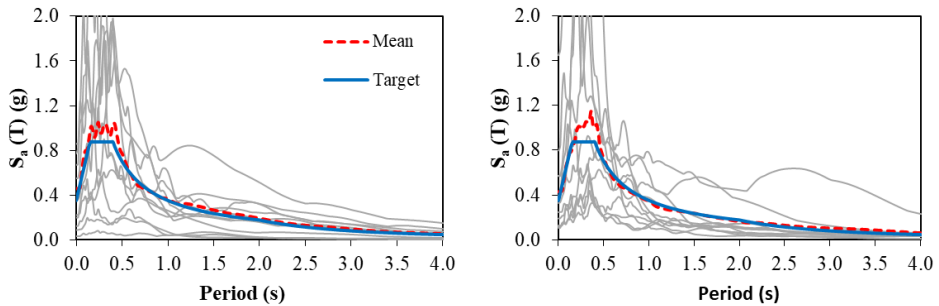


Fig. 2. Response spectral acceleration of ground motions matching with EC8 target spectrum considering NF (left) and FF (right) records for site class A

Table 2. Characteristics of earthquakes obtained for NF and FF records for soil class A

| Near Fault |                                     |       |         |                | Far Fault |                        |       |         |                |
|------------|-------------------------------------|-------|---------|----------------|-----------|------------------------|-------|---------|----------------|
| Comp       | Earthquake                          | $M_w$ | Station | $d_{Epi}$ (km) | Comp      | Earthquake             | $M_w$ | Station | $d_{Epi}$ (km) |
| X          | South Iceland (aftershock) 21/06/00 | 6.4   | ST2557  | 15             | Y         | South Iceland 17/06/00 | 6.5   | ST2496  | 31             |
| Y          | South Iceland (aftershock) 21/06/00 | 6.4   | ST2496  | 14             | Y         | Izmit 17/08/99         | 7.6   | ST770   | 78             |
| Y          | Izmit 17/08/99                      | 7.6   | ST575   | 9              | Y         | Montenegro 15/04/79    | 6.9   | ST64    | 21             |
| Y          | Valnerina 19/09/79                  | 5.8   | ST225   | 5              | X         | South Iceland 17/06/00 | 6.5   | ST2557  | 32             |

|        |                                |      |                |       |   |                            |     |        |    |
|--------|--------------------------------|------|----------------|-------|---|----------------------------|-----|--------|----|
| X      | Bingol<br>01/05/03             | 6.3  | ST539          | 14    | X | Campano Lucano<br>23/11/80 | 6.9 | ST102  | 80 |
| Y      | Mt. Hengill Area<br>04/06/98   | 5.4  | ST2495         | 18    | Y | Campano Lucano<br>23/11/80 | 6.9 | ST96   | 32 |
| Y      | Mt. Hengill Area<br>04/06/98   | 5.4  | ST2497         | 15    | Y | Umbria<br>29/04/84         | 5.6 | ST138  | 27 |
| Y      | South Iceland<br>17/06/00      | 6.5  | ST2558         | 15    | Y | Vrancea<br>30/08/86        | 7.2 | ST40   | 49 |
| Y      | Tabas<br>16/09/78              | 7.3  | ST54           | 12    | X | Avej<br>22/6/2002          | 6.5 | ST3311 | 28 |
| Y      | NE of Banja Luka<br>13/08/81   | 5.7  | ST2950         | 10    | Y | Duzce 1<br>12/11/99        | 7.2 | ST3136 | 23 |
| X      | South Iceland<br>17/06/00      | 6.5  | ST2486         | 5     | X | Friuli<br>06/05/76         | 6.5 | ST20   | 23 |
| X      | Lazio Abruzzo<br>07/05/84      | 5.9  | ST140          | 5     | X | Campano Lucano<br>23/11/80 | 6.9 | ST100  | 26 |
| Y      | Calabria<br>11/03/78           | 5.2  | ST45           | 10    | Y | Montenegro<br>15/04/79     | 6.9 | ST68   | 65 |
| PUL164 | San Fernando1<br>09/02/71      | 6.61 | Pacoima<br>Dam | 11.86 | X | Izmit<br>17/08/99          | 7.6 | ST561  | 47 |
| Y      | Izmit (aftershock)<br>13/09/99 | 5.8  | ST575          | 15    | Y | Campano Lucano<br>23/11/80 | 6.9 | ST93   | 23 |

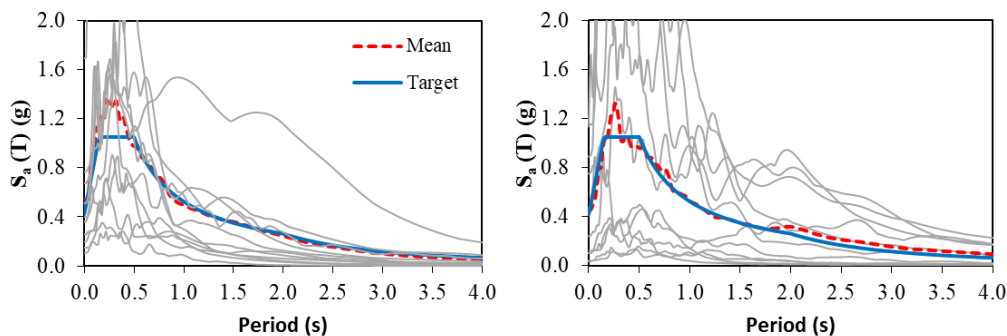


Fig. 3. Response spectral acceleration of ground motions matching with EC8 target spectrum considering NF (left) and FF (right) records for site class B

Table 3. Characteristics of earthquakes obtained for NF and FF records for soil class B

| Near Fault |                           |                |         |                       | Far Fault |                            |                |         |                       |
|------------|---------------------------|----------------|---------|-----------------------|-----------|----------------------------|----------------|---------|-----------------------|
| Comp       | Earthquake                | M <sub>w</sub> | Station | d <sub>Epi</sub> (km) | Comp      | Earthquake                 | M <sub>w</sub> | Station | d <sub>Epi</sub> (km) |
| Y          | South Iceland<br>17/06/00 | 6.5            | ST2482  | 15                    | X         | Campano Lucano<br>23/11/80 | 6.9            | ST99    | 33                    |
| Y          | Firuzabad<br>20/06/94     | 5.9            | ST3297  | 7                     | X         | Aigion 15/06/95            | 6.5            | ST1332  | 42                    |
| X          | Skydra-Edessa<br>18/02/86 | 5.3            | ST1306  | 2                     | X         | Montenegro<br>15/04/79     | 6.9            | ST63    | 24                    |
| Y          | Ano Liosia<br>07/09/99    | 6              | ST1258  | 14                    | X         | Montenegro<br>15/04/79     | 6.9            | ST62    | 25                    |

|   |                            |     |        |    |              |                             |      |        |       |
|---|----------------------------|-----|--------|----|--------------|-----------------------------|------|--------|-------|
| Y | Kalamata<br>03/01/04       | 5.9 | ST164  | 10 | X            | South Aegean<br>23/05/94    | 6.1  | ST1310 | 45    |
| X | Ano Liosia<br>07/09/99     | 6   | ST1257 | 18 | X            | Umbria Marche<br>26/09/97   | 6    | ST231  | 78    |
| X | Ano Liosia<br>07/09/99     | 6   | ST1259 | 14 | Y            | Panislir<br>30/10/83        | 6.6  | ST133  | 33    |
| Y | Campano Lucano<br>23/11/80 | 6.9 | ST276  | 16 | CHY028<br>-E | Chi-Chi, Taiwan<br>21/09/99 | 7.62 | CHY028 | 32.67 |
| X | Montenegro<br>15/04/79     | 5.4 | ST63   | 18 | 1875y        | Griva<br>21/12/90           | 6.1  | ST1306 | 36    |
| Y | Kalamata<br>03/01/04       | 5.9 | ST163  | 11 | ABBAR-<br>T  | Manjil, Iran<br>21/06/90    | 7.37 | ABBAR  | 40.43 |
| X | Erzincan<br>13/03/92       | 6.6 | ST205  | 13 | TAB-LN       | Tabas, Iran<br>16/09/78     | 7.35 | Tabas  | 55.24 |
| Y | Patras<br>14/07/93         | 5.6 | ST1330 | 10 | Y            | Campano Lucano<br>23/11/80  | 6.9  | ST103  | 72    |
| Y | South Iceland<br>17/06/00  | 6.5 | ST2484 | 7  | X            | Tabas<br>16/09/78           | 7.3  | ST59   | 57    |
| Y | Montenegro<br>15/04/79     | 6.9 | ST67   | 16 | Y            | Izmit<br>17/08/99           | 7.6  | ST544  | 93    |
| Y | Umbria Marche<br>26/09/97  | 6   | ST60   | 11 | Y            | Umbria Marche<br>26/09/97   | 6    | ST228  | 38    |

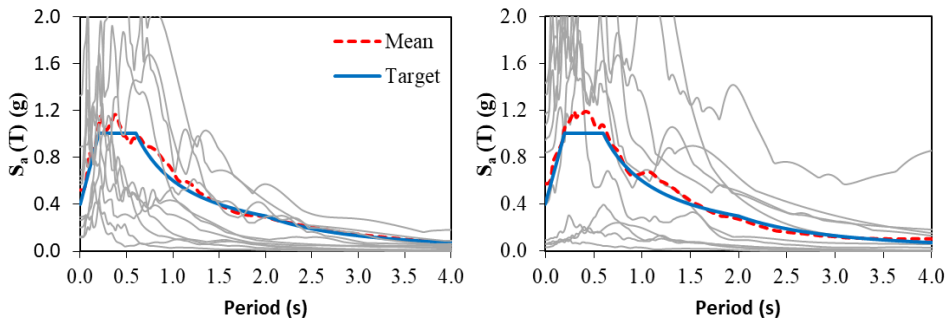


Fig. 4. Response spectral acceleration of ground motions matching to EC8 target spectrum considering NF (left) and FF (right) records for site class C

Table 4. Characteristics of earthquakes obtained for NF and FF records for soil class C

| Near Fault   |                                 |                |                 |                       | Far Fault    |                             |                |                       |                       |
|--------------|---------------------------------|----------------|-----------------|-----------------------|--------------|-----------------------------|----------------|-----------------------|-----------------------|
| Comp         | Earthquake                      | M <sub>w</sub> | Station         | d <sub>Epi</sub> (km) | Comp         | Earthquake                  | M <sub>w</sub> | Station               | d <sub>Epi</sub> (km) |
| X            | Faial<br>07/09/98               | 6.1            | ST87            | 11                    | Y            | Cubuklu<br>17/08/99         | 5.5            | ST65                  | 34                    |
| Y            | Lazio Abruzzo<br>07/05/84       | 5.9            | ST147           | 16                    | H-<br>E08140 | Imperial Valley<br>15/10/79 | 6.53           | Imperial<br>Valley-06 | 28.09                 |
| A-<br>OBR270 | WHITTIER<br>NARROWS<br>01/10/87 | 5.99           | OBREGON<br>PARK | 9.05                  | PAR—L        | Northridge 01<br>17/01/94   | 6.69           | Pardee –<br>SCE       | 25.65                 |
| X            | Friuli<br>06/05/76              | 6              | ST33            | 9                     | Y            | Lazio Abruzzo<br>07/05/84   | 5.9            | ST148                 | 45                    |

|              |                                |      |                              |       |              |                             |      |                     |       |
|--------------|--------------------------------|------|------------------------------|-------|--------------|-----------------------------|------|---------------------|-------|
| X            | Ano Liosia<br>07/09/99         | 6    | ST1253                       | 19    | RIO360       | Cape Mendocino<br>25/04/92  | 7.01 | RIO DELL<br>OVERPAS | 53.34 |
| Y            | Dinar<br>01/10/95              | 6.4  | ST271                        | 8     | X            | Duzce 1<br>12/11/99         | 7.2  | ST3139              | 28    |
| X            | Alkion<br>2/25/81              | 6.6  | ST122                        | 19    | Y            | Seferihisar<br>10/04/03     | 5.7  | ST858               | 42    |
| KJM000       | Kobe, Japan<br>17/01/95        | 6.9  | KJMA                         | 18.27 | X            | Duzce 1<br>12/11/99         | 7.2  | ST541               | 39    |
| Y            | Duzce 1<br>12/11/99            | 7.2  | ST553                        | 8     | TCU065<br>-E | Chi-Chi, Taiwan<br>21/09/99 | 7.62 | TCU065              | 26.67 |
| X            | Patras<br>14/07/93             | 5.6  | ST10                         | 10    | C02065       | PARKFIELD1<br>28/09/04      | 6    | CHOLAM<br>E         | 31.04 |
| H-<br>BCR230 | Imperial Valley<br>15/10/79    | 6.53 | BONDS<br>CORNER              | 6.2   | Y            | Patras<br>14/07/93          | 5.6  | ST215               | 37    |
| NGI270       | San Salvador<br>13/02/01       | 5.8  | NATL<br>GEOGRAF<br>ICAL INST | 9.54  | G03000       | Loma Prieta<br>18/10/89     | 6.93 | GILROY<br>ARRAY     | 31.4  |
| SCS052       | Northridge<br>17/01/94         | 6.69 | SYLMAR-<br>CONVERT<br>ER     | 13.11 | Y            | Chenoua<br>29/10/89         | 5.9  | ST2881              | 29    |
| B-<br>PTS225 | Superstition Hills<br>24/11/87 | 6.54 | Parachute<br>Test Site       | 15.99 | X            | Umbria Marche<br>26/09/97   | 6    | ST223               | 22    |
| X            | Umbria Marche<br>26/09/97      | 5.5  | ST221                        | 7     | X            | Filippias<br>16/06/90       | 5.5  | ST126               | 44    |

### 3. Results and discussions

#### 3.1 DRF Models Used for Comparison Analysis

In this section, Lin and Chang [30] (called LC04 hereafter) and Hatzigeorgiou [2] (called H10 hereafter) models are presented and compared with the results obtained in this study since these models consider the influence of soil conditions.

As already mentioned, DRFs are adjusting factors to be applied to the 5% damped spectral ordinates and they are frequently obtained from the different viscous damping considering the displacement response of elastic SDOF systems as given in (Eq. 1). In addition to (Eq. 1), DRFs can also be calculated by two other definitions (Eq. 2), namely, pseudo-spectra related to displacement of the structure, which are the pseudo-velocity spectrum  $S_{pv}$  and pseudo-acceleration spectrum  $S_{pa}$ . They are often used to study the true response spectra ( $S_v$  and  $S_a$ ) to construct the design spectra [28].

$$S_{pv}(T, \xi) = \frac{2\pi}{T} S_d(T, \xi) \tag{1}$$

$$S_{pa}(T, \xi) = \frac{2\pi}{T} S_v(T, \xi) = \frac{4\pi^2}{T^2} S_d(T, \xi) \tag{2}$$

DRFs adopted by seismic codes are often defined as the ratio between the displacement or acceleration spectra,  $S_d(T, \xi)$  or  $S_a(T, \xi)$ , and 5% damped displacement or acceleration spectrum,  $S_d(T, 5\%)$  or  $S_a(T, 5\%)$ , respectively, as described in (Eq. 3) and (Eq. 4) [2], [3], [29], [30].

$$DRFd(T, \xi) = \frac{S_d(T, \xi)}{S_d(T, 5\%)} = \frac{S_{pa}(T, \xi)}{S_{pa}(T, 5\%)} \tag{3}$$

$$DRFa(T, \xi) = \frac{S_a(T, \xi)}{S_a(T, 5\%)} \tag{4}$$

In EC8, the damping effect is introduced via the damping correction factor ( $\eta$ ) defined by (Eq. 5) and  $\eta=1$  for the reference value of 5% viscous damping. In the equation, the damping ratio is expressed in percentage and the damping correction factor should be equal or greater than 0.55, as recommended by EC8.

$$\eta = \sqrt{10/(5 + \xi)} \tag{5}$$

Lin and Chang [30] have performed a statistical study to predict the damping reduction factors considering 1037 seismic records on three types of soil classes (A to D) according to NEHRP [15]. The proposed models are given in (Eq. 6) and (Eq. 7). They are based on the spectrum different constant values which are used to estimate the DRFs (see Tables 5 and 6).

$$DRFd = 1 - \frac{aT^b}{(T + 1)^c} \tag{6}$$

Table 5. Site- and damping-dependent coefficients for DRFd [30]

| Site class | <i>a</i>                 | <i>b</i> | <i>c</i> |
|------------|--------------------------|----------|----------|
| AB         | 1.1637+0.3885ln( $\xi$ ) | 0,229    | 0.505    |
| C          | 1.4532+0.4872ln( $\xi$ ) | 0.354    | 0.810    |
| D          | 1.3243+0.4426ln( $\xi$ ) | 0.311    | 0.664    |

Hatzigeorgiou [2] proposed a new model (Eq. 8) to predict DRFs dependent on displacement and acceleration response spectra accounting the impact of soil and ground motion types (i.e., NF and FF earthquakes), in addition to viscous damping ratio and vibration period.  $c_1$  to  $c_5$  are the constants of equation and they are given in the Tables 7 and 8 for DRFd and DRFa, respectively.

$$DRFa = d + eT \tag{7}$$

Table 6. Site- and damping-dependent coefficients for DRFa [30]

| Site class | <i>d</i>             | <i>e</i>                            |
|------------|----------------------|-------------------------------------|
| AB         | 0.391 $\xi^{-0.304}$ | 0.0057+0.383 $\xi^{-1}/15,929\xi^2$ |
| C          | 0.309 $\xi^{-0.392}$ | 0.0151+0.474 $\xi^{-1}/10,241\xi^2$ |
| D          | 0.326 $\xi^{-0.371}$ | 0.0348+0.248 $\xi^{-1}/8,250\xi^2$  |

$$DRF(T, \xi) = 1 + (\xi - 5) \cdot [1 + c_1 \cdot \ln(\xi) + c_2 \cdot (\ln(\xi))^2] \cdot [c_3 + c_4 \cdot \ln(T) + c_5 \cdot (\ln(T))^2] \tag{8}$$

Table 7. Coefficient values in (Eq. 8) for DRFs dependent on displacement spectra [2]

|       | Far-fault |          | Near-fault |                  |
|-------|-----------|----------|------------|------------------|
|       | Site A    | Site B   | Site C     | All Site classes |
| $c_1$ | -0.30453  | -0.29404 | -0.29406   | -0.30241         |
| $c_2$ | 0.2184    | 0.01963  | 0.0199     | 0.02183          |
| $c_3$ | -0.07729  | -0.09299 | -0.09014   | -0.08926         |
| $c_4$ | 0.00229   | 0.00897  | -0.00001   | 0.01097          |
| $c_5$ | 0.00229   | 0.01219  | 0.01196    | 0.01007          |

Table 8. Coefficient values in (Eq. 8) for DRFs dependent on acceleration spectra [2]

|                | Site A   | Far-fault<br>Site B | Site C   | Near-fault<br>All Site classes |
|----------------|----------|---------------------|----------|--------------------------------|
| c <sub>1</sub> | -0.36725 | -0.36051            | -0.36128 | -0.36227                       |
| c <sub>2</sub> | 0.03526  | 0.03498             | 0.03494  | 0.03495                        |
| c <sub>3</sub> | -0.02634 | -0.04093            | -0.05435 | -0.04517                       |
| c <sub>4</sub> | 0.0323   | 0.03379             | 0.02907  | 0.03454                        |
| c <sub>5</sub> | -0.01047 | -0.00191            | 0.00612  | -0.0024                        |

### 3.2 Effect of Near- And Far-Fault Ground Motions on the DRFd

In Figures 5 to 7, the mean values of the DRFs calculated for NF and FF earthquakes and all ground motions (i.e., combination of results of near- and far-faults) for a structural damping ratio of 10%, 20%, and 40%, are plotted separately. It can be stated from the figures that DRFd values generally increase with increasing damping ratios and vibration periods.

Figure 5 shows the trend of the computed DRFs as well as the predictive models and it is seen that the LC04 model is comparable with NF and FF DRFs. The trend of the H10 model seems to be in agreement with DRFs for NF earthquakes, but DRFs produced by the H10 model for FF earthquakes is not satisfactory compared to the NF results. The misfit of FF DRFs increases with increasing damping ratio. Since the EC8 model is not dependent on the periods, the values are constant for all periods and DRFs are decreasing with increasing damping. According to Figure 5, target DRFs fluctuated around DRFs produced by EC8 for damping ratio lower than 40%, implying less misfit between them.

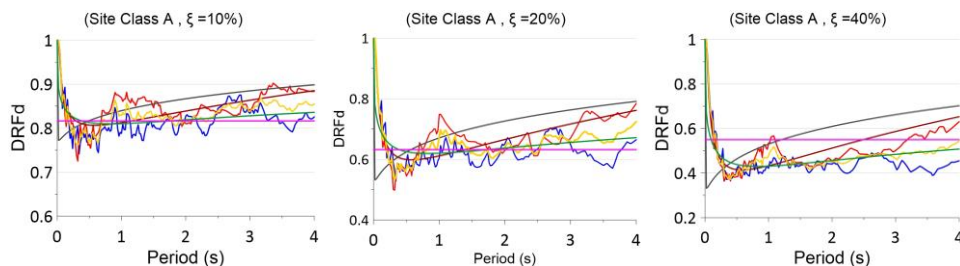


Fig. 5. DRFd values for NF and FF earthquakes for soil A

DRFd values obtained for soil B are plotted in Figure 6 with code-based results and prediction models. It is observed that the H10 model slightly differs from the analysis results for soil B for  $T > 2.0s$  and damping ratios of 10% and 20%. Distribution of DRFd values between NF and FF motions diverged and this becomes more evident with increasing damping ratios in soil B Compared to soil A. DRFd values of NF motions are greater than those of FF motions by 16%, 38%, and 58%, for  $\xi=10\%$ , 20% and 40%, respectively. Compared to soil B, DRFd values, calculated for NF and FF earthquakes shown in Figure 7, are less scattered in soil C. It appears that the accuracy of LC04 and H10 models increases and the H10 model seems slightly in better agreement with target DRFs compared to LC04 and this becomes more evident for high natural periods and damping ratios. It is obvious from the figures that DRFd values according to the EC8 definition are non-conservative, especially for  $T > 1.5s$  and  $\xi \leq 20\%$ . Owing to the fixed condition given by EC8 ( $\eta \geq 0.55$ ), the DRFd values provided by the code are conservative since the code-based values are larger than the target values for 40% damping, especially for periods less than 3s for A and B soil types, and periods less than 2.5s for C soil type.



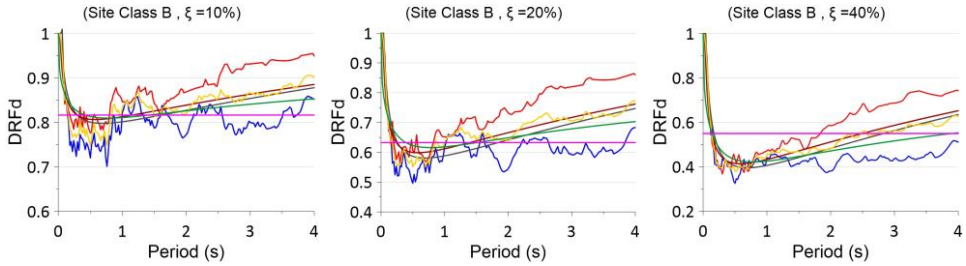


Fig. 6. DRF<sub>d</sub> values for NF and FF earthquakes for soil B

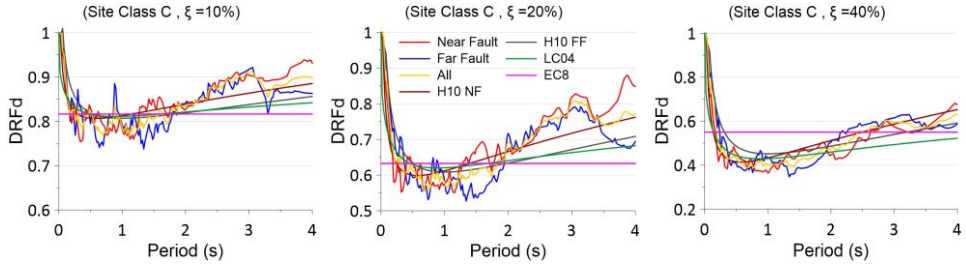


Fig. 7. DRF<sub>d</sub> values for NF and FF earthquakes for soil C

To examine the results quality of the prediction models and code based DRFs in a quantitative manner, root mean square error (RMSE) and mean absolute error (MAE) are computed for considered period ranges between the target (i.e., determined from code compatible earthquakes) and the prediction models. The results are plotted in Fig. 8. It should be noted that these error measures (i.e., RMSE and MAE) are calculated for NF and FF earthquakes separately and they were averaged for comparison purposes. It can be said that the lower RMSE and MAE can be attributed to less error or biased results, which can be also described as showing better correlation.

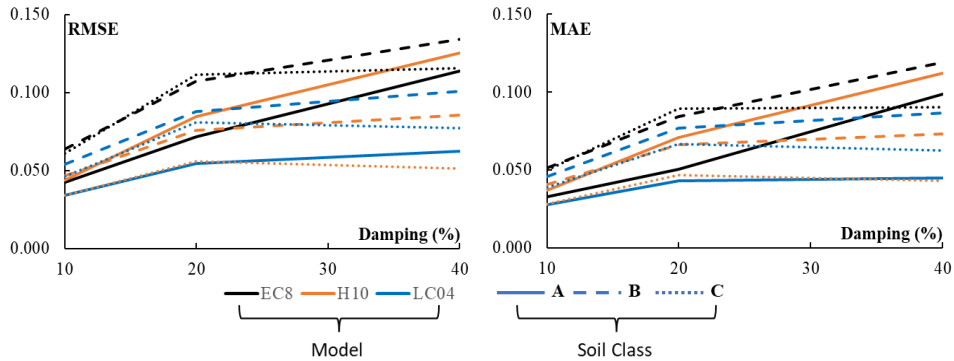


Fig. 8. Comparison of RMSE (left) and MAE (right) distribution of the models in terms of displacement DRFs for different soil classes and damping ratios

It can be viewed from Fig. 8 that values of RMSE and MAE are increasing with increasing damping ratio, in general, and this situation is more apparent with the code-based values. According to the results, LC04 model predictions are less biased compared to H10 and code based DRFs for soil class A. In addition, it seems that H10 model is more biased compared to EC8 for soil class A since the RMSE and MAE values are the average of NF and FF. The evaluations revealed that this situation is mainly related to FF predictions of H10 model as can be also observed in Fig. 5. On the other hand, NF values produced by the H10 model (RMSE < 0.03) is considerably lower than the EC8 model (RMSE > 0.04) and the H10 model

(RMSE < 0.06) is less biased compared to EC8 (RMSE > 0.09) and LC04 (RMSE > 0.07) for soil classes of B and C for all damping ratios. In the right side of Fig. 8, MAE results imply that the trends of LC04 and H10 models are almost comparable. It can be said that, in general, H10 and LC04 models are less biased (RMSE < 0.07 and MAE < 0.06 in average) than EC8 DRFs which means a better correlation with DRFs determined from the selected real earthquakes.

In Figure 9, the ratio of DRFd values, for NF and FF earthquakes are plotted for all damping ratios and soil types considered. It can be observed from the figures that despite the fluctuations between the ratios, the ratio shown for soil class B differs significantly from those of soil A and soil C, especially for  $T > 1.5s$ . The discrepancies between the ratios increase as the damping ratio increases. The maximum values of the ratios determined from class B are 1.20, 1.45 and 1.71 for 10, 20, and 40% ratios, respectively. The results also align with Lin & Chang [30] model for soil B.

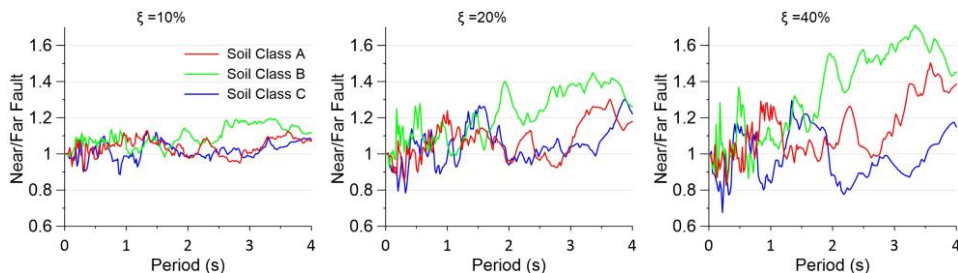


Fig. 9. Comparison of DRFd ratios of near/far-fault earthquakes for  $\xi = 10\%$ ,  $20\%$  and  $40\%$

### 3.3 Effect of Near- And Far-Fault Ground Motions on the DRFa

The effect of NF and DD motions is also examined for acceleration spectra based DRF values considering different damping ratios and A, B and C soil classes defined in EC8. Figures 10 to 12 show the distribution of code based DRFa values according to damping ratios and for NF and FF earthquakes corresponding to A, B and C classes, respectively. The distribution of DRFa values in Figure 10 indicates that the LC04 model is almost compatible with the target DRFs even at high damping ratios regarding site class A.

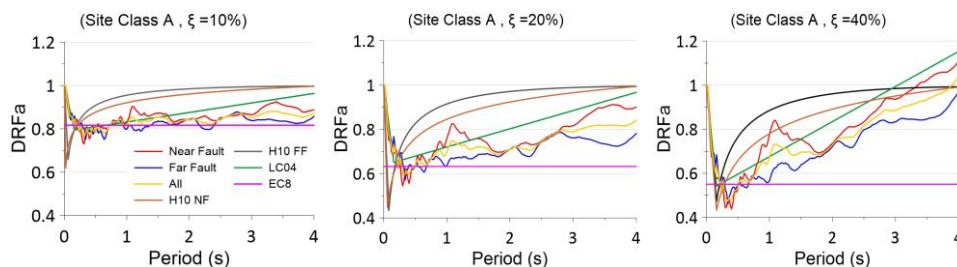


Fig. 10. DRFa values for NF and FF earthquakes for soil A

However, the H10 model produced larger values than the target DRFa values for all damping ratios and for near- and far-fault earthquakes. As observed in earlier section, DRFs produced by EC8 are constant and the code based DRFs seem consistent with DRF values determined from the selected earthquakes. However, compatibility of code based DRF values are significantly decreasing with increasing period, especially high periods (e.g.,  $T > 1.0s$ ).

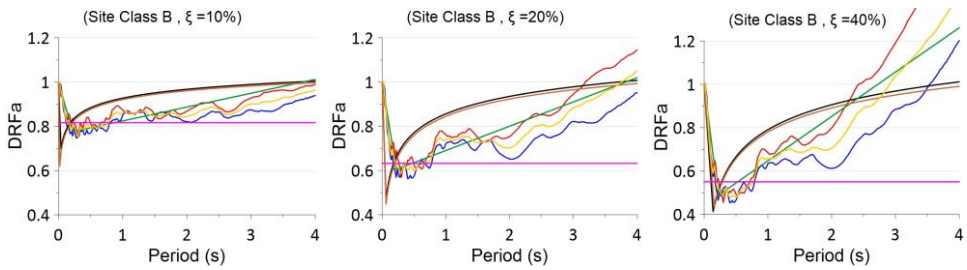


Fig. 11. DRFa values for NF and FF earthquakes for soil B

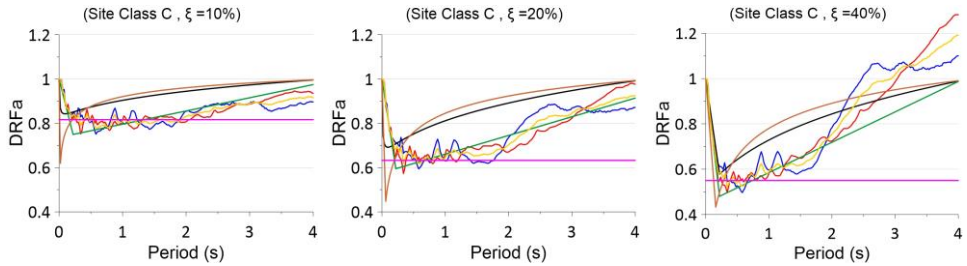


Fig. 12. DRFa values for NF and FF earthquakes for soil C

The distribution of DRFa values corresponding to soil B (see Figure 11) is also similar to the distribution observed for soil A. It can be said that the distribution of DRF values determined from the acceleration spectra is smoother than DRF values determined from the displacement spectra. The effect of NF and DD can also be seen for soil class B, but DRFa values are higher than those of DFRd. The same observations given for soils A and B can also be made for soil class C (see Figure 12). In addition, it can be said that compatibility of H10 model is slightly increasing compared to DRF values for A and B classes, and the values determined from the analysis.

The DRFd values are always lower than the unit value for all soil types and damping ratios. However, DRFa values may be higher than the unit value (i.e.,  $DRFa > 1.0$ ) at high vibration periods (for example for  $T > 2.5s$ ). When the code based DRFs are evaluated with target DRFa values, it can be said that the code-based results are generally lower than the computed DRFa values and this issue becomes more apparent at high damping ratios. Despite the slight fluctuations computed from the code compatible real earthquakes, especially at low to medium structural periods ( $T < 2.0s$ ), the code-based values seem to be relatively compatible with DRFa values at low damping ratios (i.e., 10%). On the other hand, the code based DRF values are quite lower than target DRFs for all soil classes and periods higher than 2.0s with increasing damping ratios.

RMSE and MAE are also computed for DRFa values to compare the compatibility of model results with target values and so these are plotted in Fig. 13. It is apparent from both error measures that the LC04 model is consistently less biased ( $RMSE < 0.1$  and  $MAE < 0.1$ ) compared to H10 and EC8 model DRFs for all soil classes and damping ratios. According to RMSE and MAE results, the H10 model is more biased especially for  $\xi = 10\%$  compared to EC8 for all soil classes. Similar observations were also made for DRF values determined from displacement spectra, but the biases became more pronounced when DRFa values are used. This situation can be again attributed to the considerations of very short period region ( $T < 0.50s$ ). Nevertheless, it should be noted that EC8 produces more biased result as the soil becomes softer ( $RMSE > 0.2$  and  $MAE > 0.2$  for soil class of B and C). MAE results (i.e., right side of Fig. 13) also confirm the conclusions drawn from RMSE results. When RMSE and MAE values determined from DRFd and DRFa results are compared (i.e., Fig. 8

and Fig. 13), it can be said that DRFa values are more biased than DRFd values since RMSE and MAE values are higher.

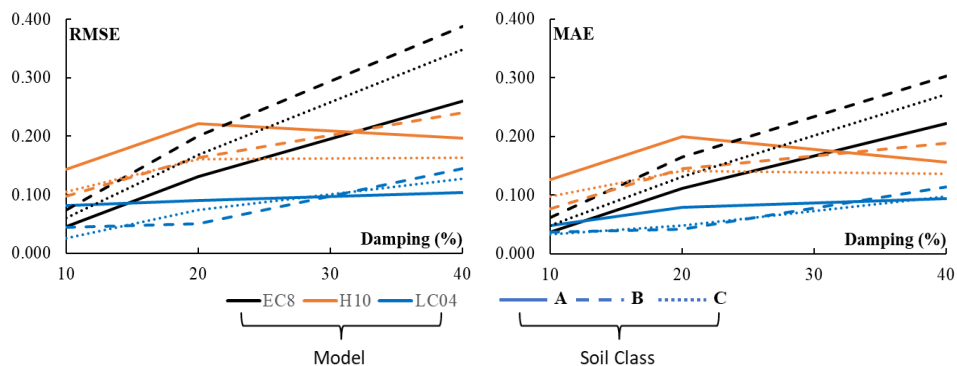


Fig. 13. Comparison of RMSE (left) and MAE (right) distribution of the models in terms of acceleration DRFs for different soil classes and damping ratios

The comparison of DRFa values between NF and FF motions, for various damping ratios and soil classes, is drawn in Figure 14. The curves show that the ratios fluctuated in the short to medium period ranges, such as 0.02 to 1.50s. At high period values (i.e.,  $T > 1.5s$ ), DRFa curves are smoother and the ratios of near/far fault for soil B are higher than for other soil types mainly when the damping ratio increases. In general, the near/ far fault ratios increase with increasing damping ratio and range between 0.9 and 1.1, 0.85 and 1.2, and 0.8 and 1.4 for  $\xi = 10\%$ , 20% and 40%, respectively.

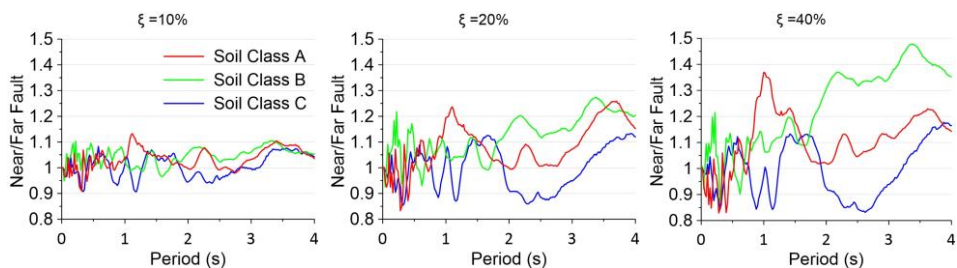


Fig. 14. Comparison of DRFa ratios of near/ far-fault earthquakes for  $\xi = 10\%$ , 20% and 40%

#### 4. Conclusions

In this study, DRFs were calculated based on the code-based target spectrum. The EC8 design acceleration spectra were used as the target for the ground motion selection. Therefore, real ground motion records were collected from different ground motion databases and divided into two groups, based on epicentral distance to represent the near- and far-fault type earthquakes. Then, the ground motions were selected and scaled to match the EC8 spectra regarding the A, B and C soil types defined in the code. The damping reduction factors were calculated based on the displacement and acceleration response spectra for damping ratios of 10, 20, and 40%, and compared with EC8 and two known DRF models from the literature for evaluation purposes. The following implications can be made:

- The distribution of DRF values indicated that the DRFa results are smoother than those of DRFd over the natural periods. The results also highlighted that DRF

values are more sensitive to ground motion type, vibration period and damping ratios.

- It was observed that the local site conditions have limited effect on DRFs. However, it was found that the DRF ratios of near- to far- field determined from acceleration and displacement spectra are especially exaggerated on site class B. This aligns with the conclusions made by Lin and Chang [30].
- It was observed that DRFd values determined from near-fault type motions are generally higher than those of far- fault type motions around 16, 38 and 58% on average for  $\xi=10; 20$  and 40%, respectively. In addition, it was found that the ratio of DRFd/DRFa is around 1.25 on average, implying the higher DRFd values.
- To evaluate and then compare the code-based and predictions of known models (i.e, H10 and LC04), RMSE and MAE error measures were computed. The computations indicated that regardless of model, soil type and damping ratio, DRFa values (RMSE  $\approx 0.145$ ) were more biased than DRFd (RMSE  $\approx 0.075$ ) values.
- Based on the measurements, it was noted that LC04 (RMSE  $\approx 0.066$ ) and H10 (RMSE  $\approx 0.067$ ) models were comparable on average and less biased compared to EC8 (RMSE  $\approx 0.091$ ) in terms of DRFd. MAE results also confirm this observation (MAE  $\approx 0.055, 0.057$  and  $0.074$  for LC04, H10 and EC8, respectively).
- Based on the comparisons, it can be stated that the DRF values provided by EC8 are more biased and the difference between the target and code based DRF values increases as the soil becomes softer, such as RMSE  $> 0.2$  and MAE  $> 0.2$  for soil classes B and C for DRFa. Accordingly, it is thought that code-based definitions should be refined to consider important parameters that affect DRFs.

It should be noted that, although the number of selected records recommended by EC8 is satisfied, the required number of records complying with the code-based record selection recommendations and complying with the near- and far- fault earthquakes were not adequate. Due to the insufficient number of ground motion records, only 15 earthquake records could be selected, for which DRF values were evaluated. However, in future studies, complying code-compatible records other than near- and far- field ground motions could be considered to increase the number of sets including seven or more ground motions to make further evaluations of code-based DRF values.

### Acknowledgement

The Institute for Infrastructure & Environment of Heriot-Watt University, Edinburgh, is deeply acknowledged for hosting the main author as Visiting Scholar.

### References

- [1] Atkinson GM, Pierre J-R. Ground-motion response spectra in eastern North America for different critical damping values. *Seismol Res Lett.* 2004;75(4):541-545. <https://doi.org/10.1785/gssrl.75.4.541>
- [2] Hatzigeorgiou GD. Damping modification factors for SDOF systems subjected to near-fault, far-fault and artificial earthquakes. *Earthq Eng Struct Dyn.* 2010;39(11). <https://doi.org/10.1002/eqe.991>
- [3] Hao A, Zhou D, Li Y, Zhang H. Effects of moment magnitude, site conditions and closest distance on damping modification factors. *Soil Dyn Earthq Eng.* 2011;31(9):1232-1247. <https://doi.org/10.1016/j.soildyn.2011.05.002>
- [4] Newmark NM, Hall WJ. Seismic design criteria for nuclear reactor facilities. In: *Proceedings of the 4th World Conference on Earthquake Engineering.* 1969. Vol. 4, p. 37-50.
- [5] Newmark NM, Hall WJ. *Earthquake spectra and design.* Eng Monogr Earthq Criteria. 1982.

- [6] Comartin CD. Seismic evaluation and retrofit of concrete buildings. Vol. 40. Seismic Safety Commission, State of California; 1996.
- [7] Federal Emergency Management Agency. NEHRP guidelines for the seismic rehabilitation of buildings. FEMA-273. Washington DC; 1997.
- [8] UBC. Uniform Building Code. International Conference of Building Officials, Whittier, CA; 1994, 1997.
- [9] ASCE. Minimum design loads for buildings and other structures. ASCE/SEI 7-05. Reston, Va; 2006.
- [10] Federal Emergency Management Agency. NEHRP prestandard and commentary for the seismic rehabilitation of buildings. FEMA-356. Washington DC; 2000.
- [11] Kawashima K, Aizawa K. Modification of earthquake response spectra with respect to damping. *Doboku Gakkai Ronbunshu*. 1984;1984(344):351-355. <https://doi.org/10.2208/jscej.1984.351>
- [12] Caltrans, California Department of Transportation. Seismic Design Criteria, 1.4. Sacra., Cal.; 2006.
- [13] Ashour SA. Elastic seismic response of buildings with supplemental damping. University of Michigan; 1987.
- [14] UBC-94. Uniform Building Code. International Conference of Building Officials, Whittier, CA; 1994.
- [15] Federal Emergency Management Agency. Recommended Provisions for Seismic Regulations for New Buildings. Washington, DC; 1994.
- [16] Bommer JJ, Elnashai AS, Weir AG. Compatible acceleration and displacement spectra for seismic design codes. In: *Proceedings of the 12th World Conference on Earthquake Engineering*. 2000. Vol. 8.
- [17] Eurocode 8: Design of structures for earthquake resistance-part 1: general rules, seismic actions and rules for buildings. Brussels Eur Comm Stand. 2005.
- [18] Ramirez OM. Development and evaluation of simplified procedures for the analysis and design of buildings with passive energy dissipation systems. State University of New York at Buffalo; 2001.
- [19] Federal Emergency Management Agency. Recommended provisions for seismic regulations for new buildings and other structures. NEHRP-2003. Washington, DC; 2003.
- [20] S., Otani K. Japanese state of practice in design of seismically isolated buildings. In: *The Fourth U.S.-Japan Workshop on Performance-Based Earthquake Engineering Methodology for Reinforced Concrete Building Structures*; Sep. 2002.
- [21] Ministry of Vehicle Infrastructure and Transport. Guidelines for Calculation Procedure and Technical Standard on Seismically Isolated Structures (in Japanese). Building Center of Japan; 2001.
- [22] Priestley MJN. Myths and fallacies in earthquake engineering. *Concr Int*. 1997;19(2):54-63.
- [23] Zhou F, Wenguang L, Xu Z. State of the art on applications, R&D and design rules for seismic isolation in China. In: *Proceedings of the 8th World Seminar on Seismic Isolation, Energy Dissipation and Active Vibration Control of Structures*. 2003. p. 6-10.
- [24] China Code. Seismic Design Code for Buildings (GB 50011-2001). China Archit Ind Press. Beijing, China; 2001.
- [25] Benahmed B. Formulation of damping reduction factor for the Algerian seismic code. *Asian J Civ Eng*. 2018;19(4). <https://doi.org/10.1007/s42107-018-0023-6>
- [26] National Center of Earthquake Applied Research (CGS). Re'gles Parasismiques Alge'riennes., RPA99 (2003 Version). D.T.R. -B.C. 2.48. Algiers, Algeria; 2003.
- [27] Hubbard DT, Mavroeidis GP. Damping coefficients for near-fault ground motion response spectra. *Soil Dyn Earthq Eng*. 2011;31(3):401-417. <https://doi.org/10.1016/j.soildyn.2010.09.009>

- [28] Pu W, Kasai K, Kabando EK, Huang B. Evaluation of the damping modification factor for structures subjected to near-fault ground motions. *Bull Earthq Eng.* 2016;14(6). <https://doi.org/10.1007/s10518-016-9885-8>
- [29] Li H, Chen F. Damping modification factors for acceleration response spectra. *Geod Geodyn.* 2017;8(5). <https://doi.org/10.1016/j.geog.2017.04.009>
- [30] Lin Y-Y, Chang K-C. Effects of Site Classes on Damping Reduction Factors. *J Struct Eng.* 2004;130(11):1667-1675. [https://doi.org/10.1061/\(ASCE\)0733-9445\(2004\)130:11\(1667\)](https://doi.org/10.1061/(ASCE)0733-9445(2004)130:11(1667))
- [31] Zhao JX, et al. Effects of earthquake source, path, and site conditions on damping modification factor for the response spectrum of the horizontal component from subduction earthquakes. *Bull Seismol Soc Am.* 2019;109(6):2594-2613. <https://doi.org/10.1785/0120190105>
- [32] Fernandez-Davila VI, Mendo AR. Damping modification factors for the design of seismic isolation systems in Peru. *Earthq Spectra.* 2020;36(4). <https://doi.org/10.1177/8755293020926189>
- [33] American Society of Civil Engineers. Minimum design loads and associated criteria for buildings and other structures. 2017.
- [34] Benahmed B, Moustafa A, Badaoui M. Comparison between DRF for displacement and acceleration spectra with uncertain damping for EC8. *J Mater Eng Struct «JMES».* 2019;6(3):345-358.
- [35] Abdelhamid A, Benahmed B, Palanci M, Aidaoui L. Assessment of uncertainties in damping reduction factors using ANN for acceleration, velocity and displacement spectra. *Electron J Struct Eng.* 2023;8-13. <https://doi.org/10.56748/ejse.23395>
- [36] Pavlou EA, Constantinou MC. Response of elastic and inelastic structures with damping systems to near-field and soft-soil ground motions. *Eng Struct.* 2004;26(9):1217-1230. <https://doi.org/10.1016/j.engstruct.2004.04.001>
- [37] Daneshvar P, Bouaanani N. Damping modification factors for eastern Canada. *J Seismol.* 2017;21(6). <https://doi.org/10.1007/s10950-017-9678-9>
- [38] Dávalos H, Miranda E, Bantis J, Cruz C. Response spectral damping modification factors for structures built on soft soils. *Soil Dyn Earthq Eng.* 2022;154. <https://doi.org/10.1016/j.soildyn.2022.107153>
- [39] Zhang H, Zhao YG. Damping Modification Factor of Acceleration Response Spectrum considering Seismological Effects. *J Earthq Eng.* 2022;26(16). <https://doi.org/10.1080/13632469.2021.1991521>
- [40] Fiore A, Greco R. Influence of Structural Damping Uncertainty on Damping Reduction Factor. *J Earthq Eng.* 2022;26(4). <https://doi.org/10.1080/13632469.2020.1747573>
- [41] Dicleli M, Kara E. Damping reduction equation for the equivalent linear analysis of seismic isolated structures subjected to near fault ground motions. *Eng Struct.* 2020;220. <https://doi.org/10.1016/j.engstruct.2020.110834>
- [42] Zhou J, Zhao JX. A damping modification factor prediction model for horizontal displacement spectrum from subduction slab earthquakes in Japan accounting for site conditions. *Bull Seismol Soc Am.* 2020;110(2):647-665. <https://doi.org/10.1785/0120190156>
- [43] Miranda S, Miranda E, de la Llera JC. The effect of spectral shape on damping modification factors. *Earthq Spectra.* 2020;36(4). <https://doi.org/10.1177/8755293020936691>
- [44] Ambraseys NN, et al. Dissemination of European strong-motion data, Volume 2. 2004.
- [45] Ancheta TD, et al. NGA-West2 database. *Earthq Spectra.* 2014;30(3):989-1005. <https://doi.org/10.1193/070913EQS197M>
- [46] Kayhan AH, Demir A, Palanci M. Multi-functional solution model for spectrum compatible ground motion record selection using stochastic harmony search algorithm. *Bull Earthq Eng.* 2022;20(12):6407-6440. <https://doi.org/10.1007/s10518-022-01450-8>

- [47] Demir A, Palanci M, Kayhan AH. Evaluation of supplementary constraints on dispersion of EDPs using real ground motion record sets. Arab J Sci Eng. 2020;45(10):8379-8401. <https://doi.org/10.1007/s13369-020-04719-9>
- [48] Palanci M, Demir A, Kayhan AH. A statistical assessment on global drift ratio demands of mid-rise RC buildings using code-compatible real ground motion records. Bull Earthq Eng. 2018;16(11):5453-5488. <https://doi.org/10.1007/s10518-018-0384-y>
- [49] Kayhan AH, Demir A, Palanci M. Statistical evaluation of maximum displacement demands of SDOF systems by code-compatible nonlinear time history analysis. Soil Dyn Earthq Eng. 2018;115:513-530. <https://doi.org/10.1016/j.soildyn.2018.09.008>
- [50] Demir A, Palanci M, Kayhan AH. Probabilistic assessment for spectrally matched real ground motion records on distinct soil profiles by simulation of SDOF systems. Earthquakes Struct. 2021.
- [51] Palanci M, Demir A, Kayhan AH. The investigation of displacement demands of single degree of freedom models using real earthquake records compatible with TBEC-2018. Pamukkale Üniversitesi Mühendislik Bilim Derg. 2021;27(3):251-263. <https://doi.org/10.5505/pajes.2020.47936>
- [52] Graizer V, Kalkan E. Prediction of spectral acceleration response ordinates based on PGA attenuation. Earthq Spectra. 2009;25(1):39-69. <https://doi.org/10.1193/1.3043904>
- [53] Demir A, Palanci M, Kayhan AH. Evaluation the effect of amplitude scaling of real ground motions on seismic demands accounting different structural characteristics and soil classes. Bull Earthq Eng. 2023. <https://doi.org/10.1007/s10518-023-01780-1>
- [54] Palanci M, Demir A, Kayhan AH. Quantifying the effect of amplitude scaling of real ground motions based on structural responses of vertically irregular and regular RC frames. In: Structures. 2023. Vol. 51, p. 105-123. <https://doi.org/10.1016/j.istruc.2023.03.040>
- [55] Demir A, Kayhan AH, Palanci M. Response-and probability-based evaluation of spectrally matched ground motion selection strategies for bi-directional dynamic analysis of low-to mid-rise RC buildings. In: Structures. 2023. Vol. 58, p. 105533. <https://doi.org/10.1016/j.istruc.2023.105533>
- [56] Bommer JJ, Acevedo AB. The use of real earthquake accelerograms as input to dynamic analysis. J Earthq Eng. 2004;8(spec01):43-91. <https://doi.org/10.1080/13632460409350521>
- [57] Chopra AK. Dynamics of structures. Pearson Education India; 2007.



## Review on base and inter storey seismic isolation systems for high rise buildings

Gudipati Chaitanya Avinash<sup>\*,a</sup>, N. Lingeshwaran<sup>b</sup>

Department of Civil Engineering, Koneru Lakshmaiah Education Foundation (Deemed to be University), Vaddeswaram, Guntur, Andhra Pradesh- 522302, India

### Article Info

### Abstract

#### Article history:

Received 17 Jan 2024

Accepted 26 May 2024

#### Keywords:

High-rise buildings;  
Vibration control systems;  
Structural stability;  
Isolation bearings;  
Base isolation;  
Inter-storey isolation

In recent decades, the construction of high-rise buildings has accelerated in modern urban areas as a response to the world's expanding population and demand for efficient space utilization. These high-rise buildings are inherently more susceptible to hazards such as strong winds, earthquakes, and human activities, which could jeopardize structural stability. However, when this rapid growth in high-rise construction continues in earthquake-prone regions it highlights the need for cautious design and oversight measures to guarantee the comfort of occupants and overall safety of buildings. So, the necessity to adopt vibration control strategies in structural engineering is therefore becoming more and more clear. As technology is advancing, several control strategies were created and implemented for high-rise buildings around the world. This review article provides a comprehensive overview of base-isolation and inter-storey isolation systems for high-rise buildings, which is accomplished by extracting useful insights from analytical and design features of real-life high-rise buildings equipped with these base isolation and inter-storey isolation systems. In detail the article explores the basic concept and the characteristics of the Base isolation system, and types of isolation bearings used for buildings. The fundamental concepts and benefits of inter-storey isolation system over base isolation. Additionally, the importance of vibration control strategy for buildings, and the different types of vibration control systems were also discussed.

© 2024 MIM Research Group. All rights reserved.

## 1. Introduction

Tall or "high-rise" buildings are constructed to a degree that distinguishes from low or medium rise structures in terms of their architectural and structural design considerations, construction methodology used, its multipurpose usage and its unique engineering among buildings in a region [1]. Many nations, like Singapore, China, the United States, the United Kingdom, and Japan are working to advance construction of tall buildings as they add prestige and demonstrate a nation's economic power [2]. According to Indian standards (IS 16700), categorized these tall buildings when larger than 50 meters and smaller or equals to 250 meters in height [3]. The CTBUH (Council on Tall Buildings and Urban Habitat), characterized the buildings based on architectural height into the following categories. The buildings are classified as "tall" or "high-rise" if their height is 100 meters (328 feet), "super-tall" if it exceeds 300 meters (984 feet), and "Mega tall" if it exceeds 600 meters (2000 feet) [1,4]. Moreover, the high-rise buildings in earthquake prone regions are inherently more vulnerable to earthquake forces due to their height, slender profiles, and complex structural systems. In a typical earthquake resistant design for buildings, the columns and beams are designed to be strong and flexible enough

\*Corresponding author: [2201020006@kluniversity.in](mailto:2201020006@kluniversity.in)

<sup>a</sup> <https://orcid.org/0009-0001-8431-7536>; <sup>b</sup> <https://orcid.org/0000-0003-2998-7315>

DOI: <http://dx.doi.org/10.17515/resm2024.156st0117rv>

Res. Eng. Struct. Mat. Vol. 11 Iss. 1 (2025) 231-271

to resist ground motions [5]. But during a strong ground motion, these buildings might behave with inelastic action causing plastic deformation in the structural components such as beams, columns, and damage to non-structural components of buildings, which are difficult to repair and restore after the earthquake. Then seismic design of high-rise buildings through ductility, mass variation or higher stiffness alone could not avoid the structural damages during a strong earthquake [6]. So, the use of response (or) vibration control strategies plays a crucial role mainly in structures such as fire stations, hospitals, schools, radio stations, nuclear power plants, and other structures which are to be safeguarded for functionality during and after a seismic event [7-9].

### 1.1. Vibration or Response Control Systems for Buildings

The vibration control approach's primary intent is to protect the structure from seismic risk by mitigating vibrational energy that avoids resonance at each segment of structure and to restore the lateral integrity of structure after earthquake and wind induced vibrations [10,11]. The vibration control also provides some instant of time for occupant of structure to reach safe destination. This response control can either be achieved by construction with lateral load resisting systems or isolation of structure from its supporting ground. In general, this vibration control originates from structure's flexibility, which intends to increase the natural period of building [12]. Based upon the magnitude of vibration control to be achieved for the buildings, selection of the type of dampers or control devices required is done. The response control systems for buildings could be classified as passive, active, or semi-active, hybrid (figure1) on the energy source requirement for energy dissipation during a seismic event [13].

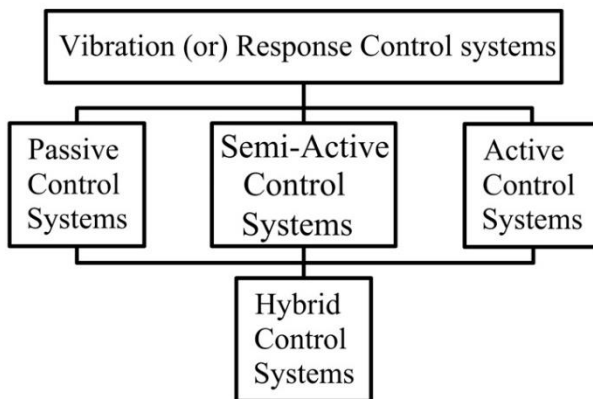


Fig. 1. Classification of vibration control systems

#### 1.1.1 Passive Control Systems

The Passive response control systems are those which do not demand any external energy source, the structure's motion during earthquake being utilized for energy dissipation [14,15,16]. Passive response control devices like seismic isolators, fluid viscous dampers (FVD), friction dampers, pressurized sand dampers (PSD), viscoelastic dampers and other dynamic vibration absorbers such as tuned mass damper (TMD), tuned mass damper with inerter (TMDI), tuned liquid column dampers systems (TLCD) are currently in practice. Passive Fluid Viscous Dampers are composed of a piston rod moving through a hollow cylinder filled with a viscous fluid (such as silicon oil). These FVDs under dynamic excitation, the movement of piston within the cylinder, forces the viscous fluid to flow through provided orifices at piston head. This movement produces a damping force that opposes the motion of the structure, which reduces the structural response [17-19]. Torre

Mayor, a 57-storey building in Mexico City skyline was the first high-rise building to utilize the FVDs as their primary means for vibration control system [20]. Numerous bridge structures such as San Francisco Oakland bay bridge [21], 91/5 highway overcrossing bridge [22] were equipped with fluid viscous dampers.

Friction Damper is a passive control type device that shows hysteretic behaviour and dissipates the kinetic energy by friction generated from sliding in between two solid surfaces. These friction dampers tend to downtrend motion of structure by principle of "bracing rather than breaking" [18,23–27]. These devices were less affected by number of load cycles, temperature changes, load frequencies and exhibits the rigid plastic behaviour [28]. Pall A S et al. [29] proposes X- braced damper, a type of friction damper which shows equal energy dissipation in both tension and compression braces due to presence of four links. This phenomenon will take place under the condition when the slippage of device is adequate to completely align any deformed braces. The three-story and nine-storey steel frame structures employed with friction dampers were experimented on shake table at University of British Columbia in 1985 and University of Berkeley in 1987. The shake table results have shown that responses of friction damped braces were far superior to the responses of moment-resisting braced frame and the members of friction damped frame remained elastic till 0.84g acceleration, while the moment resisting frame yielded at 0.3g acceleration. Tsampras G et al. [30] conducts numerical and experimental investigations on a full-scale deformable connection designed to link the floor system of a flexible gravity load resisting system to the stiff lateral force resisting system (LFRS) in earthquake-resistant buildings. In this study the deformable connection comprises a friction device (FD) and carbon fiber-reinforced bonded low-damping rubber bearings (RB) referring to the FD + RB connection. The experimental results validate that force-deformation responses of this FD + RB connection was stable under earthquake loading histories, quasi-static sinusoidal, and dynamic sinusoidal. The results also shown that FD's elastic stiffness regulates the overall elastic stiffness of the FD + RB connection, while the FD's frictional force governs the shift from elastic to post-elastic behaviour.

Pressurized sand damper (PSD) is a type of particle damper and a passive control system used to mitigate the vibrations from structures. The development of these PSD's was motivated from the failures of fluid dampers such as failure of end seals leading to detrimental leaking while accommodating for longer strokes, occurrence of occasional displacement limitations in buckling-restrained braces [31]. These PSDs mainly composes of moving piston in damper housing with pressurized sand. The sand particles in damper are enclosed within a sealed chamber and subjected to pressure, causing them to behave like a semi-solid material [32]. This allows the pressurized sand to shear that generates significant energy dissipation over a wide range of frequencies. The pressurized sand diminishes the vibrations through friction and deformation, converting kinetic energy into heat, which is then harmlessly dissipated [33,34]. These PSDs can be implemented in areas with extreme high and low temperatures, where use of fluid dampers may be challenging. Karimipetanlar M et al. [35] provides a numerical model by discrete element method to explain the mechanical behaviour of pressurized sand dampers subjected to cyclic loading. Different computational simulations of PSD were trialed and compared with different initial pressures and stroke amplitudes. The results regarding the energy dissipation have increased with increment in stroke amplitude. The specific damping capacity in all cases of simulations was shown to be near to one.

Viscoelastic Dampers are one of the earliest types of passive control systems used for high rise structures to mitigate seismic and wind induced vibrations. The viscoelastic material involved in dampers is usually made from copolymers or glassy substances that exhibit both viscous and elastic characteristics. These dampers combine the properties of both elastic solids and viscous fluids, offering to dissipate energy through material deformation

and internal friction and respond to deformation with time dependent strain that provides damping effect to the structure [36,37]. The dual behaviour of viscoelastic damper makes effective in structural applications demanding both instant response to sudden loads and long-term resistance to cyclic loads. Real life examples such as twin towers of World trade centre buildings in New York (38,39) and Columbia Sea First building in Washington (38,39) are first buildings to use viscoelastic dampers in practical implementation. Xu ZD et al. [40] explores the efficacy of viscoelastic dampers utilized with several kinds of viscoelastic material based on different matrix rubber developed. The high-order equivalent fractional derivative model was developed for numerical analysis to describe the characteristics of viscoelastic dampers. Viscoelastic dampers based on silicone rubber (SR) matrix and nitrile butadiene rubber (NBR) matrix used for experimentation. The results indicated that the performance of viscoelastic dampers is dependent on viscoelastic material's energy dissipation properties. The viscoelastic dampers based on NBR matrix have shown stable performance under different loading conditions when compared to dampers based on SR matrix.

Rubber or seismic isolators also known as base isolators are devices installed between foundation of structure and its super structure to mitigate the effects of seismic activity on crucial structures such as hospitals, bridges, etc. These seismic isolators behave as a flexible interface allowing the super structure to move independently to ground motions [41]. These seismic isolators are used to accommodate the movements in structures, such as both static and dynamic displacements due to creep and shrinkage and thermal effects [42]. Furthermore, the seismic isolators are classified based on several factors such as their characteristic behavior, material used for system and desired level of seismic mitigation are discussed in section 2.2.

Dynamic vibration absorbers are a class of passive control systems, which achieve energy dissipation through transference of some part vibrational energy to absorber rather than direct dissipation. The system typically configures with secondary mass, stiffeners and damping components, whose dynamic properties must be matched to those of primary structure. Devices such as Tuned mass dampers (TMD), Tuned mass damper with inerter (TMDI), Tuned Liquid Column Damper (TLCD) are some examples of dynamic vibration absorbers present in practical usage [28].

Passive Tuned mass Damper (TMD) contains an oscillating secondary mass connected by means of linear stiffeners and with dashpots (viscous dampers) to the top of the primary (hosting) structure, that oscillates in response to the structural vibrations [43]. The TMD's working efficiency in controlling the structural response counts on its adjustment to match the fundamental mode of vibration of the hosting structure at fixed attached mass, with its damping and stiffness properties [44]. In other words, when TMD tunes to frequency closer to the hosting structure's natural frequency, TMD resonates itself by vibrations in structure and dissipates maximum kinetic energy of primary structure during major earthquakes [45]. However, TMD systems are successfully installed in many tall skyscrapers for wind response control, bridges such as the Taipei-101 Tower (508m) in Taiwan [46], the Millennium bridge in London [47].

While TMD's have demonstrated its effectiveness in mitigating vibration across various practically engineered structures, it suffers from "detuning" of seismic and wind induced vibrations due to several reasons such as the primary structure's non-linear behaviour and uncertainties caused to dynamic properties of primary structure over time. These detuning affects could significantly influence the vibration suppression ability of TMDs [48]. The vibration suppression abilities of TMDs are closely related to its inertial characteristics: larger the TMD's mass, more the reliability and resilient the TMD behaves against quakes in structural properties [49,50]. Nevertheless, such practical constraints influenced by

architectural and structural considerations have an impact on maximum weight and volume of TMD that can be incorporated into the primary structure. Such constraint might be critical for tall buildings, where the TMD's mass typically remains below 0.5 to 1% of total building's mass [51]. To address such constraints in TMD's and utilize them for tall buildings to mitigate wind induced vibrations, Marian L et al. [52] introduces optimally engineered the Tuned Mass Damper with Inerter (TMDI), represents a passive vibration damping system. It integrates the conventional tuned mass damper (TMD) with an inerter device, designed to supply enough additional damping force proportional to the relative acceleration response of structure. This damping force was regulated by its inertial constant termed "inertance", capitalizes the mass amplification phenomenon and higher-mode damping effects of inerter device to improve vibration suspension capacity of conventional TMDs and mitigates relative acceleration responses on building [53–57]. Several recent studies have been conducted on optimal design of TMDI's, Marian L et al. [43] analytically demonstrates the efficiency of optimally designed TMDI's to reduce variance in displacement for undamped single degree of freedom (SDOF) systems under white noise excitations. Furthermore, the study validates the effectiveness of TMDI's through a numerical optimization in 3-Degree of freedom (3-DOF) damped primary structure when subjected to stationary noise excitations. The study concludes that inclusion an inerter into the TMDI can either diminish the required vibrating mass for lightweight passive vibration control or enhance the performance of the conventional TMD for a given mass. Pietrosanti D et al. [58] conducts a shake table testing under harmonic excitations to evaluate the performance of Tuned mass Damper Inerter (TMDI) in structures with non-ideal inerter behaviour and non-linear responses. The study utilizes a single degree of freedom (SDOF) structure specimen equipped with a custom-built rack and pinion Fly wheel inerter to link the TMDI secondary mass to ground. The experimental data highlighted the practical advantage of TMDI to showcase improved vibration suppression when compared conventional TMD through increasing inertance without increasing the TMD's mass and maintained for non-linear structures.

Tuned Liquid Column Damper (TLCD) comprises of a rigid piping system integrated into the primary structure and partially filled with viscous fluid, preferably water. The oscillating motion of TLCD facilitates the transfer of vibrational energy from primary structure to TLCD, consequently initiating a movement in the water column. This transferred energy was mitigated utilizing by viscous and turbulent fluid damping, that can be controlled by installation of hydraulic resistances (e.g. orifice plates) to attain desired damping characteristics [59, 60]. In Japan a 26-storey hotel was constructed with adopting a TLCD based bi-directional vibration control system [61].

However, these passive control systems might face major drawbacks in adapting to changes in structural design and various loading conditions to building [62-64].

### *1.1.2 Active Control Systems*

Active response control systems are considered as logical extension of the passive control technology [65]. These systems mainly depend on continuous supply of energy source for the operation of control devices like sensors, actuators, and computers that produce control forces in relation to the seismic response feedback into structure which counteracts the intensity of ground motion [62,66]. Active tuned mass damper (ATMD) and active tendon systems are some examples of Active control systems [67]. Active tuned mass damper (ATMD) works on similar mechanism to conventional TMD, usually consists of actuator connecting the oscillating secondary mass to primary structure. The continuous monitoring of structural response collects feedback from sensors installed in primary structure. Then a control algorithm computes optimal control force for actuator to drive the secondary mass to oscillate, there by dissipating the vibrational energy in

primary structure under wind excitations [68]. The Shanghai World financial Center is tallest building in China with height of 492 m and utilizes an active control based tuned mass damper to mitigate wind induced vibrations in structure [69]. Active Tendon system consists of pre-stressed cables that can be positioned in between floors of a structure or at ends of cables of cable-stayed bridges. In the active tendon system, these cables were pinned to a location in a structure and subsequently threaded through pulleys to be connected to linear actuators. Then computed tensile forces are applied to cables by actuators, which can diminish wind-induced excitations in structure [68, 70]. Yanik A [71] adopts an 8-storey 2D shear building model with fully active tendon-control system to propose an optimized control performance index for active control of structures during seismic excitations. However, some key differences between tuned mass dampers as passive and active systems were discussed in Table1 and Table 2.

Table 1. Differences between passive and active tuned mass dampers

| Passive Tuned Mass Damper (TMD)  | Active Tuned Mass Damper (ATMD)  |
|--|--|
| The Passive Tuned Mass Damper (TMD) system consists of secondary mass attached to the main structure through linear stiffeners and dashpots [44].  | The Active Tuned Mass Damper (ATMD) system consists of secondary mass attached to the main structure by means of a mechanical actuator, sensors around the main structure for collection of structural response feedback [70].                                   |
| Under Dynamic loading, the TMD counteracts the vibrations in structure in passive (not utilizing any power source for operation). These vibrations are dampened through dissipating kinetic energy on utilizing the mass-spring-damper mechanism [43]. | Under Dynamic loading, the ATMD counteracts the vibrations in structure in active (on utilizing a power source for operations). These vibrations are dampened through dissipating kinetic energy on utilizing the damping forces generating from actuators [68]. |
| The damping effect of TMD mostly depends on its tuning to structural response, stiffness, and damping properties of dampers provided.  | The damping effect of ATMD depends on feedback from sensors, control algorithm and stiffness, continuous power supply for operation of computer control, sensors, and actuators.   |
| It facilitates effective damping for a limited range of frequencies (determined on its design), which potentially exposes the structure to higher frequencies.   | It facilitates effective damping for a broader range of frequencies by actively adjusting the damping forces in real time, thereby providing more protection to structure at higher frequencies.   |
| The installation of TMD system was simple, cost effective, and less requirement for maintenance and operational oversight compared to ATMD due to its passively operating nature and no power requirement.   | The installation of ATMD system was complex, expensive and more requirement for maintenance and operational oversight due to its actively operating nature.  |

**Table 2. Key Differences between Conventional TMD, Tuned mass damper with Inerter (TMDI) and Active Tuned mass damper (ATMD)**

| Characteristics                                       | Conventional Tuned Mass Damper (TMD)  | Tuned Mass Damper with Inerter (TMDI)  | Active Tuned Mass Damper (ATMD)  |
|---|---|--|--|
| Type of response control system                       | Passive   | Passive  | Active   |
| Components  | Consists of Secondary mass, linear stiffeners, and dampers                            | Consists of Secondary mass, damper, linear stiffeners and an inerter device                            | Consists of Secondary mass, damper, linear stiffeners, actuators, and control systems  |
| Tuning Mechanism                                      | TMD tunes to match the natural frequency of structure.                                | TMDI also uses frequency matching technique.   | ATMD utilizes real time feedback control using sensors and actuators to adapt for uncertainties and frequencies in real time                   |
| Energy Dissipation                                    | Dissipates energy through dampers   | Dissipates energy through dampers and inerter  | Dissipates energy through dampers and actuators  |
| Frequency range and Effectiveness in High Frequencies | Effective over narrow frequency range, mainly tuned to a specific resonance frequency | Effective over a broader range of frequencies and more effective in higher frequencies due to inerter. | Effective over a broader range of frequencies and highly effective at higher frequencies, leveraging active control and real time adjustments. |

However, in practical execution, these active control systems could run into difficulties such as modelling errors, errors in generating control forces, and the unavailability of a power source during a seismic event [63,66]. The utilization of external energy makes the active control setup costlier compared to passive control system.

### *1.1.3 Semi-Active Control Systems*

Unlike passive response control systems, which does not acclimate with structural changes and rely on fixed elements like dampers, and active systems, which involve continuous energy input, researchers have developed the semi-active control systems utilizes the structure’s motion to produce large control forces and these control forces are regulated typically by a small external energy source (e.g.. battery) [15,62,66,72]. They include adaptive controls which increase efficiency and intelligence of the system [28]. Semi-active control systems differ over an active system by their lower power utilization for operation (in order of tens of watts) and semi active systems can even be powered during a seismic event [11,15]. Electrorheological (ER) dampers, Magnetorheological (MR) dampers are

examples of semi active control devices [28]. Electrorheological (ER) dampers are semi automotive suspension devices, filled with a mixture of low viscous fluid and particles sensitive to electric field, also known as electrorheological fluids [73]. When a structure is exposed to vibrations, a computer control receives feedback from sensors that are integrated into the structure. This feedback enables the computer control to adjust the electric field that is applied to the damper. The application of this electric field causes the electrorheological fluids to act as a viscoelastic material. This means that these fluids exhibit ideal behavior like that of a solid when subjected to lower stresses, but flow like a viscous fluid when the forces applied surpass their yielding stress [74]. This viscoelastic behavior of fluid allows ER dampers to have adaptive damping control and effectively mitigate structural vibrations. Magnetorheological (MR) dampers are semi automotive hydraulic devices similar to Electrorheological (ER) dampers, filled with mixture of low viscous fluid and micro-sized suspended magnetic particles which are sensitive to magnetic field, also known as Magnetorheological fluids [75]. In MR dampers at absence of magnetic field, allow fluid to flow without any restraint, resulting in minimal damping. Whereas a higher magnetic field creates an unyielding damper filled with semisolid fluid [76]. This variation of the magnetic field alters the fluid's damping characteristics, which allows for a precise control over damping force and mitigation of structural vibrations.

#### *1.1.4 Hybrid Vibrational Control System*

By amalgamating different vibration control systems such as passive, active, and semi-active devices, the hybrid vibrational control system attempts to control structural response as well as address the drawbacks in these devices there by achieving optimal performance, stability, and efficiency [11,77]. These systems offer several benefits, including enhanced structural safety, improved occupant comfort, and reduced maintenance costs. Hybrid mass damper (HMD) is one example of hybrid vibrational control systems. The Hybrid Mass Damper (HMD) system composes of passive control device such as Tuned mass damper (TMD) and active control devices for suppression of vibrations in high-rise buildings during strong winds and moderate earthquakes. These HMDs work on similar principle of ATMDs and much more energy efficient for vibration control, which uses about 1/3rd-1/4th of ATMD's consumption [78]. Maebayashi K et al. [79] proposed a hybrid mass damper system which aims at fulfilling the demand for mitigating earthquake and wind induced loads on structures. A prototype of HMD system was also installed at a 7-storey building, built in 1991 at the Institute of technology of Shimizu Corporation. The HMD system is composed of actuators driven by AC servo motors and an auxiliary mass anchored to multi-stage rubber bearings. Forced vibration tests were conducted in both x and y directions of building evaluating the dynamic characteristics of building and HMD system. The experimental findings also confirmed that HMDs could be suitable solution for mitigation of earthquake and wind induced vibrations in tall buildings.

## **2. Base Isolation System (BIS)**

The Base Isolation System (BIS) is one of the popular passive structural control design approaches, in which the superstructure and substructure of building are disintegrated through a low friction interface layer also known as base or seismic isolators, which allows the superstructure to move independently from the foundation when subjected to wind-induced vibrations or earthquakes. This relative movement allows to dissipate seismic energy and reduces the forces transmitted to the building [80-83]. These systems are crucial in regions prone to earthquakes, as they help protect structures and occupants from damage and injury. The installation of an isolation system at base prevents the seismic forces entering the structure directly [84]. The concept of seismic isolation has spread around the world especially in earthquake prone regions of countries such as Japan, China,



United states, Indonesia, New Zealand etc. However, this seismic isolation system is most used and economically appealing in low-rise to medium-rise buildings.

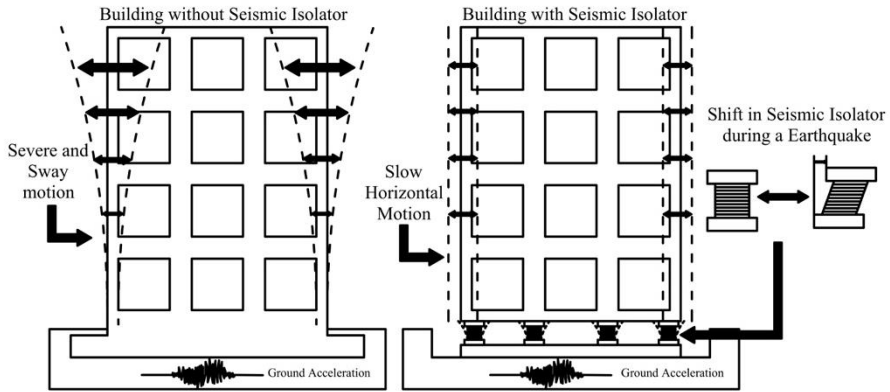


Fig. 2. Comparison between fixed base and base isolated building

Since the 1970s, the first application of base isolation was to an elementary school in Skopje, Yugoslavia. The three-storey concrete frame structure, Pestalozzi school was equipped with unreinforced rubber bearings disparte the recently exploited bearings. These unreinforced rubber bearings were developed to bulge sideways under the weight of the structure.

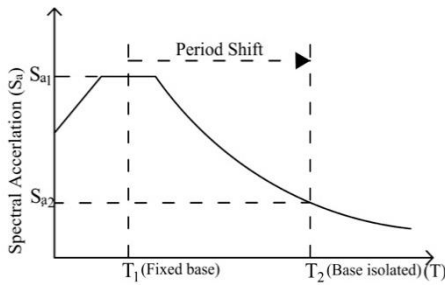


Fig. 3. Spectral Acceleration vs Natural period without isolation effect [12,87,88]

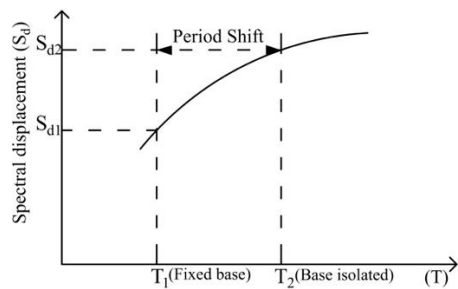


Fig. 4. Spectral Displacement vs Natural period without isolation effect [12,87,88]

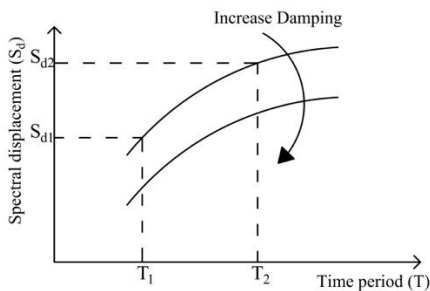


Fig. 5. Spectral Acceleration vs Natural period with isolation effect [12,87,88]

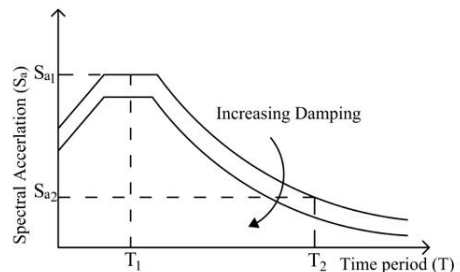


Fig. 6. Spectral Displacement vs Natural period with isolation effect [12,87,88]

Glass blocks were introduced as seismic fuses, which break after a certain limit of seismic loading. The swaying back and forth motion of structure during the seismic events has resulted from its isolation system's equal approximation in horizontal and vertical stiffness [85]. In general, the natural period of a fixed base building is significantly lower such that could correlate with the natural period of a major earthquake. Moreover, this could result in an inelastic action that increases accelerations at every floor from bottom to top. This increase in floor accelerations might induce distress within the columns between floors [86]. The building with base isolation work on principle to diminish the response accelerations on building compared to a fixed base structure in acceleration response spectrum perspective by shifting or lengthen the building's fundamental natural period away from the span of the frequencies for which greater impacts of amplification of ground waves are anticipated, (i.e.) from  $T_1$  of fixed base to  $T_2$  of base isolated structure as illustrated in figure 3 [10]. The extension in the building's natural period lowers the floor accelerations, but it could record higher displacements with the superstructure in displacement response spectrum perspective, as shown in figure 3&4. These higher displacements and accelerations are compensated through strong dampening characteristics of the isolation system to an acceptable limit, in displacement and acceleration response spectrum perspective as illustrated in figure 5&6 [12,87,88].

Furthermore, the period shift caused by base isolation system alters the structure's fundamental mode of vibration. This alteration transforms the structure's behavior from cantilever mode, characterized by significant inter-storey drifts and storey shear forces, to rigid (isolation) mode. In this rigid mode the deformation responses concentrated at the isolation level, allowing the superstructure to experience minimal storey shear forces and inter-storey drifts [89]. The reduction in demands, the superstructure remains to be elastic or virtually elastic after a design-level seismic event [90]. In some exceptional cases by installing external mechanical dampers or by incorporating additional damping in isolation system, the excessive displacement response that the base isolators are susceptible to can be mitigated [67, 91].

### **2.1. Characteristics of Isolation Systems**

The Base isolation system for a structure mainly composes a group of flexible pads also known as base isolators or bearings are located underneath super structure to offer resistance against lateral displacements [92]. During an earthquake the isolator sways in lateral direction as shown in figure 2 due to its low horizontal stiffness and its excessive deflection is controlled through steel shims in between rubber layers in case of elastomeric bearing or through higher coefficient of friction in between slider and surface plate in case of sliding bearings. Malu G et al. & Beirami Shahabi A et al. [93,94] points out that most of isolators do not absorb seismic energy, rather they collectively deflect and dissipate the seismic energy by making use of dynamics of system and other effective techniques. This filtration of seismic energy allows only partial amounts of ground accelerations to impart the structure. Some of the crucial parameters that influence the efficiency of an isolation system are the energy dissipation rate of an isolator, the superstructure's flexibility, and the mass ratio between the isolation system and the superstructure [6,95]. These isolators are meant to be built effectively, if the structure's seismic behavior can be dominated by simply the initial mode of vibration and when storey drifts in structure can be relatively lowered [8,85]. Some of the prerequisites of a good seismic isolator are as follows [96-98]:

- Horizontally flexible (or) low horizontal stiffness enough to extend the structure's natural period.
- Vertically stiff to withstand vertical or gravity loads (i.e., isolators to have a high compressive modulus).

- Should have adequate capacity to dissipate seismic energy (damping) for minimizing storey drifts during an earthquake.
- Should have ability to cut down the contributions from the higher modes of vibration.
- Provide adequate rigidity to the structure under service loading.
- Should have self-centering capability after a seismic event.
- Repeated cyclic loading on isolator should not suffer loss in its force-resisting capacity.

## **2.2. Types of Isolation System**

Several nations prepared guidelines for seismic design of structures suggests that the feasibility in design can be achieved with accurate prediction of seismic response and selection of isolation systems to be utilized, analytical procedure for structures. Based on characteristic behavior of isolation systems have been categorized into Elastomeric bearing approach and bearings with sliding approach for hands-on usage in structures such as buildings, bridges, etc [90,99-102].

### *2.2.1 Elastomeric Bearing Approach*

It's the most common approach practiced in construction of seismically isolated structures due to its simple design and installation process. This approach comprises of several bearing systems such as Natural Rubber Bearings (NRB), Lead Core Rubber Bearings (LCRB), High Damping Rubber Bearings (HDRB). Natural Rubber Bearings are also referred as elastomeric bearings, are a common type of base isolator used in structures.

Natural rubber bearings (NRB's) also known as Laminated Rubber Bearings primarily composed of layers of elastomeric material, made from synthetic or natural rubber compounds. These elastomeric layers are added on top of reinforcing thin steel shims (or) plates, together bonded by process of vulcanization [85]. NRB's behave flexibly under lateral loads and hold up higher vertical loads, where the steel shims can provide stiffness in the longitudinal direction and rubber can make it resist shearing in lateral direction [6].

Primitively, these NRB's are more extensively used in providing seismic protection for bridges [103]. The initial application of these NRB's (laminated) was for a school at Lambesc near Marseilles, France [104]. The school was supported on total of 152 isolators with 300 mm in diameter in size and 40mm in thickness. These isolators can be utilized for low-income housing buildings. one such demonstration of isolators using these NRB's has been shown for Four-storey low-income housing having confined masonry in Santiago, Chile [105]. Lead Core Rubber Bearings (LCRB) are developed from the constraints within the NRB's and composes of several elastomeric layers, steel plates placed in alternate and a lead plug at core of rubber bearing [106]. The lead core yields in shear under lateral loading, providing additional rigidity and hysteretic damping to dissipate energy against strong winds and minor seismic events [72]. these bearings achieve effective isolation on reducing structural response to 1/2-1/8 of traditional structural response [92]. Following a seismic event, these bearings can retreat their original shape and position with the help of lead core and get ready to adapt for future seismic events. In the early ages of invention LRB's, it gained more popularity as retrofitting strategy. However, several historical buildings such as first retrofitted building in United States, Salt Lake City and County Building located in Utah [107], Oakland city hall located in California [108] were retrofitted utilizing these LRB's. These LRB's were employed in construction of real-life crucial structures such as Wellington Central Police station located at New Zealand in late 1980's [109], Bhuj district Hospital in 2001[110].

High Damping Rubber Bearings (HDRB) are the most adopted isolators for construction and retrofitting of crucial infrastructure such as hospitals, bridges, and emergency centers

where serviceability of structure during and after a seismic event is essential. The HDRB's are made from elastomeric layers and the steel shims, placed in alternate layers similar kind to NRBs [111,112]. In contrast to LCRB's, the HDRB bearings are more viable in structures with special requirements as they retain greater stiffness before yielding and show better breaking effect when subjected to wind load [113]. These HDRB bearings adapt rubber made from materials such as carbon black which provide high damping capacity for isolator explicitly between 10 to 20% of critical damping at its full shear strain capacity to provide a higher level of energy dissipation, horizontal flexibility, and high vertical stiffness to compensate for similarities with NRBs. These HDRB's were primitively used for Foot hill Communities 'law and Justice Center, California built in 1984 [114]. However, HDRB's have gained huge popularity by its economic aspects and engineers have started to adapt them for vital structures such as hospitals and emergency centres. Several such examples of vital structures include a Medical Centre at Italian Navy, Ancona, Italy built in 1991[115], The Los Angeles County Fire Command and Control Centre, a 2-story steel structure located in City Terrace area of East Los Angeles. Moreover, these HDRB's were also utilized as retrofitting strategy in such as Mackay School of Mines located in Reno, Nevada [108] and Oliveto G et al. [116] conducts an analytical investigation on two identical residential buildings located at Solarino town, East Sicily which were retrofitted through using hybrid type of isolation system that contain mixed use of laminated rubber and slide bearing systems. This laminated bearing system is composed of three distinct types of bearing include Lower Damping (LDRB's), Medium Damping (MDRB's) and High Damping rubber bearings (HDRB's). One of the residential buildings employed with this Hybrid system was subjected to free vibrations to assess the behavior of Hybrid isolation system.

### *2.2.2 Bearings with Sliding Approach*

The bearings with sliding approach, often referred to as sliding isolation systems commonly used as retrofitting strategy and known for their operational simplicity [117]. This approach uses the principle of friction as a working mechanism. The bearings are composed of flat or spherically polished surface stainless-steel plates coated with sliding composites such as high-density polyethylene (HDPE) or PTFE (polytetrafluoroethylene) which is commonly known as Teflon and an articulated slider in between these plates that starts sliding or a low-friction movement between super structure and substructure when seismic excitation is greater than the frictional force in sliding isolators [118]. Harvey PS et al. [119] gives a complete review about historical and future developments in sliding or rolling type isolation approach that includes explanation of its basic concepts, types and applications of sliding or rolling type isolators. Roller bearings are type of sliding seismic isolators, typically comprises of series of cylindrical or spherical rollers to facilitate the controlled horizontal movement in structure that reduces the forces transmitted to structures during seismic events, thus protecting structural integrity of structures [120]. The isolators are simple in design, cost-effective to fabricate which renders them suitable for application in low income countries and for light weight structures [121,122]. Katsamakos A A et al. [123] studies effectiveness of rolling bearings by utilizing grout filled tennis balls rolling on concrete plates as a seismic isolator. This proposed isolation system can be available at low cost in low-income countries for isolation of light weight structures. The study focuses on characterizing the axial response of proposed isolation system by comprehensive testing of isolators at full-scale under combination of compressive and lateral cyclic loading. The key findings of experimentation have indicated an increment in rolling friction coefficient within these isolators unlike the sliding isolators with increase in compressive loads and independent to influence of velocity and temperature changes. Lee G C et al. [124] has developed roller seismic isolator for use of highway bridges. This isolator to achieve seismic isolation utilizes rolling of cylindrical rollers on V-shaped

sloping. The isolation system was characterized by its self-centering capability, an essential property for seismic applications. These isolators reduce seismic response on structures through its in-built sliding friction mechanism. The study presented performance of proposed rolling bearings when subjected to base excitations. Katsamakos AA et al. [102] conducted an experimental investigation on low-cost isolators used for houses in low-income countries. The low-cost isolator design is mainly based on rolling rubber sphere on spherical or flat surfaces. The experimental results showed effective reduction of acceleration responses in building. The author suggests such a type of isolation device for low rise structures. Fenez D M et al. [125] introduces sliding isolation bearings with adaptive behaviour. Furthermore, the study explores the operational principles and force displacement relationships of three innovative spherical sliding isolation bearings. These relationships are important to understand and predict the bearings mechanism. These sliding isolation bearings are passive control devices but still demonstrate adaptive damping and adaptive stiffness. This adaptive behaviour aids the sliding isolation bearings to be optimized for various levels of seismic event. The fabrication of these sliding isolation bearings composes of several concave surfaces and the adaptive behaviour was imposed by various combinations of surfaces upon sliding surface on which sliding occurs. The variation of stiffness and effective friction in these bearings occurs accordingly to variations in surfaces upon which sliding occurs. Furthermore, the study provides a procedure to identify the surfaces which are active and to derive the force-displacement relationships, which was grounded by first principles.

In relation to the advancement of sliding type isolation bearings, it was initially proposed with Pure friction isolation system (P-F) comprises an articulated slider positioned in between two flat stainless-steel plates, slides over these plates surface under seismic excitations. It is a basic type of isolator in all base isolation system that works on sliding friction [126,127]. Under the principle of Coulomb friction damping, the initiation of motion in slider happens when the external disturbance force overcomes the sliding friction of the interface. As a result, the slider will move accordingly to the sliding surface, thereby initiating the desired seismic isolation functionality [128]. Sometimes the isolator's flat geometric surface could contribute unnecessary movement in buildings even under low earthquake motions [93]. To use this isolation system, a structure must be designed either with an appropriate coefficient of friction or should include complementary devices along the isolator [85]. Etedali S et al. [129] conducts parametric study to assess the efficacy of Pure Friction (P-F) and Resilient friction (R-F) isolation systems which were employed in eight storey building models and compared to fixed base building models. The results shown during seismic excitations the restoring device of R-F system has the capability to reduce displacements at base storey and position back to original point. While increase in damping ratio of restoring device showed reduction in base displacement, raise in top story displacements and drifts and no effect on residual base displacements of building. Wei B et al. [130] conducts numerical investigation on a pure friction isolation (P-F) system using shake table test models to inspect whether the friction action would scale in practical modern buildings. The investigation concludes that P-F systems could result in unallowable errors in mitigation of vibrations on scaling of friction action due to its flat geometric surface. The author suggests that it is possible to reduce unallowable errors through proportionally varying the friction coefficient and geometric surface through the sliding surfaces. Avinash AR et al. [118] explains about the deficiency of restoring mechanism in P-F system that could shift the building permanently from its initial position after an earthquake. This constraint leads engineers to adapt sliding systems with restoring ability.

Friction Pendulum Isolation system (FPI) is designed to overcome the main constraint of P-F system which do not contain an appropriate restoring mechanism. The FPI system

consists of an articulated slider positioned within the two reinforcing steel plates and having a true spherical concave surface [88,118,131,132]. During an earthquake, the pendulum effect and concavity in sliding surface of isolator provides necessary restoring force to restore its original position and dissipating energy [93]. The selection of radius of curvature ( $r$ ) of concave surface and type of friction bearing material used can influence the natural period of structure [133]. In general, These FPI's are utilized in Medium-rise to High-rise structures. These FPI's have been notable all over the world for its precise control over structural displacements, which made it adopt for many historical structures such as Burex Arts building [134] and U.S Court of Appeals, San Francisco [134], which was one of largest building to be base isolated till date as retrofitting strategy. Cardone D et al. [135] has investigated the re-centering capability of friction pendulum isolation system, which involved nonlinear analyses of finite no of SDOFs. A regression analysis was performed to obtain a relation between residual displacements and parameters that influence the dynamic behavior of Friction pendulum system. However, FPI systems when intended for a specific intensity of excitation may perform ineffective over higher or lower range of earthquake frequencies than specified [136]. Due to the constant radius of curvature ( $r$ ) of the isolator surface, the building may come to resonance for smaller frequency of ground motions. To overcome constraints in FPI and P-F systems Pranesh et al [136] have proposed an isolator namely the variable frequency pendulum isolator (VFPI) contains non spherical surface chosen to provide a progression in period lengthen at different response levels and softens the restoring mechanism at larger displacements. In the case of low earthquake frequencies, VFPI exhibits behavior akin to FPI, while in case of big earthquake frequencies, it exhibits behavior akin to that of the P-F system [137,138]. The researchers have also developed isolations based on friction to have multiple sliding surfaces such as double concave friction bearings, Triple friction bearings (TP) which have 4 concave surfaces [118].

### **2.3. Advantages of Base Isolation System**

The utilization of base isolation technique has been a crucial aspect of earthquake engineering over years, used to mitigate the adverse effects of seismic and wind induced vibrations on structures. In contrast to Conventional fixed-base structures, these base isolated buildings have been demonstrated a range of following benefits:

- Show improved structural performance: The studies shown improved structural performance of a structure to seismic, and wind induced vibrations with use of base isolation technique is attributed from its main key factor, reduced transfer of seismic and wind forces with separation of superstructure from ground by the low friction interface [139].
- The base isolation system ensures protection of both structural and non-structural systems by dissipating the seismic or wind excitations through its low friction interface. To evaluate the performance of secondary systems at isolated structures, several industrial experts have conducted through finite element modelling of analytical models and the shake table testing for full scale test models equipped with secondary systems or non-structural components such as ceiling, electrical appliances and isolation systems subjected to substantial loading conditions [140,141]. Dolce M et al. [142] carries out seismic simulation tests for isolated building specimens to study impact of different of isolation systems on the damage sustained by equipment and contents. The study focuses to investigate the effectiveness of a newly developed shape-memory alloy isolation device. The results suggest that highly nonlinear isolation systems in particularly those characterized by metallic yielding induced damping induce vibrations of high frequency. Moreover, the study reveals that existing analytical techniques effectively captures the frequency content of the acceleration

response. Wolff E.D et al. [143] summarized the response of secondary systems in isolated structures through analytical and experimental investigations. A six-story building model equipped with both Lead core rubber and Friction pendulum bearings were tested through shake table in order to obtain characteristics of isolation system for analytical modelling. The results indicated that an increment in energy dissipation, whether through hysteretic or nonlinear viscous damping, results in reduction in isolator displacement while causing an increment in primary and secondary system response. Morgan T A [144] investigated the sensitivity of non-structural component's response parameters to the properties of isolated buildings. The study includes subjecting the Two moment-frame buildings, each with different natural periods, to seismic records with different source characteristics and soil types. The research considered isolation systems with bilinear behaviour, with variation of characteristic strength and elastic period. The key findings from the study indicated that the considered isolation systems exhibited favourable response in non-structural when compared to the conventional structure. However, during the analyses several challenges were confronted, particularly related to numerical instabilities that could impact high-frequency acceleration response in the isolated building. Furthermore, the study accounts the impact of modification in isolator characteristics over long-term as well as the influence of vertical acceleration and these effects later have shown least importance in speculating the secondary system's response. Van Enegele N.C et al. [145] explains that base isolation technique provides enough protection for both Structural components such as beams, columns, slabs, etc and Non-structural or secondary components such as ceiling walls, ducts, partitions walls, cladding, windows in a structure by mitigation of wind and seismic forces that may exert on a building by employing of isolation devices beneath super structure, thus safety of occupants and passers-by will be ensured [146]. Kumar P et al. [147] compares the seismic performance of non- structural (secondary) systems held in base isolated and non-base isolated buildings. The study considers two similar 3-storey reinforced concrete frame buildings, one with conventional foundation and other being isolated with lead core rubber bearings (LCRB's) as Structural (primary) system, while a steel frame was depicted as non-structural (secondary) system. The numerical simulations have shown significant reduction of acceleration response in building employed with isolation system and ensured with minimal damage in secondary system when compared to building with conventional foundation. The base isolation systems could contribute to long-term durability of a building by reducing the cumulative damage caused by repeated seismic events. Occupants in important buildings such as schools, hospitals, offices etc can remain safe and safe destinations from collapse of buildings and allow to maintain the functionality of structure during and after an earthquake [148].

- Retrofitting of existing buildings and incorporation into new construction projects with seismic isolation can be integrated in building's design with minimal disruption and be replaced if damaged during its lifespan, makes it a cost-effective technique compared to traditional strengthening methods [99]. Over the few decades several historical buildings such as Salt Lake City and county building [107], constructed in masonry and bridges such as South Rangitikei Rail Bridge [104] were being retrofitted through use of base isolation technique.
- The initial construction costs of base isolated buildings might be higher when compared to conventional building construction, but they show savings and benefits in the long-term. These long-term benefits include reduced structural damage, lower maintenance costs, and insurance premiums. Melkumyan [149]

mentions that retrofitting of existing building with isolation system at base or roof nearly costs three to five times in comparison to cost of conventional retrofitting technique. Ryan K.L [150] conducts cost-benefit analysis for base isolated and conventional buildings. the author finds out the life cycle benefits of base isolated buildings are more significant when compared to conventional and more cost effective for businesses which are unable to relocate after large seismic events.

#### **2.4. Base Isolation Systems for High Rise buildings**

The primary concern with base isolation system lies in constraining the large relative displacements within the isolator without amplifying the ground accelerations into structural and non-structural elements in superstructure. Then application of these isolation systems for high-rise buildings in seismically active regions might present with greater difficulties such as insufficient structural stiffness, development of tension in vertical members due to their slender profile, longer natural vibration period, weight distribution, and adaptability to local seismic conditions. So, the Base isolation system's effectiveness is limited for low to medium rise buildings or in buildings whose natural period is less than one second [13]. However, several research experts in the field of extensive research have pointed out a few constraints for ineffectiveness of base isolation in high-rise buildings. Shinozaki Y et al. [151] identified possible constraints such as in increase with construction costs, slender high-rise buildings are susceptible to uplift due to vertical loads during large seismic events and overturing which might damage the isolators at corner. Takewaki I et al. [152] has numerically illustrated through a two degree of freedom model that overall damping in structure diminishes on increase in number of stories and concluded that robustness of base isolated high-rise building is smaller than low or medium rise base isolated buildings. Ariga T et al. [153] concluded that base isolated high-rise buildings mainly buildings with friction type bearings are near to resonance for an intensity of long period ground motion recorded in Japan. Ogura K et al. [154] conducted parametric analysis using lumped mass approach for base isolated high rise building and concludes that Base isolation system achieves response reduction effect irrespective of structure's range of fundamental periods yet depend on whether structure is a low or high-rise. Following above Literature review demonstrates that the conventional approach in base isolation system for High rise buildings could present certain disadvantages in terms of cost, intricacy of design and its partial effectiveness within a specific range of ground frequencies.

#### **2.5. Real-life Application of Base Isolation adopted in High-Rise building - Sendai MT Building: A Case Study**

The 18-storey office building, SENDAI MT was constructed in 1995 at Sendai City, Miyagi Prefecture, East Japan (figure 7). At 85 meters high, it is the first base-isolated high-rise building constructed in Japan. Its construction has a strong emphasis on seismic resilience and maintainability even after a seismic event and incorporated with several notable features in structural design as follows [151]:

- The Sendai MT building utilizes high-grade steel rebars (SD 490) for longitudinal reinforcement and high-strength concrete (Maximum of 60 N/mm<sup>2</sup> for columns, joints, and Maximum of 48 N/mm<sup>2</sup> for beams, slabs) in precast to ensure both quality and economy in construction.
- Figure 8 represents the structural frame elevation, incorporated with hybrid structural beams of 15-meter-long span composing of steel in mid part connected with reinforced concrete at both ends of span to have an optimized space for office use.



- For effective seismic performance of building, an innovative application of base isolation system known as Hybrid TASS system was being utilized. The Hybrid TASS system in Sendai MT Building composes with two type of isolation bearings namely rubber bearings(1100mmØ,1200mmØ) and sliding bearings(1300mmØ) with varied sizes and properties are arranged as shown in figure 9 at isolation level, below ground storey to achieve effective seismic performance. The sliding bearing's damping ratio in the isolation level is designed to maintain a yield force that exceeds the wind force and were positioned beneath inner columns, where variation in axial forces due to earthquake is minimum. The rubber bearing's shape and rubber stiffness are designed to have soft stiffness following yield which excepts good seismic performance in case of large earthquakes.



Fig. 7. Exterior View of Sendai MT [196]

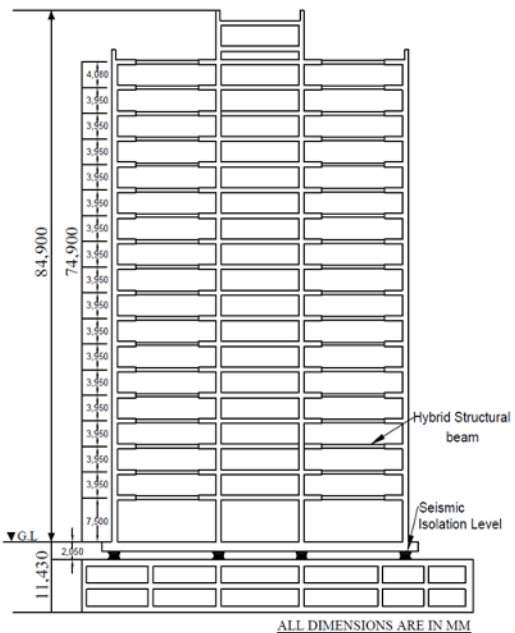


Fig. 8. Frame elevation of Sendai MT [155]

Komuro T et al. [155] compared the force-deformation relation of Hybrid TASS and ordinary isolation systems as presented in figure 10, which explains that TASS system was designed to have yield force which can exceed the design wind force and achieve good seismic performance at a large seismic event as stiffness after yield is equivalently soft.

A dynamic analysis was performed on utilizing a lumped mass model under several earthquakes. The recorded input ground motions of earthquakes such as El Centro (1940 NS), Hachinohe (1968 NS), Sendai TH-038, Taft (1952 EW) are categorized from level 1 to 3 based on probability of occurrence during building's service life. The analytical results of level 1 defined the design base shear coefficient of super structure to 8%, the drift gradient is smaller than 1/330 rad for level 2 and smaller than 1/230 rad for level 3 shown in figure 11.

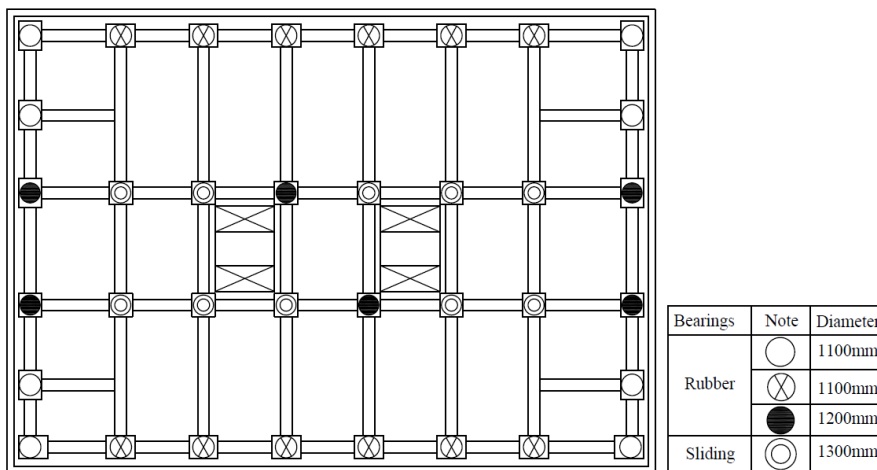


Fig. 9. Arrangement of Different Isolators in Hybrid TASS System [155]

The author reaches a conclusion that Hybrid TASS system or other structural systems along with base isolation systems brings an advantage for construction in terms of cost and seismic performance, can used in low to high-rise buildings. The Base Isolation system in high-rise buildings could still shows significant reduction in responses and building can be protected from huge earthquakes by employing with proper design of isolators [10]. So far, the Base isolation has been employed in several notable high-rise buildings, such as the Thousand Tower in Kawasaki City and Shimizu Corporation headquarters in Tokyo [156]. Furthermore, this technique has been utilized as retrofitting strategy for Historical high-rise structures like the Los Angeles City Hall, the San Francisco City Hall, and the Utah State Capitol building [13].

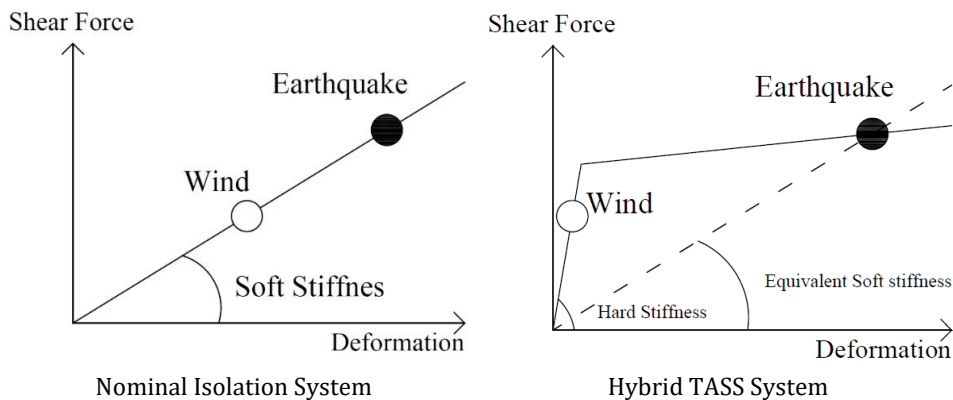


Fig. 10. Force-Deformation relation of different Isolation systems [151]

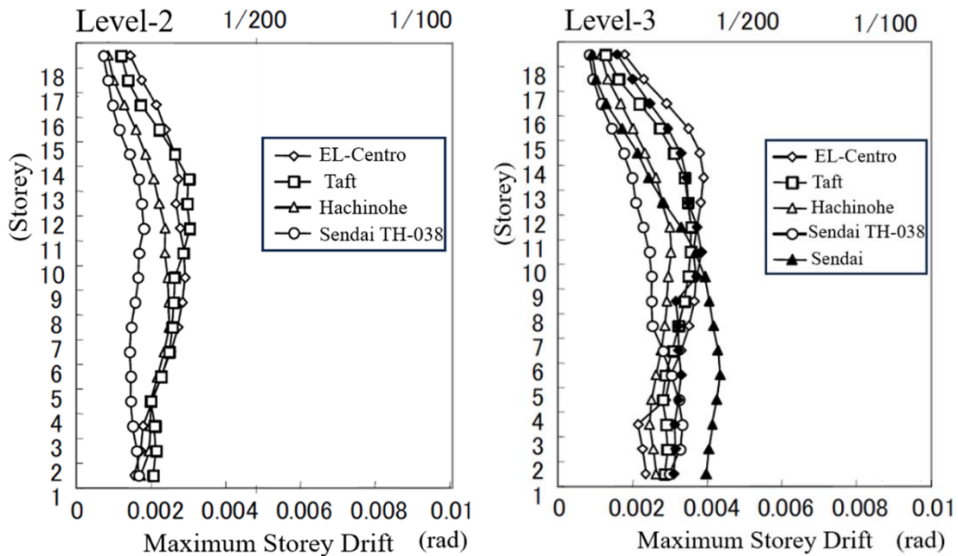


Fig. 11. Maximum Response storey Drift (in radians) for Level 2 & 3 Ground Motions [151]

### 3. Inter-Storey Isolation Systems

Over years of extended research in base isolation, the research professionals have recognized infeasible in medium and high-rise buildings due to super structure's flexibility and overturning behavior, provision of seismic gap or moat wall around structure to accommodate for significant relative displacements at the isolation level and prevent building pounding with adjacent structures often arise aesthetics concerns which is infeasible in densely built regions [157-161]. So, the necessity to address the concerns related to architectural and functionality, to enhance the construction feasibility particularly at densely populated areas, promoted the researchers to propose the Inter-storey Isolation System (IIS), which serves as an alternative to base isolation system and effective approach to provide seismic protection to buildings [162-164]. The Inter-storey or Middle-storey isolation system includes employing a flexible isolation level akin to BI's, positioned either at mid height or at a specific level within building's height. This shift of isolation level divides the super structure into upper and lower structure as shown in figure 12(a) allowing the upper structure to move independently of lower structure during an earthquake. The upper structure represents as a base isolated structure and as a mass damper mounted on top of the lower structure which demonstrates a Combined effect of seismic isolation and mass damping (unlike tuned mass damper) thus, enhancing the seismic performance of a building subjected to significant earthquake excitations [165, 166]. In elaborate, the response reduction effect occurs in lower structure with unconventional Tuned mass damper (TMD) effect from upper structure, in which a portion of upper structure's structural mass appears to be a mass absorber, while retaining to their structural and control function [158,167,168].

The seismic response reduction effect on upper structure occurs with its isolation from ground created by the lower structure and depends on mass ratio (i.e. ratio between the mass of upper structure and total mass of superstructure of building) [169]. While the response reduction effect on lower structure occurs with suitably optimized damping and stiffness characteristics of the isolation system in relation to isolated mass ratio [166].

Middle storey-isolation systems are akin to Inter-storey isolation but exhibit the variation in response reduction due to presence of isolation level at mid height of structure.

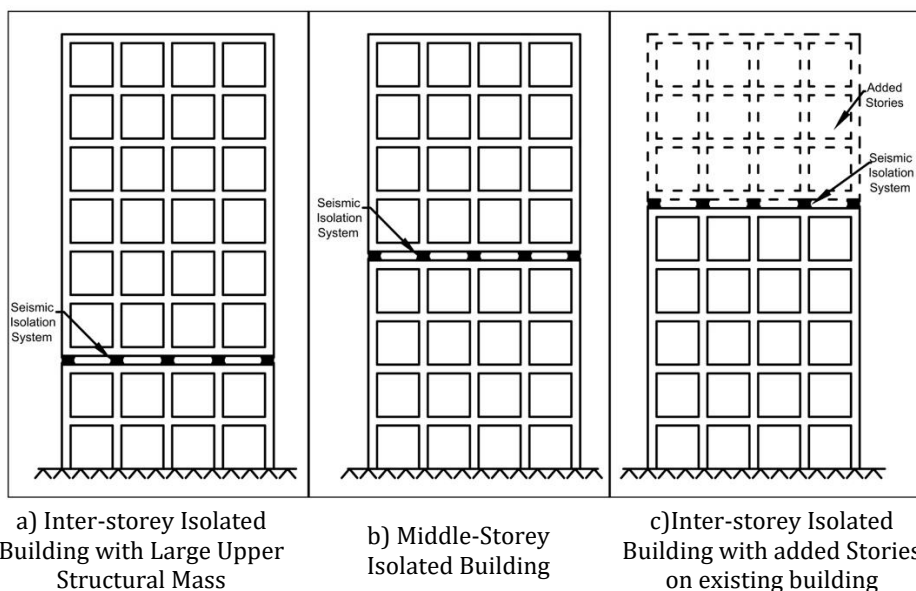


Fig. 12. Inter-storey Isolation System in building at various Heights

The Middle-storey isolation system separates the building's super structure into two structures as shown in figure 12(b), which are approximately equal in height and structural mass. This separation has shown effective seismic performance when adopted for high-rise buildings such as Shiodome Sumitomo Building [170]. These Inter-storey or middle storey isolation systems consist of isolation bearings such as HDRB's, FPS, LCRB's akin to base isolation system, designed to have high shearing strain, high damping and vertical load carrying capacity. In Inter-storey Isolated buildings, the location of Isolation level is mainly chosen based on type of structure, required level of response mitigation, cost implementation and many other factors [171]. The dynamic properties of Inter-storey Isolated buildings are characterized using simplified two-degree, three-degree, or multi-degree of freedom models due to presence of complex mechanisms rather than in base isolated buildings [162]. The unconventional TMD in Inter-storey system can overrule the constraint of inadequate added tuned mass which limits response reduction effect in structures with conventional TMD. Several researchers likely designated these Inter storey isolation systems also as building mass damper (BMD), non-conventional Tuned Mass Damper, mid or middle-storey isolation, or added storey isolation systems [172].

### 3.1. Advantages with Inter-storey Isolation Systems

The utilization of Inter-storey Isolation System adds on following advantages:

- These Inter-storey Isolation systems always permit for greater flexibility in both structural and architectural design for tall and multi-purpose buildings. Consequently, a sustainable solution for buildings allows for saving land use in densely built areas [173,174].
- Eliminates the accommodation of seismic gap or an expansion joint around the structure during construction of base isolated structures which allows for larger relative displacements at isolation level during earthquakes, presenting the economic feasibility and aesthetic desirability of these isolation systems [175,176].

- Eliminates the framing of base slab over isolators when located at base reduces the complexity in construction of foundation in such as erection of retaining walls [162].
- The Inter storey isolation systems at multiple level separates the structure into distinct individual occupancies which are diverse in both structural and functional characteristics, allowing for contrary arrangement of all the structural elements and columns at each occupancy [177].
- This IIS technique has potential to be utilized as a seismic retrofitting strategy for existing buildings as shown in figure 12(c), allowing to accommodation for additional stories without increasing the base shear and maximum acceleration response on structure which is termed as added storey Isolation system and exhibit better seismic performance and feasibility rather than base isolation [178-181].

However, These Inter-storey isolation systems can be effectively utilized in structures where use of base isolation might not be appropriate in such as offshore structures and densely built areas, in buildings with irregularity requirement (such as parking structures), mixed-use type buildings and for medium rise to high-rise buildings especially in regions of high seismic activity [178].

### **3.2. Inter-storey Isolation Systems for High-Rise Buildings**

The concept of Inter-storey isolation system for High-rise Buildings is currently widespread and gaining a lot of traction, especially in Japan despite the fact more than sixty real-life applications were developed over the course of nearly two decades [182]. Some notable examples of high-rise structures with Inter-storey isolation systems in Tokyo include the Iidabashi first building [84], the Roppongi Grand Tower [183], Shiodome Sumitomo Building [170], Nakanoshima Festival Tower [184]. However, Several Experimental and analytical studies were undertaken to review the effectiveness of Inter-storey isolation for High-rise buildings.

Villaverde R et al. [185] conducted a feasibility study out of a 13 - storey building with the roof isolation system which intends diminish the response of a structure during seismic events. The proposed isolation system comprises of isolators in between a building's roof level and columns supporting the roof and were also complemented with viscous dampers connected in between the isolation level. This feasibility study investigates the assessment of the building's response with and without the proposed isolation system using a two-dimensional analytical model under severe ground motions, which determines the required size and properties of an isolation system. The study finds out that the proposed system shows effectiveness in response mitigation and has the potential of attractive solutions for low-rise and medium-rise buildings.

Taylor P et al. [177] conducted a feasibility study on inter-storey isolation systems using both linear and nonlinear devices. The study investigated the efficacy of inter-storey isolation systems using a linear and non-linear Time History analysis for building models installed with linear and non-linear isolation devices at different levels. Three distinct approaches were proposed for choosing the optimum design deformation of a non-linear inter-storey isolation system. The findings in study revealed that stiffness in isolators decreased with the shift of inter-storey isolation system vertically up for a structure, as result of smaller portion of mass being isolated and the roof isolation system is proven to hold a merit as economical retrofit application.

Wang SJ et al. [162] carried out an experimental investigation on base and mid-storey isolated building models using shake table analysis to study their dynamic behavior. The results of the shaking table test reveal that the middle-storey isolated building has a

smaller number of modal quantities (fundamental) compared to a base-isolated. During the study it observed that lower structure's seismic response is directly influenced by its fundamental mode of vibration, whereas the lower structure's seismic response is influenced by higher mode responses. The author suggested the Response Spectrum Analysis for the initial design of middle-storey isolated structures before performing a nonlinear time history analysis.

Chey MH et al. [186] investigated the efficacy of an innovative seismic retrofitting strategy for buildings namely the "added stories isolation" systems (ASIs). The added stories isolation system comprises of newly added upper stories isolated on top of existing building, acts as a storey mass damper (unlike conventional Tuned mass damper) to overcome the requirement for larger tuned mass in structure with conventional Tuned mass dampers. The evaluation of seismic performance was analyzed for "12+2" and "12+4" Storey moment resisting frame models using the time history analysis. The study concluded that the proposed ASI system has potential to mitigate the seismic response for multi-degree-of-freedom systems across a wide range of ground motions without requiring troublesome additional mass.

Faiella D et al. [187] explored the productivity of an Inter-storey isolation system through its two distinct real-life case studies. The selected buildings, the Iidabashi first building (IB), the Shiodome Sumitomo building (SSB), elevates Japan's advancement in design practice of the inter-storey isolation systems for high-rise buildings. Frequency and Modal response analyses were executed for simplified two or three degree-of-freedom models, where these models of reduced-order could influence the governing design parameters of the dynamic problem. Whereas for multi degree of freedom (MDOF) models, the Modal response and non-linear time history analyses were conducted. The study concludes that a good seismic performance can be expected through a proper balance in dynamic characteristics of structural portions and adopting for larger mass ratio and longer isolation period.

Forcellini D et al. [188] analyzed the proficiency of inter-storey isolation for high-rise buildings on utilizing the 20-floor building models (B0, B1, B2) with isolation layer at several heights. The resultant performance of each model was analyzed for assessing the best location of isolation layer throughout the structure's height. The seismic behavior improvement was observed from the mass damping effects of this system on the substructure. Several important aspects such as dynamic effects of building at higher modes, P-delta effects, material non-linearities, stability effects of isolators by interaction of horizontal and vertical loads, etc. were considered during this study. The Analytical results prove that B2 building model with isolation system at mid height has been effective approach to diminish the acceleration responses on building and improve the seismic performance. Even though implementation of inter-storey isolation effectively diminishes the acceleration responses and deformations in between the stories of the structure, its practical application might contain several constraints.

Saha A et al. [167] demonstrated the hostile effects of pulse type motions (near fault) on the performance of Inter-storey Isolation systems (IIS). An Extensive Non-linear dynamic analysis has been executed for a group of buildings models ranging from low to high rise designed from the steel moment resisting frames and HDRB isolators placed at intermediate storey level and exposed to two groups of non-pulse type and one-directional pulse ground motions concerning to various hazard levels. These pulse type motions were exhibited to deteriorate the competence of an inter-storey isolation system and expand the seismic demands. The observed deficit of the bearing displacements been underestimated in the FEMA formulae was suggested with a revision, by accumulation of a modification factor. The results showed that low-rise to medium rise IIS building models are highly

sensitive to medium pulse type ground motions, whereas the high-rise IIS building models are sensitive to extended period pulse type ground motions.

Dona M et al. [189] highlighted the necessity for additional damping to diminish the P-Delta effects triggered from drift between the structural parts of lower and upper structure separated by isolation system. As a solution, the Fluid Viscous Dampers (FVD) were introduced in complement to these inter-storey isolation systems for additional energy dissipation. The use of FVD's allows for the isolation systems to be designed at low activation forces despite the expected earthquake forces [190]. Duan C et al. [191] highlighted the consequences of implementing inter-storey isolation systems in high-rise structures. These isolated buildings, under substantial dynamic loading might induce an overturning moment and excessive deformations at isolation level and result an irreversible damage to the bearings. As a solution, a Dual Isolation System based on Friction Pendulum isolation System (FPS) in combination with inter-storey and base isolation system was introduced. These Dual isolation systems avoids the cause tensile damage within the isolators that arises from larger deformations at isolation level, diminishes the seismic response of buildings with high aspect ratio (height to width ratio) at higher modes and enhances the ability of high-rise buildings to resist the overturning effect.

The literature review provides summary that the inter-storey isolation is an effective seismic isolation approach rather than base isolation for High-rise buildings. However, the utilization of this isolation system alone for high-rise buildings might not be an effective solution to fulfill seismic demand. It was indeed true in some cases, especially when exposed to pulse type motions (near fault), long period ground motions, substantial dynamic loading due to heavy winds, blast loads. The researchers suggested that addition of structural damping components such as Fluid viscous dampers, shear walls, outrigger systems, steel bracings in isolated buildings and inclusion of appropriate considerations during the preliminary design and analysis phase of isolation system, allows to achieve an enhanced seismic performance in high-rise buildings. The considerations included the location optimization of isolation level, P-delta effects, influence of higher modes, material non-linearities, local seismic conditions. Furthermore, the proper selection of the mass ratio of upper and lower structures ( $\alpha$ ), Isolation period ( $T_n$ ), type of isolation bearings, method of dynamic analysis, type of ground motions and building's structural configuration. Finally, it includes that IIS technique can be utilized as seismic retrofitting strategy during the additional storey construction over an existing structure, which is termed as added-storey isolation strategy as shown in figure 12(c). Some notable examples of real-life buildings with added-storey isolation systems includes The International Library of Children's Literature in Tokyo [192], The Munashino City Disaster Prevention and Safety Center [193].

### **3.3. Real-life Application of Inter-Storey Isolation adopted in High-Rise building -Marunouchi Tekko Building: A Case Study**

Marunouchi Tekko Building is a multi-purpose, seismically isolated high-rise building, built about 200 meters wide near Tokyo Station (figure 13). This mixed-use type building consists of various commercial amenities such as business support service centres, shops, lounge for bus service, restaurants, located at low-rise and basement level. This Tekko building mainly consists of the Main Building on the north side with 136.5 meters in height, and the South building on the south side of building site with 98.5 meters in height and both integrated on 3-storey basement levels.



Fig. 13. The Tekko Building [197]

### 3.3.1 Structural Features of Tekko Building

The Main Building comprises of 26 stories and a 2-storey penthouse, the South building has 19 stories and 1-storey penthouse and together sharing a 3-storey basement. The Main building houses for office spaces and South Building for high stay serviced apartments on the 6th floor and above [194].

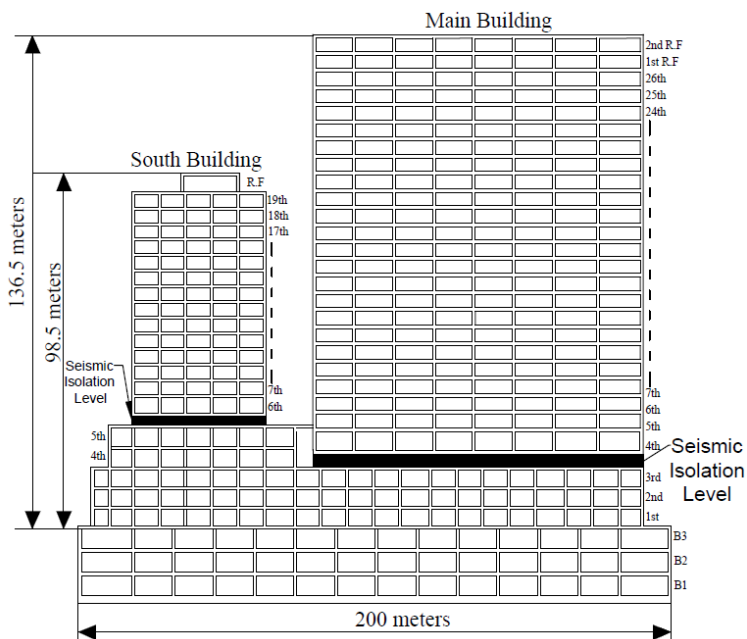


Fig. 14. Cross-Sectional View of Tekko Building

The Tekko building is so called “an intermediate-storey seismic isolated structure”, consisting of 2-seismic isolated buildings on an integrated lower part. The seismic isolation level is located in between the 3rd and 4th stories of the Main building and for South



building between the 5th and 6th stories as shown in figure 14. The Main building composes of structural steel above ground and steel framed reinforced concrete below ground, with combination of piles and mat foundation. The office areas are more spacious as provided with no columns in between for longer span about 18 m. To ensure stiffness of structural frame the intermediate seismic columns are provided in the short direction within the core. Additionally, Steel bracings were provided at higher stories (9<sup>th</sup>, 17<sup>th</sup> and 24<sup>th</sup> Floors). The South Building above the Seismic Isolation level is a 2-span structure in shorter direction and intermediate columns started from floors above seismic isolation level.

### 3.3.2 The Seismic Isolation Strategy

The seismic isolation layer for the Main Building composes of 48 units of laminated natural rubber bearings (LNRB's) of distinct sizes (1000 Ø to 1500 Ø mm), 40 units of oil dampers in 8 with locking mechanism and 30 units of U-shaped steel dampers (Figure 15). While the South building composes of 10 units of laminated natural rubber bearings (LNRB's) with varied sizes (800 Ø to 1200 Ø mm), 8 units of oil dampers and a TMD mounted on top of building [194]. The Isolation levels of the Main building and the South Building were employed below the 4th floor and 6th floor, respectively. The oil dampers with a locking system are provided in short direction of building, to avoid the elevator's shafts from deformation during stronger winds. The oil dampers with a locking mechanism operate as normal oil dampers under nominal conditions, yet during the intense winds the oil dampers were locked with a return period of 4-5 years. This locking mechanism releases on using a timer, often released at a certain time after the locking mechanism being activated and can be controlled manually. The locking mechanism gets activated when an earthquake occurs, whereby the lock is released based on accelerometer measurements.

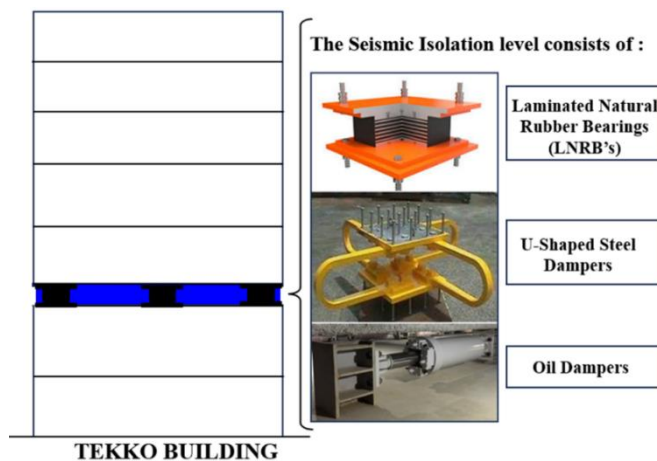


Fig. 15. Common Isolation devices used for Tekko Building

### 3.3.3 Seismic Design Strategy:

The seismic authentication of this isolated high-rise building was investigated through a Response Time History Analysis (RTHA). The Time history analysis used a set of predefined ground motions of Level 1 (rarely occurring) and Level 2 (extremely rarely occurring), categorized by probability of occurrence during building's service life. The ground motions include 3 calibrated waves from the past Hachinohe 1968 NS, Taft 1952 EW, and El Centro 1940 NS, and 3 waves prescribed from Kobe, Hachinohe, and an arbitrary phase. A coupled lumped-mass model was adopted for the vibration response analysis, where these two buildings were positioned in parallel to lower-rise integrated

part below them. The structural frame of the Main and the South building were modelled as 23 lumped masses and 16 lumped respectively. The 1st to 3rd floor masses of the main, south building and boundary arranged in parallel are presumed to be rigid as illustrated in figure 16.

### 3.3.4 Wind Design Strategy

The wind load consideration also plays curial role in the initial design and construction phase of a high-rise structure. These wind loads show detrimental effects on shape, structural properties of tall structures. The Analytical framework included two levels of wind loading for design of building against wind. The analysis for the structural frame of building was executed under two levels of wind loads, whereas for seismic isolation system under the Level 2 wind load. The Response Time History Analysis was executed undertaking the elastic-plastic characteristics of isolation bearings and a fatigue analysis was carried out for U-shaped steel dampers.

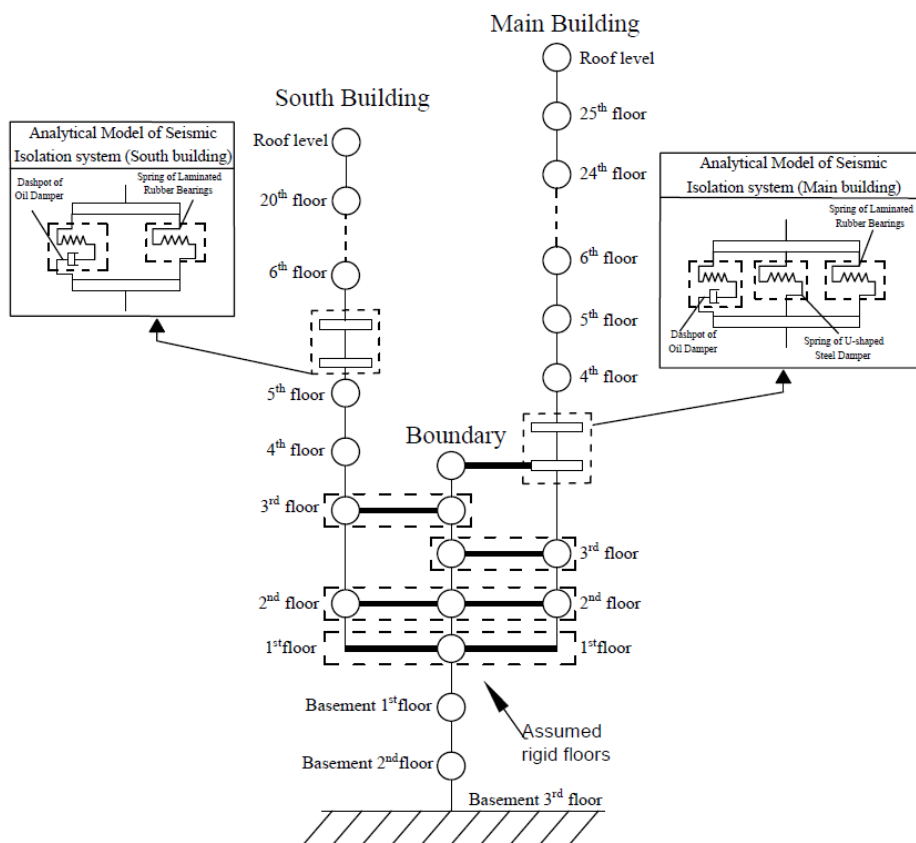


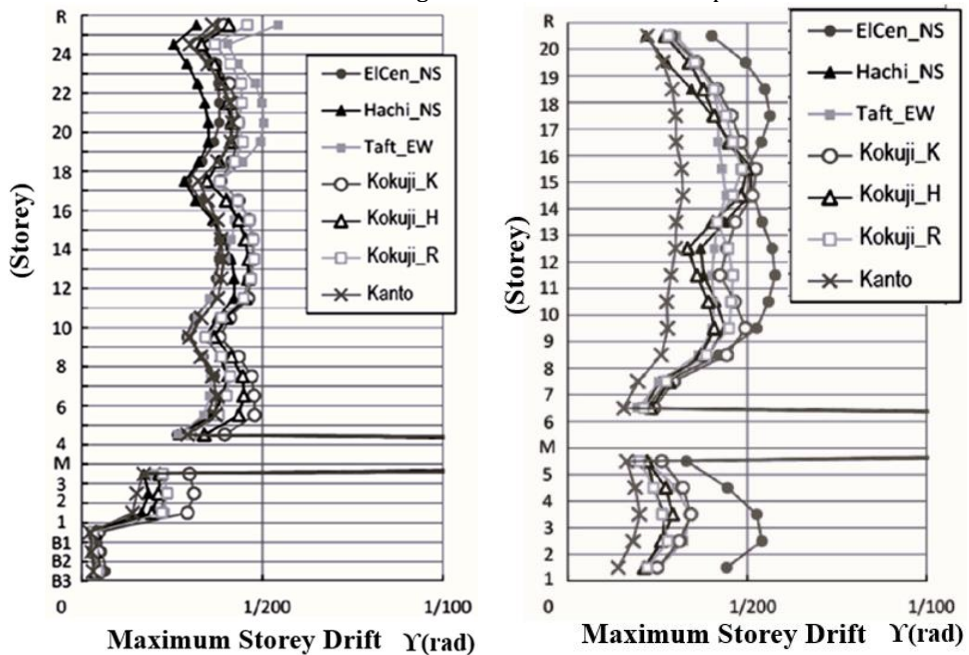
Fig.16. Vibration control analytical model for Tekko Building

### 3.3.5 Analytical Results

Tamari M et al. [195] conducted analytical studies considering seismic design and wind design strategies for Marunouchi Tekko Building and include the following findings:

- The fundamental natural period for the South building was recorded as 5.68 seconds and whereas for the Main Building with equivalent stiffness and when the deformation is 30 cm was recorded as 5.38 seconds.

- The maximum storey drift (in radians) under the Level 2 ground motions in Y direction recorded as 1/184 for the Main Building, and 1/173 for the South Building. (figure17)
- The Main Building exhibits a deformation of 336 mm at seismic isolation level, whereas for South Building with deformation of 251 mm (figure 18). Despite the consideration of variation in the seismic isolation devices, still encountered a deformation of 376 mm for the Main Building and deformation of 285 mm for the South Building.
- The wind load analysis results include that the response shear forces for both buildings are less than design shear forces, whereas the shear stresses under the Level 2 wind load are less than the short-term allowable stresses.
- Under the influence of Level 2 wind load, the storey above the seismic isolation level experiences the shear forces in proportion to the design shear forces about 41% for South Building and 84% for Main Building.
- The seismic isolation level under Level 2 wind load exhibits a maximum deformation of 98.7 mm for the Main Building and 269 mm for the South Building.
- After a year completion of construction, the seismic measurements for building under earthquake intensity of 3 were measured twice, which each of them confirmed the seismic isolation effect. While the wind measurements for building were measured by a rapid maximum wind velocity for 2 days, during which shown the activation of locking mechanism of the oil dampers.



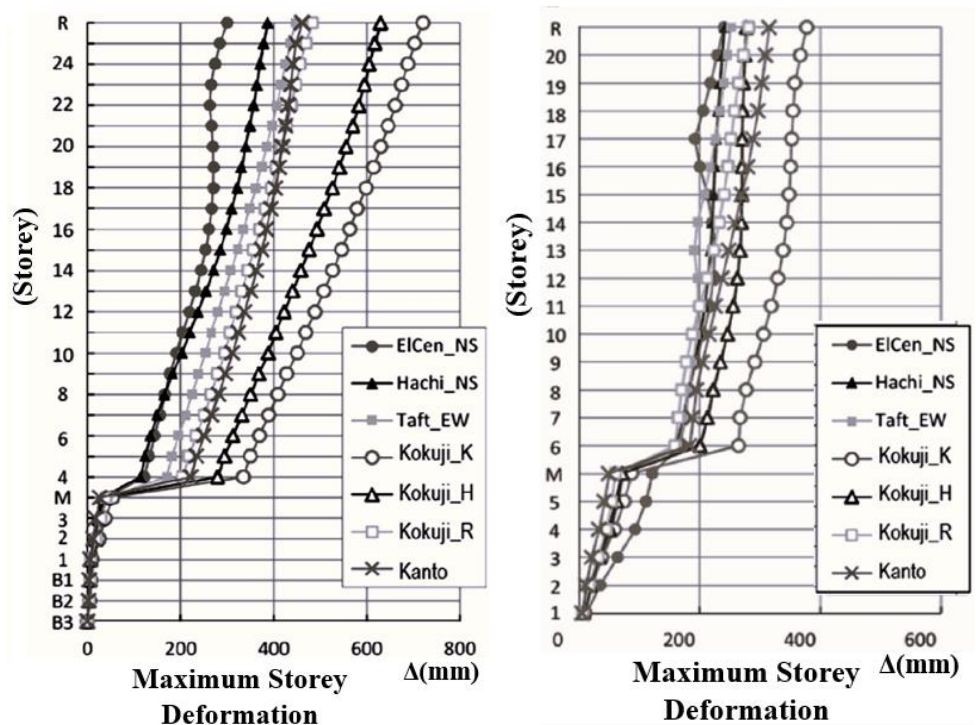
a) Main Building

b) South Building

Fig. 17. Maximum Response Storey Drift (in radians) [195]

On Conclusion, the author describes that adopted structural scheme and the design strategies carried out while checking that there are no resonance effects for the Tekko Building are worked more effective at extreme conditions. Moreover, use of additional structural elements such as U-shaped steel dampers and oil dampers with locking

mechanism have shown their effectiveness in mitigation of strong earthquake and wind forces.



a) Main Building

b) South Building

Fig. 18. Maximum Response Storey Deformation (in mm) [195]

#### 4. Conclusions

In Conclusion, the vibration control design is a key factor in ensuring the resilience and safety of tall or high-rise buildings in earthquake prone regions. This review article provides a comprehensive overview of base-isolation and Inter-storey isolation systems for High-rise buildings, which is accomplished by extracting useful insights from analytical and design features of real-life high-rise buildings equipped with these base isolation and inter-storey isolation systems. In detail the article explores the basic concept and the characteristics of the base isolation system, and the types of isolation bearings used for buildings. the fundamental concept and the benefits of inter-storey isolation system over base isolation. Additionally, the importance of vibration control strategy for buildings, and the different types of vibration control systems were also discussed. From the literature of this present study, the following main highlights and conclusions can be obtained:

- The implementation of Base isolation and inter-storey isolation systems serves as viable solutions for shifting the building’s natural period away from range of frequencies which show greater impacts on amplification of ground motions. However, these systems employ distinct mechanisms to enhance seismic performance of a structure.
- The Base isolated high-rise buildings are identified to have less robustness and tend to resonate at higher modes of vibration and under long period ground

motions. So, these base isolation systems are viable for low rise to medium rise buildings.

- The Inter-storey isolation systems for buildings utilize a combination of seismic isolation and TMD approach to achieve enhanced seismic performance when compared to base isolated buildings.
- The Inter-storey isolation system is also presented as a seismic retrofit strategy during the additional storey construction on top of an existing structure, which is termed as added-storey isolation strategy.

On study of distinct features of base isolation and inter-storey isolation techniques, several key differences were discussed as shown in table 2.

Table 2. Key differences between base isolation and inter-storey isolation technique

| Base Isolation Technique   | Inter-Storey Isolation Technique   |
|--|--|
| The base isolation technique comprises placing flexible bearings, namely isolators between the building's super structure and substructure (foundation). | The Inter-storey Isolation technique uses isolators akin to base isolation but employed between consecutive floors of a building.                          |
| The technique aims mitigate the transfer of seismic forces to structure by decoupling the building from ground motion.                                   | The technique aims to mitigate the transfer of seismic forces to adjacent floors of building, thereby minimizing inter-storey drifts and accelerations.    |
| The technique targets to provide protection for entire structure from ground motions with low to medium range of frequencies.                            | The technique targets to provide localized protection to individual floors in structures form ground motions with medium to higher range of frequencies.   |
| The technique requires provision of moat wall or seismic gap to allow for deformations at isolation level.   | The technique does not require provision of seismic gap for allowing deformations.   |
| The technique can be commonly used for low to medium-rise buildings.   | The technique can be commonly used for medium to high-rise buildings.  |
| The technique is cost effective in construction of new and existing structures as a retrofitting strategy when compared to conventional strategy.        | The technique is cost effective in construction of existing and added storey structures as a retrofitting strategy when compared to base isolation system. |

So far, these two case studies explore that use of traditional seismic isolation might not achieve to fulfill the seismic demand of high-rise buildings. Moreover, the use of other structural elements such as dampers, shear walls, outriggers along with seismic isolation system has shown effectiveness in mitigation of seismic and wind forces.

### 5. Acknowledgement

The Corresponding Author wishes to thank Dr. Lingeshwaran N, Assistant Professor, Department of Civil Engineering, KL University, Guntur, Andhra Pradesh for extended support on Ideology, Conceptualization, Planning the work, Qualitative and Quantitative analysis of results, Writing, Reviewing and Editing.

## References

- [1] Yüksel İ. An Overview on Tall Buildings from The Point of Structural Engineering. *Journal of Innovative Science and Engineering*. 2019 Dec 31;3(2):86–101. <https://doi.org/10.38088/jise.590738>
- [2] Abbood I, Jasim MA, Weli SS. High rise buildings: design, analysis, and safety. *International Journal of Architectural Engineering Technology*. 2021 May 2; 8:1–13. <https://doi.org/10.15377/2409-9821.2021.08.1>
- [3] IS 16700. Criteria for structural safety of tall concrete buildings.2017
- [4] Simmonds P. Tall, Supertall, and Mega tall Building Systems.
- [5] Nakamura Y, Okada K. Review on seismic isolation and response control methods of buildings in Japan. *Geoenvironmental Disasters*. 2019 Jun 3;6(1). <https://doi.org/10.1186/s40677-019-0123-y>
- [6] Amir M, Hamid NH. Hysteresis Loops of Base Isolation System - An Overview. *Key Engineering Materials*. 2021 Mar 1; 879:189–201. <https://doi.org/10.4028/www.scientific.net/kem.879.189>
- [7] Ozer E, İnel M, Çaycı BT. Seismic behaviour of LRB and FPS type isolators considering torsional effects. *Structures*. 2022 Mar 1; 37:267–83. <https://doi.org/10.1016/j.istruc.2022.01.011>
- [8] Naderpour H, Naji N, Burkacki D, Jankowski R. Seismic Response of High-Rise Buildings Equipped with Base Isolation and Non-Traditional Tuned Mass Dampers. *Applied Sciences*. 2019 Mar 21;9(6):1201. <https://doi.org/10.3390/app9061201>
- [9] Matsagar V, Jangid RS. Influence of isolator characteristics on the response of base-isolated structures. *Engineering Structures*. 2004 Oct 1;26(12):1735–49. <https://doi.org/10.1016/j.engstruct.2004.06.011>
- [10] MA F C, Zhang YH, Tan P, Zhou FL. Seismic Response of Base-Isolated High-Rise Buildings under Fully Nonstationary Excitation. *Shock and Vibration*. 2014 Jan 1; 2014:1–11. <https://doi.org/10.1155/2014/401469>
- [11] Thenozhi S, Yu W. Advances in modelling and vibration control of building structures. *Annual Reviews in Control*. 2013 Dec 1;37(2):346–64. <https://doi.org/10.1016/j.arcontrol.2013.09.012>
- [12] Torunbalci N. Seismic Isolation and Energy Dissipating Systems in Earthquake Resistant Design. *13th World Conference on Earthquake Engineering*. 2004;78(11):74–6.
- [13] EL Ouni MH, Abdeddaim M, Elias S, Kahla NB. Review of Vibration Control Strategies of High-Rise Buildings. *Sensors*. 2022 Nov 7;22(21):8581. <https://doi.org/10.3390/s22218581>
- [14] Kasai K, Nakai M, Nakamura Y, Asai H, Suzuki Y, Ishii M. Building passive control in Japan. *Journal of Disaster Research*. 2009 Jun 1;4(3):261–9. <https://doi.org/10.20965/jdr.2009.p0261>
- [15] Symans MD, Constantinou MC. Semi-active control systems for seismic protection of structures: a state-of-the-art review. *Engineering Structures*. 1999 Jun 1;21(6):469–87. [https://doi.org/10.1016/s0141-0296\(97\)00225-3](https://doi.org/10.1016/s0141-0296(97)00225-3)
- [16] Downey A, Cao L, Laflamme S, Taylor D, Ricles J. High-capacity variable friction damper based on band brake technology. *Engineering Structures/Engineering Structures*. 2016 Apr 1; 113:287–98. <https://doi.org/10.1016/j.engstruct.2016.01.035>
- [17] Makris N, Constantinou MC. Spring-viscous damper systems for combined seismic and vibration isolation. *Earthquake Engineering and Structural Dynamics/Earthquake Engineering & Structural Dynamics*. 1992 Jan 1;21(8):649–64. <https://doi.org/10.1002/eqe.4290210801>
- [18] Makris N, Chang SP. Effect of viscous, viscoelastic and friction damping on the response of seismic isolated structures. *Earthquake Engineering and Structural*

- Dynamics/Earthquake Engineering & Structural Dynamics. 2000 Jan 1;29(1):85–107. [https://doi.org/10.1002/\(sici\)1096-9845\(200001\)29:1<85::aid-eqe902>3.0.co;2-n](https://doi.org/10.1002/(sici)1096-9845(200001)29:1<85::aid-eqe902>3.0.co;2-n)
- [19] Zoccolini L, Bruschi E, Cattaneo S, Quaglini V. Current Trends in Fluid Viscous Dampers with Semi-Active and Adaptive Behavior. *Applied Sciences*. 2023 Sep 15;13(18):10358. <https://doi.org/10.3390/app131810358>
- [20] Taylor DP, Katz I. Seismic Protection with Fluid Viscous Dampers for the Torre Mayor, a 57-Story Office Tower in Mexico City, Mexico. 2002.
- [21] Reno ML, Pohll M. Seismic retrofit of San Francisco-Oakland Bay Bridge West Crossing. *Transportation Research Record*. 1998 Jan 1;1624(1):73–81. <https://doi.org/10.3141/1624-09>
- [22] Makris N, Zhang J. Seismic Response Analysis of a Highway Overcrossing Equipped with Elastomeric Bearings and Fluid Dampers. *Journal of Structural Engineering*. 2004 Jun 1;130(6):830–45. [https://doi.org/10.1061/\(asce\)0733-9445\(2004\)130:6\(830\)](https://doi.org/10.1061/(asce)0733-9445(2004)130:6(830))
- [23] Cao L, Downey A, Laflamme S, Taylor D, Ricles J. Variable friction device for structural control based on duo-servo vehicle brake: Modeling and experimental validation. *Journal of Sound and Vibration*. 2015 Jul 1;348:41–56. <https://doi.org/10.1016/j.jsv.2015.03.011>
- [24] Cao L, Laflamme S, Taylor D, Ricles J. Simulations of a variable friction device for multihazard mitigation. *Journal of Structural Engineering*. 2016 Dec 1;142(12). [https://doi.org/10.1061/\(asce\)st.1943-541x.0001580](https://doi.org/10.1061/(asce)st.1943-541x.0001580)
- [25] Constantinou MC, Soong TT, Dargush GF. Passive energy dissipation systems for structural design and retrofit. 1998.
- [26] Jaisee S, Yue F, Ooi YH. A state-of-the-art review on passive friction dampers and their applications. *Eng Struct* [Internet]. 2021;235(September 2020):112022. <https://doi.org/10.1016/j.engstruct.2021.112022>
- [27] Chen K, Tsampras G, Lee K. Structural connection with predetermined discrete variable friction forces. *Resilient Cities and Structures*. 2023;2(1):1–17. <https://doi.org/10.1016/j.rcns.2023.02.006>
- [28] Saaed TE, Nikolakopoulos G, Jonasson JE, Hedlund H. A state-of-the-art review of structural control systems. *Journal of Vibration and Control*. 2013 Jul 11;21(5):919–37. <https://doi.org/10.1177/1077546313478294>
- [29] Pall A S, Pall R. Friction-Dampers for Seismic Control of Buildings “A Canadian Experience.” Eleventh World Conference on Earthquake Engineering, Paper 497. 1996. p. 497.
- [30] Tsampras G, Sause R, Fleischman RB, Restrepo JI. Experimental study of deformable connection consisting of friction device and rubber bearings to connect floor system to lateral force resisting system. *Earthquake Engineering and Structural Dynamics*. 2017 Nov 29;47(4):1032–53. <https://doi.org/10.1002/eqe.3004>
- [31] Makris N, Palios X, Moghimi G, Bousias S. Pressurized sand damper for earthquake and wind engineering: design, testing, and characterization. *Journal of Engineering Mechanics*. 2021 Apr 1;147(4). [https://doi.org/10.1061/\(asce\)em.1943-7889.0001902](https://doi.org/10.1061/(asce)em.1943-7889.0001902)
- [32] Moghimi G, Makris N. Seismic Response of Yielding Multistory Steel Buildings Equipped with Pressurized Sand Dampers. *Journal of Structural Engineering*. 2022 Jul 1;148(7). [https://doi.org/10.1061/\(asce\)st.1943-541x.0003364](https://doi.org/10.1061/(asce)st.1943-541x.0003364)
- [33] Kalfas KN, Makris N. Estimation of the design parameters of pressurized sand dampers from experiments. 2022;(June).
- [34] Kalfas KN, Makris N, Shamy UE. Assessment of the Effect of Design Parameters of Pressurized Sand Dampers from Component Testing. *Journal of Engineering Mechanics*. 2023 Oct 1;149(10). [https://doi.org/10.1061/\(enmdt\)emeng-7013](https://doi.org/10.1061/(enmdt)emeng-7013)
- [35] Karimipetanlar M, Shamy UE, Kalfas KN, Makris N. Numerical Simulations of Particle Behavior and Crushing within a Pressurized Sand Damper Subjected to Cyclic Loading.

- Journal of Engineering Mechanics. 2024 Jan 1;150(1).  
<https://doi.org/10.1061/jenmdt.emeng-7365>
- [36] Xu Y, He Q, Guo YQ, Huang XH, Dong YR, Hu ZW, et al. Experimental and theoretical investigation of viscoelastic damper by applying fractional derivative method and internal variable theory. *Buildings*. 2023 Jan 14;13(1):239.  
<https://doi.org/10.3390/buildings13010239>
- [37] Zhou XQ, Yu DY, Shao XY, Zhang SQ, Wang S, The Institute of Mechanical Science and Engineering, et al. Research and applications of viscoelastic vibration damping materials: A review. *Composite Structures*. 2016.  
<http://dx.doi.org/10.1016/j.compstruct.2015.10.014>
- [38] Samali B, Kwok KCS. Use of viscoelastic dampers in reducing wind- and earthquake-induced motion of building structures. *Engineering Structures/Engineering Structures*. 1995 Nov 1;17(9):639–54. [https://doi.org/10.1016/0141-0296\(95\)00034-5](https://doi.org/10.1016/0141-0296(95)00034-5)
- [39] Tsai CS, Lee HH. Applications of viscoelastic dampers to High-Rise buildings. *Journal of Structural Engineering*. 1993 Apr 1;119(4):1222–33.  
[https://doi.org/10.1061/\(asce\)0733-9445\(1993\)119:4\(1222\)](https://doi.org/10.1061/(asce)0733-9445(1993)119:4(1222))
- [40] Xu ZD, Liao YX, Ge T, Xu C. Experimental and Theoretical Study of Viscoelastic Dampers with Different Matrix Rubbers. *Journal of Engineering Mechanics*. 2016 Aug 1;142(8). [https://doi.org/10.1061/\(asce\)em.1943-7889.0001101](https://doi.org/10.1061/(asce)em.1943-7889.0001101)
- [41] Kalfas KN, Mitoulis SA, Konstantinidis D. Influence of steel reinforcement on the performance of elastomeric bearings. *Journal of Structural Engineering*. 2020 Oct 1;146(10). [https://doi.org/10.1061/\(asce\)st.1943-541x.0002710](https://doi.org/10.1061/(asce)st.1943-541x.0002710)
- [42] Kalfas KN, Mitoulis SA, Katakalos K. Numerical study on the response of steel-laminated elastomeric bearings subjected to variable axial loads and development of local tensile stresses. *Engineering Structures*. 2017 Mar 1; 134:346–57.  
<https://doi.org/10.1016/j.engstruct.2016.12.015>
- [43] Marian L, Giaralis A. Optimal design of a novel tuned mass-damper-inerter (TMDI) passive vibration control configuration for stochastically support-excited structural systems. *Probabilistic Engineering Mechanics*. 2014;38(November):156–64.  
<http://dx.doi.org/10.1016/j.probengmech.2014.03.007>
- [44] Petrini F, Giaralis A, Wang Z. Optimal tuned mass-damper-inerter (TMDI) design in wind-excited tall buildings for occupants' comfort serviceability performance and energy harvesting. *Engineering Structures*. 2020 Feb 1; 204:109904.  
<https://doi.org/10.1016/j.engstruct.2019.109904>
- [45] Murudi MM, Mane SM. Seismic Effectiveness of Tuned Mass Damper (TMD) for Different Ground Motion Parameters. *13th World Conference on Earthquake Engineering*. 2004;325.
- [46] Poon DCK, Shieh S, Joseph LM, Chang C. Structural design of Taipei 101, the world's tallest building. *Proc CTBUH 2004 Seoul Conf Seoul, Korea*. 2004;271–8.
- [47] Dallard P, Fitzpatrick AJ, Flint A, Flint & Neill Partnership, Le Bourva S, Low A, et al. *The London Millennium Footbridge*. Vol. 79, *The Structural Engineer*. 2001 November.
- [48] Marian L, Giaralis A. The tuned mass-damper-inerter for harmonic vibrations suppression, attached mass reduction, and energy harvesting. *Smart Structures and Systems*. 2017 Jun 1;19(6):665–78.
- [49] Petrini F, Giaralis A, Wang Z. Optimal tuned mass-damper-inerter (TMDI) design in wind-excited tall buildings for occupants' comfort serviceability performance and energy harvesting. *Engineering Structures*. 2020 Feb 1;204:109904.  
<https://doi.org/10.1016/j.engstruct.2019.109904>
- [50] De Angelis M, Perno S, Reggio A. Dynamic response and optimal design of structures with large mass ratio TMD. *Earthquake Engineering and Structural Dynamics/Earthquake Engineering & Structural Dynamics*. 2011 Apr 1;41(1):41–60.  
<https://doi.org/10.1002/eqe.1117>



- [51] Giaralis A, Petrini F. Wind-Induced vibration mitigation in tall buildings using the tuned Mass-Damper-Inerter. *Journal of Structural Engineering*. 2017 Sep 1;143(9). [https://doi.org/10.1061/\(asce\)st.1943-541x.0001863](https://doi.org/10.1061/(asce)st.1943-541x.0001863)
- [52] Marian L, Giaralis A. Optimal design of inerter devices combined with TMDs for vibration control of buildings exposed to stochastic seismic excitation. In: CRC Press eBooks. 2014. p. 1025–32. <https://doi.org/10.1201/b16387-151>
- [53] Li C, Liang M, Wang Y, Dong Y. Vibration suppression using two-terminal flywheel. Part I: Modeling and characterization. *Journal of Vibration and Control*. 2011 Oct 18;18(8):1096–105. <https://doi.org/10.1177/1077546311419546>
- [54] Li C, Liang M, Wang Y, Dong Y. Vibration suppression using two-terminal flywheel. Part II: application to vehicle passive suspension. *Journal of Vibration and Control*. 2011 Oct 3;18(9):1353–65. <https://doi.org/10.1177/1077546311419547>
- [55] Sarkar S, Fitzgerald B. Vibration control of spar-type floating offshore wind turbine towers using a tuned mass-damper-inerter. *Structural Control & Health Monitoring/Structural Control and Health Monitoring*. 2019 Nov 11;27(1). <https://doi.org/10.1002/stc.2471>
- [56] Weber F, Huber P, Borchsenius F, Braun C. Performance of TMDI for tall building damping. *Actuators*. 2020 Dec 15;9(4):139. <https://doi.org/10.3390/act9040139>
- [57] Kang X, Huang Q, Wu Z, Tang J, Jiang X, Lei S. A review of the Tuned Mass Damper Inerter (TMDI) in Energy Harvesting and Vibration Control: Designs, analysis and applications. *Computer Modeling in Engineering & Sciences*. 2023 Jan 1;0(0):1–10. <https://doi.org/10.32604/cmescs.2023.043936>
- [58] Pietrosanti D, De Angelis M, Giaralis A. Experimental study and numerical modeling of nonlinear dynamic response of SDOF system equipped with tuned mass damper inerter (TMDI) tested on shaking table under harmonic excitation. *International Journal of Mechanical Sciences*. 2020 Oct 1;184:105762. <https://doi.org/10.1016/j.ijmecsci.2020.105762>
- [59] Hochrainer MJ. Tuned liquid column damper for structural control. *Acta Mechanica*. 2004 Dec 16;175–57:57–76. <https://doi.org/10.1007/s00707-004-0193-z>
- [60] Yang F, Sedaghati R, Esmailzadeh E. Vibration suppression of structures using tuned mass damper technology: A state-of-the-art review. *Journal of Vibration and Control*. 2021;1–25. <https://doi.org/10.1177/1077546320984305>
- [61] Terramara A, Yoshida O. Development of vibration control system using U-shaped water tank. 11th World Conference on Earthquake Engineering. 1996. p. Paper No. 1343.
- [62] Jin S, Yang J, Sun S, Deng L, Chen Z, Gong L, et al. Magnetorheological elastomer base isolation in civil engineering: A review. *Journal of Infrastructure Intelligence and Resilience*. 2023 Jun 1;2(2):100039. <https://doi.org/10.1016/j.iintel.2023.100039>
- [63] Stanikzai MH, Elias S, Chae Y. Recent advances in Hybrid Vibration-Control systems. *Practice Periodical on Structural Design and Construction*. 2022 Aug 1;27(3). [https://doi.org/10.1061/\(asce\)sc.1943-5576.0000685](https://doi.org/10.1061/(asce)sc.1943-5576.0000685)
- [64] Casciati F, Rodellar J, Yildirim U. Active and semi-active control of structures – theory and applications: A review of recent advances. *Journal of Intelligent Material Systems and Structures*. 2012 May 6;23(11):1181–95. <https://doi.org/10.1177/1045389x12445029>
- [65] Soong TT. State-of-the-art review. Active structural control in civil engineering. *Eng Struct*. 1988;10(2):74–84.
- [66] Datta TK. A state-of-the-art review on Active Control of Structures. *ISET Journal of Earthquake Technology*. 2003;40(1):1–17.
- [67] El-Khoury O, Adeli H. Recent advances on vibration control of structures under dynamic loading. *Archives of Computational Methods in Engineering*. 2013 Oct 17;20(4):353–60. <https://doi.org/10.1007/s11831-013-9088-2>

- [68] Jafari M, Alipour A. Methodologies to mitigate wind-induced vibration of tall buildings: A state-of-the-art review. *Journal of Building Engineering*. 2021 Jan 1; 33:101582. <https://doi.org/10.1016/j.jobe.2020.101582>
- [69] Li X, Li P, Guo X, Shi W, Liu J. Vibration control using ATMD and site measurements on the Shanghai World Financial Center Tower. *the Structural Design of Tall and Special Buildings*. 2012 Jun 7;23(2):105–23. <https://doi.org/10.1002/tal.1027>
- [70] Fisco N, Adeli H. Smart structures: Part I—Active and semi-active control. *Scientia Iranica*. 2011 Jun 1;18(3):275–84. <https://doi.org/10.1016/j.scient.2011.05.034>
- [71] Yanik A. Absolute Instantaneous Optimal Control Performance Index for Active Vibration Control of Structures under Seismic Excitation. *Shock and Vibration*. 2019 Nov 12; 2019:1–13. <https://doi.org/10.1155/2019/4207427>
- [72] Ikeda Y. Active and semi-active vibration control of buildings in Japan-Practical applications and verification. *Structural Control and Health Monitoring*. 2009 Nov 1; 16:703–23. <https://doi.org/10.1002/stc.315>
- [73] Stanway R, Sproston JL, El-Wahed AK. Applications of electro-rheological fluids in vibration control: a survey. *Smart Materials and Structures*. 1996 Aug 1;5(4):464–82. <https://doi.org/10.1088/0964-1726/5/4/011>
- [74] Vivas-López CA, Hernández-Alcantara D, Morales-Menéndez R, Ramírez-Mendoza RA, Ahuett-Garza H. Method for modeling electrorheological dampers using its dynamic characteristics. *Mathematical Problems in Engineering*. 2015 Jan 1; 2015:1–15. <https://doi.org/10.1155/2015/905731>
- [75] Khuntia S, Yadav R, Singh R, Rastogi V. Design, development, and analysis of a magnetorheological damper. *IOP Conference Series Materials Science and Engineering*. 2020 Apr 1;804(1):012009. <https://doi.org/10.1088/1757-899x/804/1/012009>
- [76] Aly AM. Vibration control of buildings using magnetorheological damper: a new control algorithm. *Journal of Engineering*. 2013 Jan 1; 2013:1–10. <https://doi.org/10.1155/2013/596078>
- [77] Da Silva Brandão F, Miguel LFF. A New Methodology for Optimal Design of Hybrid Vibration Control Systems (MR + TMD) for Buildings under Seismic Excitation. *Shock and Vibration*. 2023 Sep 4; 2023:1–14. <https://doi.org/10.1155/2023/8159716>
- [78] Saito T, Shiba K, Tamura K. Vibration control characteristics of a hybrid mass damper system installed in tall buildings. *Earthquake Engineering and Structural Dynamics/Earthquake Engineering & Structural Dynamics*. 2001 Jul 5;30(11):1677–96. <https://doi.org/10.1002/eqe.87>
- [79] Maebayashi K, Shiba K, Mita A, Inada Y. Hybrid Mass damper system for response control building. *Tenth World Conference on Earthquake Engineering*. 1992. p. 2359–64.
- [80] De Luca A, Guidi L. State of art in the worldwide evolution of base isolation design. *Soil Dynamics and Earthquake Engineering*. 2019 Oct 1; 125:105722. <https://doi.org/10.1016/j.soildyn.2019.105722>
- [81] Vetturayasudharsanan R, Harini KK, Rajakumari S, Aarthi S, Sivashanmugam T, Vishalraj P V. Analytical Study of Base Isolation- A Review. *E3S Web Conference*. 2023; 399:1–12
- [82] Markou AA, Stefanou G, Manolis GD. Stochastic response of structures with hybrid base isolation systems. *Engineering Structures*. 2018 October 1; 172:629–43. <https://doi.org/10.1016/j.engstruct.2018.06.051>
- [83] Jangid RS, Datta TK. Seismic Behaviour of Base-Isolated Buildings: A State-of-the Art Review. *Proceedings of the Institution of Civil Engineers Structures and Buildings/Proceedings of ICE Structures and Buildings*. 1995 May 1;110(2):186–203. <https://doi.org/10.1680/istbu.1995.27599>
- [84] Murakami K, Kitamura H, Ozaki H, Teramoto T. Design and Analysis of a Building with the Middle-Story Isolation Structural System. *12WCEE*. 2000;(813):1–8.

- [85] F. Naeim and J. M. Kelly. Design of seismic isolated Structures: from theory to practice. Earthquake Spectra. 1999. <http://earthquakespectra.org/doi/abs/10.1193/1.1586135>
- [86] Kelly JM. Aseismic base isolation: review and bibliography. Soil Dynamics and Earthquake Engineering. 1986 Oct 1;5(4):202–16. [https://doi.org/10.1016/0267-7261\(86\)90006-0](https://doi.org/10.1016/0267-7261(86)90006-0)
- [87] Robinson WH. Passive Control of Structures, the New Zealand Experience. Vol. 35, ISET Journal of Earthquake Technology. 1998. p. 63–75.
- [88] Islam A, Jameel M, Jumaat MZ. Seismic isolation in buildings to be a practical reality: Behavior of structure and installation technique. Journal of Engineering and Technology. 2011;3(4):99–117. <http://www.academicjournals.org/JETR/PDF/pdf/2011/Apr/Islam.pdf>
- [89] Banerjee S, Matsagar V. Hybrid Vibration Control of Hospital Buildings against Earthquake Excitations Using Unbonded Fiber-Reinforced Elastomeric Isolator and Tuned Mass Damper. Buildings. 2023 July 6;13(7):1724. <https://doi.org/10.3390/buildings13071724>
- [90] Warn GP, Ryan KL. A Review of Seismic isolation for Buildings: Historical development and research needs. Buildings. 2012 Aug 3;2(3):300–25. <https://doi.org/10.3390/buildings2030300>
- [91] Soto MG, Adeli H. Vibration control of smart base-isolated irregular buildings using neural dynamic optimization model and replicator dynamics. Engineering Structures. 2018 Feb 1; 156:322–36. <https://doi.org/10.1016/j.engstruct.2017.09.037>
- [92] Lipte SP, Rathi VR, Kolase PK. Seismic Response Control of RC Building by using Base Isolation System. 2022;8(895):895–909.
- [93] Malu G, Murnal P. Sliding Isolation Systems: State-of-the-Art Review. Second International Conference on Emerging Trends in Engineering (SICETE). IOSR Journal of Civil Engineering. 2013; 6:30–35.
- [94] Beirami Shahabi A, Ahari GZ, Barghian M. Base isolation systems-a state of the art review according to their mechanism. Journal of Rehabilitation Civil Engineering. 2020;8(2):37–61.
- [95] Sugihardjo H, Lesmana Y. The seismic performance of residential housing under strong earthquake shaking. International Journal of Civil Engineering and Technology. 2019;10(1):2195–209.
- [96] Athira VS, Minnu SN, Mohan SC. Seismic Performance of Buildings in Hilly Regions with and Without Base Isolation and Cable Support System. Vol. 188, Lecture Notes in Civil Engineering. Springer Singapore; 2022. 145–159 p. [http://dx.doi.org/10.1007/978-981-16-5673-6\\_12](http://dx.doi.org/10.1007/978-981-16-5673-6_12)
- [97] Buckle IG, Mayes RL. Seismic Isolation: History, Application, and Performance—A World View. Earthquake Spectra. 1990 May 1;6(2):161–201. <https://doi.org/10.1193/1.1585564>
- [98] Ferritto JM. Studies on seismic isolation of buildings. Journal of Structural Engineering-ASCE. 1991 Nov 1;117(11):3293–314. [https://doi.org/10.1061/\(asce\)0733-9445\(1991\)117:11\(3293\)](https://doi.org/10.1061/(asce)0733-9445(1991)117:11(3293))
- [99] Olariu I, Olariu F, Sarbu D. Base isolation for seismic retrofitting of existing structures. Seismic Design Practice in the Next Century. 2022;13(November):417–24. <https://doi.org/10.1201/9780203740026-57>
- [100] Penelis GG. Seismic isolation and energy dissipation systems. Concrete Building Seismic Regulation. 2018;(January):729–56.
- [101] Ramallo JC, Johnson EA, Spencer BF. “Smart” base isolation systems. Journal of Engineering Mechanics. 2002 October 1;128(10):1088–99. [https://doi.org/10.1061/\(asce\)0733-9399\(2002\)128:10\(1088\)](https://doi.org/10.1061/(asce)0733-9399(2002)128:10(1088))
- [102] Katsamakos AA, Belser G, Vassiliou MF, Blondet M. Experimental investigation of a spherical rubber isolator for use in low-income countries. Engineering Structures. 2022;250(January):113522. <https://doi.org/10.1016/j.engstruct.2021.113522>

- [103] Forcellini D, Kalfas K. 3D Numerical Simulations of Multi-Layered Elastomeric Bearings (EB) Subjected to Combined Vertical and Horizontal Loads. COMPDYN Proceedings. 2023 Jan 1; <https://doi.org/10.7712/120123.10585.21044>
- [104] Makris N. Seismic isolation: Early history. Earthquake Engineering and Structural Dynamics. 2018 Sep 23;48(2):269–83. <https://doi.org/10.1002/eqe.3124>
- [105] Sarrazin M, Moroni MO. Design of a base isolated confined masonry building. Proceedings of the 10th World Conference on Earthquake Engineering. 1992. p. 2505–8.
- [106] Roeder CW, Stanton JF. Elastomeric Bearings: State-of-the-Art. Journal of Structural Engineering. 1983 Dec 1;109(12):2853–71. [https://doi.org/10.1061/\(asce\)0733-9445\(1983\)109:12\(2853\)](https://doi.org/10.1061/(asce)0733-9445(1983)109:12(2853))
- [107] Bailey JS, Allen EW. Seismic isolation retrofitting of the Salt Lake City and County Building. Nuclear Engineering and Design. 1991 Jun 1;127(3):367–74. [https://doi.org/10.1016/0029-5493\(91\)90060-u](https://doi.org/10.1016/0029-5493(91)90060-u)
- [108] Kelly JM. Implementation of base isolation in the United States. Vol. 256 pt 2, American Society of Mechanical Engineers, Pressure Vessels and Piping Division (Publication) PVP. 1993. p. 159–70.
- [109] Smart CA. Wellington Central Police Station base isolation maintenance. Bulletin of the New Zealand Society for Earthquake Engineering/NZSEE Quarterly Bulletin. 2013 Sep 30;46(3):141–56. <https://doi.org/10.5459/bnzsee.46.3.141-156>
- [110] Sharpe RD. Kiwi technology to protect Indian hospital from earthquakes. Nzsee 2002. 2002;(2).
- [111] Markou AA, Manolis GD. Mechanical models for shear behavior in high damping rubber bearings. Soil Dynamics Earthquake Engineering. 2016; 90:221–6. <http://dx.doi.org/10.1016/j.soildyn.2016.08.035>
- [112] Belbachir A, Benanane A, Ouazir A, Harrat ZR, Hadzima-Nyarko M, Radu D, et al. Enhancing the Seismic Response of Residential RC Buildings with an Innovative Base Isolation Technique. Sustainability. 2023 Jul 27;15(15):11624. <https://doi.org/10.3390/su151511624>
- [113] Gu Z, Lei Y, Qian W, Xiang Z, Hao F, Wang Y. An Experimental Study on the Mechanical Properties of a High Damping Rubber Bearing with Low Shape Factor. Applied Sciences. 2021 Oct 27;11(21):10059. <https://doi.org/10.3390/app112110059>
- [114] Fuller KNG, Gough J, Pond TJ, Ahmadi H. High damping natural rubber seismic isolators. Journal of Structural Control. 1997 Dec 1;4(2):19–40. <https://doi.org/10.1002/stc.4300040202>
- [115] Forni M, Antonucci R, Arcadi A, Occhiuzzi A. A Hybrid Seismic Isolation System Made of Rubber Bearings and Semi-Active Magneto-Rheological Dampers. Control. 2004;(2177).
- [116] Oliveto G, Athanasiou A, Oliveto ND. Analytical earthquake response of 1D hybrid base isolation systems. Soil Dynamics Earthquake Engineering. 2012; 43:1–15. <http://dx.doi.org/10.1016/j.soildyn.2012.05.021>
- [117] Iemura H, Taghikhany T, Jain SK. Optimum design of resilient sliding isolation system for seismic protection of equipments. Bulletin of Earthquake Engineering. 2006 May 9;5(1):85–103. <https://doi.org/10.1007/s10518-006-9010-5>
- [118] Avinash AR, Krishnamoorthy A, Kamath K, Chaithra M. Sliding Isolation Systems: historical review, modeling techniques, and the contemporary Trends. Buildings. 2022 Nov 16;12(11):1997. <https://doi.org/10.3390/buildings12111997>
- [119] Harvey PS, Kelly KC. A review of rolling-type seismic isolation: Historical development and future directions. Engineering Structures. 2016; 125:521–31. <http://dx.doi.org/10.1016/j.engstruct.2016.07.031>
- [120] Katsamakos AA, Vassiliou MF. Experimental parametric study and phenomenological modeling of a deformable rolling seismic isolator. Journal of

- Earthquake Engineering. 2023 Mar 24;27(16):4664–93. <https://doi.org/10.1080/13632469.2023.2189978>
- [121] Foti D. Rolling devices for seismic isolation of lightweight structures and equipment. Design and realization of a prototype. *Structural Control and Health Monitoring*. 2018 Dec 21;26(3):e2311. <https://doi.org/10.1002/stc.2311>
- [122] Gilsalar H, Constantinou MC. Behavior of a spherical deformable rolling seismic isolator for lightweight residential construction. *Bulletin of Earthquake Engineering*. 2019 Apr 26;17(7):4321–45. <https://doi.org/10.1007/s10518-019-00626-z>
- [123] Katsamakas AA, Del Giudice L, Reyes SI, Candebat-Sanchez D, Vassiliou MF. Experimental and numerical assessment of grout-filled tennis balls as seismic isolation bearings [Internet]. Vol. 294, *Engineering Structures*. 2023 p. 116716. <https://doi.org/10.1016/j.engstruct.2023.116716>
- [124] Lee GC, Ou Y, Liang Z, Niu TC, Song JW. Principles and performance of roller seismic isolation bearings for highway bridges. 2007.
- [125] Fenz DM, Constantinou MC. Spherical sliding isolation bearings with adaptive behavior: Theory. *Earthquake Engineering and Structural Dynamics/Earthquake Engineering & Structural Dynamics*. 2007 Aug 20;37(2):163–83. <https://doi.org/10.1002/eqe.751>
- [126] Etedali S, Hasankhoie K, Sohrabi MR. Optimal design of pure-friction isolators with and without restoring device: A multi-objective cuckoo search-based approach for seismic-excited structures. *Structures*. 2020;25(April):708–19. <https://doi.org/10.1016/j.istruc.2020.03.041>
- [127] Gong Y, Cao L, Laflamme S, Ricles JM, Quiel SE, Taylor D. Variable friction cladding connection for seismic mitigation. *Engineering Structures*. 2019 Jun 1; 189:243–59. <https://doi.org/10.1016/j.engstruct.2019.03.066>
- [128] Yang CY, Wang SJ, Lin CK, Chung LL, Liou MC, National Center for Research on Earthquake Engineering, et al. Analytical and experimental study on sloped sliding-type bearings. *Struct Control Health Monit*. 2021. <https://doi.org/10.1002/stc.2828>
- [129] Etedali S, Hasankhoie K, Sohrabi MR. Seismic responses and energy dissipation of pure-friction and resilient-friction base-isolated structures: A parametric study. *Journal of Building Engineering*. 2020;29(January):101194. <https://doi.org/10.1016/j.jobe.2020.101194>
- [130] Wei B, Zuo C, He X, Jiang L. Numerical investigation on scaling a pure friction isolation system for civil structures in shaking table model tests. *International Journal of Non-Linear Mechanics*. 2018; 98:1–12. <https://doi.org/10.1016/j.ijnonlinmec.2017.09.005>
- [131] Mokha AS, Constantinou MC, Reinhorn AM, Zayas VA. Experimental study of Friction-Pendulum isolation System. *Journal of Structural Engineering*. 1991 Apr 1;117(4):1201–17. [https://doi.org/10.1061/\(asce\)0733-9445\(1991\)117:4\(1201\)](https://doi.org/10.1061/(asce)0733-9445(1991)117:4(1201))
- [132] Castaldo P, Tubaldi E. Influence of FPS bearing properties on the seismic performance of base-isolated structures. *Earthquake Engineering and Structural Dynamics*. 2015 Aug 10;44(15):2817–36. <https://doi.org/10.1002/eqe.2610>
- [133] Zayas VA, Low SS, Mahin SA. A simple pendulum technique for achieving seismic isolation. *Earthquake Spectra*. 1990 May 1;6(2):317–33. <https://doi.org/10.1193/1.1585573>
- [134] Mokha AS, Amin NR, Constantinou MC, Zayas VA. Seismic isolation retrofit of large historic building. *Journal of Structural Engineering*. 1996 Mar 1;122(3):298–308. [https://doi.org/10.1061/\(asce\)0733-9445\(1996\)122:3\(298\)](https://doi.org/10.1061/(asce)0733-9445(1996)122:3(298))
- [135] Cardone D, Gesualdi G, Brancato P. Restoring capability of friction pendulum seismic isolation systems. *Bulletin of Earthquake Engineering*. 2015;13(8):2449–80. <http://dx.doi.org/10.1007/s10518-014-9719-5>
- [136] Pranesh M, Sinha R. VFPI: an isolation device for aseismic design. *Earthquake Engineering and Structural Dynamics*. 2000 May 1;29(5):603–27. [https://doi.org/10.1002/\(sici\)1096-9845\(200005\)29:5<603:aid-eqe927>3.0.co;2-w](https://doi.org/10.1002/(sici)1096-9845(200005)29:5<603:aid-eqe927>3.0.co;2-w)

- [137] Malu G, Pranesh M. Comparative Study of Sliding Isolation System for Low Frequency Ground Motion. Proc fifteenth world Conf Earthq Eng. 2012;(2000).
- [138] Krishnamoorthy A. Seismic isolation of bridges using variable frequency and variable friction pendulum isolator system. Structural Engineering International. 2010 May 1;20(2):178–84. <https://doi.org/10.2749/101686610791283632>
- [139] Stanton JF, Roeder CW. Advantages and limitations of seismic isolation. Earthquake Spectra. 1991 May 1;7(2):301–24. <https://doi.org/10.1193/1.1585630>
- [140] Konstantinidis D, Makris N. Experimental and analytical studies on the response of freestanding laboratory equipment to earthquake shaking. Earthquake Engineering and Structural Dynamics. 2008 Dec 10;38(6):827–48. <https://doi.org/10.1002/eqe.871>
- [141] Konstantinidis D, Makris N. Experimental and analytical studies on the response of 1/4-scale models of freestanding laboratory equipment subjected to strong earthquake shaking. Bulletin of Earthquake Engineering. 2010 Jun 9;8(6):1457–77. <https://doi.org/10.1007/s10518-010-9192-8>
- [142] Dolce M, Cardone D. Seismic protection of light secondary systems through different base isolation systems. Journal of Earthquake Engineering. 2003 Apr 1;7(2):223–50. <https://doi.org/10.1080/13632460309350447>
- [143] Wolff ED, Constantinou MC, University at Buffalo, State University of New York. Experimental study of seismic isolation systems with emphasis on secondary system response and verification of accuracy of dynamic response history analysis methods. University at Buffalo (UB) MCEER: Earthquake Engineering to Extreme Events. 2004 Jan. Report No.: MCEER-04-0001.
- [144] Morgan TA, Mahin SA. Pacific Earthquake Engineering The Use of Base Isolation Systems to Achieve Complex Seismic Performance Objectives Tokyo Institute of Technology. Engineering. 2011;(July)
- [145] Van Engelen NC, Konstantinidis D, Tait MJ. Structural and non-structural performance of a seismically isolated building using stable unbonded fiber-reinforced elastomeric isolators. Earthquake Engineering and Structural Dynamics. 2015 Oct 19;45(3):421–39. <https://doi.org/10.1002/eqe.2665>
- [146] Carr, A & Puthanpurayil A. Base isolation: the good, the bad and the ugly. NZSEE 2021 Annual Conference. 2021; <http://13.237.132.70/handle/nzsee/2396>
- [147] Kumar P, Petwal S. Seismic performance of secondary systems housed in isolated and non-isolated buildings. Earthquakes and Structures. 2019 Apr 25;16(4):401–13. <https://doi.org/10.12989/EAS.2019.16.4.401>
- [148] Ismail MIS. Seismic isolation of structures. Part I: Concept, review and a recent development. HormigÓN Y Acero. 2018 May 1;69(285):147–61. <https://doi.org/10.1016/j.hya.2017.10.002>
- [149] Melkumyan M. Seismic Isolation vs. Conventional Construction. International Journal of Research Engineering and Science ISSN: 2320-9356. 2022;10(March):31–40.
- [150] Cutfield MR, Ma QT, Ryan KL. Cost-benefit analysis of base isolated and conventional buildings: A case study. In: New Zealand Society for Earthquake Engineering 2014 Conference. 2014
- [151] Shinozaki Y, Hosozawa O, Komuro T. Structural design of base-isolation system for tall building in Japan. CTBUH 2005 Seoul Conference. 2004;195–200.
- [152] Takewaki I. Robustness of base-isolated high-rise buildings under code-specified ground motions. The Structural Design of Tall and Special Buildings. 2007 Jun 18;17(2):257–71. <https://doi.org/10.1002/tal.350>
- [153] Ariga T, Kanno Y, Takewaki I. Resonant behaviour of base-isolated high-rise buildings under long-period ground motions. The Structural Design of Tall and Special Buildings. 2006 Jan 1;15(3):325–38. <https://doi.org/10.1002/tal.298>

- [154] Ogura K, Kawabata I, Komuro T, Soya K, Terashima T. Seismic response characteristics of high-rise buildings with base isolation system. *AIJ Journal of Technology and Design*. 1997 Jan 1;3(5):47–51. <https://doi.org/10.3130/aijt.3.47>
- [155] Komuro T, Nishikawa Y, Kimura Y, Isshiki Y. Development and realization of base isolation system for High-Rise buildings. *Journal of Advanced Concrete Technology*. 2005 Jan 1;3(2):233–9. <https://doi.org/10.3151/jact.3.233>
- [156] Nakagawa K, Shimazaki D. Application of Seismic Isolation Systems in Japanese High-Rise Buildings. *CTBUH J*. 2015;(2):36–40.
- [157] Pan T, Ling S, Cui W. Seismic response of segmental buildings. *Earthquake Engineering & Structural Dynamics*. 1995 Jul 1;24(7):1039–48. <https://doi.org/10.1002/eqe.4290240708>
- [158] Reggio A, De Angelis M. Optimal energy-based seismic design of non-conventional Tuned Mass Damper (TMD) implemented via inter-story isolation. *Earthquake Engineering & Structural Dynamics*. 2015 Jan 20;44(10):1623–42. <https://doi.org/10.1002/eqe.2548>
- [159] Phocas MC, Pamboris G. Structures with multiple seismic isolation levels. In: *WIT transactions on state-of-the-art in science and engineering* [Internet]. 2012. p. 77–86. <https://doi.org/10.2495/978-1-84564-672-1/07>
- [160] Zhang R, Phillips BM, Taniguchi S, Ikenaga M, Ikago K. Shake table real-time hybrid simulation techniques for the performance evaluation of buildings with inter-story isolation. *Structural Control & Health Monitoring*. 2016 Dec 21;24(10). <https://doi.org/10.1002/stc.1971>
- [161] Bolvardi V, Pei S, van de Lindt JW, Dolan JD. Direct displacement design of tall cross laminated timber platform buildings with inter-story isolation. *Engineering Structures*. 2018; 167:740–9. <https://doi.org/10.1016/j.engstruct.2017.09.054>
- [162] Wang SJ, Chang K, Hwang JS, Hsiao JY, Lee BH, Hung YC. Dynamic behaviour of a building structure tested with base and mid-story isolation systems. *Engineering Structures*. 2012 September 1; 42:420–33. <https://doi.org/10.1016/j.engstruct.2012.04.035>
- [163] Wang SJ, Hwang JS, Chang K, Lin MH, Lee BH. Analytical and experimental studies on midstory isolated buildings with modal coupling effect. *Earthquake Engineering & Structural Dynamics*. 2013 May 11;42(2):201–19. <https://doi.org/10.1002/eqe.2203>
- [164] Yamane K, Tsubaki H, Tanaka T, Sumi A. Isolation Story Structure of Umeda Tower, Osaka, Japan. *Structural Engineering International*. 2003 Nov 1;13(4):225–7. <https://doi.org/10.2749/10168660377964351>
- [165] Esposito F, Argenziano M, Faiella D, Mele E. Intermediate Isolation System with Nonlinear Lower Structure, and Isolation System. *Applied Sciences*. 2023 April 4;13(7):4590. <https://doi.org/10.3390/app13074590>
- [166] Bernardi E, Donà M, Da Porto F, Tan P. Investigations on inter-storey seismic isolation as a technique for adding upper storeys. *COMPdyn Proceedings*. 2021 January 1; <https://doi.org/10.7712/120121.8709.18889>
- [167] Saha A, Mishra SK. Amplification of seismic demands in inter-storey-isolated buildings subjected to near fault pulse type ground motions. *Soil Dynamics and Earthquake Engineering*. 2021 August 1; 147:106771. <https://doi.org/10.1016/j.soildyn.2021.106771>
- [168] Ikeda Y. Fundamental equation based on pole allocation for inter-story seismic isolation of buildings. *Structural Control & Health Monitoring*. 2020 Dec 23;28(3). <https://doi.org/10.1002/stc.2687>
- [169] Tsuneki Y, Torii S, Murakami K, Sueoka T. Middle-Story isolated structural system of High-Rise building. *Journal of Disaster Research*. 2009 Jun 1;4(3):229–38. <https://doi.org/10.20965/jdr.2009.p0229>

- [170] Suekoa T, Torii S, Tsuneki Y. The application of response control design using middle-story isolation system to high-rise Building. 13th World Conference on Earthquake Engineering. August 1-6, 2004; Paper No. 3457.
- [171] Cruciat R, Pricopie A, Cretu D, Technical University of Civil Engineering Bucharest. Optimization of an inter-storey isolated structure using genetic algorithms. Conference Paper. 2013 May. <https://doi.org/10.13140/2.1.1820.9601>
- [172] Wang SJ, Lin WC, Yang CY. Recent Progress in Taiwan on Seismic Isolation, Energy Dissipation, and Active Vibration Control. 2017;(Liou 2010):1–11.
- [173] Forcellini D, Gallanti L. Seismic assessment of storey isolation on tall buildings. *Innovative Infrastructure Solutions*. 2018 July 24;3(1). <https://doi.org/10.1007/s41062-018-0163-2>
- [174] Phocas MC, Pamboris G. Multi-storey Structures with Seismic Isolation at Storey-Level. In: Computational methods in applied sciences. 2016. p. 261–84. [https://doi.org/10.1007/978-3-319-47798-5\\_9](https://doi.org/10.1007/978-3-319-47798-5_9)
- [175] Ping T, Ying Z, Fulin Z. Optimal Design and Control Mechanism Study on Story Isolation System. 14th World Conference Earthquake Engineering. 2008.
- [176] Charmpis DC, Phocas MC, Komodromos P. Optimized retrofit of multi-storey buildings using seismic isolation at various elevations: assessment for several earthquake excitations. *Bulletin of Earthquake Engineering*. 2015 Feb 28;13(9):2745–68. <https://doi.org/10.1007/s10518-015-9737-y>
- [177] Taylor P, Ryan KL, Earl CL. Analysis and Design of Inter-Story Isolation Systems with Nonlinear Devices Analysis and Design of Inter-Story Isolation Systems with Nonlinear Devices. 2010;(July 2014):37–41. <https://doi.org/10.1080/13632461003668020>
- [178] Zhou Q, Singh MP, Huang X. Model reduction and optimal parameters of mid-story isolation systems. *Engineering Structures*. 2016 Oct 1; 124:36–48. <https://doi.org/10.1016/j.engstruct.2016.06.011>
- [179] Guo WD, Liu SD, Liu JY, Zhang RH. Analysis of using interlayer seismic isolation technology in Storey-Adding Structure. *Advanced Materials Research*. 2012 November 1;594–597:1702–6. <https://doi.org/10.4028/www.scientific.net/amr.594-597.1702>
- [180] Hur MW, Park TW. Seismic Performance of Story-Added Type Buildings Remodeled with Story Seismic Isolation Systems. *Buildings*. 2022 Feb 24;12(3):270. <https://doi.org/10.3390/buildings12030270>
- [181] Ma XT, Bao C, Doh SI, Lu H, Zhang LX, Ma ZW, et al. Dynamic response analysis of story-adding structure with isolation technique subjected to near-fault pulse-like ground motions. *Physics and Chemistry of the Earth*. 2021 February 1; 121:102957. <https://doi.org/10.1016/j.pce.2020.102957>
- [182] Mele E, Faiella D. Inter-Story Isolation Systems (IIS) for tall buildings: design considerations. *Structural Engineering*. CTBUH. 2018;(1i):34–41.
- [183] Nakamizo D, Koitabashi Y. Structural design of Mid-Story Isolated High-Rise Building - Roppongi Grand Tower. *International Journal of High-Rise Buildings*. 2018 Jan 1;7(3):233–42. <http://www.koreascience.or.kr/article/JAKO201834663385096.pag>
- [184] Okada K, Yoshida S. Structural design of Nakanoshima Festival Tower. *International Journal of High-Rise Buildings*. 2014 Jan 1;3(3):173–83. <https://www.koreascience.kr:443/article/JAKO201408160369336.pdf>
- [185] Villaverde R. Aseismic Roof Isolation System: Feasibility Study with 13-Story Building. *Journal of Structural Engineering-ASCE*. 2002 Feb 1;128(2):188–96. [https://doi.org/10.1061/\(asce\)0733-9445\(2002\)128:2\(188\)](https://doi.org/10.1061/(asce)0733-9445(2002)128:2(188))
- [186] Chey MH, Chase JG, Mander JB, Carr AJ. Innovative seismic retrofitting strategy of added stories isolation system. *Frontiers of Structural and Civil Engineering*. 2013 Jan 23;7(1):13–23. <https://doi.org/10.1007/s11709-013-0195-9>
- [187] Faiella D, Mele E. Insights into inter-story isolation design through the analysis of two case studies. *Engineering Structures*. 2020 July 1; 215:110660. <https://doi.org/10.1016/j.engstruct.2020.110660>



- [188] Forcellini D, Kalfas KN. Inter-story seismic isolation for high-rise buildings. *Engineering Structures*. 2023 January 1; 275:115175. <https://doi.org/10.1016/j.engstruct.2022.115175>
- [189] Donà M, Bernardi E, Zonta A, Tan P, Zhou F. Evaluation of optimal FVDs for inter-storey isolation systems based on surrogate performance models. Vol. 19, *Bulletin of Earthquake Engineering*. Springer Netherlands; 2021. 4587–4621 p. Available from: <https://doi.org/10.1007/s10518-021-01134-9>
- [190] Liu Y, Wu J, Donà M. Effectiveness of fluid-viscous dampers for improved seismic performance of inter-storey isolated buildings. *Engineering Structures*. 2018;169(May):276–92. <https://doi.org/10.1016/j.engstruct.2018.05.031>
- [191] Duan C. Experimental and Numerical Analysis of a High-Rise Structure with a Dual FPS Isolation System. *Advances in Civil Engineering*. 2022 Mar 18; 2022:1–16. <https://doi.org/10.1155/2022/1567182>
- [192] Masanori T, Mōri N, Yamamoto H, Murakami K, Sueoka T. Applying seismic isolation to buildings in Japan — retrofitting and Middle-Story isolation. *Structures Congress 2008*. 2008 Oct 14; [https://doi.org/10.1061/41000\(315\)12](https://doi.org/10.1061/41000(315)12)
- [193] Tsuneki Y, Torii S, Murakami K, Sueoka T. Middle-Story Isolated Structural System of High-Rise Building. 2009;4(3):229–38.
- [194] Faiella D, Mele E. Insights into inter-story isolation design through the analysis of two case studies. *Engineering Structures/Engineering Structures*. 2020 Jul 1; 215:110660. <https://doi.org/10.1016/j.engstruct.2020.110660>
- [195] Tamari M, Yoshihara T, Miyashita M, Ariyama N, Nonoyama M. Structural design and performance evaluation of a mid-story seismic Isolated High-Rise building. *International Journal of High-Rise Buildings*. 2017 Sep 1;6(3):227–35. <https://doi.org/10.21022/ijhrb.2017.6.3.227>
- [196] Mt-reit.jp. Available from: <https://www.mt-reit.jp/file/portfolio/f014e48d99c4ae339c3c2248ff060635b6c3d67f.jpg?timestamp=1705416251885>.
- [197] Imgur.com. Available from: <https://i.imgur.com/QtRkWGd.jpg>.

Blank Page

Research Article

## Study on performance of multiwall carbon nanotubes and functionalized multiwall carbon nanotubes/ poly aryl ether ketone polymer composite gears

Rai Sujit Nath Sahai<sup>1,a</sup>, Pravin Nana Jadhav<sup>1,2,b</sup>, Achyut Sahebrao Raut<sup>3,c</sup>, Sumit Shahaji Surve<sup>3,d</sup>

<sup>1</sup>Department of General Engineering, Institute of Chemical Technology, Mumbai, India

<sup>2</sup>Department of Mechanical Engineering, Gharda Institute of Technology, Lavel, Ratnagiri, India

<sup>3</sup>Department of Mechanical Engineering, Rajendra Mane College of Engineering & Technology, Ambav, India

### Article Info

### Abstract

#### Article history:

Received 24 Mar 2024

Accepted 02 Jun 2024

#### Keywords:

*Poly aryl ether ketone;  
Multiwalled carbon  
nanotube;  
Functionalized  
multiwalled carbon  
nanotube;  
Polymer composite  
gears*

This study investigates the thermal and wears resistance performance of polymer gears made of pristine poly aryl ether ketone (PAEK) and PAEK polymer matrix incorporating both pristine multi walled carbon nanotube (MWCNT) and functionalized MWCNT polymer composites under different operating conditions. The investigation involves the thermal behavior, wear performance and surface roughness of gears at different torques (0 Nm, 6 Nm, 8 Nm, and 10 Nm) and at rotational speeds such as 1000 rpm and 1500 rpm. The polymer composite materials are prepared by using a twin-screw extruder and the gears of these materials are manufactured by using an injection molding machine. The gears are examined using a gear test rig. The surface temperature, specific wear rate and surface roughness are the parameters that are measured at different torques and rotational speeds using a gear test rig, before and after the running operations of these gears. The gears made of PAEK and amine functionalized MWCNT composite materials exhibits improved performance in terms of wear resistance and thermal behavior.

© 2024 MIM Research Group. All rights reserved.

## 1. Introduction

Gears are the major element in various mechanical systems used for power transmission. The transformation of power and motion using gears is better than other transmission systems such as belt, rope and chain drive due to less slippage between two mating gears [1]. The polymer gears have gained significant attention due to unique set of inherent properties such as light weight, low noise, and self-lubrication, ability to resist shock and impact load, ease of manufacturing [2]. These properties have driven polymer gears adoption for metal gears replacement in industrial applications such as automotive, aerospace, textile, robotics, industrial machinery, and consumer products.eg. Lightweight gearboxes [3]. The load, temperature, surface roughness, wear and rotational speed are the major analyzing parameters to investigate the performance of polymer gears [4][5]. The teeth of polymer gears experience fatigue loads while operating conditions. It produces heat internally and, on the surface, due to contact stress when the gear pairs are in motion under loading conditions [6].

Several studies have indicated that polymer composite gears showed improved results than pristine polymer gears in terms of overall performance improvement [7-9]. In recent

\*Corresponding author: [pnjadhav@git-india.edu.in](mailto:pnjadhav@git-india.edu.in)

<sup>a</sup>orcid.org/0000-0003-1539-9520; <sup>b</sup>orcid.org/0000-0002-6646-1905; <sup>c</sup>orcid.org/0000-0003-2324-2304;

<sup>d</sup>orcid.org/0000-0002-3577-2727

DOI: <http://dx.doi.org/10.17515/resm2024.217na0324rs>

Res. Eng. Struct. Mat. Vol. 11 Iss. 1 (2025) 273-285

years, there has been extensive research conducted on polymer composite gears reinforced with glass and carbon fibers in polymer matrix materials. These studies have consistently demonstrated enhanced performance of wear resistance, durability under specific loads, and other relevant properties and the results showed improvements in overall performance of gears [10, 11]. Thermoplastic materials, such as nylon, acetal, polycarbonate etc. find extensive use in industrial applications, including the manufacturing of gears and seals etc. [12]. The study of gears made of these thermoplastics and its composites were widely explored [13, 14]. The graphene reinforcement in nylon and acetal polymer composites gears exhibited superior performance in terms of wear resistance [7, 15]. The investigation of gears made with incorporation of different fillers such as multilayer graphene nanoplatelets, clay, graphite in polyamide (PA6) matrix, showed enhancement in mechanical, thermal and tribological properties [16-18]. The gears manufactured by high performance polymer composites i.e. poly ether ketone (PEEK) and carbon fiber exhibits enhanced results for load capabilities and wear performance [19]. The relative performance of PEEK and steel gears are also investigated and it showed superior performance [20, 21]. PAEK gears have been studied under dry, greased, and lubricated conditions, demonstrated superior performance at elevated temperatures and lubricated conditions [22]. MWCNTs are considered the most suitable nanofiller for polymer composites due to their exceptional properties. These properties include high mechanical strength, excellent electrical conductivity, and superior thermal stability, which significantly enhance the performance and durability of the polymer composites in which they are incorporated. Additionally, MWCNTs exhibit a large surface area and strong interfacial interaction with polymer matrices, leading to improved load transfer and dispersion within the composite material. This makes MWCNTs an ideal choice for applications requiring enhanced material properties [23-25]. The behavior of commodity and engineering polymer gears considering different performance parameters are widely explored to achieve better power transmission.

This study specifically focuses on the performance of gears manufactured using high temperature polymer such as poly aryl ether ketone (PAEK) and PAEK based nanocomposite reinforced with multiwalled carbon nanotube (MWCNT) and functionalized MWCNT. The investigation encompasses the examination of wear and thermal properties of these gears under different loading conditions.

## **2. Materials and Methods**

### **2.1 Materials**

The semi-crystalline granular polymer material PAEK 1200G, utilized for the injection molding process, was sourced from Gharda Chemicals Ltd., Panoli, Gujarat, India. This PAEK material exhibits a density of 1.3 g/cc, a melting temperature of 152°C, and a glass transition temperature of 372°C. The nanomaterials employed in this study include MWCNT and amine-functionalized MWCNT were procured from Adnano Technologies Pvt. Ltd., Shimoga, Karnataka, India. These powdered nanomaterials possess a surface area ranging from 110 to 350nm, with outer diameters falling within the range of 10-30nm, inner diameters between 5-10nm, 99% purity level and a length of 10 μm.

### **2.2 Preparation of Composites**

The uniform mixtures at concentrations of 0.5% weight of MWCNT and functionalized MWCNT nanofillers were carefully mixed and dispersed in PAEK matrix using a high-speed mechanical mixer for duration of 15 minutes to achieve a homogeneous mixture. As an additional measure, Tris Nonyl phenyl phosphite (TNPP) at a concentration of 0.02% by weight was incorporated as an antioxidant.

Table 1. Temperatures at different zones

| Zones       | Zone 1 | Zone 2 | Zone 3 | Zone 4 |
|-------------|--------|--------|--------|--------|
| Temperature | 380°C  | 385°C  | 390°C  | 400°C  |

The compounding process was carried out by utilizing a twin-screw extruder, featuring a screw diameter of 26mm and a length to diameter ratio of 40:1. The temperatures at different zones within the twin-screw extruder are shown in table 1. The screw speed was maintained at 300 rpm. Following compounding, the resulting strands were prepared through extrusion and subsequently chopped by a cutter to produce samples of composites in granular form [26].

### 2.3 Manufacturing of Gears

The gears are manufactured using injection moulding machines with PAEK based polymer composite materials. Prior to the injection moulding process, the materials underwent a preheating process at a temperature of 220°C for 3 hours. This preheating served the purpose of eliminating moisture content and drying of the mixture. The gears are manufactured by injection molding process at A.K. Engineers, Mumbai, using an injection molding machine of 40-tonnage capacity manufactured by R.K. Techniques, Mumbai, India. During the injection molding process, specific parameters were carefully controlled to ensure optimal results. The injection time was set at 22 seconds and holding time of 8 seconds. The temperature settings for different zones in the injection moulding machine were adjusted as follows: 380°C for temperature zone 1, 385°C for zone 2, 390°C for zone 3, and 400°C for zone 4. These temperature zones spanned from the feed zone to the nozzle, playing a critical role in the moulding process. In addition to the machine temperature settings, the mould temperature was maintained at 220°C. This temperature control was essential for ensuring the proper moulding of the materials and achieving the desired properties in the final product of gears. The controlled operating temperatures of extruder and mould contributed to the successful fabrication of the injection-moulded gears. The detailed information about materials, parameters and manufacturing method of test gears are given in table 2 and manufactured gears are shown in fig. 1.

Table 2. Detail information of test gears

| Parameters                       | Specifications  |
|----------------------------------|---|
| 1. Materials                     | 1. PAEK<br>2. PAEK+ 0.5 weight % MWCNT<br>3. PAEK + 0.5 weight % Amine functionalized MWCNT |
| 2. Module                        | 2.5   |
| 3. Pitch circle diameter (mm)    | 60  |
| 4. Number of teeth (No's)        | 22  |
| 5. Addendum circle diameter (mm) | 60  |
| 6. Dedendum circle diameter (mm) | 52  |
| 7. Pressure angle (Degree)       | 20°   |
| 8. Face width (mm)               | 20  |
| 9. Manufacturing process         | Injection moulding  |

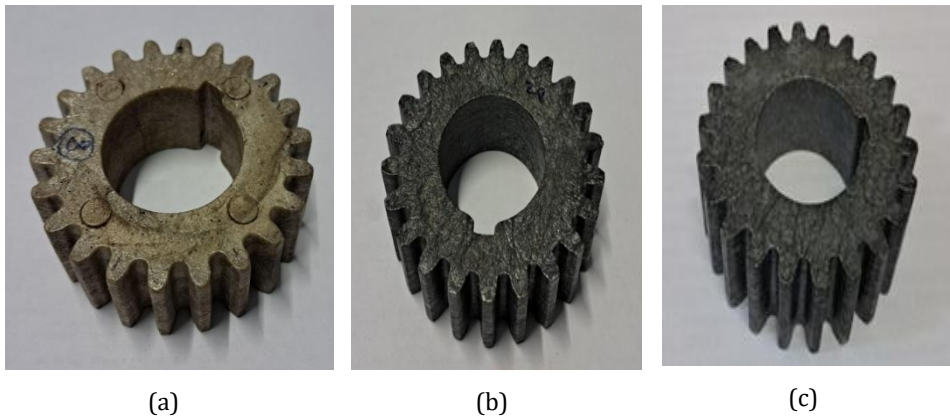


Fig. 1 Gear images (a) PAEK gear, (b) PAEK+ MWCNT gear, (c) PAEK +Amine functionalized MWCNT gear

### 2.4 Testing of the Gears

The gears were tested using a gear test rig shown in fig. 2 Each gear underwent testing for a duration of 1 hour and 40 minutes including different speeds (1000 rpm and 1500 rpm) and at different torque conditions (0 Nm, 6 Nm, 8 Nm and 10 Nm). The test gears are run for  $1 \times 10^5$  and  $1.5 \times 10^5$  revolutions for comparative analysis of these gears. The speed of motor was controlled by using variable frequency drive (VFD). The surface temperature of gears was monitored using an infrared thermometer throughout the testing process. Additionally, the weight of each gear was measured using a digital weighing machine before and after the running operations.

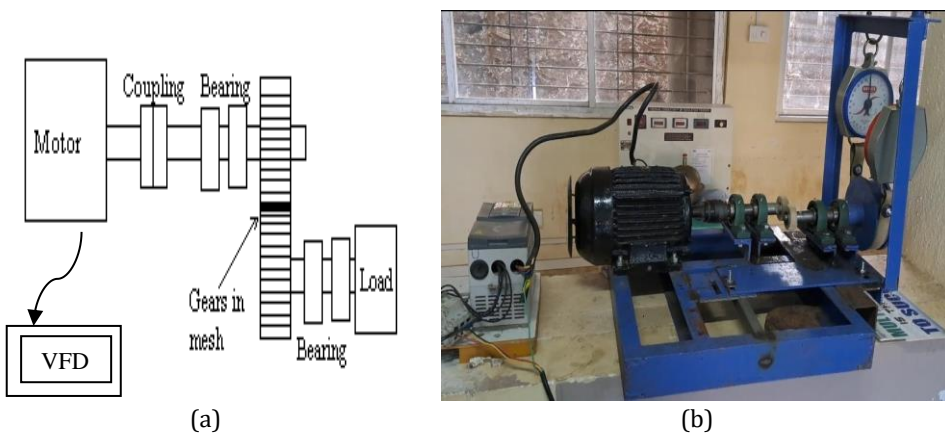


Fig. 2 Gear test rig (a) Schematic diagram of gear test rig, (b) Photograph of gear test rig

To assess surface conditions of the major affected area such as the face surface of gear teeth, a surface roughness tester (Mitutoyo, resolution -  $0.01 \mu\text{m}$ ) was used for both prior to and following the operation. By comparing the pre and post operation gear surface temperature, weights and roughness, the assessment provides insights into factors such as thermal behavior, wear rate and roughness that may have occurred during the testing period. Specific wear rate ( $W_s$ ) of polymer gears is calculated using the following equation.

$$W_s = W_v / (2zmbN_T) \quad (1)$$

Where,  $W_v$  is the wear volume ( $\text{mm}^3$ ),  $z$  is the number of gear teeth,  $m$  is the module (mm),  $b$  is the tooth face width (mm),  $N_T$  is the number of revolutions.

### 3. Results and Discussion

The performance of gears is significantly influenced by the surface temperature, wear and roughness as the mechanical properties of polymer materials are closely tied to it. All these three types of gears made of three different materials exhibit distinct behaviors attributed to their physical and chemical properties. These gears are tested for 0 Nm, 6Nm, 8 Nm and 10Nm torques and rotational speeds of 1000 rpm and 1500 rpm. These gears are operated for  $1 \times 10^5$  and  $1.5 \times 10^5$  revolutions.

#### 3.1 Surface Temperature of Polymer Gears

The surface temperature of gears produced with PAEK, PAEK reinforced with MWCNT nanofiller and PAEK reinforced with amine functionalized MWCNT nanofiller materials is shown in fig. 3, 4 and 5. Figures indicated that, temperature of gear surface increases with rise in torques. Additionally, it reveals that the temperature of the gear surface rises with an increase in rotational speeds. This pattern was observed in all three types of gears. The increase in gear surface temperature was comparatively low in amine-functionalized MWCNT-reinforced PAEK composite gears than PAEK and PAEK reinforced with MWCNT composite gears, under the same operating conditions, including torques and rotational speeds. Furthermore, it was noted that the surface temperature of the driver gear was consistently higher than that of the driven gear for all three types of gears at these different torques and speeds.

The elevation in temperature weakens the hydrogen bonds between polymer chains, leading to the degradation of mechanical properties. While in operation, the interaction of gears during meshing induces heat at both the tooth surface and within the bulk material. This heat generation stems from several factors, including friction, hysteresis, fatigue load, and higher contact stresses resulting from the sliding and rolling actions of the gears [7, 27].

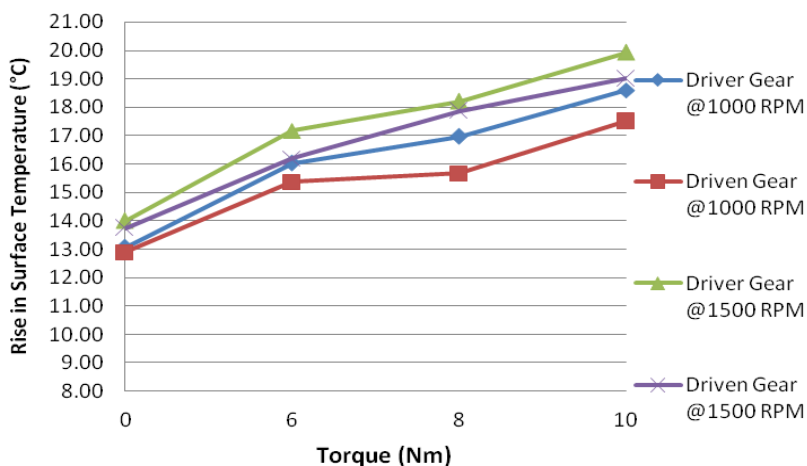


Fig. 3. Surface temperature of PAEK driver and driven gears at 1000 rpm and 1500 rpm

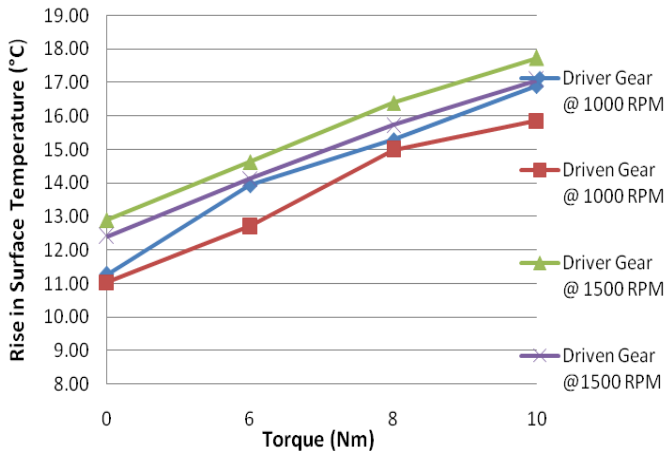


Fig. 4. Surface temperature of PAEK reinforced with MWCNT driver and driven gears at 1000 rpm and 1500 rpm

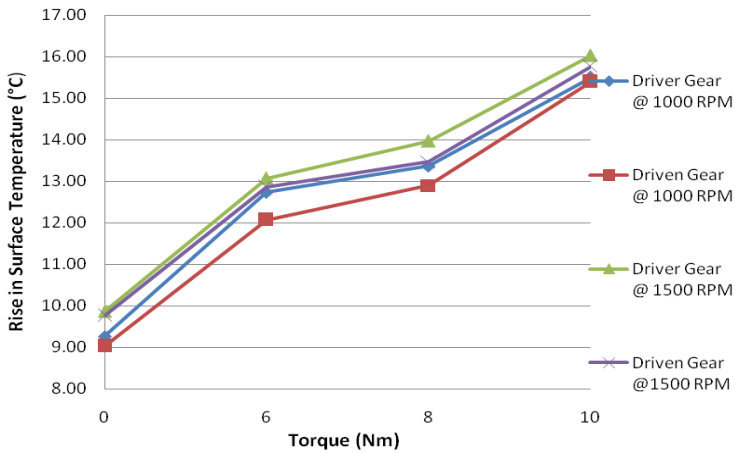


Fig. 5. Surface temperature of PAEK reinforced with an amine functionalized MWCNT driver and driven gears at 1000 rpm and 1500 rpm

The substantial increase in rotational speed leads to a considerable rise in loading frequency due to repetition of contacts and concurrently rises the surface temperature of gears. The surface temperature increases with higher surface roughness and contact area [28][29]. Hence, at low torque levels and at 1000 rpm rotational speed, there was minimal frictional heating of gear teeth, while at high torque levels and 1500 rpm speed, there was an increase in frictional heating resulting in a rise in temperature of gears teeth at high torque and at higher rotational speed. This observed phenomenon is a result of the proportional increase in heat generation driven by the factors such as slightly higher friction, high contact stresses, higher fatigue load and hysteresis loss, coinciding with an increase in both the rotational speeds and torques of the gears [13].

The heat generation in reinforced composite gears than unreinforced gears [13]. The enhancement in thermal properties is attributed to the reinforcing effect of MWCNT in the polymer composites, owing to their tensile modulus, stiffness, and thermal properties [30][31]. The improved mechanical performance of PAEK composites was achieved by



incorporating functionalized MWCNTs compared to PAEK composites with non-functionalized MWCNTs. This enhancement is attributed to the improved interfacial interaction and better heat dissipation resulting from the surface treatment of MWCNTs [32]. The functionalized MWCNTs enhance thermal conductivity and mechanical stability, reducing the temperature rise in polymer composites under operational conditions [33]. Similarly, those amine-functionalized MWCNTs significantly improve the dispersion within the polymer matrix, leading to better load transfer and thermal management [34]. Hence, gears made of PAEK materials incorporated with amine-functionalized MWCNTs demonstrated a lesser temperature rise in comparison to gears made from standard PAEK and PAEK reinforced with MWCNTs, across varying torque levels.

The driver gear drives the driven gear during running the meshing gears. Therefore, there are higher active and reactive forces exerted on the driver gears compared to driven gears when gears are in motion. As a result, the temperature rise in driver gears is comparatively higher than the driven gear.

### 3.2 Wear Performance

Fig. 6 and 7 illustrates the wear performance of gears manufactured from PAEK, PAEK reinforced with MWCNT nanofiller and PAEK reinforced with amine-functionalized MWCNT nanofiller materials at 1000rpm and 1500 rpm respectively. Figures indicated that the rise in specific wear rate of gears with rise in torques and rotational speeds of gears. This trend was observed in all three varieties of gears. Notably, amine-functionalized MWCNT gears exhibit a lower specific wear rate compared to PAEK and MWCNT-reinforced PAEK gears under identical operating conditions, including torques and rotational speeds. Moreover, it was observed that, across various torques and speeds, the specific wear rate of the driver gear remained higher than that of the driven gear for all three gear types.

The wear rate of these meshed gears was slightly higher at higher rotational speeds compared to lower rotational speeds, primarily due to increased friction resulting from repeated contact between the surfaces within a minimal time period. Additionally, a higher wear rate was observed at higher torque levels, due to the elevated stresses experienced in comparison to lower torque conditions. Hence, the higher wear rate is observed for higher rotational speed i.e. 1500 rpm and higher torque such as 10 Nm.

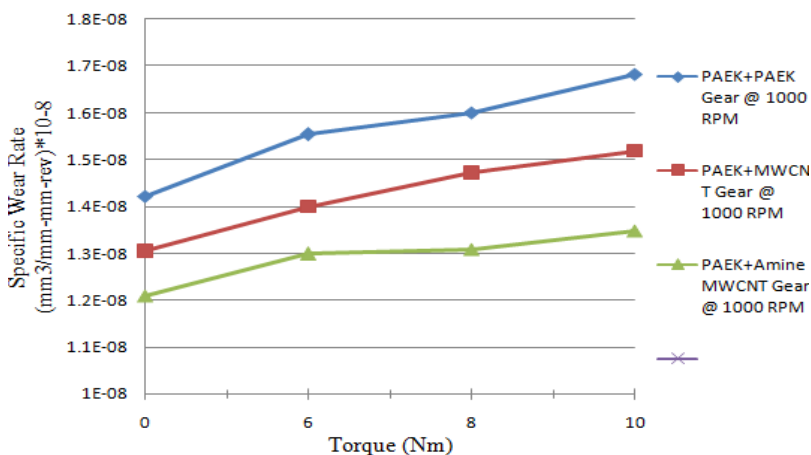


Fig. 6. Wear performance of PAEK and its composites with MWCNT and amine-functionalized MWCNT gears at 1000 rpm

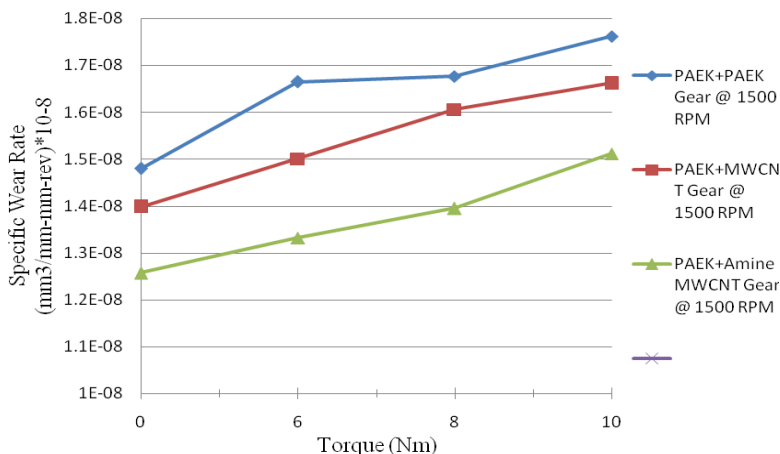


Fig. 7. Wear performance of PAEK and its composites with MWCNT and amine-functionalized MWCNT gears at 1500 rpm

The aspect ratio, smaller in size and excellent mechanical properties of MWCNTs improves the mechanical properties such as stiffness, hardness, rigidity, tensile modulus, fatigue properties and the strengths of MWCNTs reinforced polymer composites [35, 36]. But, functionalized MWCNT improves the cross-link density, dispersion and interfacial interaction by increasing dispersibility and surface polarity resulting in the enhancement in the strength of composites, fatigue properties and reduces asperity deformation than MWCNT reinforced composites [6, 37]. Hence, the mechanical strengths of amine functionalized MWCNT incorporated PAEK composites are higher than MWCNT reinforced PAEK composites and pristine PAEK polymer [26]. Therefore, the wear performance of gears made of PAEK/amine functionalized MWCNT composites is superior to gears made of PAEK and PAEK/MWCNT composites.

During meshing, the gear tooth slides, and the direction reverses at the pitch point. The driver gear rotates towards the pitch point, while the driven gear consistently slides away from the pitch point. The relative direction of sliding and rolling actions plays a significant role for wear of gears [38][39]. Therefore, the driver gear experiences a higher rate of wear compared to the driven gear, caused by the more active and reactive forces experienced by the driver gear as compared to the driven gear. Wear was noticed on the gear tooth faces rather than the flanks, primarily due to the larger contacting surface area while gears are in motion. The melting temperature and glass transition temperature of PAEK and PAEK based composites is high as these materials are high temperature and high performance in category [40]. Therefore, these studied materials do not undergo softening at these temperature rises. Hence, there was no failure of teeth or no more wear rate of these gears due to the excellent mechanical and thermal properties of all these three types of gear materials.

### 3.3 Surface Roughness of Gears

Fig. 8 and 9 depicts the surface roughness of gears made from PAEK, PAEK reinforced with MWCNT nanofiller, and PAEK reinforced with amine-functionalized MWCNT nanofiller materials at 1000 rpm and 1500 rpm respectively. These figures reveal an increase in surface roughness (Ra) value with the elevation of torques and rotational speeds of the gears. This trend was consistent across all three gear types. This phenomenon can be attributed to the intensified friction, contact stresses, and sliding actions experienced by

the gear teeth under higher torque and rotational speed conditions [41]. Notably, amine-functionalized MWCNT gears exhibit a lower surface roughness value compared to PAEK and MWCNT-reinforced PAEK gears under identical operating conditions, including torques and rotational speeds. Furthermore, it was observed that, across various torques and speeds, the surface roughness value of the driver gear was consistently higher than that of the driven gear for all three gear types. The excellent properties such as hardness, lower asperity deformation, improved adhesion and reduced friction of the MWCNT and amine functionalized MWCNT incorporated PAEK composites gears exhibited lower roughness (Ra value) than PAEK gears after the running operation [42].

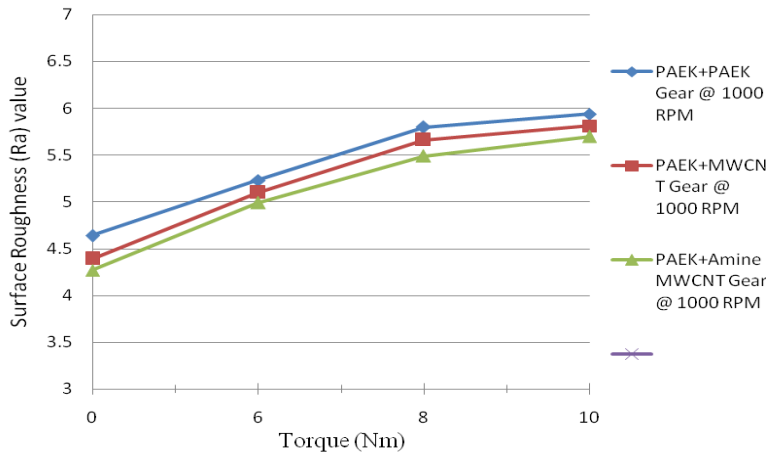


Fig. 8. Surface roughness of PAEK and its composites with MWCNT and amine-functionalized MWCNT gears at 1000 rpm

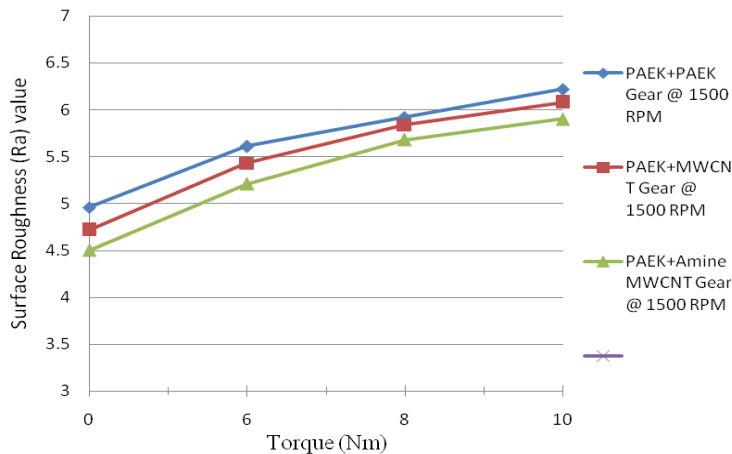


Fig. 9. Surface roughness of PAEK and its composites with MWCNT and amine-functionalized MWCNT gears at 1500 rpm

In the driving gear, the frictional force consistently acts away from the pitch point, whereas in the driven gear, it acts towards the pitch point. As a result, the frictional forces in the driving gear tend to separate the surfaces, leading to increased roughness on the teeth surface of the driver gear [6]. The surface roughness of gears was influenced by factors

such as material composition, operational conditions, and the presence of additives like MWCNTs. Gears incorporating amine-functionalized MWCNTs demonstrate reduced

#### 4. Conclusions

The investigation conducted on running meshed gears made of PAEK, MWCNT reinforced PAEK and amine-functionalized MWCNT reinforced PAEK materials under various operating conditions has led to several key conclusions are as follows:

- With increasing speed and torque, there is a concurrent increase in the surface temperature and wear rate of all these three types of gears. Notably, the contribution of torque to the rise in surface temperature is proportionally higher than that of rotational speed.
- Gears composed of amine-functionalized MWCNT reinforced PAEK materials exhibit slightly superior performance compared to those made from PAEK and MWCNT reinforced PAEK. This advantage can be attributed to the comparatively higher mechanical and thermal properties of amine-functionalized MWCNTs, enhancing the overall durability and reliability of these gears.
- The surface temperature and wear rate of driver gears are slightly higher than those of the driven gears. This discrepancy can be attributed to the differential distribution of frictional forces and contact stresses experienced by the gears during operation.
- No instances of tooth failure or abnormal wear rates were observed in any of the gears tested. This can be attributed to the high inherent strengths of PAEK and MWCNTs nanofiller, ensuring the structural integrity and longevity of the gears under the specified operating conditions.
- Post-operation analysis revealed that the surface roughness of gears composed of amine-functionalized MWCNT reinforced PAEK materials was lower than that of gears made from PAEK and MWCNT reinforced PAEK. This indicates a good surface finish and potentially improved performance in terms of friction and wear characteristics. These gears can be useful at the high temperature and loading working conditions.
- The investigation highlights the significant influence of operating conditions and material composition on the performance of meshed gears. The superior properties of amine-functionalized MWCNT reinforced PAEK materials suggest their potential for applications requiring high durability and reliability in dynamic mechanical systems.

#### References

- [1] Singh PK, Siddhartha, Singh AK. An investigation on the thermal and wear behavior of polymer-based spur gears. *Tribol Int.* 2018 Feb 1; 118:264–72. <https://doi.org/10.1016/j.triboint.2017.10.007>
- [2] Mao K, Greenwood D, Ramakrishnan R, Goodship V, Shroufi C, Chetwynd D, et al. The wear resistance improvement of fibre reinforced polymer composite gears. *Wear.* 2019 Apr 30; 426–427:1033–9. <https://doi.org/10.1016/j.wear.2018.12.043>
- [3] Soudmand BH, Shelesh-Nezhad K. Study on the gear performance of polymer-clay nanocomposites by applying step and constant loading schemes and image analysis. *Wear.* 2020 Oct; 458–459:203412. <https://doi.org/10.1016/j.wear.2020.203412>
- [4] Zorko D, Demšar I, Tavčar J. An investigation on the potential of bio-based polymers for use in polymer gear transmissions. *Polym Test.* 2021 Jan; 93:106994. <https://doi.org/10.1016/j.polymertesting.2020.106994>

- [5] Targett J, Nightingale JE. Paper 23: Thermoplastic Gears. Proceedings of the Institution of Mechanical Engineers, Conference Proceedings. 1969 Sep 17; 184(15):184–226. [https://doi.org/10.1243/PIME\\_CONF\\_1969\\_184\\_458\\_02](https://doi.org/10.1243/PIME_CONF_1969_184_458_02)
- [6] Gurunathan C, Kirupasankar S, Gnanamoorthy R. Wear characteristics of polyamide nanocomposite spur gears. In: Proceedings of the Institution of Mechanical Engineers, Part J: Journal of Engineering Tribology. 2011. p. 299–306. DOI: [10.1177/1350650111401282](https://doi.org/10.1177/1350650111401282)
- [7] Rajamani G, Paulraj J, Krishnan K. Analysis of wear behaviour of graphene oxide – Polyamide gears for engineering applications. Surface Review and Letters. 2017 Nov 9; 24(Supp02):1850018. DOI: [10.1142/S0218625X1850018X](https://doi.org/10.1142/S0218625X1850018X)
- [8] Mohsenzadeh R, Majidi H, Soltanzadeh M, Shelesh-Nezhad K. Wear and failure of polyoxymethylene/calcium carbonate nanocomposite gears. Proceedings of the Institution of Mechanical Engineers, Part J: Journal of Engineering Tribology. 2020 Jun 31; 234(6):811–20. DOI: [10.1177/1350650119867530](https://doi.org/10.1177/1350650119867530)
- [9] Kirupasankar S, Gurunathan C, Gnanamoorthy R. Transmission efficiency of polyamide nanocomposite spur gears. Mater Des. 2012 Aug; 39:338–43. <http://dx.doi.org/10.1016/j.matdes.2012.02.045>
- [10] Kurokawa M, Uchiyama Y, Iwai T, Nagai S. Performance of plastic gear made of carbon fiber reinforced polyamide 12. Wear. 2003; 254(5–6):468–73. doi:[10.1016/S0043-1648\(03\)00020-6](https://doi.org/10.1016/S0043-1648(03)00020-6)
- [11] Tavcar J, Grkman G, Duhovnik J. Accelerated lifetime testing of reinforced polymer gears. Journal of Advanced Mechanical Design, Systems and Manufacturing. 2018; 12(1). DOI: [10.1299/jamdsm.2018jamdsm0006](https://doi.org/10.1299/jamdsm.2018jamdsm0006)
- [12] Mao K. A new approach for polymer composite gear design. Wear. 2007 Feb 4; 262(3–4):432–41. <https://doi.org/10.1016/j.wear.2006.06.005>
- [13] Senthilvelan S, Gnanamoorthy R. Effect of rotational speed on the performance of unreinforced and glass fiber reinforced Nylon 6 spur gears. Mater Des. 2007; 28(3):765–72. <https://doi.org/10.1016/j.matdes.2005.12.002>
- [14] Letzelter E, Guingand M, Vaujany JP De, Schlosser P. A new experimental approach for measuring thermal behaviour in the case of nylon 6/6 cylindrical gears. Polym Test. 2010 Dec; 29(8):1041–51. <https://doi.org/10.1016/j.polymertesting.2010.09.002>
- [15] Ramanjaneyulu S, Suman KNS, Phani Kumar S, Suresh Babu V, Professor A. Design and Development of Graphene reinforced Acetal copolymer plastic gears and its performance evaluation-review under responsibility of the Committee Members of International Conference on Advancements in Aeromechanical Materials for Manufacturing (ICAAMM-2016) [Internet]. Vol. 4. 2017. Available from: [www.sciencedirect.com/www.materialstoday.com/proceedings](http://www.sciencedirect.com/www.materialstoday.com/proceedings)
- [16] Afifi EM, Elshalakny AB, Osman TA, Kamel BM, Zian H. Investigation of gear performance of MLNGPs as an additive on polyamide 6 spur gear. Fullerenes, Nanotubes and Carbon Nanostructures. 2018 Jun 3; 26(6):351–9. <https://doi.org/10.1080/1536383X.2018.143841>
- [17] Srinath G, Gnanamoorthy R. Sliding wear performance of polyamide 6–clay nanocomposites in water. Compos Sci Technol. 2007 Mar; 67(3–4):399–405. <https://doi.org/10.1016/j.compscitech.2006.09.00>
- [18] Unal H, Mimaroglu A. Friction and wear performance of polyamide 6 and graphite and wax polyamide 6 composites under dry sliding conditions. Wear. 2012 Jun 15; 289:132–7. <http://dx.doi.org/10.1016/j.wear.2012.04.004>
- [19] Kurokawa M, Uchiyama Y, Nagai S. Performance of plastic gear made of carbon fiber reinforced poly-ether-ether-ketone: Part 2 [Internet]. Vol. 33, Tribology International. 2000. Available from: [www.elsevier.com/locate/triboint](http://www.elsevier.com/locate/triboint)
- [20] Yu G, Liu H, Mao K, Zhu C, Wei P, Lu Z. An Experimental Investigation on the Wear of Lubricated Steel Against PEEK Gears. J Tribol. 2020 Apr 1; 142(4).

- [21] Wood AK, Williams V, Weidig R. The Relative Performance of Spur Gears Manufactured from Steel and PEEK [Internet]. 2010. Available from: [www.geartechnology.com58](http://www.geartechnology.com58)
- [22] Weidig R, Rösler J. Performance of HT-Thermoplastic Spur Gears Made Out of Polyaryletherketone (PAEK). In 2001. <https://doi.org/10.4271/2001-01-1142>
- [23] Demircan Ö, Sufyan S, Basem AM. Tensile and charpy impact properties of CNTs integrated PET/ Glass Fiber thermoplastic composites with commingled yarn. Research on Engineering Structures and Materials. 2022; <http://dx.doi.org/10.17515/resm2022.442ma0606>
- [24] Demircan Ö, Uzunoglu FB, Ansaroudi NR. Influence of multi-walled carbon nanotubes on tensile and flexural properties of polyamide 66/short glass fiber composites. Research on Engineering Structures and Materials. 2022. <http://dx.doi.org/10.17515/resm2022.443ma0607>
- [25] Demircan Ö. Compression after impact properties of glass fiber/epoxy/MWCNT composites. Research on Engineering Structures and Materials. 2019. <http://dx.doi.org/10.17515/resm2019.137ma0702>
- [26] Jadhav PN, Sahai RSN, Biswas D, Samui AB. Comparative Study of Mechanical Properties of Multiwall Carbon Nanotubes and Functionalized Multiwall Carbon Nanotubes/Poly Aryl Ether Ketone Nanocomposites. Iranian Journal of Materials Science and Engineering. 2023 Dec 1; 20(4). DOI: 10.22068/ijmse.3446
- [27] Kalin M, Kupec A. The dominant effect of temperature on the fatigue behaviour of polymer gears. Wear. 2017 Apr; 376–377:1339–46. <https://doi.org/10.1016/j.wear.2017.02.003>
- [28] Dong HL, Hu JB, Li XY. Temperature Analysis of Involute Gear Based on Mixed Elastohydrodynamic Lubrication Theory Considering Tribo-Dynamic Behaviors. J Tribol. 2014 Apr 1; 136(2). <https://doi.org/10.1115/1.4026347>
- [29] Britton RD, Elcoate CD, Alanou MP, Evans HP, Snidle RW. Effect of Surface Finish on Gear Tooth Friction. J Tribol. 2000 Jan 1; 122(1):354–60. <https://doi.org/10.1115/1.555367>
- [30] Chouit F, Guellati O, Boukhezar S, Harat A, Guerioune M, Badi N. Synthesis and characterization of HDPE/N-MWNT nanocomposite films. Nanoscale Res Lett. 2014; 9(1):1–6. <http://www.nanoscalereslett.com/content/9/1/288>
- [31] Spitalsky Z, Tasis D, Papagelis K, Galiotis C. Carbon nanotube–polymer composites: Chemistry, processing, mechanical and electrical properties. Prog Polym Sci. 2010 Mar; 35(3):357–401. <https://doi.org/10.1016/j.progpolymsci.2009.09.003>
- [32] Ardjmand M, Omidi M, Choolaei M. The effects of functionalized multi-walled carbon nanotube on mechanical properties of multi-walled carbon nanotube/epoxy composites. Oriental Journal of Chemistry. 2015; 31(4):2291–301. <http://dx.doi.org/10.13005/ojc/310457>
- [33] Kim K, Yang J, Kim J. The Study of Multi-walled Carbon Nanotube Surface and Matrix Structure for Thermal Conductive Composite Material. Polymer Korea. 2018 Sep 30; 42(5):776–83. DOI: 10.7317/pk.2018.42.5.776
- [34] Ma PC, Siddiqui NA, Marom G, Kim JK. Dispersion and functionalization of carbon nanotubes for polymer-based nanocomposites: A review. Compos Part A Appl Sci Manuf. 2010 Oct; 41(10):1345–67. <https://doi.org/10.1016/j.compositesa.2010.07.003>
- [35] Yetgin SH. Effect of multi walled carbon nanotube on mechanical, thermal and rheological properties of polypropylene. Journal of Materials Research and Technology. 2019 Sep; 8(5):4725–35. <https://doi.org/10.1016/j.wear.2018.12.043>
- [36] Hosur M V., Rahman T, Brundidge-Young S, Jeelani S. Mechanical and Thermal Properties of Amine Functionalized Multi-walled Carbon Nanotubes Epoxy-Based Nanocomposite. Compos Interfaces. 2010 Jan 2; 17(2–3):197–215. <http://dx.doi.org/10.1163/092764410X490608>

- [37] Breeds AR, Kukureka SN, Mao K, Walton D, Hooke CJ. Wear behaviour of acetal gear pairs. *Wear*. 1993 Jun; 166(1):85–91. [https://doi.org/10.1016/0043-1648\(93\)90282-Q](https://doi.org/10.1016/0043-1648(93)90282-Q)
- [38] Wright NA, Kukureka SN. Wear testing and measurement techniques for polymer composite gears. Vol. 251, *Wear*. 2001. [DOI:10.1016/S0043-1648\(01\)00793-1](https://doi.org/10.1016/S0043-1648(01)00793-1)
- [39] Remanan M, Rao RS, Bhowmik S, Varshney L, Abraham M, Jayanarayanan K. Hybrid nanocomposites based on poly aryl ether ketone, boron carbide and multi walled carbon nanotubes: Evaluation of tensile, dynamic mechanical and thermal degradation properties. *E-Polymers*. 2016 Nov 1; 16(6):493–503. [DOI10.1515/epoly-2016-0162](https://doi.org/10.1515/epoly-2016-0162)
- [40] Sazali N, Ibrahim H, Jamaludin AS, Mohamed MA, Salleh WNW, Abidin MNZ. Degradation and stability of polymer: A mini review. *IOP Conf Ser Mater Sci Eng*. 2020 Apr 1; 788(1):012048. [10.1088/1757-899X/788/1/012048](https://doi.org/10.1088/1757-899X/788/1/012048)
- [41] Lee GW, Park M, Kim J, Lee JI, Yoon HG. Enhanced thermal conductivity of polymer composites filled with hybrid filler. *Compos Part A Appl Sci Manuf*. 2006 May; 37(5):727–34. [10.1016/j.compositesa.2005.07.006](https://doi.org/10.1016/j.compositesa.2005.07.006)
- [42] Her SC, Lai CY. Effect of Functionalized MWCNTs on Mechanical Properties of Polymer Matrices. *Asian Journal of Chemistry*. 2014; 26(17):5709–11. <https://doi.org/10.14233/ajchem.2014.18189>

Blank Page



Research Article

## Research on nonlinear corrosion law of epoxy coating on steel bridges based on image processing

Yi Zhang<sup>a</sup>, Tian Su<sup>\*,b</sup>

Department of Engineering and Management, International College, Krirk University, Bangkok, Thailand

### Article Info

### Abstract

#### Article history:

Received 25 Mar 2024  
Accepted 05 June 2024

#### Keywords:

Image processing;  
Steel bridge coating;  
Non linearity;  
Corrosion law

This paper adopted the accelerated corrosion test method to study the corrosion law of epoxy coatings on steel bridges. An image processing algorithm based on MATLAB was used to perform grayscale conversion, normalized histogram drawing, and binary image processing on the surface morphology images of coated specimens. Four coated specimens were prepared and placed in the cyclic accelerated corrosion environment. The coated specimens were subjected to the accelerated corrosion test for 90 days, observed changes in coating thickness and corrosion area rate and analyzing the corrosion laws of epoxy coatings in different corrosion environments. Using image processing technology to process images of coating corrosion and analyze the corrosion mechanism of coatings. The research results indicate that the corrosion rate of epoxy coatings exhibits a non-linear corrosion law of slow corrosion in the early stage and accelerated corrosion in the middle and later stages. The corrosion rate of epoxy coatings in saltwater corrosive environments is faster than in freshwater corrosive environments. Based on the corrosion laws and mechanisms of coatings, a nonlinear corrosion function model for epoxy coatings on steel bridges under different accelerated corrosion environment was established, which has a high correlation with experimental data.

© 2024 MIM Research Group. All rights reserved.

## 1. Introduction

Corrosion is a phenomenon in which metals undergo chemical or electrochemical reactions with the surrounding environment, causing significant economic losses and social harm to various industries [1-2]. Steel exposed to the atmosphere is prone to chemical reactions caused by the combined effects of environmental factors such as oxygen and rainwater (acid rain), leading to the formation of rust [3-5]. If severe corrosion occurs in key parts of the steel bridge, it may pose a threat to the structural bearing capacity of the steel bridge. To prevent the corrosion of steel by air and water, anti-corrosion coating technology has emerged as the most commonly used means to slow down the corrosion rate of steel bridges. The principle of most coatings for corrosion prevention is mainly physical corrosion prevention, which is achieved by coating the steel surface to avoid direct contact between air and water on the steel [6-8]. At present, the most widely used anti-corrosion method for steel bridges is to apply coatings on the surface of the steel bridge. However, during the service of steel bridges, the coating will also undergo corrosion and aging due to environmental factors such as oxygen, rainwater, and ultraviolet radiation. As the corrosion intensifies, the protective effect of the coating on the steel bridge becomes increasingly worse. Therefore, in order to effectively control the corrosion of steel bridges and extend their service life, the corrosion law of steel bridge coatings has become a topic worthy of in-depth research.

\*Corresponding author: [sutiancivil@foxmail.com](mailto:sutiancivil@foxmail.com)

<sup>a</sup> orcid.org/0009-0001-6911-8125; <sup>b</sup> orcid.org/0000-0002-1851-2288

DOI: <http://dx.doi.org/10.17515/resm2024.219ma0325rs>

Res. Eng. Struct. Mat. Vol. 11 Iss. 1 (2025) 287-304

During the visual inspection process by coating inspectors, due to the diverse types and complex presentation of coating defects, it is difficult for inspectors to identify the specific types of defects. Moreover, visual errors can also make it difficult to detect subtle defects, such as pitting, micro bubbles, and filamentous cracks, when observed with the naked eye. When measuring defects, traditional measuring instruments are used, and ensuring the measurement accuracy required for corrosion inspection in an on-site environment is difficult. Moreover, there are no effective measuring tools for irregular coating defects, such as those for measuring the area of rust and peeling. With the development of image acquisition technology and image processing technology, the identification and measurement of corrosion defects encountered in the inspection process of coating defects mentioned above will be effectively improved. Image processing technology is a technique that uses image processing algorithms to process and optimize images captured by digital cameras and other tools to achieve the desired results [9]. The main steps of image processing include contrast enhancement, filtering, threshold segmentation, morphological processing, feature extraction and classification [10].

In the field of corrosion, the form and characteristics of corrosion damage can be represented by corrosion images to evaluate the type of corrosion and analyze the degree of corrosion. The corrosion images become an important basis for studying corrosion laws. By establishing appropriate segmentation criteria and recognition models, quantitative description of corrosion areas can be obtained. Corrosion detection problems can be transformed into computer vision problems [11-13]. The traditional image processing method is to use wavelet transform to extract energy and entropy values from each sub image of the corrosion image, and use them to detect the corrosion area in the image [14-15]. Scholars have used the color difference between corroded and non-corroded areas to segment images [16]. Some scholars also believe that as corrosion intensifies, the roughness of the metal surface also changes, which is reflected in the corrosion image [17]. The gray scale values of pixels at the corrosion edge are different from those at other locations, and this distinguishes between corroded and non-corroded areas [18-19]. Furthermore, several scholars have proposed using Non-Destructive Evaluation (NDE) to analyze texture changes on corroded surfaces, combined with Self Organizing Feature Mapping (SOFM) networks for corrosion damage classification, or training Support Vector Machines (SVM) for corrosion classification and detection, based on the color characteristics of the corroded area [20-22].

In the study of coating corrosion laws, the commonly used method is to compare and evaluate the physical, chemical, and electrochemical properties of coatings as they decay with exposure time, in order to establish a model for the variation of coating corrosion laws. Many scholars have conducted research on the corrosion laws of coatings. Kim et al. [23] conducted accelerated exposure tests on five commonly used coating systems for Japanese steel bridges and discussed the corrosion degradation caused by initial coating defects. Hirohata et al. [24] developed an accelerated exposure experimental system to simulate seawater environment. The acceleration coefficient of this experimental system is based on the study of the actual corrosion depth of structural steel components exposed to seawater environment for more than 19 years. Kallias et al. [25] reviewed the mechanisms that lead to coating degradation, with a focus on the main types of coatings. Based on the classification of corrosive environments and response function models, research was conducted to quantify the impact of corrosion, and an atmospheric corrosion model was proposed. Kendig et al. [8] studied the anti-corrosion performance of organic coatings using electrochemical impedance method and established a life prediction model for organic coatings. Lee et al. [26] studied the life of coatings through on-site exposure tests and artificial accelerated aging tests, and established aging models for three coating systems: chlorinated rubber, polyurethane, and inorganic zinc rich. Through regression

analysis, the life prediction formulas for the three coating systems were obtained, and the life of the three coating systems were found to be 20.8 years, 26.6 years, and 17.8 years, respectively. Fredj et al. [27-29] used electrochemical impedance spectroscopy to study the protective performance of organic coatings under the coupling effect of load and corrosive environment. By comparing and analyzing the effects of different loads and stress symbols on the protective performance of organic coatings, the results showed that tensile stress accelerated the degradation of coatings, while compressive stress slowed down the loss of coating performance. The S6-cycle corrosion test was carried out on structural steels for 30, 60, 90, 120 and 150 days and metal coating films for 100, 200 and 300 days [30]. The purpose of this study was to determine correlation between an accelerated cyclic corrosion test (S6-cycle test) specified in Japanese Industrial Standards K5621 and field exposure tests. Merachtsaki et al. [31] studied the corrosion behavior of steel coated with epoxy-(organo) clay nanocomposite films by using salt spray exposures, optical and scanning electron microscopy examination, open circuit potential, and electrochemical impedance measurements. Rachid [32] reviewed the chemical corrosion mechanism and calculation method of the corrosion behavior of epoxy anti-corrosion coatings in 3.5% NaCl solution.

Based on image processing technology, this paper adopted the accelerated corrosion test method to study the corrosion law of epoxy coatings on steel bridges. Four coated specimens were prepared and placed in a cyclic accelerated corrosion environment. The coated specimens were subjected to a 90-day accelerated corrosion test to observe changes in coating thickness and corrosion area rate, and to analyze the corrosion laws of epoxy coatings in different corrosion environments. Image processing technology was used to process images of coating corrosion and analyze the corrosion mechanism of coatings. The research results indicate that the corrosion rate of epoxy coatings exhibits a nonlinear corrosion pattern of slow corrosion in the early stage and accelerated corrosion in the middle and later stages. The corrosion rate of coatings in saline corrosive environments is faster than in freshwater corrosive environments. Based on the corrosion laws and mechanisms of coatings, a nonlinear corrosion function model for epoxy coatings on steel bridges under different accelerated corrosion environments was established, which has a high correlation with experimental data.

## 2. Materials and Experimental Procedure

### 2.1. Materials

The coating systems widely used on steel bridges mainly include epoxy coating systems, acrylic polyurethane coating systems, and fluorocarbon coating systems. The research object of this paper is the epoxy coating system. Details of epoxy coating in this paper are as shown in table 1. Four epoxy coated specimens were prepared with specimen numbers HY01, HY02, HY03, and HY04, respectively. Q235 low-carbon steel with a size of 140mm×70mm×4.5mm was selected as the sample steel plate, which has good thermal conductivity and corrosion resistance.

Table 1. Details of epoxy coating in this paper

| Parameters         | Epoxy Coating               |
|--------------------|-----------------------------|
| Substrate          | Mild steel                  |
| preparation grades | Sa 2.5                      |
| primer             | inorganic zinc rich (50 μm) |
| intermediate coat  | epoxy cloud iron (100μm)    |
| top coat           | epoxy topcoat (50μm)        |
| Color              | gray                        |
| Dry film thickness | (200±40)μm                  |

Prior to abrasion, the Q235 cold-rolled mild steel panels were cleaned with a metal cleaner, used to remove excess oil from the surface of the steel panels, and then dried at room temperature [33]. The surfaces of both the sample and the base plate were pretreated before painting, a polishing machine was used to polish them to the Sa2.5 level, and then the sample was prepared by painting [34]. After each coating, the samples were cured at room temperature for 24 hours, after which the second layer of paint was applied at room temperature. After each coating was brushed and cured, a coating thickness gauge was used for testing to achieve the required coating thickness range. The coating thickness standard was inorganic zinc-rich (50 μm) + epoxy cloud iron (100 μm) + epoxy topcoat (50 μm), with a spraying thickness not exceeding 20% of the standard thickness. The coated specimens are as shown in Fig. 1.

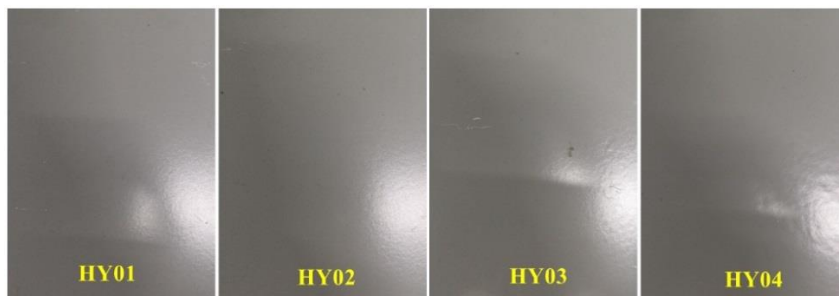


Fig. 1. Preparation of coated specimens

### 2.2. Cyclic Accelerated Corrosion Test

To simulate the service environment of steel bridges more realistically, this paper designs a cyclic accelerated corrosion test involving a water environment immersion test and an accelerated aging test. The cycling program for the accelerated corrosion test was set as follows: 144 h accelerated aging test+72 h water environment immersion test.

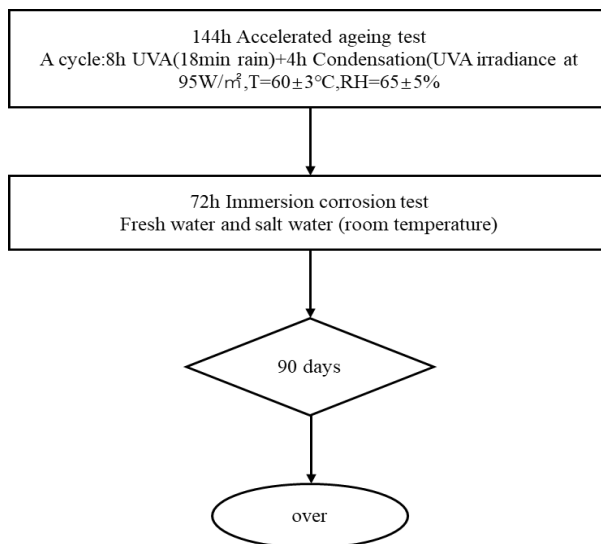


Fig. 2. Cyclic Accelerated Corrosion Test Procedure

The cyclic accelerated corrosion test procedure is shown in Fig. 2. To complete the water environment corrosion test, a water environment corrosion test chamber was constructed, and a total of two water environment corrosion test chambers were prepared: a freshwater environment corrosion test chamber (the water source for the devices inside the chamber was tap water) and a saline environment corrosion test chamber (the water source for the devices inside the chamber was 3.5% sodium chloride solution). The accelerated aging test is completed through an accelerated aging environment test chamber, which can control the intensity, humidity, and temperature of ultraviolet radiation. The cycle program of the accelerated aging test included 8 hours of ultraviolet radiation (including 18 minutes of rain) +4 hours of condensation, where the ultraviolet intensity was  $95 \text{ W/m}^2$ , the temperature was  $60 \pm 3^\circ\text{C}$ , and the relative humidity was  $65 \pm 5\%$ . The duration of the experimental plan in this article was 90 days, and the coating thickness and corrosion area rate of each coated specimen were measured every 10 days. After measurement, the initial coating thickness of all 4 coated specimens was  $200 \mu\text{m}$ , and the initial corrosion area rate was 0%. The test environment for epoxy coated specimens is shown in Table 2.

Table 2. Test environment for coating specimens

| Coating test piece number | Test environment                    |
|---------------------------|-------------------------------------|
| HY01                      | Freshwater + Accelerated aging test |
| HY02                      |                                     |
| HY03                      | Saltwater + Accelerated aging test  |
| HY04                      |                                     |

### 2.3. Coating Performance Testing Methods

A CT-220 coating thickness gauge was used to measure the thickness changes of the coating during the corrosion process. Before measurement, the instrument was calibrated on a standard metal block to confirm that the measurement accuracy met the requirements. Each coating specimen was measured at 5 points, and the arithmetic mean of the 5 measurement values was taken as the coating thickness of the specimen; A camera was used to capture photos of the coating surface, image processing technology was used to process the surface appearance image of the corroded coating, and the change in the rust area rate of the coating was calculated.

## 3. Test Results

### 3.1. Coating Thickness

The transmission of corrosive media such as water and oxygen in coatings conforms to Fick's diffusion law, and when a coating is used to protect the surface of a steel plate, a coating film is formed on the surface of the steel plate. This coating film can block the contact between corrosive media and the steel substrate. Based on this theory, many scientific and technological workers believe that increasing the coating thickness can increase the protective effect of the coating on the steel, thereby extending the service life of the coating. Therefore, coating thickness is one of the important indicators reflecting the corrosion process of coatings.

Fig. 3 and Fig. 4 respectively show the variation of coating thickness and coating thickness loss rate with test time for epoxy coated specimens placed in different accelerated corrosion environments. From the graph, it can be seen that the coating thickness of the freshwater environment specimens (HY01 and HY02) increased from the initial thickness of  $200 \mu\text{m}$  during a 90 day accelerated corrosion test time dropped to  $173 \mu\text{m} \sim 174 \mu\text{m}$ . The loss value of coating thickness is  $26 \mu\text{m} \sim 27 \mu\text{m}$ . The loss rate of coating thickness is

13.0%~13.5%. During a 90-day accelerated corrosion test, the coating thickness of the saltwater environment specimens (HY03 and HY04) increased from the initial thickness of 200 $\mu\text{m}$  dropped to 170 $\mu\text{m}$  ~171 $\mu\text{m}$ . The loss value of coating thickness is 29 $\mu\text{m}$  ~30 $\mu\text{m}$ . The loss rate of coating thickness is 14.5%~15.0%. The phenomenon of coating thickness loss is due to the combined effect of factors such as ultraviolet radiation, water, and oxygen on the coating in an accelerated corrosion environment, especially the significant impact of ultraviolet radiation on the decrease of coating thickness. Ultraviolet radiation can decompose the ion bonds between the high polymers of the coating, leading to aging and degradation of the coating. The surface of the coating gradually becomes powdery, and the residue of coating decomposition gradually separates from the coating under the washing of water. This pulverization and erosion effect leads to a gradual decrease in coating thickness. The experimental results show that regardless of whether it is in a freshwater or saline environment, the coating thickness gradually decreases with the extension of the test time, and shows a slow decrease in coating thickness in the early stage of corrosion, and a faster decrease in coating thickness in the middle and later stages of corrosion. This indirectly indicates that the corrosion rate of the coating follows a non-linear corrosion pattern of slow corrosion in the early stage and accelerated corrosion in the middle and later stages.

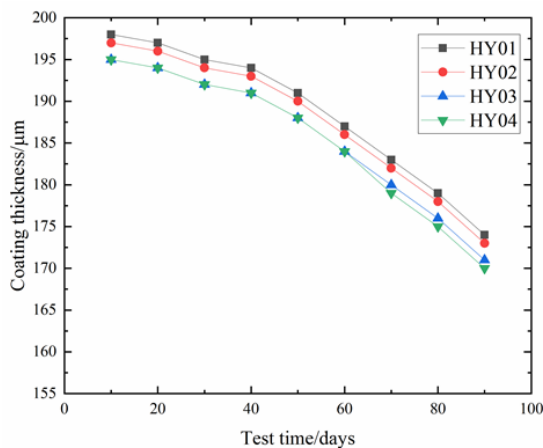


Fig. 3. The variation law of coating thickness with test time

According to the change in coating thickness data, the coating thickness of specimen HY01 decreased by 26 $\mu\text{m}$ , and the coating thickness of specimen HY03 decreased by 29 $\mu\text{m}$ . From the perspective of coating thickness loss, the coating thickness loss of specimens in saline environment (HY03 and HY04) is greater than that of specimens in freshwater environment (HY01 and HY02). This indicated that the corrosion rate of epoxy coatings on steel bridges in saline accelerated corrosion environment is faster than that in freshwater accelerated corrosion environment. For epoxy coatings, in saline corrosive environments, they not only face corrosion from UV rays, water, oxygen, etc., but also from chloride ions. Chloride ions can accelerate the chemical reaction that occurs during coating corrosion, leading to an accelerated rate of molecular decomposition of the coating. The experimental results indicate that chloride ions in saline environments can accelerate the corrosion rate of epoxy coatings.

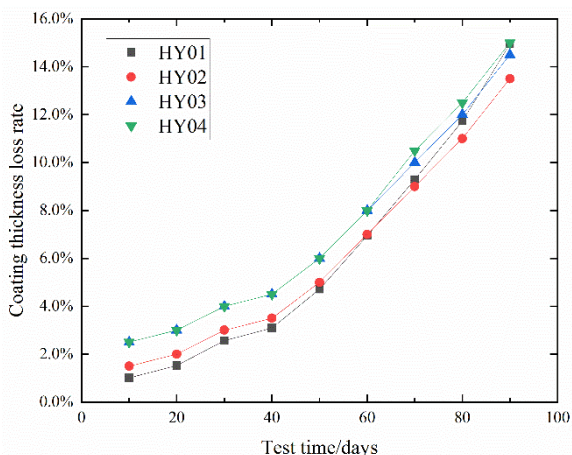


Fig. 4. The variation law of coating thickness loss rate with test time

### 3.2. Corrosion Area Rate

The corrosion area of the coating is the most effective indicator for characterizing the corrosion process and health status of the coating. When the corrosion area rate reaches a specific value, it can be considered that the coating has failed. This article takes the corrosion area rate of coatings as one of the research indicators to analyze the corrosion laws of coatings.

Fig. 5 shows the variation in the corrosion area rate of epoxy coated steel bridge specimens in different accelerated corrosion environments over time. The graph shows that during the 90-day accelerated corrosion test period, the corrosion area rate of the freshwater environment specimens increased from 0% to 1.90%. In the range of 0-40 days, the corrosion area rate of the coating remained at 0%. In the range of 40-90 days, the corrosion area rate of the coating gradually increased, and the slope of the increase became increasingly larger. During the 90-day accelerated corrosion test period, the corrosion area rate of the saline environment specimens increased from 0% to 2.40%. In the range of 0-20 days, the corrosion area rate of the coating remained at 0%. In the range of 20-90 days, the corrosion area rate of the coating gradually increased, and the slope of the increase became increasingly larger. The experimental results show that with increasing test time, the corrosion area rate gradually increases, the corrosion area rate slowly increases in the early stage of corrosion, and the corrosion area rate rapidly increases in the middle and late stages of corrosion, indicating that the coating corrosion process follows a nonlinear corrosion law. The increase in corrosion area is due to the combined effect of factors such as UV radiation, water, and oxygen on the coating in an accelerated corrosion environment, leading to electrochemical reactions of the coating. The coating gradually undergoes corrosion degradation, losing its protective effect on the steel bridge structure. The nonlinear corrosion law may be because in the early stage of corrosion, the loss of coating thickness is relatively small, and the insulating effect of the coating against external erosion factors is still strong. Oxygen, water, chloride ions, etc. need a long time to enter the coating substrate; In the middle and later stages of corrosion, as the thickness of the coating decreases and the porosity of the coating gradually increases, corrosion factors are more likely to enter the coating substrate and undergo chemical reactions, accelerating the electrochemical reaction process of coating corrosion. The accumulation rate of corrosion products is greatly accelerated, characterized by an accelerated increase in the corrosion area rate of the coating.

From the perspective of the change in corrosion area rate, the corrosion area rate of specimens in saline environment (HY03 and HY04) increased faster than that in freshwater environment (HY01 and HY02), indicating that the corrosion rate of the epoxy coating on steel bridges in saline accelerated corrosion environment is faster than that in freshwater accelerated corrosion environment. By comparing the composition factors of saline corrosion environment and freshwater corrosion environment, it can be concluded that chloride ions are the main factor affecting coating corrosion in saline corrosion environment. For epoxy coatings, chloride ions have a smaller radius and are more likely to penetrate the coating and enter the coating/metal interface. Prolonged exposure of chloride ions in aqueous solutions can accelerate corrosion reactions and easily penetrate the protective film on the metal surface, causing crevice corrosion and pore corrosion.

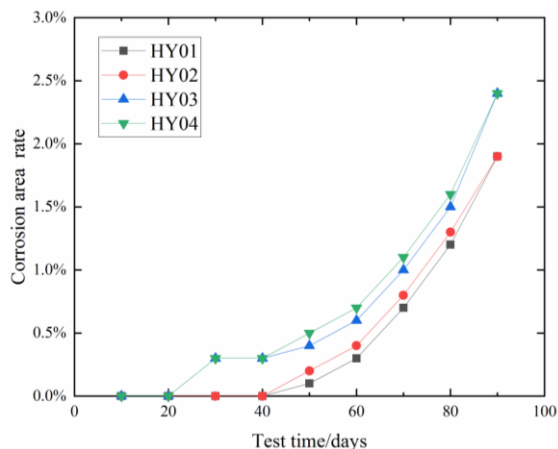


Fig. 5. The variation law of corrosion area rate with test time

### 3.3. Coating Corrosion Morphology Based on Image Processing

At present, the quality inspection of coating surfaces mainly relies on manual work. The manual corrosion detection of coating surfaces is limited by its subjectivity, making it difficult to objectively quantify the characteristics of corrosion. In recent years, image processing technology has gradually been applied in the field of coating corrosion. The form and characteristics of coating corrosion damage can be represented by corrosion images to evaluate the type of corrosion and analyze the degree of corrosion. This is important basis for studying corrosion laws.

To obtain clearer and easier to recognize images of the coating corrosion morphology, this paper adopts an image processing algorithm based on MATLAB to perform grayscale conversion, normalized histogram drawing, and binary image processing on the surface morphology images of coated specimens. Fig. 6 shows the corrosion morphology image of the coating after cyclic accelerated corrosion test. From the graph, it can be seen that the number of corrosion rust points in the saltwater environment coated specimens is significantly higher than that in the freshwater environment coated specimens, which is consistent with the variation law of the corrosion area rate of the coating. This indirectly confirms that chloride ions can accelerate the corrosion of the coating. Compared with the initial morphology of the coating, the color of the coating has undergone significant changes. This is mainly because the pigment molecules in the coating are excited to form free radicals after being exposed to ultraviolet radiation, leading to molecular breakage and chemical changes, resulting in a change in color. Fig. 7 shows a grayscale image of



coating corrosion morphology, which is generated by converting a three-dimensional RGB image into a two-dimensional grayscale image through image processing algorithms. Fig. 8 and Fig. 9 show the normalized histograms of coating corrosion morphology images, which can directly reflect the ratio of different grayscale levels. The horizontal axis represents the grayscale level of each pixel in the image, and the vertical axis represents the number or probability of pixels with different grayscale levels appearing in the image. Normalized histograms are of great significance in obtaining the optimal threshold for images.

Fig. 10 and Fig. 11 show binary images of coating corrosion morphology. The method of generating binary images is to obtain the assumed optimal threshold of the image based on the normalized histogram, calculate the center values of the foreground and background at this threshold. When the average value of the center values of the foreground and background is the same as the assumed optimal threshold, the iteration is terminated. This value is used as the threshold for binarization. From the graph, it can be seen that after the cyclic accelerated corrosion test for 90 days, the surface of the coated specimens showed varying degrees of corrosion. The corrosion area rate of the coated specimens in a saline environment was greater. Therefore, image processing algorithms based on MATLAB can clearly present the corrosion morphology and degree of coating corrosion.

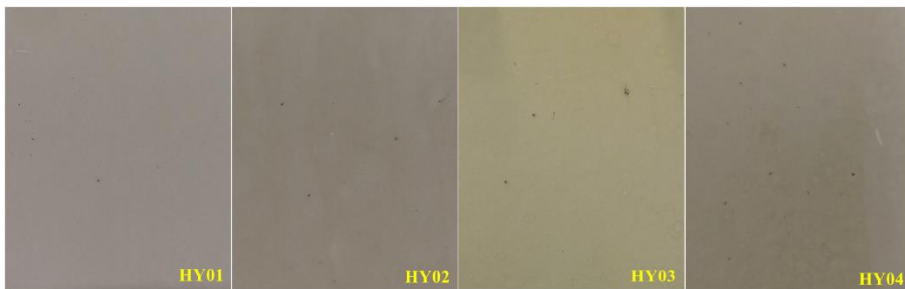


Fig. 6. Coating corrosion morphology at 90 days

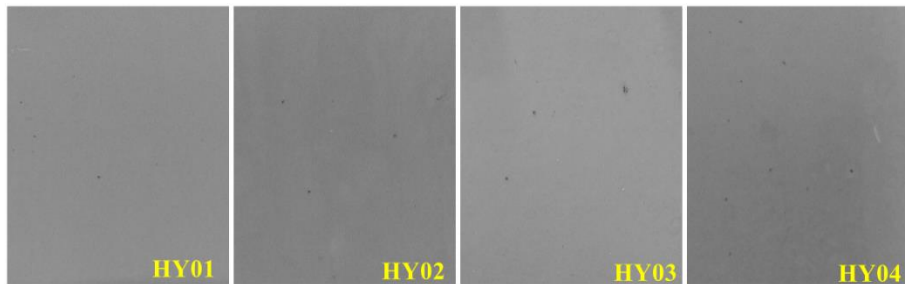


Fig. 7. Gray scale image of coating corrosion morphology at 90 days

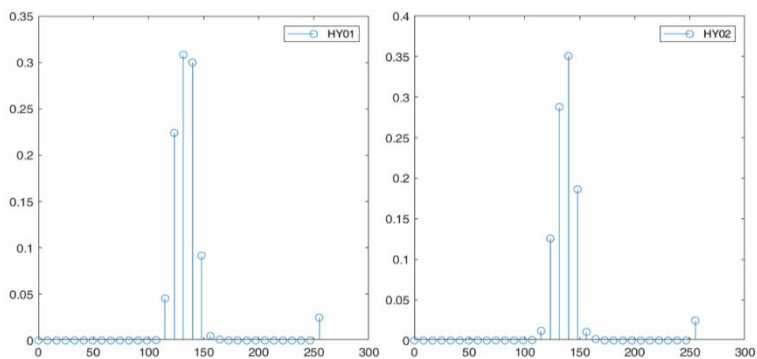


Fig. 8. Normalized histogram of coating corrosion images at 90 days (HY01 and HY02)

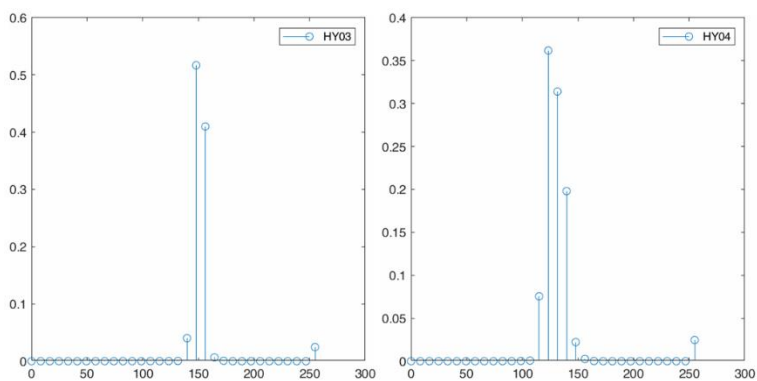


Fig. 9. Normalized histogram of coating corrosion images at 90 days (HY03 and HY04)

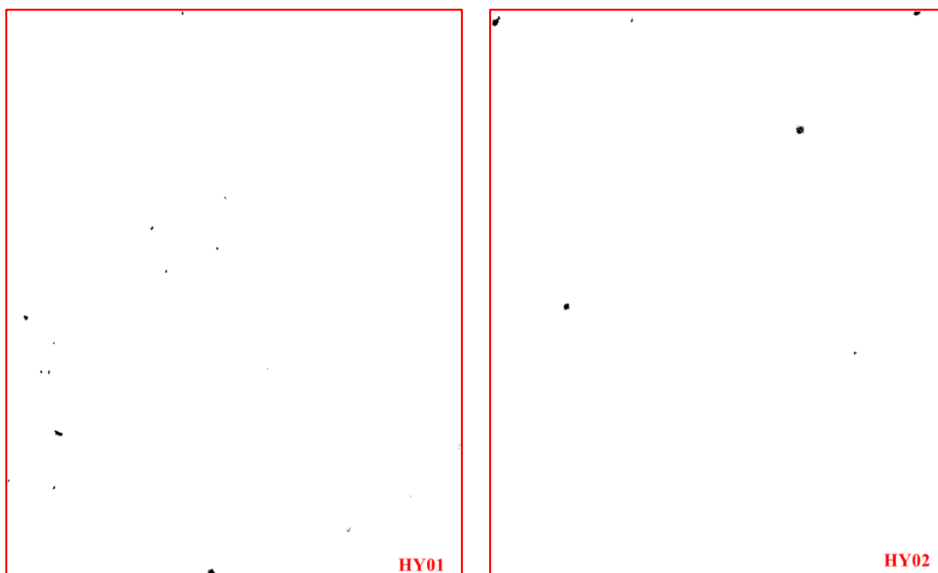


Fig. 10. Binary image of coating corrosion morphology (HY01 and HY02)

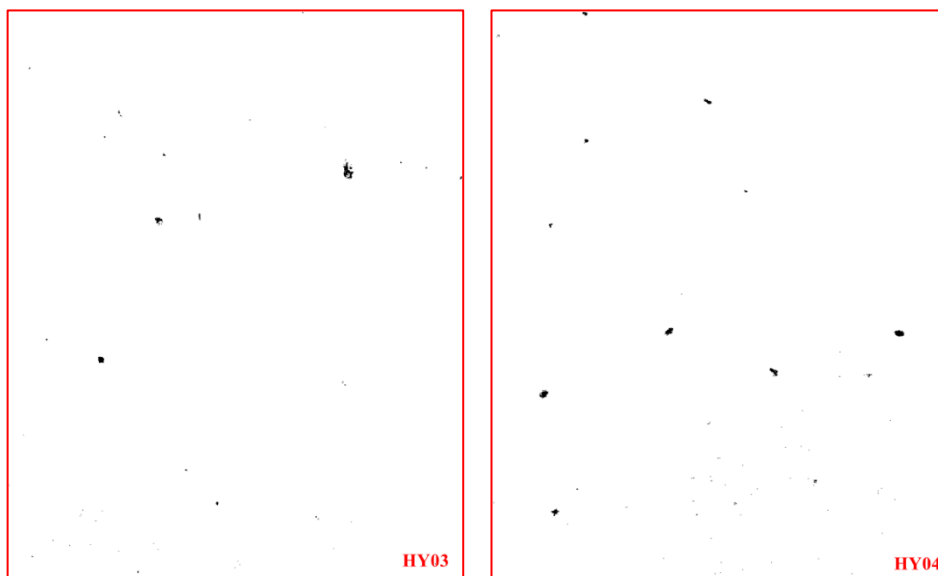


Fig. 11. Binary image of coating corrosion morphology (HY03 and HY04)

#### 4. Discussion

##### 4.1. Analysis of Corrosion Data

To reduce the error of experimental data, the average coating thickness loss rate of epoxy coated specimens was fitted and analyzed. Nonlinear corrosion function fitting was performed for two corrosion conditions, namely epoxy coating in freshwater environment and epoxy coating in saltwater environment, respectively. Fig. 12 and Fig. 13 respectively show the fitting curves of coating thickness loss rate under different corrosion environment. After fitting with Origin Pro2019 software, there is a high correlation between the coating thickness loss rate and the quadratic polynomial.

$$H = n + B_1 \times t + B_2 \times t^2 \tag{1}$$

Where,  $H$  represents the loss rate of coating thickness,  $t$  represents the corrosion time of the coating (in days).  $n$ ,  $B_1$ , and  $B_2$  are constants (different corrosion environment correspond to different values, see Table 3 for parameter values).

Table 3. Parameter values under different corrosion environment

| Corrosion Environment | $n$    |                | $B_1$   |                | $B_2$   |                | $R^2$       |
|-----------------------|--------|----------------|---------|----------------|---------|----------------|-------------|
|                       | Value  | Standard Error | Value   | Standard Error | Value   | Standard Error | Correlation |
| Freshwater            | 0.0047 | 0.0027         | 2.26E-4 | 1.42E-4        | 1.43E-5 | 1.52E-6        | 0.99        |
| Saltwater             | 0.0090 | 0.0047         | 6.08E-4 | 2.42E-4        | 1.01E-5 | 2.59E-6        | 0.98        |

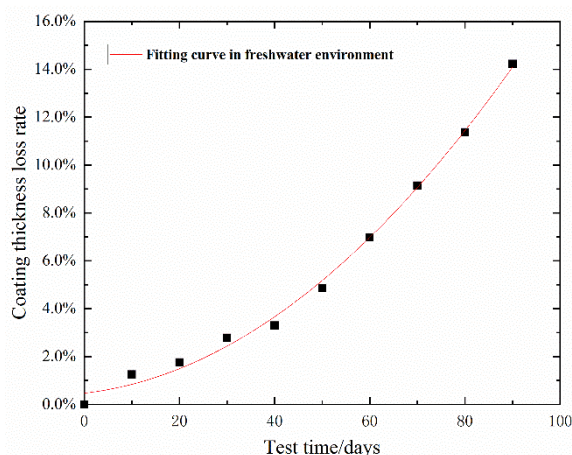


Fig. 12. Fitting curve of thickness loss rate of epoxy coating in freshwater environment

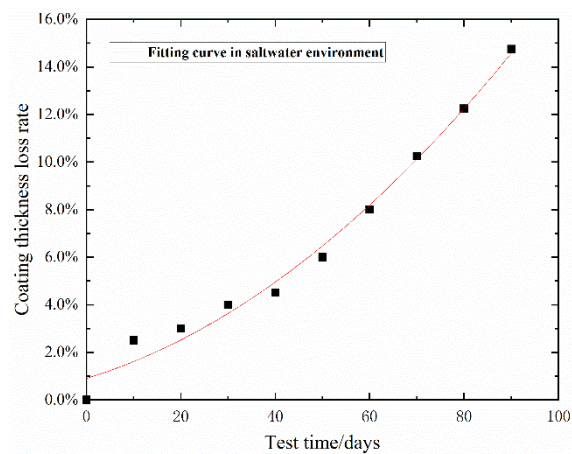


Fig. 13. Fitting curve of thickness loss rate of epoxy coating in saltwater environment

Due to the possibility of deviation in the corrosion area rate of individual coated specimens, this article takes the average corrosion area rate of specimens under the same conditions for data fitting to reduce model errors. Nonlinear corrosion function fitting is performed on epoxy coatings in freshwater and saline environment. Fig. 14 and Fig. 15 respectively show the fitting curves of corrosion area rate under different corrosion environment. After fitting with Origin Pro2019 software, there is a high correlation between the corrosion area rate of the coating and the following functional models.

$$S = a \times b^t \tag{2}$$

Where, S: corrosion area rate, t: corrosion time (days), a and b: constant (different corrosion environment correspond to different values, see Table 4 for parameter values).

Table 4. Parameter values under different corrosion environment

| corrosion environment | <i>a</i> |                | <i>b</i> |                | R <sup>2</sup> |
|-----------------------|----------|----------------|----------|----------------|----------------|
|                       | value    | standard error | value    | standard error | correlation    |
| Freshwater            | 2.98E-10 | 2.22E-10       | 4.00     | 0.1677         | 0.99           |
| Saltwater             | 3.76E-08 | 3.81E-08       | 2.96     | 0.2302         | 0.98           |

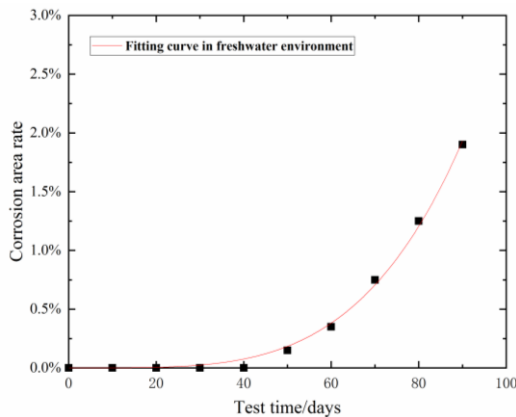


Fig. 14. Fitting curve of corrosion area rate of epoxy coating in freshwater environment

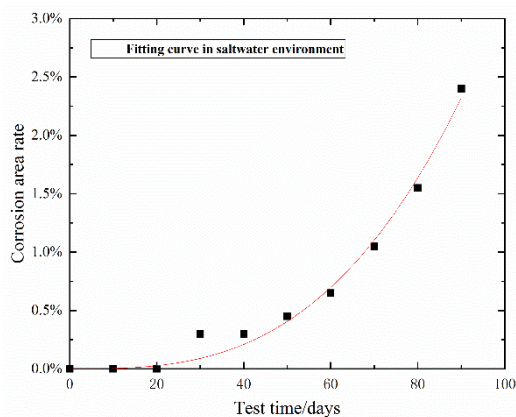


Fig. 15. Fitting curve of corrosion area rate of epoxy coating in saltwater environment

**4.2. Analysis of Corrosion Mechanism of Epoxy Coatings**

The experimental results of this paper indicate that the corrosion rate of epoxy coatings exhibits a non-linear corrosion pattern of slow corrosion in the early stage and accelerated corrosion in the middle and later stages. The schematic diagram of the coating corrosion process is shown in Fig. 16. Based on the experimental phenomena and results in this article, the corrosion mechanism of epoxy coatings on steel bridges is analyzed as follows the epoxy coating is a multi-layer structure, and in the early stage of corrosion, the pores of the coating are very dense, making it difficult for corrosive substances such as air, water, and chloride ions to pass through the coating and reach the coating/metal substrate

interface. With the passage of time, the effects of ultraviolet radiation, temperature changes, humidity changes, and other factors cause the polymer structure of the coating to continuously age and degrade. The pores of the coating become less dense, and substances such as oxygen and water can partially enter the interior of the coating through the pores and undergo chemical reactions. Therefore, in the early stage of coating corrosion, it is generally manifested as coating powdering, color difference, loss of glossiness, etc. There will be no rust spots, coating peeling in the early stage of coating corrosion. With the development of corrosion process, the corrosion rate continues to accelerate, and the decomposition rate of coating material structure is also accelerating.

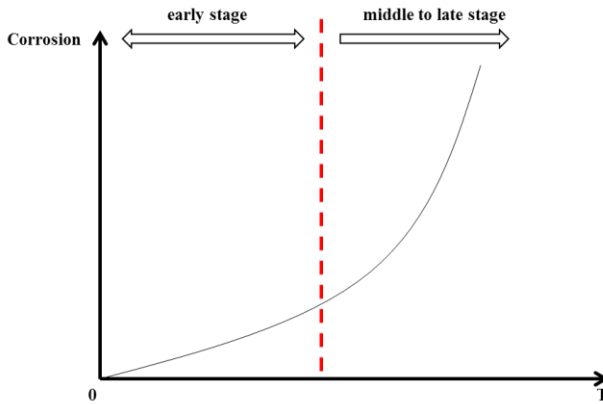


Fig. 16. The schematic diagram of the coating corrosion process

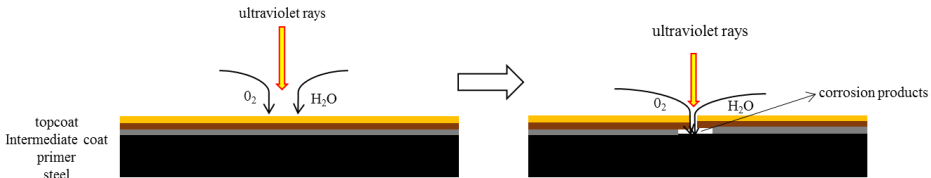


Fig. 17. The corrosion mechanism of epoxy coating under freshwater environment

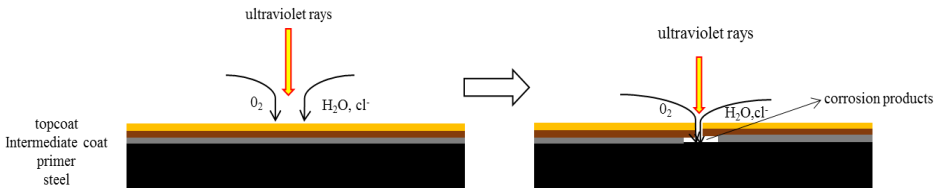


Fig. 18. The corrosion mechanism of epoxy coating under freshwater environment

The chemical reaction rate at the coating/metal matrix interface continues to accelerate. The generated chemical reaction products continue to accumulate and increase. The coating will expand, forming obvious corrosion problems such as rust spots, bubbles, and even coating peeling. Therefore, when the corrosion process reaches the middle and later stages, the rate of coating corrosion will greatly accelerate, and the products of coating corrosion degradation will continue to increase, ultimately manifested as the continuous expansion of the corrosion area rate. When the corrosion area rate increases to a specific

value, it can be considered that the coating has failed and decision measures for repairing or repainting the coating are needed.

### 4.3. Corrosion Function Model of Epoxy Coating on Steel Bridges

According to the corrosion laws and mechanisms of coatings, the corrosion area rate and thickness of coatings exhibit nonlinear patterns with corrosion time. Research has shown that coating thickness and coating corrosion area rate can effectively characterize the degree of coating corrosion. Therefore, this paper takes coating thickness and coating corrosion area rate as model indicators to establish a nonlinear corrosion function model for epoxy coatings on steel bridges under accelerated corrosion environment. Dr. Yamamoto Takashi, a Japanese anti-corrosion expert, proposed the theory of coating corrosion life, which suggests that coating corrosion goes through two stages [35]. The first stage is corrosion before the coating is perforated, and the second stage is corrosion after the coating is perforated. This theory is consistent with the corrosion law obtained through experiments in this paper.

Based on the corrosion law of coatings and Dr. Yamamoto Takashi's coating life theory, this paper divides the corrosion process of epoxy coatings on steel bridges into two stages: the early stage of corrosion, the middle and later stage of corrosion. The early stage of corrosion refers to the period from the service of the coating to the occurrence of corrosion rust spots. During this stage, the corrosion of the coating is mainly characterized by a decrease in coating thickness. The middle and later stage of corrosion is from the appearance of corrosion rust spots to the failure of the coating. During this stage, the corrosion of the coating is mainly characterized by an increase in the corrosion area. Therefore, this paper divides the nonlinear corrosion function model of epoxy coating on steel bridges under accelerated corrosion environment into two parts. In the early stage of corrosion, the loss rate of coating thickness is used as the model indicator, and a function model for the early stage of epoxy coating corrosion on steel bridges under accelerated corrosion environment is established. In the middle and later stages of corrosion, the corrosion area rate of coating is used as the model indicator, and a function model for the middle and later stages of epoxy coating corrosion on steel bridges under accelerated corrosion environment is established.

The nonlinear corrosion function model of epoxy coatings on steel bridge in the early stage is shown in the Eq (3).

$$H = n + B_1 \times t + B_2 \times t^2 \tag{3}$$

Where,  $H$ : coating thickness loss rate,  $t$ : corrosion time (days),  $n$ : initial coating thickness loss rate (the initial coating thickness loss rate of the new coating is 0),  $B_1$  and  $B_2$ : constant (the values vary under different corrosive environments, as shown in Table 5).

Table 5. Parameter values of new coating under different corrosion environment

| corrosion environment  | $n$   | $B_1$   | $B_2$   |
|------------------------|-------|---------|---------|
|                        | value | value   | value   |
| Freshwater environment | 0     | 2.26E-4 | 1.43E-5 |
| Saltwater environment  | 0     | 6.08E-4 | 1.01E-5 |

The nonlinear corrosion function model of epoxy coatings on steel bridge in the middle and later stages is shown in the Eq (4).

$$S = a \times b^t \tag{4}$$

Where,  $S$ : corrosion area rate,  $t$ : corrosion time (days),  $a$  and  $b$ : constant (the values vary under different corrosive environments, as shown in Table 6).

Table 6. Parameter values under different corrosion environment

| corrosion environment  | $a$      | $b$   |
|------------------------|----------|-------|
|                        | value    | value |
| Freshwater environment | 2.98E-10 | 4.00  |
| Saltwater environment  | 3.76E-08 | 2.96  |

## 5. Conclusions

This paper adopted the accelerated corrosion test method to study the corrosion law of epoxy coatings on steel bridges. An image processing algorithm based on MATLAB was performed grayscale conversion, normalized histogram drawing, and binary image processing on the surface morphology images of coated specimens. From the test results, the following conclusions could be drawn:

- Whether in freshwater or saltwater corrosion environment, the coatings on steel bridge will undergo varying degrees of corrosion, manifested by a decrease in coating thickness and an increase in corrosion area rate. The corrosion rate of the coating exhibits a non-linear corrosion pattern of slow corrosion in the early stage and accelerated corrosion in the middle and later stages.
- The experimental results indicate that the corrosion rate of epoxy coatings on steel bridges is faster in saltwater environment than in freshwater environment. Chlorine ions in salt environment can accelerate the corrosion of coatings. Chlorine ions are more likely to penetrate the coating and enter the coating/metal interface. Prolonged exposure to aqueous solutions can accelerate the corrosion reaction and easily penetrate the protective film on the metal surface, causing crevice corrosion and pitting corrosion.
- According to the analysis of coating morphology, it can be concluded that the surface of the coated specimens showed varying degrees of corrosion after the cyclic accelerated corrosion test for 90 days. The corrosion area rate of the coated specimens in a saline environment was higher. The image processing algorithms based on MATLAB can clearly present the corrosion morphology and degree of coating corrosion.

Based on the analysis of the mechanism of coating corrosion and the results of accelerated corrosion test, a nonlinear corrosion function model for steel bridge coatings in an accelerated corrosion environment was established. This function model has a high correlation with experimental data. Nonlinear corrosion function models were established for epoxy coatings in freshwater and saline environments, respectively.

## Acknowledgement

This research did not receive any specific grant from funding agencies in the public, commercial, or not-for-profit sectors.

## References

- [1] Abass AO. Recent advances on organic coating system technologies for corrosion protection of offshore metallic structures. *Journal of Molecular Liquids*, 2018, 269: 572-606. <http://doi.org/10.1016/j.molliq.2018.08.053>
- [2] Sørensen PA, Kiil S, et al. Anticorrosive coatings: a review. *J. Coat. Technol. Res.* 2009; 6: 135-176. <http://doi.org/10.1007/s11998-008-9144-2>



- [3] Meng F, Liu Y et al. Studies on Mathematical Models of Wet Adhesion and Lifetime Prediction of Organic Coating/Steel by Grey System Theory. *Materials*. 2017; 10: 1-15. <http://doi.org/10.3390/ma10070715>
- [4] Mansfeld F, Kenkel JV. Electrochemical Measurements of Time-of-Wetness and Atmospheric Corrosion Rates. *Corrosion*. 1977; 33: 13-16. <https://doi.org/10.5006/0010-9312-33.1.13>
- [5] Mansfeld F, Kendig MW, Tsai S. Evaluation of Corrosion Behavior of Coated Metals with AC Impedance Measurements. *Corrosion*. 1982; 38: 478-485. <https://doi.org/10.5006/1.3577363>
- [6] Salmasifar A, Sarabi AA, Mohammadloo HE. Anticorrosive performance of epoxy/clay nanocomposites pretreated by hexafluorozirconic acid based conversion coating on St 12. *Corros. Eng. Sci. Technol*. 2015; 50: 372-379. <http://doi.org/10.1179/1743278214Y.0000000233>
- [7] Lee CY, Lee SK, Park JH, et al. Novel approach to correlate degree of surface deterioration to coating impedance for laboratory test panels coated with two types of primers. *Corros. Eng. Sci. Technol*. 2012; 47: 411-420. <http://doi.org/10.1179/1743278212Y.000000015>
- [8] Kendig M, Scully J. Basic Aspects of Electrochemical Impedance Application for the Lifetime Prediction of Organic Coatings on Metals. *Corrosion*. 1990; 46: 22-29. <https://doi.org/10.5006/1.3585061>
- [9] Kirthiga, R., Elavenil, S. A survey on crack detection in concrete surface using image processing and machine learning. *J Build Rehabil*. 2024; 9:15. <http://doi.org/10.1007/S41024-023-00371-6>
- [10] Shengan Z, et al. Detection method of interface defects of titanium nitride thin film coating materials based on image processing. *International Journal of Materials and Product Technology* 65.1(2022):41-51. <http://doi.org/10.1504/IJMPT.2022.124256>
- [11] Sprague A, et al. Automatic Nondestructive Detection of Damages in Thermal Barrier Coatings Using Image Processing and Machine Learning. *Microscopy and Microanalysis* 28.S1(2022):3068-3072. <http://doi.org/10.1017/S1431927622011448>
- [12] Wenjun Y, et al. A novel method for evaluating the slurry coating characteristics of sized yarns based on the starch-iodine color reaction principle and image processing. *Textile Research Journal* 91.11-12(2021):1302-1312. <http://doi.org/10.1177/0040517520980805>
- [13] Perumal P, et al. Investigation of TiN coating uniformity and its corrosion behaviour using image process. *Materials Research Express* 6.4(2019):046411-046411. <http://doi.org/10.1088/2053-1591/aafae9>
- [14] Fernández-Isla C, Navarro J P, Alcover M P. Automated Visual Inspection of Ship Hull Surfaces Using the Wavelet Transform. *Mathematical Problems in Engineering*; 2013, 27(5): 211-244. <http://doi.org/10.1155/2013/101837>
- [15] Jahanshahi MR, Masri SF. Effect of color space, color channels, and sub-image block size on the performance of wavelet-based texture analysis algorithms: an application to corrosion detection on steel structures. *Computing in Civil Engineering*; 2013: 685-692. <https://doi.org/10.1061/9780784413029.086>
- [16] Son H, Hwang N, et al. Rapid and automated determination of rusted surface areas of a steel bridge for robotic maintenance systems. *Automation in Construction*; 2014, 42: 13-24. <http://doi.org/10.1016/j.autcon.2014.02.016>
- [17] Xie X. A review of recent advances in surface defect detection using texture analysis techniques. *ELCVIA: Electronic Letters on Computer Vision and Image Analysis*, 2008, 7(3): 1-22. <http://doi.org/10.5565/rev/elcvia.268>
- [18] Zaidan BB, Zaidan AA, Alanazi HO, et al. Towards corrosion detection system. *International Journal of Computer Science*, 2010, 7(3): 33-36.

- [19] Acosta MRG, Diaz JCV, Castro NS. An innovative image-processing model for rust detection using perlin noise to simulate oxide textures. *Corrosion Science*, 2014, 88: 141-151. <http://doi.org/10.1016/j.corsci.2014.07.027>
- [20] Chen PH, Shen HK, Lei CY, et al. Fourier-transform-based method for automated steel bridge coating defect recognition. *Procedia Engineering*, 2011, 14: 470-476. <https://doi.org/10.1016/j.proeng.2011.07.058>
- [21] Aijazi AK, Malaterre L, Tazir ML, et al. Detecting and analyzing corrosion spots on the hull of large marine vessels using colored 3d lidar point clouds. *ISPRS Annals of Photogrammetry Remote Sensing & Spatial Informa*, 2016, 33: 153-160.
- [22] Igoe D, Parisi AV. Characterization of the corrosion of iron using a smartphone camera. *Instrumentation Science and Technology*, 2016, 44(2): 139-147. <http://doi.org/10.1080/10739149.2015.1082484>
- [23] Kim I T, Itoh Y. Accelerated exposure tests as evaluation tool for estimating life of organic coatings on steel bridges. *Corros. Eng. Sci. Technol.* 2007; 42: 242-252. <http://doi.org/10.1179/174327807X214833>
- [24] Hirohata M, Takemi J, Itoh Y. Corrosion accelerated exposure experiment simulating under seawater environment for organic coated steel materials. *Corros. Eng. Sci. Technol.* 2014; 50: 449-461. <http://doi.org/10.1179/1743278214Y.0000000238>
- [25] Kallias, Alexandros N, et al. Performance profiles of metallic bridges subject to coating degradation and atmospheric corrosion. *Structure and Infrastructure Engineering*, 2017, 13(4):440-453. <http://doi.org/10.1080/15732479.2016.1164726>
- [26] Lee CY, Chang T. Service Life Prediction for Steel Bridge Coatings with Type of Coating Systems. *Korean Society of Steel Construction*. 2016; 28: 325-335. <http://doi.org/10.7781/kjoss.2016.28.5.325>
- [27] Fredj N, Cohendoz S, Feaugas X, et al. Ageing of marine coating in natural and artificial seawater under mechanical stresses. *Prog. Org. Coat.* 2012; 74: 391-399. <http://doi.org/10.1016/j.porgcoat.2011.10.002>
- [28] Fredj N, Cohendoz S, Feaugas X et al. Effect of mechanical stress on kinetics of degradation of marine coatings. *Prog. Org. Coat.* 2008; 63: 316-322. <http://doi.org/10.1016/j.porgcoat.2008.05.001>
- [29] Fredj N, Cohendoz S, Feaugas X, et al. Effect of mechanical stress on marine organic coating ageing approached by EIS measurements. *Prog. Org. Coat.* 2011; 72: 260-268. <http://doi.org/10.1016/j.porgcoat.2011.04.014>
- [30] Itoh Y, Kim IT. Accelerated cyclic corrosion testing of structural steels and its application to assess steel bridge coatings. *Anti-Corros. Methods Mater.* 2006; 53: 374-381. <http://doi.org/10.1108/00035590610711723>
- [31] Merachtsaki D, Xidas P, Giannakoudakis P, Triantafyllidis K, Spathis P. Corrosion Protection of Steel by Epoxy-Organoclay Nanocomposite Coatings. *Coatings*. 2017; 7(7):84. <https://doi.org/10.3390/coatings7070084>
- [32] Rachid H. Review on epoxy polymers and its composites as a potential anticorrosive coatings for carbon steel in 3.5% NaCl solution: Computational approaches. *Journal of Molecular Liquids*. 2021;336. <https://doi.org/10.1016/j.molliq.2021.116307>
- [33] ISO 8501-2007, "Preparation of steel substrates before application of paints and related products-Visual assessment of surface cleanliness-Part 1: Rust grades and preparation grades of uncoated steel substrates and of steel substrates after overall removal of previous coatings". Geneva, Switzerland: ISO 2007.
- [34] GB/T 1727-2021, "General methods for preparation of coating films". Beijing, China: GB/T 2021.(in Chinese)
- [35] Fang Z. Simple talk about the forecast theory about coating's life. *Paint Coat. Plat.* 2005; 3: 3-5. (in Chinese)

# Enhancing the seismic performance of a concentrically braced reinforced concrete frame using an I-shaped shear link made of low yield point steel

Sara Hadidi<sup>1,a</sup>, Denise-Penelope N. Kontoni<sup>\*2,3,b</sup>, Imran Karimi<sup>4,c</sup>

<sup>1</sup>Department of Civil Engineering, University of Kurdistan, Sanandaj, Iran

<sup>2</sup>Department of Civil Engineering, School of Engineering, University of the Peloponnese, 26334 Patras, Greece

<sup>3</sup>School of Science and Technology, Hellenic Open University, GR-26335 Patras, Greece

<sup>4</sup>Department of Civil Engineering, University of Tabriz, Tabriz, Iran

## Article Info

## Abstract

### Article history:

Received 01 May 2024

Accepted 21 June 2024

### Keywords:

Seismic performance;  
Reinforced concrete frame;  
Concentric brace;  
Low yield point (LYP) steel;  
I-shaped shear link;  
Ductility;  
Energy dissipation

The experience of previous earthquakes has shown that reinforced concrete frames are susceptible to earthquake damage; therefore, several techniques have been suggested by researchers to enhance their efficiency. Although the reinforcement of RC frames with concentric braces does enhance the frame's stiffness and lateral resistance, it does not have much effect on its ductility. Hence, in this article, an I-shaped shear link as a damper is investigated with the aim of strengthening RC frames. This damper designed for ease of production and post-earthquake replacement, not only improves the frame's stiffness and resistance, but also augments its ductility and plastic behavior. Considering that the damage is expected to be limited in the damper, other structural components will remain in the elastic region. Although the addition of such dampers increases the ductility, it reduces the stiffness of the system. To compensate for this weakness, the damper using low yield point (LYP) steel is discussed and investigated. Furthermore, the effect of the thickness of the damper flanges on the seismic behavior of the frame is examined. The results show that the use of LYP steel in the construction of the studied shear damper can improve the stiffness and resistance of the reinforced concrete frame as well as the amount of energy dissipation. However, the mere use of LYP steel does not guarantee the improvement of the frame's behavior, and this is subject to the thickness of the damper's flanges.

© 2024 MIM Research Group. All rights reserved.

## 1. Introduction

During recent severe earthquakes, reinforced concrete (RC) structures experienced structural damage at various levels due to the lack of ductility, insufficient strength, etc. [1-3]. Consequently, the losses caused by these major earthquakes highlight the importance of further investigation to enhance the seismic performance of RC structures.

The improvement of the seismic response of RC buildings using the base isolation technique has been studied by various researchers, including Kontoni & Farghaly [4], Farghaly & Kontoni [5], and Belbachir *et al.* [6]. The mitigating effect of tuned mass dampers (TMDs) on the seismic response of RC high-rise buildings, considering soil-structure interaction (SSI), has been investigated by Kontoni & Farghaly [4], Farghaly & Kontoni [5], etc. Moreover, the mitigation of seismic pounding between RC high-rise buildings, considering SSI, through the use of base isolation, tuned mass dampers (TMDs) and pounding tuned mass dampers (PTMDs) has been explored by Farghaly & Kontoni [5]

\*Corresponding author: [kontoni@uop.gr](mailto:kontoni@uop.gr); [kontoni.denise@ac.eap.gr](mailto:kontoni.denise@ac.eap.gr)

<sup>a</sup> orcid.org/0009-0004-6260-0076; <sup>b</sup> orcid.org/0000-0003-4844-1094; <sup>c</sup> orcid.org/0009-0006-1410-8671

DOI: <http://dx.doi.org/10.17515/resm2024.263st0105rs>

Res. Eng. Struct. Mat. Vol. 11 Iss. 1 (2025) 305-332

and Farghaly & Kontoni [7]. In reinforced concrete buildings with a moment frame system, seismic energy is dissipated by relying on the formation of plastic joints at both ends of the beam [8]. Considering that the floor beam, in addition to the task of energy absorption and lateral load, is also responsible for gravity load, so it is highly difficult to replace and repair it after an earthquake. On the other hand, the lateral and gravity loads increase its vulnerability.

In many reinforced concrete buildings, a change of use or a change in seismic requirements, damages caused after an earthquake, or the need to change the area or the number of floors of the buildings, confirm the necessity of retrofitting the buildings. In general, the strengthening of reinforced concrete buildings is done by two methods: local and general strengthening. Local reinforcements include the use of FRP [9,10], the use of steel jackets [11-13], the use of concrete jackets [14-16], the use of UHPC concretes to strengthen joints [17-19], and it is also the use of SMA [20,21], which usually do not have a significant effect on the stiffness and lateral strength of the structure. In cases where a structure needs to increase its stiffness or strength, only using the general strengthening method including the addition of structural elements such as steel shear wall [22-24], concrete shear wall [24-27], concentric brace [28-30], eccentric brace [30-33], BRB brace [34-36], and dampers [37-41] are prevalent. Although the addition of concrete shear walls increases the stiffness and lateral resistance, it brings disadvantages such as increasing the weight of the structure, complexity of implementation and formatting, and disturbance in the use of the building. Furthermore, despite the efficiency and adaptability of steel shear walls, employing steel sheets as the primary load-bearing component leads to the transmission of high stresses to the surrounding frame. This requires beams and columns with a high moment of inertia, which may sometimes be unachievable. It should be noted that convergent braces also do not perform well against bidirectional loads, so it has not been accepted as a successful method, particularly in areas with a high risk of earthquakes. On the other hand, the eccentrically braced frame (EBF) system is another method which has exhibited good ductility during previous earthquakes. Nevertheless, due to the fact that the connecting beam is integrated into the floor beam in this system, repairing or replacing the connecting beam after a severe earthquake is complicated [42]. Also, the shear capacity of the connecting beam causes significant axial forces to be applied to the columns around the brace, which must be considered in the design and seismic analysis process. Researchers addressed the complexities related to the construction and design of the diverging system by employing a perpendicular shear link at the junction of the beam and braces (beneath the beam). In the new system with vertical shear link (V-EBF), the shear link is not subjected to axial loading and this system is known as an alternative strategy for improving the seismic behavior and strengthening of reinforced concrete buildings. After the initiative of V-EBF, some researchers have suggested metal dampers such as added stiffness and damping dampers (ADAS), oval added stiffness and damping (EDAS), triangular added stiffness and damping (TADAS), U-shaped, ring, box and other types of dampers, in order to improve the behavior of convergent frame braces (CBF).

In the last few decades, the philosophy of designing important buildings against earthquakes has shifted from traditional and conventional methods, which are solely focused on increasing the strength and stiffness of the structure, to the use of energy dissipation systems. In the modern approach to designing structures, engineers constantly strive to enhance the structure's plasticity by utilizing some items of equipment known as dampers and energy absorbers. In this design philosophy, dampers act as a fuse and are yielded earlier than the rest of the members in order to prevent the occurrence of large non-linear deformations in the main members. This design approach is especially important in regions with high seismic activity, as it not only ensures the stability of the structure during an earthquake, but also allows for the replacement of energy-absorbing

components without damaging the remaining primary elements. As a result, the costs associated with repairing and reconstructing structures after an earthquake could be significantly reduced. By incorporating energy dissipation systems in a well-planned and suitable design, numerous benefits can be attained in both the construction of new buildings and the retrofitting of existing ones. With regard to these advantages, the following can be mentioned: increasing the damping and energy absorption of the structure, significantly reducing the acceleration and relative displacement of the floors, minimizing disruptions in structural service, reducing destructive deformations in structural and non-structural components, and minimizing damages related to internal equipment. These advantages encompass a significant increase in the structure's damping and energy dissipation, leading to a considerable reduction in floor acceleration and relative displacement.

There are various types of dampers, including friction dampers, viscous dampers, metal dampers, buckling dampers, and others. Energy dissipation in the mentioned systems has different mechanisms compared to each other. Among the existing steel dampers, shear dampers are of more interest due to their ease of construction, installation, repair and replacement after an earthquake, as well as their favorable performance in seismic behavior confirmed by laboratory and numerical studies. With the addition of a damper to the bracing member, the stiffness is obtained from the sum of the stiffness of the equivalent series springs. Based on this, although the utilization of shear dampers directly connected to the braces can prevent the buckling of the diagonal members within the concentric frame and enhance the system's energy absorption capacity, this approach simultaneously reduces the elastic stiffness of the lateral load-bearing system.

In this study, the effect of using LYP steel, in an I-shaped shear link, as a method to increase the seismic performance of the RC frame in terms of ultimate strength, stiffness, energy absorption and ductility is investigated. For the considered I-shaped shear link used as a damper, twelve models with different thicknesses of the damper's flanges and also various combinations of steel types (ST37 and LYP) have been compared to determine to what extent the RC frame is influenced and in which cases its seismic performance is notably improved.

## **2. Damper Details**

Although the acceptable performance of the damper under seismic loading is an important factor in evaluating the damper as a ductile element under the influence of seismic loads, the ease of construction, installation, and replacement after an earthquake are also considered as other important factors in the assessment of the damper. Thus, the damper shown in Figure 1 is suggested to strengthen the reinforced concrete frames, which fulfills both important factors of ease of construction and installation. As shown in Figure 1, these dampers are connected to the beginning of the concentrically braced elements, and by being yielded before the beam elements prevent their buckling. Therefore, it is expected to act like a ductile fuse. Also, their placement is such that they can be easily replaced after a severe earthquake.

For the construction of this damper, the use of both ST37 steel and LYP steel is feasible. The use of low yield point (LYP) steel is preferred for two reasons: 1) Although the system strength using low yield point steel is equal to that of conventional steels, the shear displacement of the system using LYP steel is less than that of other high carbon steels. 2) The ductility and energy dissipation capacity of LYP steel are much higher than conventional steel.

According to AISC 341-16, the damper's performance as a shear link is classified into three modes: Shear mechanism in the case that  $\rho \leq 1.6$ , shear-flexural mechanism in the case that

$2.6 > \rho > 1.6$ , and flexural mechanism by  $\rho \geq 2.6$ , where  $\rho = \frac{e}{M_p/V_p}$ . Studies in this field [43-46] have indicated that I-shaped links with shear yielding demonstrate better performance than links with flexural yielding; therefore, it is suggested that the proposed damper should be designed in such a way that the shear yielding mode occurs. Regarding article F3.5b.2 of AISC 341-16, design shear strength is determined using the expression of  $V_n \phi_v$ . Since the shear mechanism used for the damper is  $V_n = V_p$ , in this case, according to AISC 341-16 regulations, its shear strength is calculated from Equation (1):

$$V_p = 0.6 F_{yw} A_w \tag{1}$$

In Equation (1), the net section area of the web,  $A_w$ , equals  $bt_w$ , where  $b$  is the net depth of the web, and  $t_w$  is the web thickness. Additionally,  $F_{yw}$  stands for yield stress of the steel material utilized in the web.

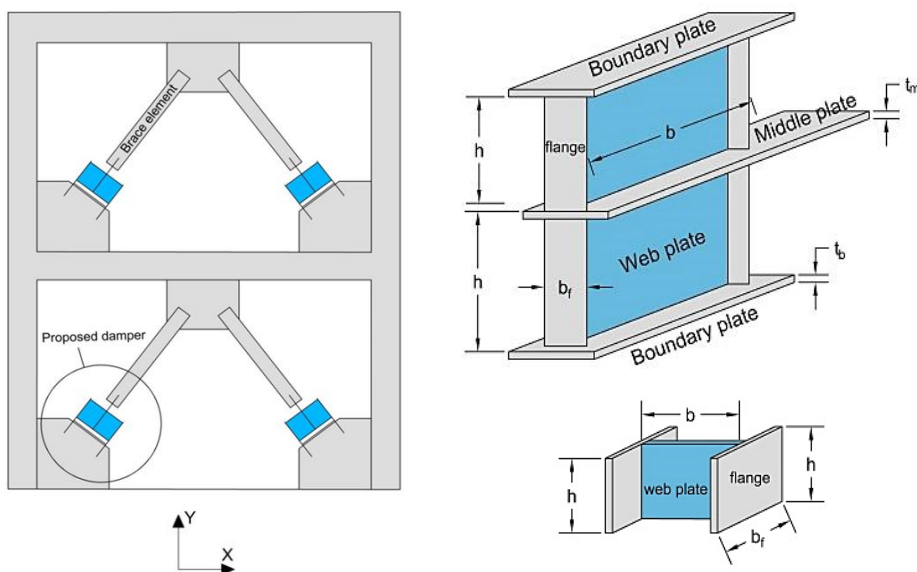


Fig. 1. Proposed damper

Although in AISC 341-16, the flange strength in shear capacity is ignored, in this article, referring to previous studies [47-50], the contribution of the flange in the shear capacity of the damper has been considered. Since two I-shaped dampers are utilized in the construction of the damper, a factor of 2 is applied; therefore, the shear capacity ( $V_d$ ) of the damper is suggested as follows:

$$V_d = 2(V_p + V_f) \tag{2}$$

In the above relationship,  $V_f$  is the shear capacity of the flange, which can be calculated from Equation (3).

$$V_f = \frac{4M_f}{h} \tag{3}$$

In above Equation (3),  $h$  represents the shear link height, which is shown in Figure 1. Additionally,  $M_f$  denotes the flexural capacity of the damper flange, which is obtained from

Equation (4), where  $F_{yf}$  represents the yield stress of the material of the flanges. Moreover,  $b_f$  and  $t_f$  stand for flanges width and thickness, respectively.

$$M_f = \frac{b_f t_f^2}{4} F_{yf} \quad (4)$$

$$V_{design} = \max \left\{ \begin{array}{l} 1.25 R_y V_d \\ \Omega V_d \end{array} \right. \quad (5)$$

After designing the shear damper, the brace has been designed for the intensified force according to Equation (5). The purpose of brace design for a force greater than the capacity of the damper is to yield the damper before the diagonal of the damper to ensure the fuse-like operation of the damper. In the above relation,  $R_y$  and  $\Omega$  are the ratio of ultimate stress to the yield stress of the damper material, and the over-strength factor of the damper, respectively.

### 3. Method of Study

In this article, a fixed thickness of 6 mm was considered for the damper web in all the examined models in the case that the steel type used is ST37, because when the steel material is changed to LYP, the thickness corresponding to the yield stress needs to be modified. Other dimensions of the damper such as the height of the web and the width of the flanges are unchanged in the studied models, while the thickness effect of the flange was examined in different cases with different steel materials. First, a damper was designed as a base model, in which the thickness of the web is 6 mm, the thickness of the flange is 20 mm, the width of the flange is 150 mm, and the depth of the web is 150 mm. After calculating the shear capacity of the brace using Equation (5), the steel braces within the reinforced concrete frame were designed for the obtained shear force, which was considered 2UNP120 for each brace. Then, the longitudinal and transverse reinforcements of the reinforced concrete frame were designed with the initial assumption of beam and column sections of 400×400 ( $mm^2$ ).

Table 1. Material properties of steel sections

| Material                 | Yield stress,<br>$F_y$ (MPa) | Ultimate tensile<br>strength,<br>$F_u$ (MPa) | Modulus of<br>elasticity,<br>$E$ (MPa) | Ultimate<br>strain |
|--------------------------|------------------------------|--|--|--------------------|
| ST37                     | 240                          | 370  | 200000                                 | 0.065              |
| Rebar ( $\emptyset 10$ ) | 486                          | 600  | 210000                                 | 0.15               |
| LYP100                   | 100                          | 257  | 153100                                 | 0.02               |

The details of reinforcements were designed for the lateral horizontal force resulted from the combined effects of the braces forces designed using ETABS [51] software. Figure 2 illustrates the specific details of the designed frame, and Table 1 provides the material specifications. To assess the impact of flange thickness on the shear strength of the damper, keeping other variables constant, dampers with a flange thickness of 5, 10, and 15 mm were analyzed. Also, to evaluate the effect of the type of steel on the performance of the system, dampers with two types of steel, ST37 and LYP, were investigated. Considering that the yield strength of LYP steel is about 2.4 times less than that of ST37, therefore, when using LYP, the thickness of that section was increased by 2.4 times to keep the shear strength constant. In Figure 2, details related to the dimensions of the concrete frame, the diagonal elements of the brace, and the dimensions and information of the beam and column sections can be observed. Within the ABAQUS [52] software, a single-floor frame (with one opening) was modeled and analyzed from the mentioned frame.

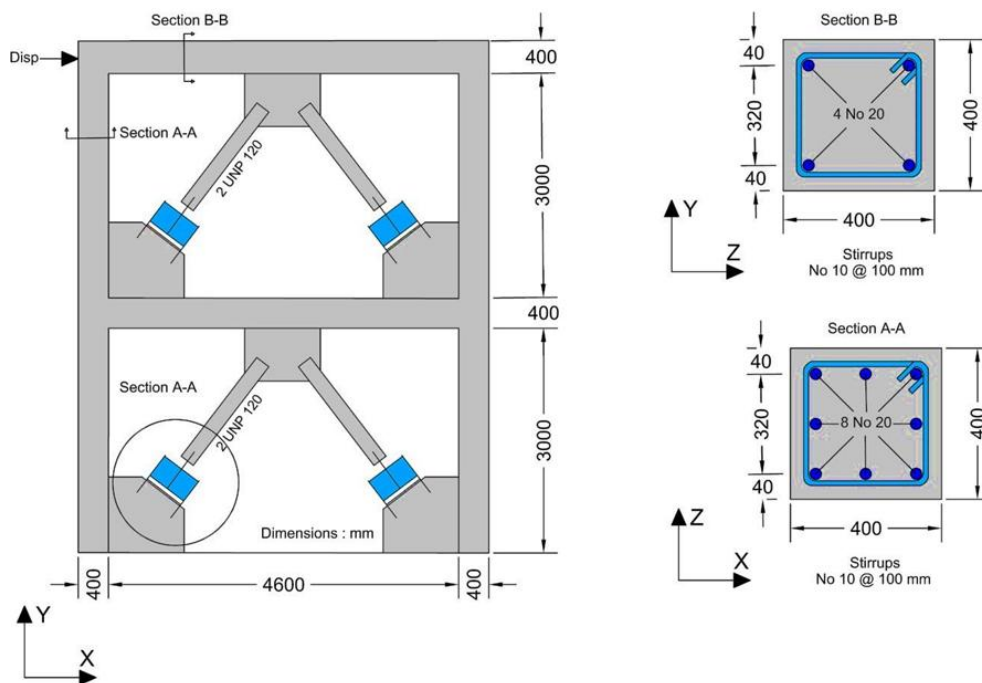


Fig. 2. Details of the frame (Dimensions in mm)

## 4. Numerical Study

### 4.1. Numerical Models

As described in the previous section, twelve models were analyzed, and categorized into four groups: 1) three damper models made of ST37 with flange thicknesses of 5mm, 10mm and 15mm, along with a 6mm web thickness; 2) three damper models with flange thicknesses of 5mm, 10mm and 15 mm made of ST37 steel, and the corresponding web thickness of 15 mm made of LYP100 steel; 3) three damper models with flanges and webs made of LYP, featuring flange thicknesses of 5mm, 10mm and 15mm, and a web thickness of 15mm; 4) three damper models with both the web and flanges made of LYP100 material, featuring flange thicknesses of 12mm, 24mm, and 36mm, and a web thickness of 15mm. It is necessary to mention that when changing the steel material from ST37 to LYP100, the corresponding thickness related to the yield stress must be taken into account. In other words, the web thickness of 6mm, which is initially used with ST37 steel, should be adjusted in order to account for the change in steel type to LYP100 with the coefficient  $\frac{F_{yw}(ST37)}{F_{yw}(LYP)} = \frac{240}{100} = 2.4$ ; therefore, when using LYP steel for the damper web, the thickness of the web is increased in this way:  $6 \times 2.4 = 14.4 \cong 15mm$ . Thus, the thickness of the components whose steel is changed from ST37 to LYP100 is modified in the mentioned way. Since the value of the parameter  $b$ , representing the depth of the I-shaped section, is constant in all models, according to Equation (1), the shear capacity in both corresponding cases is equal to each other. Table 2 displays the details related to the thickness and the utilized steel of the damper components in the studied models. In this Table, for each numerical model, a name has been chosen as  $M_f-t_f-M_w-t_w$ , which respectively represents



the material type of the flange plate, the thickness of the flange plate, the material type of the web plate, and the thickness of the web plate.

Table 2. Properties of models

| Model     | $t_f(mm)$ | $t_w(mm)$ | $M_f$  | $M_w$  |
|-----------|-----------|-----------|--------|--------|
| S-5-S-6   | 5         | 6         | ST37   | ST37   |
| S-10-S-6  | 10        | 6         | ST37   | ST37   |
| S-15-S-6  | 15        | 6         | ST37   | ST37   |
| S-5-L-15  | 5         | 15        | ST37   | LYP100 |
| S-10-L-15 | 10        | 15        | ST37   | LYP100 |
| S-15-L-15 | 15        | 15        | ST37   | LYP100 |
| L-5-L-15  | 5         | 15        | LYP100 | LYP100 |
| L-10-L-15 | 10        | 15        | LYP100 | LYP100 |
| L-15-L-15 | 15        | 15        | LYP100 | LYP100 |
| L-12-L-15 | 12        | 15        | LYP100 | LYP100 |
| L-24-L-15 | 24        | 15        | LYP100 | LYP100 |
| L-36-L-15 | 36        | 15        | LYP100 | LYP100 |

#### 4.2. Verification of Finite Element Results

In this article, the ABAQUS [52] software was used to simulate numerical models. In order to ensure the accuracy of the modeling and analysis of the finite element models, the laboratory test of TahamouliRoudsari *et al.* [53] was chosen for validation, which is similar to the model discussed in this article in terms of boundary conditions and the use of steel elements in the concrete frame. In Figure 3, the finite element modeling of the laboratory model derived from the referenced article [53] is displayed.

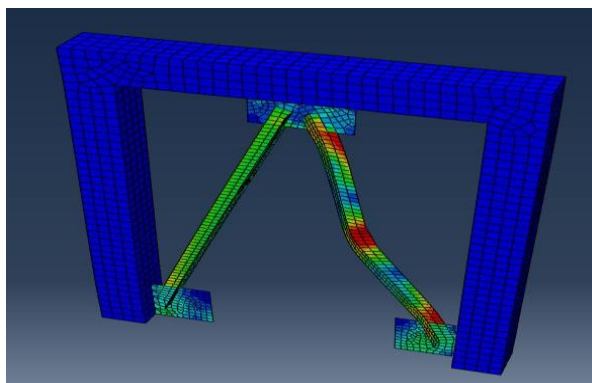


Fig. 3. The stress status of the validated FE model

The geometric and mechanical details, as well as the loading and boundary conditions, were applied according to the referenced paper [53] in the ABAQUS [52] software. Solid elements were used for modeling concrete elements, while shell elements were utilized for modeling the brace and gusset plates. Comparing the experimental results of

TahamouliRoudsari *et al.* [53] and the finite element results, as presented in Figure 4, shows the high accuracy of the FE modeling.

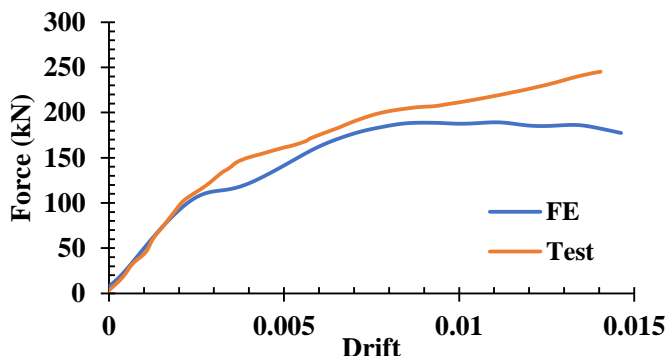


Fig. 4. Comparing the results of the experimental test model with the FE model

## 5. Results and Discussion

### 5.1. Investigating the Effect of Flanges Thickness on The Stiffness and Strength of The Studied Frame

The push-over and bilinear curves of the models can be seen in Figures 5, 6 and 8 in terms of investigating the effect of increasing the flanges thickness. In the models of the diagram in Figure 5, a comparison has been made between the models in which all damper components are made of ST37 steel. The diagrams in Figure 6 are related to the models in which the damper web is made of LYP steel, and the damper flanges are made of ST37. The graphs in Figure 8 compare the models in which the entire damper components are made of LYP steel. Also, all the results of the analysis of the models are given in Table 3.

In Figure 5, as the thickness of the damper flanges increases, the slope of the bilinear curves in the elastic region, which represents the stiffness of the frame, also increases. Moreover, the increase in the ultimate strength of the studied frame with the increase in the thickness of the flanges is clearly observable in this diagram. According to Table 3, by increasing the flanges thickness from 5 mm to 10 mm, the frame stiffness is increased by 8 percent. Furthermore, with an increase in the flanges thickness from 5 mm to 15 mm, the percentage increase in stiffness reaches 16%. This indicates that in models where all the damper components are made from ST37, the frame stiffness is improved by increasing the flanges thickness from 5 mm to 15 mm. Regarding the system shear strength, based on Table 3, it can be inferred that a rise in the flanges thickness from 5 mm to 10 mm results in a 13% growth in shear strength. This percentage increase in strength, when the flanges thickness of damper changes from 5 mm to 15 mm, reaches 25%. Therefore, in the group of models where all damper components are made of ST37, the final strength of the frame improves with an increase in the thickness of the flanges.

According to the graphs in Figure 6, it can be seen that with the growth in the thickness of the damper flanges, the stiffness of the system is grown. Although the stiffness of the system in this group, in which the damper is made of LYP, is increased with the rise of the thickness of the flanges, the ultimate strength of the system is decreased. As the values in Table 3 show, the stiffness of the frame rises by 5% as the thickness of the damper flanges is increased from 5 mm to 10 mm, and this stiffness growth in the case where the thickness of the damper flanges is increased from 5 mm to 15 mm, is reached 11 percent. However,

by increasing the thickness from 5 mm to 10 mm, the shear strength of the system has decreased by 3%, and by increasing the thickness of the damper flanges from 5 mm to 15 mm, the system strength has declined by 13%. With regard to Figure 7, it is evident that with an increase in the thickness of LYP flanges from 5 mm to 10 mm, the ultimate strength, stiffness, and energy absorption grow by a percentage of 2-5%. Furthermore, in model L-15-L-15, despite a negligible decrease in the ultimate strength compared to model L-5-L-15, the stiffness and energy absorption of the frame show a rise of 9% and 7%, respectively.

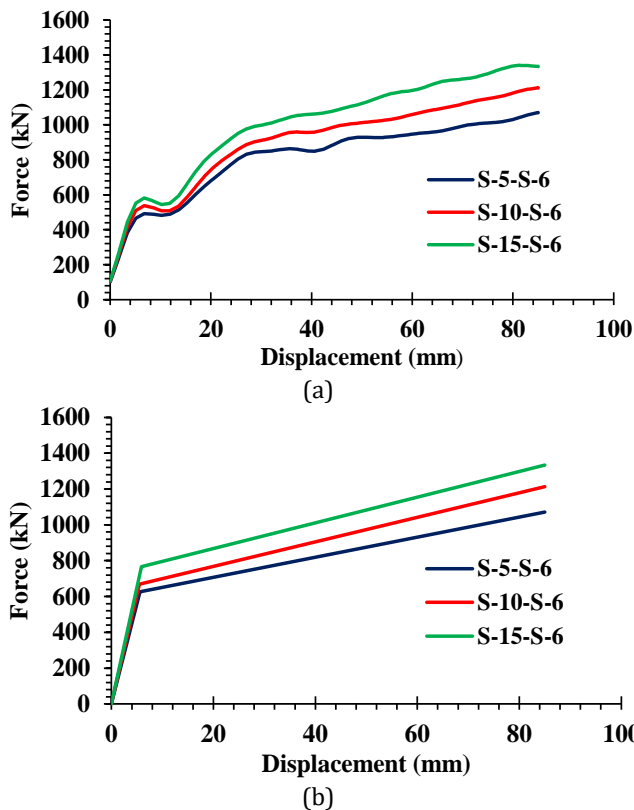


Fig. 5. Comparing the models whose dampers are made from ST37: (a) push-over curves, (b) bilinear graphs of (a)

By analyzing the graphs in Figure 8, it can be observed that by increasing the thickness of the damper flanges from 12 mm (thickness corresponding to 5 mm in the state of flanges made from ST37) to 24 and 36 mm (thicknesses corresponding to 10 and 15 mm in the state of flanges made from ST37, respectively), the stiffness of the frame is grown. The results in Table 3 show that with the rise in thickness from 12 mm to 24 mm, the stiffness of the frame is increased by 12%. In addition, when the thickness of flanges changes from 12 mm to 36 mm, the percentage increase in the frame stiffness reaches 22 percent.

Additionally, the frame shear strength is reduced by 7% with the increase in the thickness of the flanges from 12 mm to 24 mm. However, with the growth in the thickness of the flanges from 12 to 36 mm, the system shear strength shows a slight increase of 1%. Thus, in the comparison made for Figures 5, 6, and 8, it is concluded that the stiffness rises with the growth in the thickness of the flanges. However, considering the impact of increasing the flanges thickness on system strength in Figures 6 and 8, it can be inferred that while the increase in flanges thickness contributes to a decrease in frame strength, this reduction

is generally not a significant magnitude. Consequently, increasing the thickness of the flanges within the range of 5 to 15 mm notably enhances the stiffness and strength of the analyzed frame in most models.

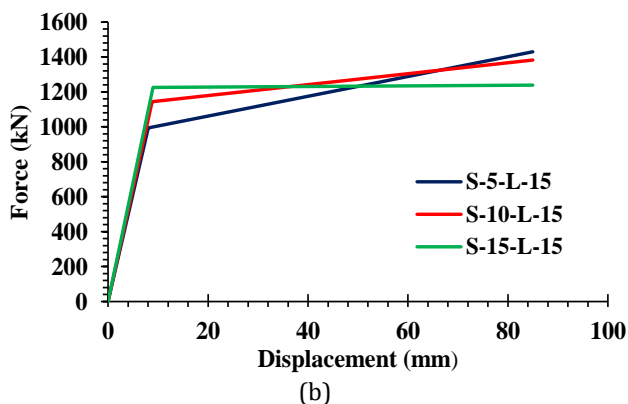
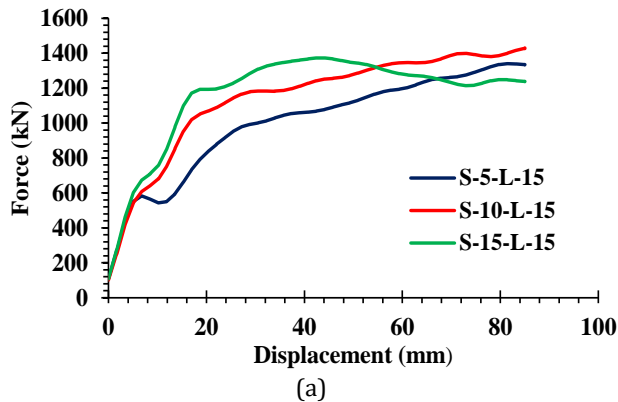
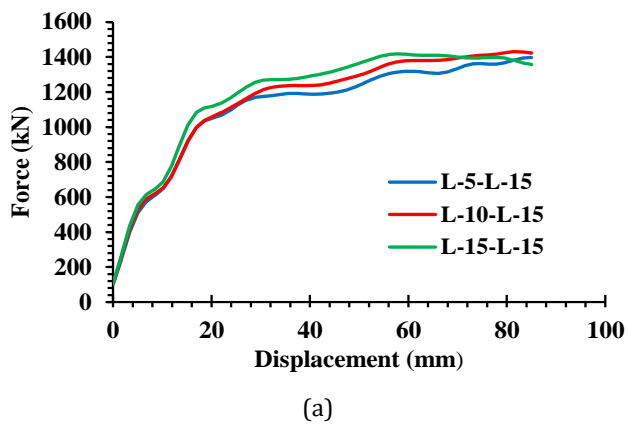
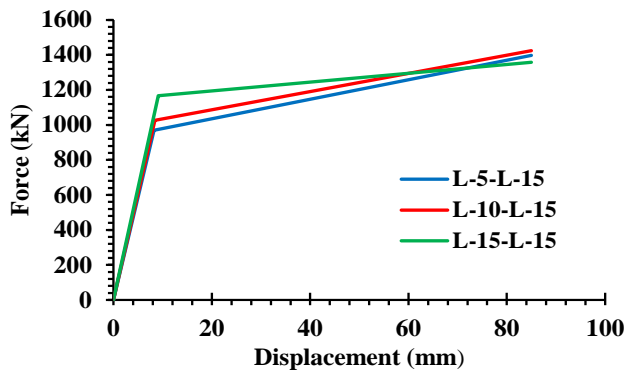


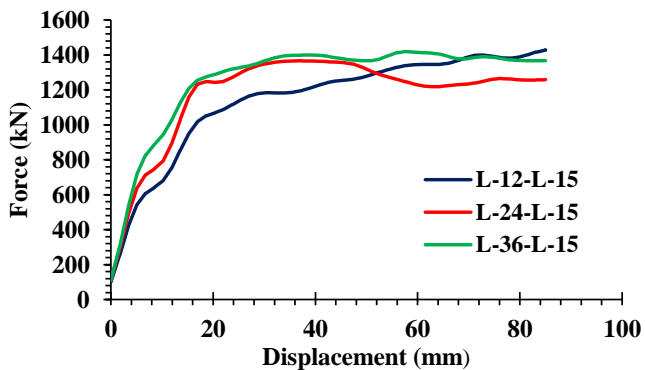
Fig. 6. Comparing the models whose webs of dampers are only made from LYP: (a) push-over curves, (b) bilinear graphs of (a)



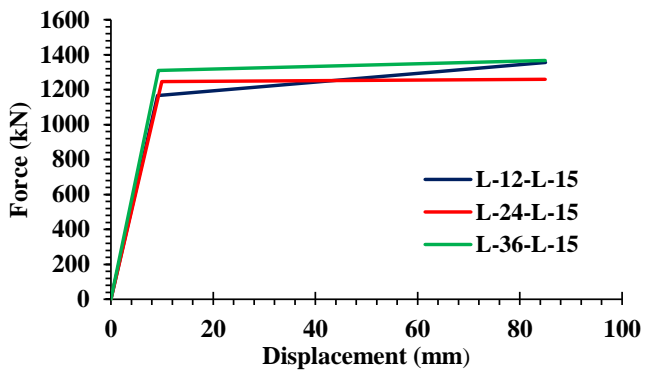


(b)

Fig. 7. Comparing the models whose all plates of dampers are made from LYP: (a) push-over curves, (b) bilinear graphs of (a)



(a)



(b)

Fig. 8. Comparing the models whose all plates of dampers are made from LYP: (a) push-over curves, (b) bilinear graphs of (a)

Table 3. Comparison of values based on increasing thickness of damper's flanges

| Model     | Ultimate strength, $V_u$ (kN) | $\psi^*$ | Stiffness, $K$ ( $\frac{kN}{mm}$ ) | $\psi^*$ | Energy absorption, EA (kN.mm) | $\psi^*$ |
|-----------|-------------------------------|----------|------------------------------------|----------|-------------------------------|----------|
| S-5-S-6   | 1071.07                       |          | 111.97                             |          | 69173.37                      |          |
| S-10-S-6  | 1212.41                       | 1.13     | 121.42                             | 1.08     | 76624.23                      | 1.11     |
| S-15-S-6  | 1334.32                       | 1.25     | 129.9                              | 1.16     | 85364.20                      | 1.23     |
| S-5-L-15  | 1429.48                       |          | 123.47                             |          | 97219.09                      |          |
| S-10-L-15 | 1383.14                       | 0.97     | 129.86                             | 1.05     | 101297.78                     | 1.04     |
| S-15-L-15 | 1238.69                       | 0.87     | 136.49                             | 1.11     | 99172.13                      | 1.02     |
| L-5-L-15  | 1398.27                       |          | 117.68                             |          | 94894.65                      |          |
| L-10-L-15 | 1424.61                       | 1.02     | 122.34                             | 1.04     | 98176.37                      | 1.03     |
| L-15-L-15 | 1358.46                       | 0.97     | 128.47                             | 1.09     | 101185.11                     | 1.07     |
| L-12-L-15 | 1355.99                       |          | 128.19                             |          | 101021.76                     |          |
| L-24-L-15 | 1258.93                       | 0.93     | 143.52                             | 1.12     | 100176.55                     | 0.99     |
| L-36-L-15 | 1366.79                       | 1.01     | 156.3                              | 1.22     | 107409.77                     | 1.06     |

\* The ratio of values to the base model in each category.

## 5.2. Investigating The Effect of Flanges Thickness on The Behavior Factor and Over-Strength Coefficient of The Studied Frame

In Table 4, the results of the behavior factor and over-strength coefficient related to the investigated models are evident. In the group of models in which the entire damper plates are made of ST37 steel, with the increase in flanges thickness from 5 mm to 10 mm and 15 mm, the coefficient of behavior is increased by a negligible amount of 1% and 3% (respectively). Regarding the over-strength coefficient, by increasing the flanges thickness from 5 mm to 10 mm, no significant effect can be seen in this parameter (one percent decrease).

Table 4. Comparison of behavior factor (R) and over-strength ( $\Omega$ ) based on increasing damper's flange

| Model     | R     | $\psi^*$ | $\Omega$ | $\psi^*$ |
|-----------|-------|----------|----------|----------|
| S-5-S-6   | 10.37 |          | 1.65     |          |
| S-10-S-6  | 10.49 | 1.01     | 1.63     | 0.99     |
| S-15-S-6  | 10.7  | 1.03     | 1.74     | 1.05     |
| S-5-L-15  | 11.7  |          | 2.37     |          |
| S-10-L-15 | 11.65 | 0.99     | 2.6      | 1.10     |
| S-15-L-15 | 11.25 | 0.96     | 2.65     | 1.12     |
| L-5-L-15  | 11.85 |          | 2.43     |          |
| L-10-L-15 | 11.83 | 0.99     | 2.48     | 1.02     |
| L-15-L-15 | 11.72 | 0.98     | 2.68     | 1.10     |
| L-12-L-15 | 11.72 |          | 2.69     |          |
| L-24-L-15 | 11.02 | 0.94     | 2.52     | 0.94     |
| L-36-L-15 | 10.95 | 0.93     | 2.44     | 0.91     |

\* The ratio of values to the base model in each category.

Also, by increasing the thickness of the flanges from 5 mm to 15 mm, this coefficient is increased by 5 percent. In the second group of models in which only the web plate of the damper is made of LYP, by increasing the thickness of the damper flange from 5 mm to 10 and 15 mm, no significant effect on the behavior coefficient can be seen, while this amount of growth in the thickness of the flanges is led to an increase of about 10% in the over-strength coefficient amount. According to the third group of models with LYP flanges and webs, there is no remarkable improvement in the behavior factor (R) by changing the thickness of the flanges from 5mm to 10mm and 15mm. However, model L-15-L-15 indicates a growth of 10% in the over-strength factor ( $\Omega$ ) in comparison with model L-5-L-15. Also, in the group of models where the entire damper plates are made of LYP, the increase in the thickness of the damper flanges results in a 6-7% decrease in the behavior coefficient. Also, this trend in the thickness of the damper flanges leads to a decrease in the over-strength coefficient (a decrease between 5 and 10%).

### **5.3. Investigating The Impact of Damper Steel Type on The Strength, Stiffness, And Energy Absorption of The Analyzed Frame**

In Figures 9 to 23, the models have been compared to examine the impact of steel type on the structural parameters of the system. Figure 9 clearly demonstrates the positive effect of using LYP steel in the damper. The stiffness of model S-5-L-15 increases by 10% compared to the base model in this group (S-5-S-6). Additionally, the frame strength in this comparison rises by 33%.

In Figure 10, a comparison has been made between the model in which all damper components are made from LYP and the case where all damper components are made of ST37. The positive effect of using steel with low yield stress on stiffness and strength can be seen in this diagram. As it is evident from Table 5, using LYP steel in all damper components results in a 14% growth in system stiffness and a 27% increase in ultimate strength. It can be observed that this process of enhancing stiffness and strength is apparent in the remaining diagrams, except for the model in Figure 22. According to the diagram in Figure 22 and as indicated in Table 5, the model with the characteristic S-15-L-15, compared to the base model of this group (S-15-S-6), has shown a 7% reduction in strength. As a result, it can be generally concluded that when steel with low yield stress is used in the damper components, although in some cases the ultimate strength value may decrease by less than 10%, the system's overall improvement is evident across all comparisons in terms of system stiffness. Moreover, according to Table 5 and the comparative Figures in this section, the system's energy absorption is significantly improved due to the usage of LYP in the damper web or the entire damper, instead of using ST37 steel.

Regarding to Figures 13 to 15, the models in the third group show better performance in terms of energy absorption and ultimate resistance than the ST37 models (the first group of models). In this comparison, the stiffness of the frame is almost constant and without significant change. According to Figures 16 to 18, the third group of models does not show a remarkable difference in ultimate strength, stiffness, and energy absorption when they are compared to the second group peer-to-peer. However, Figure 24 shows that the stress distribution in the third group is significantly better than in the second group. While Figures 19 to 21 and Figure 24 demonstrate that the fourth group of models exhibits higher stiffness and energy absorption compared to the third group, the stress distribution in the studied frame is more favorable when using the third group of damper models.

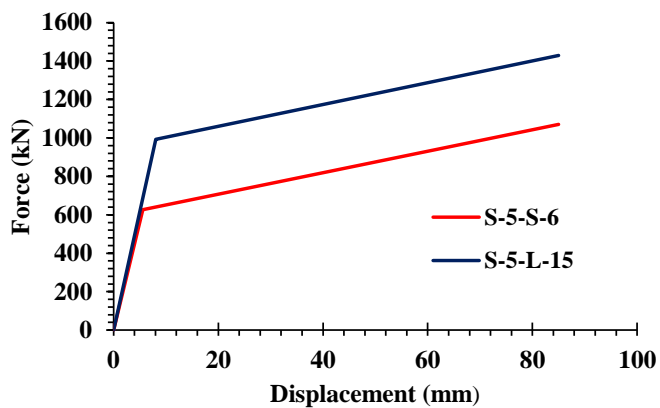


Fig. 9. Comparing S-5-S-6 with S-5-L-15

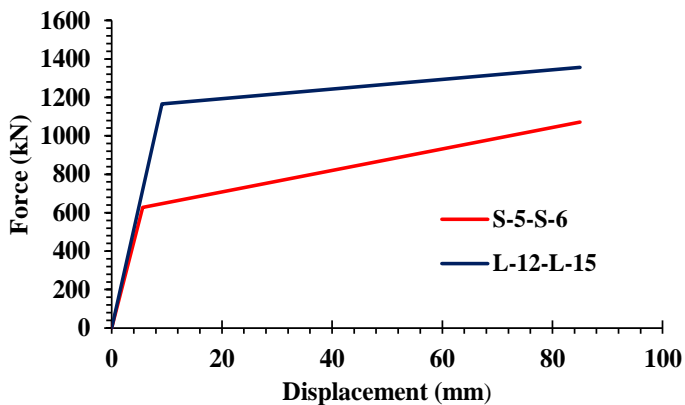


Fig. 10. Comparing S-5-S-6 with L-12-L-15

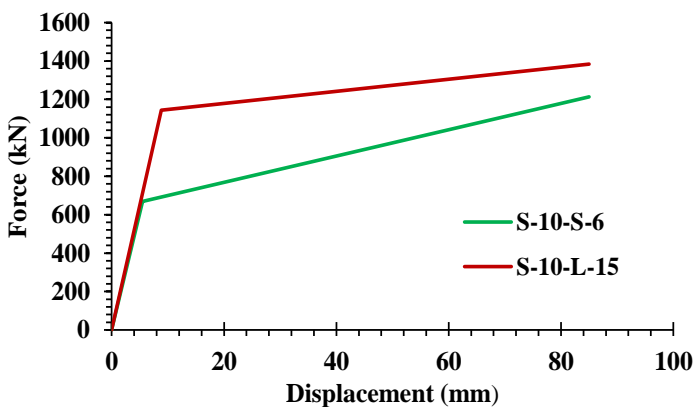


Fig. 11. Comparing S-10-S-6 with S-10-L-15



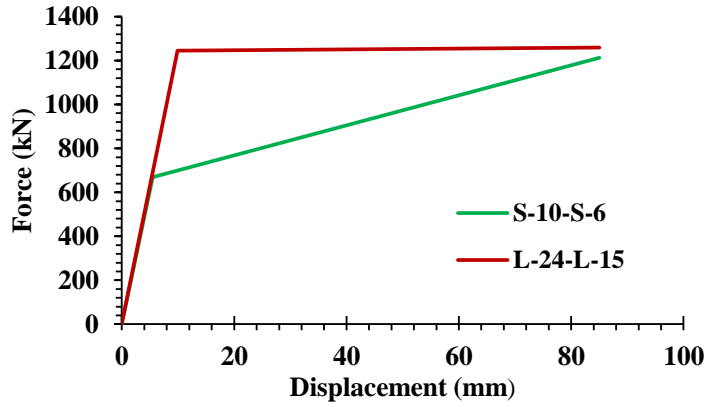


Fig. 12. Comparing S-10-S-6 with L-24-L-15

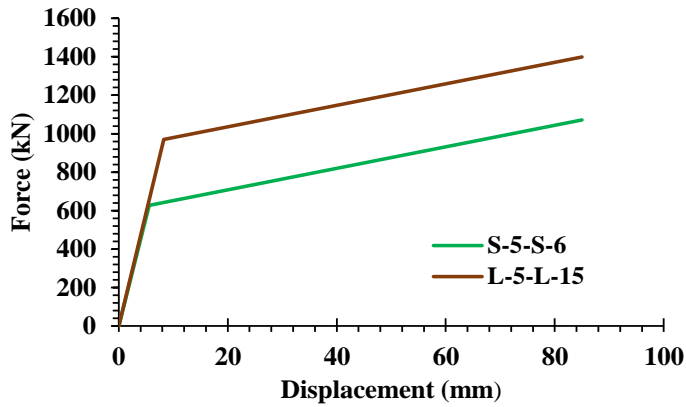


Fig. 13. Comparing S-5-S-6 with L-5-L-15

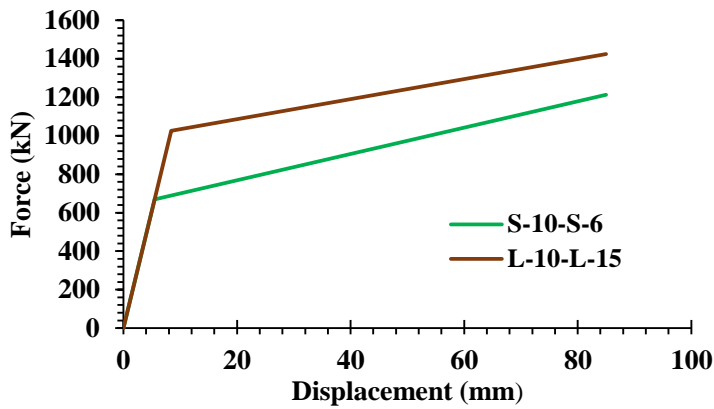


Fig. 14. Comparing S-10-S-6 with L-10-L-15

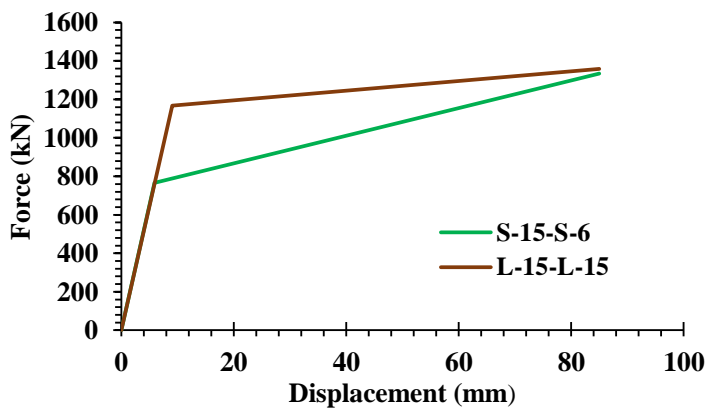


Fig. 15. Comparing S-15-S-6 with L-15-L-15

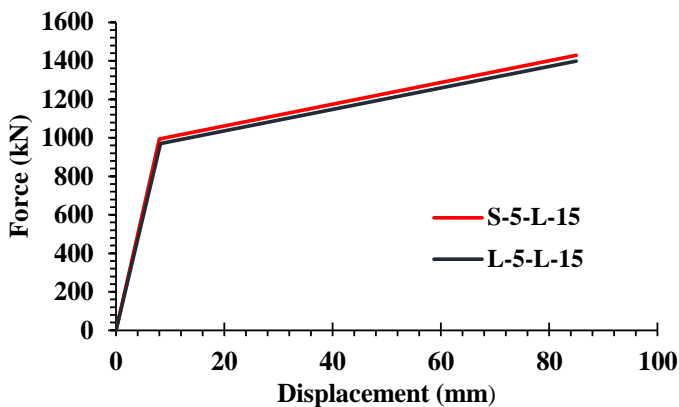


Fig. 16. Comparing S-5-L-15 with L-5-L-15

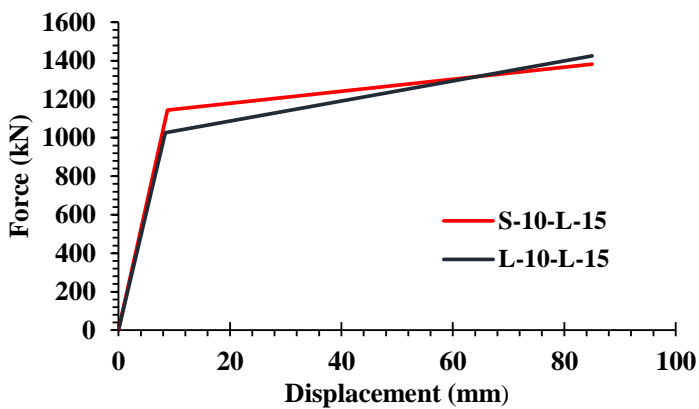


Fig. 17. Comparing S-10-L-15 with L-10-L-15

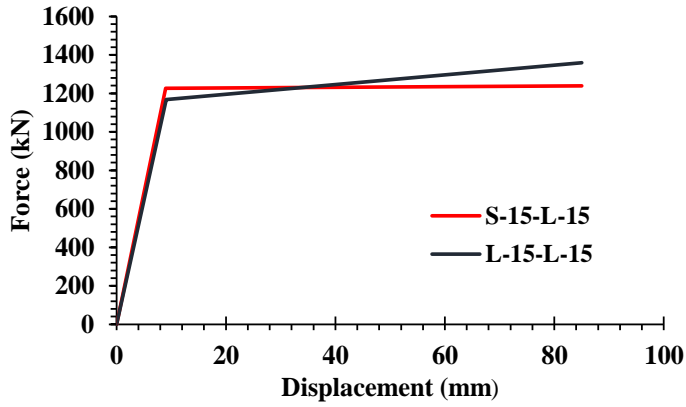


Fig. 18. Comparing S-15-L-15 with L-15-L-15

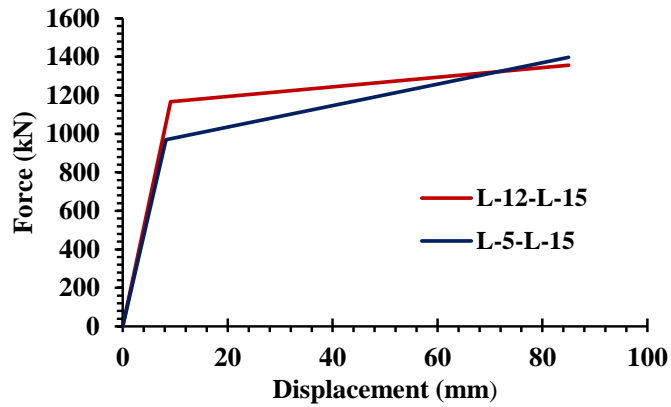


Fig. 19. Comparing L-12-L-15 with L-5-L-15

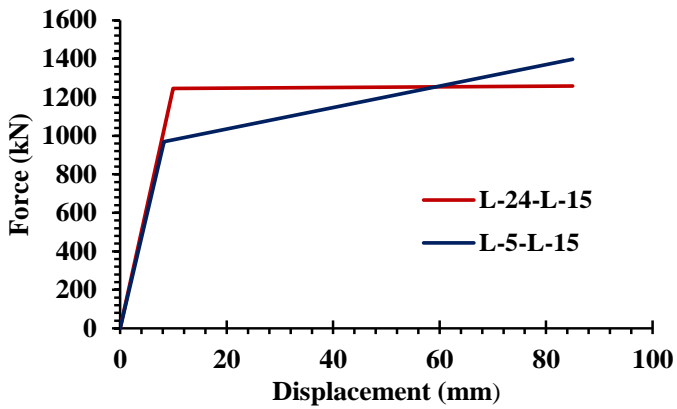


Fig. 20. Comparing L-24-L-15 with L-5-L-15

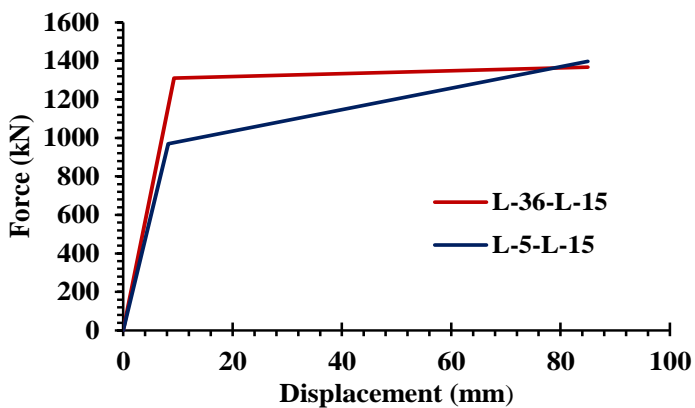


Fig. 21. Comparing L-36-L-15 with L-5-L-15

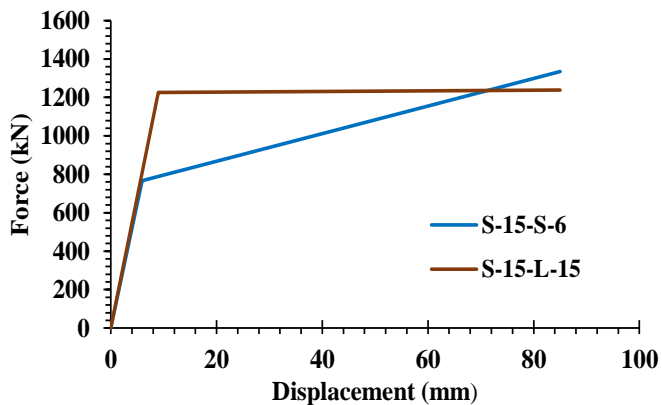


Fig. 22. Comparing S-15-S-6 with S-15-L-15

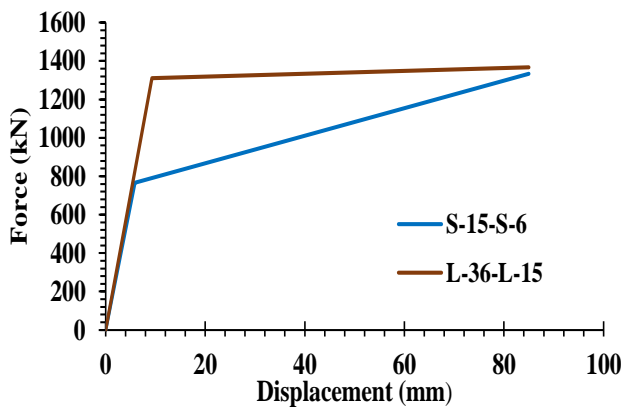


Fig. 23. Comparing S-15-S-6 with L-36-L-15

Table 5. The structural parameters of the LYP damper divided by the parameters of the ST37 damper

| Model     | Ultimate strength, $V_u(kN)$ | $\psi^*$ | $\psi^{**}$ | Stiffness, $K(\frac{kN}{mm})$ | $\psi^*$ | $\psi^{**}$ | Energy Absorption, EA (kN.mm) | $\psi^*$ | $\psi^{**}$ |
|-----------|------------------------------|----------|-------------|-------------------------------|----------|-------------|-------------------------------|----------|-------------|
| S-5-S-6   | 1071.07                      |          |             | 111.97                        |          |             | 69173.37                      |          |             |
| S-10-S-6  | 1212.41                      |          |             | 121.42                        |          |             | 76624.23                      |          |             |
| S-15-S-6  | 1334.32                      |          |             | 129.9                         |          |             | 85364.20                      |          |             |
| S-5-L-15  | 1429.48                      | 1.33     |             | 123.47                        | 1.10     |             | 97219.09                      | 1.41     |             |
| S-10-L-15 | 1383.14                      | 1.14     |             | 129.86                        | 1.07     |             | 101297.78                     | 1.32     |             |
| S-15-L-15 | 1238.69                      | 0.93     |             | 136.49                        | 1.05     |             | 99172.13                      | 1.16     |             |
| L-5-L-15  | 1398.27                      | 1.30     | 0.98        | 117.68                        | 1.05     | 0.95        | 94894.65                      | 1.37     | 0.98        |
| L-10-L-15 | 1424.61                      | 1.18     | 1.03        | 122.34                        | 1.01     | 0.94        | 98176.37                      | 1.28     | 0.97        |
| L-15-L-15 | 1358.46                      | 1.02     | 1.10        | 128.47                        | 0.99     | 0.94        | 101185.11                     | 1.18     | 1.02        |
| L-12-L-15 | 1355.99                      | 1.27     | 0.95        | 127.98                        | 1.14     | 1.04        | 101021.76                     | 1.46     | 1.04        |
| L-24-L-15 | 1258.93                      | 1.04     | 0.91        | 125.3                         | 1.03     | 0.96        | 100176.55                     | 1.31     | 0.99        |
| L-36-L-15 | 1366.79                      | 1.02     | 1.10        | 140.89                        | 1.08     | 1.03        | 107409.77                     | 1.26     | 1.08        |

$$\psi^*: \left(\frac{S-L-i-L-15}{S-i-S-6}\right), \psi^{**}: \left(\frac{L-i-L-15}{S-i-L-15}\right)$$

#### 5.4. Investigating The Impact Of Damper Steel Type On The Behavior Factor and Over-Strength Coefficient of The Analyzed Frame

Referring to Table 6, while the utilization of steel with low yield stress, either in the damper web or in all its components, increases the behavior factor to some extent, the substantial rise in the values of the over-strength coefficient is more significant (approximately an increase of 40% and 60%).

Table 6. Behavior factor (R) and over-strength ( $\Omega$ ) coefficient of the LYP damper divided by factors of the ST37 damper

| Model     | R     | $\psi^*$ | $\psi^{**}$ | $\Omega$ | $\psi^*$ | $\psi^{**}$ |
|-----------|-------|----------|-------------|----------|----------|-------------|
| S-5-S-6   | 10.37 |          |             | 1.65     |          |             |
| S-10-S-6  | 10.49 |          |             | 1.63     |          |             |
| S-15-S-6  | 10.7  |          |             | 1.74     |          |             |
| S-5-L-15  | 11.7  | 1.13     |             | 2.37     | 1.44     |             |
| S-10-L-15 | 11.65 | 1.11     |             | 2.6      | 1.60     |             |
| S-15-L-15 | 11.25 | 1.05     |             | 2.65     | 1.52     |             |
| L-5-L-15  | 11.85 | 1.14     | 1.01        | 2.43     | 1.47     | 1.03        |
| L-10-L-15 | 11.83 | 1.13     | 1.02        | 2.48     | 1.52     | 0.95        |
| L-15-L-15 | 11.72 | 1.10     | 1.04        | 2.68     | 1.54     | 1.01        |
| L-12-L-15 | 11.72 | 1.13     | 1           | 2.69     | 1.63     | 1.14        |
| L-24-L-15 | 11.02 | 1.05     | 0.946       | 2.52     | 1.55     | 0.97        |
| L-36-L-15 | 10.95 | 1.02     | 0.973       | 2.44     | 1.40     | 0.92        |

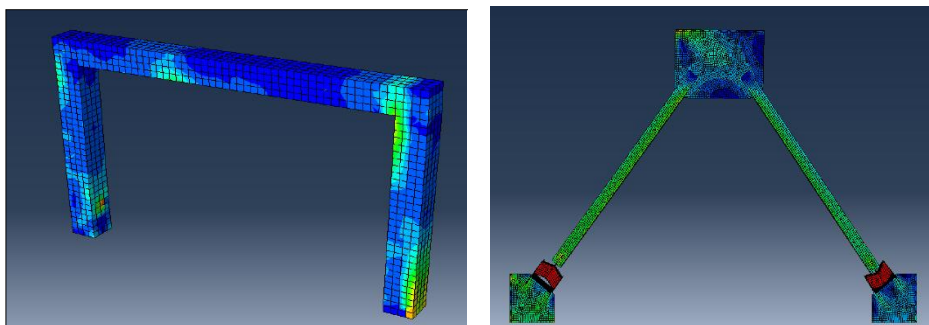
$$\psi^*: \left(\frac{S-L-i-L-15}{S-i-S-6}\right), \psi^{**}: \left(\frac{L-i-L-15}{S-i-L-15}\right)$$

Consequently, the use of LYP steel instead of ST37 elevates the behavior and over-strength coefficients of the studied frame, and this elevation is more pronounced in the case of the over-strength coefficient.

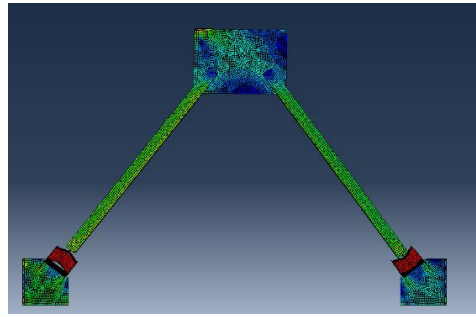
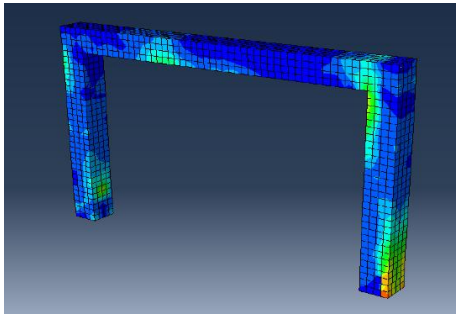
### 5.5. Reviewing the Stress Distribution In Structural Members

To consider the impact of adding the proposed damper to the RC frame on the stress distribution, the status of the stresses is shown in Figure 24. The stresses in the RC frame and the steel elements are shown separately for each case to provide a clearer understanding of the stress distribution. Referring to Figure 24, in the cases of (a), (b) and (c), the dampers are obviously yielded, whereas the other parts of the structures remain elastic. Since the studied frame in this paper was designed based on the capacity of the damper made of ST37 steel (as described in section 3), in the presented models in which all damper components are made of ST37 steel, the provided equation (5) for the damper design is satisfied, and the damper acts as a ductile fuse, as was shown in Figures 24(a), 24(b), and 24(c).

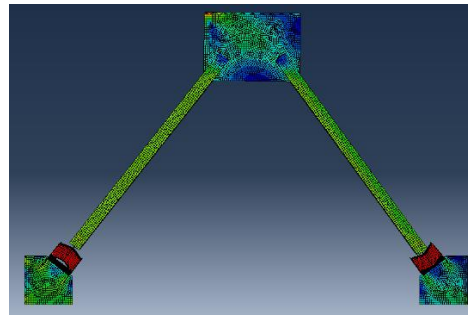
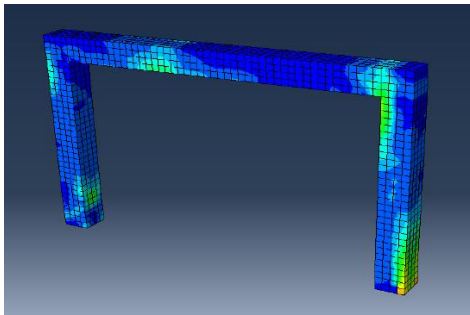
On the other hand, by utilizing LYP steel, in some cases such as (e), (f), (k) and (l), stress is transferred from the damper to the brace elements. This difference in stress distribution of ST37 and LYP models, despite identical shear capacities for ST37 and LYP models, is due to the distinct behavior of LYP steel. In fact, it is expected that based on the equations proposed to predict the shear behavior of each shear plate (or shear link), the shear capacity will be obtained based on the yield stress and its thickness. Therefore, to maintain this shear strength in both types of ST37 and LYP dampers, the same capacity was considered to predict and evaluate their nonlinear behavior. Expected results according to Figure 24 show that owing to the strain-hardening impact of the LYP steel, the ultimate strength of the LYP dampers is greater than the expected value. For this reason, if the LYP damper is designed based on the relationships governing the ST37 damper, the damper may cause buckling of the brace elements. Therefore, the members outside the LYP damper should be designed for amplified forces. Additionally, the LYP models exhibited higher energy absorption, stiffness, ultimate strength, behavior factor, and over-strength compared to the ST37 models, as shown in Table 5, demonstrating LYP effectiveness in enhancing the seismic performance. The LYP models (g), (h) and (i) with lower thickness of flanges indicate better status of stress distribution compared to models (j), (k), and (l), which suggests that the mere use of LYP steel does not guarantee the improvement of the frame's behavior, and this is subject to the thickness of the damper's flanges.



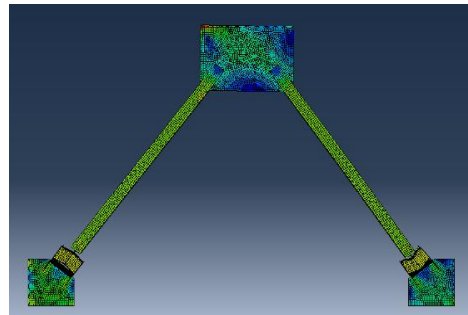
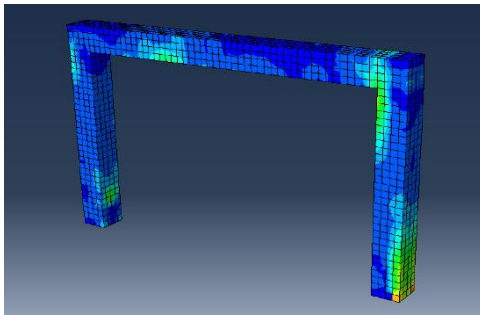
(a) S-5-S-6



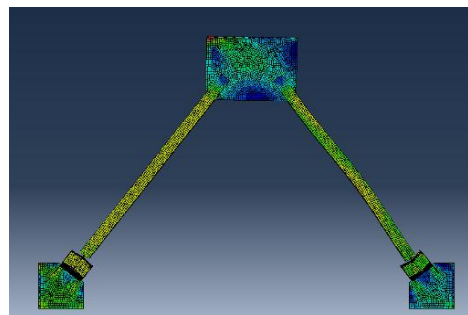
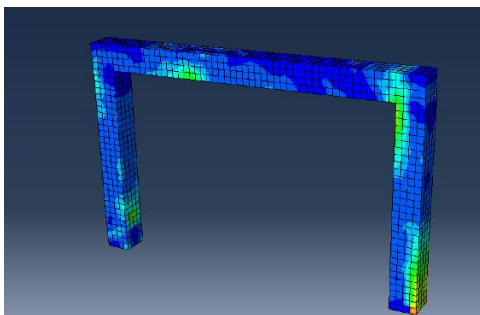
(b) S-10-S-6



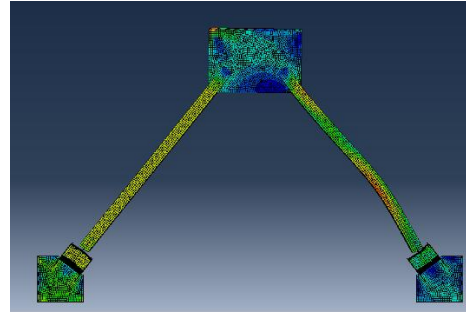
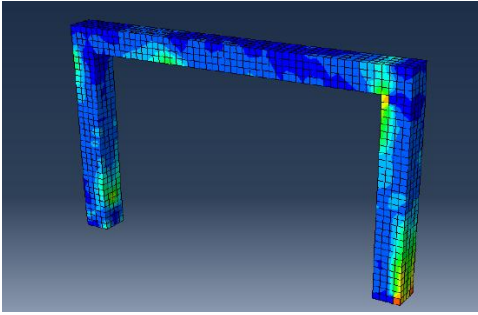
(c) S-15-S-6



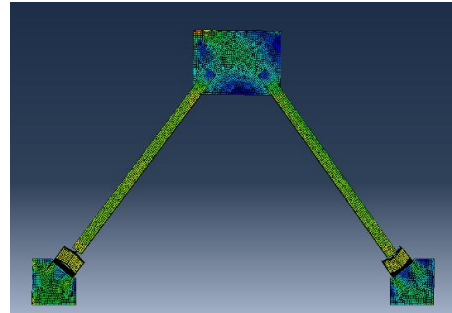
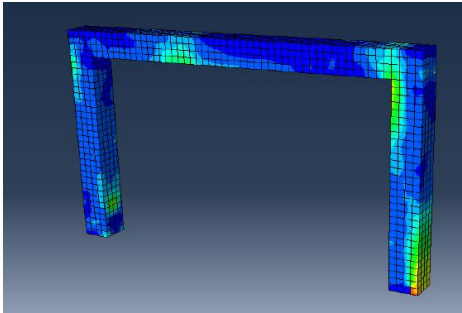
(d) S-5-L-15



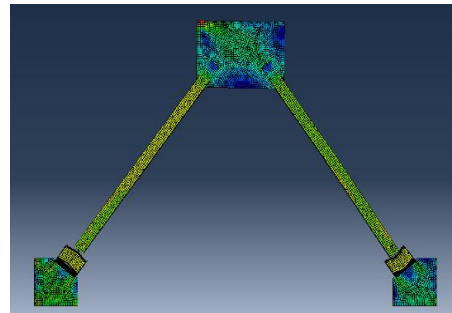
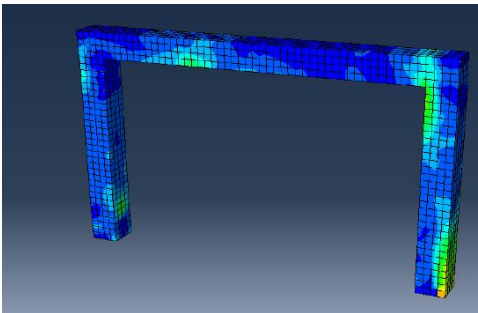
(e) S-10-L-15



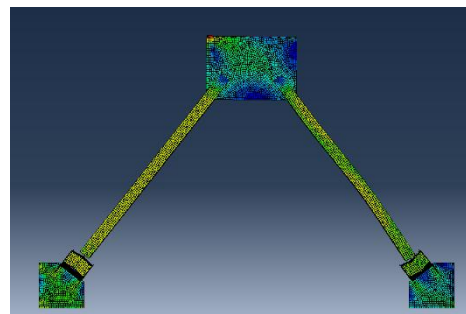
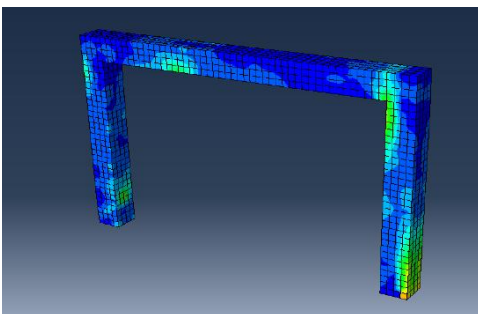
(f) S-15-L-15



(g) L-5-L-15

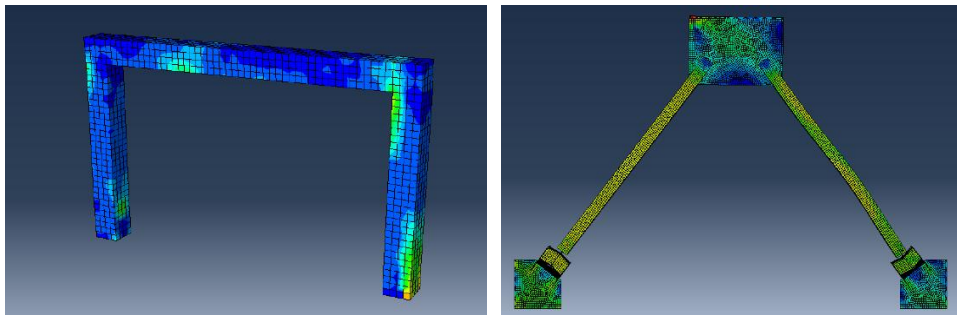


(h) L-10-L-15

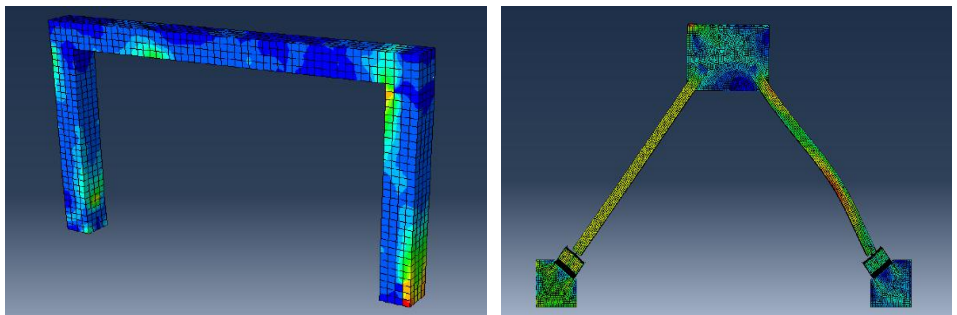


(i) L-15-L-15

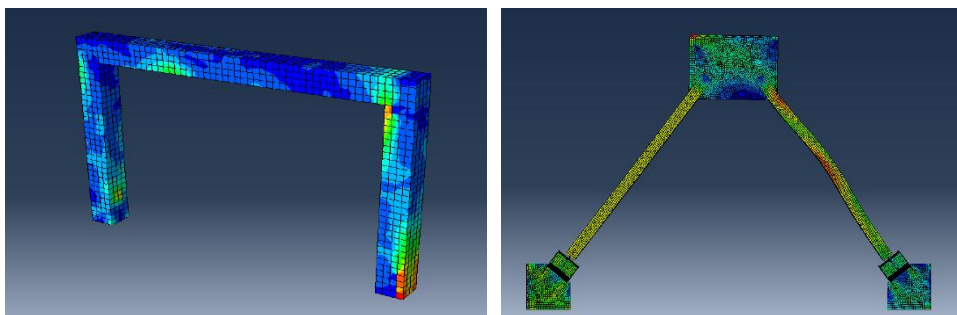




(j) L-12-L-15



(k) L-24-L-15



(l) L-36-L-15

Fig. 24. Distribution of stresses

## 6. Conclusions

In this paper, the effects of the steel type and the thickness of the damper flanges, pertaining to an I-shaped shear link, on the ultimate strength, stiffness, energy absorption, behavior factor, and over-strength coefficient were investigated. The findings are summarized in the following:

- In the group of models where all damper components are made of ST37 steel, an increase in the thickness of damper flanges leads to an increase in the system's stiffness, ultimate strength, and energy absorption. Furthermore, this growth in

damper flange thickness indicates an increase in the behavior and over-strength coefficient by 1 to 5 percent.

- With reference to the models where only the damper web is constructed using LYP steel, an increase in the thickness of the damper flanges has led to a decrease in ultimate strength by 3 to 13 percent, while the system's stiffness and energy absorption are increased. Additionally, the behavior coefficient is decreased by 1 to 4 percent, while the additional resistance coefficient is increased by 10 percent.
- In the group of models where the entire damper is made of LYP, increasing the thickness of the damper flanges has resulted in a reduction in strength by approximately 7 percent. Meanwhile, both stiffness and energy absorption are increased. Additionally, there is a decrease of approximately 5 to 10 percent in both the behavior coefficient and the over-strength coefficient.
- Using LYP steel is led to an increase in the parameters of stiffness, ultimate strength, energy absorption, behavior coefficient, and over-strength coefficient. However, the positive impact of using LYP on the energy absorption parameter and the over-strength coefficient is more noticeable. This indicates that the use of LYP steel not only improves the system's stiffness and strength, but also enhances the energy absorption capacity and ductility of the system.
- The LYP models in the third group demonstrate that using LYP steel enhances the seismic behavior of the RC frame in terms of ultimate strength, stiffness, energy absorption, behavior factor, and over-strength compared to the ST37 models.
- A comparison of the third and fourth groups of models reveals that while LYP steel can enhance the seismic behavior of the frame, the degree of improvement is contingent upon the thickness of the damper plates.
- The use of LYP steel in the studied I-shaped shear link has a significant role in enhancing the performance of concentrically braced reinforced concrete frames in terms of ultimate strength, stiffness, ductility, and energy absorption, provided that the related equations for the damper design are satisfied.

## References

- [1] Avcil F, Işık E, İzol R, Büyüksaraç A, Arkan E, Arslan MH, Aksoyulu C, Eyisüren O, Harirchian E. Effects of the February 6, 2023, Kahramanmaraş earthquake on structures in Kahramanmaraş city. *Natural Hazards*, 2024; 120: 2953-2991. <https://doi.org/10.1007/s11069-023-06314-1>
- [2] Işık E, Avcil F, İzol R, Büyüksaraç A, Bilgin H, Harirchian E, Arkan E. Field Reconnaissance and Earthquake Vulnerability of the RC Buildings in Adıyaman during 2023 Türkiye Earthquakes. *Applied Sciences*, 2024; 14(7): 2860. <https://doi.org/10.3390/app14072860>
- [3] Akar F, Işık E, Avcil F, Büyüksaraç A, Arkan E, İzol R. Geotechnical and structural damages caused by the 2023 Kahramanmaraş Earthquakes in Gölbaşı (Adıyaman). *Applied Sciences*, 2024; 14(5): 2165. <https://doi.org/10.3390/app14052165>
- [4] Kontoni D-PN, Farghaly AA. The effect of base isolation and tuned mass dampers on the seismic response of RC high-rise buildings considering soil-structure interaction. *Earthquakes and Structures*, 2019; 17(4): 425-434. <https://doi.org/10.12989/eas.2019.17.4.425>
- [5] Farghaly AA, Kontoni D-PN. Mitigation of seismic pounding between RC twin high-rise buildings with piled raft foundation considering SSI. *Earthquakes and Structures*, 2022; 22(6): 625-635. <https://doi.org/10.12989/EAS.2022.22.6.625>
- [6] Belbachir A, Benanane A, Ouazir A, Harrat ZR, Hadzima-Nyarko M, Radu D, Işık E, Louhibi ZSM, Amziane S. Enhancing the Seismic Response of Residential RC Buildings with an Innovative Base Isolation Technique. *Sustainability*, 2023; 15(15): 11624. <https://doi.org/10.3390/su151511624>

- [7] Farghaly AA, Kontoni D-PN. Mitigation of seismic pounding between two L-shape in plan high-rise buildings considering SSI effect. *Coupled Systems Mechanics*, 2023; 12(3): 277-295. <https://doi.org/10.12989/csm.2023.12.3.277>
- [8] Huang H, Yuan Y, Zhang W, Li M. Seismic behavior of a replaceable artificial controllable plastic hinge for precast concrete beam-column joint. *Engineering Structures*, 2021; 245: 112848. <https://doi.org/10.1016/j.engstruct.2021.112848>
- [9] Naser MZ, Hawileh RA, Abdalla JA. Fiber-reinforced polymer composites in strengthening reinforced concrete structures. *Engineering Structures*, 2019; 198: 109542. <https://doi.org/10.1016/j.engstruct.2019.109542>
- [10] Frascadore R, Di Ludovico M, Prota A, Verderame GM, Manfredi G, Dolce M, Cosenza E. Local strengthening of reinforced concrete structures as a strategy for seismic risk mitigation at regional scale. *Earthquake Spectra*, 2015; 31(2): 1083-1102. <https://doi.org/10.1193/122912EQS361M>
- [11] Di Trapani F, Malavisi M, Marano GC, Sberna AP, Greco R. Optimal seismic retrofitting of reinforced concrete buildings by steel-jacketing using a genetic algorithm-based framework. *Engineering Structures*, 2020; 219: 110864. <https://doi.org/10.1016/j.engstruct.2020.110864>
- [12] Aldhafairi F, Hassan A, Abd-EL-Hafez LM, Abouelezz AEY. Different techniques of steel jacketing for retrofitting of different types of concrete beams after elevated temperature exposure. *Structures*, 2020; 28: 713-725. <https://doi.org/10.1016/j.istruc.2020.09.017>
- [13] Villar-Salinas S, Guzmán A, Carrillo J. Performance evaluation of structures with reinforced concrete columns retrofitted with steel jacketing. *Journal of Building Engineering*, 2021; 33: 101510. <https://doi.org/10.1016/j.jobe.2020.101510>
- [14] Vandoros KG, Dritsos SE. Concrete jacket construction detail effectiveness when strengthening RC columns. *Construction and Building Materials*, 2008; 22(3): 264-276. <https://doi.org/10.1016/j.conbuildmat.2006.08.019>
- [15] Alhadid MMA, Youssef MA. Analysis of reinforced concrete beams strengthened using concrete jackets. *Engineering Structures*, 2017; 132: 172-187. <https://doi.org/10.1016/j.engstruct.2016.11.014>
- [16] Nechevska-Cvetanovska G, Roshi A, Bojadjieva J. Seismic strengthening of existing RC buildings structures using concrete jacketing and FRP materials. *Advances in Civil and Architectural Engineering*, 2019; 10(19): 68-80. <https://hrcak.srce.hr/ojs/index.php/acae/article/view/20041>
- [17] Jang HO, Lee HS, Cho K, Kim J. Experimental study on shear performance of plain construction joints integrated with ultra-high performance concrete (UHPC). *Construction and Building Materials*, 2017; 152: 16-23. <https://doi.org/10.1016/j.conbuildmat.2017.06.156>
- [18] Xue W, Hu X, Song J. Experimental study on seismic behavior of precast concrete beam-column joints using UHPC-based connections. *Structures*, 2021; 34: 4867-4881. <https://doi.org/10.1016/j.istruc.2021.10.067>
- [19] Farzad M, Shafieifar M, Azizinamini A. Experimental and numerical study on bond strength between conventional concrete and Ultra High-Performance Concrete (UHPC). *Engineering Structures*, 2019; 186: 297-305. <https://doi.org/10.1016/j.engstruct.2019.02.030>
- [20] Alam MS, Moni M, Tesfamariam S. Seismic overstrength and ductility of concrete buildings reinforced with superelastic shape memory alloy rebar. *Engineering Structures*, 2012; 34: 8-20. <https://doi.org/10.1016/j.engstruct.2011.08.030>
- [21] Raza S, Shafei B, Saiidi MS, Motavalli M, Shahverdi M. Shape memory alloy reinforcement for strengthening and self-centering of concrete structures—State of the art. *Construction and Building Materials*, 2022; 324: 126628. <https://doi.org/10.1016/j.conbuildmat.2022.126628>

- [22] Driver RG, Kulak GL, Elwi AE, Kennedy DL. FE and simplified models of steel plate shear wall. *Journal of Structural Engineering*, 1998; 124(2): 121-130. [https://doi.org/10.1061/\(ASCE\)0733-9445\(1998\)124:2\(121\)](https://doi.org/10.1061/(ASCE)0733-9445(1998)124:2(121))
- [23] Nie J, Fan J, Liu X, Huang Y. Comparative study on steel plate shear walls used in a high-rise building. *Journal of Structural Engineering*, 2013; 139(1): 85-97. [https://doi.org/10.1061/\(ASCE\)ST.1943-541X.0000613](https://doi.org/10.1061/(ASCE)ST.1943-541X.0000613)
- [24] Kontoni D-PN, Farghaly AA. Enhancing the Earthquake Resistance of RC and Steel High-Rise Buildings by Bracings, Shear Walls and TMDs considering SSI, *Asian Journal of Civil Engineering*, 2023; 24: 2595-2608. <https://doi.org/10.1007/s42107-023-00666-6>
- [25] Ile N, Reynouard JM. Nonlinear analysis of reinforced concrete shear wall under earthquake loading. *Journal of Earthquake Engineering*, 2000; 4(02): 183-213. <https://www.worldscientific.com/doi/pdf/10.1142/S136324690000102?download=true>
- [26] Mohamed N, Farghaly AS, Benmokrane B, Neale KW. Experimental investigation of concrete shear walls reinforced with glass fiber-reinforced bars under lateral cyclic loading. *Journal of Composites for Construction*, 2014; 18(3): A4014001. [https://doi.org/10.1061/\(ASCE\)CC.1943-5614.0000393](https://doi.org/10.1061/(ASCE)CC.1943-5614.0000393)
- [27] Abualreesh AM, Tuken A, Albidah A, Siddiqui NA. Reliability-based optimization of shear walls in RC shear wall-frame buildings subjected to earthquake loading. *Case Studies in Construction Materials*, 2022; 16: e00978. <https://doi.org/10.1016/j.cscm.2022.e00978>
- [28] Shen J, Seker O, Akbas B, Seker P, Momenzadeh S, Faytarouni M. Seismic performance of concentrically braced frames with and without brace buckling. *Engineering Structures*, 2017; 141: 461-481. <https://doi.org/10.1016/j.engstruct.2017.03.043>
- [29] Kheyroddin A, Sepahrad R, Saljoughian M, Kafi MA. Experimental evaluation of RC frames retrofitted by steel jacket, X-brace and X-brace having ductile ring as a structural fuse. *Journal of Building Pathology and Rehabilitation*, 2019; 4(1): 11. <https://doi.org/10.1007/s41024-019-0050-z>
- [30] Ahiwale DD, Kontoni D-PN, Darekar PL. Seismic performance assessment of reinforced concrete frames with different bracing systems. *Innovative Infrastructure Solutions*, 2023; 8(3): 102. <https://doi.org/10.1007/s41062-023-01071-3>
- [31] Kawamata S, Ohnuma M. Strengthening effect of eccentric steel braces to existing reinforced concrete frames. *Proceedings of the Seventh World Conference on Earthquake Engineering (7WCEE)*, pp. 513-520, Istanbul, Turkey, 8-13 September 1980. [http://www.iitk.ac.in/nicee/wcee/article/7\\_vol4\\_513.pdf](http://www.iitk.ac.in/nicee/wcee/article/7_vol4_513.pdf)
- [32] Ghobarah A, Abou Elfath H. Rehabilitation of a reinforced concrete frame using eccentric steel bracing. *Engineering Structures*, 2001; 23(7): 745-755. [https://doi.org/10.1016/S0141-0296\(00\)00100-0](https://doi.org/10.1016/S0141-0296(00)00100-0)
- [33] Omrani R, Kafi MA, Kheyroddin A. Evaluation and Comparison of Divergent and Convergent Bracing Performance in Strengthening of Reinforced Concrete Frames. *Journal of Structural and Construction Engineering*, 2021; 8(9): 96-116. <https://doi.org/10.22065/jsce.2020.211332.2021>
- [34] Xie Q. State of the art of buckling-restrained braces in Asia. *Journal of Constructional Steel Research*, 2005; 61(6): 727-748. <https://doi.org/10.1016/j.jcsr.2004.11.005>
- [35] Hoveidae N, Rafezy B. Overall buckling behavior of all-steel buckling restrained braces. *Journal of Constructional Steel Research*, 2012; 79: 151-158. <https://doi.org/10.1016/j.jcsr.2012.07.022>
- [36] Zhou Y, Shao H, Cao Y, Lui EM. Application of buckling-restrained braces to earthquake-resistant design of buildings: A review. *Engineering Structures*, 2021; 246: 112991. <https://doi.org/10.1016/j.engstruct.2021.112991>

- [37] Dyke SJ, Spencer Jr BF, Sain MK, Carlson JD. An experimental study of MR dampers for seismic protection. *Smart Materials and Structures*, 1998; 7(5): 693. <https://doi.org/10.1088/0964-1726/7/5/012>
- [38] Lee D, Taylor DP. Viscous damper development and future trends. *The Structural Design of Tall Buildings*, 2001; 10(5): 311-320. <https://doi.org/10.1002/tal.188>
- [39] Kaleybar RS, Tehrani P. Effects of using different arrangements and types of viscous dampers on seismic performance of intermediate steel moment frames in comparison with different passive dampers. *Structures*, 2021; 33: 3382-3396. <https://doi.org/10.1016/j.istruc.2021.06.079>
- [40] Ghamari A, Kim C, Jeong SH. Development of an innovative metallic damper for concentrically braced frame systems based on experimental and analytical studies. *The Structural Design of Tall and Special Buildings*, 2022; 31(8): e1927. <https://doi.org/10.1002/tal.1927>
- [41] Ghamari A, Jeong SH, Thongchom C, Jaya RP. An innovative shear links as dampers compound of shear plates and round HSS sections. *Journal of Materials Research and Technology*, 2023; 25: 6134-6149. <https://doi.org/10.1016/j.jmrt.2023.07.042>
- [42] Vetr MG, Ghamari A. Experimentally and analytically study on eccentrically braced frame with vertical shear links. *The Structural Design of Tall and Special Buildings*, 2019; 28(5): e1587. <https://doi.org/10.1002/tal.1587>
- [43] Ghamari A, Kim YJ, Bae J. Utilizing an I-shaped shear link as a damper to improve the behaviour of a concentrically braced frame. *Journal of Constructional Steel Research*, 2021; 186: 106915. <https://doi.org/10.1016/j.jcsr.2021.106915>
- [44] Alshimmeri AJH, Kontoni D-PN, Ghamari A. Improving the seismic performance of reinforced concrete frames using an innovative metallic-shear damper, *Computers and Concrete*, 2021; 28(3): 275-287. <https://doi.org/10.12989/cac.2021.28.3.275>
- [45] Ghamari A, Alzebaree R, Thongchom C. Developing an innovative stiffened shear damper for concentrically braced frames. *Structures*, 2023; 50: 734-744. <https://doi.org/10.1016/j.istruc.2023.02.079>
- [46] Kontoni D-PN, Ghamari A, Thongchom C. Experimental and numerical study of a steel plate-based damper for improving the behavior of concentrically braced frames, *Steel and Composite Structures*, 2023; 47(2): 185-201. <https://doi.org/10.12989/scs.2023.47.2.185>
- [47] Ghamari A, Khaloo A. Strengthening the RC Frames Using an Innovative Steel Damper with Shear Mechanism. *Journal of Concrete Structures and Materials*, 2020; 5(2): 16-31. [http://www.jcsm.ir/article\\_119456\\_336076b0a84b822d34b0dd530a185460.pdf?lang=en](http://www.jcsm.ir/article_119456_336076b0a84b822d34b0dd530a185460.pdf?lang=en)
- [48] Alshimmeri AJH, Kontoni D-PN, Ghamari A. Improving the Performance of I-Shaped Dampers Using Stiffeners. *Proceedings of the 9th International Conference on Computational Methods in Structural Dynamics and Earthquake Engineering (COMPdyn 2023)*, Athens, Greece, 12-14 June 2023. [https://files.eccomasproceedia.org/papers/compdyn-2023/C23\\_21378.pdf?mtime=20231027201710](https://files.eccomasproceedia.org/papers/compdyn-2023/C23_21378.pdf?mtime=20231027201710)
- [49] Ghamari A, Thongchom C, Putra Jaya R, Sithole T. Utilizing Low Yield Point Steel to Improve the Behavior of the I-Shaped Shear Links as Dampers. *Buildings*, 2023; 13(2): 554. <https://doi.org/10.3390/buildings13020554>
- [50] Kontoni D-PN, Ghamari A, Kheiri J, Ilia G. An innovative I-shaped low-yield steel shear damper directly connected to the concentrically braced frame. *Proceedings of the 10th Eurosteel Conference (EUROSTEEL 2023)*, jointly organized by TU Delft, ETH Zurich and Bouwen met Staal, and supported by ECCS, Amsterdam, 12-14 September 2023. *ce/papers - Proceedings in Civil Engineering*, 6: 925-929. <https://doi.org/10.1002/cepa.2604>

- [51] ETABS® Version 2015. *Integrated Software for Structural Analysis and Design of Buildings*. Computers and Structures, Inc., Walnut Creek, CA and New York, NY, USA, 2015.
- [52] ABAQUS Version 6.14. *Documentation-Manuals*. Dassault Systemes Simulia Corporation, Providence, RI, USA, 2014.
- [53] TahamouliRoudsar M, Entezari A, Hadidi M, Gandomian O. Experimental assessment of retrofitted RC frames with different steel braces. *Structures*, 2017; 11: 206-217. <https://doi.org/10.1016/j.istruc.2017.06.003>



Research Article

## A study on the quantitative recrystallization of cold deformed copper affected by tin-lead solder

Mohammad Salim Kaiser<sup>\*1,a</sup>, S Reaz Ahmed<sup>2,b</sup>

<sup>1</sup>Innovation Centre, International University of Business Agriculture and Technology, Dhaka-1230, Bangladesh

<sup>2</sup>Dept. of Mechanical Eng., Bangladesh University of Engineering and Technology, Dhaka-1000, Bangladesh

### Article Info

### Abstract

#### Article history:

Received 28 Dec 2023

Accepted 22 June 2024

#### Keywords:

Cu-alloy;  
Sn-Pb solder;  
Work hardening;  
Recrystallization;  
Precipitate;  
Microstructure

It has been observed that the fractional recrystallization characteristics of commercially pure copper is affected by the presence of individual or both the constituent elements of the Sn-Pb solder alloy. In order to design the experiment, commercially pure Cu, binary copper alloys (Cu-Sn and Cu-Pb) and ternary copper alloy, Cu-Sn-Pb are investigated. Cast alloys are homogenized, solution treated, and then quenched to complete the thermal treatment. In order to recrystallize, alloys are cold rolled to a 75% thickness and then annealed at 700°K isothermally for varying durations, up to 3600 seconds. In this experiment, the fractional recrystallization of annealed samples is evaluated as the normalized difference in microhardness recorded at various time steps. Additionally, in an attempt to verify the experimental results, the well-known Johnson-Mehl-Avrami-Kolmogorov equation is also used to predict the associated recrystallization behavior. From the study, it can be inferred that the presence of Sn-Pb solder-alloy elements have a positive impact on the recrystallization behavior of pure copper due to the solid solution strengthening, in which the effect of tin is greater than that of lead. Quantitative analysis indicates that recrystallization of pure Cu, Cu-Sn, Cu-Pb, and Cu-Sn-Pb alloys attains 99.4%, 95.4%, 98.4%, and 89.5%, respectively. Sn forms intermetallic with Cu but Pb does not. Additionally, Sn forms different intermetallic with impurities and has a BCC crystal structure dissimilar to the FCC of Cu and Pb. As a result, the formation of GP zones and the intermetallic phases during annealing show greater differences in the recrystallization behavior between the two approaches. By combination, microstructural studies of the cold-rolled alloys reveal the elongated grains of the second phases, and the alloys almost completely re-crystallized after 1800 seconds of annealing at 700°K.

© 2024 MIM Research Group. All rights reserved.

## 1. Introduction

The numerous benefits of copper, including its exceptional electrical and thermal conductivity, resistance to atmospheric corrosion, and antibacterial properties with robust resistance to chemical attack, became more and more significant as industrialization expanded [1-4]. Copper can be combined with an extensive variety of metals to form alloys, and a multitude of alloy systems are currently on the market that allow for the controlled modification of mechanical and technological properties like hardness, tensile properties, and resistance to wear and corrosion [5, 6]. It should be noted that the addition of elements to an alloy can improve certain properties while affecting others in different ways. In the literature, there are lot of information on the influence of alloying elements in copper [2, 4, 6]. For example, alloying with Sn provides strength and precipitation hardening, but reduces ductility and conductivity [7]. The addition of Al shows similar behavior but

\*Corresponding author: [dkaiser.res@iubat.edu](mailto:dkaiser.res@iubat.edu)

<sup>a</sup> orcid.org/0000-0002-3796-2209; <sup>b</sup> orcid.org/0000-0002-8382-0711

DOI: <http://dx.doi.org/10.17515/resm2024.136ma1228rs>

Res. Eng. Struct. Mat. Vol. 11 Iss. 1 (2025) 333-349

decreases the corrosion properties [8]. When Si is added, it improves tensile strength as well as machineability but is less corrosion-resistant than other types of Cu alloys. While Ni-added alloys have high thermal stability, which enables them to keep their mechanical characteristics even at high temperatures, but their machinability is a result of their high toughness [3, 9]. Alloyed with Zr refines the grain structure and thermal stability of the alloys, and Sc furthermore provides precipitation strengthening [10, 11]. High conductivity, including thermal and electrical conductivities, and high strength are the two most desirable characteristics of high-performance copper alloys. Such property profiles could have a wide range of present and future uses in automotive and electronic industries, including busbars in commutators, casting molds, die-casting plungers, electric motors, generators, relays, switches, and welding electrodes. When Cu is used as the primary conductor in the above electrical sector, wires or parts are to be joined by using solders. Note that, at earlier stages, Sn-Pb solder alloys are mostly used for the joining processes. Therefore, the corresponding recycled copper would contain a small amount of Sn-Pb solder elements as well as trace impurities [12, 13].

Once more, it might be suggested that using copper purposefully or under certain conditions requires plastic deformation. It is established that cold working is a simple and common method to improve strength by changing the crystal structure of common materials. When alloying elements are added, the quality of the improved strength of the base material varies. Obviously, the presence of Sn-Pb solder will play an important role in strength through significant dislocation hardening and grain refinement [3, 14, 15]. When worked again at a high temperature beyond half of its melting temperature, a group of processes known as recrystallization can release the stored energy, the deformed grains are replaced by a new set of original defect-free grains, etc. As a result, radically decrease in strength [16-18]. Once it comes to pure metals, the single crystal's original orientation determines the values of stored energy and recrystallization temperature. When elements are present in small amounts, they can occasionally have the opposite effect of pure metals, increasing the recrystallization temperature and reducing the stored energy. This depends on the properties, quantity, and rate of deformation of the elements [19, 20].

There is no mention of the copper's reusable qualities, especially when affected by Sn-Pb solder. In order to thoroughly study and appropriately identify the engineering applications of scraped Cu for optimal exploitation toward the advancement of civilization, it is necessary to discover a number of its qualities. Recrystallization behavior is one of them. It may be investigated in several ways. Dynamic and isothermal resistivity measurements have been used by previous researchers to examine this attribute [21]. The most straightforward way to investigate the behavior of recrystallization is to use optical microscopy to calculate the fraction that has been recrystallized [22]. Vickers microhardness techniques and differential scanning calorimetry may also be used to investigate it [23]. It is challenging to discern between the recrystallized and deformed microstructures in severely deformed copper, though, the recrystallized fraction has also been ascertained by other indirect techniques. Considering all circumstances, microhardness data is the easiest procedure to determine the fractional recrystallization of the materials [24]. Consequently, the focus of this study is on how Sn-Pb solder affects the fractional recrystallization behavior of copper that has undergone significant plastic deformation. To compare and isolate the effect of individual elements on the recrystallization behavior, the same reduction ratio and subsequent annealing are employed for commercially pure Cu, Cu-Sn, and Cu-Pb alloys. It also takes into account the specific amounts of Sn and Pb based on the composition of the solder. Another, since the Johnson-Mehl-Avrami-Kolmogorov (JMAK) relationship follows the isothermal kinetics of the recrystallization process of the specific material system, an effort is made to analyze



and compare the results of the experimental study derived from the difference in micro-hardness values for these trial alloys [25].

## 2. Experimental Methods

### 2.1. Preparation of Alloys

To prepare the copper-solder alloy (Cu-Sn-Pb), copper wires as well as soldered connecting structures after extensive use were collected from various sources, which was then melted using a suitable flux cover in a pit furnace powered by natural gas in a traditional manner. Optical emission spectroscopy has shown that the resulting cast copper contains trace amounts of lead and tin as well as few other elements with negligible amount. It was a Cu-Sn-Pb alloy composed of about one percent each of tin and lead. Simultaneously, based on the above minor alloying elements, three more samples of commercially pure Cu, Cu-Sn, and Cu-Pb were prepared to establish the impact of individual components of the solder. The chemical compositions of the major element are listed in Table 1, in which the negligible elements, like, Si, Fe, P, etc., are not included. One can however see from the table that the binary alloys, that is, Cu-Sn and Cu-Pb contain negligible amounts of Pb and Sn, respectively.

Table 1. Alloy chemical composition by wt.%

| Alloy    | Cu     | Sn    | Pb    |
|----------|--------|-------|-------|
| Pure Cu  | 99.986 | 0.0   | 0.0   |
| Cu-Sn    | 98.456 | 1.134 | 0.012 |
| Cu-Pb    | 98.433 | 0.002 | 1.197 |
| Cu-Sn-Pb | 97.113 | 1.257 | 1.195 |

### 2.2. Preparation of The Test Specimen

The above four cast samples were homogenized for eight hours at 773°K and air-cooled to allow the release of internal stresses and to achieve the equilibrium conditions of solidification. Again, the solution treatment was done at 973°K for two hours and quenched into ice-salt water to get a super saturated single-phase region. To apply cold rolling, the samples were machined to assume the dimension of 300 × 15 × 12 mm. The cold working operation was then performed using a laboratory-scale 10HP cold rolling machine under 1 mm reduction per pass. Consequently, the samples' thickness decreased from 12 mm to 3 mm as they deformed by 75%. To study the recrystallization behavior, isothermal annealing of cold rolled samples was performed for a duration of 3600 seconds at 700°K. Additionally, all four samples were annealed at 773°K for four hours to achieve a fully recrystallized state [12]. For different tests, the finished surface was prepared with sandpaper and polished to a size of 15 x 15 x 3 mm.

### 2.3. Working Instruments and Test data collection methods

#### 2.3.1 Hardness Test

A Mitutoyo HM-200 Series 810-Micro Vickers Hardness Testing Machine was used to measure the hardness of various alloys at various annealed conditions. Diamond Indenter was applied to the sample with a load of 100 grams for a dwell time of 20 seconds. On each polished surface of the aged samples, at least eleven indentations were made at various locations of three test specimens prepared from each of the four categories.

#### 2.3.2 Resistivity Measurement

The electrical conductivity of alloys under various conditions was measured using an Electric Conductivity Meter (type 979). In order to plot the graph, the conductivity data

was then converted to electrical resistivity. Likewise, the case of hardness, a minimum of eleven measurements were taken at different places on each polished surface of three test specimens prepared from each of the four categories.

### 2.3.3 Microstructural Study

Finally, to ascertain the microstructure and granular texture of the materials, an optical microscopic observation was performed on the cold rolled and annealed samples. An OEM BW-S500 optical electronic microscope was used for this study. The samples were ultimately polished with alumina to reveal the microstructure. The same combination of ammonium hydroxide and hydrogen peroxide (3%) was employed for metallographic copper etching. In addition, the surface morphologies of deformed samples were investigated with the help of a field emission scanning electron microscope model JEOL JSM-7600F. An electron dispersive spectrometer (JEOL EX-37001 model) connected to the setup to capture the samples' EDX spectra. Microstructural images were taken at different locations of the sample with various magnifications, and the representative images are presented.

## 3. Results and Discussion

### 3.1. Isothermal Annealing

Figure 1 shows the change in average microhardness over time of commercially pure Cu, tin-doped binary Cu alloy (Cu-Sn), lead-doped binary Cu alloy (Cu-Pb), and the ternary Cu alloy, Cu-Sn-Pb under isothermal annealing at 700°K. The hardness values corresponding to the initial state, that is, at zero time, represent the hardness of 75% cold-rolled samples without any influence of annealing. It is clearly demonstrated that all alloys soften with time at different rates. Copper shows a relatively rapid and steeper decrease in hardness following a more or less constant value at higher time durations. The alloy samples also exhibit variation in hardness and follow trends nearly similar to that of pure Cu, although some variations may be noticed in higher time domain ( $1200 \leq t \leq 3600$  sec). From the results it is observed that, at the steady-state condition (higher time domain) pure Cu assumes the lowest and the ternary alloy the highest hardness, and the hardness of the binary alloys remain in between. More specifically, tin is identified to be more influential than lead in assuming higher hardness of the binary alloys in the steady-state condition. All the samples were plastically deformed by 75%.

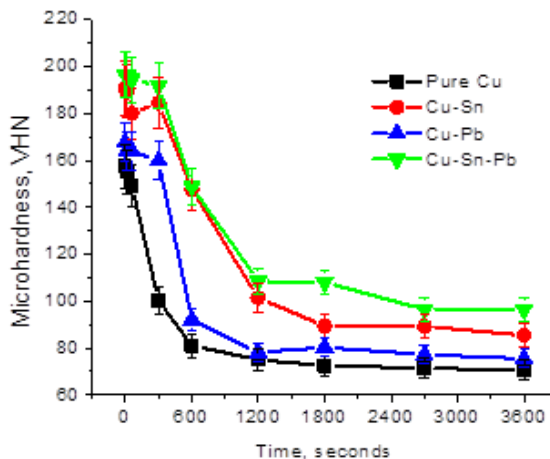


Fig. 1. Microhardness variation, isothermal annealing at 700°K

A highly cold deformed alloy consists of huge dislocations, which result in its developed hardness. Hardness reduction in the early stages of annealing may be associated with rearrangement of dislocations as well as stress-relieving and higher annealing times for recovery, recrystallization, and grain growth [12, 26]. An elevated temperature during annealing for any metal that has been deformed and hardened will eventually nullify the effect of strain hardening. Formation of a defect free new grain structure during the recrystallization process is the primary cause of softening [27, 28]. Initially, higher hardness is observed for minor-added alloys compared to pure copper because the solid solution is strengthened through the Sn and Pb phases. The higher hardness of the Sn-added alloy is due to its BCC crystal lattice, which differs from that of Cu's FCC crystal lattice, and Pb has a similar FCC crystal lattice to Cu. The FCC and BCC lattice alloys exhibit different supersaturated solid solution patterns of higher internal stress than those of both similar lattices. One thing may be noted that atomic size of the Sn is higher than Pb as well as Cu. As a result, the addition of Sn to the Cu matrix accelerates the internal stress. The Pb element does not form any intermetallic with Cu. Nonetheless, Sn not only forms different intermetallic with Cu, but it also forms intermetallic with other negligible impurities as deposited during casting, which play an important role in strengthening the alloy [13, 29, 30]. The main stable intermediate phases are  $\text{Cu}_3\text{Sn}$ ,  $\text{Cu}_{41}\text{Sn}_{11}$ ,  $\text{Cu}_{10}\text{Sn}_3$ , and  $\text{Cu}_6\text{Sn}_5$ , where  $\text{Cu}_3\text{Sn}$  and  $\text{Cu}_6\text{Sn}_5$  two intermetallic, primarily have a significant impact on hardness [31]. Solder affected alloys bear the highest hardness for both alloying effects. At the initial stage of annealing, the element added alloys show a fluctuating nature of hardness due to the formation of different intermetallic. These intermetallic hinder the dislocation movement during the annealing, so such a type of nature is observed.

### 3.2. Recrystallized Fraction

In general, the maximum and minimum values of hardness represent the important characteristics of any material's microstructure; therefore, recrystallization kinetics may be expressed in terms of fractional softening, as demonstrated by earlier researches [26, 32]. Following the standard procedure of the above literature, the fractional recrystallization,  $X$  is defined as the ratio of change in hardness, which is as follows:

$$X = \frac{H_{max} - H_i}{H_{max} - H_{min}} \quad (1)$$

Where,  $H_{max}$  and  $H_{min}$  represent the maximum and minimum hardness corresponding to the initial cold-rolled and the completely recrystallized state of the sample, whereas the hardness at any time step after applying thermal annealing is denoted by  $H_i$ . For the present material, no change in hardness is encountered at time intervals of 2, 4, 6, 8 hours, for example, after applying annealing at 773°K, which basically represents the state of full recrystallization, which has also been found in the work of reference [12]. Table 2 lists the maximum and minimum microhardness values of the experimental alloys under two conditions: unannealed and annealed for four hours at 773°K. Fig. 2 shows the variation of fractional recrystallization,  $X$  for the four samples annealed at 700°K as a function of annealing time, which is obtained based on Eq. (1) and Table 2. According to the figure, copper has the largest percentage of recrystallization. Pb-doped and Sn-doped Cu alloys as well as the Cu-Sn-Pb alloy respectively follow the gradually decreasing trends of recrystallization. The above recrystallization behavior of the alloys may be realized by the formation the different intermetallics that hinder the dislocation movement of the alloys. Note that it has already been discussed about the influence of individual and both the elements of Sn-Pb solder on the microhardness under annealing treatment. Similar observations were also found for other trace or minor added alloys [33].

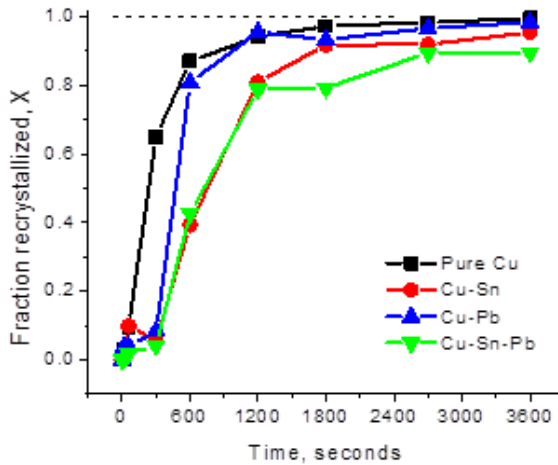


Fig. 2. Difference in the kinetics of recrystallization with annealing time derived from microhardness data

The Johnson-Mehl-Avrami-Kolmogorov model (JMAK equation) may be used to investigate the kinetics of a material’s recrystallization [32, 34]. In order to theoretically study the fraction recrystallization as a function of annealing time, the JMAK equation can be stated as:

$$X = 1 - \exp[-(kt)^n] \tag{2}$$

where  $t$  is the applied time for annealing, and  $k$  and  $n$  are the temperature dependent constants and the JMAK exponent, respectively. The parameters are contingent upon the conditions of the material and processing. Following a logarithmic operation, the JMAK equation can be reduced to a linear relationship as follows:

$$\ln\left[\ln\left(\frac{1}{1-X}\right)\right] = n\ln(t) + n\ln(k) \tag{3}$$

When plotted on a logarithmic scale,  $\ln\{1/(1 - X)\}$  vs.  $t$  should show a straight line. The parameters can be obtained from Fig. 3 by way of the linear relationship whose slope is equal to the JMAK exponent. The kinetics of recrystallization of alloys annealed at 700°K can be obtained using the values of the JMAK exponent  $n$  and parameter  $k$ . The comparison of recrystallization kinetics for commercially pure Cu, binary tin, and lead-added alloys, as well as ternary tin-lead solder affected alloys obtained micro-hardness data and JMAK type investigation, is shown in Fig. 4-7. The experimental alloys exhibit different softening under annealing treatment and, as a result, exhibit varying slopes for their recrystallization performance.

$$X = 1 - \exp[-(0.002114 \times t)^{0.98744}] \text{ for pure Cu} \tag{4}$$

$$X = 1 - \exp[-(0.000894 \times t)^{0.99975}] \text{ for Cu-Sn alloy} \tag{5}$$

$$X = 1 - \exp[-(0.001292 \times t)^{1.02257}] \text{ for Cu-Pb alloy} \tag{6}$$

$$X = 1 - \exp[-(0.000705 \times t)^{1.37267}] \text{ for Cu-Sn-Pb alloy} \tag{7}$$

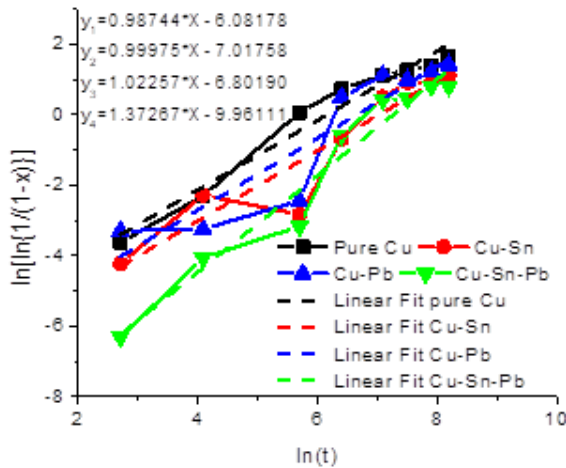


Fig. 3. Plot of  $\ln\{1/(1-X)\}$  Vs.  $(t)$  in logarithmic scale, to obtain linear relationship

Table 2. Measured maximum and minimum microhardness of alloys with JMAK exponent

| Alloy    | $H_{max}$ | $H_{min}$ | n       | k        |
|----------|-----------|-----------|---------|----------|
| Pure Cu  | 157.3     | 70.0      | 0.98744 | 0.002114 |
| Cu-Sn    | 190.8     | 80.3      | 0.99975 | 0.000894 |
| Cu-Pb    | 167.6     | 74.0      | 1.02257 | 0.001292 |
| Cu-Sn-Pb | 196.4     | 84.7      | 1.37267 | 0.000705 |

The experimental Cu sample displays the lowest disparity among two methods of fraction recrystallization (Fig. 4). Doped by Sn and Pb alloys, there are the higher differences between the two respective methods, as seen respectively in Fig. 5 and Fig. 6. The reason for this phenomenon is that the finely dispersed particles typically slow down the process of recrystallization, which has a greater slowing effect on nucleation than on growth.

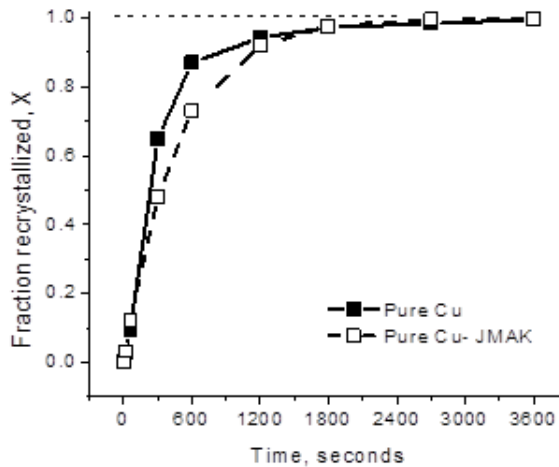


Fig. 4. Inconsistency of recrystallization kinetics determined by both JMAK type study and micro-hardness data for commercially pure Cu

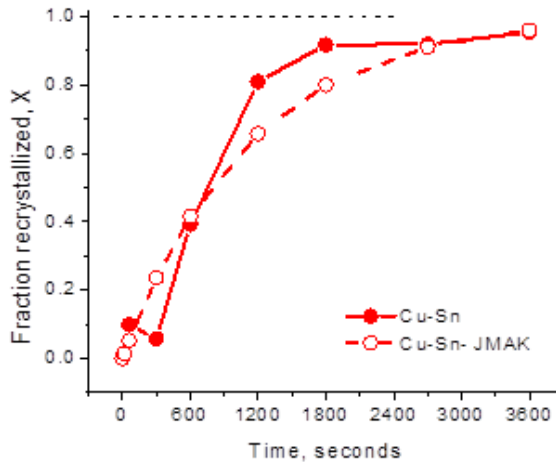


Fig. 5. Inconsistency of recrystallization kinetics determined by both JMAK type study and micro-hardness data for Cu-Sn alloy

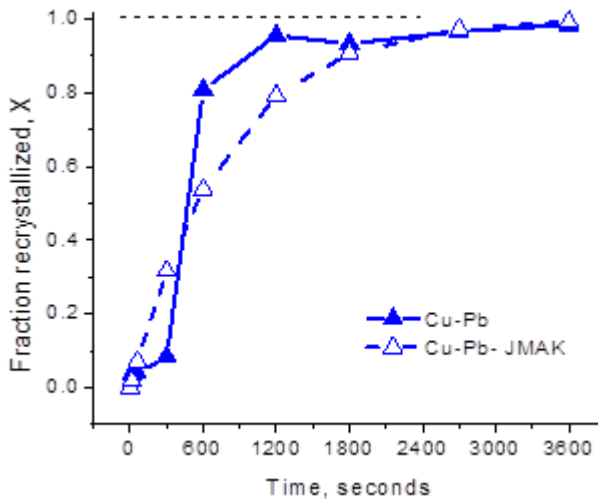


Fig. 6. Inconsistency of recrystallization kinetics determined by both JMAK type study and micro-hardness data for Cu-Pb alloy

Consequently, the orientation dependent nucleation provides a rationale for the texture changes. In the case of commercially pure Cu, trace impurities may be exerted from the melt environment during casting, which forms an insignificant amount of intermetallic during the process of annealing, so some effect may be felt [18, 35]. In the case of Sn addition, dissolution of different phases and different intermetallic formations with Cu and impurities in the course of annealing treatment make the differences higher [31]. Pb addition shows a relatively low value as it does not form any intermetallic with copper. Solder-affected alloy displays the maximum variation because of the presence of both elements (Fig. 7). Finally, it can be summarized that Eq. (1) describes the experimental results of fractional recrystallization based on the actual measurements of hardness, whereas the JMAK equation gives the corresponding theoretical prediction of the behavior.

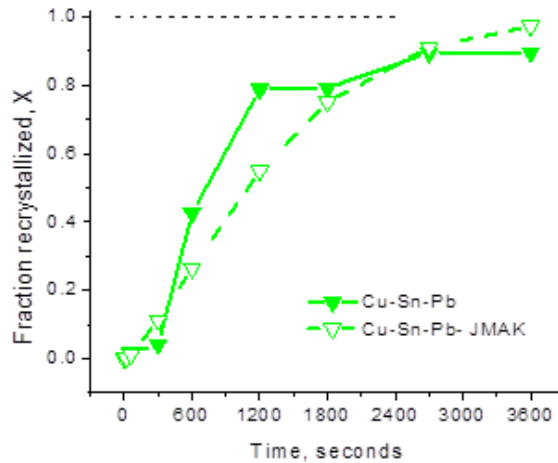


Fig. 7. Inconsistency of recrystallization kinetics determined by both JMAK type study and micro-hardness data for Cu-Sn-Pb alloy

A comparison of the results shown in Figs. 4-7 reveals that, the discrepancy between the two approaches is basically observed in the early stages of the annealing treatment, showing good agreement in the steady-state regions. It can be noted that, for annealing under such higher temperature, the formation of intermetallic occurs within a very short period of time, which would be the probable reason for the above discrepancy.

### 3.3 Resistivity

In this section, the electrical resistivity of pure copper as well as its binary and ternary alloys is recorded in an attempt to assess the electrical conduction characteristics of the alloy samples during the process of fractional recrystallization as a function of annealing time. The resistivity curves of the alloy samples at the same annealing condition mentioned earlier are presented in Fig. 8, which show an initial drop, followed by a small increase, and finally a slow but steady decrease of resistivity. During isothermal ageing of the test alloys, the first drop in resistivity occurs due to dislocation rearrangement as well as the recovery phenomena of the cold-worked alloy.

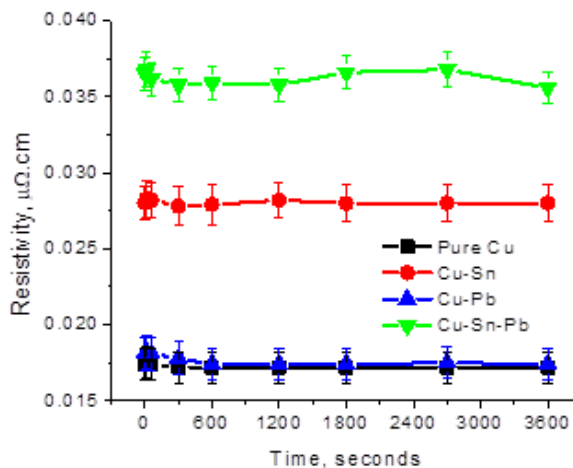
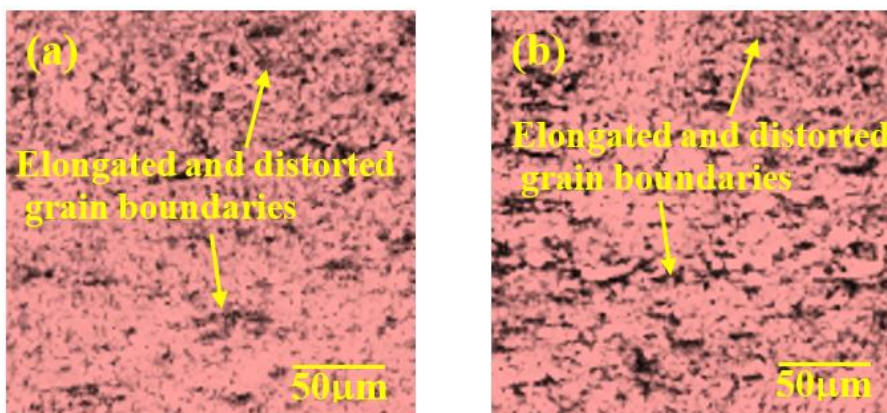


Fig. 8. Resistivity fluctuation, isothermal annealing at 700°K

The rate of resistivity reduction is the highest for solder-affected alloy because they consist of the highest dislocation density created by both elements. The second minor increase in resistivity of all alloys is linked to different intermetallic formations. The fine precipitate inhibits free electron movement, resulting in increased resistivity in alloys. The chemical composition previously stated that during the casting process, all alloys consist of different trace impurities, so they form different intermetallic through heat treatment. In the final stage of annealing, there is a slow and steady decrease in resistivity due to the following factors: particle coarsening, grain coarsening, and recrystallization, ultimately resulting in a decrease in electron anomalous scattering [36, 37]. Again, Sn added alloy normally demonstrates all the cases of higher intensity than Pb-added alloy and pure Cu has the lowest. Since Sn has a BCC lattice difference from the Cu FCC lattice, the lattice distortion is higher than that of the FCC Pb alloy. Additionally, Sn forms different intermetallic with Cu and trace impurities, resulting in a higher alloy resistivity than Pb. The alloy that is affected by the solder has an impact, which demonstrates the resistive effect of both elements.

### 3.4 Optical images of Grains

Optical micrographs of commercially pure Cu, tin-added Cu-Sn, lead added Cu-Pb, and solder affected Cu-Sn-Pb alloys at the combination of solution treated and cold-rolled by 75% are displayed in Fig. 9a-d. Every single grain in the microstructure is heterogeneous and distributed in rolling directions. Extensive plastic deformation destroys grain boundaries to form sub grains. A minor addition of elements does not provide the foremost differences. But some deviations can be distinguished between alloys, as grain boundaries are relatively thin for Cu, followed by Pb-doped, Sn-doped and solder-affected alloys. Copper materials contain the minimum number of impurities, such as Fe, C, P, etc., so the intermetallic are smaller in both size and quantity during solution treatment. Tin forms denser grain boundaries than lead because alloys with FCC Cu and BCC Sn lattices exhibit different supersaturated solid solution patterns than similar lattices of both Cu and Pb. Additionally, the atomic size of Sn is larger than that of Pb as well as Cu, so it tends to be allocated to grain boundaries, resulting in denser grain boundaries for alloys containing Sn. Both material effects dominate the dense boundary of the solder affected Cu [38]. After 30 minutes of annealing at 700°K, the appearance of the alloys' microstructures entirely changed. The microstructure completely lacks elongated grains; most residual phases dissolve into the  $\alpha$ -Cu matrix, the grain boundaries are clearly defined, and the grain outlines are equiaxed (Fig. 10a-d).





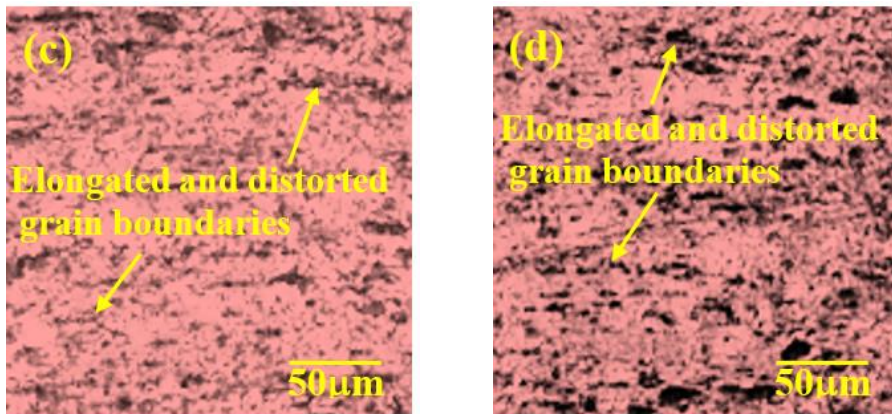


Fig. 9. Optical images of cold rolled (a) pure Cu, (b) binary Cu-Sn alloy, (c) binary Cu-Pb alloy and (d) ternary Cu-Sn-Pb alloy

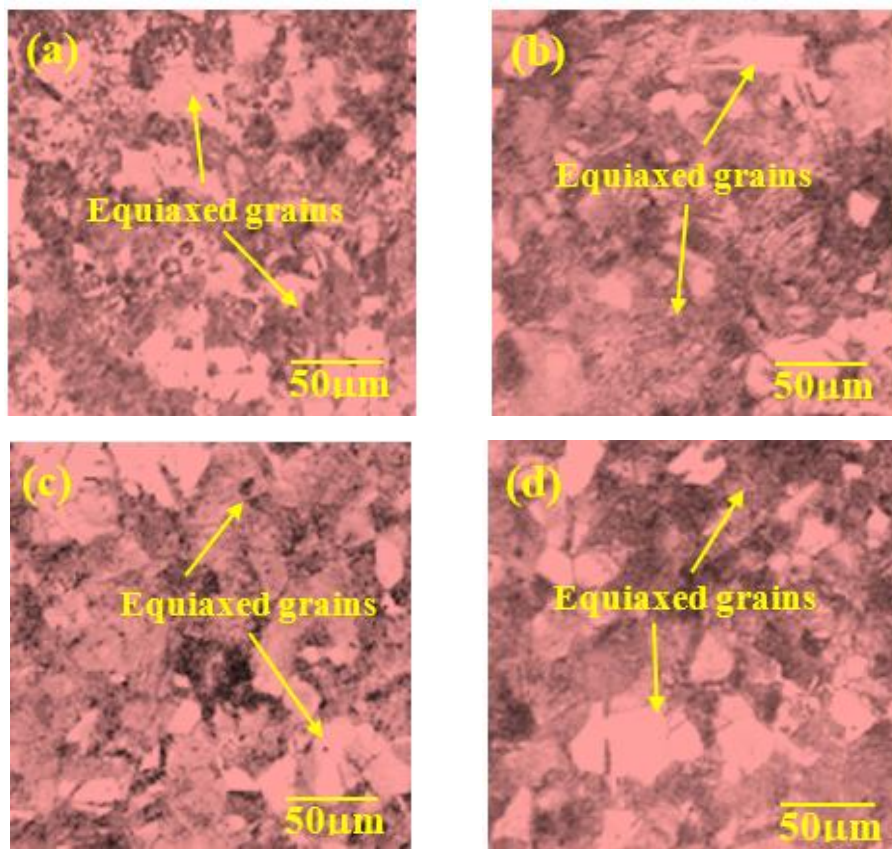


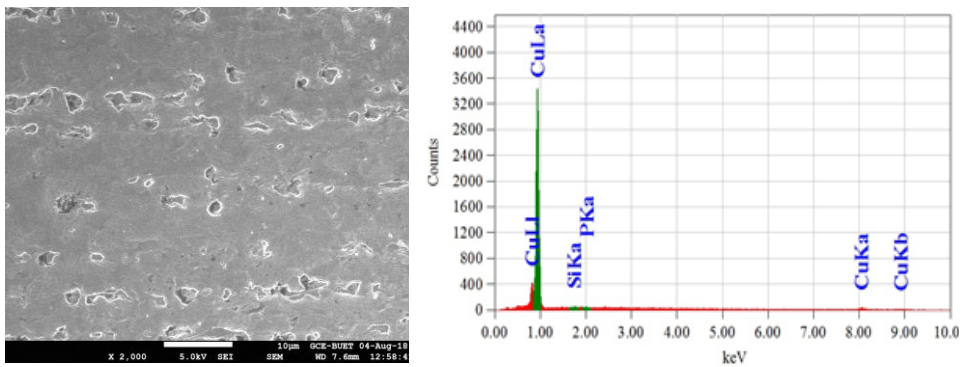
Fig. 10. Optical images of cold rolled (a) pure Cu, (b) binary Cu-Sn alloy, (c) binary Cu-Pb alloy and (d) ternary Cu-Sn-Pb alloy annealed at 700°K for 1800 seconds

The alloys contain a variety of trace impurities and small additional elements that can form intermetallic particles during the casting and annealing processes. However, most of these

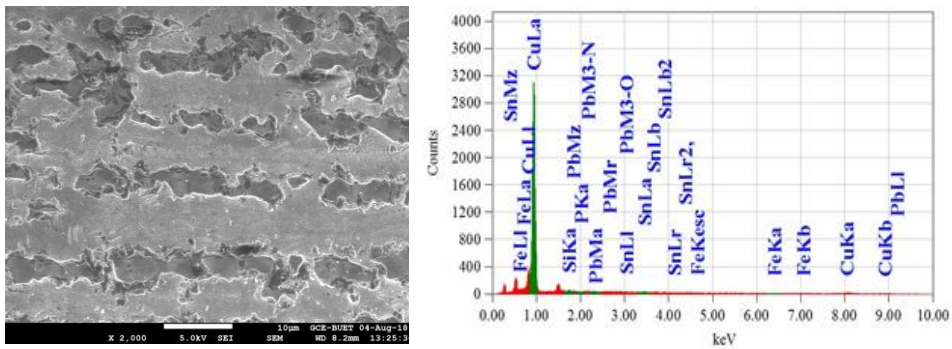
precipitates are distributed along grain boundaries at higher annealing temperatures and times. For phases containing elements of Si and Fe, the dissolution temperature is very high. These phases are so tiny that they can still be found inside grains and next to grain boundaries [6].

### 3.5 SEM and EDX Analysis

In order to comply with the optical microstructure, the SEM images and the respective EDX spectra of cold-rolled alloys are shown in Figure 11a-d. The EDX spectra are included mainly to demonstrate the elemental analysis of the SEM images of pure copper and its alloys. Due to plastic deformation, equiaxed grains elongate regularly in the rolling direction. For severe deformation, the crystal grains become blurred, and the crystal grains are difficult to distinguish. Thus, the microstructure of pure Cu consists of the solid phases of  $\alpha$ -Cu and insignificant intermetallic produced by trace impurities. The alloy microstructure of tin is composed of primary copper,  $\beta$ -tin, and various impurity intermetallic. Since it has the BCC crystal structure, which is different from the FCC of Al, it tends to distribute at grain boundaries, resulting in dense grain boundaries. Similarly, alloys containing lead show primary aluminum,  $\alpha$ -lead, and impurities distributed in the microstructure. But grain boundaries are not very thick because both Pb and Al alloys have the FCC crystal structure. The solder affected alloy reflects the addition of both elements [31].



(a)



(b)

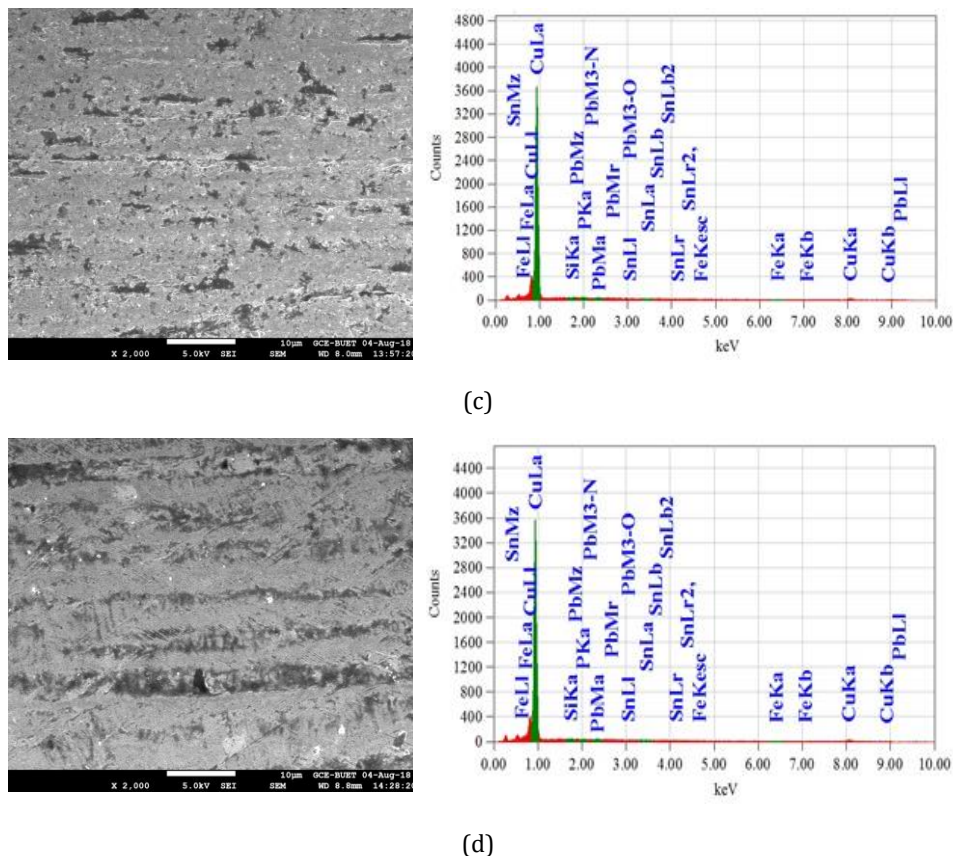


Fig. 11. SEM images along with EDX spectra of cold rolled (a) pure Cu, (b) binary Cu-Sn alloy, (c) binary Cu-Pb alloy and (d) ternary Cu-Sn-Pb alloy

The corresponding EDX for each alloy conforms to the chemical composition listed in Table 1. The EDX of the matching SEM of Cu reveals the following chemical composition by weight percentage: 99.70% Cu, 0.09% Si and 0.21% P. The EDX scan reveals the following chemical composition by the weight percentage of Cu-Sn Alloy: 97.18% Cu, 1.14% Sn, 0.25 % Pb and 0.41% Si and 0.82% Fe. Similarly, the Cu-Pb alloy shows 97.52% Cu, 1.00% Pb, 0.20% Si, 0.22% P, and 1.07% Fe. The solder affected Al-Sn-Pb alloy consists of 96.99% Cu, 0.75% Sn, 0.95% Pb, 0.15% Si, 0.29% P, and 0.87% Fe.

#### 4. Conclusions

The main findings from the present study of fractional recrystallization behaviour of pure copper containing the elements of Sn-Pb solder alloy are as follows:

- The presence of the elements of Sn-Pb solder alloy shows positive effect on the fractional recrystallization characteristic of commercially pure copper. The cold-rolled pure copper (75% deformation) is found to recrystallize 99.4% when it is annealed for a period of one hour at 700°K, whereas the same for the ternary copper alloy (Cu-Sn-Pb) is found to take place only 89.5% under the same condition. More specifically, when the results are analyzed in the perspective of individual constituent elements of the solder alloy, the effect of tin is identified to be more influential than lead in preventing the recrystallization of copper. This is because of

the fact that FCC Cu and BCC Sn lattice alloys exhibit different supersaturated solid solution patterns of higher internal stress than those of both similar lattices of Cu and Pb. Additionally, tin forms different intermetallic with Cu as well as trace impurities, but lead does not form any intermetallic with Cu.

- Under isothermal annealing, the resistivity of heavily cold-rolled alloys demonstrates an initial drop in resistivity, followed by a small increase, and finally a slow but steady decrease. The initial drop of this property is associated with dislocation, rearrangement, and recovery phenomena; secondly, the minor increase is related to different intermetallic formation; and finally, a slow and steady decrease in resistivity is due to particle coarsening, grain coarsening, and recrystallization. The rate of change of resistivity for the ternary Cu alloy is all concomitances the highest because both the elements Sn and Pb play a part in creating dislocation density.
- Pure Cu demonstrates almost identical fractional recrystallization behavior in micro-hardness data and JMAK analyses. The Sn added alloy shows the greater divergence between the two methods, followed by the individual Pb addition. In the early stage of annealing, various trace impurities create diverse intermetallic, particularly with Sn. Furthermore, Sn has a different crystal structure than Cu as well as Pb. As a result, the binary Cu-Pb alloy is less stable than the Cu-Sn alloy as well as the ternary copper alloy. When both the elements of the solder alloy are present in Cu, the resulting alloy eventually makes the discrepancy between the two methods quite significant.
- All the alloys reached a state of almost fully recrystallized after annealing at 700°K for a period of 1800 seconds, but the ternary copper alloy demonstrates a higher fraction of the dissolved second phase in the microstructure and developed grain boundaries.

### Acknowledgement

The corresponding author would like to express sincere gratitude to the authority of the International University of Business Agriculture and Technology, Dhaka, for their encouragement in promoting research activities in the university. Their efforts in fostering collaboration with other institutions are also worthy of recognition.

### References

- [1] Islak S, Çaligülü U, Hraam HRH, Özorak C, Koç V. Electrical conductivity, microstructure and wear properties of Cu-Mo coatings. *Research on Engineering Structures and Materials*, 2019; 5(2): 137-146. <http://dx.doi.org/10.17515/resm2018.58is0716>
- [2] Kaiser S, Kaiser MS. Influence of Aluminium and Zinc Additives on the Physical and Thermal Behaviour of Cast Copper. *Journal of Sustainable Structures and Materials*, 2020; 3(1): 1-9. <http://dx.doi.org/10.26392/SSM.2020.03.01.001>
- [3] Afifeh M, Hosseinipour SJ, Jamaati R. Manufacturing of pure copper with extraordinary strength-ductility-conductivity balance by cryorolling and annealing. *CIRP Journal of Manufacturing Science and Technology*, 2022; 37: 623-632. <https://doi.org/10.1016/j.cirpj.2022.03.010>
- [4] Davis JR. Introduction and Overview of Copper and Copper Alloys. *Metals Handbook Desk Edition (2nd Edition)*, ASM International, Materials Park, Ohio, USA, 1998. <https://doi.org/10.31399/asm.hb.mhde2.9781627081993>
- [5] Liu J, Liu J, Wang X. Study on Phase Transformation Dynamics, Microstructure, and Properties of the Cu-2.7Ti-2.5-Ni-0.8V Alloy. *Archives of Metallurgy and Materials*, 2023; 68(4): 1383-1390. <https://doi.org/10.24425/amm.2023.146204>

- [6] Kaiser S, Kaiser MS. Impact of cold plastic deformation and thermal post-treatment on the physical properties of copper based alloys Al-bronze and  $\alpha$ -brass. *Journal of Acta Metallurgica Slovaca*, 2021; 12(2): 103-108. <https://doi.org/10.36547/ams.27.3.951>
- [7] Zeng C, Zhang B, Ettefagh AH, Wen H, Yao H, Meng WJ, Guo S. Mechanical, thermal, and corrosion properties of Cu-10Sn alloy prepared by laser-powder-bed-fusion additive manufacturing. *Additive Manufacturing*, 2020; 35: 1-8. <https://doi.org/10.1016/j.addma.2020.101411>
- [8] Khan AA, Kaiser S, Kaiser MS. Electrochemical corrosion performance of copper and uniformly alloyed bronze and brass in 0.1 M NaCl solution. *Revista Mexicana de Física*, 2023; 69(5):1-10. [10.31349/RevMexFis.69.051002](https://doi.org/10.31349/RevMexFis.69.051002)
- [9] Constantinescu S, Popa A, Groza JR, Bock I. New high-temperature copper alloys. *Journal of Materials Engineering and Performance*, 1996; 5: 695-698. <https://doi.org/10.1007/BF02646904>
- [10] Haque MS, Khan SAR, Kaiser MS. Effect of Sc and Zr on Precipitation Behaviour of Wrought Al- Bronze. *IOP Conference Series Materials Science and Engineering*, 2022; 1248(1):1-12. <https://doi.org/10.1088/1757-899X/1248/1/012037>
- [11] Tylecote RF. *The Prehistory of Metallurgy in the British Isles*: 5, 1<sup>st</sup> edition, 1986, Taylor & Francis, London, UK. <https://doi.org/10.4324/9781351199476>
- [12] Rahman MM, Ahmed SR, Kaiser MS. On the investigation of reuse potential of SnPb-solder affected copper subjected to work-hardening and thermal ageing. *Materials Characterization*, 2021; 172(3): 1-19. <https://doi.org/10.1016/j.matchar.2021.110878>
- [13] Ahmed A, Iqbal N, Kaiser MS, Ahmed SR. Thermo-mechanical and optical characteristics of cold-rolled copper with natural melting impurities. *AIP Conference Proceedings*, 2021; 2324(1): 0300171-7. <https://doi.org/10.1063/5.0037516>
- [14] Kaiser MS. Fractional recrystallization behavior of impurity-doped commercially pure aluminum. *Journal of Energy, Mechanical, Material, and Manufacturing Engineering*, 2020; 5(2): 37-46. <https://doi.org/10.22219/jemmm.v5i2.11675>
- [15] Minggao Y, Qingsui W, Kuangdi X. Recovery and Recrystallization. In: Xu, K. (eds) *The ECPH Encyclopedia of Mining and Metallurgy*. 2023, Springer, Singapore. [https://doi.org/10.1007/978-981-19-0740-1\\_931-1](https://doi.org/10.1007/978-981-19-0740-1_931-1)
- [16] Benchabane G, Boumerzoug Z, Gloriant T, Thibon I. Microstructural characterization and recrystallization kinetics of cold rolled copper. *Physica B: Condensed Matter*, 2011; 406(10): 1973-1976. <https://doi.org/10.1016/j.physb.2011.02.068>
- [17] Rokon N, Haque MS, Kaiser MS. On the mechanical behaviour of thermally affected non-heat-treatable aluminium alloys, *Journal of Chemical Technology and Metallurgy*, 2023; 58(6): 1153-1162. <https://doi.org/10.59957/jctm.v58i6.156>
- [18] Shen K, Guo M, Wang M. Recrystallization characteristics of a fine grained copper alloy. *Materials Chemistry and Physics*, 2010; 120(2-3): 709-714. <https://doi.org/10.1016/j.matchemphys.2009.12.019>
- [19] Haessner F, Hoschek G, Tölg G. Stored energy and recrystallization temperature of rolled copper and silver single crystals with defined solute contents. *Acta Metallurgica*, 1979; 27(9): 1539-1548. [https://doi.org/10.1016/0001-6160\(79\)90176-7](https://doi.org/10.1016/0001-6160(79)90176-7)
- [20] Kaiser MS. Precipitation and softening behaviour of cast, cold rolled and hot rolling prior to cold rolled Al-6Mg alloy annealed at high temperature. *Journal of Mechanical Engineering, The Institution of Engineers, Bangladesh*, 2015; ME45(1): 32-36. <https://doi.org/10.3329/jme.v45i1.24381>
- [21] Freudenberger J, Kauffmann A, Klaub H, Marr T, Nenkov K, Sarma VS, Schultz L. Studies on recrystallization of single-phase copper alloys by resistance measurements. *Acta Materialia*, 2010; 58(7): 2324-2329. <https://doi.org/10.1016/j.actamat.2009.12.018>

- [22] Tarasiuk J, Gerber P, Bacroix B. Estimation of recrystallized volume fraction from EBSD data. *Acta Materialia*, 2002; 50(6): 1467-1477. [https://doi.org/10.1016/S1359-6454\(02\)00005-8](https://doi.org/10.1016/S1359-6454(02)00005-8)
- [23] Benchabane G, Boumerzoug Z, Thibon I, Gloriant T. Recrystallization of pure copper investigated by calorimetry and microhardness. *Materials Characterization*, 2008; 59(10): 1425-1428. <https://doi.org/10.1016/j.matchar.2008.01.002>
- [24] Rokon SMN, Kaiser MS, Shorowordi KM. Fractional recrystallization kinetics in non-heat-treatable aluminium alloys. *AIP Conference Proceedings*, 2021; 2324(1): 0600061-6. <https://doi.org/10.1063/5.0037948>
- [25] Kalu PN, Waryoba DR. A JMAK-microhardness model for quantifying the kinetics of restoration mechanisms in inhomogeneous microstructure. *Materials Science and Engineering: A*, 2007; 464(1-2): 68-75. <https://doi.org/10.1016/j.msea.2007.01.124>
- [26] Morozova A, Dolzhenko A, Odnobokova M, Zhilyaev AP, Belyakov A, Kaibyshev R. Annealing Behavior and Kinetics of Primary Recrystallization of Copper. *Defect and Diffusion Forum*, 2018; 385, 343-348. <https://doi.org/10.4028/www.scientific.net/ddf.385.343>
- [27] Zhang Z, Wang R, Peng C, Feng Y, Wang X, Wu X, Cal Z. Effect of elevated-temperature annealing on microstructure and properties of Cu-0.15Zr alloy. *Transactions of Nonferrous Metals Society of China*. 2021; 31(12): 3772-3784. [https://doi.org/10.1016/S1003-6326\(21\)65763-1](https://doi.org/10.1016/S1003-6326(21)65763-1)
- [28] Alaneme KK, Okotete EA. Recrystallization mechanisms and microstructure development in emerging metallic materials: A review. *Journal of Science: Advanced Materials and Devices*, 2019; 4(1): 19-33. <https://doi.org/10.1016/j.jsamd.2018.12.007>
- [29] Yang P, He D, Shao W, Tan Z, Guo X, Lu S, Anton K. Study of the microstructure and mechanical properties of Cu-Sn alloys formed by selective laser melting with different Sn contents. *Journal of Materials Research and Technology*, 2023; 24: 5476-5485. <https://doi.org/10.1016/j.jmrt.2023.04.198>
- [30] Kim JC, Ko BH, Moon IH. On some physical properties of nanostructured Cu-Pb alloy prepared by mechanical alloying. *Nanostructured Materials*, 1996; 7(8): 887-903. [https://doi.org/10.1016/S0965-9773\(96\)00059-1](https://doi.org/10.1016/S0965-9773(96)00059-1)
- [31] Leineweber A. The Cu-Sn System: A Comprehensive Review of the Crystal Structures of its Stable and Metastable Phases. *Journal of Phase Equilibria and Diffusion*, 2023; 44, 343-393. <https://doi.org/10.1007/s11669-023-01041-3>
- [32] Humphreys FJ, Hatherly M. *Recrystallization and related annealing phenomena*. 2<sup>nd</sup> edition, 2004, Elsevier, Oxford, UK. <https://doi.org/10.1016/B978-0-08-044164-1.X5000-2>
- [33] Kaiser MS. Fractional Recrystallization Behaviour of Al-Mg Alloy with Different Sc Addition Content. *International Journal of Materials Science and Engineering*, 2014; 2(2): 136-140, 2014. <https://doi.org/10.12720/ijmse.2.2.136-140>
- [34] Dutta S, Kaiser MS. Recrystallization Kinetics in Aluminum Piston. *Procedia Engineering*, 2014; 90: 188-192. <https://doi.org/10.1016/j.proeng.2014.11.835>
- [35] Jiang Y, Gu RC, Peterlechner M, Liu YW, Wang JT, Gerhard Wilde, Impurity effect on recrystallization and grain growth in severe plastically deformed copper. *Materials Science and Engineering: A*, 2021; 824: 141786-790. <https://doi.org/10.1016/j.msea.2021.141786>
- [36] Gierlotka W, Chen S, Lin S. Thermodynamic description of the Cu-Sn system. *Journal of Materials Research*, 2007; 22(11): 3158-3165. <https://doi.org/10.1557/JMR.2007.0396>
- [37] Li R, Wang E, Zuo X. Co-Precipitation, Strength and Electrical Resistivity of Cu-26 wt % Ag-0.1 wt % Fe Alloy. *Materials*, 2017, 10(12): 1-17. <https://doi.org/10.3390/ma10121383>

- [38] Peng J, Li J, Liu B, Fang Q, Liaw PK. Origin of thermal deformation induced crystallization and microstructure formation in additive manufactured FCC, BCC, HCP metals and its alloys. *International Journal of Plasticity*, 2024; 172: 1-21. <https://doi.org/10.1016/j.ijplas.2023.103831>

Blank Page



## Statistical models for porous asphalt mixtures containing pulverized surface dressed pavement material/low-density polyethylene waste

Hassan Shuaibu Abdulrahman<sup>1,a</sup>, Ali Almusawi<sup>2,b</sup>, Julide Oner<sup>\*3,c</sup>, Nasiru Ibrahim Ahmed<sup>1,d</sup>

<sup>1</sup>Department of Civil Engineering, Federal University of Technology Minna, Niger, Nigeria

<sup>2</sup>Department of Civil Engineering, Çankaya University, Ankara, Türkiye

<sup>3</sup>Department of Civil Engineering, Uşak University, Uşak, Türkiye

### Article Info

### Abstract

#### Article History:

Received 01 Nov 2024

Accepted 13 Jan 2025

#### Keywords:

Porous asphalt;  
Pulverized surface dressed pavement material;  
Bitumen;  
Low-density polyethylene;  
Durability test

Porous asphalt (PA) mixtures typically contain a high proportion of coarse aggregates with minimal fine aggregates, along with a binder that creates ample space for water drainage. Since road construction consumes large quantities of aggregates, recycling and reusing materials have become common practices. This study focuses on developing PA by partially replacing traditional aggregates with pulverized surface-dressed pavement material (PSM) and modifying bitumen with low-density polyethylene (LDPE). The mixtures were produced using 60/70 penetration grade bitumen modified with 2%, 4%, and 6% LDPE waste and 20%, 40%, 60%, and 80% PSM. Adding LDPE waste to the bitumen altered key properties, such as the softening point, penetration, flashpoint, and ductility, resulting in a stiffer binder. Replacing aggregates with PSM reduced both stability and flow, leading to a lower Marshall quotient. Flow values for all trial mixes did not meet AAPA (2004) standards, while stability values slightly decreased as LDPE content increased from 2% to 6%. Despite this, all samples met the AAPA (2004) stability standard. The sample containing 2% LDPE and no PSM exhibited the highest Marshall quotient. Linear regression models were developed from experimental data to highlight the relationships between the measured responses and the variables. These polynomial equations demonstrated a strong correlation, indicated by high coefficients of determination. The study introduces an innovative approach by incorporating PSM and LDPE, largely unexplored in PA production, especially in Nigeria. The major societal benefits include reducing environmental pollution through plastic waste reuse, conserving natural aggregates, and promoting cost-effective construction practices. By advancing the use of recycled materials, this research supports sustainable infrastructure development while maintaining compliance with industry standards.

© 2025 MIM Research Group. All rights reserved.

## 1. Introduction

Porous asphalt (PA) is an innovative pavement technology widely applied across the globe. Designed as a specialized wearing course, it improves road safety, especially under wet conditions. The permeable friction layer in PA rapidly drains water from the surface, offering numerous safety, economic, and environmental benefits [1,2]. European countries extensively use PA to enhance driving quality, visibility during wet weather, and reduce road traffic noise [3].

\*Corresponding author: [julide.oner@usak.edu.tr](mailto:julide.oner@usak.edu.tr)

<sup>a</sup>orcid.org/ 0000-0002-5960-0321; <sup>b</sup>orcid.org/ 0000-0002-4507-2492; <sup>c</sup>orcid.org/ 0000-0003-3229-152X;

<sup>d</sup>orcid.org/ 0009-0007-2261-2779

DOI: <http://dx.doi.org/10.17515/resm2025-512ma1101rs>

Res. Eng. Struct. Mat. Vol. 11 Iss. 1 (2025) 351-368

Structurally, PA is an open-graded asphalt mixture composed of coarse aggregates, minimal fine aggregates, binder, and high air voids [4]. Its high content of coarse aggregates creates a porous structure with 25%-30% voids. This porosity allows water from rain and snow to drain effectively from the road surface, improving slip resistance and reducing braking distances [5].

PA pavement offers significant advantages over traditional asphalt pavement, particularly in terms of drainage, noise reduction, skid resistance, and other functional properties. To enhance and expand the capabilities of road pavements, PA pavement has become a key area of research in highway engineering [6]. The most notable feature of PA is its high air void content exceeding 20% compared to the 3-6% air voids found in traditional asphalt pavements [5]. This high porosity enables rainwater to infiltrate the road surface and drain through interconnected pores to the road edges. However, PA mixtures also have some drawbacks. These include aging, stripping, raveling, drain down, reduced porosity over time, higher maintenance requirements, and a shorter service life. Addressing these issues is important for the effective use of porous asphalt.

Studies suggest that improvements in PA can be made by enhancing the properties and gradation of aggregates, modifying bituminous binders, and reinforcing the mixture with fibers [7]. Ashour investigated the stability and permeability of PA and provided reliable results on both aspects [8]. The study focused on optimizing aggregate mix ratios to achieve the desired permeability while maintaining the necessary stability. The findings showed that the tested samples exhibited excellent permeability, highlighting the effectiveness of these adjustments. Mayuni et al. evaluated PA mixtures by varying bitumen content, using a specific type of aggregate native to the West Kalimantan region of Indonesia [9]. The structural performance of the PA mixes was assessed using Marshall stability and Cantabro tests, while the functional performance was evaluated through an analysis of volumetric properties. This comprehensive approach allowed for an in-depth understanding of how bitumen content and aggregate properties affect the overall performance of porous asphalt.

The improvement of PA quality through the use of polymer-modified asphalt, other additives, and coarse aggregates has been widely studied [10,11,12]. The durability of PA mixtures is typically evaluated based on their resistance to traffic impact, abrasion, and aggregate stripping, with the Cantabro test being a common method for measuring these properties [13]. Additionally, the Marshall stability test is frequently used to determine the stability of compacted PA mixes, ensuring they can withstand loads and maintain structural integrity. In a study exploring the mechanical characteristics of PA pavement, the influence of polymer modifications and aggregate compositions was examined. The research revealed that mixtures containing conventional bitumen failed to meet the Cantabro loss test criteria of a maximum 20% loss. However, polymer-modified asphalt mixtures demonstrated significantly superior performance in terms of permeability, Cantabro loss, and the ratio of indirect tensile strength, highlighting the impact of polymer modifications on improving the essential mechanical properties of PA [14]. Gupta et al. evaluated bitumen modified with high vinyl content SBS polymer. PA mixtures prepared with 4.5% polymer-modified bitumen exhibited higher elasticity, better fatigue resistance, and improved rutting behavior [7]. Ma et al. explored additives like SBS-modified bitumen, hydrated lime, and fibers. They found that hydrated lime improved moisture stability, while fibers enhanced durability and low-temperature cracking resistance of PA mixtures [15]. Zhang et al. assessed four fiber types (lignin, polyester, basalt, polyacrylonitrile) and their effects on PA. Fiber modifications improved drainage, rutting resistance, and fatigue life, with polyester fiber providing the best overall performance [16]. Sarsam compared PA and stone mastic asphalt under repeated tensile stresses. While stone mastic asphalt showed higher tensile strength ratios, PA with carbon fiber modifications had better resistance to moisture damage [17]. Ranieri et al. investigated Warm Mix Asphalt (WMA) technologies for PA in cold climates. Results showed that PA could be laid at temperatures 20°C lower without significant performance loss, though further study is recommended [18].

Road construction and rehabilitation consume large quantities of virgin materials, resulting in high costs, particularly for highways. Surface-dressed roads, typically used for light traffic, consist of aged chippings embedded in bitumen. These reclaimed materials, primarily made up of coarse aggregates and bitumen, may be suitable for open-graded mixes [19]. Developing porous asphalt

by partially replacing traditional aggregates with pulverized surface-dressed pavement material (PSM) and modifying bitumen with low-density polyethylene (LDPE) presents a promising approach to enhancing pavement performance and sustainability [20]. Incorporating recycled materials like PSM into porous asphalt mixtures can improve environmental sustainability and resource efficiency. Reclaimed asphalt pavement (RAP), a similar recycled material, has been successfully used in various pavement applications, demonstrating that recycled aggregates can maintain or even enhance pavement performance when properly processed and integrated. Modifying bitumen with LDPE enhances corrosion resistance and the mechanical properties, offers low moisture permeability of asphalt mixtures [21]. LDPE is generally used in the form of films as well as in the production of bags for food and other products [22]. Studies have shown that adding LDPE to asphalt binders improves resistance to deformation and aging, leading to longer-lasting pavements [23]. Combining PSM as a partial aggregate replacement with LDPE-modified bitumen in porous asphalt mixtures could synergistically enhance pavement performance. The recycled aggregates contribute to sustainability and cost-effectiveness, while the polymer-modified binder improves mechanical properties and durability. This integrated approach aligns with sustainable construction practices by reducing waste and conserving natural resources [24].

In Nigeria, many surface-dressed roads are being upgraded to dense asphalt mixes. Reclaiming these materials presents a valuable alternative, especially for porous asphalt, which requires a significant amount of coarse aggregates. Nigeria generates approximately 2.5 million tons of plastic waste annually, placing it ninth globally among contributors to plastic pollution [25,26]. Unfortunately, most of this plastic waste remains unrecycled. The use of Recycled Surface-dressed Pavement (RSP) and LDPE in hot mix asphalt has similarities to studies incorporating recycled asphalt pavement (RAP) and LDPE in porous asphalt. However, the use of RSP and LDPE in developing PA remains largely unexplored, particularly in Nigeria. Globally, Nigeria ranks 28th in publications on porous asphalt, with only three studies published between 1974 and 2022 [9]. Although many experimental works have been carried out to determine the properties of PA containing recyclable materials like LDPE and PSM, yet to the best of our knowledge, no models have been introduced to predict the properties of such material. Therefore, the aim of this study is to explore the potential of utilizing PSM and LDPE in the development of porous asphalt, focusing on their effects on the performance characteristics of the mix using statistical models.

## 2. Materials

### 2.1. Material Characterization

For the purpose of this research, the following materials were used:

- *Aggregates*: Two types of aggregates were used in this experimental study, which include:

*Pulverized Surface-Dressed Pavement Material (PSM)*: This material was obtained from an old surface-dressed road in Bida, Niger State. It was then pulverized into smaller sizes, as shown in Fig. 1. RAP has been used in several studies in different percentages ranging from 5 to 100% in PA mixtures with varying levels of success [27,28]. The material used in this study is quite similar to RAP. They are pulverized surface dressed pavements materials that are aged with aggregate chippings embedded in bitumen physically [19]. Since bulk of this type of treatment is coarse aggregates and bitumen, they might be good for open graded mixes. For this study 20%, 40%, 60%, 80% of PSM was replaced with conventional aggregate by weight.

*Virgin Aggregates*: This crushed granite was obtained from local vendors in Minna, Niger State.

- *Bitumen 60/70*: The bitumen was obtained from Dantata Construction Company in Abuja, Nigeria.
- *Low-Density Polyethylene Bags*: The LDPE was obtained from Sani Basket Plastic Company in Minna, Niger State (Fig. 2). The LDPE used is colorless and has a density of  $0.92 \text{ g/cm}^3$  and a melting temperature between  $110\text{--}160^\circ\text{C}$ . Many studies have used LDPE in asphalt mixtures in various percentages ranging from 1 to 15% [29-32]. The optimum binder content used by them was 5%. Optimum Binder Content (OBC) refers to the percentage of

binder in the mix that optimizes performance parameters such as stability, flow, and durability while meeting the required standards. This study uses 2%, 4%, and 6% LDPE as a modifier for bitumen at an OBC of 5%. This is because PSM is already coated with aged bitumen; thus, higher percentages of LDPE and OBC were not used, as higher percentages might affect the stability of the mixtures. At more than 6% LDPE, the stability of the mix decreases [32].






Fig. 1. Pulverized surface dressed pavement material



Fig. 2. Shredded LDPE

Table 1. Bitumen tests

| No | Test Standards                   | Image of the tests |
|----|----------------------------------|--------------------|
| 1  | Penetration test<br>ASTM D5 [36] |                    |

|   |  |
|---|--|
| <p>2 Softening point test<br/>ASTM D36 EN 1427 [37]</p> |    |
| <p>3 Specific gravity<br/>ASTM D113 [40]</p>            | <p>-</p>   |
| <p>4 Flash point<br/>ASTM D92 [39]</p>                  |   |
| <p>5 Ductility<br/>(ASTM D70) [38]</p>                  |  |

Sieve Analysis [33], specific gravity test [34], water absorption [35], Flakiness and Elongation tests were carried out on both virgin aggregates and PSM aggregates. The following tests on bitumen and binder (bitumen + LDPE) were conducted to characterize the binder. For porous asphalt, an asphalt binder with a penetration value higher than that of conventional asphalt types is used. Additional properties and details of the procedures can be found in the relevant standards, as shown in Table 1.

### 3. Methods

This study primarily focuses on the development of PA using readily available materials, such as PS) and bitumen modified with LDPE. The experimental procedure encompasses the following steps: material characterization, mix design, sample preparation, and testing of PA properties. Material characterization includes evaluating aggregates (sieve analysis, specific gravity, water absorption, flakiness, and elongation) and bitumen (penetration, softening point, flashpoint, and ductility). The mix design involves creating PA mixtures with varying proportions of PSM (20%, 40%, 60%, 80%) and LDPE (2%, 4%, 6%) based on ASTM D704. The prepared samples undergo mechanical, hydraulic, and durability testing, such as stability, flow, permeability, and Cantabro loss evaluations. Statistical modeling techniques are applied to analyze the relationships between the variables and assess compliance with industry standards. An experimental procedure flowchart has been added and is shown in Fig. 3 to illustrate these steps clearly. The findings from these tests

provide insights into the performance of PA mixtures and their suitability for sustainable road construction.

### 3.1. Mix Design

In order to achieve the set-out objectives virgin aggregates are blended together with PSM aggregates and are both mixed together with the binder with varying percentage of LDPE. Mixing multiple types of aggregates with different gradations is a crucial first step in producing any asphalt mix. The design criteria used are based on ASTM D704. The aggregate gradation, as outlined by NAPA, is presented in Table 2.

Table 2. Porous asphalt aggregate gradation

| SN | Sieve Sizes(mm) | Gradation limits (% passing) |
|----|-----------------|------------------------------|
| 1  | 19              | 100                          |
| 2  | 12.5            | 85-100                       |
| 3  | 9.5             | 55-75                        |
| 4  | 4.75            | 10-25                        |
| 5  | 2.36            | 5-10                         |
| 6  | 0.075           | 2-4                          |

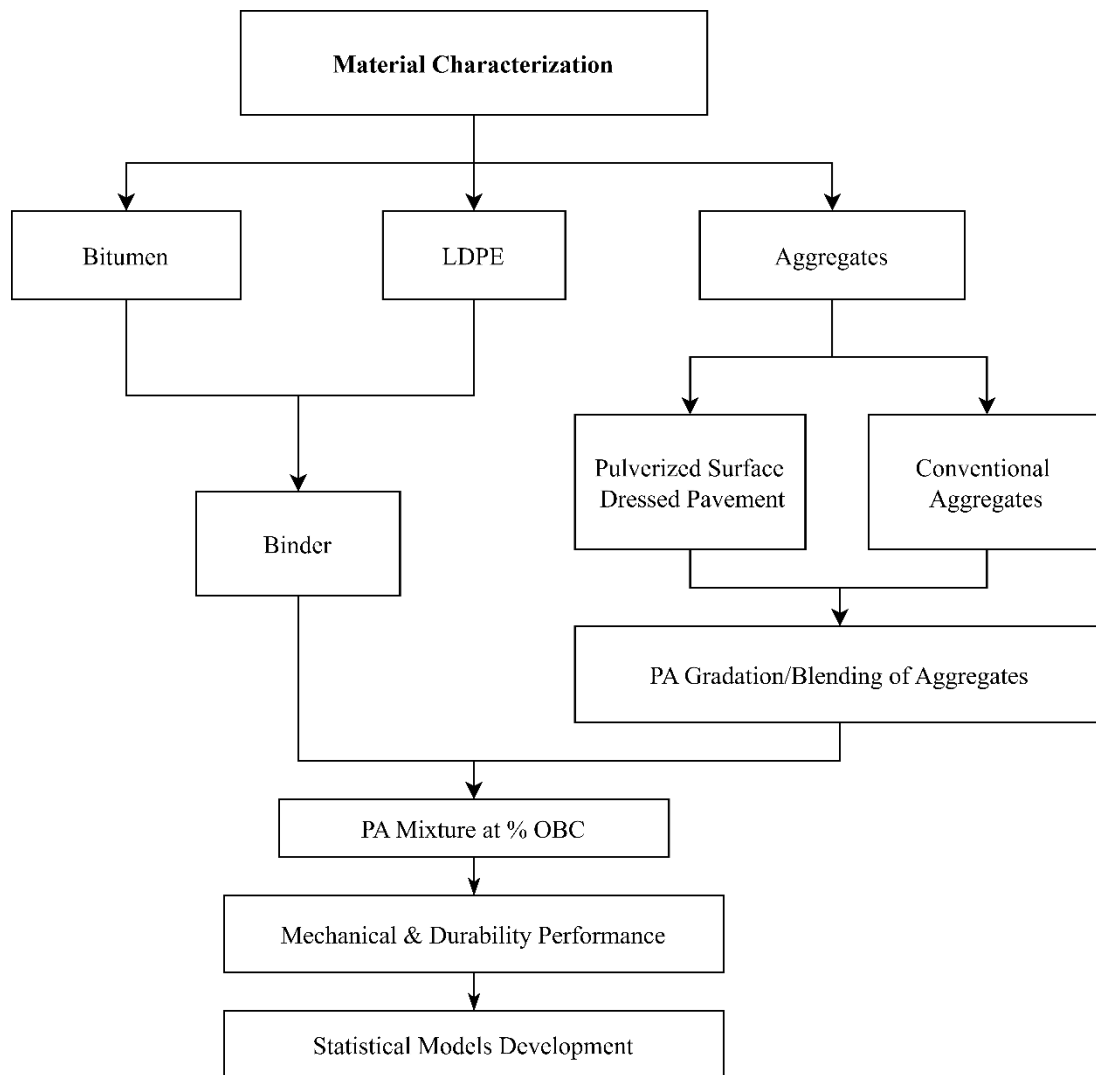


Fig. 3. Experimental procedure flowchart

### 3.2. Mechanical and Durability Performance

The PA mixtures was produced using a LDPE modified bitumen previously produced from optimum bitumen content of 5% and varying 0%, 2%, 4%, 6%, of LDPE. The binder was now mixed with 1200 g of blended aggregates 20,40,60.80% PSM by weight of conventional aggregates to produce a test sample  $63.5 \pm 1.27$  mm thick. Cylindrical samples of 50 mm diameter and 100 mm height were used for the Marshall hammer test which used 75 blows on each face following the ASTM standards. The porous asphalt mix are then subjected to the following tests presented in Table 3 based on ASTM standards.

The Drain down test was carried out to determine the portion of material which separates itself from the sample as a whole and is placed outside the wire basket during the test. The drained material could be either asphalt binder or a combination of asphalt binder, additives, or fine aggregate. The test was performed on one un compacted sample


Marshall Properties of the asphalt mix such as stability and flow was carried out on compacted samples and the Cantabro abrasion test was performed based to determine the abrasion loss of porous asphalt samples where the test was performed on un-aged compacted samples for each binder content. Also the permeability of porous asphalt was carried out on the samples. All standards used can be found in Table 3.

### 3.3 Statistical Modelling

Statistical analysis including correlation analysis, covariance analysis, trend lines, and regression analysis were employed to assess the strength of relationship between the variables. The models were created based on experimental data only to illustrate the relationships between the measured responses and variables and the interactions among the measured responses.

Microsoft Excel package was used for the model development since all the models considered here is one parameter model. This is to allow validation of the models through statistical analysis. The regression was done at 95% confidence interval.

Table 3. Mechanical and durability performance

| No | Properties/specification        | Image  |
|----|---------------------------------|--|
| 1  | Permeability<br>ASTM D5084 [41] |  |

|   |   |
|---|---|
| <p>2 Particle Loss (Cantabro)<br/>(%) Maximum<br/>ASTM D7064 [42]</p> |   |
| <p>3 Bitumen Drain down<br/>(%), Max<br/>ASTM D6390 [43]</p>          |   |
| <p>4 Marshal Stability<br/>ASTM D6927/AASHTO T<br/>245-13 [44]</p>    |  |

## 4. Results and Discussion

### 4.1. Physical Properties of Materials and Mechanical/Durability of the Mix

The results of the physical properties of the virgin and recycled surface-dressed aggregates used in this study are presented in Table 4.

Table 4. Physical properties of Virgin and PSM aggregates

| Test             | Statistics         | Virgin Aggregates | Recycled Surface-dressed Aggregates | Units |
|------------------|--------------------|-------------------|-------------------------------------|-------|
| Specific gravity | Mean               | 2.64              | 2.45                                | -     |
|                  | Standard deviation | 0.04              | 0.17                                |       |
| Water Absorption | Mean               | 5.04              | 4.30                                | %     |
|                  | Standard deviation | 0.96              | 0.23                                |       |
| Flakiness        | Mean               | 10                | 5                                   | %     |
|                  | Standard deviation | 0.14              | 1.41                                |       |
| Elongation       | Mean               | 44                | 15                                  | %     |
|                  | Standard deviation | 0.7               | 1.12                                |       |

From Table 4, the specific gravity of virgin aggregate is higher than that of PSM, as the specific gravity of PSM is typically reduced due to the inclusion of asphalt binder. The water absorption of virgin aggregate is slightly higher, indicating a dense rock with fewer pores. While asphalt binder may expose more pores, the characteristics of the original parent aggregate before coating with bitumen are unknown. The elongation and flakiness indices of both aggregates provide insights



into their quality and suitability for road construction, and both meet the NAPA 2003 general specifications.

Table 5 presents the percentage passing of the aggregate blends comprising virgin aggregates (VA) and PSM aggregates. It illustrates the different blends of virgin aggregates and PSM in varying proportions and their gradation for porous asphalt. These gradations meet the standards specified by NAPA 2003.

Table 5. Percentage passing of Virgin and PSM aggregates

| Test   | Percentage Passing |         |                  |                  |                  |                  |
|--------|--------------------|---------|------------------|------------------|------------------|------------------|
|        | 100% PSM           | 100% VA | 80% VA & 20% PSM | 60% VA & 40% PSM | 40% VA & 60% PSM | 20% VA & 80% PSM |
| 20mm   | 86.96              | 81.67   | 81.93            | 79.25            | 82.33            | 84.80            |
| 14mm   | 54.16              | 70.77   | 71.43            | 57.18            | 57.36            | 60.03            |
| 10mm   | 26.58              | 53.67   | 40.99            | 34.96            | 39.45            | 34.62            |
| 6.30mm | 13.14              | 40.23   | 24.80            | 21.78            | 27.66            | 21.22            |
| 5.00mm | 9.33               | 34.83   | 19.70            | 18.67            | 23.78            | 17.58            |
| Pan    |                    |         |                  |                  |                  |                  |

The physical properties of the bitumen and binder (bitumen + LDPE) are shown in Table 6. All tests were repeated 3 times and the average values and standard deviations are shown in Table 6. The physical properties of the bitumen + LDPE mixture show that as the proportion of LDPE increases, significant changes occur in the material's behavior. The penetration test results reveal a decrease in penetration values from 62 (0% LDPE) to 51 (6% LDPE), indicating that the bitumen becomes stiffer with the addition of LDPE. This increased stiffness enhances the mixture's resistance to deformation under load, making it more suitable for applications requiring high stability. The softening point test shows a clear trend of increased temperature stability, with the softening point rising from 55°C at 0% LDPE to 74.5°C at 6% LDPE. This suggests that the bitumen + LDPE mixture can withstand higher temperatures before softening, which is crucial for pavement performance in hot climates. However, the ductility test results indicate a reduction in flexibility as the LDPE content increases, with ductility dropping from 57 cm at 0% LDPE to 25.67 cm at 6% LDPE. This reduction in ductility means the material becomes more brittle and less capable of elongating without breaking, which could affect its crack resistance under heavy traffic. Furthermore, the flash point improves with the addition of LDPE, increasing from 104°C to 167°C as the LDPE content rises. This higher flash point suggests that the bitumen + LDPE mixture is less prone to ignition at high temperatures, contributing to overall safety during handling and application. The results of the physical properties of the LDPE modified bitumen are quite similar and to the results reported by recent studies [29,30,31,32].

Similarly, the mechanical and durability tests were repeated 3 times and the average values and are shown in Table 7.

Table 6. Physical properties of bitumen and binder (bitumen + LDPE)

| Test                 | Statistics         | 0% LDPE | 2% LDPE | 4% LDPE | 6% LDPE |
|----------------------|--------------------|---------|---------|---------|---------|
| Penetration          | Mean               | 62      | 60      | 55      | 51      |
|                      | Standard deviation | 1       | 1       | 1       | 1.41    |
| Softening point test | Mean               | 55      | 62.5    | 69      | 74.5    |
|                      | Standard deviation | 1.41    | 0.7     | 0       | 0.7     |
| Specific gravity     | Mean               | 1.0845  | 0.769   | 0.602   | 0.59    |
|                      | Standard deviation | 0.04    | 0.12    | 0.16    | 0.16    |
| Flash point          | Mean               | 104     | 127     | 149     | 163     |
|                      | Standard deviation | 2.87    | 0.82    | 2.05    | 10      |
| Ductility            | Mean               | 104     | 127     | 149     | 163     |
|                      | Standard deviation | 2.87    | 0.82    | 2.05    | 10      |

The Stability values marginally decreases as LDPE content increases from 2 to 6% at 0% PSM, but all the samples meet AAPA standard (> 500 kg) [45]. But as the PSM content increases all stability values (< 400 kg) do not meet this standard. The PSM materials has been coated with bitumen which will increase the bitumen content which will affect the stability of the porous asphalt mix. Flow values for all trial mixes do not meet the standards of 2-6% [45]. Even though a general trend shows that the addition of LDPE and PSM decreases the flow values closer to the standards.

The Cantabro loss shows marginally changes with addition of LDPE. However, as the percentage of RSM increases in the mix, the value exceeds the standards of less than 20%. The drain down value of < 0.3% is desired for porous asphalts. Most of the samples do not meet this standard. Only samples with no PSM materials meets the standards. This is connected with the fact that no fibres were used to prevent the drain down of the bitumen hence high values were recorded. Also because PSM materials are already coated with bitumen, so as the temperature increases, the more bitumen will melt and drain down. The occurrence of binder drain down through the specimen will reduce the permeability of mix. The addition of LDPE and PSM decreases permeability values. Since most agencies do not have standard values for the coefficient of permeability or permeability value It is therefore recommended that the standard values be selected based rainfall intensity of the pavement location in question [46].

Table 7. Mechanical and durability properties of porous asphalt mixtures

| SN | PSM (%) | LDPE (%) | Stability (kg) | Flow (mm) | Permeability (m/s) | Drain down (%) | Cantabro (%) |
|----|---------|----------|----------------|-----------|--------------------|----------------|--------------|
|    |         |          | Mean           | Mean      | Mean               | Mean           | Mean         |
| 1  | 0       | 2        | 650            | 9.3       | 449                | 0              | 6.94         |
| 2  | 20      | 2        | 370            | 7.3       | 413                | 0.8            | 8.14         |
| 3  | 40      | 2        | 360            | 7.6       | 278                | 5.5            | 11.42        |
| 4  | 60      | 2        | 290            | 9.9       | 275                | 9.4            | 14.52        |
| 5  | 80      | 2        | 285            | 9.6       | 222                | 28.9           | 14.7         |
| 6  | 0       | 4        | 590            | 9.6       | 397.5              | 0              | 6.72         |
| 7  | 20      | 4        | 395            | 7.8       | 303.97             | 0              | 8.52         |
| 8  | 40      | 4        | 380            | 8.3       | 283.13             | 4.7            | 14.25        |
| 9  | 60      | 4        | 395            | 9.5       | 300.61             | 8.5            | 15.56        |
| 10 | 80      | 4        | 295            | 7.7       | 293.83             | 19.2           | 19.72        |
| 11 | 0       | 6        | 640            | 8.6       | 235.13             | 0              | 6.36         |
| 12 | 20      | 6        | 395            | 8.2       | 279.4              | 0              | 8.92         |
| 13 | 40      | 6        | 572            | 9.7       | 223.17             | 0.9            | 16.37        |
| 14 | 60      | 6        | 520            | 9.5       | 329.4              | 5.7            | 21.52        |
| 15 | 80      | 6        | 480            | 7.9       | 294.77             | 14.9           | 21.9         |

### 4.2. Statistical Model Development

Correlation analysis, covariance analysis, trend lines, and regression analysis were employed to develop these models. The models were created based on experimental data to illustrate the relationships between the measured responses and variables and the interactions among the measured responses.

#### 4.2.1 Correlation Analysis

This analysis demonstrates the strength and direction of the relationship between the variables. The values range from -1 to 1, with a value close to 1 indicating a strong relationship, and the sign denoting the direction of the relationship. Tables 8-10 present the relationships for 2%, 4%, and 6% LDPE while varying the content of PSM. The correlation coefficients are generally high, but the strength and direction vary depending on the specific relationship between variables. For instance, as the stability of the mix improves, the flow decreases, leading to a negative correlation. Similarly, the correlation between stability and the Cantabro value is also negative, indicating that as the stability of the mix decreases, the Cantabro value increases, suggesting poorer resistance to wear, tear, and disintegration. Similar trends can be observed in Tables 8 to 10.

Table 8. Correlation analysis for LDPE 2%

| Factors                              | Flow (mm) | Permeability *(10 <sup>-3</sup> m/s) | Drain down test | Cantabro test (%) | Stability (kg) |
|--------------------------------------|-----------|--------------------------------------|-----------------|-------------------|----------------|
| Flow (mm)                            | 1         |                                      |                 |                   |                |
| Permeability *(10 <sup>-3</sup> m/s) | -0.99327  | 1                                    |                 |                   |                |
| Drain down test (%)                  | 0.772308  | -0.809254379                         | 1               |                   |                |
| Cantabro test (%)                    | 0.97284   | -0.954629844                         | 0.794474        | 1                 |                |
| Stability (kg)                       | -0.7998   | 0.811538002                          | -0.59368        | -0.81971          | 1              |

Table 9. Correlation analysis for LDPE 4%

| Factors                                 | Permeability*<br>(10 <sup>-3</sup> m/s) | Drain down test<br>(%) | Cantabro test<br>(%) | Stability<br>(kg) | Flow<br>(mm) |
|---|---|------------------------|----------------------|-------------------|--------------|
| Permeability*<br>(10 <sup>-3</sup> m/s) | 1                                       |                        |                      |                   |              |
| Drain down test                         | -0.60055                                | 1                      |                      |                   |              |
| Cantabro test (%)                       | -0.76669                                | 0.936227               | 1                    |                   |              |
| Stability (kg)                          | 0.861298                                | -0.89128               | -0.98573             | 1                 |              |
| Flow (mm)                               | -0.67103                                | 0.945931               | 0.950756             | -0.91213          | 1            |

Table 10. Correlation analysis for LDPE 6%

| Factors                                 | Permeability*<br>(10 <sup>-3</sup> m/s) | Drain down test<br>(%) | Cantabro test<br>(%) | Stability<br>(kg) | Flow<br>(mm) |
|---|---|------------------------|----------------------|-------------------|--------------|
| Permeability*<br>(10 <sup>-3</sup> m/s) | 1                                       |                        |                      |                   |              |
| Drain down test                         | -0.8435                                 | 1                      |                      |                   |              |
| Cantabro test (%)                       | -0.96523                                | 0.773785               | 1                    |                   |              |
| Stability (kg)                          | 0.968204                                | -0.89698               | -0.93679             | 1                 |              |
| Flow (mm)                               | -0.98812                                | 0.873321               | 0.970246             | -0.95289          | 1            |

#### 4.2.2 Covariance Analysis

The covariance matrix further aids in understanding the direction of linear relationships between variables. Positive values indicate that the variables increase together, suggesting a direct relationship, while negative values signify an inverse relationship, where one variable increases as the other decreases. The results of the covariance analysis are presented in Tables 11 to 13.

Table 11. Covariance analysis for LDPE 2%

| Factors                                 | Flow<br>(mm) | Permeability*<br>(10 <sup>-3</sup> m/s) | Drain<br>down test<br>(%) | Cantabro<br>test (%) | Stability (kg) |
|---|--------------|---|---------------------------|----------------------|----------------|
| Flow (mm)                               | 1.1544       |   |                           |                      |                |
| Permeability*<br>(10 <sup>-3</sup> m/s) | -93.536      | 7681.84                                 |                           |                      |                |
| Drain down test (%)                     | 8.7552       | -748.368                                | 111.3256                  |                      |                |
| Cantabro test (%)                       | 3.33224      | -266.7376                               | 26.72352                  | 10.16326             |                |
| Stability (kg)                          | -115.24      | 9538.6                                  | -840.02                   | -350.444             | 17984          |

Table 12. Covariance analysis for LDPE 4%

| Factors                                 | Permeability*<br>(10 <sup>-3</sup> m/s) | Drain down<br>test<br>(%) | Cantabro test<br>(%) | Stability<br>(kg) | Flow (mm) |
|---|---|---------------------------|----------------------|-------------------|-----------|
| Permeability*<br>(10 <sup>-3</sup> m/s) | 1719.117                                |                           |                      |                   |           |
| Drain down<br>test                      | -177.132                                | 50.6056                   |                      |                   |           |
| Cantabro test<br>(%)                    | -150.97                                 | 31.62988                  | 22.55454             |                   |           |
| Stability (kg)                          | 3656.884                                | -649.26                   | -479.378             | 10486             |           |
| Flow (mm)                               | -21.0716                                | 5.0964                    | 3.41972              | -70.74            | 0.5736    |

Table 13. Covariance analysis for LDPE 6%

| Factors                                 | Permeability*<br>(10 <sup>-3</sup> m/s) | Drain down<br>test<br>(%) | Cantabro<br>test<br>(%) | Stability<br>(kg) | Flow (mm) |
|---|---|---------------------------|-------------------------|-------------------|-----------|
| Permeability<br>*(10 <sup>-3</sup> m/s) | 1522.212                                |                           |                         |                   |           |
| Drain down<br>test(%)                   | -187.821                                | 32.572                    |                         |                   |           |
| Cantabro test<br>(%)                    | -240.317                                | 28.1812                   | 40.72246                |                   |           |
| Stability (Kg)                          | 3129.594                                | -424.12                   | -495.272                | 6863.84           |           |
| Flow (mm)                               | -27.3041                                | 3.53                      | 4.38508                 | -55.912           | 0.5016    |

4.2.3 Relationships Between Responses and Proportion of LDPE and PSM

The results illustrated in Figs. 4-8 can be understood by looking at the contrasting characteristics of PSM and LDPE. The PSM tends to be rigid and somewhat brittle, while LDPE is a more flexible, ductile material. When these two materials are combined in pavement mixtures, they produce various effects on the mechanical and functional qualities of the final product. For instance, the decreasing stability seen in Fig.4 can be linked to PSM's rigidity. It seems to weaken the mix's cohesion and binding strength. The more PSM you include, the less stable the pavement becomes. LDPE, though flexible, doesn't quite make up for the cohesion loss caused by PSM particles. On the other hand, Fig. 5 shows that the flow increases as the PSM content rises, suggesting that PSM and LDPE together contribute to a more flexible and deformable mixture. LDPE's elasticity adds to the material's ability to endure deformation, while PSM adds bulk. However, too much PSM can result in too much deformation, making the pavement vulnerable to rutting under heavy loads.

Fig. 6 highlights how the Cantabro loss rises with higher PSM levels, which likely comes from the reduced cohesion and adhesion when more PSM is introduced. The rigid structure of PSM, particularly in large amounts, lowers the pavement's durability, increasing surface wear. This effect is more pronounced when LDPE is not present in sufficient quantities to maintain a flexible and cohesive binder. The rise in drain down (Fig. 7) with higher PSM content suggests that the binder has trouble staying in place. RSP, because of its rigidity and granular nature, separates from the binder, which leads to more binder loss. Although LDPE enhances the mixture's elasticity, it can't stop the binder from draining, especially as PSM content grows.

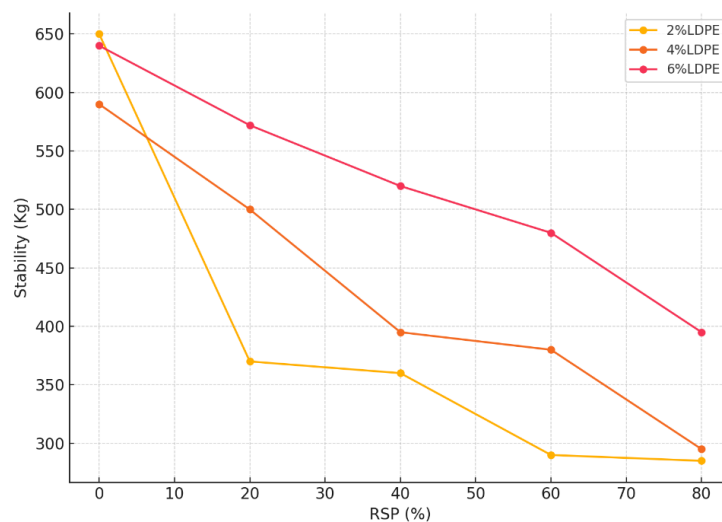


Fig. 4. Stability versus percentage PSM

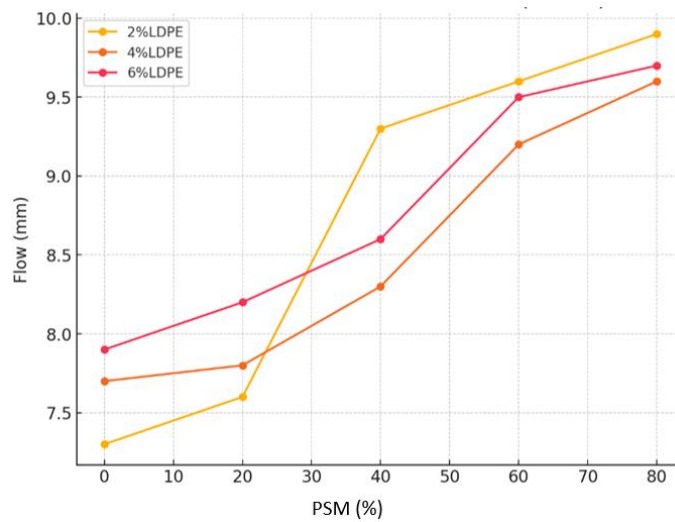


Fig. 5.: Flow versus percentage PSM

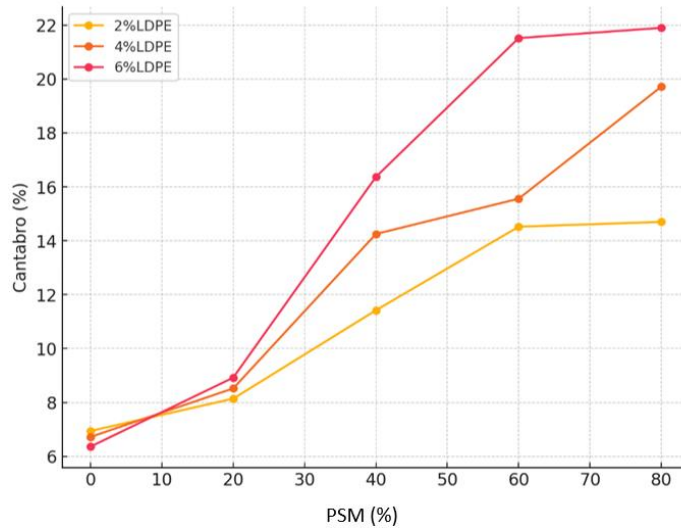


Fig. 6. Cantabro versus percentage PSM

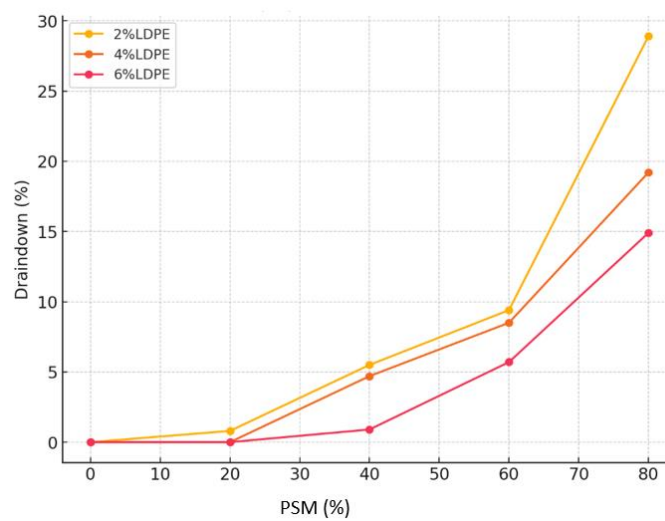


Fig. 7. Drain down versus percentage PSM

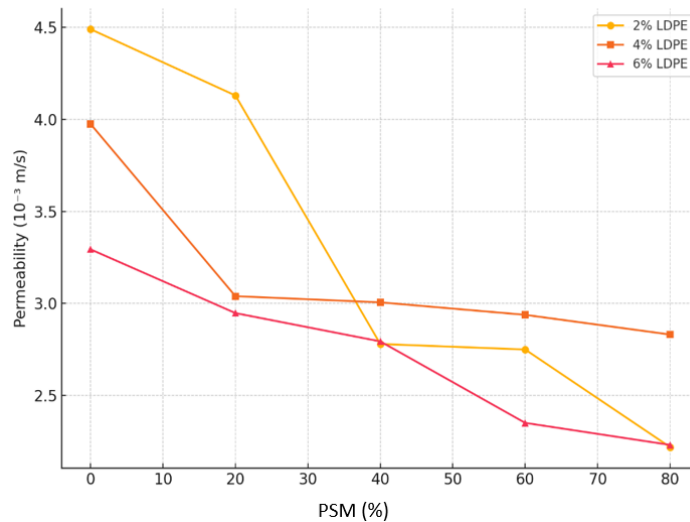


Fig. 8. Permeability versus percentage PSM

Lastly, the decrease in permeability shown in Fig. 8 can be attributed to the increased density and decreased porosity as more PSM is added. The relatively non-porous nature of PSM makes it harder for water to penetrate the mixture. LDPE fills in voids and forms a continuous matrix, further reducing permeability. However, too much PSM might make the pavement overly impermeable, which can cause problems with surface water drainage. In summary, the combination of PSM and LDPE shows a balance between stiffness and flexibility, and the results clearly demonstrate how these materials interact to influence pavement properties like stability, flow, durability, and permeability.

#### 4.2.4 Regression Analysis of the Impact of PSM and LDPE Content on Pavement Properties

The regression analysis conducted on the relationship between pavement properties and the percentage of PSM at varying levels of LDPE content offers valuable insight into how these materials behave. For pavements containing 2% LDPE (Table 14), the results reveal a robust link between RSP content and permeability, with an R-squared value of 0.912, indicating a well-fitting model. This suggests that permeability decreases significantly as RSP increases, a trend further supported by a negative coefficient of -2.96 and a low P-value, which confirms the statistical relevance of the result. However, while stability also diminishes with more RSP, the model for this behavior is weaker, as shown by a lower R-squared of 0.729 and a P-value of 0.065, which suggests less confidence in this connection. Flow, by contrast, shows a strong positive relationship, as indicated by an R-squared of 0.898, meaning that as RSP rises, flow increases. For Cantabro loss, which is a measure of durability, the model demonstrates a strong fit with an R-squared of 0.943, and the positive coefficient points to reduced durability. Drain down also increases moderately as RSP content goes up, reflected by an R-squared of 0.792.

When LDPE content is raised to 4% (Table 15), the analysis suggests stronger correlations. The reduction in permeability with increasing PSM is even more pronounced, with an R-squared of 0.947, and is statistically significant. Similarly, the decrease in stability follows the same downward trend observed at the 2% LDPE level but with a better fit (R-squared of 0.935). Flow rates spike sharply, as seen by a very high R-squared value of 0.979, while Cantabro loss continues to increase, indicating a decline in durability. The drain down also rises significantly as PSM levels increase, with a reliable fit shown by an R-squared of 0.940. For pavements containing 6% LDPE (Table 16), the trends are consistent with the previous two LDPE levels. Permeability further decreases as PSM content rises, supported by a strong model fit (R-squared of 0.946). Stability continues to drop, again, with a very strong model fit (R-squared of 0.974). Flow increases further, with an R-squared of 0.947, while Cantabro loss continues to rise but with slightly less statistical strength than at lower LDPE levels. Drain down also increases, though its statistical significance is weaker.

In conclusion, these findings show clear linear relationships between PSM content and various pavement properties. As PSM content rises, permeability and stability decrease, while flow, Cantabro loss, and drain down increase. The models are reliable based on the high R-squared values, but the strength of statistical significance varies, particularly for Cantabro loss and drain down. These trends underscore the trade-off between incorporating recycled materials for environmental benefits and the associated drawbacks in terms of durability and cohesion, with LDPE offering some resilience but not entirely offsetting the effects of PSM.

Table 14. Regression Statistics for 2% LDPE

| Statistics /Relationships  | R <sup>2</sup> | Adjusted R <sup>2</sup> | F     | Significance F | P-value   |          | Coefficient |          |
|----------------------------|----------------|-------------------------|-------|----------------|-----------|----------|-------------|----------|
|                            |                |                         |       |                | Intercept | Variable | Constant    | variable |
| Permeability versus %PSM   | 0.91           | 0.88                    | 31.26 | 0.01           | 0.0004    | 0.0112   | 445.8       | -2.96    |
| Stability versus %PSM      | 0.72           | 0.63                    | 8.09  | 0.06           | 0.004     | 0.0653   | 553         | -4.05    |
| Flow versus %PSM           | 0.89           | 0.86                    | 26.44 | 0.01           | 0.0001    | 0.0142   | 10.18       | -0.036   |
| Cantabro (%) versus %PSM   | 0.94           | 0.92                    | 50.39 | 0.00           | 0.002     | 0.005    | 6.764       | 0.1095   |
| Drain down (%) versus %PSM | 0.79           | 0.72                    | 11.42 | 0.04           | 0.43      | 0.043    | -4.36       | 0.332    |

Table 15. Regression Statistics for 4% LDPE

| Statistics /Relationships  | R <sup>2</sup> | Adjusted R <sup>2</sup> | F     | Significance F | P-value   |          | Coefficient |          |
|----------------------------|----------------|-------------------------|-------|----------------|-----------|----------|-------------|----------|
|                            |                |                         |       |                | Intercept | Variable | Constant    | variable |
| Permeability versus %PSM   | 0.94           | 0.92                    | 35.62 | 0.026          | 0.000     | 0.026    | 312.71      | -0.34    |
| Stability versus %PSM      | 0.93           | 0.90                    | 28.76 | 0.033          | 0.003     | 0.033    | 550         | -3.15    |
| Flow versus %PSM           | 0.97           | 0.96                    | 92.30 | 0.010          | 0.000     | 0.010    | 7.15        | 0.03     |
| Cantabro (%) versus %PSM   | 0.94           | 0.92                    | 37.39 | 0.025          | 0.065     | 0.025    | 5.785       | 0.17     |
| Drain down (%) versus %PSM | 0.93           | 0.90                    | 31.30 | 0.030          | 0.137     | 0.030    | -7.25       | 0.30     |

Table 16. Regression Statistics for 6% LDPE

| Statistics /Relationships  | R <sup>2</sup> | Adjusted R <sup>2</sup> | F     | Significance F | P-value   |          | Coefficient |          |
|----------------------------|----------------|-------------------------|-------|----------------|-----------|----------|-------------|----------|
|                            |                |                         |       |                | Intercept | Variable | Constant    | variable |
| Permeability versus %PSM   | 0.94           | 0.91                    | 35.28 | 0.02           | 0.00      | 0.02     | 322.88      | -1.29    |
| Stability versus %PSM      | 0.97           | 0.96                    | 75.0  | 0.01           | 0.00      | 0.01     | 634.5       | -2.85    |
| Flow versus %PSM           | 0.94           | 0.92                    | 35.5  | 0.02           | 0.00      | 0.02     | 7.65        | 0.02     |
| Cantabro (%) versus %PSM   | 0.88           | 0.82                    | 15.1  | 0.05           | 0.18      | 0.05     | 6.15        | 0.22     |
| Drain down (%) versus %RSP | 0.87           | 0.81                    | 14.2  | 0.06           | 0.19      | 0.06     | -7          | 0.24     |

### 4.3. Failure Modes of Samples

The failure modes of the porous asphalt (PA) samples were carefully assessed during the mechanical and durability testing phases. These observations provide critical insights into the performance of the mixtures under various conditions and offer guidance for optimizing mix design. Samples with higher Pulverized Surface-Dressed Pavement Material (PSM) content exhibited a brittle failure mode, characterized by visible cracks forming under load during the Marshall Stability Test. Conversely, samples with higher Low-Density Polyethylene (LDPE) content demonstrated a ductile failure mode, with significant deformation but delayed cracking. The brittleness in PSM-heavy samples is attributed to the reduced flexibility of aged aggregates. LDPE content enhanced elasticity, counteracting brittleness but requiring optimal proportions for effectiveness. This highlights the trade-off between rigidity and flexibility in PA mix design. Excessive PSM reduces load-bearing capacity, while LDPE improves deformation tolerance. Surface raveling and aggregate dislodgment were observed during the Cantabro Abrasion Test in samples with insufficient binder content. High PSM content exacerbated this effect due to reduced cohesion. The aged and granular nature of PSM decreased binder adhesion, increasing Cantabro loss. Optimized LDPE content mitigated these effects, enhancing resistance to disintegration. Maintaining sufficient binder content and incorporating LDPE is critical for durability under abrasion. During the Permeability Test, clogging and reduced water flow occurred in samples with excessive PSM content, impairing permeability. Balanced LDPE and PSM contents preserved structural integrity and functional porosity. The compacted structure of PSM-heavy samples



reduced voids, while LDPE enhanced void space continuity. Proper proportioning of PSM and LDPE is vital to retain permeability, a key functional property of PA.

Binder drainage was prevalent during the Drain Down Test in samples with low LDPE content, resulting in binder separation. This issue was mitigated in samples with higher LDPE content. LDPE increased binder viscosity and adhesion, reducing the likelihood of binder separation during mixing and compaction. Optimal LDPE content ensures uniform binder distribution and minimizes material loss.

Excessive flow and reduced stability were noted in samples with high PSM content, leading to structural instability under load. The rigidity of PSM decreased cohesive strength, while LDPE improved flexibility but required precise optimization. Achieving a balance between stability and flow is essential to prevent deformation or premature cracking. These failure modes underline the importance of balancing PSM and LDPE proportions in PA mix design. Excessive PSM compromises cohesion and stability, while insufficient LDPE limits elasticity and binder performance. By optimizing these components, durable and functional PA mixtures can be developed, meeting both performance and sustainability objectives.

## 5. Conclusions

From the results of this study, the following conclusions can be drawn:

- **Aggregate Standards:** The aggregates, including granite and recycled surface-dressed pavement (RSP), were shown to meet porous asphalt (PA) standards. The specific gravity of virgin aggregates was 2.64, slightly higher than RSP (2.45), reflecting their suitability for PA applications.
- **Binder Property Enhancement:** Adding low-density polyethylene (LDPE) significantly improved binder properties, increasing the softening point from 55°C to 74.5°C and flashpoint from 104°C to 167°C. However, ductility decreased from 57 cm to 25.67 cm, indicating reduced flexibility.
- **Porous Asphalt Performance:** Porous asphalt mixtures were successfully produced with local materials, incorporating RSP as an aggregate replacement and LDPE as a binder modifier. These mixtures demonstrated sufficient stability and met most industry standards.
- **Stability and Permeability Trends:** Stability decreased with increasing RSP content, and flow values were inconsistent, indicating room for optimization. Permeability also decreased due to reduced void spaces, impacting water drainage efficiency.
- **Sustainability and Hydraulic Benefits:** The use of RSP and LDPE reduces reliance on virgin aggregates, providing a cost-effective and environmentally sustainable solution for road construction. Additionally, PA's higher permeability enhances stormwater management and mitigates urban flooding, making it ideal for road shoulders and other applications.
- **Societal and Academic Contributions:** This research offers practical solutions for managing plastic waste and reclaiming road materials, promoting sustainable infrastructure development. Academically, it fills a gap by introducing statistical models to predict PA performance and provides valuable insights for further studies on sustainable materials in road construction.

## 6. Limitations and Recommendations

- **Limitations:** The study primarily focused on laboratory-scale testing, and the performance of porous asphalt mixtures with RSP and LDPE under real-world traffic and environmental conditions was not assessed. Additionally, the flow values of the mixtures require further refinement to meet AAPA (2004) standards.
- **Recommendations for Future Work:** Future studies should include long-term field performance evaluations under varying traffic loads and environmental conditions. Exploring the use of additional modifiers, such as fibers or alternative polymers, could help optimize the flow properties and overall durability of the mixtures. Research on the environmental impact and lifecycle assessment of these mixtures would also enhance their adoption in sustainable construction practices.

## References

- [1] Hao G., He M, Lim SM, Ong GP, Zulkati A, Kapilan S. Recycling of plastic waste in porous asphalt pavement: Engineering, environmental, and economic implications. *Journal of Cleaner Production*, 2024; 440: 140865. <https://doi.org/10.1016/j.jclepro.2024.140865>
- [2] Hao G, Lim SM, He M, Ong GP, Zulkati A, Kapilan S, Tan JH. Long-term performance of porous asphalt pavement incorporating recycled plastics. *Resources, Conservation and Recycling*, 2025; 212: 107979. <https://doi.org/10.1016/j.resconrec.2024.107979>
- [3] Lyons KR, Putman BJ. Laboratory evaluation of stabilizing methods for porous asphalt mixtures. *Construction and Building Materials*, 2013; 49: 772-780. <https://doi.org/10.1016/j.conbuildmat.2013.08.076>
- [4] Sun Y, Zhang X, Chen J, Liao J, Shi C, Huang C. Mixing design and performance of porous asphalt mixtures containing solid waste. *Case Studies in Construction Materials*, 2024; 21: e03644. <https://doi.org/10.1016/j.cscm.2024.e03644>
- [5] Lokesh Y, Parate HR, Swamy HM, Ali H. Development of prediction model for structural behavior and gradation of porous asphalt pavement. *Discover Civil Engineering*, 2024; 1(1): 1-11. <https://doi.org/10.1007/s44290-024-00012-y>
- [6] Rodzi AM, Masri KA, Shahnewaz SM, Ferdaus R, Abd Ghani NAA, Arshad AK. Microstructure analysis and permanent deformation of porous asphalt incorporating steel fiber. In *IOP Conference Series: Earth and Environmental Science*, 2024; 1296 (1): 012018. <https://doi.org/10.1088/1755-1315/1296/1/012018>
- [7] Gupta A, Rodriguez-Hernandez J, Castro-Fresno D. incorporation of additives and fibers in porous asphalt mixtures: A review. *Materials*, 2019; 12: 3156. <https://doi.org/10.3390/ma12193156>
- [8] Ashour B. The Relationship between mechanical properties and initial temperature of compacted asphalt mixture of binder course. M.Sc Dissertation, Islamic University of Gaza, Palestine, 2017.
- [9] Mayuni S, Wardani SPR, Setiadji BH. Science mapping of porous asphalt pavement and open graded friction course (OGFC). *Civil Engineering and Architecture*, 2022; 11(1): 36-50. <https://doi.org/10.13189/cea.2023.110104>
- [10] Chen JS, Lee CT, Lin YY. Influence of engineering properties of porous asphalt concrete on long term performance. *Journal of Materials in Civil Engineering*, 2016; 29(4):0416246. [https://doi.org/10.1061/\(ASCE\)MT.1943-5533.0001768](https://doi.org/10.1061/(ASCE)MT.1943-5533.0001768)
- [11] Shirini B, Imaninasab R. Performance evaluation of rubberized and SBS modified porous asphalt mixtures. *Construction and Building Materials*, 2016; 107: 165-171. <https://doi.org/10.1016/j.conbuildmat.2016.01.006>
- [12] Hassan Q, Viktor P, Al-Musawi T J, Ali BM, Algburi S, Alzoubi HM, Jaszczur M. The renewable energy role in the global energy Transformations. *Renewable Energy Focus*, 2024; 48: 100545. <https://doi.org/10.1016/j.ref.2024.100545>
- [13] Poulidakos LD, Gubler R, Partl MN, Pittet M, Arnaud L, Junod A, Simond E. Mechanical properties of porous asphalt, recommendations for standardization. *Swiss Federal Laboratory for Materials Testing and Research, Empa, Dübendorf, Switzerland*, 2006.
- [14] Ibis AB, Sengoz B, Almusawi A, Ozdemir DK, Topal A. Mechanical characteristics of environmentally friendly permeable pavement: Enhanced porous asphalt. *Jordan Journal of Civil Engineering*, 2024; 18(2): 212-223. <https://doi.org/10.14525/IJCE.v18i2.05>
- [15] Ma X, Li Q, Cui YC, Ni AQ. Performance of porous asphalt mixture with various additives. *International Journal of Pavement Engineering*, 2018; 19(4): 355-361. <https://doi.org/10.1080/10298436.2016.1175560>
- [16] Zhang J, Huang W, Zhang Y, Lv Q, Yan C. Evaluating four typical fibers used for OGFC mixture modification regarding drainage, raveling, rutting and fatigue resistance. *Construction and Building Materials*, 2020; 253: 119131. <https://doi.org/10.1016/j.conbuildmat.2020.119131>
- [17] Sarsam SI. Comparative evaluation of moisture susceptibility for porous and stone matrix asphalt concrete. *Indian Journal of Engineering*, 2021; 18: 424-432.
- [18] Ranieri V, Kowalski KJ, Berloco N, Colonna P, Perrone P. Influence of wax additives on the properties of porous asphalts. *Construction and Building Materials*, 2017; 145: 261-271. <https://doi.org/10.1016/j.conbuildmat.2017.03.181>
- [19] Alhassan M, Alhaji MM, Saidu AE. Investigating the performance of full depth reclaimed surface-dressed pavement treated with cement and calcium carbide residue as road base. *Nigerian Journal of Engineering and Applied Sciences: Federal University of Technology, Minna*, 2022.
- [20] Alghrafi YM, Abd Alla ESM, El-Badawy SM. Rheological properties and aging performance of sulfur extended asphalt modified with recycled polyethylene waste. *Construction and Building Materials*, 2021; 273: 121771. <https://doi.org/10.1016/j.conbuildmat.2020.121771>
- [21] Awwad MT, Shbeeb L. The use of polyethylene in hot asphalt mixtures. *American Journal of Applied Sciences*, 2007; 4(6): 390-396. <https://doi.org/10.3844/ajassp.2007.390.396>

- [22] Bensaada A, Soudani K, Haddadi S. Effects of short-term aging on the physical and rheological properties of plastic waste-modified bitumen. *Innovative Infrastructure Solutions*, 2021; 6: 1-12. <https://doi.org/10.1007/s41062-021-00471-7>
- [23] Roja KL, Masad E, Krishnamoorthy SK, Ouederni M. Ageing characteristics of polyethylene-modified asphalt binders blended with different compatibilisers. *Road Materials and Pavement Design*, 2023; 24(1): 672-689. <https://doi.org/10.1080/14680629.2023.2181123>
- [24] Junaid M, Jiang C, Eltwati A, Khan D, Alamri M, Eisa MS. Statistical analysis of low-density and high-density polyethylene modified asphalt mixes using the response surface method. *Case Studies in Construction Materials*, 2024; 21: e03697. <https://doi.org/10.1016/j.cscm.2024.e03697>
- [25] Anichebe E. Plastic Plague in Nigeria: Lessons from Other Nations. [https://www.thisdaylive.com/index.php/2019/12/16/plastic-plague-in-nigeria-lessons-from-other-/,](https://www.thisdaylive.com/index.php/2019/12/16/plastic-plague-in-nigeria-lessons-from-other-/) 2019.
- [26] Dumbili E, Henderson L. The Challenge of plastic pollution in Nigeria. *Plastic Waste and Recycling*. Academic Press, 2020: 569-583. <https://doi.org/10.1016/B978-0-12-817880-5.00022-0>
- [27] Qiu J., Huurman M, Bruin B, Demmink EW, Frunt MHT. Towards 90% warm re-use of porous asphalt using foaming technology. *Journal of Cleaner Production*, 2018; 190: 251-260. <https://doi.org/10.1016/j.jclepro.2018.04.086>
- [28] Goh SW, You Z. Mechanical properties of porous asphalt pavement materials with warm mix asphalt and RAP. *Journal of Transportation Engineering*, 2012; 138(1): 90-97. [https://doi.org/10.1061/\(ASCE\)TE.1943-5436.0000307](https://doi.org/10.1061/(ASCE)TE.1943-5436.0000307)
- [29] Kolo SS, Jimoh YA. Dissolved wastewater sachet as a modifier of optimum bitumen content in asphalt mixes. *Epistemics in Science, Engineering and Technology*, 2011; 1(4): 176-184.
- [30] Rokade S. Use of waste plastic and waste rubber tyres in flexible highway pavements. In *International conference on future environment and energy, IPCBEE (Vol. 28)*, 2012.
- [31] Nkanga UJ, Joseph JA, Adams FV, Uche OU. Characterization of bitumen/plastic blends for flexible pavement application. *Procedia Manufacturing*, 2017; 7: 490-496. <https://doi.org/10.1016/j.promfg.2016.12.051>
- [32] Eme DB, Nwaobakata C. Effect of low density polyethylene as bitumen modifier on some properties of hot mix. *Nigerian Journal of Technology (NIJOTECH)*, 2019; 38 (1): 1-7. <https://doi.org/10.4314/njt.v38i1.1>
- [33] American Standards for Testing of Materials ASTM C 127. Annual Book of ASTM Standards.
- [34] American Standards for Testing of Materials ASTM C128. Annual Book of ASTM Standards.
- [35] American Standards for Testing of Materials ASTM C136. Annual Book of ASTM Standards
- [36] American Standards for Testing of Materials ASTM D5 EN 14264. Annual Book of ASTM Standards.
- [37] American Standards for Testing of Materials ASTM D36 EN 1427. Annual Book of ASTM Standards.
- [38] American Standards for Testing of Materials ASTM D70. Annual Book of ASTM Standards.
- [39] American Standards for Testing of Materials ASTM D92. Annual Book of ASTM Standards.
- [40] American Standards for Testing of Materials ASTM D113. Annual Book of ASTM Standards.
- [41] American Standards for Testing of Materials ASTM D5084. Annual Book of ASTM Standards.
- [42] American Standards for Testing of Materials ASTM D7064. Annual Book of ASTM Standards.
- [43] American Standards for Testing of Materials ASTM D6390. Annual Book of ASTM Standards.
- [44] American Standards for Testing of Materials ASTM D6927. Annual Book of ASTM Standards.
- [45] Australian Asphalt Pavement Association (AAPA) (2004). National Asphalt Specification.
- [46] Alvarez AE, Martin AE, Estakhri C. A review of mix design and evaluation research for permeable friction course mixtures. *Construction and Building Materials*, 2011 25: 1159-1161. <https://doi.org/10.1016/j.conbuildmat.2010.09.038>

Blank Page

Research Article

## Enriching asphalt binders' rheology by joining nano-copper oxide as a modifier

Baran Ramadhan Omer<sup>\*,1,a</sup>, Ganjeena J. Khoshnaw<sup>2,b</sup>

<sup>1</sup>Department of Civil Engineering, College of Engineering, University of Duhok, Duhok, Iraq

<sup>2</sup>Road Construction Department, Erbil Technology College, Erbil Polytechnic University, Erbil, Iraq

### Article Info

### Abstract

#### Article History:

Received 02 Jan 2025

Accepted 13 Jan 2025

#### Keywords:

Nanomaterials;  
Nano-copper oxide;  
Asphalt conventional tests;  
Bending beam rheometer;  
Dynamic shear rheometer

The durability of road surfaces faces persistent challenges due to increasing traffic loads and the vulnerability of traditional asphalt binders to aging, temperature fluctuations, and fatigue cracking. To address these issues, researchers have explored the integration of nanomaterials into asphalt binders to enhance their durability and rheological performance. Bitumen 60/70 Penetration Grade, commonly produced in Iraq, is rarely used locally due to its sensitivity to temperature variations. In this study, Nano-Copper Oxide was incorporated as a modifier into the asphalt binder at concentrations of 2%, 4%, 6%, and 8% by weight. The modified binders underwent conventional tests such as Penetration, Softening Point, and Ductility, alongside rheological tests including the Dynamic Shear Rheometer and Bending Beam Rheometer. The results revealed significant improvements in penetration reaching about 25% and 37% at 6% content for both unaged and aged samples, respectively. While the lowest temperature susceptibility found at 4% content. Additionally, the viscoelastic behavior was improved, as indicated by higher  $G^*$  values and lower  $\delta$  values compared to the original binder with enhanced stiffness and reduced aging effects as confirmed by the Rolling Thin Film Oven Test. Furthermore, the nano-modified binders met SuperPave™ specifications and exhibited resistance to low-temperature cracking only at -6 °C and failed at -12 °C. These findings suggest the potential for extended pavement service life and increased durability through the use of nano-modified asphalt binders.

© 2025 MIM Research Group. All rights reserved.

## 1. Introduction

The success of any modifier for asphalt binder can be assessed built on two main criteria: (a) its behavior while performing, which includes features such as resistance to rutting, moisture damage, fatigue, and low-temperature thermal cracking once applied on sites; and (b) its practical requirements before site usage, including modifier dispersal within the asphalt binder medium, stability at high storage temperatures, resistance to aging throughout the construction phase, and workability [1-4]. Although currently applied modifiers, such as crumb rubber, polymers, and additives have demonstrated significant improvements in in-service performance, they still face challenges related to phase separation at high temperatures and poor compatibility before field application. Additionally, unmodified asphalt binders tend to become stiffer before application due to a higher degree of oxidation, presenting another functional challenge [5, 6].

Researchers are therefore working to address these challenges in modified binders while also seeking to improve the performance of unmodified asphalt binders through the use of innovative materials. Recently, nanotechnology has raised as a potential field, using elements such as nano-clay, nano-silica ( $\text{SiO}_2$ ), nano-alumina ( $\text{Al}_2\text{O}_3$ ), nano-copper oxide ( $\text{CuO}$ ), carbon nanotubes (CNT),

\*Corresponding author: [baran.omer@uod.ac](mailto:baran.omer@uod.ac)

<sup>a</sup>orcid.org/ 0009-0000-6447-2566; <sup>b</sup>orcid.org/ 0000-0001-9424-779X

DOI: <http://dx.doi.org/10.17515/resm2025-607ma0102rs>

nano-titanium oxide (TiO<sub>2</sub>) and other nanomaterials to improve the characteristics of bitumen. This technique provides unique options for sustainable and durable asphalt infrastructures, with several nano-sized elements demonstrating potential in enhancing the physicochemical characteristics of bitumen [7-9]. This advanced technology is regarded as the most recent innovation for creating safe and sustainable pavement infrastructure. Despite many years of research and exploration by scientists, material manufacturers, and engineers, the application of nanotechnology has remained restricted. Thus, there has been renewed effort and investigation into developing nanomaterials for pavement applications, focusing on enhancing the nanoscale rheological properties and the durability of the mixtures [10-15].

Numerous studies have demonstrated the potential of nanomaterials in enhancing bitumen properties. Yao et al. found that nano silica significantly improved rheological properties, stiffness, and resistance to rutting and aging, with optimal results at 4–6% concentrations [16]. Cheraghian et al. highlighted the benefits of fumed silica nanoparticles in enhancing binder stability and aging resistance [17], while Masri et al. identified 2% nano silica as optimal for maintaining viscoelastic behavior and minimizing strain under stress. Similarly [18], Alhamali et al. and Zghair et al. observed improved performance at higher nano silica concentrations, though challenges like reduced ductility and storage stability were noted [19, 20]. Also, recent studies by Ashish and Singh and Amini et al. demonstrated the use of nano-CuO with multi-wall carbon nanotubes to improve temperature susceptibility, viscosity, and resistance to aging and rutting, showcasing the potential for hybrid nanocomposites [12, 21]. Also, nanomaterials' role in improving moisture damage resistance, aging resistance, and high-temperature performance has been emphasized by reviewer [22, 23]. Other study by Yang and Tighe, explored the effectiveness of various nanoparticles like nano clay, nanotubes, and nano-titanium dioxide, with improvements in crack resistance, fatigue resistance, and environmental sustainability [24].

Despite extensive research on enhancing asphalt binders, limited studies have focused exclusively on the use of nanomaterials, such as nano-CuO, either independently or without combining them with other compounds. This gap is critical, as it pertains to understanding the unique impact of nanoparticles on the performance of asphalt binders, offering the potential for more cost-effective and efficient alternatives. The primary objective of this study is to address the shortcomings of traditional asphalt binders, particularly in terms of aging resistance, temperature susceptibility, and fatigue cracking, which collectively contribute to the premature deterioration of asphalt pavements. This study aims to enhance the durability and performance of asphalt binders through the direct incorporation of nano-CuO, without the inclusion of other additives such as polymers, elastomers, rubbers, or chemical additives.

## 2. Materials and Methods

### 2.1. Materials

#### 2.1.1. Asphalt Binder

In this study, a 60/70 penetration grade asphalt binder, supplied by the Directorate of Roads and Bridges – Duhok, was used in this study. Conventional tests according to American Society for Testing and Materials (ASTM) standards were conducted to analyze the rheological properties of the original asphalt binder, as detailed in Table 1. The results of the tests indicate that the asphalt binder generally meets the requirements specified by ASTM D946M-15, which is related to the standard specification for penetration-graded asphalt binder for use in pavement construction.

Table 1. Asphalt binder properties per ASTM D946M-15

| Tests (Unit)                              | Requirements | Results    |
|---|--------------|------------|
| Penetration at 25°C (0.1mm)               | 60-70        | 68.8       |
| Ductility at 25°C (cm)                    | Min. 100     | 106        |
| Softening Point (°C)                      | Min. 46      | 47         |
| Ductility after RTFOT (cm)                | Min. 50      | 93         |
| Retained Penetration after RTFOT (%)      | 50 +         | 78         |
| Rotational Viscosity at 135°C, 165°C (cp) | -            | 365, 112.5 |

The penetration value of 68.8 (0.1 mm) indicates adequate stiffness, while the ductility of 106 cm reflects excellent resistance to cracking under tensile stress. The softening point of 47°C exceeds the required minimum, ensuring thermal stability during temperature fluctuations. The retained penetration value of 78% and ductility of 93 cm after rolling thin film oven test (RTFOT) confirm the binder's strong resistance to short-term aging, maintaining flexibility and durability. Additionally, rotational viscosity values at 135°C (365 cP) and 165°C (112.5 cP) ensure good workability during mixing and paving

### 2.1.2. Nano-Material

Nano-Copper Oxide, appears as a black to brown powder as shown in Fig. 1, was used to modify the asphalt binder, which were ordered from Hebei Suoyi New Material Technology Co., Ltd. – China. The nanomaterial properties are presented in Table 2.

Table 2. Nanomaterial's properties

| Properties            | Nano-Copper               |
|-----------------------|---------------------------|
| Chemical Formula      | CuO                       |
| Appearance            | Black to Brown powder     |
| Purity                | 99%                       |
| Particle size         | 45nm                      |
| Particle Morphology   | Spherical                 |
| Specific surface area | 100-200 m <sup>2</sup> /g |
| pH                    | 5.5-6.5                   |
| Molecular weight      | 79.55g/mol                |
| Melting point         | 1201°C                    |



Fig. 1. Nano-copper oxide powder

## 2.2. Asphalt Binder Sample Preparation

### 2.2.1. Sample

An oven is used to heat the original asphalt binder to achieve liquidity, slightly above its softening point, to allow easy pouring into the mixing pan. Precise amounts of nano-copper oxide, comprising 2%, 4%, 6%, and 8% by weight of the asphalt binder, are then carefully measured and gradually added to the liquefied binder. Then a high shear mixer was used for mixing. Initially, the speed of the mixer was 4500 rpm for 5 minutes to ensure uniform dispersion of the nanomaterials, avoid clumping, and manage floating particles and bubbles [20]. After this, the mixer's speed is increased to 15000 rpm for 15 minutes, with the mixing temperature kept at  $157 \pm 1^\circ\text{C}$ , which is determined in accordance with ASTM D2493 guidelines. The mixing criteria were selected based on findings from previous studies, which indicate a relationship between mixing time and speed. Specifically, when the mixing speed is high, the required mixing time decreases, and vice versa, to ensure optimal dispersion of materials [25-29]. Once the desired dispersion is achieved, the modified

bitumen is cooled and stored in sealed containers for subsequent testing and application. Fig. 2 illustrates the procedure for sample preparation.

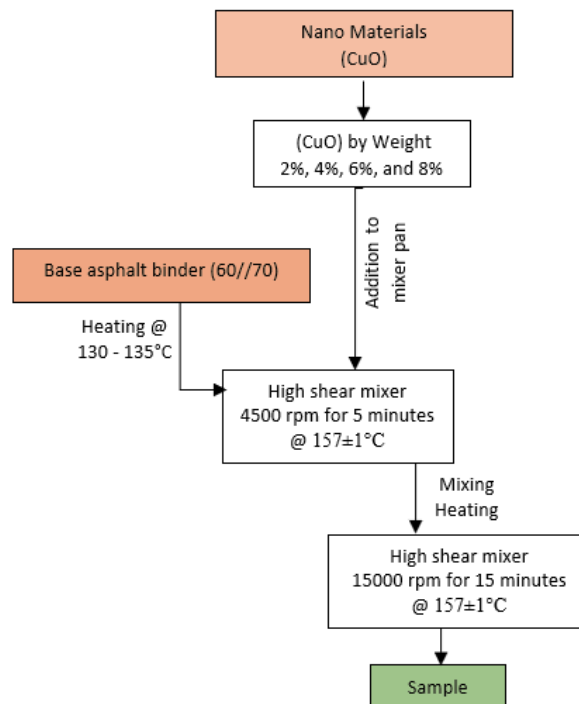


Fig. 1. Asphalt binder sample preparation procedure

### 2.2.2. Aging Process

Bitumen gradually ages due to exposure to various environmental and operational factors, resulting in oxidation and volatilization [30, 31]. Volatilization and oxidation are the primary processes responsible for the formation of carbonyl and sulfoxide groups, which contribute to the aging of asphalt binders. These processes increase the viscosity of the binder, resulting in stiffer mixes and subsequently leading to various pavement distresses, such as raveling, fatigue cracking, and thermal cracking [32]. Short-term aging takes place throughout storage, mixing, transportation, and paving activities. To simulate this aging process in a controlled environment, the RTFOT test was conducted following ASTM D2872 standards [33]. In RTFOT test, a thin layer of asphalt binder is exposed to heat and air in a rotating oven to simulate oxidative aging. The test is carried out at 163°C for 85 minutes to ensure uniform exposure, and the results, which include changes in penetration, softening point, and viscosity, offer information about the binder's resistance to aging and suitability for practical uses.

### 2.3. Rheological Properties of Asphalt Binder

Conventional laboratory experiments were performed on the binder both before and after the aging process. These tests included assessments of ductility in accordance with ASTM D113-2007 guidelines, the softening point following ASTM D36/D36M-14 standards, penetration according to ASTM D5/D5M-13 specifications, and thermal susceptibility evaluated by the penetration index (PI). The Penetration Index (PI), derived from the softening point and penetration test results, measures the binder's susceptibility to temperature variations. A higher PI indicates a lower susceptibility of binder samples to temperature variations, which is preferable in terms of temperature sensitivity. The PI value, determined by equation 1, ranges from -3 (high susceptibility) to +7 (low susceptibility), providing insight into the binder's resilience to temperature fluctuations. [34-36].

$$PI = \frac{1952 - 500 \log (Pen_{25}) - 20SP}{50 \log (Pen_{25}) - SP - 120} \quad (1)$$



To evaluate short-term aging resistance, researchers focus on two primary factors: the increase in softening point (ISP) and retained penetration (RP). ISP measures the change between the softening points of aged and unaged samples, while RP represents the percentage of penetration retained in aged samples compared to their original unaged state. These parameters are calculated using Equations 2 and 3 [15].

$$ISP (^{\circ}C) = SP_{aged} - SP_{unaged} \quad (2)$$

$$RP (\%) = \frac{\text{Penetration before aging}}{\text{Penetration after aging}} * 100 \quad (3)$$

Where; PI is Penetration Index, SP is Softening point ( $^{\circ}C$ ), and Pen25 is Penetration value at  $25^{\circ}C$ . As the asphalt binder ages, its penetration value decreases, and simultaneously, its softening point and viscosity increase. Generally, for aging resistance of bitumen, higher ISP and lower RP values are indicative of better aging resistance. Therefore, a higher ISP and lower RP value help to reverse further aging of the asphalt binder samples [15, 25].

Typically, a rise in viscosity after aging is detected, representing higher stiffness. Although, at elevated temperatures, raised viscosity can advance rutting resistance, extreme stiffness may lead to cracking, particularly under low temperatures or frequent loads. Conversely, a reduction in ductility post-aging suggests less flexibility, causing the binder more prone to thermal and fatigue cracking.

## 2.4. Dynamic Rheologic Parameters for Nano-Modified Asphalt Binders

The dynamic rheological parameters of nano-modified asphalt binders assess the material's response to applied stress or strain under varying temperatures and frequencies using both DSR and BBR tests.

### 2.4.1. Dynamic Shear Rheometer Test

Concerning the rheological characteristics of the binder at intermediate to high temperatures, a dynamic shear rheometer tester (Anton Paar RheoCompass™), as shown in Fig. 3, was utilized in accordance with AASHTO T315 [16]. The test was performed at a mean temperature of  $70.0^{\circ}C$  using a frequency of 10 rad/s (1.59 Hz) and a strain of 12%. The sample geometry included a parallel plate setup with 25mm diameter and 1mm thick. Each test included 10 data points, with significant values determined by averaging the results. For instance, the mean complex shear modulus ( $|G^*|$ ) was 0.968 kPa, and the  $|G^*|/\sin(\delta)$  value was 0.9685 kPa, with a standard deviation of 0.0003 kPa and a 95% confidence interval of 0.9683–0.9687 kPa. The dynamic shear rheometer DSR test results yield two key parameters: the complex shear modulus ( $G^*$ ) and the phase angle ( $\delta$ ) [37]. These parameters aim to assess both the elastic and viscous behaviors of the modified asphalt binders. The asphalt binder specimen is subjected to frequent shearing which deforms the specimen and the overall specimen resistance to this deformation is known as complex modulus ( $G^*$ ), while the shift between the resulting shear strain and the practiced shear stress is called the phase angle ( $\delta$ ) which describes the relationship between components of the viscous and elastic behaviors [38-40]. Fatigue cracking and rutting are two indicators obtained from the ( $G^*$ ) and ( $\delta$ ) results [41]. A higher  $G^*$  value is associated with greater stiffness, which enhances rutting resistance at high temperatures by limiting permanent deformation under repetitive loads. Conversely, the phase angle ( $\delta$ ) quantifies the lag between applied stress and resultant strain, with lower  $\delta$  values indicating a more elastic behavior. This elastic behavior contributes to improved load recovery, further mitigating rutting potential. At low temperatures, cracking resistance is influenced by the binder's ability to relax thermal stresses, which is related to its viscous properties. While higher  $G^*$  values enhance stiffness, they may reduce flexibility, increasing susceptibility to thermal cracking if not balanced by a sufficiently high  $\delta$  value. The ratio  $G^*/\sin(\delta)$ , commonly referred to as the rutting factor, is used to evaluate high-temperature performance, with higher values indicating superior resistance to rutting deformation [14, 23]. After RTOFT aging, a greater ( $G^*$ ) value suggests improved stiffness and resistance to rutting, but if it is not balanced with an appropriate phase angle, it may also indicate a risk of brittleness.

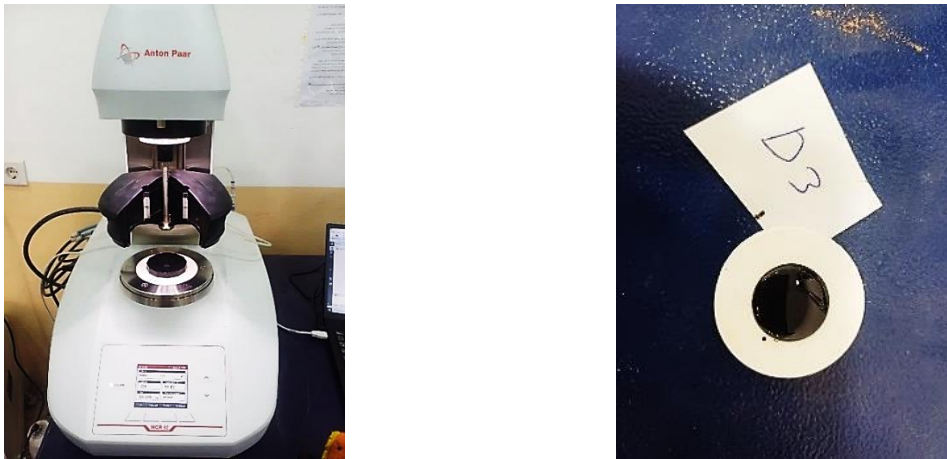


Fig. 3. DSR tester

#### 2.4.2. Bending Beam Rheometer Test

The Bending Beam Rheometer test was conducted on both original and modified asphalt binders, in accordance with AASHTO T313 standards, to assess the thermal cracking susceptibility of the binder samples, as shown in Fig. 4. This test was performed at temperatures of  $-6^{\circ}\text{C}$  and  $-12^{\circ}\text{C}$  and its increment, with a constant load applied for 240 seconds to measure the binder's ability to resist thermal cracking. The specimen geometry consisted of beams measuring 125 mm in length, 12.5 mm in width, and 6.25 mm in thickness. The equipment used included a calibrated bending beam rheometer capable of maintaining precise temperature control. Each test involved multiple repetitions to ensure reliability, with significant values determined by averaging the results. This test aids in evaluating the stiffness and relaxation properties of asphalt binders at low temperatures, which is essential for predicting their performance in cold climates [7, 17, 42-44].



Fig. 4. BBR tester

#### 2.5. Morphology of the Nano-Modified Binder

The energy-dispersive X-ray spectrometer and scanning electron microscope were used in tandem to provide information on the elemental composition of samples, identifying the elements present along with their concentration and dispersal. The EDX was operated at a magnification of 1000x and a voltage acceleration of 15kV to generate an elemental map for evaluating the dispersion of nanomaterials within the sample. Utilizing an X-ray spectrum, the EDX compresses compositional and topographical information of the sample into a single view. The elemental dispersion is then visualized with a colored map, where each color represents an element present in the sample [45-48]

### 3. Results and Discussions

#### 3.1. Conventional Tests

Throughout the aforementioned process, the integration of Nano-copper oxide into the asphalt binder has yielded notable enhancements in its physical characteristics. Fig. 5, Fig. 6, and Fig. 7 illustrate its impact dosages on both aged and unaged samples concerning penetration, resistance to short-term aging, and susceptibility to thermal changes.

Regarding the penetration, adding nano-copper oxide led to improvements in the penetration of unaged and aged modified asphalt binders. As illustrated in Fig. 5, the penetration value decreased with the increase in (CuO) ratio up to 6%, then started to increase with (CuO) 8%. This increase might be attributed to the excessive concentration of nanoparticles within the asphalt binder matrix, which can lead to particle agglomeration and subsequently increase the stiffness.

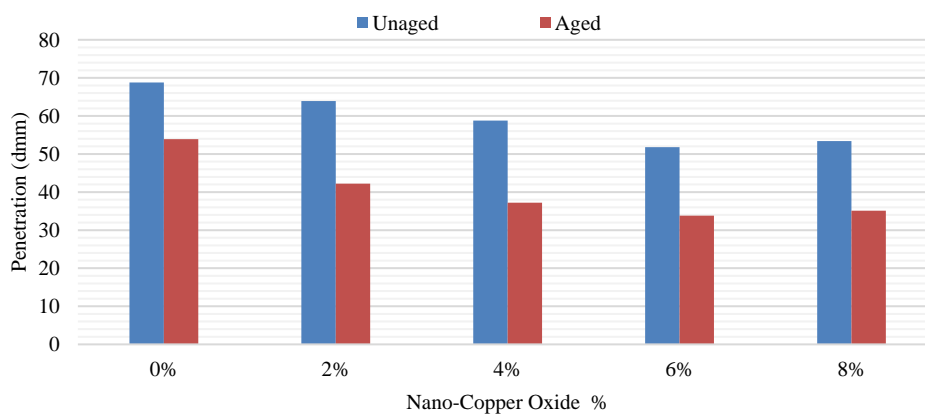


Fig. 5. Penetration test results

The data presented in Fig. 6 (a) and Fig. 6 (b) indicate that the lowest RP and maximum ISP value occurs at a concentration of 4%, respectively. Therefore, the 4% nano-copper oxide concentration exhibits the lowest RP and highest ISP values, demonstrating superior short-term aging resistance. Furthermore, 4% gives the lowest PI which demonstrate the lowest temperature susceptibility as shown in Fig. 7.

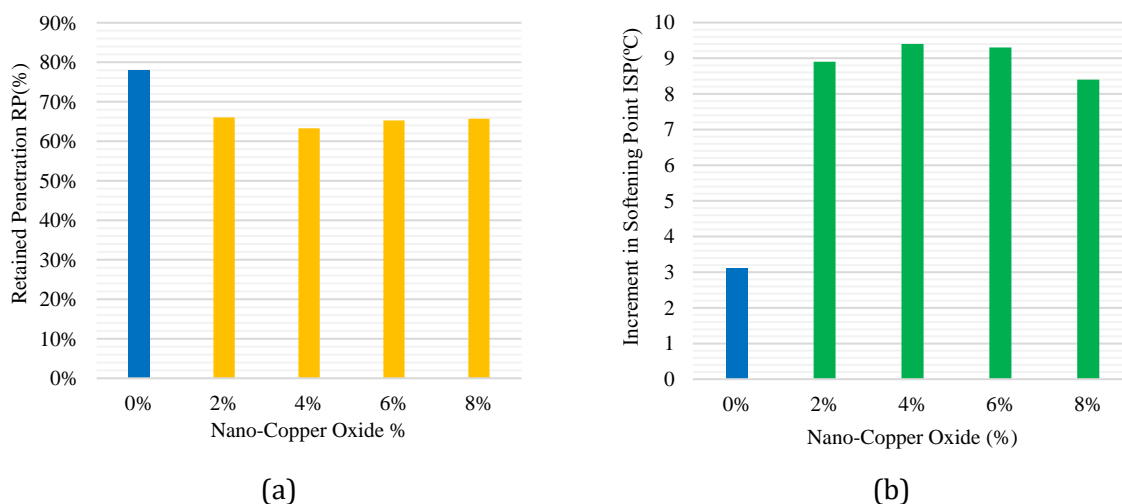


Fig. 6. Retained penetration-RP (%) and Increment in softening point-ISP results (°C)  
(a) RP % (b) ISP (°C)

The ductility test results are utilized to assess the anti-deformation and anti-cracking characteristics of modified asphalt binders. As depicted in Fig. 8, for unaged and aged modified binder asphalts, improvements in ductility cannot be observed except for unaged 2% content

sample which exhibits improvements about 4% compared to the original asphalt binders. This is attributed to the elasticity characteristics of the nano-CuO, which is not viscoelastic.

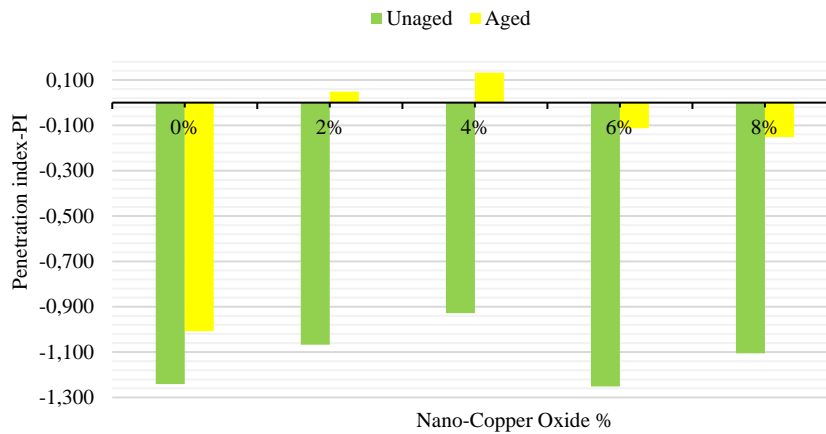


Fig. 7. Penetration Index (PI) results

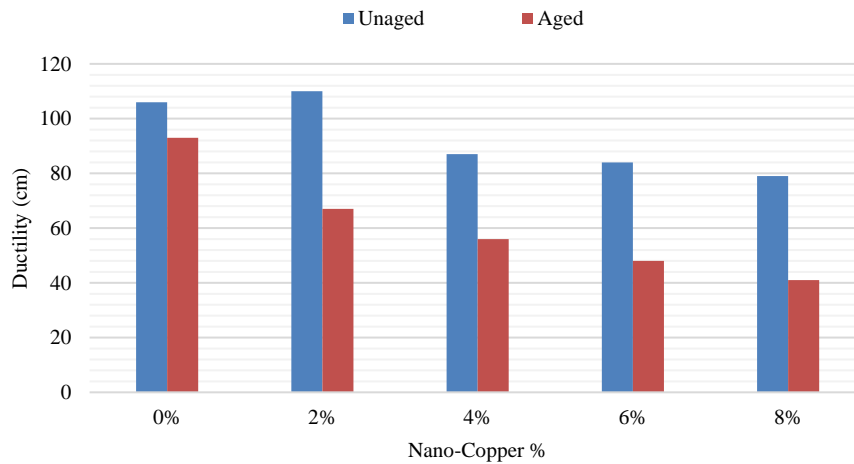


Fig. 8. Ductility test results

### 3.2. Rheological Tests

#### 3.2.1. Dynamic Shear Rheometer Test (DSR)

This study evaluated modified asphalt binders in both aged and unaged states. Fig. 9 and Fig. 10 display the complex shear modulus ( $G^*$ ) and phase angle ( $\delta$ ) of modified asphalt binder mixes across a range of temperatures. An increase in temperature resulted in a reduction of the complex shear modulus and a concurrent rise in the phase angle. Thus, higher temperatures led to increased viscosity in the asphalt binder. Notably, all modified asphalt binder samples demonstrated higher  $G^*$  values and lower  $\delta$  values compared to the original binder at the same temperatures, indicating enhanced stiffness and elastic properties in both aged and unaged samples. The effect of aging on the complex shear modulus ( $G^*$ ) and phase angle ( $\delta$ ) provides critical insights into the performance of asphalt binders. Aging typically increases  $G^*$  due to stiffening of the binder, improving rutting resistance at high temperatures but potentially reducing flexibility. The phase angle ( $\delta$ ) generally decreases with aging, indicating a shift toward more elastic behavior. This effect is temperature and frequency-dependent, as higher temperatures and lower frequencies tend to amplify the viscoelastic changes caused by aging, which could influence the binder's susceptibility to thermal and fatigue cracking under varying field conditions.

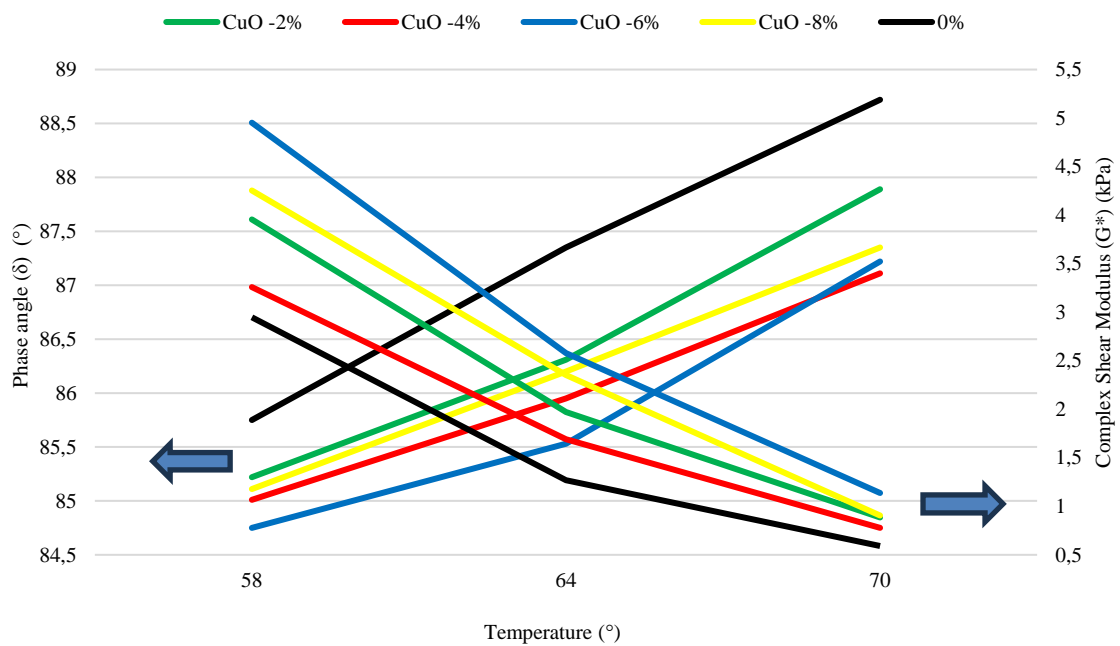


Fig. 9. Unaged DSR results - complex shear modulus ( $G^*$ ) and phase angle ( $\delta$ )

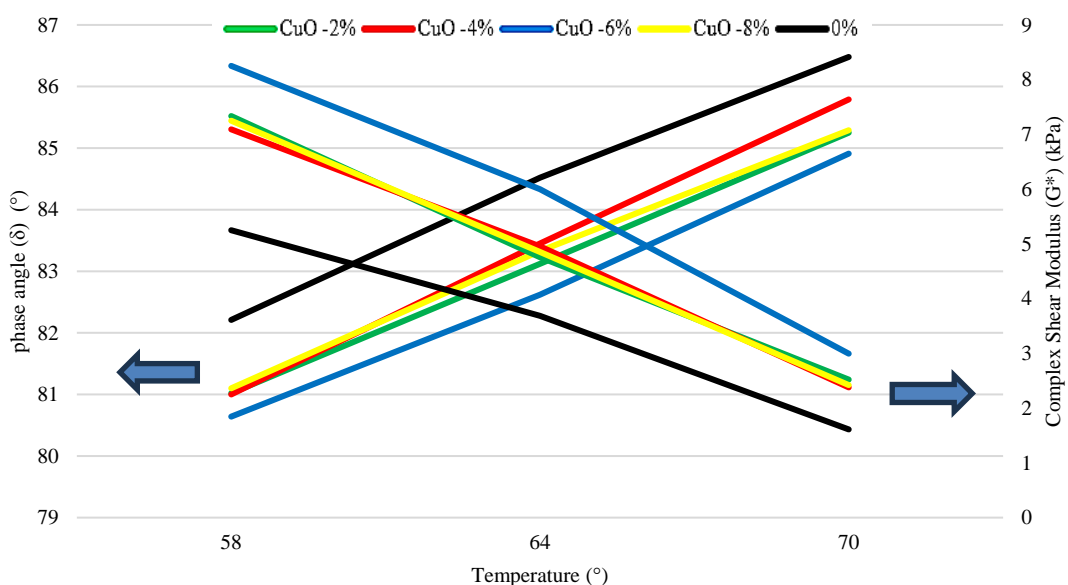


Fig. 10. RTOFT aged DSR results - complex shear modulus ( $G^*$ ) and phase angle ( $\delta$ )

### 3.2.2. Bending Beam Rheometer Test

To evaluate the impact of nanomaterial modifications on low-temperature performance, the creep stiffness and m-value parameters were assessed. The results, as illustrated in Fig. 11 and Fig. 12, demonstrate the effects of integrating nano-copper oxide into the asphalt binder. Notably, there were improvements in certain mix contents, particularly with 6% Content, where the m-value increased by approximately 3%, which reflect better stress relaxation capabilities, allowing the binder to dissipate thermal stresses more effectively, and creep stiffness decreased by about 10% indicating improved flexibility, reducing the binder's brittleness and enhancing its ability to resist thermal cracking at low temperatures. However, some contents showed a decline in performance. Despite these variations, all samples met the SuperPave™ requirements at a low temperature of -6°C, with an m-value of  $\geq 0.3$  and a creep stiffness of  $\leq 300$  MPa. Nevertheless, all samples failed to meet these requirements at -12°C. This indicates that differences in the chemical composition of

the nanoparticles and the asphalt binder, as well as their interaction, may be the primary cause of the failure at lower temperatures.

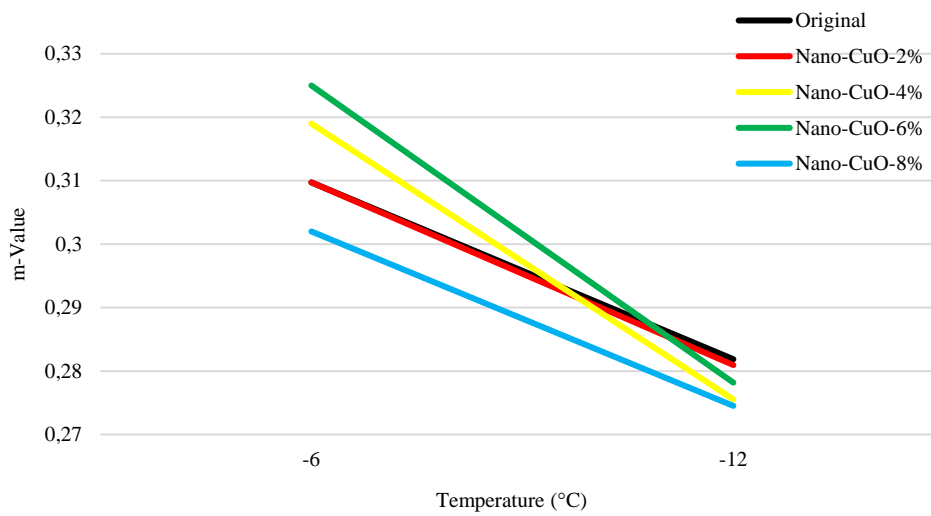


Fig. 11. m-Value

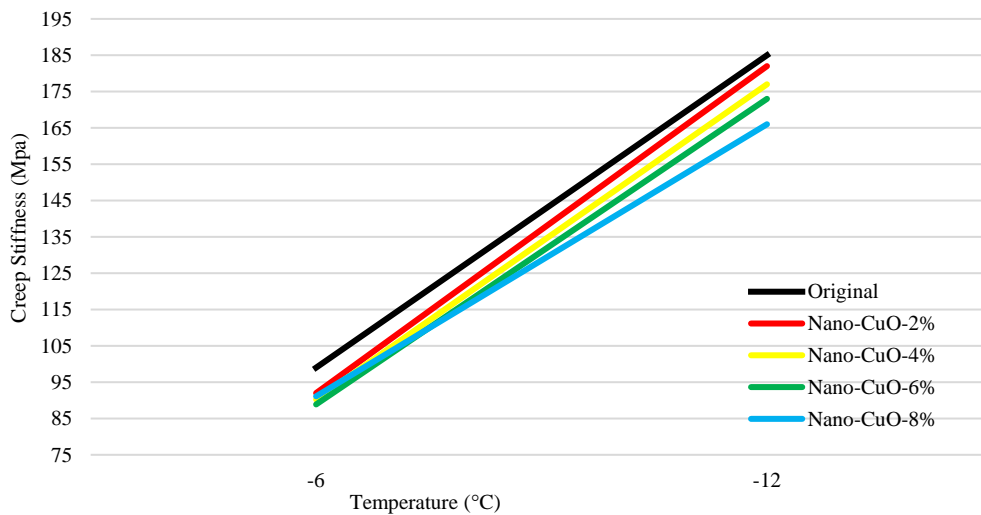


Fig.12. Creep Stiffness

### 3.3. Morphology of the Sample

Employing the Energy-dispersive X-ray (EDX) analysis method alongside scanning electron microscopy (SEM) enables the evaluation of sample chemical compositions and the distribution of nanomaterials within asphalt binder mixes. This technique assigns a unique color to each element, allowing for the construction of an elemental map by overlaying all elements present, thus illustrating the sample's elemental composition. SEM images, along with elemental EDX maps and EDX spectra of nano-copper modified asphalt binders, is presented in Fig. 13. The SEM images indicate a high-quality dispersion achieved through the mixing technique utilized across all samples. Moreover, the EDX spectrum provides insight into X-ray intensities and their relative concentrations emitted from the sample in relation to their energy levels. By identifying the peak of each element, the EDX spectrum aids in determining the presence of these elements in each modified asphalt binder sample.

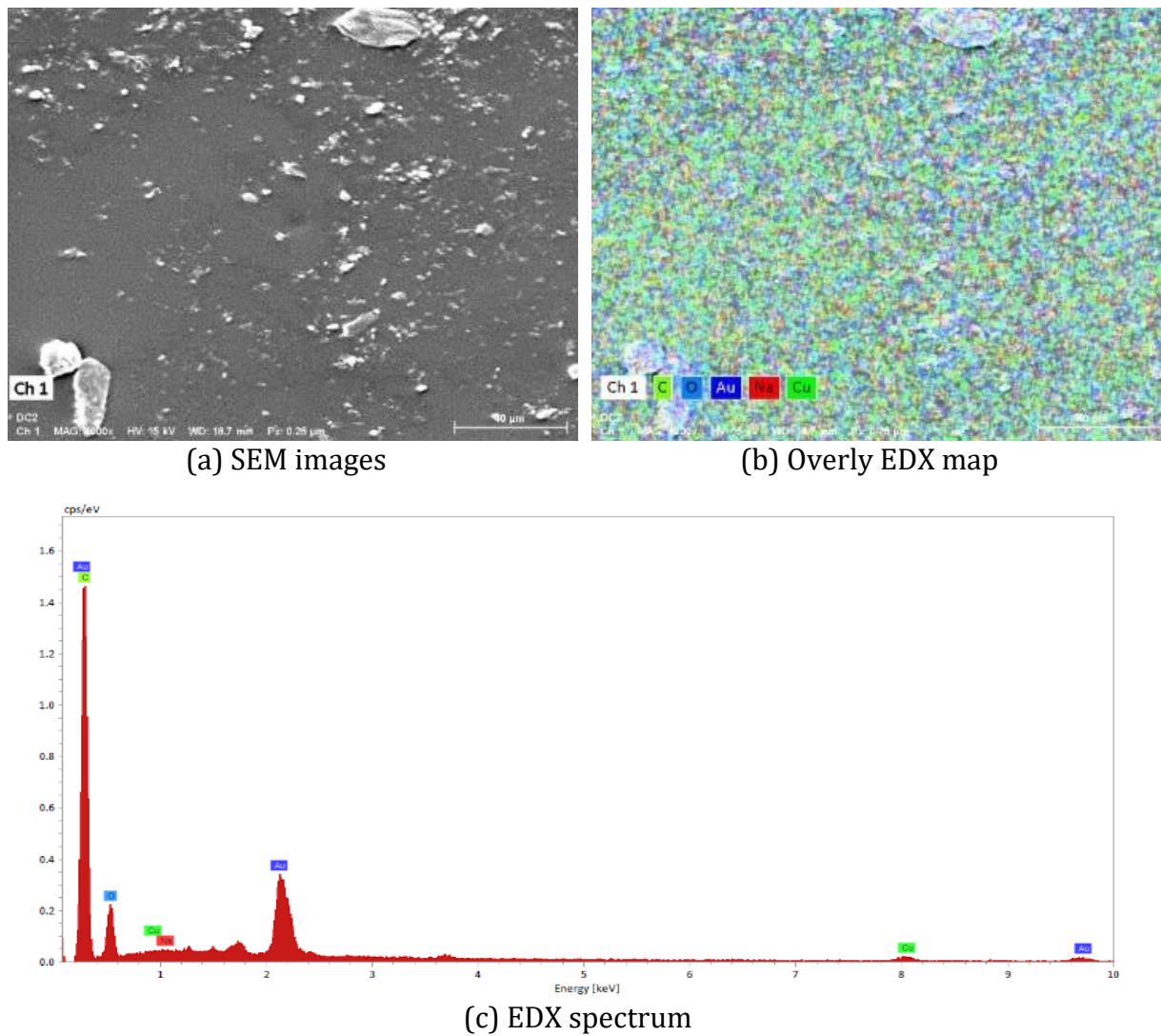


Fig.13. SEM/EDX elemental scan, Spectrum and map for nano-copper oxide modified binder

#### 4. Conclusion

This investigation explored into the durability and physical assets of asphalt binder when subjected to modification with nano-copper oxide. The subsequent findings are as follows:

- The conditions used for mixing, including time, speed, and temperature, have resulted in a good dispersion of nanomaterials throughout the mixes which was established by utilizing EDX analysis and SEM images;
- The integration of Nano-Copper oxide has vital impact on improving the penetration for both aged and unaged modified asphalt binders. The best improvement has found at 6% in which reached about 25% for unaged samples and 37% for aged ones at the same concentration level;
- Significant improvements in short-term aging resistance were discerned in the modified asphalt binders with 4% ratio, characterized by increased increment in softening point ISP with 67% and reduced retained penetration RP with 19.2%, compared to the original asphalt binder samples;
- The susceptibility of temperature, evaluated by the penetration index (PI), experienced a significant boost with 4% samples for each of aged and unaged modified asphalt binder reaching 25% and 113% for unaged and aged samples, respectively;

- Due to the brittleness of the Nano-Copper oxide, the addition of high ratios of (more than 2%) led to decrease in ductility for unaged modified asphalt binders. However, post short-term aging (RTFOT), the ability to endure low-temperature performance and resist cracking did not commonly improve across all mix contents; instead, some samples experienced brittle; and
- Dynamic Shear Rheometer (DSR) testing revealed that the integration of nanomaterials notably bolstered resistance against rutting deformation and minimized bitumen's resistance to cracking and deformation under high temperatures. Furthermore, RTFOT-aged samples exhibited heightened stiffness, improved elasticity, and a greater rutting factor  $G^*/\sin(\delta)$  upon incorporation of Nano-copper oxide, indicative of their exceptional capacity to withstand aging during construction, thereby ensuring prolonged durability for practical applications.
- Although all the asphalt binder samples successfully met the SuperPave™ criteria for low-temperature performance at -6°C, they failed to meet the required specifications at the more stringent temperature of -12°C, indicating a potential limitation in their low-temperature cracking resistance at colder climates or extreme condition.

Although the initial cost of nano-CuO may be higher, its long-term benefits can offset these expenses. By improving the durability and performance of asphalt binders, nano-CuO can reduce maintenance and operational costs over time. Furthermore, its cost-effectiveness during the service life of the asphalt binder makes it a favorable option for environmental sustainability, as it can lead to fewer repairs and longer-lasting road infrastructure. Therefore, In this context, further investigation may be conducted in future studies, including the incorporation of additional nanomaterials to create composite nanomaterials and evaluating their cost-effectiveness in road applications.

## Acknowledgements

The authors express their appreciation to the Duhok Central Construction Lab for providing experimental support through the research.

## References

- [1] Alhamali DI, Wu J, Liu Q, Hassan NA, Yusoff NIM, Ali SIA. Physical and rheological characteristics of polymer modified bitumen with nanosilica particles. Arab J Sci Eng. 2016;41(4):1521-1530. <https://doi.org/10.1007/s13369-015-1964-7>
- [2] Carraher CE Jr. Seymour/Carraher's Polymer Chemistry. CRC Press; 2007. <https://doi.org/10.1201/9781420051032>
- [3] Hunter RN, Self A, Read J, Hobson E. The Shell Bitumen Handbook. Ice Publishing; 2015. <https://doi.org/10.1680/tsbh.58378>
- [4] Fettahoğlu A, Genes M. Design charts for linear elastic pavements. Res Eng Struct Mater. 2020;6(4).
- [5] Masri K, et al. Visco-elastic characteristic of bitumen incorporating nano silica. Int J Mater Sci Eng. 2019;7:45-49.
- [6] Ramadhansyah PJ, et al. Nanoparticle in asphalt binder: a state-of-the-art review. IOP Conf Ser Mater Sci Eng. 2020;712(1):012023. <https://doi.org/10.1088/1757-899X/712/1/012023>
- [7] Xiao F, Amirkhanian AN, Amirkhanian SN. Long-term ageing influence on rheological characteristics of asphalt binders containing carbon nanoparticles. Int J Pavement Eng. 2011;12(6):533-541. <https://doi.org/10.1080/10298436.2011.560267>
- [8] Yang X, You Z, Dai Q, Mills-Beale J. Mechanical performance of asphalt mixtures modified by bio-oils derived from waste wood resources. Constr Build Mater. 2014;51:424-431. <https://doi.org/10.1016/j.conbuildmat.2013.11.017>
- [9] Yu Q. Application of nanomaterials in alkali-activated materials. In: Nanotechnology in Eco-efficient Construction. Elsevier; 2019. p. 97-121. <https://doi.org/10.1016/B978-0-08-102641-0.00005-0>
- [10] Abdel-Wahed T, Rashwan NK, Maurice AE. The physical properties of bitumen modified with ilmenite and bentonite nanoparticles. HBRC J. 2020;16(1):335-350. <https://doi.org/10.1080/16874048.2020.1834904>
- [11] Ahmad Faizul MFR. The physical and engineering properties of 80/100 bitumen with carbon black additive. 2013.



- [12] Amini N, Latifi H, Hayati P. Effects of Nano-CuO, MWCNT and SBS on the aging of asphalt binder: FTIR and XRD analyses. *Jordan J Civ Eng.* 2021;15:277-291.
- [13] Badgujar P. Imprint of nano-silica particles on ageing of bitumen. *Int J Res Appl Sci Eng Technol.* 2018;6:238-242. <https://doi.org/10.22214/ijraset.2018.5038>
- [14] Golestani B, Nam BH, Moghadas Nejad F, Fallah S. Nanoclay application to asphalt concrete: characterization of polymer and linear nanocomposite-modified asphalt binder and mixture. *Constr Build Mater.* 2015;91:32-38. <https://doi.org/10.1016/j.conbuildmat.2015.05.019>
- [15] Jahromi SG, Khodaii A. Effects of nanoclay on rheological properties of bitumen binder. *Constr Build Mater.* 2009;23(8):2894-2904. <https://doi.org/10.1016/j.conbuildmat.2009.02.027>
- [16] Yao H, et al. Properties and chemical bonding of asphalt and asphalt mixtures modified with nanosilica. *J Mater Civ Eng.* 2012;25. [https://doi.org/10.1061/\(ASCE\)MT.1943-5533.0000690](https://doi.org/10.1061/(ASCE)MT.1943-5533.0000690)
- [17] Cheraghian G, Wistuba MP, Kiani S, Barron AR, Behnood A. Rheological, physicochemical, and microstructural properties of asphalt binder modified by fumed silica nanoparticles. *Sci Rep.* 2021;11(1):11455. <https://doi.org/10.1038/s41598-021-90620-w>
- [18] Masri KA, Awang H, Jaya RP, Ali MI, Ramli NI, Arshad AK. Moisture susceptibility of porous asphalt mixture with nano silica modified asphalt binder. *IOP Conf Ser Earth Environ Sci.* 2019;244(1):012028. <https://doi.org/10.1088/1755-1315/244/1/012028>
- [19] Alhamali D, Wu J, Liu Q, Hassan N, Yusoff NIM, Ali SIA. Physical and rheological characteristics of polymer modified bitumen with nanosilica particles. *Arab J Sci Eng.* 2015;41:12/15. <https://doi.org/10.1007/s13369-015-1964-7>
- [20] Zghair H, Joni H, Hassan M. Rheological characteristics of nano silica modified asphalt binder material. 2020. <https://doi.org/10.1109/IEC47844.2019.8950636>
- [21] Ashish PK, Singh D. Study on understanding functional characteristics of multi-wall CNT modified asphalt binder. *Int J Pavement Eng.* 2020;21(9):1069-1082. <https://doi.org/10.1080/10298436.2018.1519190>
- [22] Ashish PK, Singh D. Use of nanomaterial for asphalt binder and mixtures: a comprehensive review on development, prospect, and challenges. *Road Mater Pavement Des.* 2021;22(3):492-538. <https://doi.org/10.1080/14680629.2019.1634634>
- [23] Shah PM, Mir MS. Application of nanotechnology in pavement engineering: a review. *Can J Civ Eng.* 2020;47(9):1037-1045. <https://doi.org/10.1139/cjce-2019-0395>
- [24] Yang J, Tighe S. A review of advances of nanotechnology in asphalt mixtures. *Procedia Soc Behav Sci.* 2013;96:1269-1276. <https://doi.org/10.1016/j.sbspro.2013.08.144>
- [25] Crucho J, Picado-Santos L, Neves J, Capitão S. A review of nanomaterials' effect on mechanical performance and aging of asphalt mixtures. *Appl Sci.* 2019;9(18):3657. <https://doi.org/10.3390/app9183657>
- [26] Hasaninia M, Haddadi F. Studying engineering characteristics of asphalt binder and mixture modified by nanosilica and estimating their correlations. *Adv Mater Sci Eng.* 2018;2018:4560101. <https://doi.org/10.1155/2018/4560101>
- [27] Yusoff NIM, Breem AAS, Alattug HNM, Hamim A, Ahmad J. The effects of moisture susceptibility and ageing conditions on nano-silica/polymer-modified asphalt mixtures. *Constr Build Mater.* 2014;72:139-47. <https://doi.org/10.1016/j.conbuildmat.2014.09.014>
- [28] Mansourian A, Gholamzadeh S. Moisture susceptibility of hot mix asphalt containing asphalt binder modified with nanocomposite. *Road Mater Pavement Des.* 2017;18(6):1434-47. <https://doi.org/10.1080/14680629.2016.1211961>
- [29] Zafari F, Rahi M, Moshtagh N, Nazockdast H. The improvement of bitumen properties by adding nanosilica. *Stud Civ Eng Archit.* 2014;3(1):62-9.
- [30] Mousavi M, Aldagari S, Fini EH. Adsorbing volatile organic compounds within bitumen improves colloidal stability and air quality. *ACS Sustain Chem Eng.* 2023;11(26):9581-94. <https://doi.org/10.1021/acssuschemeng.3c00539>
- [31] Zare-Shahabadi A, Shokuhfar A, Ebrahimi-Nejad S. Preparation and rheological characterization of asphalt binders reinforced with layered silicate nanoparticles. *Constr Build Mater.* 2010;24(7):1239-44. <https://doi.org/10.1016/j.conbuildmat.2009.12.013>
- [32] Hamzah M, Omranian S, Golchin B. A review on the effects of aging on properties of asphalt binders and mixtures. *Constr Build Mater.* 2015;4:15-34.
- [33] Oliviero Rossi C, Caputo P, Ashimova S, Fabozzi A, D'Errico G, Angelico R. Effects of natural antioxidant agents on the bitumen aging process: an EPR and rheological investigation. *Appl Sci.* 2018;8(8):1405. <https://doi.org/10.3390/app8081405>
- [34] Zhang L, Gao X, Wang W, Wang H, Zheng K. Laboratory evaluation of rheological properties of asphalt binder modified by Nano-TiO<sub>2</sub>/CaCO<sub>3</sub>. *Adv Mater Sci Eng.* 2021;2021:5522025. <https://doi.org/10.1155/2021/5522025>

- [35] Gunay T. Investigation of physical properties of base and SBS modified bitumens by rheological test methods. *Rev Constr.* 2022;21(2):281-94. <https://doi.org/10.7764/RDLC.21.2.281>
- [36] Wang W, Cheng Y, Tan G, Liu Z, Shi C. Laboratory investigation on high- and low-temperature performances of asphalt mastics modified by waste oil shale ash. *J Mater Cycles Waste Manag.* 2018;20:1710-23. <https://doi.org/10.1007/s10163-018-0737-2>
- [37] Baldino N, Gabriele D, Lupi FR, Oliviero Rossi C, Caputo P, Falvo T. Rheological effects on bitumen of polyphosphoric acid (PPA) addition. *Constr Build Mater.* 2013;40:397-404. <https://doi.org/10.1016/j.conbuildmat.2012.11.001>
- [38] Xiao F, Amirkhanian AN, Amirkhanian SN. Influence of carbon nanoparticles on the rheological characteristics of short-term aged asphalt binders. *J Mater Civ Eng.* 2011;23(4):423-31. [https://doi.org/10.1061/\(ASCE\)MT.1943-5533.0000184](https://doi.org/10.1061/(ASCE)MT.1943-5533.0000184)
- [39] Lee SJ, Amirkhanian SN, Shatanawi K, Kim KW. Short-term aging characterization of asphalt binders using gel permeation chromatography and selected Superpave binder tests. *Constr Build Mater.* 2008;22(11):2220-7. <https://doi.org/10.1016/j.conbuildmat.2007.08.005>
- [40] Galooyak SS, Dabir B, Nazarbeygi AE, Moeini A. Rheological properties and storage stability of bitumen/SBS/montmorillonite composites. *Constr Build Mater.* 2010;24(3):300-7. <https://doi.org/10.1016/j.conbuildmat.2009.08.032>
- [41] Bachir SD, Dekhli S, Mokhtar AK. Rheological properties and storage stability of SEBS polymer modified bitumens. *Int J Eng Sci Technol.* 2013;5:1031-8.
- [42] He R, Wu S, Wang X, Wang Z, Chen H. Temperature sensitivity characteristics of SBS/CRP-modified bitumen after different aging processes. *Materials (Basel).* 2018;11(11):1-14. <https://doi.org/10.3390/ma11112136>
- [43] Amini N, Hayati P. Effects of CuO nanoparticles as phase change material on chemical, thermal and mechanical properties of asphalt binder and mixture. *Constr Build Mater.* 2020;251:118996. <https://doi.org/10.1016/j.conbuildmat.2020.118996>
- [44] Karki B. Effect of nanomaterials on binder and mix performance [dissertation]. Grand Forks: The University of North Dakota; 2017.
- [45] Abdalfattah IA, Mogawer WS, Stuart K. Quantification of the degree of blending in hot-mix asphalt (HMA) with reclaimed asphalt pavement (RAP) using energy dispersive X-ray spectroscopy (EDX) analysis. *J Clean Prod.* 2021;294:126261. <https://doi.org/10.1016/j.jclepro.2021.126261>
- [46] Jiang Y, Gu X, Zhou Z, Ni F, Dong Q. Laboratory observation and evaluation of asphalt blends of reclaimed asphalt pavement binder with virgin binder using SEM/EDS. *Transp Res Rec.* 2018;2672(28):69-78. <https://doi.org/10.1177/0361198118782023>
- [47] Zhu X, Yuan Y, Li L, Du Y, Li F. Identification of interfacial transition zone in asphalt concrete based on nano-scale metrology techniques. *Mater Des.* 2017;129:91-102. <https://doi.org/10.1016/j.matdes.2017.05.015>
- [48] Lin PC, Lin S, Wang PC, Sridhar R. Techniques for physicochemical characterization of nanomaterials. *Biotechnol Adv.* 2014;32(4):711-26. <https://doi.org/10.1016/j.biotechadv.2013.11.006>

## Forecasting California bearing ratio (CBR) of soil using machine learning algorithms: A review

Nabam Tado<sup>a</sup>, Salam Medhajit<sup>b</sup>, Dibyendu Pal<sup>\*c</sup>

Department of Civil Engineering, North Eastern Regional Institute of Science and Technology, Nirjuli-791109, Arunachal Pradesh, India

### Article Info

### Abstract

#### Article History:

Received 15 Jan 2025

Accepted 29 Jan 2025

#### Keywords:

California bearing ratio;  
Machine learning;  
Support vector machine;  
Artificial neural networks;  
Atterberg limits;  
Compaction parameters

Traditionally California bearing ratio (CBR) is obtained by conducting laboratory testing, which is often time-consuming, laborious, and costly. This delays the design and construction processes of important structures. Recently, several researchers have predicted CBR using ML algorithms. This study focused on understanding the uses of various ML algorithms in the prediction of CBR of treated and natural soils, and other applications. Factors like OMC (30%), MDD (29%), LL (25%), PL (20%), and PI (19%) were mostly used as contributing factors for estimating CBR. ANN, RF, and CNN were the best models for predicting settlement of shallow foundation, bearing capacity of piles and slope stability, and landslide identification, respectively. DNN, GEP, and ELM-CSO were the best models in estimating CBR for granular soil, fine-grained soil, and lateritic soil, respectively, and RFR, AB-DT, LR, and ANN for other types of soils. ANN and BBO-MLP were the best models for expansive clay soil treated with HARHA, and pond ash treated with lime and lime sludge, whereas ANN was for lateritic soil treated with cement and RHA, sand with quartz, feldspar, calcite, corund, amorphous, and clay with pozzolan and lime powder, respectively. The quality and quantity of available training data were fundamental to observing the capacity of models, highlighting the importance of richer, better-labeled datasets.

© 2025 MIM Research Group. All rights reserved.

## 1. Introduction

California bearing ratio (CBR) is widely used as a key factor to assess the strength of subgrade and determine pavement thickness. CBR determines the relative force required to penetrate a soil sample compared to a standard material. CBR is determined in the laboratory by placing a standard diameter plunger into a sample of compacted soil [1]. This evaluates the relative quality of subgrade soil. These laboratory tests encountered numerous obstacles such as inappropriate compaction, difficulties in preserving proper moisture content, improper alignment of the pistol during penetration, swelling in soil samples after soaking, and errors in recording test results. The traditional method of CBR test requires a substantial amount of time (minimum 4 days per sample per composition), money, and experienced and trained laboratory staff. The field test of CBR comprises driving a piston into the soil mass and soil subgrade using a loading jack. This requires more labor for carrying bulky instruments, making boreholes in the field, and skilled operators to get proper results. Field compaction may not accurately match with laboratory compaction which may lead to erroneous results [2]. This delays the design and construction processes of important structures. Recently, there has been an increasing demand for a faster, more precise, and much less expensive alternative, especially given the increasing complexity of infrastructure projects and new sustainable construction practices. This has attracted

\*Corresponding author: [dpl@nerist.ac.in](mailto:dpl@nerist.ac.in) / [pal\\_here00@yahoo.co.in](mailto:pal_here00@yahoo.co.in)

<sup>a</sup>orcid.org/0009-0001-2756-6835; <sup>b</sup>orcid.org/0009-0009-1934-005X; <sup>c</sup>orcid.org/0000-0002-6419-4639

DOI: <http://dx.doi.org/10.17515/resm2025-623ml0115rv>

Res. Eng. Struct. Mat. Vol. 11 Iss. 1 (2025) 383-398

considerable interest in exploring machine learning (ML) algorithms as predictive tools for estimating CBR [3]. Over the last decade, numerous ML methods have been investigated to forecast the CBR value. This includes Artificial Neural Network (ANN) [4], Decision Tree (DT) [5], Support Vector Machine (SVM) [6], and ensemble models such as Random Forest (RF) [7], Extreme Gradient Boosting (XGB) [1], and Light Gradient Boosting (LightGBM) [8]. The training of such models mainly takes on data relating to soil characteristics; including particle size distribution (fine content (FC), gravel content (GC), sand content (SC)), Atterberg limits (liquid limit (LL), plasticity index (PI), plastic limit (PL), shrinkage limit (SL)), compaction parameters (maximum dry density (MDD), optimum moisture content (OMC)), natural moisture content (NMC), Specific gravity (G) [9]. The MDD is a key variable, with studies indicating its substantial impact on CBR predictions [10]. While MDD is important, other factors like particle size distribution, including gravel and sand content, were essential for accurate CBR prediction [9, 5]. ML models depend on data quality, quantity, and choices of appropriate algorithms. Issues such as overfitting, model interpretability, and generalizability for diverse soil types were still a challenge [3]. This study is an effort to overview the ML model that functions superior in predicting the CBR value of soil. Efforts have also been made to find the most common soil properties being used to build such a model. This paper elaborates on the studies conducted using ML algorithms to predict various soil properties and narrates the review related to the prediction of CBR from natural soil as well as treated/stabilized soil. It also briefly summarizes the reviews and highlights the conclusions and future direction of this study.

## 2. Uses of Machine Learning (ML) in Geotechnical Engineering

The application of ML offers numerous advantages with respect to conventional approaches in the field of geotechnical engineering, through enhanced forecasting capabilities and efficiency in data processing. In comparison to regression, the ML model can handle several outputs and responses, whereas regression models can handle a single response at a time [11]. ML techniques, such as ANN, DT, and SVM, excel in modeling complex, non-linear relationships of geotechnical materials like soil, which traditional methods often struggle to capture due to their reliance on simplified assumptions [12-13].

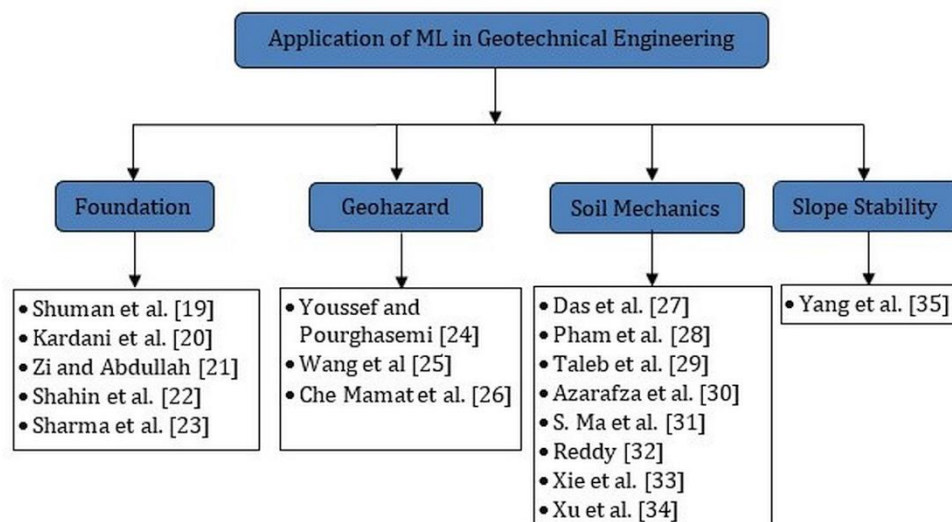


Fig. 1. Structure of the study on application of ML in Geotechnical Engineering

ML can significantly enhance site characterization and scour assessment, providing more reliable estimation and real-time monitoring capabilities [14]. However, challenges persist, including the need for large, high-quality datasets and the chances of overfitting, which can undermine model reliability [15]. Additionally, traditional methods, while laborious, often provide a more straightforward interpretable framework that can be beneficial in certain contexts, highlighting

the need for a balanced approach that integrates both methodologies for optimal outcomes in geotechnical applications [13]. The ML techniques, contrary to the traditional statistical and empirical methods that depend on previously available data regarding relationships in data, have very much been adapted to represent the complex behavior of geotechnical engineering materials [16]. Similarly, a novel parameter estimation model was presented by [17] in a study on Backpropagation (BP) neural networks along with geotechnical properties using MATLAB. They chose the expert system method from the BP neural network theory to forecast geotechnical parameters because it had a convenient programming function and strong nonlinear fitting ability and did not need the distribution of the drilling hole. The data source for their study was mainly from geotechnical investigation and engineering geological survey including hydrogeological survey. It was concluded that the forecasting capability of the model satisfied the requirement. A structure of the study showing the flow of the application of ML in geotechnical engineering is presented in Fig. 1.

## **2.1 Foundations**

Finite Element Methods (FEM) are precise but resource-demanding and Boundary Element Methods (BEM) reduce computational load but are incapable of handling heterogeneous and nonlinear conditions [18]. Researchers [19] predicted the settlement of bigger-diameter helical piles in cohesive soil using ML algorithms. They have created a complete database by linking fields and calibrating numerical models. A total of 40 load cases were considered to develop a database of 3600 numerical models for training and validating four different ML algorithms such as DT, RF, ANN, and Adaboost. They evaluated the models using cross-validation techniques and assessed them on a separate dataset. The results confirmed that the DT ( $R^2$  values of 0.92) and RF ( $R^2$  values of 0.96) models had high accuracy. Moreover, ML algorithms also demonstrated great potential in projecting the bearing capacity of piles. Researchers [20] carried out an ML analysis to estimate the bearing capacity of piles. They used cohesionless soil for the study. A dataset of 59 cases was employed to train and validate six different ML models. They were optimized by using the particle swarm optimization (PSO) algorithm. From the results, it was observed that among all, the optimized XGB model was superior with an  $R^2$  value of 0.9615, and the PSO algorithm is efficient in hyperparameter tuning. Researchers [21] investigated the use of ML in predicting the geotechnical axial capacity of reinforced concrete-driven piles. A dataset of 439 piles from six projects in Penang, Malaysia was used. 80% of the data set was used to train the model. The remaining 20% was used for testing the model. The RF model stood to be the superior for forecasting pile geotechnical axial capacity with an  $R^2$  value of 0.962. Researchers [22] examined the ability of ANNs to predict foundation settlement more effectively. The model predictions were also evaluated with three traditional methods. A total of 189 case histories were compiled from existing literature. Input parameters included the footing width, average SPT blow count, footing geometry, applied pressure, and embedment ratio; and the target variable was the settlement. It was found that ANN outperformed the traditional approaches. The ANN was particularly excellent in predicting a wide interval of settlements between 0.6 and 121 mm, while the other traditional methods showed limitations for large settlements. Sensitivity analysis showed SPT blow count, footing width, and applied pressure as the most relevant factors with 33.3%, 23.2%, and 17.7%, respectively. Researchers [23] discussed the usage of ML techniques to forecast the dynamic response of geogrid-reinforced foundation beds for industrial machines using ANN and GP. The consultant ANN and GP models based on field test data were written for parameters such as geogrid depth, shear strain, excitation angle, damping ratio, natural frequency, shear modulus, and operating frequency. They found that both the GP and ANN models can be successfully used to estimate the dynamic response, although GP turned out to be a slightly better model. The most critical parameter was operating frequency.

## **2.2 Geohazard Assessment**

Researchers [24] used ML algorithms for mapping landslide susceptibility prediction in the Abha Basin, Saudi Arabia. They used an inventory map of landslides and twelve landslide-conditioning factors to train and validate seven different ML models. The models were assessed through a

comparison of the predicted susceptibility to the actual landslide occurrences. It was found that linear discriminant analysis (LDA) and RF model performed with good accuracy. Researchers [25] gave a new approach that combined both deep learning and ML methods to recognize landslides of natural terrain through integrated geotechnical data. In this research, they used landslide-related data, such as topographic, geological, and rainfall, to build three general-purpose geodatabases. They implemented and compared five different algorithms RF, LR, SVM, CNN, and boosting methods, over the datasets. They have also shown an application of the current method with a case study that was executed at Lantau in Hong Kong. They found that CNN was the best model with an accuracy of 92.5% in the ReCLD dataset and that it outperformed other algorithms. Boosting methods were the second most accurate and then RF, LR, and SVM. Similarly, researchers [26] used SVM to predict maximum ground surface settlement (MGS) beneath a road embankment, with embankment height, applied surcharge, and side slope as inputs. Four kernel functions were used to design the SVM network. The RBF kernel function outperforms the SVM (mean absolute relative error (MARE) = 0.048 and root mean square error (RMSE) = 0.007). The SVM model was compared with an ANN for performance evaluation, and it was found that SVM RBF improves MGS prediction accuracy over neural networks.

### **2.3 Soil Mechanics**

Researchers [27] estimated the residual angle of friction of clay soil using characteristics such as index properties of the soil to train and validate different models based on ANN and SVM. From the result, it was seen that the SVM model was superior compared to ANN models in forecasting the residual strength of clay soils. A comparison of four ML algorithms for forecasting the shear strength of soft soil was carried out [28]. The datasets were obtained from 188 samples of plastic clay soil gathered from bridge construction projects in Vietnam. For predicting shear strength, the four ML techniques were Genetic Algorithm Adaptive Network based Fuzzy Inference System (GANFIS), ANN, Particle Swarm Optimization Adaptive Network based Fuzzy Inference System (PANFIS), and SVR. Evaluation of performance was done using different criteria such as RMSE and Pearson coefficient of correlation (R). The PANFIS model showed the highest accuracy in prediction (R=0.601, RMSE=0.038) of the strength of the soil. Researchers [29] used ANNs to estimate the plasticity index, MDD, and OMC of Clayey soil (CH, CL, and MH classes) stabilized with lime. The ANN model was validated on a fresh data set. The sensitivity of each parameter was also carried out. They concluded that the ANN model predicted PI, MDD, and OMC of a lime-stabilized clayey soil with high accuracy. Researchers [30] provided a series of procedures for creating a deep learning predictive model (DNN) predicting the geo-mechanical attributes of samples of marlstone sampled from the South Pars region of southwest Iran. They have predicted unconfined compressive strength (UCS), specific gravity (G), elasticity modulus (E), and an angle of internal friction. The models were used on a dataset obtained by conducting multiple geotechnical tests while evaluating the geotechnical parameters of 120 samples. They suggested that the proposed DNN-based model showed peak accuracy (=0.95), precision (=0.97), and the minimum error rate (RMSE = 0.17, mean absolute error (MAE) = 0.13, and mean square error (MSE) = 0.11). This model was an accurate predictor of geotechnical indices in terms of  $R^2$  (0.925 for E, 0.941 for G, 0.933 for UCS, and 0.954 for the angle of internal friction). Researchers [31] developed an ML algorithm to predict permeability by optimizing the image sample data enhancement process to get a sufficient training dataset. They trained an extreme learning machine neural network to predict the permeability of sandstone and compared its relative error with other established ML methods. They applied the same data collection and forecasting method to granite and bentonite to verify the correctness of the technique. The recommended method accurately predicted the gas permeability of different geomaterials with low error rates (4.1782% for sandstone and granite, 3.2479% for bentonite). RF as an ML algorithm in geotechnical engineering was used by [32] for forecasting the UCS of soil. The key features were soil content, water-holding capacity, relative density, OMC, and plasticity index. The model was assessed using correlation coefficient (R), MAE, and RMSE. They observed that the RF model could efficiently predict UCS values for a wide range of soils with higher accuracy than those of conventional empirical models. Researchers [33] have developed a broad-based model for

machine-learned geotechnical subsurface modeling that essentially includes spatial autocorrelations. They applied geotechnical distance fields (GDFs) to six local mapping ML methods: GB, ETs, RF, XGBoost, KNN, and general regression neural network (GRNN). These GDFs allowed the ML models to learn the spatial association among the sampled and unknown locations, and therefore, enhance the accuracy and spatial continuity compared with the conventional XY coordinate fields. GDF-ML is generic and applicable to multi-variable and high-dimensional datasets, as well as incomplete datasets. They concluded that the GDF-ET method results in an accurate and speedy interpretation of soil property profiles with quantified statistical uncertainty.

Researchers [34] used ML to predict key tunnel boring machines (TBM) operational parameters. The ML models employed to develop prediction models were Bayesian ridge regression (BR), nearest neighbors' regression, RF, GTB (Gradient Tree Boosting), and SVM. Two different DNNs, CNN (convolutional neural network), and long short-term memory network (LSTM) were also evaluated. The GTB and LSTM methods provided the best prediction accuracy.

## 2.4 Slope Stability Analysis

ML Algorithms are also being used to predict and analyze slope stability by finding the relationship between slope stability and influential factors based on available slope data. However, ML model accuracy depends greatly on the appropriate setting of hyperparameters. Different optimization algorithms, like the firefly algorithm (FA) and PSO were used to optimize hyperparameters while improving the accuracy of prediction [35].

Table 1. Summary of the literature on the application of ML in Geotechnical Engineering

| Reference        | Input parameter used               | Model used | R <sup>2</sup> /R | Number of data used | Target variable  |     |     |
|------------------|------------------------------------|------------|-------------------|---------------------|--|-----|-----|
| Researchers [27] | LL, PI, CF, ΔPI                    | SVM        | 0.954             | 137                 | Residual friction angle  |     |     |
|                  |                                    | ANN        | 0.888             |                     |  |     |     |
|                  |                                    | PANFIS     | 0.601             |                     |  |     |     |
| Researchers [28] | LL, PL, CC, NMC                    | GANFIS     | 0.569             | 188                 | Shear Strength   |     |     |
|                  |                                    | SVR        | 0.549             |                     |  |     |     |
|                  |                                    | ANN        | 0.49              |                     |  |     |     |
|                  |                                    | PSO-DT     | 0.9428            |                     |  |     |     |
| Researchers [20] | L, A, σ', φs, φt                   | PSO-KNN    | 0.7706            | 59                  | Bearing Capacity of piles on cohesionless soil.                |     |     |
|                  |                                    | PSO-MLP    | 0.8408            |                     |  |     |     |
|                  |                                    | PSO-RF     | 0.9235            |                     |  |     |     |
|                  |                                    | PSO-SVR    | 0.8222            |                     |  |     |     |
|                  |                                    | PSO-XGB    | 0.9807            |                     |  |     |     |
| Researchers [29] | LL, PL, LC                         | ANN        | N/A               | 280                 | PI   |     |     |
|                  |                                    | ANN        | 0.94              |                     |  | 122 | OMC |
|                  |                                    | ANN        | 0.94              |                     |  | 122 | MDD |
| Researchers [22] | B, q, N, L/B, Df/B                 | ANN        | 0.865             | N/A                 | Settlement of shallow foundations on cohesionless soils        |     |     |
| Researchers [21] | Dp, As, Ab, Ab, Sp, Ns, Nb, S1, S2 | SVM        | 0.956             | 439                 | Geotechnical axial capacity of reinforced concrete-driven pile |     |     |
|                  |                                    | RF         | 0.962             |                     |  |     |     |
|                  |                                    | DT         | 0.959             |                     |  |     |     |
|                  |                                    | KNN        | 0.919             |                     |  |     |     |

**Notation Used:** MGS = Maximum ground surface settlement, CC = Clay Content, MLP = Multilayer perceptron, L = Length of the pile, A = Cross-sectional area of the pile,  $\phi_t$  = Soil shear resistance angle at the tip of the pile,  $\phi_s$  = Soil shear resistance angle at the shaft of the pile,  $\sigma'$  = Effective stress at the tip of the pile,  $\Delta PI$  = Deviation from the A-line in casagrande's classification chart =  $PI - 0.73(LL - 20)$ ,  $\beta$  = Side slope, h = Embankment height, q = Surcharge, RBF = Radial basis function, LC = Lime content, B = Footing width, N = Average SPT blow count, L/B = Footing geometry, Df/B = Footing embedment ratio, CF = Clay fraction, Dp = Pile depth, As = Pile shaft area, Ab = Pile base area, Sp = Pile shape, Ns = Shaft SPT-N, Nb = Base SPT-N, S1 = Soil along pile shaft, S2 = Soil at pile base, Duw = Dry unit weight, CoU = Coefficient of uniformity, CoC = Coefficient of curvature, ClayA = Clay activity, LS = Liner shrinkage, DFS = Differential free swell.

From the above studies, it was observed that the best ML models depended on the specific location and data set and the predicted variable. ML algorithms were used to predict UCS, ground settlement, internal angle of friction, specific gravity, modulus of elasticity, slope stability, geotechnical axial capacity, etc. It was also observed that ML algorithms outperformed traditional statistical techniques. ANN was the best ML algorithm in many cases. RMSE, MAE, R, and MSE were used as a validation parameter for verifying the precision of the ML model. Table 1 presents the summary of the literature on the application of ML in Geotechnical Engineering.

### 3. Prediction of CBR of Natural Soil

Estimating the CBR of the soil is primarily required in geotechnical and pavement engineering for its crucial role in the design of flexible pavement. Recent advancement in artificial intelligence (AI) and ML offers alternative solutions with much-enhanced accuracy and efficiency of prediction. Initial attempts at predicting CBR were based largely on statistical correlations between soil properties and CBR values. Researchers [36] proved ANNs to be effective in predicting CBR values while identifying important input parameters by sensitivity analysis.

Recent studies have also focused on hybrid and ensemble ML models. Researchers [37] studied the impact of the physical properties of soil on the Un-soaked CBR of soil. A total of 99 soil samples were collected from Nigeria to develop a simplified CBR model using ANN and Least Square Regression (LSR). Both the ANN and LSR models forecasted CBR quite similarly to its laboratory value. The model without the percentage passing through the 200-micron sieve ranked as top. Researchers [38] hybridized ANN with optimization algorithms, such as gradient-based optimization (GBO) and firefly algorithms, and nearly perfect  $R^2$  values were obtained from the training and testing phases.

Researchers [6] compared SVM, RF, and ANN models and concluded that the RMSE and  $R^2$  values of RF were maximum. Researchers [10] forecasted the CBR of soils for pavement designs using ML algorithms. A total of 679 data were taken from published literature for this study. ML models such as MLP, KNN regressor, Support Vector Regression (SVR), Random Forest regressor (RFR), and Multilinear regression (MLR) were used. Analysis showed that RFR was the best model followed by KNN, MLP, SVR, and MLR. MDD of soils followed by the percentage of gravel was the supreme dependent parameter of CBR's outcome. Researchers [39] used five ANN models with a database of 521 records based on CBR and eight other index variables from standard laboratory tests of soil to predict CBR. Deep Neural Networks (DNNs) were applied in forecasting the CBR of subgrade soil [40] Various soil characteristics such as grain-size distribution, Atterberg limits, and compaction characteristics were considered as input variables. The results indicate that DNNs give better performance on CBR prediction compared with shallow ANNs and conventional MLR models.

Researchers [41] fused ELM with PSO to develop an accurate prediction model. They also optimized DT with meta-heuristic techniques for superior prediction accuracy ( $R^2 = 0.996$ ). Such recent findings have led to novel hybrid methods compositing various ML algorithms with optimization techniques. Researchers [5] found that the hybrid model (AB-DT) was more reliable than the single model (DT). From the result, it was revealed that the suggested AB-DT model can forecast successfully and precisely the CBR values, and MDD was the most important parameter



influencing CBR value. Researchers [42] combined meta-heuristic algorithms with Least Square Support Vector Regression for an overfitting solution. Researchers [43] highlighted the demerit of conventional statistical methods that failed to capture the complex interdependencies among the different soil properties like plasticity, gradation, and compaction-related characteristics. Researchers [44] introduced the GMDH model, which optimized network architecture based on input variables and showed better performance than MLR. Research like [45] strongly shows the ability of ML and AI to substitute empirical methods to make fast and economical CBR estimations. Table 2 represents a brief overview of various literature that employed ML algorithms to forecast the CBR value of natural soil. The ANN was the top performing and the most frequently used ML model for CBR prediction.

Table 2. Summary of the literature in predicting the CBR value of natural soil

| References       | Input Parameter                      | Model used | R <sup>2</sup> | Number of soil samples |
|------------------|--------------------------------------|------------|----------------|------------------------|
| Researchers [6]  | NMC, FC, SC, GC, G, LL, PL           | SVM        | 0.7            | 480                    |
|                  |                                      | RF         | 0.94           |                        |
|                  |                                      | MLR        | 0.3            |                        |
|                  |                                      | ANN        | 0.43           |                        |
|                  |                                      | M5 TREE    | 0.16           |                        |
| Researchers [36] | MDD, OMC, LL, PI, FC, SC, GC         | ANN        | 0.78           | 358                    |
| Researchers [10] | FC, SC, GC, LL, PL, OMC, MDD         | KNNR       | 0.86           | 697                    |
|                  |                                      | SVR        | 0.86           |                        |
|                  |                                      | RFR        | 0.93           |                        |
|                  |                                      | MLP        | 0.9            |                        |
|                  |                                      | MLR        | 0.7            |                        |
| Researchers [46] | FC, SC, GC, LL, PL, OMC, MDD         | ELM-CSO    | 0.996          | 149                    |
|                  |                                      | ELM        | 0.974          |                        |
| Researchers [39] | FC, SC, GC, LL, PL, OMC, MDD, PI     | ANN        | 0.96           | 70                     |
| Researchers [40] | FC, SC, GC, LL, PL, OMC, MDD, PI     | ANN        | 0.945          | 77                     |
| Researchers [38] | FC, SC, GC, LL, PL, OMC, MDD, PI, SL | ANN        | 0.997          | 100                    |
| Researchers [43] | FC, SC, GC, LL, OMC, $\gamma_d$ , PI | ANN        | 0.91           | 354                    |
|                  |                                      | GEP        | 0.918          |                        |
| Researchers [5]  | FC, SC, GC, LL, PL, PI, OMC, MDD     | DT         | 0.815          | 214                    |
|                  |                                      | AB-DT      | 0.967          |                        |
| Researchers [4]  | FC, LL, OMC, MDD, PL, PI             | DNN M-1    | 0.836          | 105                    |
|                  | FC, LL, OMC, MDD, PL, PI             | DNN M-2    | 0.36           | 175                    |
|                  | FC, OMC, MDD                         | DNN M-3    | 0.965          | 282                    |
| Researchers [47] | D10, D60, D30, D50, Cu, Cc           | DNN        | 0.999          | 90                     |
|                  |                                      | MLR        | 0.957          |                        |
| Researchers [48] | MDD, G                               | LR         | 0.92           | 34                     |

Hybrid models are the combination of one or more different types of ML models to enhance overall performance like combining the interpreting ability of DT and predicting ability of Neural Networks to achieve better results than a single model could achieve. For more information about

Hybrid Models, readers can refer to the cited article for RF [2], XGB [9], Light GBM [8], etc. From the above study, it was observed that ML and AI are the most accurate and fast techniques to predict the CBR of natural soil with the available dataset. However, from this study, it was not clear whether soil characteristics of different soil types can be combined or not. No study has shown the influence of different soil types on predicting CBR. Therefore, a study may be conducted to verify the impact of soil types on CBR estimation using ML and AI algorithms.

#### **4. Prediction of CBR of Treated Soil**

A soil sample mixed with admixtures such as lime, cement, rice husk, etc. to enhance the strength of the soil is known as treated soil. In this section prediction of CBR of treated soil sample data is reviewed. Prediction of CBR of treated soil is challenging as there are different additives and different treatment methods which makes it difficult to generalize prediction for different treatment methods. Developing models for this prediction requires a complex interaction between soil characteristics and additives. Moreover, Datasets of treated soil are hard to find. However, ML (for example ANN model) has the potential to address this complexity by learning the relationship and dependencies between soil properties and additive types from large datasets [49]. ML can also adapt to different soil conditions and additive types, identify patterns, and provide accurate predictions. ML can also optimize additive combinations and quantities for specific soil conditions. The geographical location of soil samples used for the training of the ML model can influence the model's predictive ability [50]. ML models offer enhanced precision in estimating CBR values compared to traditional methods [49-50].

Different researchers have used ML models for the forecasting of CBR of problematic soil such as expansive soil and black cotton soil treated with different admixtures. Researchers [51] investigated the stabilization of expansive soil subgrades for pavement construction by using bagasse ash (BA) as well as geotextile reinforcement. The CBR value of soil was estimated using the ANN model. The treated soil was 6.84% stronger than the natural soil. The MLR analysis tool was 91% reliable in predicting the CBR value. Similarly, researchers [52] used Gaussian process regression (GPR) in forecasting the CBR of expansive soil treated with hydrated lime-activated rice husk ash (HARHA). GPR performed better than the previously constructed models of ANN and GEP for the forecasting of CBR. Sensitivity analysis revealed that HARHA was the most important parameter. Researchers [53] explored the application of three distinct algorithms of an artificial neural network- namely, Levenberg-Marquardt Backpropagation, Bayesian Programming, and Conjugate Gradient algorithms-for assessing strength performance for expansive soils treated with HARHA. The study found that all the ANN algorithms could forecast the values of CBR and UCS of the HARHA-treated soil with good accuracy, and the LMBP algorithm performed better than the others. Researchers [8] validated the predictability of CBR of agricultural and industrial waste mixed expansive soils. This study used Light Gradient Boosting (LGB) as an ML algorithm. The result obtained was, Pearson correlation coefficient ( $R$ ) = 0.9452, RMSE = 0.3225, and MAE = 0.2522. The important feature in predicting the CBR value was found in order as: ash content, MDD, ash type, OMC, LL, and PL. Researchers [54] presented and compared the predictive capacity of the three ML models namely, Multivariate Adaptive Regression Splines (MARS), RF, and Gradient Boosting Machines (GBM) for the estimation of the CBR value of expansive soil stabilized with sawdust ash, ordinary Portland cement (OPC) and quarry. The RF model indicated better predictive potentiality as compared to MARS and GBM. The influence of stabilizers, incorporated into the model creation process, had considerably improved predictive accuracy. Researchers [55] applied multiple regression analysis to forecast the CBR of cement and waste glass admixture-treated black cotton soil. The model obtained had precisely predicted the CBR with a coefficient of multiple determination,  $R^2$  equal to 0.98 for the standard proctor compactive effort and 0.94 for the treated proctor compactive effort.

Similar studies were also conducted for lateritic soil. Researchers [46] discussed employing an integrated extreme learning machine-cooperation search optimizer approach toward forecasting the CBR of lateritic soils. Two models were developed namely ELM-CSO and ELM. It assesses the ability of models pertaining to minimizing the MAE, MSE, RMSE, or maximizing  $R$  and  $R^2$ . The

values of CBR were better predicted with the model ELM-CSO than with the ELM model. Researchers [56] focused on efficient model development for forecasting the CBR value of cement and RHA (Rice husk ash) mixed lateritic soil. For this study, 1288 samples were used and the data gathered was analyzed using three ANN algorithms. The model's ability was assessed by a set of statistical performance indicators, namely  $R^2$ , and RMSE. Based on the results they reported that the ANN model was the best technique for forecasting the lateritic soil's CBR values.

Similar studies were also carried out using clay soil. Researchers [57] did the strength prediction of difficult clayey soils treated with nano-scale combinations of natural source pozzolan (NNP) and lime powder (NL) using MLR, ANN, and FL. In the developed model, the performance criteria suggested that ANN as well as FL techniques predict the value of CBR and PI accurately, but in better terms, ANN is preferred compared to FL. Similarly, researchers [58] used a soft computing approach to estimate Nigerian black clay CBR values, using ANNs and MLPs. The models were trained with the feed forward back propagation algorithm to predict the unsoaked and soaked CBR value of black clay stabilized with cement kiln dust.

Researchers [59] used MR and ANN models to foresee the CBR of pond ash from a thermal power plant. The plant was stabilized with lime and lime sludge. The period of curing was the most crucial parameter affecting the estimation of treated pond ash CBR value. The ANN model was superior among the two. Similarly, in another study, researchers [7] studied the application of two ML techniques, namely RF and M5P model tree, for forecasting the CBR value of pond ash from a thermal power plant. The pond ash was mixed with lime and industrial waste lime sludge. The output of statistical parameters shows that RF performed better than M5P. The curing period was the dominating factor in estimating the CBR value.

Some researchers studied the application of ML algorithms in determining the CBR of fine-grained soil treated using admixtures. Researchers [60] estimated the soaked CBR of fine-grained plastic soils using ML algorithms. A total of 1011 data sets were taken from a highway project for this study. Three ML algorithms, GPR, Kernel Ridge Regression (KRR), and KNN were used in this study. The GPR model developed by the FCM data division method (GPRF) proved to be the superior model for predicting the CBR of fine-grained plastic soils. The K-fold data division method was also proved to be effective in preventing overfitting of the models. It was also found that the geological location of the soil samples used for developing the models can significantly affect the models' predictive ability. Researchers [61] applied soft computing systems in estimating the value of CBR for the fine-grained soil combined with QD and lime, and RHA and lime. Then, the CBR values of the soils were estimated using Simple Linear Regression (SLR), MLR, ANN, and SVM. They found that the ANN model surpassed all the models because it gave the highest  $R^2$  value for both QD-lime and RHA-lime stabilized soils. The optimal content of QD-lime stabilized soil was found to be 40% QD and 4% lime and that for RHA-lime stabilized soil was 12% RHA and 4% lime.

Similar experiments were also conducted with sand. Researchers [62] explored the application of evolutionary polynomial regressions (EPR) and ANN in forecasting the UCS and CBR of micro silica-lime stabilized sulfate silty sand. They used 90 CBR and UCS tests on sulfate silty sand treated with various percentages of micro silica and lime. Similarly, researchers [63] used ANN and MR models to estimate the CBR of Aegean sands. The work had its basis on nine different sands of the Aegean with contrasting soil properties. Laboratory tests on the sands were conducted for an extensive dataset through various parameters like the distribution of particle size, Atterberg limits, and CBR. Among both, the ANN model was superior in predicting CBR values. Researchers [64] used eight ML models, which include RF, Least Median of Squares Regression (LMSR), ANN, Elastic Net Regularization Regression (ENRR), GPR, Lazy K-star (LKS), M-5 Model Trees Alternating Model Trees (AMT) to foresee the CBR of geosynthetic reinforced subgrade. The data used for calibrating and validating the models were collected from earlier studies, covering various soil types. The input parameters for the model's development include soil properties, geosynthetic reinforcement properties, and the position of reinforcement layers.

The results showed that ANN models showed better prediction accuracy in predicting the CBR value. Numerous studies [9, 65] have shown that the accuracy of the ANN model was the highest in predicting CBR value. Researchers [9] found the effects of gradation and compaction characteristics on the CBR of granular materials in subbase and landfill liner construction. Experimental data and six different computational intelligence models ANN, GP, Evolutionary Polynomial Regression (EPR), RF, XGBoost, and Response Surface Methodology (RSM) were used to predict CBR value. Accuracy for ANN was 88%, followed by GP, EPR, and RF with a similar accuracy of 85%, while XGBoost was the least 81%. It was also found that the optimum performance of CBR depends on  $D_{50}$  (Particle size at which 50% of the sample is finer) and  $D_{60}$  (Particle size at which 60% of the sample is finer). Researchers [66] applied ANNs to foresee the CBR of remolded soils. Three types of soil normally found in the central region of India such as yellow soil, copra soil, and murum soil were used. Two ANN models, specifically GRNN and MLPN with the Levenberg-Marquardt back-propagation algorithm were developed using MATLAB. GRNN model was superior in forecasting the CBR in terms of  $R^2$ . Researchers [65] explored the usability of chemically stabilized Coal Gangue (CG), a coal mining byproduct, as a sustainable filling material for earthworks by estimating its engineering properties using ANN and RF models. The Chemicals used were lime and gypsum. Parametric analysis revealed that for obtaining maximum unsoaked and soaked CBR, the optimum contents of gypsum and lime were 1.50% and 4%, respectively, and for UCS, it was 1.50% and 6%, respectively. Both ANN and RF models demonstrated high accuracy, with ANN being slightly superior.

Table 3. Summary of literature predicted the CBR value of treated soil

| References       | Techniques used  | Additives used                               | Sample size | $R^2/R$                 | Soil Properties used     | Soil type               |
|------------------|------------------|--|-------------|-------------------------|--------------------------|-------------------------|
| Researchers [53] | ANN              | hydrated-lime activated rice husk ash        | 121         | More than 0.9           | OMC, CA, MDD, LL, PL, PI | Expansive clay Soil     |
| Researchers [66] | MLPN<br>GRNN     | Remolded the Soil                            | 60          | 0.97<br>0.99            | LL, SC, FC, PI, OMC, MDD | Yellow, Copra and Murum |
| Researchers [69] | BBO-MLP          | Lime and Lime sludge                         | 51          | 0.997                   | MDD, NMC                 | pond ash                |
| Researchers [56] | ANN              | Cement and Rice husk ash                     | 1288        | 0.99                    | LL, PI, MDD, OMC         | Lateritic               |
| Researchers [59] | ANN<br>MR        | Lime and Lime sludge                         | 51          | More than 0.96          | MDD, OMC                 | pond ash                |
| Researchers [63] | ANN<br>MR        | Quartz, Feldspar, Calcite, Corund, Amorphous | N/A         | 0.978<br>0.812          | G, Cu, Cc, MDD, OMC      | Sand                    |
| Researchers [57] | MLR<br>ANN<br>FL | Pozzolan and lime powder                     | 120         | 0.869<br>0.989<br>0.975 | G, LL, PL, OMC, MDD      | Clay                    |

Researchers [67] investigated the possibilities of AI methods in estimating the CBR of soil stabilized with alum sludge. They concluded that AI could estimate CBR with high accuracy for MAE values ranging between 0.30 to 0.51, and  $R^2$  values between 0.94 to 0.99. The number of hammers for compaction was the most important parameter, and MDD and mixture were the

least important. Researchers [68] utilized the MLR algorithm to forecast the CBR values of the Makkah area soil of Saudi Arabia, based on less complicated tests like the Los Angeles Abrasion test, sieve analysis, OMC, and MDD. The results provided a good relationship between the CBR and sieve analysis parameters, OMC, and MDD, with  $R^2 = 0.95$ . Table 3 summarizes the literature which predicted the CBR value of treated soil. From the above studies, it can be said that the CBR values obtained from treated or treated soil could easily be predicted using ML algorithms. Many researchers have considered only one or two types of additives to treat the soil to improve its capacity. However, limited research could be seen in predicting the CBR using different additives. The most effective additives of all were not compared to predicting the CBR using ML algorithms. Fig. 2 represents the soil properties used as an input parameter for CBR prediction. It is observed from Fig. 2 that OMC is the most frequently used as input for modeling CBR followed by MDD, LL, PL, and PI.

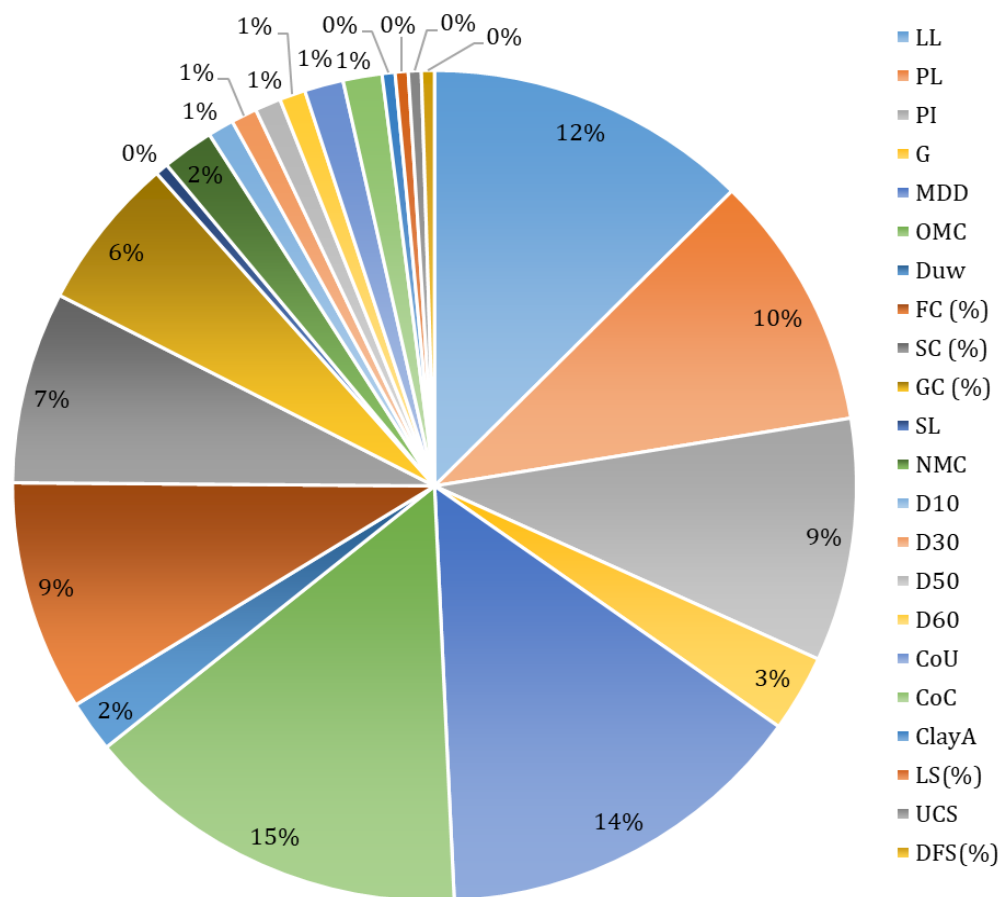


Fig. 2. Most commonly used soil properties as input parameters for CBR prediction

## 5. Summary and Conclusion

This study focuses on reviewing the literature related to the application of machine learning in forecasting the CBR of natural and treated soils. In addition to that, a few applications of machine learning in geotechnical engineering such as foundation engineering, slope stability, geohazard assessment, and soil mechanics were carried out. The important findings of the reviews are given below.

- ANN (0.865) was found to be the best model for forecasting the settlement of shallow foundations.
- The rank of ML models was RF (0.962), DT (0.959), SVM (0.956), and KNN (0.919) for forecasting load bearing capacity of the driven pile, whereas PSO-XGB (0.9807) was found to be the best model for forecasting bearing capacity of piles on cohesionless soils.

- Though SVM (0.964) was the best in terms of AUC, however, for practical consideration, RF was found to be the best model for forecasting slope stability.
- RF (AUC=0.951) was the best model in forecasting landslide susceptibility, whereas CNN was found to be the best in landslide identification.
- PANFIS, SVM, and ANN were the best models in forecasting shear strength, residual friction angle, and plasticity index, respectively for clay soil. The superior models for predicting PI, MDD, and OMC was ANN.
- In the case of CBR of natural soils, DNN (0.99), GEP (0.918), and ELM-CSO (0.996) were the best models for granular soil, fine-grained soil, and lateritic soil, respectively. Several studies have found the best models as RF (0.94), RFR (0.93), AB-DT (0.967), and LR (0.92). However, multiple studies have found that ANN (0.96/0.945/0.997/0.91/0.78) was the best model, and the most frequently used model was the ANN.
- In the case of CBR of treated soils, ANN (>0.90), BBO-MLP (0.997), ANN (0.99), ANN/MR (>0.96), ANN (0.978), ANN (0.989) was found to be the best models for expansive clay soil with HARHA, pond ash with lime and lime sludge, lateritic soil with cement and RHA, pond ash with lime and lime sludge, sand with Quartz, feldspar, calcite, corund, amorphous, and clay with pozzolan and lime powder, respectively. GRNN (0.99) was found to be the best model for yellow, copra, and murum soil remolding.
- OMC was the most frequently used input for modeling CBR followed by MDD, LL, PL, and PI.

Though ML models are advantageous over other techniques and tedious laboratory experiments, they have also certain limitations. While ML made CBR prediction easy and reliable, ML also faced challenges such as limited data availability, variation of soil properties for different soil, and difficulty in selecting input features. ML models may also suffer from overfitting, underfitting, or poor generalizability when applied to different datasets. ML also faced significant challenges when additives were used as it required complex interaction between soil characteristics and additives.

RF has superior predictive accuracy and reduces overfitting by ensemble learning but it can also be intensive with large datasets, and the complication of the model can hinder interpretability. ANN can learn complex nonlinear relations and is suitable for various types, but the training process is complex and difficult to select hyperparameters. SVM performs well with high dimensional data and has different kernel functions that can adapt to various types of data, but it takes a lot of time to train large datasets, and performance is largely dependent on parameter selection. DT is easy to visualize. It can perform numerical and categorical problems and has a certain level of robustness against missing data, but this model uses a greedy tree which may lead to getting stuck in local optimal solutions. DNN can detect complex features and has better generalizability than simple networks, but it has problems too and needs modification when problems arise since network architecture is initialized at the beginning and it depends on the family of ANN.

Future research on CBR prediction should focus on using deep learning techniques like CNN to detect complicated associations among soil properties and CBR values and developing hybrid models that integrate traditional methods with ML algorithms that could enhance interpretability and applicability. Similarly, ensemble models like RF and GB can be explored to combine the strengths of multiple algorithms and improve prediction accuracy. Moreover, Big data analytics should be utilized to handle and extract insights from large-scale geotechnical datasets, incorporating regional and global soil variability. Advanced engineering features such as automated feature selection, dimensionality reduction, and the use of domain-specific knowledge to create interaction terms, are essential to improve model inputs and understanding the interplay between influencing factors. These directions would pave the way for more robust, accurate, and generalizable predictive models in forecasting CBR.

## References

- [1] Vardhan KH, Rani KS, Babu ChVN, Satyanarayana G. Prediction of California Bearing Ratio Using Machine Learning for Stabilized Soil Subgrade. *International Journal of Research Publication and Reviews*, 2023;4(10):621–630. <https://ijrpr.com/uploads/V4ISSUE10/IJRPR18113.pdf>
- [2] Kassa SM, Wubineh BZ. Use of Machine Learning to Predict California Bearing Ratio of Soils. *Advances in Civil Engineering*, 2023;2023:1-11. <https://doi.org/10.1155/2023/8198648>
- [3] Díaz E, Spagnoli G. Natural Gradient Boosting for Probabilistic Prediction of Soaked CBR Values Using an Explainable Artificial Intelligence Approach. *Buildings*, 2024;14(2):352. <https://doi.org/10.3390/buildings14020352>
- [4] Yabi CP, Agongbe SW, Koto Tamou BC, Farsangi EN, Alamou E, Gibigaye M. Prediction of CBR by Deep Artificial Neural Networks with Hyperparameter Optimization by Simulated Annealing. *Indian Geotechnical Journal*, 2024; 54(6):2318–2334. <https://doi.org/10.1007/s40098-024-00870-4>
- [5] Ngo HTT, Bui Q-AT, Vi N Van, Thuy NTB. Application of hybrid modeling to predict California bearing ratio of soil. *Vietnam Journal of Earth Sciences*, 2024;46(3):399–410. <https://doi.org/10.15625/2615-9783/20766>
- [6] Tunbosun AJ, Ehiorobo JO, Obinna OS, Nwankwo E. Application of Soft Computing Techniques in Modelling of Soaked and Unsoaked California Bearing Ratio. *Asian Soil Research Journal*, 2022;6(2):32–46. <https://doi.org/10.9734/asrj/2022/v6i230128>
- [7] Suthar M, Aggarwal P. Modeling CBR value using RF and M5P Techniques. *Mendel*, 2019;25(1):73–78. <https://doi.org/10.13164/mendel.2019.1.073>
- [8] Tran VQ, Do HQ. Prediction of California Bearing Ratio (CBR) of Stabilized Expansive Soils with Agricultural and Industrial Waste Using Light Gradient Boosting Machine. *Journal of Science and Transport Technology*, 2021;1(1):1–8. <https://jstt.vn/index.php/en/article/view/3>
- [9] Alzara M, Onyelowe KC, Ebid AM, Hanandeh S, Yosri AM, Alshammari TO. Modeling of the Effect of Gradation and Compaction Characteristics on the California Bearing Ratio of Granular Materials for Subbase and Landfill Liner Construction. *Sci Rep*, 2024;14:23630. <https://doi.org/10.1038/s41598-024-74106-z>
- [10] Bherde V, Mallikarjunappa LK, Baadiga R, Balunaini U. Application of Machine-Learning Algorithms for Predicting California Bearing Ratio of Soil. *Journal of Transportation Engineering, Part B: Pavements*, 2023;149(4): 1-12. <https://doi.org/10.1061/jpeodx.pveng-1290>
- [11] Mahajan L, Bhagat S. Machine learning approaches for predicting compressive strength of concrete with fly ash admixture. *Res. Eng. Struct. Mater.*, 2023;9(2):431–456. <https://doi.org/10.17515/resm2022.534ma0927>
- [12] Liu H, Su H, Sun L, Dias-da-Costa D. State-of-the-art review on the use of AI-enhanced computational mechanics in geotechnical engineering. *Artificial Intelligence Review*, 2024;57:196. <https://doi.org/10.1007/s10462-024-10836-w>
- [13] Shao W, Yue W, Zhang Y, Zhou T, Zhang Y, Dang Y, et al. The Application of Machine Learning Techniques in Geotechnical Engineering: A Review and Comparison. *Mathematics*, 2023;11(18):3976. <https://doi.org/10.3390/math11183976>
- [14] Yousefpour N, Liu Z, Zhao C. Machine Learning Methods for Geotechnical Site Characterization and Scour Assessment. *Transp Res Rec*, 2024;0:0. <https://doi.org/10.1177/03611981241257512>
- [15] Yaghoubi E, Yaghoubi E, Khamees A, Vakili AH. A systematic review and meta-analysis of artificial neural network, machine learning, deep learning, and ensemble learning approaches in field of geotechnical engineering. *Neural Computing and Application*, 2024;36:12655–12699. <https://doi.org/10.1007/s00521-024-09893-7>
- [16] Puri N, Prasad HD, Jain A. Prediction of Geotechnical Parameters Using Machine Learning Techniques. *Procedia Computer Science*, 2018;125:509–517. <https://doi.org/10.1016/j.procs.2017.12.066>
- [17] Cui K, Jing X. Research on prediction model of geotechnical parameters based on BP neural network. *Neural Computing and Applications*, 2019;31:8205–8215. <https://doi.org/10.1007/s00521-018-3902-6>
- [18] Mourya VK, Pandey G, Patel D, Kumar R. Approaches considering non-linearity in soil-foundation-interaction: A State of the Art Review. *Res. Eng. Struct. Mater.*, 2023;9(3):989–1013. <https://doi.org/10.17515/resm2023.646me0117>
- [19] Shuman NM, Khan MS, Amini F. Efficient machine learning model for settlement prediction of large diameter helical pile in c— $\Phi$  soil. *AI in Civil Engineering*, 2024;3(10):1–26. <https://doi.org/10.1007/s43503-024-00028-4>
- [20] Kardani N, Zhou A, Nazem M, Shen SL. Estimation of Bearing Capacity of Piles in Cohesionless Soil Using Optimised Machine Learning Approaches. *Geotechnical and Geological Engineering*, 2020;38:2271–2291. <https://doi.org/10.1007/s10706-019-01085-8>

- [21] Xun OZ, Abdullah RA. Predicting Geotechnical Axial Capacity of Reinforced Concrete Driven Pile Using Machine Learning Technique. *Malaysian Journal of Civil Engineering*, 2023;35(3):11-23. <https://doi.org/10.11113/mjce.v35.20544>
- [22] Shahin MA, Maier HR, Jaksa MB. Predicting Settlement of Shallow Foundations using Neural Networks. *Journal of Geotechnical and Geoenvironmental Engineering*, 2002;128(9):785-793. [https://doi.org/10.1061/\(ASCE\)1090-0241\(2002\)128:9\(785\)](https://doi.org/10.1061/(ASCE)1090-0241(2002)128:9(785))
- [23] Sharma S, Venkateswarlu H, Hegde A. Application of Machine Learning Techniques for Predicting the Dynamic Response of Geogrid Reinforced Foundation Beds. *Geotechnical and Geological Engineering*, 2019;37:4845-4864. <https://doi.org/10.1007/s10706-019-00945-7>
- [24] Youssef AM, Pourghasemi HR. Landslide susceptibility mapping using machine learning algorithms and comparison of their performance at Abha Basin, Asir Region, Saudi Arabia. *Geoscience Frontiers*, 2021;12(2):639-655. <https://doi.org/10.1016/j.gsf.2020.05.010>
- [25] Wang H, Zhang L, Yin K, Luo H, Li J. Landslide identification using machine learning. *Geoscience Frontiers*, 2021;12(1):351-364. <https://doi.org/10.1016/j.gsf.2020.02.012>
- [26] Che Mamat R, Ramli A, Che Omar MBH, Samad AM, Sulaiman SA. Application of machine learning for predicting ground surface settlement beneath road embankments. *International Journal of Nonlinear Analysis and Applications*, 2021;12(Special Issue):1025-1034. <https://doi.org/10.22075/IJNAA.2021.5548>
- [27] Das SK, Samui P, Khan SZ, Sivakugan N. Machine learning techniques applied to prediction of residual strength of clay. *Central European Journal of Geosciences*, 2011;3(4):449-461. <https://doi.org/10.2478/s13533-011-0043-1>
- [28] Pham BT, Son LH, Hoang TA, Nguyen DM, Tien Bui D. Prediction of shear strength of soft soil using machine learning methods. *Catena*, 2018;166:181-191. <https://doi.org/10.1016/j.catena.2018.04.004>
- [29] Bahmed IT, Harichane K, Ghrici M, Boukhatem B, Rebouh R, Gadouri H. Prediction of geotechnical properties of clayey soils stabilised with lime using artificial neural networks (ANNs). *International Journal of Geotechnical Engineering*, 2017;13(2):191-203. <https://doi.org/10.1080/19386362.2017.1329966>
- [30] Azarafza M, Bonab MH, Derakhshani R. A Deep Learning Method for the Prediction of the Index Mechanical Properties and Strength Parameters of Marlstone. *Materials*, 2022;15(19):6899. <https://doi.org/10.3390/ma15196899>
- [31] Ma S, Liu J, Lin Y, Wang Z, Zhang T, Jian Z. Prediction of permeability of various geotechnical materials under different temperatures based on physical characteristics and machine learning. *Fuel*, 2025;379:13109. <https://doi.org/10.1016/j.fuel.2024.133109>
- [32] Reddy YR. Prediction of Ground Properties Using Machine Learning Techniques. *International Journal of Current Science (IJCS PUB)*, 2011;1(1):12-15. <https://rjpn.org/ijcs/pub/papers/IJCSP11A1004.pdf>
- [33] Xie J, Huang J, Zeng C, Huang S, Burton GJ. A generic framework for geotechnical subsurface modeling with machine learning. *Journal of Rock Mechanics and Geotechnical Engineering*, 2022;14(5):1366-1379. <https://doi.org/10.1016/j.jrmge.2022.08.001>
- [34] Xu C, Liu X, Wang E, Wang S. Prediction of tunnel boring machine operating parameters using various machine learning algorithms. *Tunnelling and Underground Space Technology*, 2021;109:103699. <https://doi.org/10.1016/j.tust.2020.103699>
- [35] Yang Y, Zhou W, Jiskani IM, Lu X, Wang Z, Luan B. Slope Stability Prediction Method Based on Intelligent Optimization and Machine Learning Algorithms. *Sustainability*, 2023;15(2):1169. <https://doi.org/10.3390/su15021169>
- [36] Al-Busultan S, Aswed GK, Almuhanza RRA, Rasheed SE. Application of Artificial Neural Networks in Predicting Subbase CBR Values Using Soil Indices Data. *IOP Conference Series: Material Science and Engineering*, 2020; 671:012106. <https://doi.org/10.1088/1757-899X/671/1/012106>
- [37] Tunbosun AJ, Ehiorobo JO, Obinna OS, Nwankwo E. Application of Machine Learning Techniques to Estimate Unsoaked California Bearing Ratio in Ekiti Central Senatorial District. *Current Journal of Applied Science and Technology*, 2021;40(35):30-37. <https://doi.org/10.9734/cjast/2021/v40i3531571>
- [38] Thapa I, Ghani S. Estimation of California bearing ratio for hill highways using advanced hybrid artificial neural network algorithms. *Multiscale and Multidisciplinary Modeling, Experiments and Design*, 2024;7:1119-1144. <https://doi.org/10.1007/s41939-023-00269-3>
- [39] Ojeda JMP, Calderon BAC, Huatangari LQ, Pintado WR. Determination of the California Bearing Ratio of the Subgrade and Granular Base Using Artificial Neural Networks. *International Journal of Engineering and Technology Innovation*, 2023;13(3):175-188. <https://doi.org/10.46604/ijeti.2023.11053>
- [40] Othman K, Abdelwahab H. The application of deep neural networks for the prediction of California Bearing Ratio of road subgrade soil. *Ain Shams Engineering Journal*, 2023;14(7):101988. <https://doi.org/10.1016/j.asej.2022.101988>



- [41] Bardhan A, Samui P, Ghosh K, Gandomi AH, Bhattacharyya S. ELM-based adaptive neuro swarm intelligence techniques for predicting the California bearing ratio of soils in soaked conditions. *Applied Soft Computing*, 2021;110:107595. <https://doi.org/10.1016/j.asoc.2021.107595>
- [42] Ma C, Shao Q, Yin M. California Bearing Ratio Prediction Based on LSSVR and Multiple Optimizers. *Journal of Applied Science and Engineering*, 2024;28(5):1095–1105. [https://doi.org/10.6180/jase.202505\\_28\(5\).0015](https://doi.org/10.6180/jase.202505_28(5).0015)
- [43] Taskiran T. Prediction of California bearing ratio (CBR) of fine grained soils by AI methods. *Advances in Engineering Software*, 2010;41(6):886–892. <https://doi.org/10.1016/j.advengsoft.2010.01.003>
- [44] Kurnaz TF, Kaya Y. Prediction of the California bearing ratio (CBR) of compacted soils by using GMDH-type neural network. *The European Physical Journal Plus*, 2019;134:326. <https://doi.org/10.1140/epjp/i2019-12692-0>
- [45] Shukla DK, Murthy YI. California bearing ratio of black cotton soil using soft computing techniques. *Asian Journal of Civil Engineering*, 2024;25:3961–3972. <https://doi.org/10.1007/s42107-024-01023-x>
- [46] Nagaraju TV, Bahrami A, Prasad CD, Mantena S, Biswal M, Islam MR. Predicting California Bearing Ratio of Lateritic Soils Using Hybrid Machine Learning Technique. *Buildings*, 2023;13(1):255. <https://doi.org/10.3390/buildings13010255>
- [47] Polo-Mendoza R, Duque J, Masin D. Prediction of California bearing ratio and modified proctor parameters using deep neural networks and multiple linear regression: A case study of granular soils. *Case Studies in Construction Materials*, 2024;20:e02800. <https://doi.org/10.1016/j.cscm.2023.e02800>
- [48] Umar IH, Salisu IM, Lin H, Hassan JI. Soil characterization, CBR modeling, and spatial variability analysis for road subgrade: a case study of Danchuwa – Jajere Road, Yobe State, Nigeria. *Engineering Research Express*, 2024;6:035119. <https://doi.org/10.1088/2631-8695/ad78a5>
- [49] Yousefpour N, Medina-Cetina Z, Hernandez-Martinez FG, Al-Tabbaa A. Stiffness and strength of stabilized organic soils—part ii/ii: Parametric analysis and modeling with machine learning. *Geosciences*, 2021;11(5):218. <https://doi.org/10.3390/geosciences11050218>
- [50] Gowda S, Kunjar V, Gupta A, Kavitha G, Shukla BK, Sihag P. Prediction of the Subgrade Soil California Bearing Ratio Using Machine Learning and Neuro-Fuzzy Inference System Techniques: A Sustainable Approach in Urban Infrastructure Development. *Urban Science*, 2024;8(1):4. <https://doi.org/10.3390/urbansci8010004>
- [51] Rajakumar C, Rao PKR, Babu GR, Sreenivasulu A. Experimental and numerical prediction of California bearing ratio of expansive soil stabilized by bagasse ash and geotextile reinforcement. *IOP Conference Series: Earth and Environmental Science*, 2021;796: 012057. <https://doi.org/10.1088/1755-1315/796/1/012057>
- [52] Ahmad M, Al-Zubi MA, Kubińska-Jabcoń E, Majdi A, Al-Mansob RA, Sabri MMS, et al. Predicting California bearing ratio of HARHA-treated expansive soils using Gaussian process regression. *Scientific Reports*, 2023;13:13593. <https://doi.org/10.1038/s41598-023-40903-1>
- [53] Onyelowe KC, Iqbal M, Jalal FE, Onyia ME, Onuoha IC. Application of 3-algorithm ANN programming to predict the strength performance of hydrated-lime activated rice husk ash treated soil. *Multiscale and Multidisciplinary Modeling, Experiments and Design*, 2021;4:259–274. <https://doi.org/10.1007/s41939-021-00093-7>
- [54] Ikeagwuani CC. Estimation of modified expansive soil CBR with multivariate adaptive regression splines, random forest and gradient boosting machine. *Innovative Infrastructure Solutions*, 2021;6:199. <https://doi.org/10.1007/s41062-021-00568-z>
- [55] Ikara IA, Kundiri AM, Mohammed A. Predicting CBR Values of Black Cotton Soil Stabilized with Cement and Waste Glass Admixture Using Regression Model. *American Journal of Traffic and Transportation Engineering*, 2019;4(1):31–36. <https://doi.org/10.11648/j.ajtte.20190401.15>
- [56] Nnochiri ES, Okokpuije IP, Tartibu LK. Artificial Neural Network Models for Predicting California Bearing Ratio of Lateritic Soil Admixed with Reinforce and Rice Husk Ash. *Revue d'Intelligence Artificielle*, 2023;37(2):305–313. <https://doi.org/10.18280/ria.370208>
- [57] Al-Swaidani AM, Meziab A, Khwies WT, Al-Bali M, Lala T. Building MLR, ANN and FL models to predict the strength of problematic clayey soil stabilized with a combination of nano lime and nano pozzolan of natural sources for pavement construction. *International Journal of Geo-Engineering*, 2024;15:2. <https://doi.org/10.1186/s40703-023-00201-1>
- [58] Salahudeen AB, Sadeeq JA. California bearing ratio prediction of modified black clay using artificial neural networks. In: LS and EE, editors. 10th Anniversary Conference, Accra: West Africa Built Environment Research (WABER) Conference; 2019, 268-281. <https://doi.org/10.33796/waberconference2019.19>
- [59] Suthar M, Aggarwal P. Predicting CBR Value of Stabilized Pond Ash with Lime and Lime Sludge Using ANN and MR Models. *International Journal of Geosynthetics and Ground Engineering*, 2018;4:6. <https://doi.org/10.1007/s40891-017-0125-3>

- [60] Verma G, Kumar B, Kumar C, Ray A, Khandelwal M. Application of KRR, K-NN and GPR Algorithms for Predicting the Soaked CBR of Fine-Grained Plastic Soils. *Arabian Journal of Science and Engineering*, 2023;48:13901–13927. <https://doi.org/10.1007/s13369-023-07962-y>
- [61] Islam MR, Roy AC. Prediction of California Bearing Ratio of Fine-Grained Soil Stabilized with Admixtures Using Soft Computing Systems. *Journal of Civil Engineering, Science and Technology*, 2020;11(1):28–44. <https://doi.org/10.33736/jcest.2035.2020>
- [62] Ghorbani A, Hasanzadehshooilli H. Prediction of UCS and CBR of microsilica-lime stabilized sulfate silty sand using ANN and EPR models; application to the deep soil mixing. *Soils and Foundations*, 2018;58(1):34–49. <https://doi.org/10.1016/j.sandf.2017.11.002>
- [63] Erzin Y, Turkoz D. Use of neural networks for the prediction of the CBR value of some Aegean sands. *Neural Computing and Application*, 2016;27:1415–1426. <https://doi.org/10.1007/s00521-015-1943-7>
- [64] Raja MNA, Shukla SK, Khan MUA. An intelligent approach for predicting the strength of geosynthetic-reinforced subgrade soil. *International Journal of Pavement Engineering*, 2022;23(10):3505–3521. <https://doi.org/10.1080/10298436.2021.1904237>
- [65] Amin MN, Iqbal M, Ashfaq M, Salami BA, Khan K, Faraz MI, et al. Prediction of Strength and CBR Characteristics of Chemically Stabilized Coal Gangue: ANN and Random Forest Tree Approach. *Materials*, 2022;15(12):4330. <https://doi.org/10.3390/ma15124330>
- [66] Kumar SA, Kumar JP, Rajeev J. Application of Machine Learning Techniques to Predict Soaked CBR of Remolded Soils. *International Journal of Engineering Research & Technology (IJERT)*, 2013; 2(6): 3019–3024. <https://www.ijert.org/research/application-of-machine-learning-techniques-to-predict-soaked-cbr-of-remolded-soils-IJERTV2IS60881.pdf>
- [67] Baghbani A, Nguyen MD, Alnedawi A, Milne N, Baumgartl T, Abuel-Naga H. Improving Soil Stability with Alum Sludge: An AI-Enabled Approach for Accurate Prediction of California Bearing Ratio. *Applied Sciences*, 2023;13(8):4934. <https://doi.org/10.3390/app13084934>
- [68] Alawi M, Rajab M. Prediction of California bearing ratio of subbase layer using multiple linear regression models. *Road Materials and Pavement Design*, 2013; 14(1):211–219. <https://doi.org/10.1080/14680629.2012.757557>
- [69] Wu J, Li J, Hu W. Applying Biogeography-Based Multi-Layer Perceptron Neural Network to Predict California Bearing Capacity Value of Stabilized Pond Ash with Lime and Lime Sludge. *Stavební Obzor - Civil Engineering Journal*, 2022;31(2):349–359. <https://doi.org/10.14311/cej.2022.02.0026>

## Using digital modelling for the partial reconstruction of Sheikh Al-Arab Hammam citadel, situated in Farshout, Qena, Egypt

Essam H. Mohamed

Archaeological conservation Dept., Faculty of Archaeology, South Valley University, Qena, Egypt

### Article Info

#### Article History:

Received 10 Jan 2025

Accepted 13 Feb 2025

#### Keywords:

Sheikh Al- Arab Hammam Citadel; Finite elements method; 3D digital modelling; The virtual partially reconstruction

### Abstract

This article proposes the virtual partially reconstruction of the missed architectural units of the citadel of Sheikh al-Arab Hammam that is located in the western mountainside, north of al-Arki village in Farshout, Qena, Egypt. In order to achieve this, the following methodology was followed: Evaluation of the current state of the citadel by two methods: firstly, evaluation of building materials by several scientific techniques, and secondly, evaluation of the structural condition of the building by numerical analysis based on finite elements method (F.E.M.). This research presents the virtual reconstruction of the citadel by Building Information Modeling, "BIM". A 3D virtual reconstruction of the citadel has been based on the archived documents in National Books and Documents House. AutoCAD (2022), Extended 3D Analysis of Building System (ETABS-2023), and Autodesk 3D Max (2022) were used to get plans, elevations, and details of the citadel with real dimensions and the appropriate drawing scale, which aim to revive the citadel and provide a way to document it. By evaluating the current status of the citadel, it was found that there are weaknesses in the properties of building materials such as High porosity and water absorption and low resistance to compressive stresses, as well as the exposure of most of the citadel walls to tensile stresses higher than the permissible limit, in addition to the missing architectural units. The study concluded that it is necessary to improve the properties of building materials and carry out restoration work for the various symptoms of damage.

© 2025 MIM Research Group. All rights reserved.

## 1. Introduction

Although adobe architectural hasn't gotten as much scholarly attention as stone architecture, mud-brick architecture was actually more prevalent in all time periods throughout Egyptian history. Unfired brick made from mud, river, or desert clay was used as the main building material for the various buildings such as citadels, mosques, monasteries, and houses [1].

Adobe architecture provided a more comfortable and versatile living and working environment compared to stone buildings. It was also more affordable and technically straightforward to construct walls and vaults [2]. Mud bricks are a part of masonry structures. Since it is an essential component of a wall mass, it must be understood both structurally and chemically. The type of raw materials used, the construction methods used, the location, the microclimatic conditions, and the mechanical and microstructural characteristics of the brick itself all affect how susceptible a mud brick is to deterioration agents [3]. Adobe buildings' durability depends on factors like soil type, construction techniques and regional climate [4, 5]. Clay sediments, commonly found in deltas and near construction sites, are the primary component of mud bricks [6]. Despite their widespread historical use, mud bricks are vulnerable to mechanical damage due to environmental factors,

\*Corresponding author: [essam.mohamed@arch.svu.edu.eg](mailto:essam.mohamed@arch.svu.edu.eg)

<sup>a</sup>[orcid.org/0000-0003-0695-6997](https://orcid.org/0000-0003-0695-6997)

DOI: <http://dx.doi.org/10.17515/resm2025-609st0110rs>

Res. Eng. Struct. Mat. Vol. 11 Iss. 1 (2025) 399-415

temperature changes carried on by sunlight or water influence, such as rainfall or seepage water carried on by variations in groundwater levels [7]. Because of atmospheric conditions that deterioration of clay bricks, buildings made of these materials are destroyed, necessitating ongoing restoration [8]. This study examines a military citadel, a significant historical building witnessing events between Prince Hammam and Ali Bey al-Kabir during the Mamluk army's invasion of Farshut, Egypt [9,10]. The citadel suffered intentional destruction, resulting in architectural units' loss and physical deterioration, in addition to its poor physical condition as a result of neglect and exposure to many different damage factors. Since the late 20th century, "virtual archaeology" leverages digital technologies to simulate and reconstruct the past [11]. Advances in video game industry technology enable improved quality and accessibility [12, 13, 14]. Virtualizing heritage involves conserving, reproducing, representing and digitally reprocessing cultural evidence using advanced virtual reality imaging [15, 16]. We live in an era of significant technical innovation. Mechatronic systems optimize computing, enhancing efficiency and effectiveness [17]. Interdisciplinary knowledge structures hierarchies for cultural heritage protection [18,19,20]. Recent studies highlight 3D GIS and BIM significance in conservation [21,22,23]. Digital models, accurate and detailed virtual reproductions, result from survey phases preceding cultural heritage digitization [24,25]. Reverse engineering produces scaled models, coherent in metric terms, enhanced with material aesthetic appearance and reflectance qualities [26, 27,28]. Digital models, accurate and detailed virtual reproductions, result from survey phases preceding cultural heritage digitization [29, 30]. Reverse engineering produces scaled models, coherent in metric terms, enhanced with material aesthetic appearance and reflectance qualities [31].

The underlying assumptions of Historical Building Information Modeling (H-BIM) differ from those of BIM applications for new structures since architectural heritage objects must have historical, cultural, and social parameters included when taking into account the building's identity. The three key issues that the architectural BIM model must address are "what," "why," and "how" each component that has to be replaced was constructed. It is not always necessary to create a 3D model of the complete structure, but often only a part of it is sufficient [32, 33].

The present study aims to:

- Monitoring various symptoms of damage.
- Evaluation of the building's current state informs material properties and structural behavior [34].
- The evaluation process identifies and categorizes citadel deterioration symptoms, focusing on material degradation and architectural integrity.
- Precise structural assessment may help to have better restoration methodologies.
- Conservation strategies require comprehensive risk assessments and material evaluations.
- The current status report may provide the basis for targeted interventions and restoration strategies.
- This study presents a virtual module approach for reconstructing missing architectural units of historical citadels, facilitating accurate restoration and preservation.

## **2. Sheikh Al Arab Hammam Citadel**

### **2.1. Historical Background of The Citadel**

In The eponymous Sheikh al-Arab Hammam Citadel commemorates Prince Sharaf al-Dawla Hammam ibn Yusuf bin Ahmad ibn Muhammad bin Hammam (1709-1769/1121-1183 AH), an influential leader in Upper Egypt's Farshût region. Sheikh al-Arab Hammam Citadel (18th century) was built by Prince Hammam bin Youssef to protect Farshout. It witnessed the war between Ali Bey al-Kabir and Prince Hammam, enduring destruction by the Mamluk army. The Sheikh Al Arab Hammam Citadel's walls stand testament to traditional construction techniques. Composed of mud bricks forged from Nile-sourced straw, sand and silt, the structure's 22x7x7 cm bricks showcase precise alternating headers and stretches. Excavations revealed foundations built upon a single layer of mud bricks, merely 15 cm high [35,36].

## 2.2. Architectural Design Of The Citadel

The Prince Hammam citadel's main building covers around (2,156) m<sup>2</sup>. It has four façades, the eastern façade is the major façade, and it looks out over the main road that leads to the village. This facade is (47.5) meters long and 6 meters high, extending from north to south. The citadel's southern tower, which is square in design and measures (5.25) meters on each side and (7) meters in height, is situated at the southern end of this facade. It extends (4.4) meters from the southern facade and (2) meters from the eastern facade. At a distance of five meters north of this tower (Fi. 1). The western façade is stretching (40) meters from north to south. The citadel's western tower rises in the southern half of the wall, dividing it into two sections: the (1.1) m long section facing south, followed by the (5)m long tower block, and the (23.5) m long section facing north. This facade is comparable to its structure, and its aesthetics are consistent with the other citadel facade, and it features viewing openings.

The citadel's southern façade, which is its secondary façade, looks out over the remains of the military barracks. Its design is similar to that of the main façade, and it is (47.5) meters long and 6 meters high, extending from east to west. Its easternmost point is the castle's eastern tower, while the secondary entrance is (15) meters away. The structure attached to the citadel is visible from the 48-meter-long northern façade, which runs from east to west. It is composed of two parts: the eastern part is (21) meters long and extends (3.5) meters from the western part, and the second component is 21 meters long and extends westward, with a length of (27) m. The southeast corner of the castle is home to the southeast corner tower. It is square in shape, with a side length of (5.25) m and a height of (7) m. It consists of two floors. The first floor is covered with a shallow dome supported by spherical triangles, and the second floor is exposed. The Western Tower is located on the western façade, (11.5m from its southern end. It is square in shape, with a side length of (5) m. It consists of two floors. The first floor is roofed with a hemispherical dome supported by spherical triangles, and the second floor is exposed. After entering through the main entrance of the citadel, which is located on the eastern wall, we see a huge courtyard whose sides, from east to west, are (9.25) m long and from north to south, (8.25) m. This courtyard opens onto a corridor that is (29.5) m long and (3.25) m wide as we head north. With a length of (19.5) m and a width of (2.6) m, it moves north until breaking to the west. A door leading south across the courtyard in front of the main entrance leads to an open architectural block that has two square rooms on the east side. This architectural block had a second level that led to the southeast tower.



Fig. 1. General site of Sheikh al Arab Hammam citadel (Google map:

[https://www.google.com/maps/@26.011198,32.1626764,1624m/data=!3m1!1e3!5m2!1e1!1e4?entry=ttu&g\\_ep=EgoyMDI1MDExNC4wIKXMDSoASAFAQAw%3D%3D](https://www.google.com/maps/@26.011198,32.1626764,1624m/data=!3m1!1e3!5m2!1e1!1e4?entry=ttu&g_ep=EgoyMDI1MDExNC4wIKXMDSoASAFAQAw%3D%3D))

### 3. Present Condition of The Citadel

The Sheikh Al Arab Hammam citadel's building materials were deteriorated due to multiple factors, including intentional destruction, resulting in architectural units loss and physical deterioration, in addition to its poor physical condition as a result of neglect and exposure to many different damage factors such as, man-made deterioration, human activity and neglectance, lack of Maintenance: Inadequate preservation accelerates decay, also climatic conditions: temperature, humidity, wind, and rainfall accelerate deterioration, biological degradation, vandalism, temperature and humidity fluctuations, structural damage, elevated groundwater levels and contaminated soil saturation. All the aforementioned causes of deterioration have led to the emergence of several symptoms, including the following: The citadel shows significant loss of its architectural elements, either partially or entirely, and detachment and losing of considerable areas of plaster layers. In addition to Human actions have led to the deterioration and loss of wall sections, the adobe materials exhibit significant thermal-induced deterioration, characterized by: Temperature stresses causing tiny cracks/fractures, plaster degradation and disintegration. Facade's damage: Detachment and losing of considerable areas of plaster, fissures, cracks, missing parts of walls, and partial collapses and losses of bricks and mortar in walls (Fig. 2). The mud-brick structures were susceptible to deterioration due to rainfall and solar exposure, exacerbated by human activity. Climate change and human intervention are primary factors in the degradation of earthen fortifications. Removal of the protective silt layer exacerbated degradation processes, affecting the citadel's mud-brick structure. The exposure duration and neglect of buildings significantly impact mud-brick deterioration, both qualitatively and quantitatively.

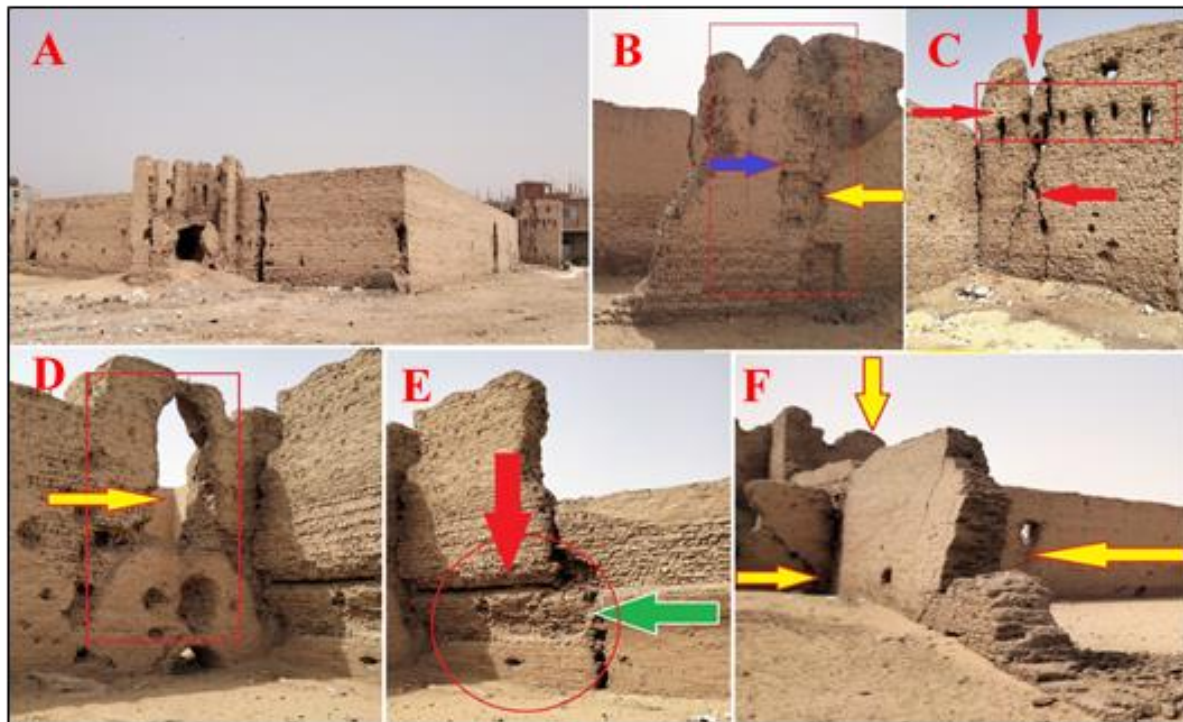


Fig. 2. A. Shows the western façade of the citadel. B. loose parts of the wall. C. fissures in along the wall (western tower). D. loose parts of the wall due man-made deterioration. E. Partial collapse and separation in the wall. F. loose parts and slanting in the wall.

### 4. Materials and Methods

#### 4.1. Materials

Mud brick samples were collected from the detached and fallen parts of the citadel's walls, the studied samples were cut into cubes  $4 \times 4 \times 4$  cm in order to conduct physical and mechanical properties tests.

## 4.2. Methods

### 4.2.1. Examination and Mineralogical Composition

Mineralogical composition analysis of mud brick samples carried out using X-ray diffraction (XRD) on a Philips PW 1840 diffract meter (Cu-K $\alpha$  radiation, 40 kV/40 mA, 2 $\theta$ : 5-50°). XRD analysis characterized mud brick mineralogy between 5° and 50° 2 $\theta$ .

Petrographic characterization employed ZEISS Axio Imager. A1m Polarized Light Microscopy (PLM) at 20 $\times$  magnification. Deteriorated mud brick samples were examined using an Olympus BX40 optical stereo microscope with digital camera recording at 40-60 $\times$  magnification. Microstructural and chemical analyses of deteriorated mud brick samples were performed using Scanning Electron Microscope (SEM) Model Quanta 250 (FEG) Field Emission Gun (Accelerating voltage 200V-30kV Operating Voltage 5-30kV, Magnification: 30X- 300kX) coupled with X-ray energy dispersive system (EDS) with accelerating voltage 30 K. V., Magnification (14X) up to (1,000,000) and resolution for Gun. In, K550X Sputter Coater, England.

### 4.2.2. Physical and Mechanical Properties of Mud Brick

The properties of building materials of the citadel carried out according to (ASTM C62-17). The bulk density was calculated by the following Eq (1):

$$\rho_{dry} = \frac{M(solid)}{V(total)} \quad (1)$$

Where,  $\rho$  = density,  $m$  = mass,  $V$  = volume. The water content was calculated by the following Eq (2):

$$WC = \frac{W_2 - W_1}{W_1} \times 100 \quad (2)$$

Where,  $W_1$ = sample weight after drying,  $W_2$ = sample weight before drying. Compressive strength carried out according to (ASTM C67/C67M-19). The compressive strength of mud brick was calculated by the following Eq (3):

$$Compressive\ strength, C = \frac{P}{A} \quad (3)$$

Where,  $P$ = maximum recorded load indicated in testing machine (N),  $A$ = Average of the gross of the upper and lower bearing surface of the specimens mm<sup>2</sup>.

## 4.2. Structural Analysis of The Citadel

3D numerical model of the citadel carried out using the finite element (FE) software (ETABS). The aim was to understand the structural behavior under the different loading conditions that citadel had subjected to. These loading included the self-weight and earthquake. ETABS 2021 was used to simulate the structural response of Sheikh Al Arab Hammam Citadel to own weight and earthquake loads, using the finite element (FE) with shell elements for walls. Data of building materials properties have been entered into ETABS software. Earthquakes loads were calculated in two orthogonal directions (X-X) and (Y-Y), structural elements were represented with consideration that the walls as load-bearing walls [37].

When calculating stresses due to loading on a building, it's essential to consider the following factors:

- Building design and construction details
- Type of materials used
- Site conditions and climate
- Architectural and engineering standards and specifications

### 4.2.1. Self-Weight Stress

The self-weight stress ( $\sigma$ ) can be calculated using the following Eq (4):

$$\text{Self – weight stress } (\sigma) = (W \times g / A) \tag{4}$$

$$\text{Self – weight stress } (\sigma) = \left( \frac{14290 \times g}{559.03} \right) = 250.60 \text{ kPa}$$

Where,  $\sigma$ = self-weight stress,  $W$ = self-weight of the building = 14290 ton,  $g$ : acceleration due to gravity= 9.8 g ,  $A$ = cross-sectional area of the building = 559.03 m<sup>2</sup> . The resulting value from the equation (250.60 kPa) is the maximum allowable stress of the building under its own self-weight. The self-weight induced stress values derived from the finite element method of the building are calculated to be 2000 KPa. Which appears as shown in (Fig. 3) deformation that appear in dark orange and dark green in the corners of the building. The deformations are shown in dark green and dark orange at the corners represent the maximum stress the building is exposed to, which is equal to 2 MPa.

#### 4.2.2. Earthquake Stress

The earthquake stress ( $\sigma$ ) can be calculated using the following Eq (5a):

$$\text{Earthquake stress } (\sigma) = (S \times W)/(A) \tag{5a}$$

$$\text{Earthquake stress } (\sigma) = \frac{1 \times 14290}{559.03} = 250.60 \text{ KPa} \tag{5b}$$

where:  $\sigma$ : earthquake stress,  $S$ : seismic coefficient (dependent on building location) = 1,  $W$ : self-weight of the building =14290 ton,  $A$ : cross-sectional area of the building = 559.03 m<sup>2</sup> ,Eq (5b). The resulting value from the equation (250.60 KPa) is the maximum allowable stress of the building under earthquake stress. The resulting value from the equation is the average shear stress of the building under earthquake loading. The earthquake induced stress values derived from the finite element method of the building are calculated to reach 5000 KPa due to stress concentrations in two orthogonal directions (X-X) and (Y-Y) as shown in (Fig. 4 - 5)

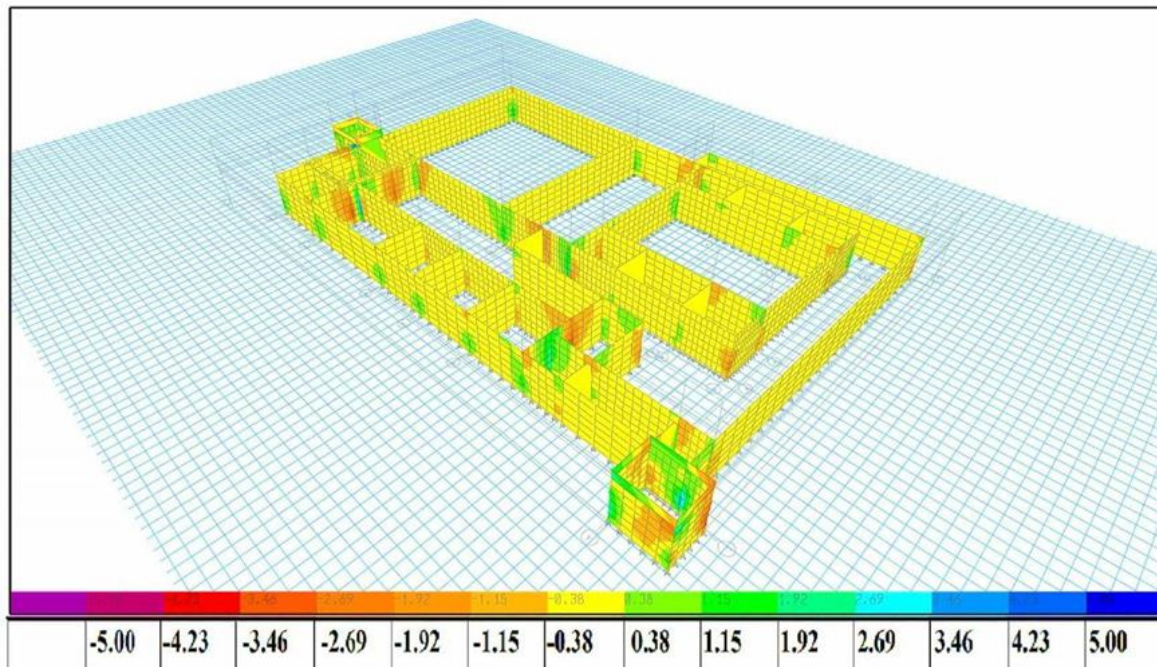


Fig. 3. Variation of the stresses (self-weight stress) in considered building (MPa)of the citadel walls.



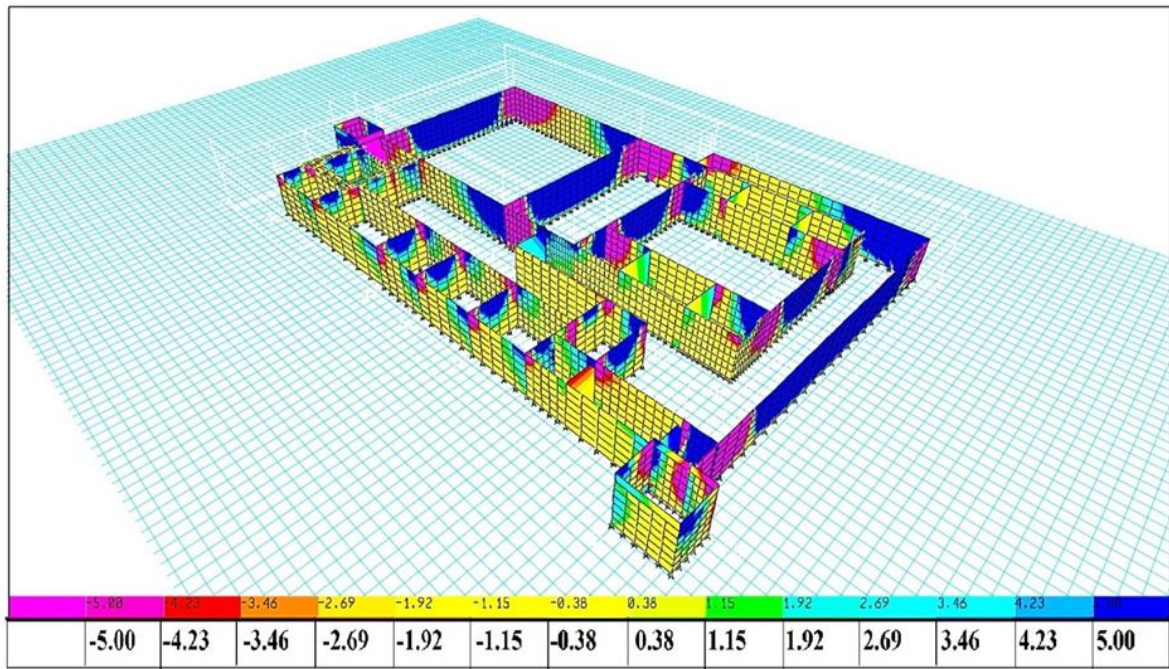


Fig. 4. Locations of the maximum principle stresses (earthquake stress) (MPa) in direction (X-X)of the citadel walls

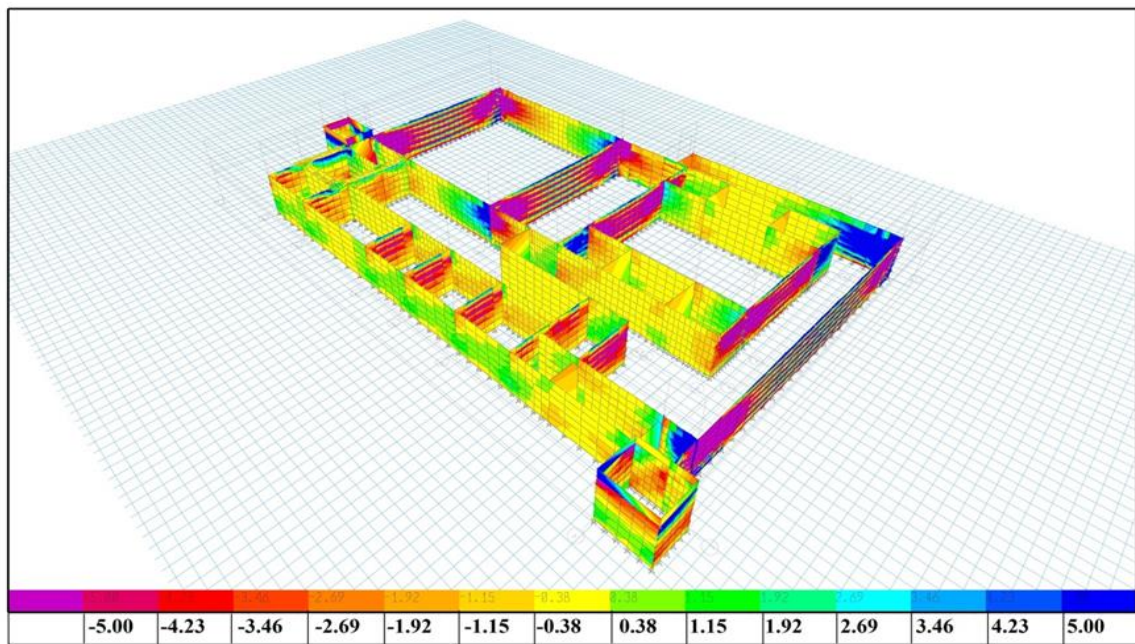


Fig. 5. Locations of the maximum principle stresses (earthquake stress) (MPa) in direction (Y-Y)of the citadel walls

## 5. Building Information Modelling for the Partial Reconstruction of The Citadel

### 5.1. Documentation of the Citadel

The study commenced with a comprehensive review of the building's historical, architectural, and construction significance, followed by material evaluation and structural analysis. A virtual model of the archaeological building was subsequently developed.

### 5.1.1. Archaeological Documentation

Sheikh Al-Arab Hammam Citadel (12th century AH/18th century AD) is a prominent Ottoman-era military fortification, officially registered as a monument under Prime Minister Resolution No. 2661 (2011) and Minister of Culture Resolution No. 661 (2011).

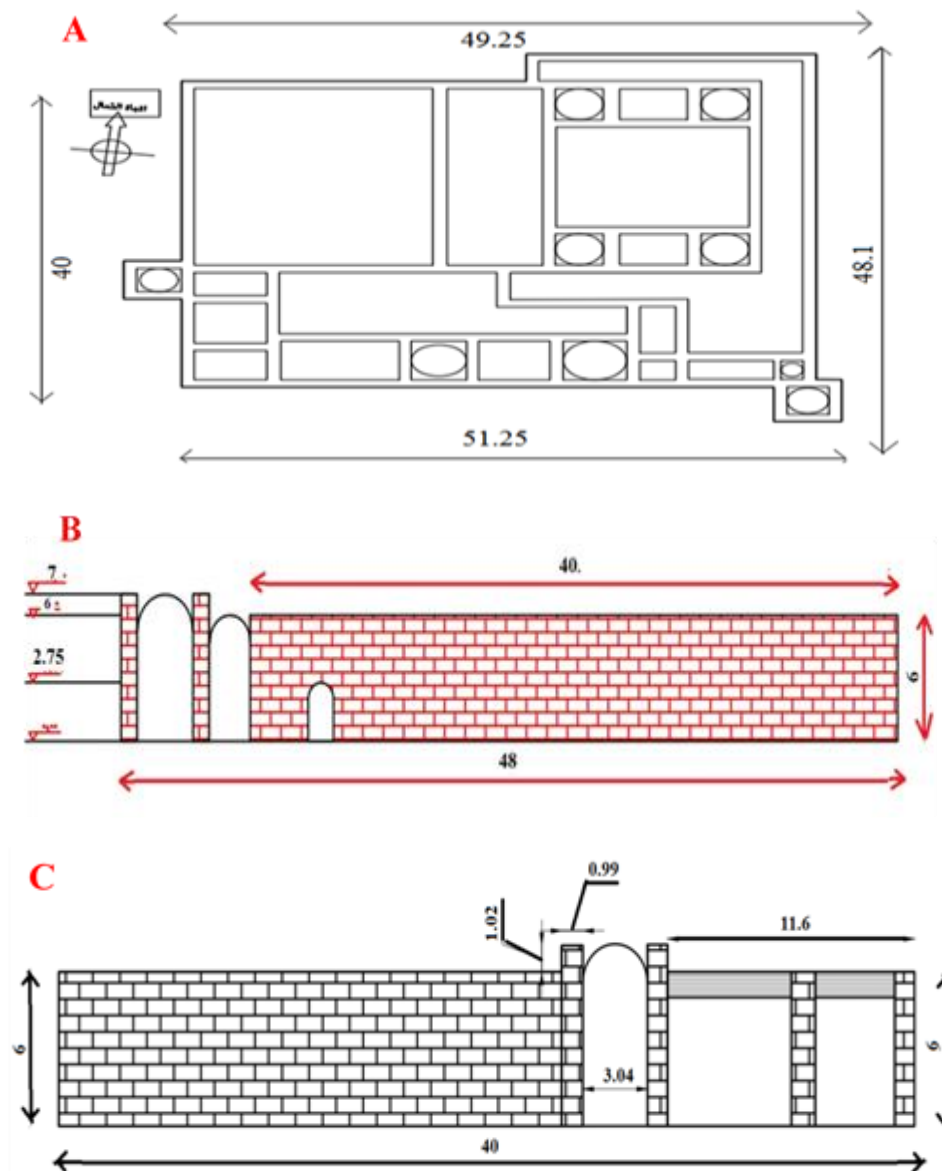
The citadel's construction is attributed to Prince Hammam bin Youssef, who, as leader of the Hawara tribes, sought to fortify Farshout, the center of his authority in Upper Egypt. Sheikh Al-Arab Hammam Citadel bears testament to the 1769 conflict between Ali Bey al-Kabir and Prince Hammam, suffering deliberate destruction by Muhammad Bey Abu al-Dahab's Mamluk forces.

### 5.1.2. Architectural Documentation

Through meticulous exterior and interior surveys, the citadel's architectural features were recorded. These dimensions facilitated the creation of detailed horizontal projections and architectural facades, revealing a main facade spanning 48.21m with a height of 6m. (Fig.6)

### 5.1.3. photographic Documentation

The citadel building was photographed from different angles to highlight on the architectural details. (Fig. 7 and Fig. 8).



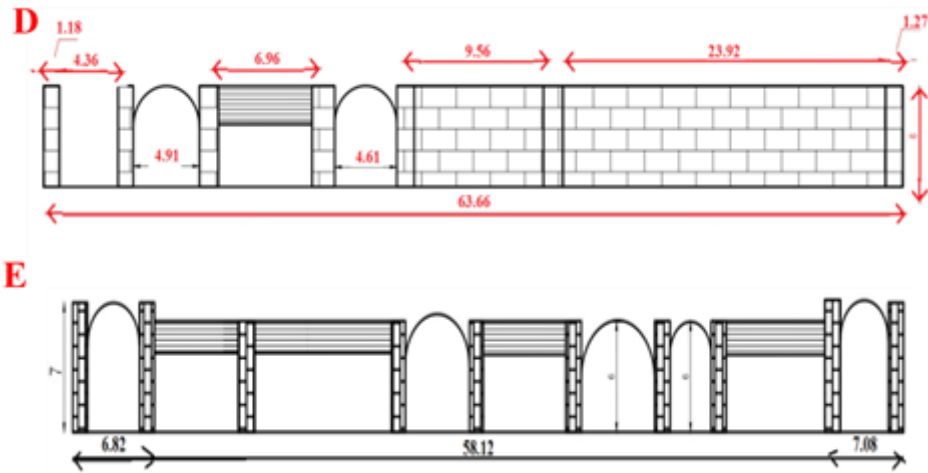


Fig. 6. A. Horizontal projection of the citadel. B. the eastern façade (the main facade). C. the western façade d. The northern facade. E. the southern façade

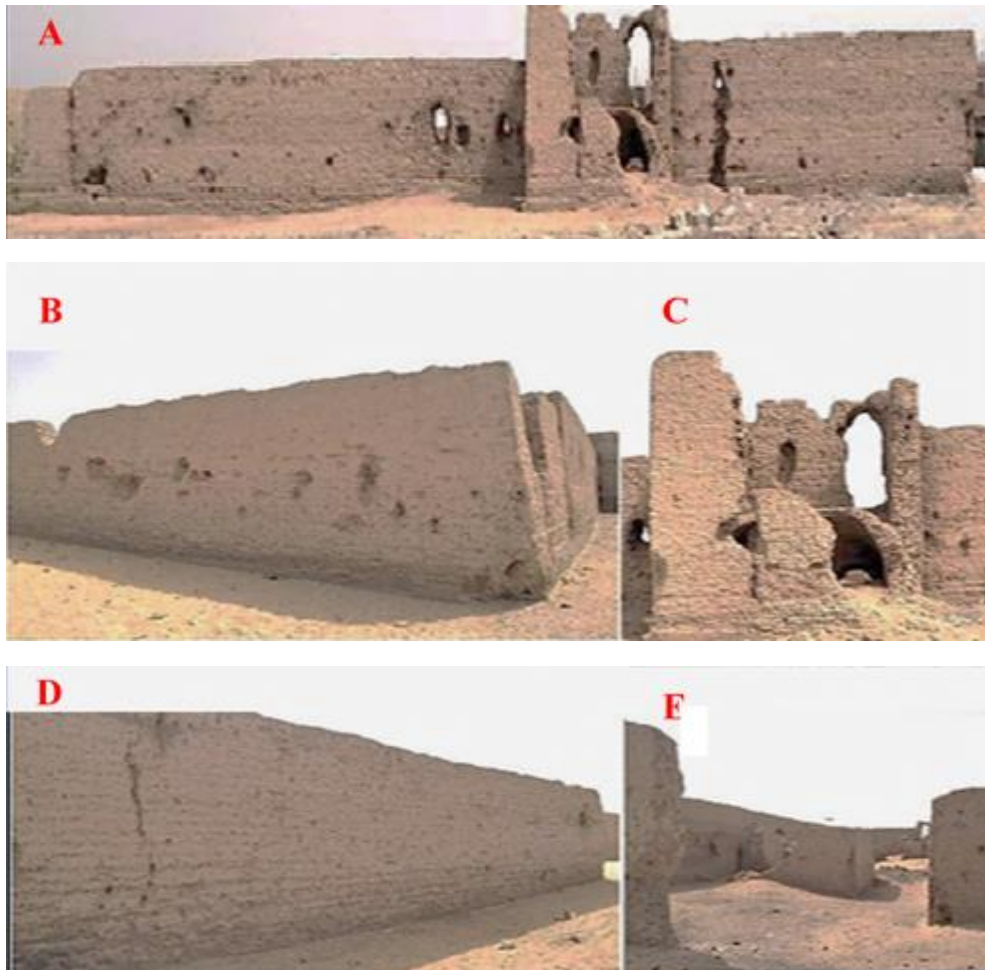


Fig. 7. A. The western façade of the citadel. B. the southern façade. C. The northern facade. D. the eastern façade (the main facade). E. The western tower F. the citadel from inside. G. the southern tower



Fig. 8. A. and B. the courtyard of the citadel. C. the destroyed architectural units of the citadel

## 5.2. Design of the Virtual Models of The Citadel

The following software applications were utilized to create the virtual model of the citadel:

### 5.2.1. Data Collection and Correction

The data collection and validation phase encompass the systematic gathering, categorization, and verification of case study data, facilitating the development of virtual models.

### 5.2.2. The Data Input and Construction of The Database

This stage entailed digitizing collected case study data, converting paper-based records into computer-readable formats to facilitate analysis and modeling.

### 5.2.3. Data Storage and Retrieval Subsystem

Data Digitization Phase: Paper-based case study data was converted into digital format for computer processing and analysis.

### 5.2.4. Data Manipulation and Analysis Subsystem

Data Processing Phase: This stage includes data standardization, error correction, updates, and calculations (e.g., measurements, spatial analysis, and distance calculations).

### 5.2.5. Data Display and Modeling Subsystem

The data visualization stage employs multidisciplinary methods (modeling, graphical representations, multimedia) to communicate refined data insights, emphasizing spatial contexts and dimensional accuracy. This phase leverages visualization techniques (2D/3D modeling, graphs, images) to facilitate comprehension of complex data, focusing on spatial relationships, measurements and feature definitions.

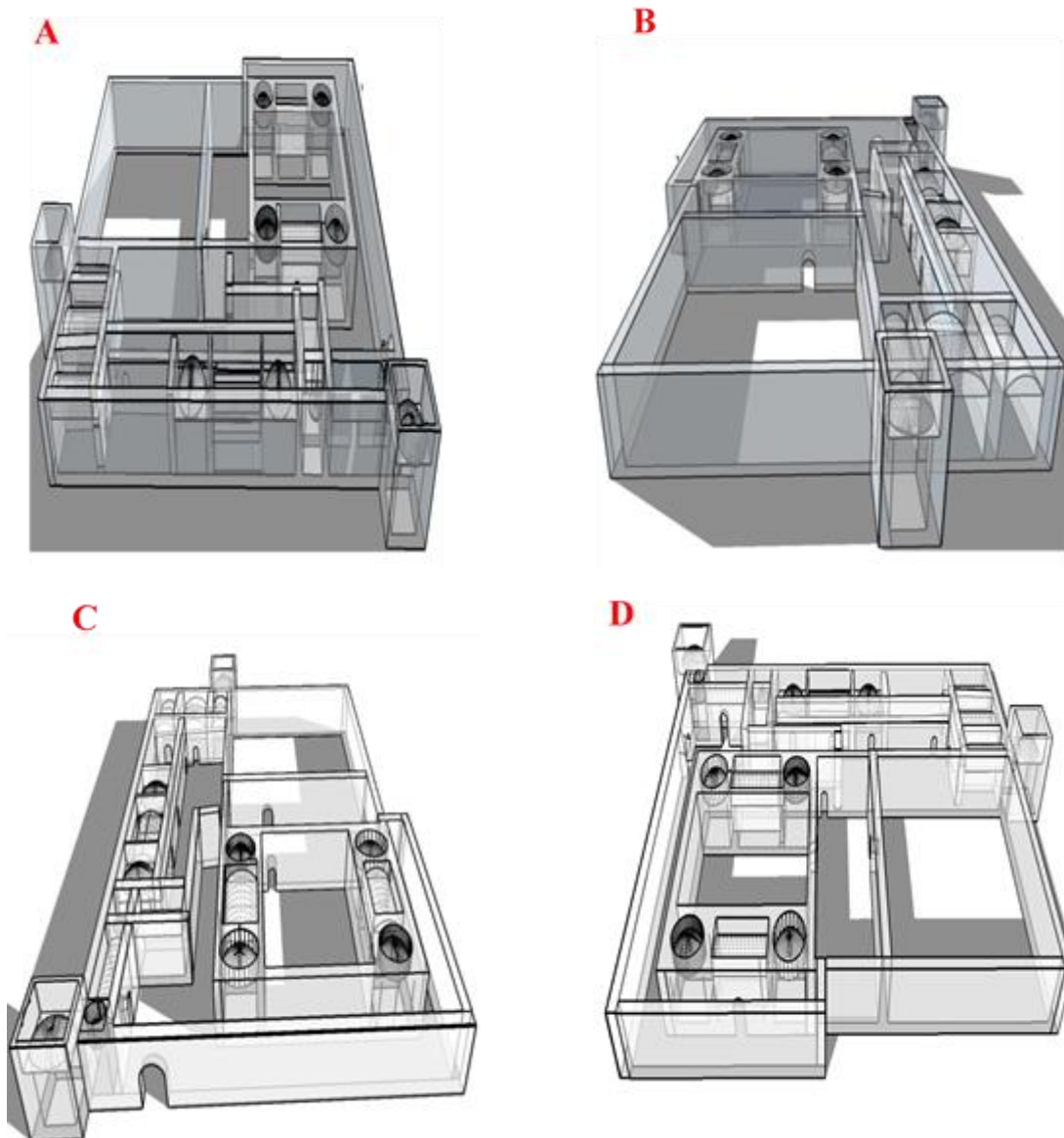


Fig. 9. The virtual models of the citadel a. the northern façade of the citadel. b. the southern façade

## 6. Results and Discussion

### 6.1. Results of Examination and Mineralogical Composition

Scientific analysis of the mud brick samples taken from Prince Hamam Castle revealed the following chemical and mineral components: X-ray diffraction patterns revealed that mud brick sample mainly consist of quartz ( $\text{SiO}_2$ ) Kaolinite  $\text{AlSi}_3\text{O}_8$  (K, Na) and Calcite ( $\text{CaCO}_3$ ), Indalite  $\text{Mg}_2\text{Al}_3(\text{AlSi}_5\text{O}_{18})$ . The analysis results showed the presence of Indalite mineral, which is a transformed form of Cordierite mineral ( $\text{MgFe})_2\text{Al}_3(\text{AlSi}_5\text{O}_{18})$ , resulting from the effect of high temperatures.

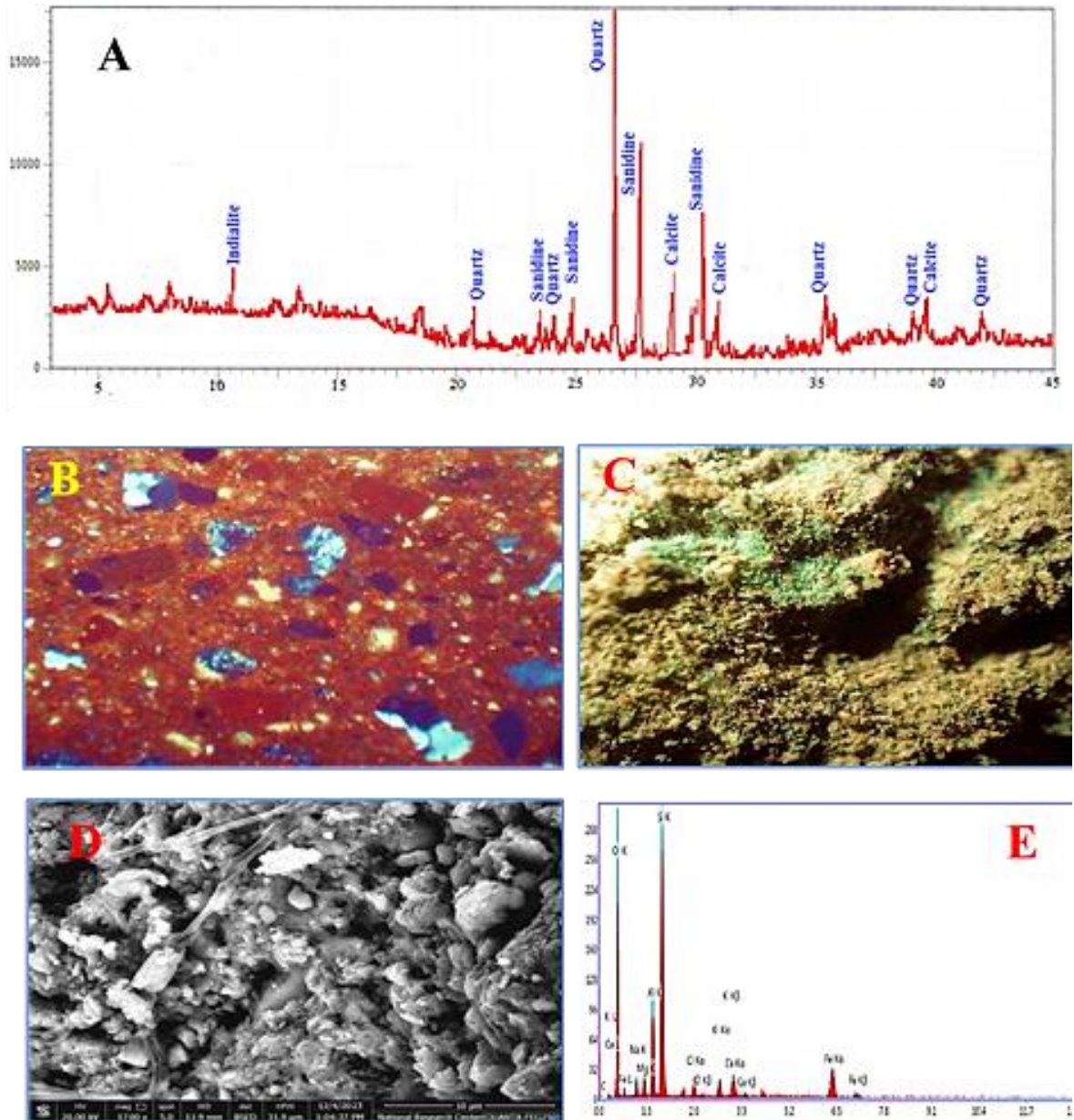


Fig. 10. A. X-ray diffraction analysis results of mud brick B. PLM investigation shows coarse texture of quartz grains. C. Stereo microscope shows granular disintegration and salt crystals. D. SEM photomicrograph shows disintegration and erosion of quartz crystals and salts . E. EDS analysis results of mud brick

Polarized Light Microscopy (PLM) analysis of mud brick thin sections revealed a coarse mosaic texture comprising quartz crystals and fragments, along with feldspar. Stereo microscopy revealed mud brick deterioration: surface roughening, relief, granular disintegration, and crystallized salt deposits. SEM analysis confirmed internal micro-cracks, quartz crystal disintegration, binding

material loss, and quartz crystal erosion (Fig. 10). Scientific analysis of mud brick samples revealed compromised physical, chemical, and mechanical properties, primarily attributed to environmental factors. An assessment of the Sheikh al-Arab Hammam Citadel's mud brick materials demonstrated significant degradation, underscoring the interplay between material properties and environmental conditions.

### 6.2. Results of Physical and Mechanical Properties of Mud Brick

The results obtained from the physical properties tests demonstrate that the mud brick specimens were taken from the case study exhibit the average density values are between 1.31 to 1.52 gm/cm<sup>3</sup>, the means values of water content are between 1.89 % and 2.96 % (as shown Table. 1). The results obtained from the mechanical properties tests demonstrate that the mud brick specimens were taken from the case study exhibit the compressive strength values between 0.5 to 2 MPa. High variation is attributable to non-uniform degradation due to durability effects. The results indicate a reduction in the density of the mud brick, accompanied by an increase in moisture content and a decrease in compressive strength

Table 1. The means values Physical and mechanical properties of mud brick

| Average of physical properties of mud brick      |                              |                            |
|--|------------------------------|----------------------------|
| Test code  | Density gm / cm <sup>3</sup> | water content %            |
| ASTM C62-17                                      | 1.31 - 1.52                  | 1.89 % - 2.96              |
| Average of Compressive strength of mud brick MPa |                              |                            |
| Test code  | Load (N)                     | Compressive strength (MPa) |
| ASTM C67/C67M-19                                 | 65.5- 75.6                   | 0.5 - 2                    |

### 6.3. Results of Digital Modelling

Finite element modeling simulations indicated that the maximum stress generated by the self-weight of the citadel (250.69kPa) is generally exceeded in wall corners. The maximum stressed sections generated by the earthquake loading of the citadel reaches values around 5 MPa which is highly above the average shear stress. Areas subjected to excessive stresses are observable on the southeast elevation of the castle, and is also apparent in the upper portions of the eastern and southwest towers.

### 6.4. Results of Design of The Virtual Models

Engineering programs were used to develop a virtual design for the partial reconstruction of the citadel as shown (Fig. 11).

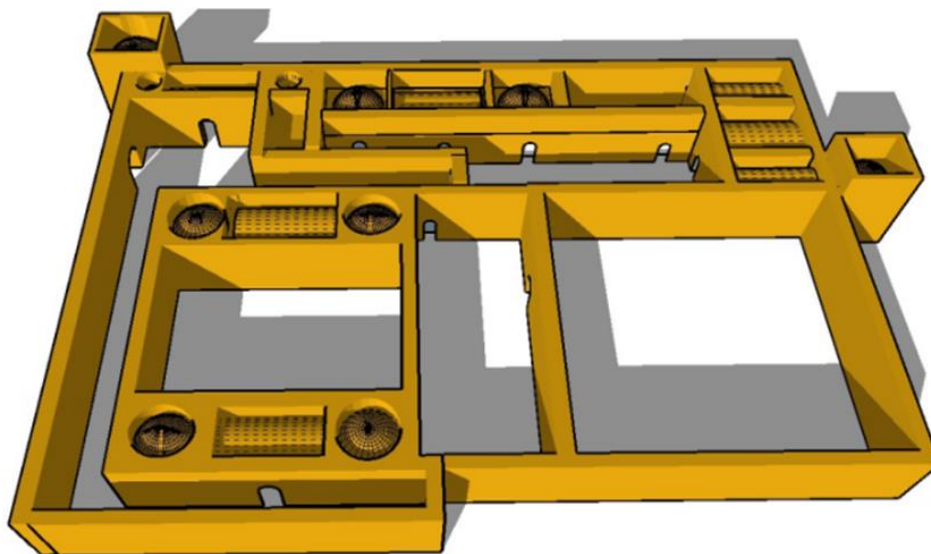


Fig. 11. The virtual model of Final appearance after a partial reconstruction the of citadel

## 7. Conclusions

This study explores the 18th-century citadel's partial ruin, attributed to Muhammad Bey Abu al-Dahab's 1769 destruction and subsequent environmental degradation, informing conservation strategies. Seismic analysis of the 3-D numerical model revealed critical structural vulnerabilities. Recommendations include material treatment, completing missing sections, and wall reinforcement prior to partial reconstruction.

The comprehensive assessment of the castle's building materials, encompassing inspections, analyses, and testing, reveals a degradation of the mud brick structure and a corresponding decline in its physical and mechanical characteristics. To mitigate these effects, the application of strengthening treatments using consolidation treatments of mud brick such as Ethyl Silicate, Wacker OH 100, Nano Estel, and Nano Silica, which are deemed necessary to restore and enhance its physical and mechanical properties.

The results of the finite element modeling simulations reveal that the castle walls necessitate structural reinforcement measures, encompassing the repair of cracks, restoration of damaged elements, and reconstruction of degraded architectural components. This comprehensive approach will effectively mitigate structural weaknesses, restore the building's integrity, and revive the castle's original visual splendor.

Undoubtedly, the first steps in the architectural restoration of the castle begin with determining the soil's ability to withstand the pressures and loads imposed on it by the various buildings above it. From here, specialists in architectural restoration try, to the best of their abilities, to treat weak soil layers and inject them with suitable chemical materials to strengthen their weak components and restore cohesion to their separated layers.

We recommend following the subsequent steps for the restoration of the citadel walls:

- Treating structural cracks in the castle, especially those extending vertically from top to bottom or from bottom to top, resulting from the imbalance between the building and the soil beneath it. This treatment is one of the most important operations and is carried out in well-defined and studied stages, the most important of which are:
- Cleaning the cracks and voids in the building walls from dust, salts, and various damage residues, then moistening these cracks and voids with a spray of pure water without affecting the brick components. Subsequently, filling these cracks and voids with a scientific mortar mixed with sand, lime, and a small proportion of gypsum, and mixing these components with a solution of silicates and siliconates.
- Breaking the edges of the cracks from the back, thoroughly cleaning and moistening them with pure water, and filling them with the aforementioned mortar.
- Rebuilding missing parts of the walls or any architectural element in the archaeological building using new brick blocks that carry the specifications of the old brick, with improvements to their physical and chemical properties using suitable chemical materials.
- As for walls on the verge of collapse, they are dismantled using scientific and technical methods known in this field, separating the brick blocks from each other, thoroughly cleaning them from various damage residues, strengthening them with the aforementioned suitable chemical materials, and rebuilding them anew.
- External coating stage: A system was followed in the castle, which is coating its external walls with a layer of mortar with good properties. Therefore, we propose coating those walls with a layer of clay mortar composed of lime and sand or clay and straw, or covering these walls with a block of mud brick similar to the old brick in its composition, with some additions to improve its properties and increase its resistance to damage factors. This method has been adopted in earthen buildings found in Mexico, Peru, Ghana, and Nigeria.
- Reinforcement with wooden panels: Walls of the castle on the verge of collapse are reinforced and strengthened with wooden supports characterized by high rigidity. The roof of the building is covered with a wooden canopy resting on supports built from mud brick. This method has been used to protect earthen buildings from wind and rain, especially in Peru and Italy during the 19th century, and is still followed in some countries.



- Reinforcing foundations with mud brick blocks: As for the castle's foundations, many mud brick blocks that have been affected by various damage factors are reinforced and completed with new brick blocks similar to the old brick, with the addition of a proportion of clay, sand, lime, and red brick powder to their components. This is done to increase their mechanical strength and ability to resist damage factors.

The article highlights on the virtual partial reconstruction of the citadel of Sheikh al-Arab Hammam through of several key conclusions:

- Technological Advancement: The use of virtual reconstruction techniques demonstrates significant advancements in architectural preservation, allowing for a more detailed understanding of historical structures.
- Cultural Heritage Preservation: By reconstructing missing architectural units, the project contributes to preserving cultural heritage and offers insights into the historical significance of the citadel.
- Educational Value: The virtual model serves as an educational tool, enabling researchers, students, and the public to engage with the site's history and architecture in an interactive manner.
- Future Restoration Projects: This reconstruction can inform future physical restoration efforts, guiding decisions on materials and techniques that align with the original design.
- Interdisciplinary Collaboration: The project illustrates the importance of collaboration among historians, architects, and technology experts to achieve a comprehensive reconstruction.
- Overall, the article emphasizes the potential of virtual reconstructions to enhance our understanding of historical sites and support preservation efforts.

## Acknowledgements

I would like to thank Eng. Barakat Heshmat Mohamed, consultant of the civil engineering of Gamaan office for engineering consultancy and geotechnical laboratories, Kingdom of Saudi Arabia for his cooperation and valuable efforts in this research.

I would like to thank Mahmoud abd el-Wahab Madani director of General of Archaeological Affairs of Upper Egypt.

## References

- [1] ZAREMBA, Małgorzata, et al. Influence of deterioration on the preservation of mud brick architecture based on the monuments from the tell el-retaba archaeological site. *International Journal of Conservation Science*, 2021, 12.1: 67-86. <https://www.researchgate.net/publication/349732145>
- [2] EMERY, Virginia L. Mud-brick architecture. *UCLA Encyclopedia of Egyptology*, 2011, 1.1. <https://escholarship.org/uc/item/4983w678>
- [3] EL-GOHARY, Mohammed. The Contrivance Of New Mud Bricks For Restoring And Preserving The Edfa Ancient Granary-Sohag, Egypt. *International Journal of Conservation Science*, 2012, 3.2. <https://research.ebsco.com/linkprocessor/plink>
- [4] PIANI, Tiziano Li, et al. The mechanical performance of traditional adobe masonry components: An experimental-analytical characterization of soil bricks and mud mortar. *Journal of green building*, 2018, 13.3: 17-44. <https://doi.org/10.3992/1943-4618.13.3.17>
- [5] ALKENANEE, Frak S.; ALRUDAINI, Thaer MS. Seismic performance of masonry buildings in Iraq. *Research on Engineering Structures and Materials (RESM)*, 2023. <http://dx.doi.org/10.17515/resm2022.489ie0801>
- [6] ILLAMPAS, R.; IOANNOU, Ioannis; CHARMPIS, Dimos C. Adobe: an environmentally friendly construction material. *WIT Transactions on Ecology and the Environment*, 2009, 120: 245-256.
- [7] KHORASANI, Fatemeh Faghih; KABIR, Mohammad Zaman. Experimental study on the effectiveness of short fiber reinforced clay mortars and plasters on the mechanical behavior of adobe masonry walls. *Case Studies in Construction Materials*, 2022, 16: e00918. <https://doi.org/10.1016/j.cscm.2022.e00918>
- [8] YUAN, Yue, et al. Evaluation Of The Organosilicon Materials For Ancient Grey Bricks Preservation. *International Journal of Conservation Science*, 2018, 9.4. <https://research.ebsco.com/c/ylm4lv/viewer/pdf/p2y327tzjn>
- [9] Madani, Mahmoud. Prince Hammam bin Youssef Castle, an archaeological documentary study, first edition, National Book and Documents House, 2010, 17.

- [10] AL-SHOKY, Ahmad. Qal'at Sheikh Hammâm (2020). (Ottoman Fortification in Upper Egypt). Bulletin archéologique des Écoles françaises à l'étranger, 2021. <https://doi.org/10.4000/baefe.3039>
- [11] SIMOU, Sana; BABA, Khadija; NOUNAH, Abderrahman. The integration of 3D technology for the conservation and restoration of ruined archaeological artifacts. History of science and technology, 2022, 12.1: 150-168. <https://doi.org/10.32703/2415-7422-2022-12-1-150-168>
- [12] VALIENTE, Ernesto Echeverria; D'AMICO, Flavio Celis; DA CASA MARTÍN, Fernando. Architecture and Archeology. Virtual Reconstruction of Ipi's Tomb TT315 in Deir-el-Bahari, Theban, Egypt. In: Digital Restoration and Virtual Reconstructions: Case Studies and Compared Experiences for Cultural Heritage. Cham: Springer International Publishing, 2023. p. 169-183. [https://doi.org/10.1007/978-3-031-15321-1\\_11169](https://doi.org/10.1007/978-3-031-15321-1_11169)
- [13] STANCO, Filippo; BATTIATO, Sebastiano; GALLO, Giovanni. Digital imaging for cultural heritage preservation. Analysis, Restoration, and Reconstruction of Ancient Artworks, 2011.
- [14] HERRERO-TEJEDOR, Tomás Ramón, et al. Documentation and Virtualisation of Vernacular Cultural Heritage: The Case of Underground Wine Cellars in Atauta (Soria). Heritage, 2023, 6.7: 5130-5150. <https://doi.org/10.3390/heritage6070273>
- [15] CULTRARO, Massimo; GABELLONE, F.; SCARDOZZI, G. The virtual musealization of archaeological sites: between documentation and communication. In: Proceedings of the 3rd ISPRS International Workshop 3D-ARCH. 2009; 25-28.
- [16] MORCILLO, Jesús Muñoz, et al. Authenticity through VR-based documentation of cultural heritage. A theoretical approach based on conservation and documentation practices. Virtual Archaeology Review, 2017, 8.16: 35-43. <http://dx.doi.org/10.4995/var.2017.5932>
- [17] CÓRDOBA-CELY, Carlos; DE LA CRUZ, Arturo. Pasto varnish: 3D virtualization of an intangible cultural heritage. Virtual Archaeology Review, 2024. <https://doi.org/10.4995/var.2024.21761>
- [18] MORALES, Antonio Javier, et al. Application of virtualisation methods in archaeology: the case of stela A from the tomb of Henenu (TT 313, Deir el-Bahari, Egypt). Virtual Archaeology Review, 2023, 15.31: 104-115. <https://doi.org/10.4995/var.2024.20670>
- [19] CHIABRANDO, Filiberto, et al. Cultural heritage documentation, analysis and management using building information modelling: state of the art and perspectives. mechatronics for cultural heritage and civil engineering, 2018, 181-202. [https://doi.org/10.1007/978-3-319-68646-2\\_8](https://doi.org/10.1007/978-3-319-68646-2_8)
- [20] BAIK, Ahmad. From point cloud to jeddah heritage BIM nasif historical house-case study. Digital applications in archaeology and cultural heritage, 2017, 4: 1-18. <https://doi.org/10.1016/j.daach.2017.02.001>
- [21] STAMPOULOGLOU, Maria, et al. Archaeological anastylosis of two Macedonian tombs in a 3D virtual environment. Virtual Archaeology Review, 2020, 11.22: 26-40. <https://doi.org/10.4995/var.2020.11877>
- [22] BANFI, Fabrizio. Building information modelling-A novel parametric modeling approach based on 3D surveys of historic architecture. In: Digital Heritage. Progress in Cultural Heritage: Documentation, Preservation, and Protection: 6th International Conference, EuroMed 2016, Nicosia, Cyprus, October 31-November 5, 2016, Proceedings, Part I 6. Springer International Publishing, 2016. p. 116-127. [https://doi.org/10.1007/978-3-319-48496-9\\_10](https://doi.org/10.1007/978-3-319-48496-9_10)
- [23] BRUMANA, Raffaella, et al. Survey and scan to BIM model for the knowledge of built heritage and the management of conservation activities. Digital Transformation of the Design, Construction and Management Processes of the Built Environment; Daniotti, B., Gianinetto, M., Della Torre, S., Eds, 2020, 391-400. [https://doi.org/10.1007/978-3-030-33570-0\\_35](https://doi.org/10.1007/978-3-030-33570-0_35)
- [24] LLOPIS VERDÚ, Jorge; GUTIÉRREZ-PÉREZ, Nicolás; CABODEVILLA-ARTIEDA, Ignacio. Virtual reconstruction of the disappeared Valencia Oil Market (Spain). Virtual Archaeology Review, 2023, 15.31: 86-103. <https://doi.org/10.4995/var.2024.21148>
- [25] CONDORELLI, Francesca; BONETTO, J. 3D digitalization and visualization of archaeological artifacts with the use of photogrammetry and virtual reality system. The International Archives of the Photogrammetry, Remote Sensing and Spatial Information Sciences, 2022, 48: 51-57. <https://doi.org/10.5194/isprs-archives>
- [26] KURAPKAT, Dietmar, et al. Digital Monument Preservation in 3D. The virtual bazaar of Aleppo (Suq al-Madina) as a discussion tool for the preservation of historical monuments. 2023. <https://doi.org/10.34780/4vcd-2sac>
- [27] TAKÁČ, Ondrej, et al. Building partial 3D models of cultural monuments. Int. J. Adv. Nat. Sci. Eng. Res, 2023, 7: 295-299. <https://as-proceeding.com/index.php/ijanser>
- [28] SARANTI, Anna, et al. From 3D point-cloud data to explainable geometric deep learning: State-of-the-art and future challenges. Wiley Interdisciplinary Reviews: Data Mining and Knowledge Discovery, 2024, 14.6: e1554. <https://doi.org/10.1002/widm.1554>
- [29] BILGIN, Hüseyin, et al. Numerical study to evaluate the structural response of the basilica of St. Sotiri. Research on Engineering Structures and Materials, 2023, 9.2. <http://dx.doi.org/10.17515/resm2023.641ea0305>

- [30] MANSURI, Lukman E., et al. A systematic mapping of BIM and digital technologies for architectural heritage. *Smart and Sustainable Built Environment*, 2022, 11.4: 1060-1080.
- [30] MANSURI, Lukman, et al. Scientometric analysis and mapping of digital technologies used in cultural heritage field. In: Association of Researchers in Construction Management, ARCOM 2019-Proceedings of the 35th Annual Conference. 2019. p. 255-264. <https://www.arcom.ac.uk/-docs/archive/2019>
- [31] AGHASI, Niloofar Haji Mirza. Application of GIS for urban traffic accidents: A critical review. *Journal of Geographic Information System*, 2019, 11.1: 82-96. <https://doi.org/10.4236/jgis.2019.111007>
- [32] LOVELL, Lucy J.; DAVIES, Richard J.; HUNT, Dexter VL. The application of historic building information modelling (HBIM) to cultural heritage: a review. *Heritage*, 2023, 6.10: 6691-6717. <https://doi.org/10.3390/heritage6100350>
- [33] MOHAMED, Essam H. Assessment of the current state of Qanibay al-Rammah Complex (908 AH/1502 AD), as a procedure precedes the restoration process. *Open Journal of Geology*, 2019, 10.1: 71-91. <https://doi.org/10.4236/ojg.2020.101004>
- [34] AL-SHOKY, Ahmad. Qal'at Cheikh Hammâm (2021).(Ottoman Fortification in Upper Egypt-2nd Season). *Bulletin archéologique des Écoles françaises à l'étranger*, 2022. <https://doi.org/10.4000/baefe.5680>
- [35] AL-SHOKY, Ahmad; IBRAHIM, Mohamed. Qal'at Sheikh al-'Arab Hammâm (2022). *Ottoman Citadel in Upper Egypt. Bulletin archéologique des Écoles françaises à l'étranger*, 2023. <https://doi.org/10.4000/baefe.8220>
- [36] Mohamed, E. H. (2019). Using of GIS technology for conservation of the ottoman bathroom and its urban surrounding in Qena—Egypt. *Archaeological Discovery*, 8(1), 26-46. <https://doi.org/10.4236/ad.2020.81002>
- [37] Alaa, A., Shokry, M. E. D., & Tarabia, A. (2023). Evaluation of the Egyptian code for Seismic design of regular frames using the performance-based design methods. *International Journal of Advances in Structural and Geotechnical Engineering*, 7(02), 1-9. <https://doi.org/10.21608/ASGE.2024.218470.1058>

# Research on Engineering Structures and Materials

